SANDIA REPORT

SAND2007-5547
Unlimited Release
Printed September 2007

Use of Composite Materials, Health Monitoring and Self-Healing Concepts to Refurbish Our Civil and Military Infrastructure

Dennis Roach, Kirk Rackow, Waylon DeLong
Steve Yepez, Dave Reedy, Scott White

Prepared by
Sandia National Laboratories
Albuquerque, New Mexico 87185 and Livermore, California 94550

Sandia is a multiprogram laboratory operated by Sandia Corporation,
a Lockheed Martin Company, for the United States Department of Energy's
National Nuclear Security Administration under Contract DE-AC04-94AL85000.

Issued by Sandia National Laboratories, operated for the United States Department of Energy by Sandia Corporation.

Available to DOE and DOE contractors from
U.S. Department of Energy
Office of Scientific and Technical Information
P.O. Box 62
Oak Ridge, TN 37831

Telephone: (865)576-8401
Facsimile: (865)576-5728
E-Mail: reports@adonis.osti.gov
Online ordering: http://www.osti.gov/bridge

Available to the public from
U.S. Department of Commerce
National Technical Information Service
5285 Port Royal Rd
Springfield, VA 22161

Telephone: (800)553-6847
Facsimile: (703)605-6900
E-Mail: orders@ntis.fedworld.gov
Online order: http://www.ntis.gov/help/ordermethods.asp?loc=7-4-0#online

SAND2007-5547
Unlimited Release
Printed September 2007

Use of Composite Materials, Health Monitoring and Self-Healing Concepts to Refurbish Our Civil and Military Infrastructure

Dennis Roach
Kirk Rackow
Waylon DeLong
Infrastructure Assurance and Nondestructive Inspection Department, 6416

Steve Yepez
Systems Engineering I Department, 5932

Dave Reedy
Applied Mechanics Development Department, 1526

Sandia National Laboratories
P. O. Box 5800
Albuquerque, NM 87185

Scott White
University of Illinois
104 South Wright Street
Urbana, Illinois 61801-2935

ABSTRACT

An unavoidable by-product of a metallic structure's use is the appearance of crack, corrosion, erosion and other flaws. Economic barriers to the replacement of these structures have created an aging civil and military infrastructure and placed even greater demands on efficient and safe repair and inspection methods. As a result of Homeland Security issues and these aging infrastructure concerns, increased attention has been focused on the rapid repair and pre-emptive reinforcement of structures such as buildings and bridges. This Laboratory Directed Research and Development (LDRD) program established the viability of using bonded composite patches to repair metallic structures. High modulus fiber-reinforced polymer (FRP) material may be used in lieu of mechanically fastened metallic patches or welds to reinforce or repair damaged structures. Their use produces a wide array of engineering and economic advantages. Current techniques for strengthening steel structures have several drawbacks including requiring heavy equipment for installation, poor fatigue performance, and the need for ongoing maintenance due

to continued corrosion attack or crack growth. The use of bonded composite doublers has the potential to correct the difficulties associated with current repair techniques and the ability to be applied where there are currently no rehabilitation options. Applications include such diverse structures as: buildings, bridges, railroad cars, trucks and other heavy machinery, steel power and communication towers, pipelines, factories, mining equipment, ships, tanks and other military vehicles.

This LDRD also proved the concept of a living infrastructure by developing custom sensors and self-healing chemistry and linking this technology with the application of advanced composite materials. Structural Health Monitoring (SHM) systems and mountable, miniature sensors were designed to continuously or periodically assess structural integrity. Such systems are able to detect incipient damage before catastrophic failure occurs. The ease of monitoring an entire network of distributed sensors means that structural health assessments can occur more often, allowing operators to be even more vigilant with respect to flaw onset. In addition, the realization of smart structures, through the use of in-situ sensors, allows condition-based maintenance to be substituted for conventional time-based maintenance practices. The sensitivity and reliability of a series of sensor systems was quantified in laboratory and real-world environments. Finally, self healing methods for composite materials were evolved - using resin modules that are released in response to the onset of delaminations - so that these components can provide a living infrastructure with minimal need for human intervention.

This program consisted of four related research elements: 1) design, installation, and performance assessment of composite repairs, 2) in-situ sensors for real-time health monitoring, 3) self healing of in-service damage in a repair, and 4) numerical modeling. Deployment of FRP materials and bonded joints requires proper design, suitable surface preparation methods, and adequate surveillance to ensure structural integrity. By encompassing all "cradle-to-grave" tasks - including design, analysis, installation, durability, flaw containment, and inspection - this program is designed to firmly establish the capabilities of composite doubler repairs and introduce technology to incorporate self-monitoring and self-healing (living structures) methodologies. A proof-of-concept repair was completed on a steel highway bridge in order to demonstrate the potential of composite doubler technology for critical infrastructure use.

This work was performed under the Sandia Laboratory Directed Research and Development program 79778. Sandia National Laboratories is a multiprogram laboratory operated by Sandia Corporation, a Lockheed Martin Company, for the United States Department of Energy's National Nuclear Security Administration under contract DE-AC04-94AL85000.

Acknowledgements

This work was sponsored by Sandia Labs under a Laboratory Directed Research and Development Program. An investigation such as this would not succeed without the support of a number of research and field personnel covering a wide range of disciplines. Dennis Dunn and Zach Jacob assisted with the initial studies to determine the optimum surface preparation method for bonding composites to steel structures. The structural and fracture mechanics testing at Sandia Labs was supported by John Laing, Brenden Rogillio, John Hofer, and Tom Crenshaw. Corrosion assessments and tests to quantify environmental affects on bond fracture were aided by Rob Sorensen. Guidance on the statistical analysis of data to quantify sensor performance was provided by Floyd Spencer. Support for the structural health monitoring work was provided by Rob Hannum at Acellent Technologies (piezoelectric sensors) and Steven Kreger at Blue Road Research (fiber optics). Andy Chilcott at Structural Monitoring Systems provided the Comparative Vacuum Monitoring (CVM) sensors and valuable guidance on the CVM performance assessment tasks. In the arena of sensor development, the authors would like to thank Jon Bryan for his support in hardware design and schematic capture. Jon provided significant input in the sensor design through both modeling and experiments. Without his support, many concepts would have gone undiscovered. Nathan Lowrie provided several contributions on the software side of the program by delivering the graphical user interface, developing the interface with the device and installing several features to both control and monitor the device. Clint Furrer also added his signature to many aspects of the embedded controller used to drive the impedance analyzer, store data, and cycle through the flow chart of activities. Additional contributions were made by Val Shulfer, who provided the original and subsequent generation of coil designs. Janelle Garcia developed the essential I2C interface between the controller and the impedance IC that is vital to the project. Scott Frederick provided much of the preliminary analysis of the required inductances and other parameters for the first coil designs. Jimmie Wolf provided many hours of testing and analysis of the doublers using sensors developed in an earlier program. For self-healing research we extend thanks to Professors Nancy Sottos, Phillipe Geubelle, and Jeffery Moore at the University of Illinois for technical advice and helpful discussions. Scanning electron microscopy was carried out in the Center for Microanalysis of Materials, University of Illinois, which is partially supported by the U.S. Department of Energy under grant DEFG02-91-ER45439. Testing was completed at the Advanced Materials Testing and Engineering Lab, University of Illinois with the assistance of Peter Kurath, Gavin Horn and Rick Rottet. The authors would also like to acknowledge the efforts of Syncrude Canada Ltd. personnel Victor del Valle, Khaled Obaia, Mal Carroll, Jeremy Wong, and Stefano Chiovelli for their support in studying the application of this technology to Syncrude equipment. Finally, the composite repair of an Interstate-10 bridge was supported by the New Mexico Department of Transportation. Special thanks go to Earl Franks, Ted Barber and their NMDOT crew for facilitating this successful proof-of-concept bridge repair.

Use of Composite Materials, Health Monitoring and Self-Healing Concepts to Refurbish Our Civil and Military Infrastructure

TABLE OF CONTENTS

Use of Composite Materials, Health Monitoring and Self-Healing Concepts to Refurbish Our Civil and Military Infrastructure

1.0 DESCRIPTION OF TECHNOLOGY AND ITS APPLICATION

Dennis Roach and Kirk Rackow

1.1 Overview of the Problem and Idea

An unavoidable by-product of a metallic structure's use is the appearance of crack and corrosion flaws. Economic barriers to the replacement of these structures have created an aging infrastructure and placed even greater demands on efficient and safe repair methods. This Sandia Lab Directed Research and Development (LDRD) program deals with the repair or reinforcement of steel structures using high modulus fiber reinforced polymer (FRP) material. The use of bonded composite doublers has the potential to correct the difficulties associated with current repair techniques and the ability to be applied where there are no rehabilitation options. It promises to be cost-effective with minimal disruption to the users of the structure. Instead of fastening or welding multiple steel plates to implement a repair, it is possible to bond a single FRP composite doubler to the damaged structure. Current techniques for strengthening steel structures have several drawbacks including requiring heavy equipment for installation, poor fatigue performance, and the need for ongoing maintenance due to continued corrosion attack.

Composite Doubler Repair Method - Extreme fatigue, temperature, erosive, and corrosive environments induce an array of equipment damage. The current weld repair techniques for these structures provide a fatigue life that is inferior to that of the original plate. Weld repair techniques may only provide a temporary fix and subsequent cracking must be revisited on a regular basis. The use of composite doublers, which do not have brittle fracture problems such as those inherent in welds, can help extend the structure's fatigue life and reduce the equipment downtime. Similarly, the uniform load transfer provided by the bonded composite joint is very efficient and free from the fatigue cracks that can arise in mechanically fastened joints. Two of the main issues for applying composite repairs to civil applications are developing an installation technique for carbon steel and accommodating large repairs on extremely thick structures. Mechanically fastened repairs involve the addition of new holes with associated stress risers and new crack initiation sites. In addition, the time and labor involved to attach such repairs can be prohibitive. Continued corrosion of traditional metallic repairs is also a major concern [1.1-1.2]. Finally, both bolted and welded repairs have inferior crack mitigation capabilities compared to bonded composite repairs.

Smart Structures and Structural Health Monitoring - The costs associated with the increasing maintenance and surveillance needs of aging structures are rising. The application of distributed sensor systems can reduce these costs by allowing condition-based maintenance practices to be substituted for the current time-based maintenance approach. Through the use of in-situ sensors,

it is possible to quickly, routinely, and remotely monitor the integrity of a structure in service. This requires the use of reliable structural health monitoring systems that can automatically process data, assess structural condition, and signal the need for human intervention. Prevention of unexpected flaw growth and structural failure can be improved if on-board health monitoring systems exist that could frequently, or even continuously, assess structural integrity. Such systems would be able to detect incipient damage before catastrophic failures occurs. Other advantages of on-board distributed sensor systems are that they can eliminate costly, and potentially damaging, disassembly, improve sensitivity by producing optimum placement of sensors with minimized human factors concerns in deployment, and decrease maintenance costs by eliminating more time-consuming manual inspections. The ease of monitoring an entire network of distributed sensors means that structural health assessments can occur more often, allowing operators to be even more vigilant with respect to flaw onset.

Goal - *The goal of this project was to establish bonded composite doublers as a reliable and cost-effective structural repair method for civil and military structures and to develop adequate real-time monitoring and self-healing systems to ensure the long-term integrity of such structures with minimal need for human intervention. This investigation proved the effectiveness of composite materials to strengthen damaged or deficient steel structures. The final deliverable from this effort was to produce and demonstrate a smart structure that is self-sustaining and applicable to a myriad of aerospace, civil and infrastructure uses. To accomplish these objectives, testing of prototype installations was coupled with theoretical modeling in the following four-element approach: 1) design, installation, and performance of composite repairs, 2) in-situ sensors for real-time health monitoring, 3) self healing of in-service damage in a repair, and 4) numerical modeling. Each of these elements is described in dedicated chapters in this report.*

This LDRD contained the self healing, smart structure, and modeling/simulation elements needed to pursue living infrastructure concepts. It also included the desired use of large composite structures to address aging transportation infrastructure concerns. This LDRD also produced new science related to distributed and continuous Structural Health Monitoring (SHM), the use of adaptive structures, and the intelligent application of advanced materials to provide a valuable tool for a wide range of critical, civil and military steel structures. Much of the technology generated by this LDRD is applicable to existing initiatives within Energy and Infrastructure Assurance (E&IA) as well as other Sandia national security activities. The SHM and sensors work is useful in other Architectural Surety applications including monitoring aging mechanisms and rapid analysis of damage due to natural and malevolent events in critical infrastructure such as bridges and hospitals. The sensing technology developed under this LDRD enhances Sandia's capability to perform continuous in-service monitoring of structures and mechanical assemblies. These sensors can be applied in retrofit applications in which reinforcements are added to an infrastructural asset, such as an aircraft, bridge, or vessel. They can help ensure safe and effective operation by allowing preventive health monitoring strategies to be implemented across a wide range of industries.

The engineering activities in this program investigated design, analysis, fatigue performance, installation, health monitoring, and adaptive healing issues. This program demonstrated the

successful application of composite doubler repairs on steel structure by successfully establishing that:

1. Composite doubler repair technology is viable for steel structures within both civil and military arenas.
2. Composite doublers are able to withstand extensive damage and non-optimum installations while improving fatigue life and ultimate strength.
3. Continuous health monitoring is possible with the necessary sensitivity and minimal need for human involvement in the SHM process.
4. Self healing concepts are feasible within working structures and can help enhance the integrity and safety of composite structures.
5. Project activities have eliminated obstacles to the use of composite doubler repairs and allow authorities to utilize their engineering and economic advantages.
6. Field installations are feasible and they can demonstrate the performance of composite materials in the repair and refurbishment of steel structures.
7. This LDRD established the viability of fieldable technology that will aid Service Life Extension Programs and provide a tool that can counteract terrorist attacks on our civil infrastructure.
8. Program recognizes the value of replacing metallic structural elements with large composite structures and the need to safely integrate their use into DOE, DOT, DOD, DHS and architectural efforts.

1.2 Bonded Composite Doubler Repair Method

Figure 1-1 shows schematics of general composite doubler designs and basic design parameters such as ply lay-up, ply orientation, patch shape and taper, and the bond layer. The number of plies and fiber orientation are determined by the nature of the reinforcement required (i.e. stress field and configuration of original structure). The taper at the edge of the doubler is used to produce a gradually increasing stress gradient in the area of primary load transfer. A top ply of fiberglass is installed to supply mechanical and environmental protection for the installation. This type of repair can often provide more cost effective and reliable repairs than those currently employed. Figure 1-2 shows two families of aircraft composite doubler repair installations on aircraft.

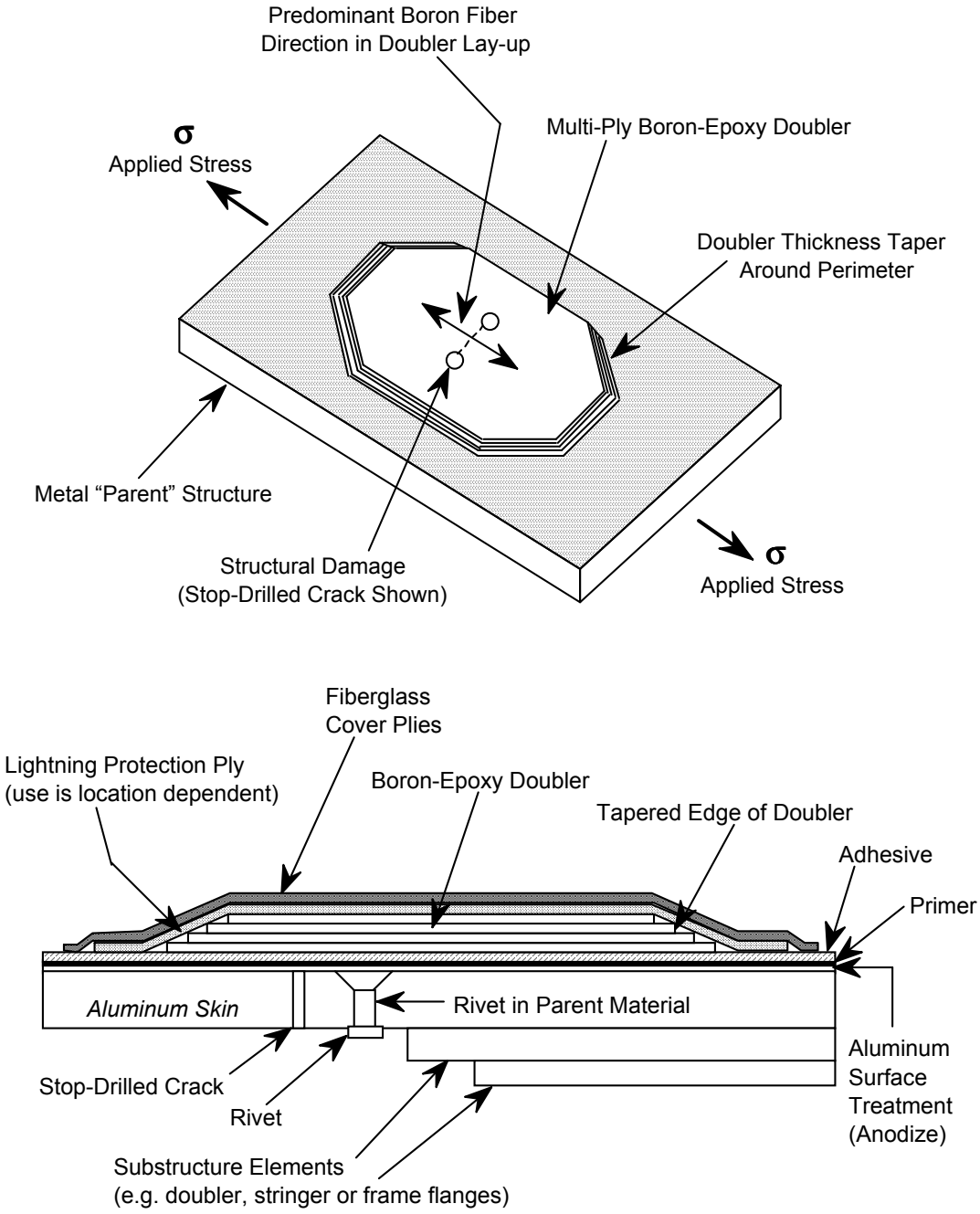

Figure 1-1: Schematics Showing the Bonded Composite Doubler Repair Method

Figure 1-2: Sample Composite Doubler Aircraft Repairs

Composite doublers offer enhanced safety through improved fatigue life and corrosion resistance [1.3]. The engineering advantages include: 1) elimination of fastener holes or weld stress risers that produce new crack initiation sites, 2) superior flaw growth mitigation performance, 3) high strength-to-weight ratio, 4) high durability, 5) ability to tailor strength to meet anisotropy needs thus eliminating the undesirable stiffening of a structure in directions other than those required, 6) corrosion resistance, and 7) formability to complex contours. The economic advantages include rapid repair installations that reduce downtime and do not require future maintenance. Cost savings associated with their use (time savings in installation) is a desirable by-product which will accelerate their introduction into routine use.

In some cases, such as in bridge and tower construction, the use of bolted or welded cover plates has been a common repair option. The current weld repair techniques for these structures only provide a temporary fix that must be revisited on a regular basis. Mechanically fastened repairs involve the addition of new holes with associated stress risers and new crack initiation sites. In addition, the time and labor involved to attach such repairs can be prohibitive. Finally, both bolted and welded repairs have inferior crack mitigation capabilities compared to bonded composite repairs. An extended description of these advantages follows.

1. A bonded repair will help relieve the residual stresses brought on by traditional welding in thick structures. Adhesive bonding eliminates stress concentrations, and new potential crack initiation sites, caused by additional fastener holes or heat-affected weld regions.
2. Bonded repairs allow for rapid, coherent joining of materials. Load transfer occurs over the entire footprint of the doubler/adhesive (vs. discrete weld seams). The doubler can be tapered to gradually introduce the reinforcing effect. This greatly reduces stress concentrations associated with discretely fastened or welded repairs. The more uniform load distribution provided by bonded joints improves fatigue life.
3. Adhesive joints provide localized support around the damaged region thus providing better crack mitigation than traditional repairs. This phenomenon is shown in Figure 1-3 where the short spring of a bonded joint performs better than the long spring represented by fasteners or fillet welds that are spaced far apart.

4. Also, composite doublers can be tailored to meet specific anisotropy needs thus eliminating the undesirable stiffening of a structure in directions other than those required. The directional stiffness of composite doublers can be tailored to address the critical loads so that reinforcement is produced only in the necessary directions.
5. This repair resists corrosion which may eliminate the onset of stress corrosion cracking.
6. Composite laminates are easily formed to fit the contour of tight radius areas or complex shapes permitting the repair of irregular components.
7. Composite doubler repairs can be quickly installed so economic advantages stem primarily from time savings in repair installation and the secondary effect of reduced equipment downtime.

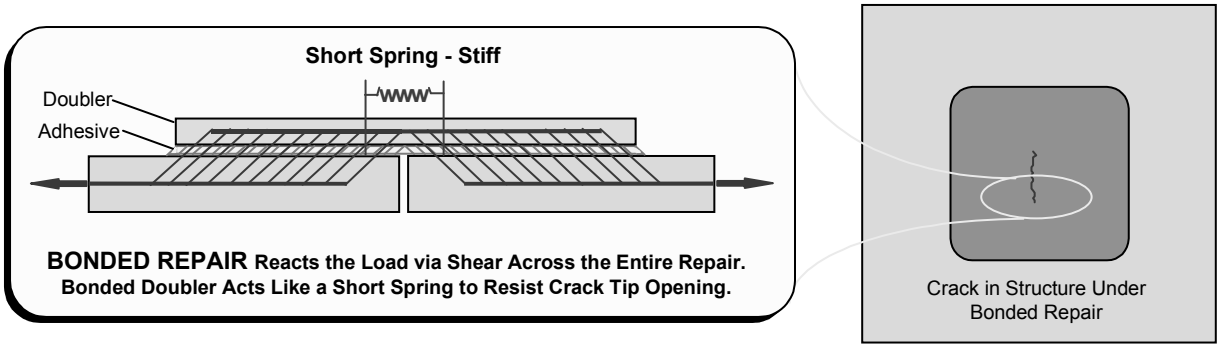

A. Joint Continuity of Bonded Doubler Reduces Stress Levels in Damaged Region

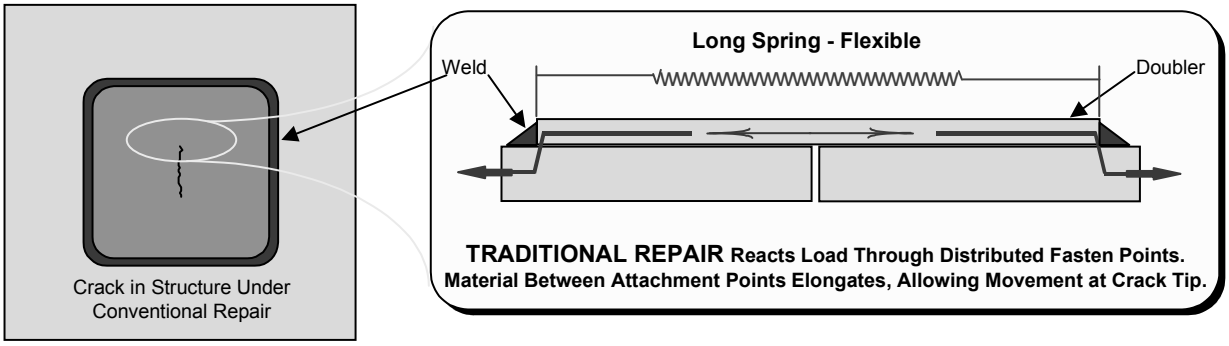

B. Local Loading and Intermittent Connection Produced by Spaced Perimeter Welds

Figure 1-3: Short Spring Representing the Localized Crack Mitigation of Bonded Doublers Versus the Longer Spring That Allows Cracks to Open and Grow More Rapidly

1.3 Applications for Composite Doubler Repairs and Living Infrastructure Concepts

As a result of Homeland Security and aging civil infrastructure concerns, increased attention has been placed on the rapid repair and pre-emptive reinforcement of buildings and bridges. Bonded composite doublers can be used in lieu of mechanically fastened metallic patches to reinforce or repair damaged structures. Recent events have demonstrated the need to address critical

infrastructure protection needs [1.4]. The key assets represent a broad array of unique facilities, sites, and structures whose disruption could have significant consequences. In this arena, composite materials can be used to reinforce critical portions of terrorism targets. This could be applied as a preventative measure to mitigate damage or avoid catastrophic failures of structures.

"Smart structures" concepts can be applied to compliment composite doubler repairs. A "smart structure" is one that is sufficiently instrumented so that the data can be synthesized to form an accurate real-time picture of the state of the structure in all its critical aspects. Leave-in-place sensors can be installed prior to installing composite repairs or for monitoring of the repaired structure. Less labor intensive and more frequent structural assessments can be performed via distributed sensor systems. Prevention of unexpected flaw growth and structural failure can be improved if on-board health monitoring systems exist that could continuously assess structural integrity. Such systems would be able to detect incipient damage before catastrophic failures occurs.

This report concludes a study into the application of composite patches to repair steel structures. The applications can include such diverse structures as: buildings, bridges, mining structures and vehicles, railroad cars, trucks and other heavy machinery, oil recovery equipment, steel towers used for telecommunications and power transmission, ships, tanks and a wide array of military structures. Damage can arise from service loads as well as from external impact or other off-design conditions. When considering the military applications it should be noted that rapid repair issues are inherent in this LDRD. This will allow for quick return-to-service of military structures and vehicles through the rapid repair of battle damage. Similarly, the proposed technology could also allow for rapid repair of damaged transportation lines (bridges) with minimal disruption to users of the structure.

Following is a brief description of some sample repair applications in order to demonstrate the wide range of uses for this technology. The evolution of this technology into smart, living structures that can both detect and repair damage is a tremendous enhancement. The accompanying sensor technology offers the potential for real-time, automatic health monitoring that will be critical for implementing self-healing techniques. Self-healing functionality expands the useful lifetime of polymeric components while incorporating a mechanism to provide increased safety associated with the repair of metallic structures. *Chapters 7-9 of this report present the living infrastructure concepts (self-monitoring and self-healing) and structural health monitoring sensors that are used to extend this advanced structural repair method into a complete smart and adaptive structure technology.*

1.3.1 Sample Uses on Civil and Military Infrastructure

In the matter of bridge refurbishment alone, the National Bridge Inventory Database (Fed. Highway Admin. 2003) indicates that 30% of the 600,000 bridges in the United States are "structurally deficient." In addition, a majority of the rail bridges in U.S. are operating beyond their initial design life. A bridge that is "structurally deficient" is still strong enough and stable enough for use; however, there are some elements that could be repaired in order to restore the structure to its original strength and stability. There are other reports that up to 40% of our US

bridges are in need of repair. That doesn't mean that 40% are about to fail; rather it means that preventative maintenance is needed to keep the bridges from further deterioration.

Tom Warne, Chairman of the Transportation Research Board has stated that "Even modest gains in the efficiency of construction and repair could yield huge overall savings." In 2006, the American Society of Civil Engineers (ASCE) issued a report in the status of the U.S. infrastructure. It assessed everything from roads to hazardous waste systems and gave the country's infrastructure an overall grade of "D". The ASCE warned that our "rotting" infrastructure poses risks to safety & economic growth and urged wholesale changes including increased research and development. For steel structures corrosion flaws reduce the cross section of members and the effect of repeated loading can generate fatigue cracks. Age is factor from the extent that corrosion and fatigue become more prevalent with time.

This composite repair or reinforcement/refurbishment process is useful to a wide range of industries. Applications include: auto and rail bridges, trains and subway vehicles, ships and naval vessels, buildings, electric nuclear power plants, energy generation equipment, aerospace vehicles, transmission towers, manufacturing factories, pressure vessels, tanker trucks, military vehicles and structures, mining equipment, offshore oil platforms, and pipelines. Aviation endeavors represent only a small percentage of potential composite doubler applications. Steel structures also require strengthening due to changes in use, demand for increases in load carrying capacity, corrosion of the existing structure, or the need to improve the fatigue performance by reducing stress levels. There is a wide range of infrastructure uses for this technology where oftentimes there are no repair or refurbish options. In many instances, it may be possible to avert a complete component replacement. Figures 1-4 through 1-16 present an array of applications for both composite doubler repairs and structural health monitoring and include some damage scenarios experienced in these structures.

1. trains and subway vehicles (Figure 1-4)
2. ships and naval vessels (Figure 1-5)
3. electric and nuclear power plants (Figure 1-6)
4. energy generation equipment (Figure 1-7)
5. pressure vessels, tanker trucks, and rail cars (Figure 1-8)
6. buildings (Figure 1-9)
7. military vehicles (Figure 1-10)
8. aerospace vehicles (Figure 1-11)
9. factories, offshore oil platforms, and pipelines (Figure 1-12)
10. bridges (Figure 1-13)

Figure 1-4: Trains and Subway Vehicles - Applications for Composite Doubler Repair and In-Situ Structural Health Monitoring Technology

Figure 1-5: Ships and Naval Vessels - Applications for Composite Doubler Repair and In-Situ Structural Health Monitoring Technology

Figure 1-6: Electric and Nuclear Power Plants - Applications for Composite Doubler Repair and In-Situ Structural Health Monitoring Technology

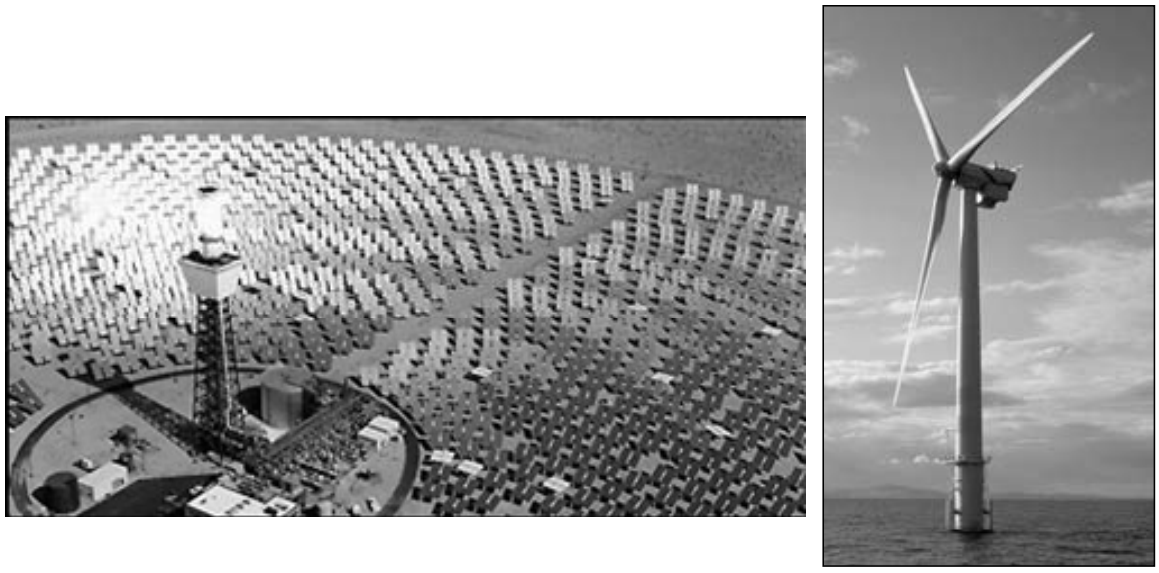

Figure 1-7: Energy Generation Equipment - Applications for Composite Doubler Repair and In-Situ Structural Health Monitoring Technology

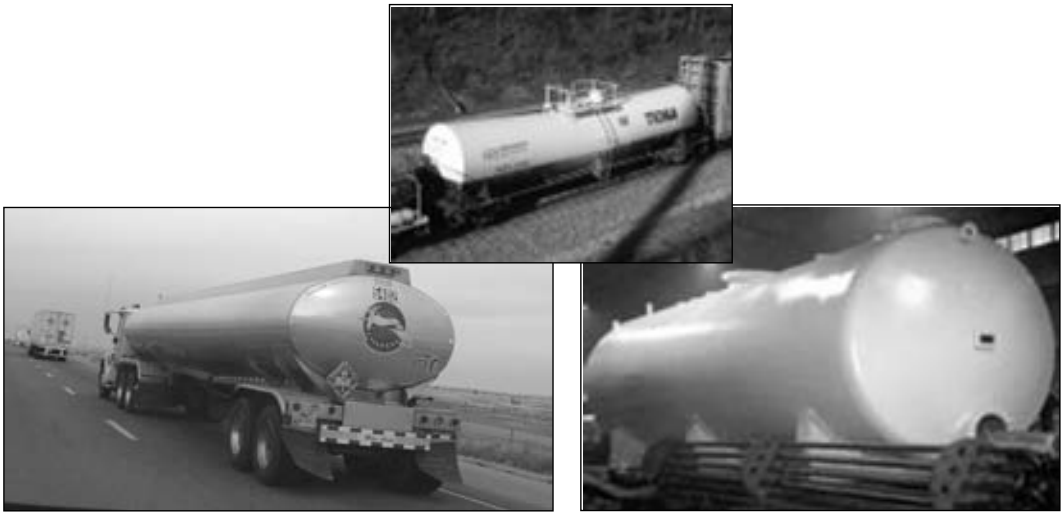

Figure 1-8: Pressure Vessels, Tanker Trucks and Rail Cars - Applications for Composite Doubler Repair and In-Situ Structural Health Monitoring Technology

Figure 1-9: Buildings - Applications for Composite Doubler Repair and In-Situ Structural Health Monitoring Technology

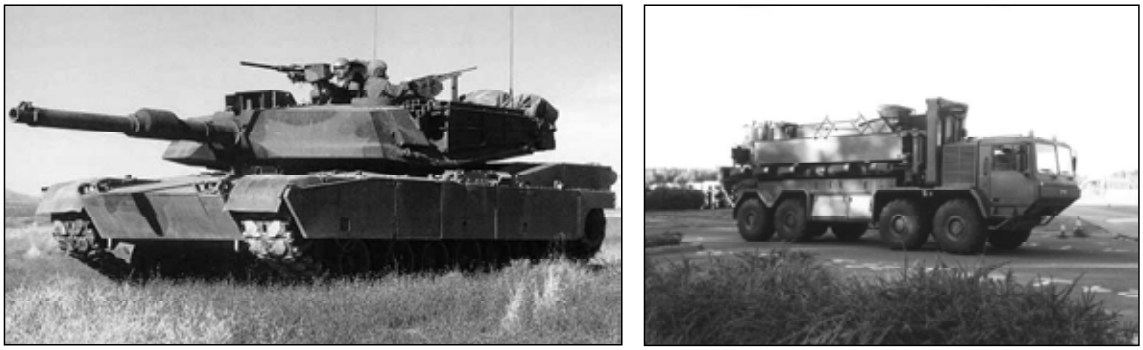

Figure 1-10: Military Vehicles - Applications for Composite Doubler Repair and In-Situ Structural Health Monitoring Technology

Figure 1-11: Aerospace Vehicles - Applications for Composite Doubler Repair and In-Situ Structural Health Monitoring Technology

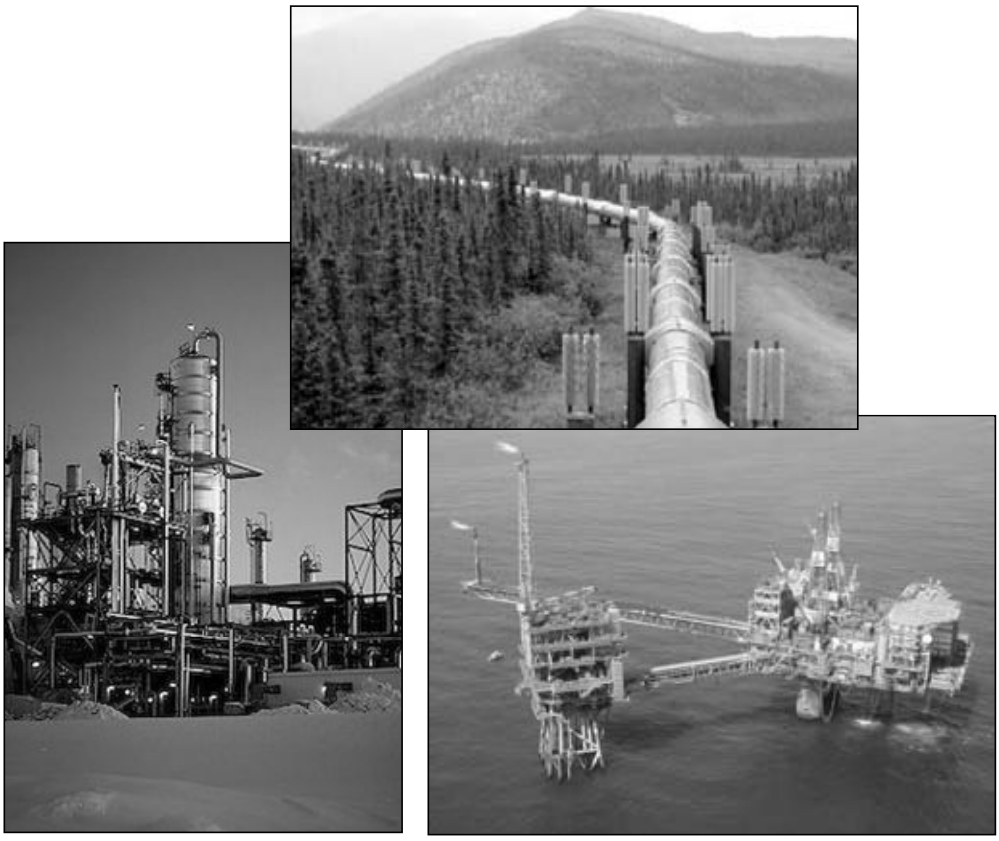

Figure 1-12: Manufacturing Factories, Offshore Oil Platforms, & Pipelines - Applications for Composite Doubler Repair and In-Situ Structural Health Monitoring Technology

Figure 1-13: Rail and Auto Bridges - Applications for Composite Doubler Repair and In-Situ Structural Health Monitoring Technology

Steel superstructure bridges built during the interstate construction boom of the 1950's and 1960's are reaching or surpassing their initial design lifetime. Depending on their level of maintenance, some bridges are showing visible signs of deterioration. Budget restrictions can limit inspections or repairs such that only the more serious problems are addressed. On September 30, 2006, part of an overpass collapsed in Laval, a suburb of Montreal. Figure 1-14 shows two bridge failures – in Montreal and Connecticut – and one bridge with a large fatigue crack that was discovered and repaired prior to any catastrophic failure.

On August 1, 2007 an interstate 35 bridge crossing the Mississippi River in Minneapolis failed (see Figure 1-15). The collapse of the interstate 35 bridge in Minneapolis prompted many questions regarding the health of similar structures around the world and their associated maintenance programs. On June 15, 2007 a bridge over the Xijiang River in south China's Guangdong province failed and in January 1999 a pedestrian bridge spanning the Qi River in southwestern China's Sichuan province collapsed. The government's plans to fix 6,000 "structural deficient" bridges by 2010 were reported recently in China Daily. The Minneapolis event is being described as a structural failure and not an act of terrorism. However, the cases of the Montreal, Minneapolis, and recent China bridge collapses are still under investigation to determine their exact cause.

In Ontario, Canada 187 bridges missed safety inspections in 2006, according to a report in the *Hamilton Spectator*. The newspaper said Ontario only finished $36 million of $210 million in bridge repairs needed in the province's Golden Horseshoe area. Last year, a provincial report in Manitoba found that of 1,200 bridges in the province, 123 had exceeded their design life of 50 years. Another 222 were at least 40 years old.

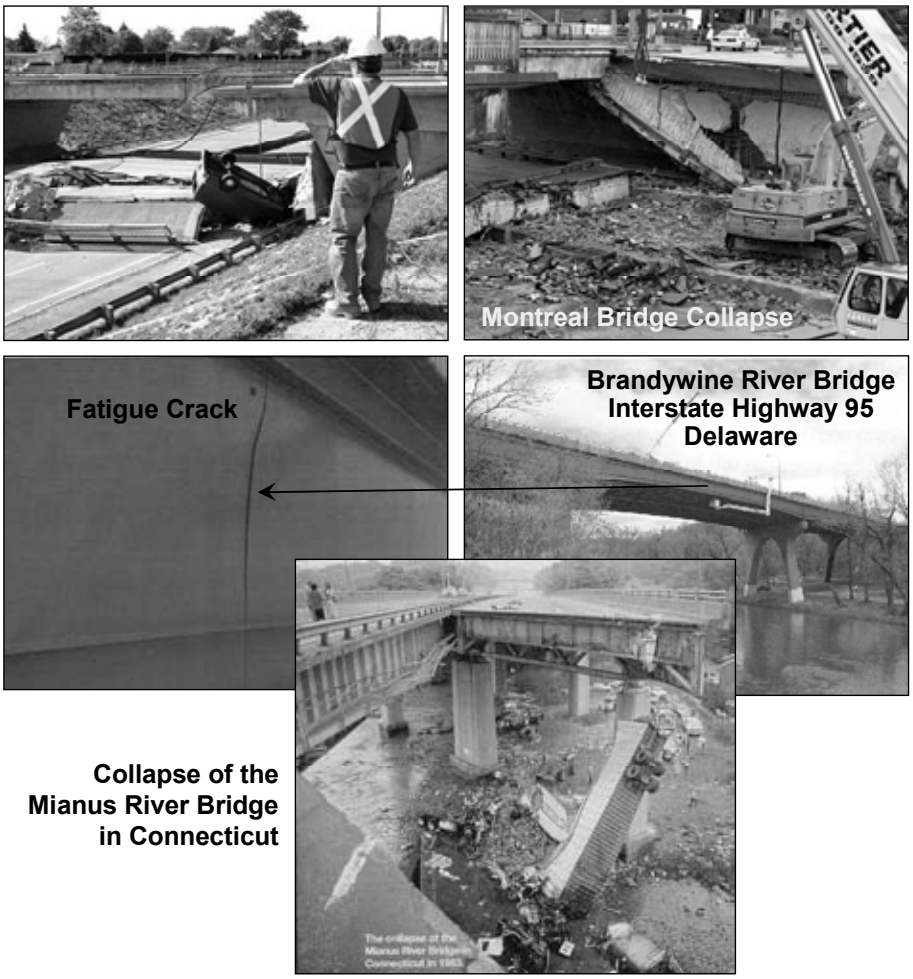

Figure 1-14: Sample Failures in Bridge Structures

1.3.2 Detailed Assessment of Oil Recovery and Mining Industries

Syncrude Canada Ltd. is one of only a few companies in the world that extracts oil from "oil sand" (bitumen) mineral deposits. The technique involves a mining operation followed by a mechanical and chemical process to produce crude oil. Equipment damage, such as the frequent occurrence of cracking, is caused by high impact loads, high fatigue cycles, low operating temperatures and large component size. Shutdowns to repair equipment can cost in excess of $1M per day. As a result, any improvement in mining equipment operation and maintenance can lead to significant reductions in yearly operating budget. Current techniques for strengthening steel structures have several drawbacks including requiring heavy equipment for installation, poor fatigue performance, heat affected zones around welds, and the need for ongoing maintenance due to continued corrosion attack and crack growth. Due to Syncrude's extreme interest in the technology described here, an in-depth investigation into the applicability of composite doubler repairs and SHM to Syncrude structures was completed.

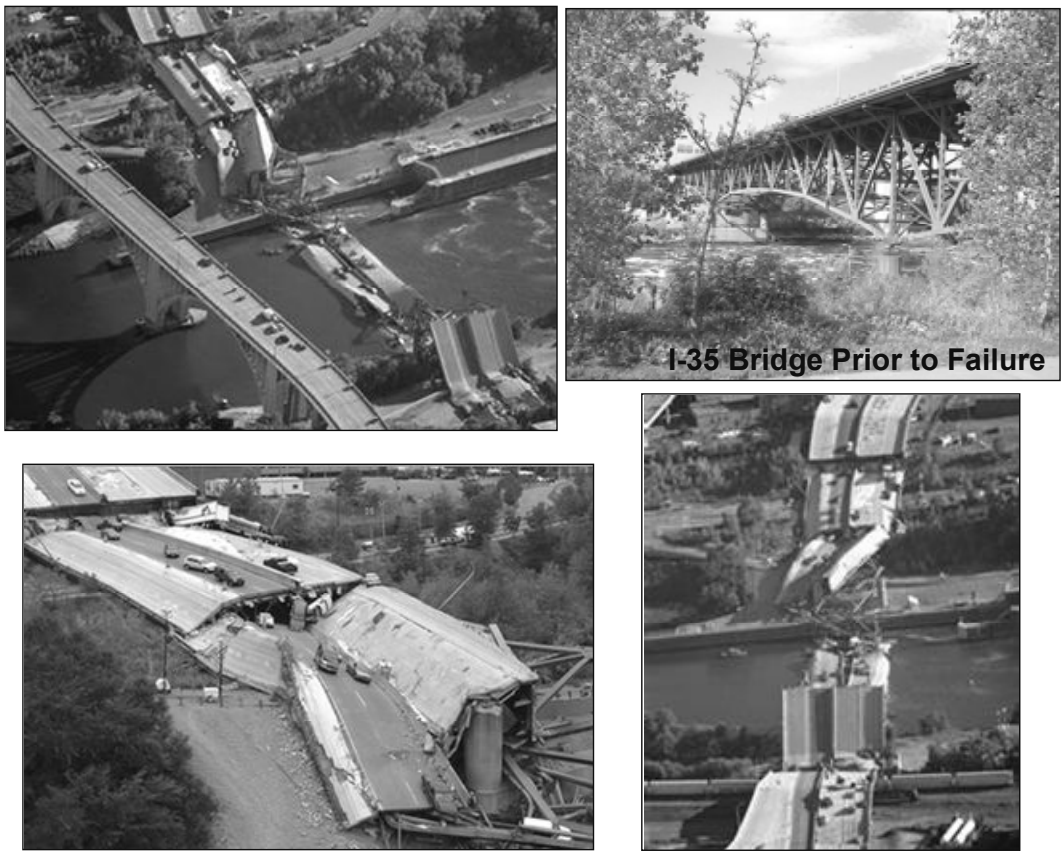

Figure 1-15: Collapse of the I-35 Bridge in Minneapolis

Figures 1-16 and 1-17 show several of the hydraulic and cable shovels along with the trucks used in the surface mining operation. The trucks hold from 240 to 380 tons of oil sand and can be filled in three to four passes of an excavation shovel. Fatigue cracks are commonly found in the body, arms, frames, and buckets of this equipment. The current weld repair techniques for these structures only provide a temporary fix that must be revisited on a regular basis. It is believed that the use of composite doublers, which do not have brittle fracture problems such as those inherent in welds, will help extend the fatigue life of this type of structure and reduce the equipment downtime during mining operations.

A general view of the oil recovery/mining process and movement of the oil sands into the upgrading plant is shown in Figures 1-18 to 1-20. These photos include a number of candidate applications for composite doublers and associated structural health monitoring. Visits to the Syncrude oil extraction site and associated meetings with plant engineers identified the following potential repair applications:

1. Hydraulic and cable shovels – primarily the shovel booms and sticks (see Figs. 1-16, 1-17)
2. Cable shovel revolving frame (body) at window cutout (see Fig. 1-16)
3. Conveyor belt truss structures (see Fig. 1-19)

4. Mechanical tumbling drums (see Fig. 1-20)
5. Fluid cylinders on tanker trucks
6. Vibrating screens for filtering (see Fig. 1-21)
7. Shovel buckets (see Figs 1-17 and 1-22)
8. Boxes on mining trucks (see Fig. 1-23)
9. Truck frames – stringers and bolsters especially at hinge region (see Fig. 1-24).

Figure 1-16: Oil Sands Recovery - Sample Syncrude Equipment that Could Utilize Composite Doubler Repair and SHM Techniques

Hydraulic Excavator

Cable Shovel

Figure 1-17: Oil Sands Recovery - Sample Syncrude Equipment that Could Utilize Composite Doubler Repair and SHM Techniques

Rock Crusher

Upgrading Plant

Figure 1-18: Plant equipment for Processing Oil Sands

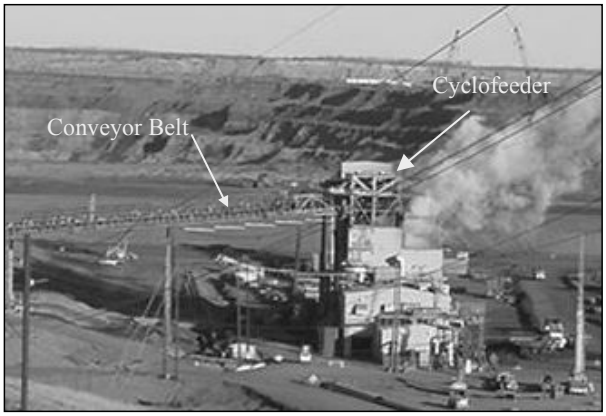

Figure 1-19: Conveyor Belts Transfer Oil Sands to Cyclofeeder for Hydrotransport

Figure 1-20: Tumblers Initiate the Separation Process in the Extraction Plant

Figure 1-21: Vibrating Screen for Filtering Initial Mining Products

Figure 1-22: Hydraulic Shovel Bucket

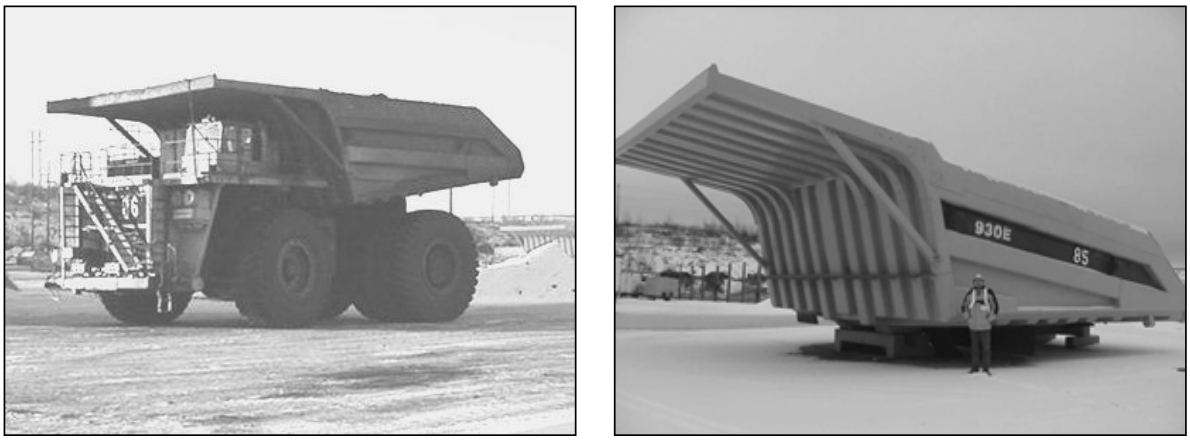

Figure 1-23: Truck and Truck Box Structure for Oil Sands Mining Operation

Figure 1-24: Mining Truck Frame and Crack Area at Bolster-to-Box ¾" Fillet Weld

Cable Shovel Boom – The Bucyrus-Erie 395B cable shovel boom was chosen as the best initial application for a composite repair. Figures 1-25 shows two views of the boom mounted and removed from the cable shovel, respectively. It can be seen that this is a split, two pronged boom. The favorable features of this repair include: manageable wall thickness (7/8" and 1 ¼"), good accessibility, relatively low expected stress levels, and no structural impediments (complex geometry). Figures 1-26 and 1-27 show close-up photos of regions repaired with fill welds only. Typical cracks found on the shovel boom are pictured in Figure 1-28. Figure 1-29 shows the temporary repair process that uses seam-welded fish plates (steel doublers) to quickly repair boom cracks so that the shovel can continue to operate until planned maintenance can complete the more robust fill-weld repair. Multiple plates are applied as the crack continued to grow across the width of the shovel boom. Figure 1-30 shows a boom plate crack as it propagates out from under the fish plate and around the corner into an adjacent boom plate. The steel plate used for the boom is a steel material that has a Canadian specification of CSA-G40.21-92 which is ASTM A633 (σ_u= 70-90 KSI; σ_y=50 KSI; elongation = 22-25%). The specific chemical composition that we are trying to match is: C_{max} 0.20, Mn 1.15/1.5, S_{max} 0.05, P_{max} 0.04, Si

0.15/0.50, and Cb 0.01/0.05. In 6 months of operation, it is estimated that the boom experiences close to 260,000 load cycles.

Figure 1-25: Cable Shovel Boom and Split Boom Removed from Shovel

Figure 1-26: Fill-Weld Repair on Boom Side Plate

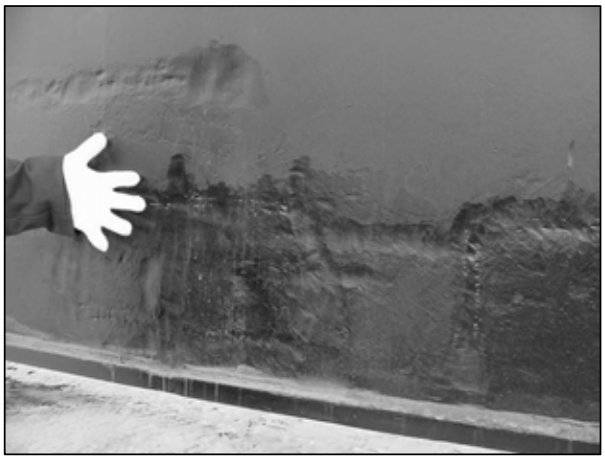

Figure 1-27: Fill-Weld Repair on Side Plate

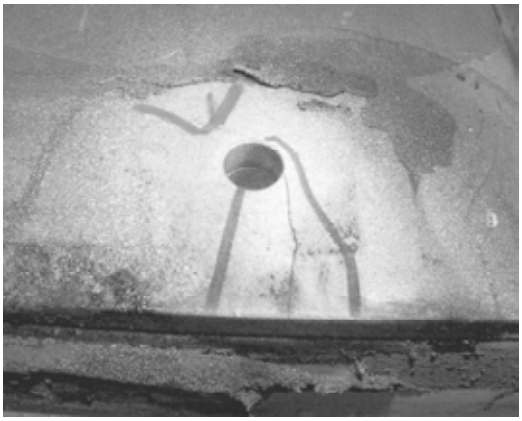

Figure 1-28: Typical Fatigue Cracks Found in the Shovel Boom

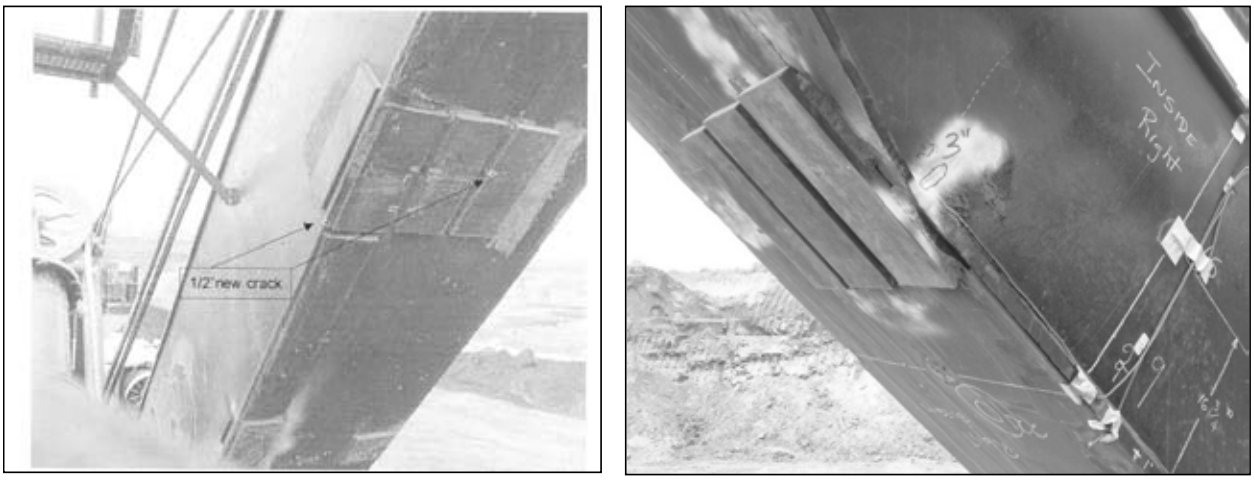

Figure 1-29: Series of Fish Plate Repairs to Slow the Growth of a Propagating Crack

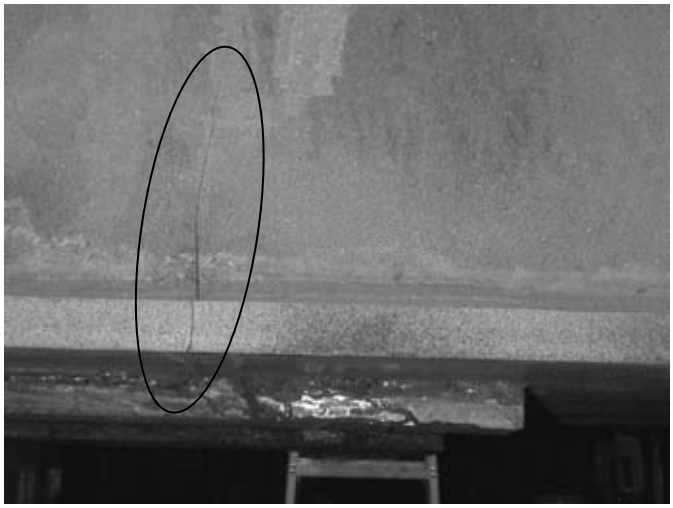

Figure 1-30: Crack in Boom Plate Emanating Around the Corner from a Fish Plate Welded Repair

1.4 R&D Technical Approach

Advances in structural adhesives have permitted engineers to contemplate the use of bonded joints in areas that have long been dominated by mechanical fasteners and welds. Although strength, modulus, and toughness have been improved in modern adhesives, the typical concerns with using these polymers still exist. These include a strong sensitivity of mechanical properties to temperature change, concerns over durability in hot/wet environments, and an inability to quantify bond strength (i.e., identify weak bonds) in adhesive joints. As a result, deployment of bonded joints requires proper design, suitable surface preparation methods and adequate surveillance to ensure long-term structural integrity.

This research program developed and proved an optimum field installation process using specific mechanical and chemical surface preparation techniques coupled with unique, in-situ heating methods. In addition, a comprehensive performance assessment of composite doubler repairs was completed to establish the viability of this technology for large, steel structures. The factors influencing the durability of composite patches in severe field environments were evaluated along with related laminate design issues. Design philosophies were evolved to accommodate materials of different moduli, ductility, and failure modes. Installation of ultra-large composite doublers for bridge or building applications were studied. This LDRD went on to develop smart structures through the use of in-situ sensors or sensors embedded in the composite structures. In addition to this self-monitoring aspect, project tasks investigated self healing methods for composite materials - using resin modules that are released in response to the onset of delaminations - so that these components can provide a living infrastructure. Finally, proof-of-concept repairs were completed in a bridge repair application to demonstrate the potential of composite doubler technology for critical infrastructure use. By encompassing all "cradle-to-grave" tasks - including design, analysis, installation, structural integrity and inspection - this program is designed to firmly establish the capabilities of composite doubler repairs. The material used for strengthening was a composite material consisting of a continuous Boron-reinforced tungsten filament in an epoxy matrix (Boron-Epoxy).

Design, Installation, and Performance Assessment of Composite Repairs - To demonstrate the capabilities of composite doubler reinforcement technology in an area of known fatigue cracking, this segment of the LDRD contained the following technical activities: 1) structural design of the doubler, 2) development of doubler installation procedures, 3) structural evaluation of the design, 4) inspection procedures, and 5) laboratory and field tests of a composite doubler installed on an operating, steel structure. The general issues which were addressed to establish the performance of composite doubler repairs in complex environments were: 1) patch installation (surface preparation, tooling, heat sinks, effect of underlying structures, field work), and 2) patch design (strength, damage tolerance, durability, reliability, flaw containment, optimum adhesive properties, and critical patch parameters). Fatigue and ultimate strength tests evaluated the overall effect of composite doublers on stress intensity, crack growth, and strength characteristics of steel structure. The structural tests: 1) assessed the potential for interply delaminations and disbonds between the steel and the laminate, and 2) determined the load transfer and crack mitigation capabilities of composite doublers in the presence of severe defects. The prebond surface treatment to which steel is subjected can significantly influence the resultant initial strengths and long-term durability provided by such bonds. In order to optimize surface preparation, the basic mechanisms of adhesion must be considered. The two basic mechanisms of adhesion for structural adhesive bonding - mechanical interlocking and chemical enhanced bonding between the polymer and the adherend surface – were studied using a tailored set of surface preparation options.

Smart Structures and Health Monitoring Sensors - The use of composite doubler repairs can be suppressed by uncertainties surrounding their application, subsequent inspection and long-term endurance. Therefore, it is imperative that methods be developed which can quickly and easily assess the integrity of the doubler. A “smart structure” is one which is sufficiently instrumented so that the data can be synthesized to form an accurate real-time picture of the state

of the structure in all its critical aspects. In this case, the absence of disbonds and delaminations indicates that the doubler is able to perform its duty. This segment of the LDRD developed an eddy current (EC) microsensor that can be permanently mounted on the structure to detect crack onset and growth. The EC sensor was designed with sufficient penetration power to detect deeply embedded, or subsurface, fatigue cracks. Other sensor approaches studied include: Comparative Vacuum Monitoring sensors, fiber-optic sensors, and piezoelectric sensors embedded within or mounted on the surface of the composite material. Because of the basic lamination concept that builds a structure from multiple composite plies, continuous fiber structural composites naturally lend themselves to embedded sensors that can monitor the structural response in real-time. Continuous or segmented fiber optic sensors were deployed to detect cracks in the steel structure beneath the composite repair and to measure the stresses in the composite doubler after it is placed into service. Irregular changes in the stress field can be used to indicate both crack onset in the steel structure and delaminations or disbands in the composite repair.

Self Healing in the Composite Laminate Repair – Self-healing materials are inspired by living systems, in which minor damage triggers an autonomic healing response. Healing is accomplished by incorporating a microencapsulated healing agent and a catalytic chemical trigger within a polymer matrix. Damage in the form of a bond dislocation serves as the triggering mechanism for self-healing. The approaching dislocation ruptures the embedded microcapsules, releasing a healing agent into the crack plane through capillary action. Polymerization of the healing agent is triggered by contact with the embedded catalyst, bonding the crack faces. Employing this self-healing research concept, this segment of the LDRD developed self-healing bond lines suitable for bonded repair of metallic structures. Repair of damage is accomplished automatically and without human intervention, improving performance and service-life. This activity included three main tasks: (1) healing system screening, (2) self-healing adhesive fabrication, and (3) mechanical property assessment. The healing efficiency of adhesive film systems was measured via carefully controlled fracture experiments. The most critical issue for the adhesive fabrication task was to identify the processing window for compaction pressure in which the microcapsules remain structurally intact throughout cure while ensuring full compaction of the laminate stack.

Numerical Modeling - Numerical modeling was used to: 1) produce an understanding of the critical elements of this technology and 2) develop design guidelines with an associated software package to aid the design process. The highest levels of monitoring hierarchy are prognostic and diagnostic assessments. In order to arrive at the necessary insights into service performance plus life and degradation evaluations, it is necessary to include a modeling effort to compliment the smart structure approach. Composite doubler design and analysis was conducted via finite element analyses. These analyses can be broken into two types corresponding to whether only the local patch region is modeled or whether the overall structure being reinforced/repaired is modeled as well. In both cases, the effects captured in the patch region included the anisotropic response of the composite patch, the gradual load transfer between the parent and patch materials over the patch taper region, the residual stresses resulting from the thermal strain mismatch between the patch and parent materials, and out-of-plane bending arising from shifting of the bending neutral axis in the patch area. Degraded adhesive properties were modeled in various sub-regions in order to investigate the effects of contamination and imperfect curing. In order to

successfully transfer composite doubler technology to industry for application, it was necessary to develop simplified models for the patch region that can be rapidly analyzed. Development of such simplified models allowed for the development of a design and analysis software package to further streamline the use of composite doubler technology.

References

1.1 Schwendeman, L., and Hedgren, A., "Fatigue and Repair Cases in Steel Bridges," JSCE, 2002.

1.2 "Maintenance and Repair of Army Structures," U.S. Army Engineering Manual, EM-1110-2-6054, December 2001.

1.3 Roach, D.P, "Damage Tolerance Assessment of Bonded Composite Doublers for Commercial Aircraft Applications", Sandia National Laboratories/ Dept. of Energy Report No. SAND98-1016, August 1998; also FAA Report SNL96ER0189 under Atlanta Aircraft Certification Office Project SP1798AT-Q, November 1997.

1.4 White House document, "*National Strategy for Physical Protection of Critical Infrastructures and Key Assets,"* February 2003.

2.0 COMPOSITE DOUBLER INSTALLATION PROCESS ON CARBON STEEL STRUCTURES

Dennis Roach, Kirk Rackow and Waylon DeLong

Metal treatment prior to bonding is a key factor for both the initial adhesion of a bonded joint and its long-term environmental durability. Current metal prebond surface preparations are either inconvenient or complex to use, contain hazardous materials (e.g. strong acids), and/or do not provide the performance necessary for successful long-term, durable bonds. Past bond failures, primarily due to inadequate surface preparation, have been a limiting factor in the current use of bonded hardware, especially for primary structure. The portion of the program presented in this chapter determined the optimum surface preparation in order to meet both the bond strength and bond durability requirements.

2.1 Surface Preparation Options

Before moving into component level and full scale testing on simulated Syncrude repairs it was first necessary to certify a chemical bonding process for steel structure and verify the associated strength of the critical adhesive layer. The prebond surface treatment to which steel is subjected can significantly influence the resultant initial strengths and long-term durability provided by such bonds. The key to structural bonding is that the adherend surfaces must be roughened and free from contamination and weak oxide layers. Proper surface preparation will produce these features on the material and will allow for a reliable joint with sufficient strength and durability [2.1]. In order to optimize surface preparation, the basic mechanisms of adhesion must be considered. The adhesive must be able to wet the entire surface of the adherend so that there is intimate molecular contact at the joint interface. There are two basic mechanisms of adhesion for structural adhesive bonding: 1) mechanical interlocking of the polymer with the adherend surface, and 2) chemical enhanced bonding of the polymer molecules with the adherend surface layer. Both of these mechanisms were pursued using a tailored set of surface preparation options.

Since this study is aimed at field installation in industrial settings, it is necessary to use simple, repeatable, and economically viable processing procedures. Sophisticated chemical surface treatments are too expensive or complicated to produce repeatable results. Ultra high temperature and high pressure processes are also not feasible in the field. The surface preparation used for many aluminum bonding operations involves a phosphoric acid anodize etch. This approach requires a tailored phosphoric acid containment system that is time consuming to apply and potentially hazardous in the repair applications for this program. Another chemical process was developed for the surface preparation procedure on carbon steel structures to produce optimum strength in the bond joint. The surface preparation options evaluated in this study were selected on the basis of strength and durability, as well as, their ability to be carried out in heavy industrial settings.

The matrix of surface preparation options is summarized in Table 2-1. The surface degrease step involved an application of Acetone followed by residue removal using Methyl Alcohol. Surface

roughening for mechanical interlocking was provided by grit blasting or a simple oxide removal and sanding process. The surface chemistry was changed in some of the options through the application of Silane, Sol-Gel, or Pasa-Jell. Finally, different primers were applied to assess any durability improvements they might provide in extreme environments. A description of each of these processes follows along with some discussion on several other surface preparation options that were eliminated from consideration prior to any testing.

Surface Roughening

Roughening surfaces prior to bonding enhances the strength of adhesive joints. The abrasive process removes contaminated layers, including hard-to-remove oxide layers, and the roughened surface provides some degree of mechanical interlocking with the adhesive. The process also forms a larger effective surface area for the bond and can introduce physical/chemical changes which affect surface energy and wettability. All of these issues must be considered in light of the characteristics of the adhesive and its ability to spread on different surface textures.

Experience has shown that any relatively smooth surface bonded to structural epoxy adhesives will suffer rapid delamination during conditions of high stress and humidity. Rougher surface morphology allows for better adhesion and resistance to the damaging effects of moisture. The task of providing a fine scale, stable, repeatable, rough surface on low carbon steels is difficult due to the surface condition, heat treatment, and metallurgical complexity of the steel materials. For these reasons, along with field installation impediments, chemical etching was eliminated from consideration.

Prior to roughening the surface, Scotch-Brite abrasion was applied to remove any oxide coating and debris. Additional grease and surface residue was removed with an alcohol cleaning. The relationship between surface texture and adhesion is complex and the relative magnitude and interactions of these different mechanisms need to be understood to optimize abrasive surface treatment processes. The grit blast process is used extensively to provide a clean and uniformly roughened surface for high strength bonding applications [2.2]. In this study, various grit blast energy levels were applied to the carbon steel plates in order to determine the best surface roughening performance for the hardness of our material. Related information from bonded repairs on aircraft was used to select grit type (aluminum oxide) and grit size (50 μm). In addition, the degree of surface roughness (≈50 μinch RMS) was chosen to match the level that produced optimized adhesion tests in aluminum bonds that utilized the same adhesive. This roughness number represents the average departure of the surface profile from the mean plane.

The relationship between the grit blast delivery pressure (energy level) and the corresponding surface roughness was determined. It was found that a 60 psi grit blast on carbon steel (ASTM 572) produced a similar surface roughness as a 40 psi grit blast on aluminum (2024-T3) during aircraft repairs. Filtering and drying systems were added to the compressed air supply line to reduce contamination. Figure 2-1 shows the test specimen preparation using the portable grit blast system. After blasting, a jet of clean air was blown across the surface to remove loose grit particles. The chemicals listed in Table 2-1 were then applied generously using brush-on or spray applications such that any contaminating residues were rinsed from the surface. To determine the feasibility of a quicker surface roughening option, hand sanding was included in

the test matrix. Zirconium oxide sanding paper was applied in two perpendicular directions to produce a scratched surface that was sufficiently roughened but much less uniform in appearance. Figures 2-2 and 2-3 compare two surfaces that were grit blasted and hand sanded. In certain instances, the containment of the grit is a concern or the space available to conduct the grit blast is limited. In such cases, it is necessary to eliminate the grit blast process; however, some surface roughening is still needed. So, a number of sanding options were pursued. In the event that the lack of uniformity and the presence of deep gouges produced by the hand sand method (Option 9) resulted in poor bond performance, then two machine sand options (Option 10 & 11) – each producing different levels of surface roughness – were also investigated.

Option	Scotch-Brite Abrade & Degrease	Grit Blast	Blow Off Surface -Oil-Free Air	Post Blast Degrease	Chemical Treatment & Heat Lamp Dry	Primer & Air/Heat Lamp Dry
1	✓	✓	✓	-	Sol-Gel	BR-6747
2	✓	✓	✓	✓	Sol-Gel *	BR-6747 *
3	✓	✓	✓	✓	Pasa-Jell *	BR-6747 *
4	✓	✓	✓	✓	-	BR-6747
5	✓	✓	✓	✓	- *	-
6	✓	✓	✓	-	Silane *	BR-6747 *
7	✓	✓	✓	-	Silane	BR-127
8	✓	✓	✓	✓	Silane	BR-6747
9	✓	SAND 180 grit Manually Applied	✓	✓	-	BR-6747
10	✓	SAND 36 grit Grind Wheel Applied	✓	✓	Silane	BR-6747
11	✓	SAND 24 grit Grind Wheel Applied	✓	✓	Silane	BR-6747

* Corrosion assessment coupons; 2 at each condition indicated

Table 2-1: Surface Preparation Options for Adhesive Bonding

Figure 2-1: Grit Blast of Steel Surface Using 50 Micron Aluminum Oxide Grit Applied at 60 PSI

Figure 2-2: 50X Microscopic View of Grit Blasted Surface at 60 PSI (Surface Roughness = 52 μinch RMS)

Figure 2-3: 50X Microscopic View of Hand Sanded Surface (Nonuniform – no roughness value)

Chemical Interlocking

Coupling Agents – Silane chemicals have been used to promote adhesion [2.3-2.4]. Use of the Silane with a chemically compatible primer provides enhanced durability in hot-wet conditions. Figure 2-4 shows a schematic of the Silane layer being produced on the metal surface to enhance the bonding process. In this study the Silane chemical was mixed with distilled water in a 99:1 ratio and then brushed directly onto the grit-blasted steel surface. The Silane was applied as follows: 1) 1% diluted mixture was brushed on with a natural hair brush such that the liquid flow was sufficient to check for a water break-free surface, 2) the surface was wetted for 10 minutes

with brush applications, 3) the surface Silane was blown off with instrument quality air, and 4) excess moisture was removed via heat lamp drying (120-150°F for 20 minutes). If streaks were noted during the blowing process, it indicated the presence of grit and the Silane wetting process was repeated to remove excess grit. In order to cure the composite doubler and adhesive film, the structure must be heated to 225°F. Since heating the massive, steel structures more than one time is impractical, this effort evaluated a co-cure process wherein final cure of the Silane was achieved simultaneously with the adhesive.

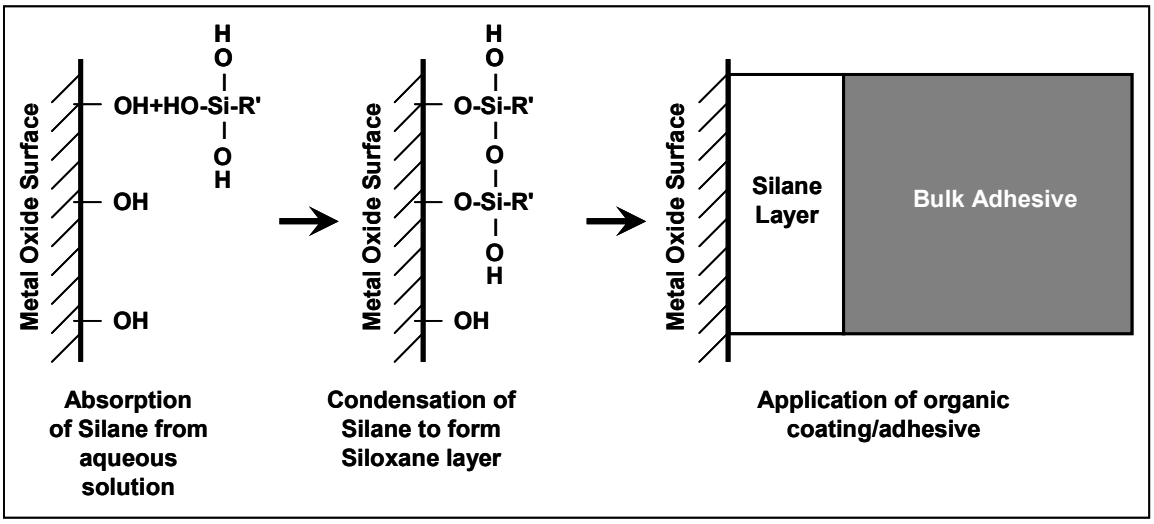

Figure 2-4: Schematic of Silane Layer Formed on Steel Surface to Promote Bonding

Sol-Gel is another prebond surface treatment that facilitates adhesive bonding to metallic surfaces [2.5]. Sol-Gel formulations developed by Boeing were designed to work optimally with aluminum alloys, however, successful testing has already been completed on stainless steel alloys. This study attempted to extend Sol-Gel use to carbon steel materials. The water based Sol-Gel chemistry develops thin coatings that produce a gradient from the metallic surface, through a hybrid inorganic/organic layer, to the organic epoxy resin (adhesive). Enhanced adhesion is produced by the chemical interaction at the interfaces between the metal and the Sol-Gel and the Sol-Gel and the primer. The Sol-Gel was applied in the same fashion as the Silane chemical mixture. It was also co-cured with the epoxy adhesive in a single heat cycle.

Conversion Coatings - A number of chemical conversion coatings have been researched as surface treatment alternatives to degreasing, grit blasting, or other coupling agents such as Silane or Sol-Gel [2.3]. These conversion coatings offer the potential for high treatment rates. They produce varying degrees of surface organic material and complex oxide coatings. Zinc and iron phosphate treatment solutions can precipitate crystallites onto the steel surface.

Surface analysis and mechanical joint testing have demonstrated high strength and durability in bonded joints prepared with these chemicals. However, one of the main problems with these chemicals is the formation of a loosely adhering layer of iron oxide "smut" that is difficult to remove before bonding but easily pulls away with the adhesive when the joint is stressed. If the

grain size is not carefully controlled, the coating thickness becomes so great that one phosphate crystal precipitates on another and a weak interface is produced. Heat cure epoxies, such as the AF-163 film adhesive used in this study, are especially susceptible to this problem as thermal stresses between the thick conversion coating and the steel substrate can create fractures in the coating. Thus, this steel treatment has a high potential to fail at the metal/metal oxide interface at lower stress levels than expected for the other surface preparation options.

Another major problem with chemical conversion coatings is that the nature of the resulting surface topology is a function of the metallurgy of the substrate. As a result they do not provide consistent results and, in general, offer no performance enhancement over the more easily monitored and uniform grit blast technique. Because of these application drawbacks and concerns over achieving repeatable results, chemical conversion coatings were eliminated from consideration in the surface preparation test matrix.

Steel Chemical Etchants - Effective chemical etching treatments for carbon steels have not been found. Unlike aluminum and titanium, iron does not form coherent, adherent oxides, so it is difficult to replicate the fine micro roughness needed for good adhesion found on other substrate materials. Although various chemical etchants have been tried for both low carbon and stainless steels for many years, none has been widely adopted or shown to be superior to grit blasting [2.6]. One traditional etching chemical for aluminum bonding was considered in this study: Pasa-Jell.

Pasa-Jell is formulated for treatment of aluminum and titanium materials and has been shown to improve bond strength in these alloys by cleaning and producing a surface micro roughness. It has a high content of nitric and chromic acids and is used for corrosion removal and surface etching. It also contains chemical activators and inhibitors that can improve the hydrolytic stability of an interface. Pasa-Jell is inorganically thickened to permit application in localized areas and on vertical or overhead surfaces. In this study, the extrapolation of Pasa-Jell to carbon steel materials was evaluated by coating the adherend surface with this paste and removing the residue with a water rinse. However, exposure times well beyond the routine 10-15 minutes failed to produce any appreciable change in the carbon steel surface. In fact, much of the oxide layer was still intact after almost 30 minutes of exposure to Pasa-Jell. These bench top tests eliminated the Pasa-Jell surface treatment (Option 3) before any specimens were manufactured. This was not a highly desirable surface treatment option anyway since it involved the use and disposal of hazardous materials.

Primers

To achieve satisfactory bonding with metals, it is often necessary to use primers. Metal surfaces that have been freshly abraded are highly reactive and will undergo rapid interaction with water or organic contaminants. Primers protect surfaces from contamination and improve overall bond performance. Based on their performance in aircraft applications and for both aluminum and steel materials, two different waterborne, chromate primers were evaluated: Cytec Fiberite BR6747 (40-72^{o}F storage) and BR127 (0^{o}F storage). The BR6747 primer is more easily applied in field applications because: 1) it can be stored at room temperature, and 2) it can be co-cured with the adhesive. The BR127 primer is designed to be cured immediately after application and

prior to installing the adhesive. However, due to the reasons cited above the BR127 primer was co-cured simultaneously with the adhesive during this investigation.

Corrosion Assessment During Surface Preparation

At various stages of the surface preparation process, test coupons were produced to assess the effects of exposure to atmospheric conditions. The tests were used to determine if corrosion or other bond inhibiting coatings would form on the steel surfaces during any steps of the surface preparation process. Two coupons were produced for each of the six conditions indicated in Table 2-1. These conditions cover before and after chemical treatment and before and after primer applications. The coupons were exposed to medium (60%) and high (90%) relative humidity for two days after the steps marked by asterisks in Table 2-1. During field repairs, it is anticipated that there will be unexpected delays in moving from one installation step to another. These tests evaluated the possible deterioration in a surface that might occur during such delays. However, the humidity chamber tests revealed that there was no degradation in the prepared surfaces nor did any corrosion form in 48 hours of exposure.

2.2 Evaluation of Surface Preparation Options

The purpose of mechanical testing of adhesive bonds is three-fold: to provide engineering design data, to serve as a quality control procedure, and to evaluate the performance and relative merits of various bonding processes. The joint strength and durability tests described below provided information on all three of these items, however, the primary goal was to rank the viability and effectiveness of the candidate surface preparation options.

The tests were performed using a series of coupon test specimens that were designed to approximate essential features and test critical elements of our repair. The adherends were mild steel (ASTM A607) similar to the highly weldable steel used in large shovel and truck construction. The specimens were lap shear, wedge-loaded, and cleavage peel coupons as shown in Figures 2-5 through 2-7, respectively.

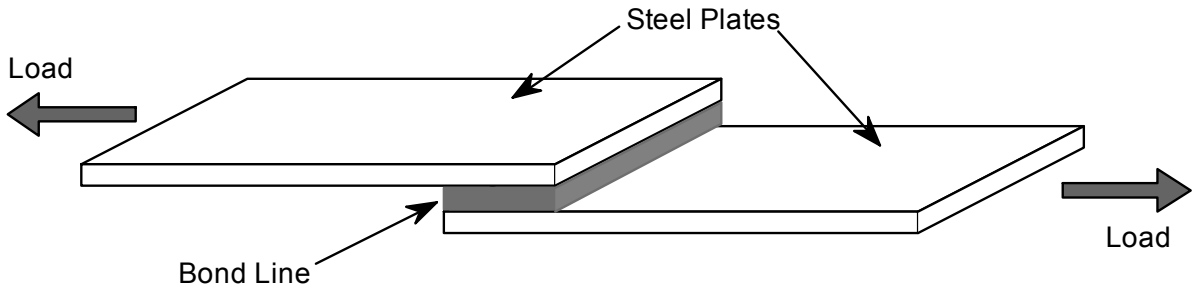

Figure 2-5: Lap Joint Shear Strength Test of Bonded Metal Specimens by Tension Loading With Secondary Bending

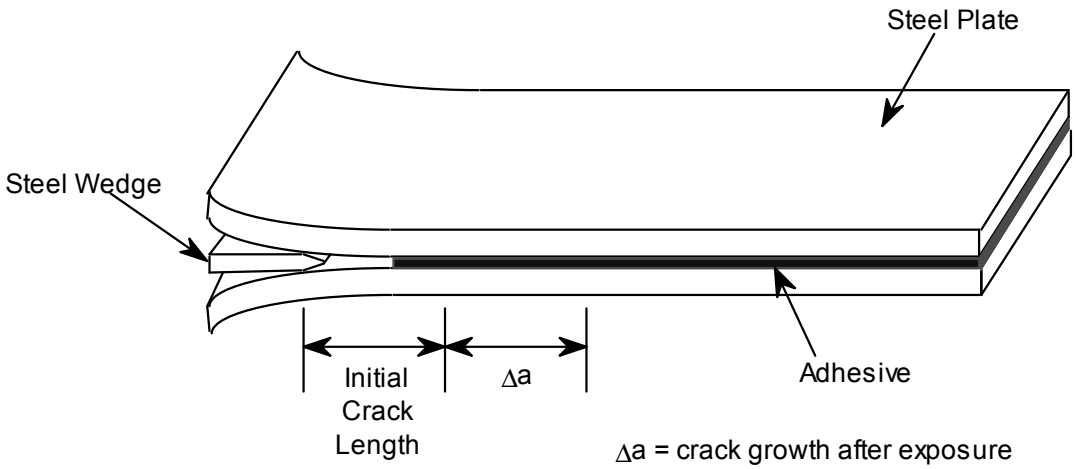

Figure 2-6: Wedge Test to Measure Durability of Adhesive-Bonded Surface

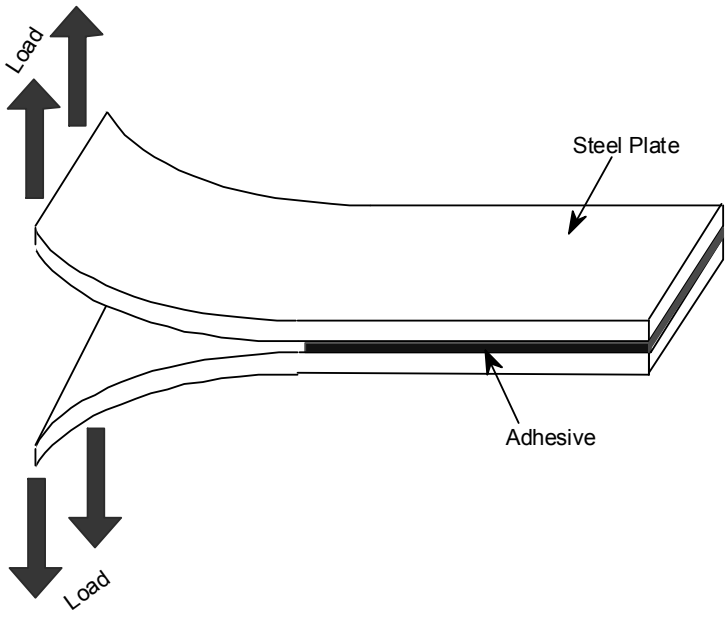

Figure 2-7: Cleavage Peel Test to Determine Crack Extension and Arrest Parameters

A series of coupon tests were conducted to quantify the strength and durability of the bonding process. Similar tests were repeated to evaluate performance in extreme operating environments. Table 2-2 lists the matrix of coupon failure tests for the specimens shown in Figures 2-5 to 2-7. Previous studies have shown that water absorption, represented by the hot/wet conditioning, is the primary cause of performance reduction. This environmental conditioning, followed by testing at temperature extremes, was included in all appropriate coupon testing.

Environmental Durability Tests – Carbon Steel Bonding Process Certification				
Test	**Test Environment**	**No. of Specimens**	**Minimum Requirement**	**Specimen Figure No.**
Lap Shear (0.125" th. adherend; 1" overlap)	75°F	5	4.2 KSI	Fig. 2-5
	-65°F	3	4.2 KSI	
	180°F	3	3.1 KSI	
	hot/wet* @75°F	5	X_{min}	
	hyd. fluid $^{\Delta}$ @75°F	3	X_{min}	
Lap Fatigue (0.125" th. adherend; 1" overlap)	75°F	3	500K cycles	Fig. 2-5
	hot/wet* @75°F	3	500K cycles at 1500 PSI	
Creep Rupture (1600 PSI load for 192 hours)	75°F	3	$\Delta d_{max} = 0.015$"	Fig. 2-5
Adhesive Crack Extension (Fixed Displ., End Bolt Load for G_{Iscc}) (Alt. Surface Durability Wedge Test)	75°F	5	$G_{Iscc} = 3.5$ lb/in	Fig. 2-6
	hot/wet* @75°F	5	70% of G_{Iscc} unconditioned	
	hot/wet* @-65°F	5	70% of G_{Iscc} unconditioned	
Adhesive Crack Extension (Split Pin Test for G_{Ia} & G_{Ic})	75°F	5	$G_{Ic} = 8$ lb/in	Fig. 2-7
	-65°F	5	$G_{Ia} = 6$ lb/in	

* Hot/wet condition represents 30 day exposure to 100% RH @ 120°F or 10% moisture absorption by weight.

Δ 7 day immersion in hydraulic fluid

$X_{min} = X_q - 3.064S_q$ where X_q and S_q are the mean and standard deviation values from unconditioned tests

G_{Ic} = Critical crack extension force (crack initiation)

G_{Ia} = Arrest crack extension force

G_{Iscc} = Environment crack extension force (crack arrest under aqueous exposure)

Table 2-2: Summary of Mechanical and Environmental Durability Tests to Assess Various Carbon Steel Bonding Processes

Lap Ultimate Shear (Fig. 2-5) - Two bonded plates are pulled apart longitudinally to determine ultimate shear strength of the adhesive.

Lap Tension Fatigue (Fig. 2-5) - Two bonded plates are cyclically loaded longitudinally in tension to determine fatigue strength of the adhesive bond.

Wedge Crack Growth (Fig. 2-6) - A wedge is inserted between two bonded steel plates. This test combines the effects of stress and aging environment.

Cleavage Peel & Critical Crack Extension (Fig. 2-7) - Two bonded plates are pulled apart perpendicularly along one edge until a crack begins to propagate along the bond line.
Cleavage Peel – Crack Arrest (Fig. 2-7) - Same as above but the crack arrest load is the maximum load that can be exerted on the joint without further crack growth.

The lap tests provided the ultimate shear strength of the adhesive bond as well as the modulus values for the adhesive. In the wedge test, a wedge is inserted 0.75" into a 1" wide by 6" long coupon. The resultant crack growth is measured over time as the bonded joint is exposed to various environmental conditions. Both test series used 3-4 specimens at each condition and the average results are reported.

A single part, heat cured film adhesive (AF-163) was used to bond all of the test specimens. This adhesive has been shown to provide high strength and durability in the extreme hot, cold, and wet conditions experienced by aircraft. The adhesive was cured for 2 hours at 225^{o}F and 8 psi (simulating vacuum pressures attainable in the field). Hot-wet conditioning was achieved by 30 day exposure to 100% RH at 140^{o}F. In addition, zero degree conditioning was used to study the performance of the bonded joints during winter operation. These environmental exposures were followed by coupon testing at the hot (140^{o}F) and cold (0^{o}F) temperature extremes. Ambient conditioning and testing was also conducted to complete the range of expected operating conditions and to provide baseline data.

2.2.1 Wedge Test

The wedge test specimen combines the effects of stress with aging environments of temperature and humidity. Figures 2-8 to 2-10 show the crack growth as a function of exposure time to the various environments. In most of the samples, a significant percentage of the total crack growth takes place in the first 48 hours when the driving force for the crack is at its maximum. The crack growth tends to stabilize towards a particular value after about 200 hours of exposure. The total crack growth, however, depends upon the surface preparation process used for the joint. The more extensive crack growth in Figure 2-10 (hot/wet), versus growth measured in the Figure 2-8 (room temperature) and 2-9 (cold) conditions, show that water absorption, represented by hot/wet conditioning, is the primary cause of performance reduction.

At ambient conditions, Figure 2-8 shows that the surface with no chemical treatment (Option 4) performed the best followed by the co-cured Silane-primer options (Options 6 & 8). As expected, all of the results are tightly clustered with only a 12% separation between the shortest and longest crack growth. At zero degrees (Figure 2-9), Option 4 continued to perform the best followed by both the Silane and Sol-Gel surface treatment options. It is here that the benefits of grit blasting begin to appear as the hand sanding Option 9 allows for almost twice the crack growth as the other grit blast processes. The primary benefits of grit blasting and the use of primers are seen in the performance of the bonds in hot/wet conditions. Figure 2-10 contains the largest spread in results with both the Silane (Options 6 & 8) and Sol-Gel (Option 2) processes performing the best. Interface durability is a major limitation in the adhesive system. The addition of Silane clearly improved interfacial durability. Use of primers – coupling agents that effectively stabilize the iron surface against corrosion – also improved the long term durability of the joint. Surprisingly, Option 4 with no chemical treatment continued to compare well, however, the lap shear results will determine if this good crack mitigation ability is accompanied

by sufficient adhesive strength. The hand sand (Option 9) and non-primer (Option 5) methods performed the worst with crack growth approximately 95% greater than the optimum processes.

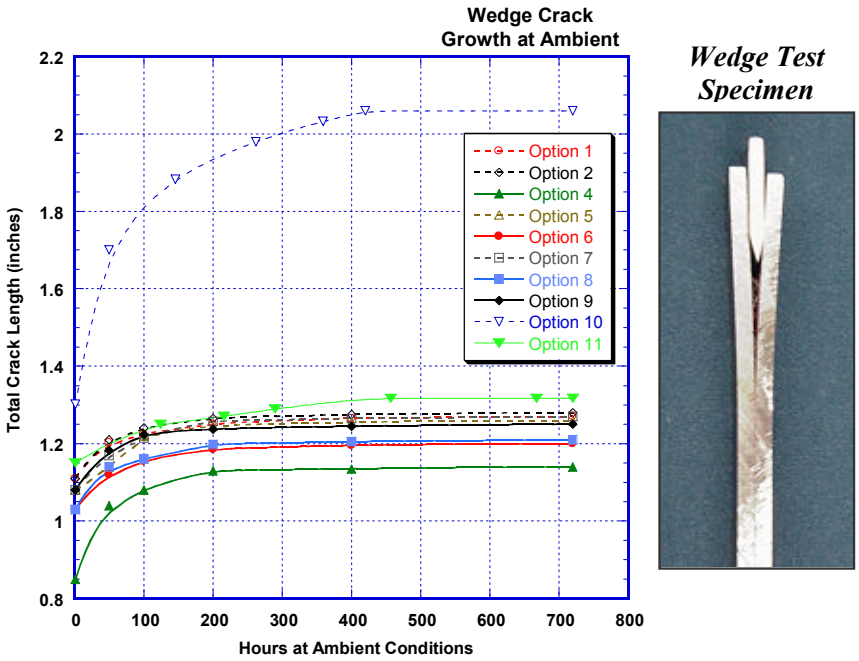

Figure 2-8: Comparison of Wedge Crack Extension for the Ten Surface Preparation Options - Carbon Steel Bonds at Ambient Conditions

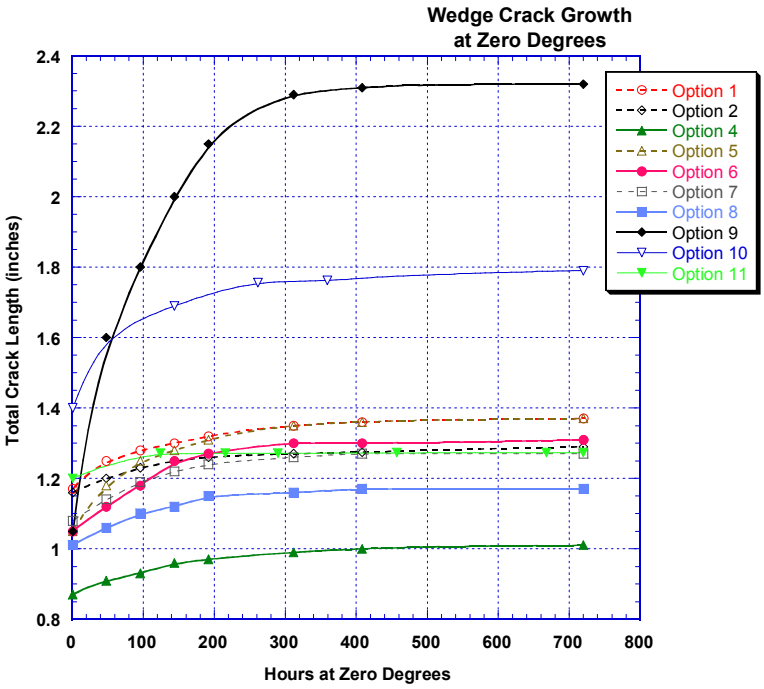

Figure 2-9: Comparison of Wedge Crack Extension for the Ten Surface Preparation Options - Carbon Steel Bonds at Zero Degree Conditions

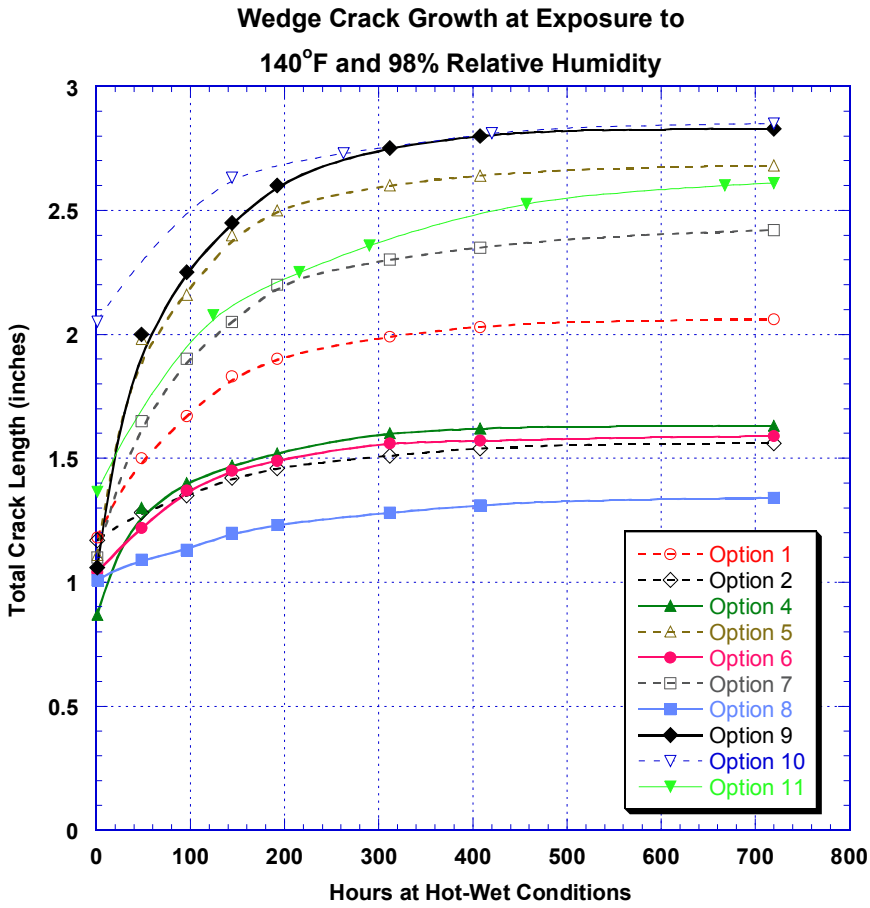

Figure 2-10: Comparison of Wedge Crack Extension for the Ten Surface Preparation Options - Carbon Steel Bonds at Hot/Wet Conditions

Figure 2-11 shows the extreme deformation required to fail the wedge test specimens. Threaded holes were machined into the ends of some wedge tests specimens. Two opposing bolts were then used to produce enough deformation to fracture the adhesive layer. The goal was to demonstrate that adhesive products would appear on each side of the mating steel plates (see lower left photo in Fig. 2-11). This indicates that the mode of failure was adhesive (vs. cohesive disbonding) and that the full strength of the adhesive material was achieved.

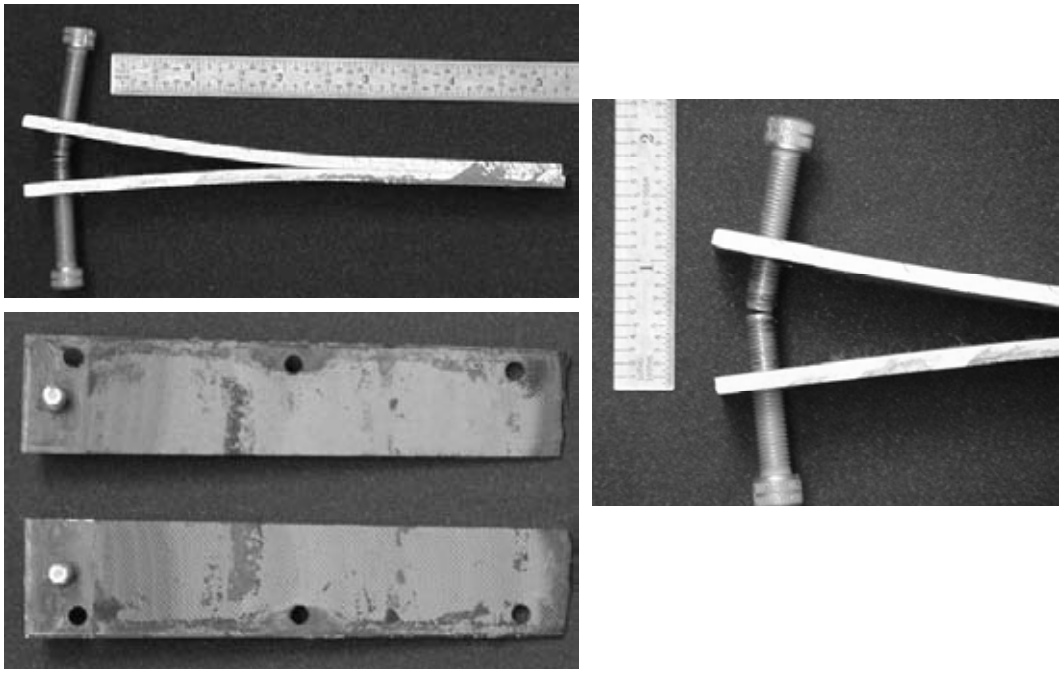

Figure 2-11: Extreme Wedge Test Needed to Fail Adhesive and Proof of Optimum Cohesive Failure Mode of the Adhesive

2.2.2 Lap Shear Ultimate Failure Tests

The lap shear results are presented as histograms in Figure 2-12. This test series used 3 to 4 specimens at each condition and the average results are reported. At ambient conditions, the Sol-Gel and Silane processes were superior with less than a 10% spread in the ultimate shear stress levels ($\gamma_{ambient} \approx 5{,}200$ psi). The zero degree exposure tests showed similar results while also revealing that the ultimate shear stress levels are increased at reduced temperatures ($\gamma_{zero} \approx 6{,}000$ psi). These results exceed the recommended minimum strength requirements listed in Table 2-2. While the hot/wet conditioning reduced the ultimate shear stress levels in all surface preparation methods ($\gamma_{hot/wet} \approx 4{,}000$ psi), processes using Silane and Sol-Gel retained most of their initial strength. Options 6 and 8 retained 82% of their shear strength vs. the ambient test specimens while Options 1 and 2 retained 78% of their full baseline strength. In all cases, the simple, primer-only approach that performed well in the wedge tests (Option 4), produced the lowest ultimate shear stress in the test specimens.

The most critical test for bonded joints is durability in humid, high stress environments. Moisture may affect adhesive joints by: 1) hydrolyzing the adhesive, 2) displacing the adhesive at the adhesive adherend interface and, 3) by promoting corrosion at the interface with the steel adherend. Thus the adhesive as well as the surface preparation process must be able to resist this type of degradation. The hot/wet condition tests revealed that mechanical preparations alone do not provide durable bonding substrates. Virgin grit-blasted steel surfaces produced joints with relatively little durability. Figure 2-10 shows that the untreated steel surfaces (Options 4, 5, & 9) experienced more rapid crack growth during humidity chamber exposure.

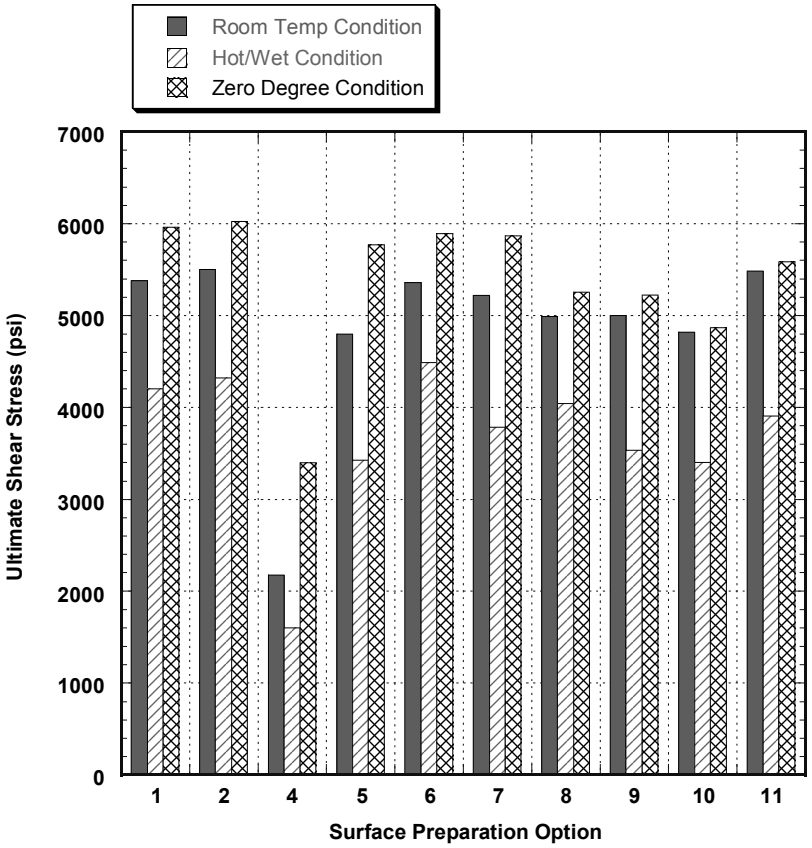

Figure 2-12: Ultimate Shear Stress Results for Each Surface Preparation Process

Clearly, the important parameters include surface roughening and chemical treatment/protection. Results from joints without chemical coupling agents and/or primer are inferior – especially when exposed to hot/wet conditions. Examination of the failure surfaces showed that undesirable adhesive failure (disbonds along bond line) occurred in surface preparation options 4, 5, and 9. Cohesive failure (fracture of the adhesive indicating that the full strength of the adhesive was achieved) was observed in the Sol-Gel and Silane surface preparation methods.

Optimum behavior of the bonded joints would cause the failure mode to be cohesive fracture of the adhesive (as opposed to adhesive disbond between the adhesive and the substrate). This would allow the full strength of the adhesive to be utilized in the joint and repairs could be designed using the entire ultimate strength of the adhesive. Since it produces a reduction in processing time, co-curing the primers with the adhesive provides a tremendous advantage over precuring the primer followed by a separate adhesive cure cycle. However, the reduction in processing time is not a benefit if durability is lost. Cohesive failure of the specimens revealed that co-curing the primer did not reduce the performance of the bonded joint.

Cohesive fracture indicates that the bonding interface is stable under the test environment and that the adhesive polymer is the limiting factor in the joint performance. On the other hand, joint

failures that are predominantly interfacial (disbond between adhesive and steel surface) indicate unpredictable joint failure which will be dependent on its stress field and environmental exposure history. These results reinforce the previously derived conclusions from the wedge tests about the efficacy of the grit blast-Silane-primer surface treatment.

2.2.3 Lap Shear Fatigue Durability Tests

In addition to the ultimate shear stress tests, tension-tension fatigue tests were conducted using the lap shear specimens. The two main potential causes of structural failure in composite doubler installations stem from crack growth in the parent steel and adhesive disbonds. When disbonds occur, they may lead to joint failures. By their nature, they occur at an interface and are, therefore, always hidden. A combination of fatigue loads and other environmental weathering effects can combine to initiate these types of flaws. The fatigue tests studied the durability of the bonded joint and the potential for critical failure between the two adherends. The upper end of the applied tension loads was 50% to 55% of the ultimate shear stress values determined by the failure tests. Figure 2-12 shows that the ultimate shear stress values were on the order of 5,000 psi so the upper tension load was 2,500 lbs. If no failure was observed in the test specimen after 245,000 cycles, the upper load level was increased to 2,750 lbs.

Figures 2-13 to 2-15 show the fatigue results for Room Temperature (70 ^{o}F), Zero Degree (0 ^{o}F), and Hot-Wet (140 ^{o}F) conditioning/testing, respectively. Once again, the Sol-Gel and the Silane options (note Options 2 and 6) produced the best results across all operating conditions. In all cases, the simple primer-only (no chemical treatment approaches) that performed well in the wedge tests (Options 4 and 5), produced the least durable joints. When subjected to hot-wet conditioning, these joints could only sustain a relatively few fatigue cycles before failing (see Fig. 2-15). A significant difference was also observed between the Option 6 Silane and the Silane processes in Options 7 and 8. These results indicate the affects of different primers and of post grit blast chemical cleaning. It appears that the Silane mixture and the BR-6747 primer are the only chemicals that should be applied after the grit blast process. The use of post grit blast cleaning chemicals degrades the joint's durability. Also, the BR-127 primer is usually cured at elevated temperature prior to the bonding process. The co-cure approach used here may have contributed to the poor performance shown in the Option 7 results.

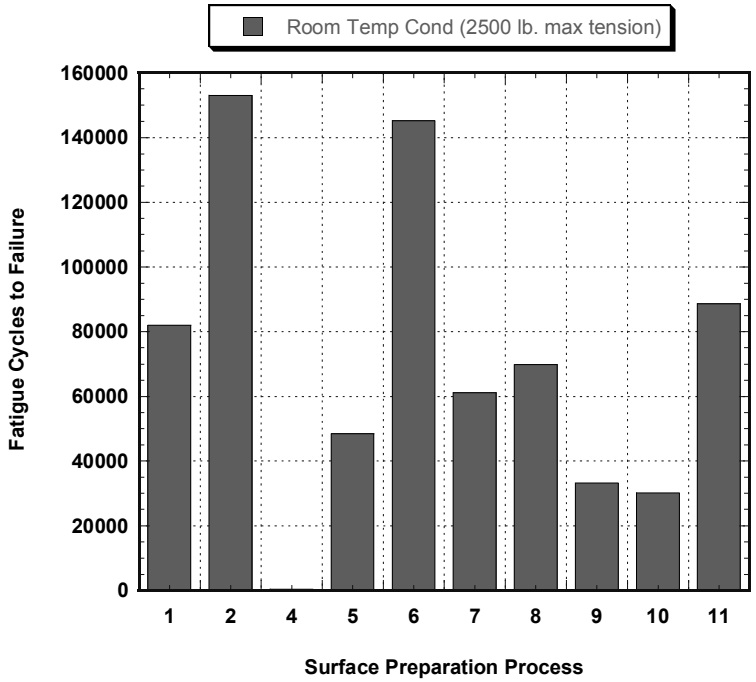

Figure 2-13: Cycles to Lap Joint Failure at Room Temperature Testing (tension-tension up to 50% of shear ultimate values)

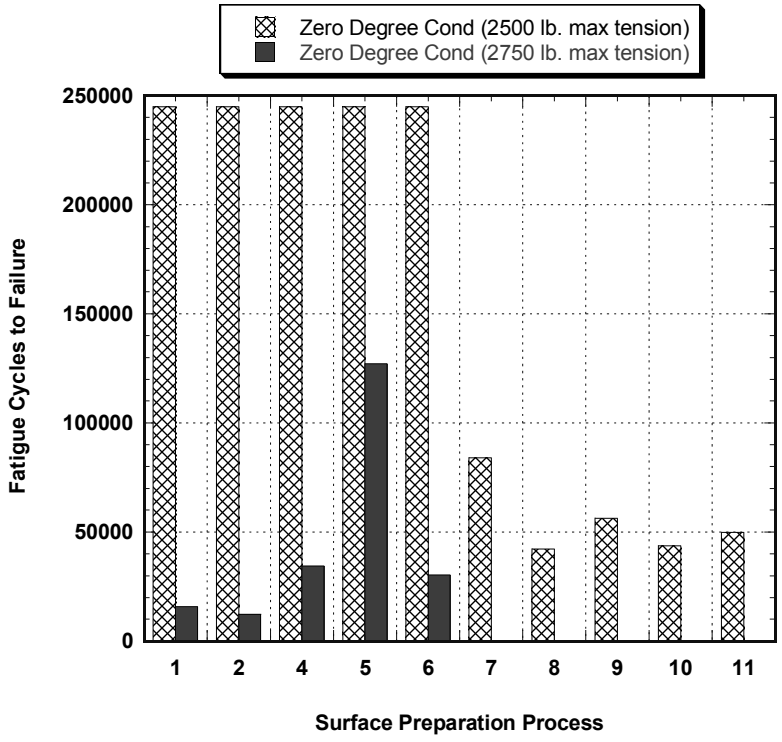

Figure 2-14: Cycles to Lap Joint Failure at Zero Degree Testing (2,500 lb. tension-tension followed by 2,750 lb. fatigue)

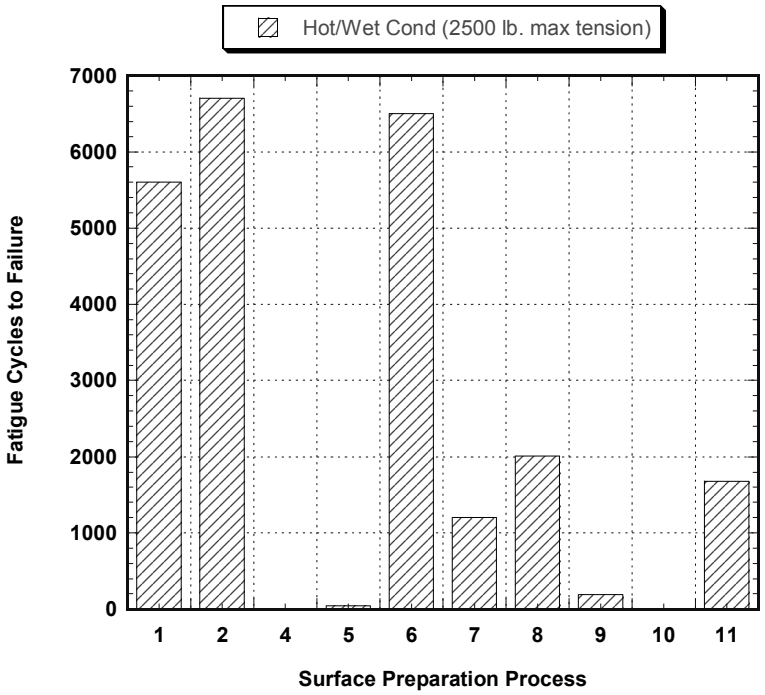

Figure 2-15: Cycles to Lap Joint Failure at Hot/Wet Testing (140^{o} F) (2,500 lb. tension-tension fatigue)

The mechanical interlocking of the hardened epoxy adhesive with the substrate increases the initial bond strength but its real importance is in improving bond durability. With the high strength epoxies used in most structural applications, moisture can completely disrupt the chemical bonds as a result of dispersion forces, leading to catastrophic failure unless interlocking is present.

2.2.4 Adhesive Modulus

Adhesives for structural applications must possess high strength and be able to maintain this strength and stiffness under all deteriorating influences. The deteriorating influences may be broadly classified as physical (stresses) and chemical (heat, moisture, foreign contaminants). One important measure of an adhesive's strength is its elastic modulus. Load-displacement data from the lap shear testing was used to arrive at modulus of elasticity values for the AF-163 adhesive. Figure 2-16 shows the adhesive modulus values for operation in Room Temperature (70 ^{o}F), Zero Degree (0 ^{o}F), and Hot-Wet (140 ^{o}F) conditions. The various surface preparation options did produce some slight differences in adhesive modulus due to microscopic fracture and slippage in the joint during the "elastic" portion of the load response. However, for the most part, the elastic constants derived from these tests were quite similar. The effect of temperature on adhesive modulus – modulus increases as operating temperature decreases – was also evident. The AF-163 modulus values were on the order of 50,000 lbs/in.^{2} at 140^{o}F, 55,000 lbs/in.^{2} at 70^{o}F and 62,000 lbs/in.^{2} at 0^{o}F.

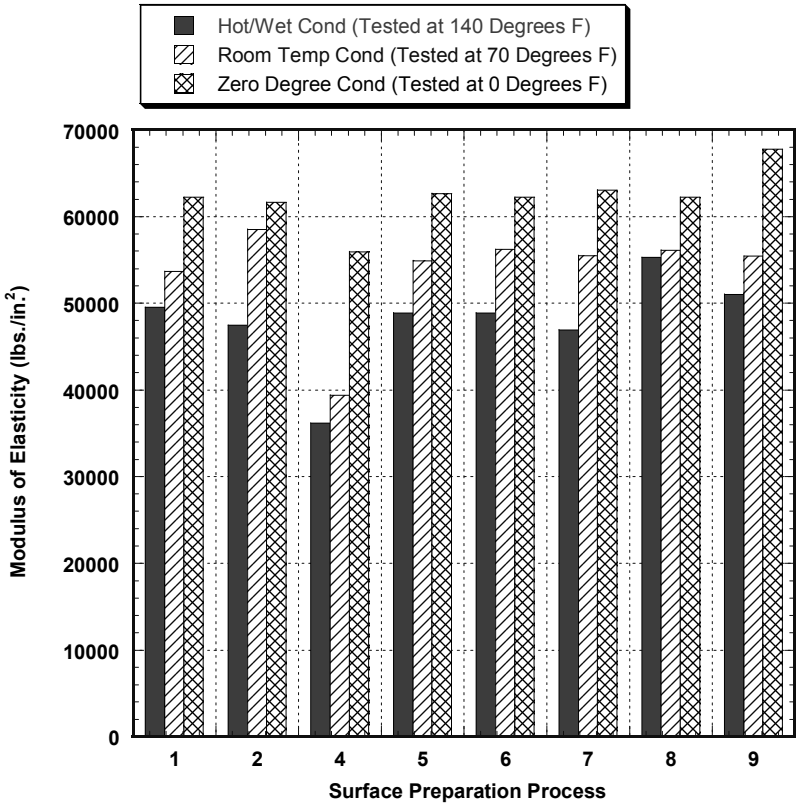

Figure 2-16: Affect of Temperature on Adhesive Modulus

2.2.5 Critical Crack Extension and Crack Arrest

A series of other parameters that can be used to study the performance of a bonded joint are the Critical Crack Extension and Crack Arrest properties. To measure these properties, the wedge test specimens shown in Figure 2-6 are used. However, the specimens are loaded in a cleavage peel arrangement shown in Figure 2-7. In the cleavage peel tests, the specimen is slowly loaded as per Fig. 2-7 (displacement control) and the following parameters are measured for each surface preparation option at the various environmental conditions:

P_c = Critical Crack Extension (load producing crack growth)

P_a = Crack Arrest Load (relief level at which crack arrests)

a_c = crack growth caused by critical load

a_a = crack growth that occurs as crack arrests

These parameters were then used to calculate the following crack extension properties:

G_{Ic} = Critical crack extension force (crack initiation)
G_{Ia} = Arrest crack extension force

Critical Crack Extension represents the minimum load required to propagate a crack along the bondline. This separation can be the result of adhesive fracture, disbond growth between the adhesive and adherend, or a combination of the two phenomena. The Crack Arrest Load is the maximum load that can be exerted on the bonded joint without further growth in the adhesion line crack. The tests were conducted at the same temperature as the associated coupon conditioning: 0^{o}F, RT, and 140^{o}F. Each specimen was loaded until a maximum load level was observed (P_c). At that point the machine crosshead was stopped and the load was allowed to drop until an equilibrium was reached (crack propagation stopped at crack arrest level). The initial (pre-test) and final (post-test) crack growths were measured optically using a 50X magnification. In both the Critical Crack Extension and Crack Arrest plots, the goal is to produce the largest load levels (solid portion of the bar charts) while minimizing the degree of crack growth (cross-hatched portion of the bar charts).

Test Procedure:

1. Mount in tensile test machine using eye bolts and clevis arrangement such that specimen is at right angle to the loading direction.
2. Observe load on the specimen while moving crosshead at 0.1 to 0.2 inch/min. When the load peaks (critical load) stop the crosshead movement.
3. With the crossheads stopped, allow the crack to stop propagating and the reducing load to reach equilibrium. Without using any additional force, place a wedge in the opening between the plates as shown in Fig. 2-6.
4. Record the peak (P_g = critical load) and the equilibrium (P_a = arrest load)
5. Measure final crack length.

The results are plotted in Figures 2-17 to 2-19. In general it can be seen that the hot-wet conditions are the most detrimental to the joint and produce the lowest crack extension and arrest values. Once again, the peel strength of the joint manufactured with the Option 4 process (no chemical treatment with primer) is shown to be quite high. However, the poor shear strength and fatigue performance of this surface preparation process removes Option 4 from consideration. Overall, the results from operation in all environments indicate that the Silane surface preparation processes produce the best bondline strengths and crack mitigation. Furthermore, Option 6 performs the best out of the three Silane processes. The process with the least resistance to moisture ingress (Option 5 with no primer protection) and the process with the non-uniform surface roughening (Option 9 with hand sanding only) produced the poorest results in the cleavage peel tests.

Ideal adhesive joint designs should utilize adhesives in the mode that makes the best use of their mechanical properties (i.e. they should be used in compression, shear, or tension). Cleavage and peeling forces should be avoided as much as possible. Many of the composite doubler repair applications involve shear joints. In addition, the repairs should be designed to produce joints that provide low average stresses and avoid high local stresses. The doubler taper, overall footprint, and thickness must be balanced to provide sufficient strength while achieving a gradual load transfer from the parent steel structure. Although the peel forces will be minimized, this is

still a good test to differentiate and quantify the capabilities of the candidate surface preparation options.

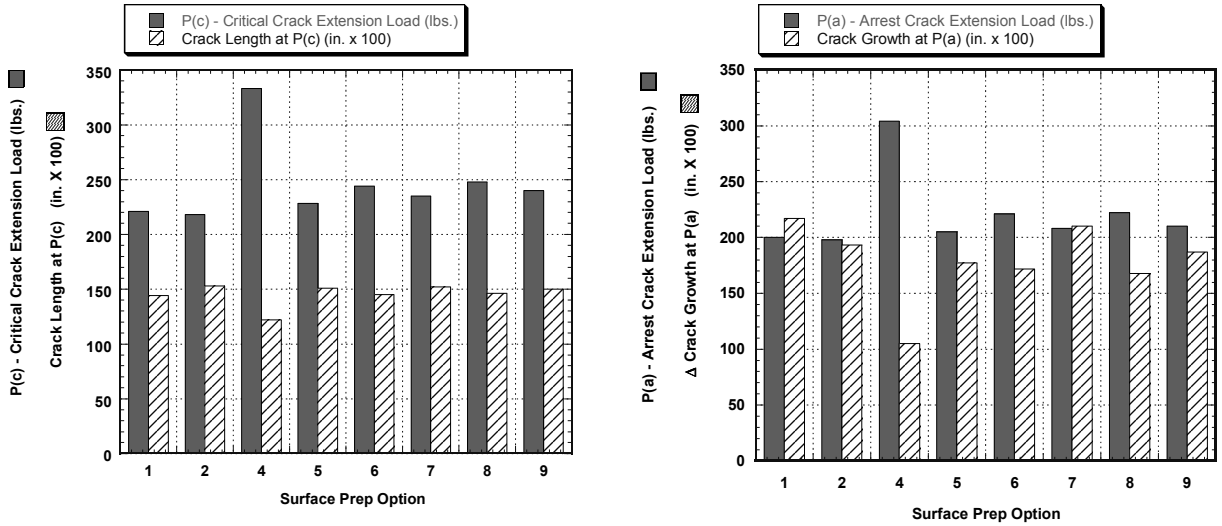

Figure 2-17: Critical Crack Extension and Crack Arrest Parameters for Room Temperature Testing (70^{o} F)

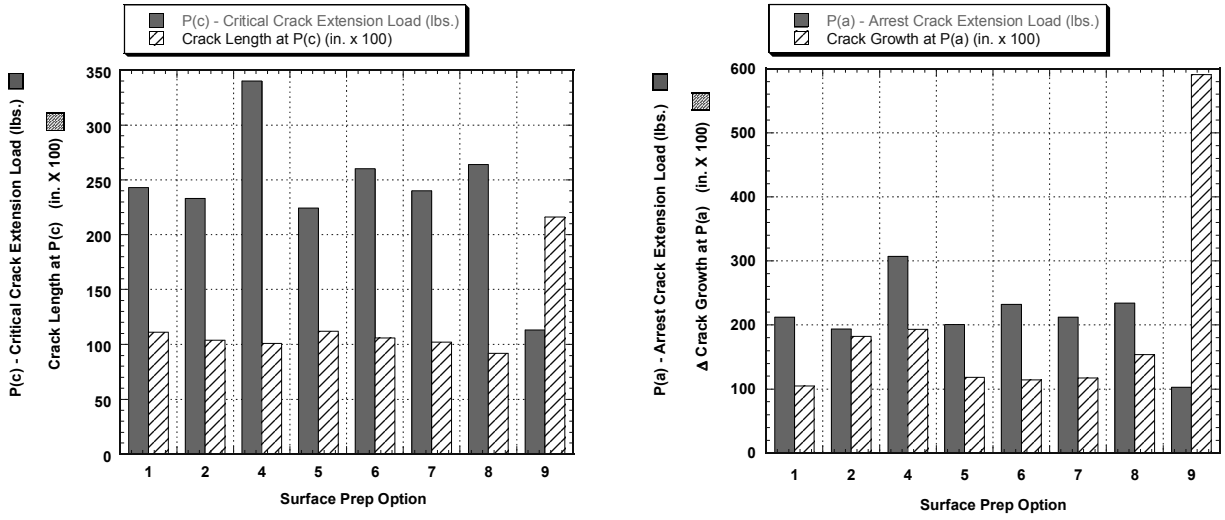

Figure 2-18: Critical Crack Extension and Crack Arrest Parameters for Zero Degree Testing (0^{o} F)

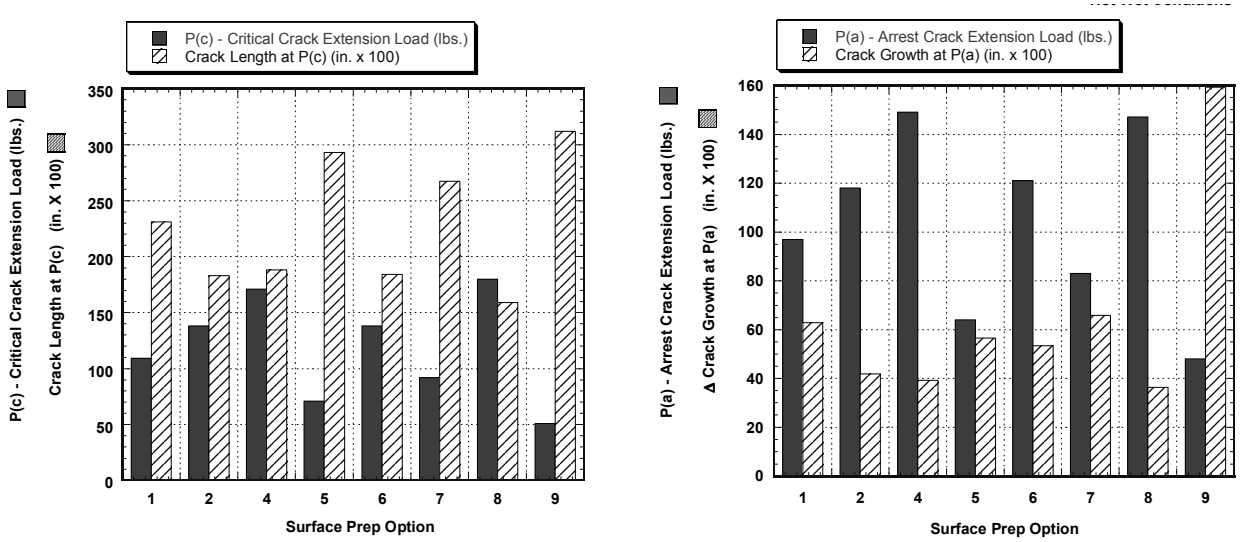

Figure 2-19: Critical Crack Extension and Crack Arrest Parameters for Hot/Wet Testing (140^{o} F)

2.2.6 Adhesive vs. Cohesive Fracture Surfaces

Failure of the adhesive joints occur as fracture of the adhesive or as a separation between the adhesive and the adherend. Figure 2-20 depicts these two failure modes which are defined as follows:

> Adhesive Failure – Joint fails by adhesive film detaching from one or both of the substrates. This is usually caused by poor surface preparation and/or the deteriorating effects of the operating environment.
>
> Cohesive Failure – Adhesive joint fails through fracture of the adhesive film. This provides the highest possible joint strength (full strength of adhesive is achieved).

The strengths measured in the lap shear tests reflect the degree of cohesive and adhesive failure in the respective joints. For example, the low ultimate shear stress values produced by the Option 4 test specimens indicate that a large percentage of the failure surface will show adhesive failures. Conversely, when inspecting Option 6-8 post-failure surfaces, it was observed that the failures did not occur at the steel/Silane interface or at the Silane/adhesive interface, but rather at the boundary layer region that is strengthened by the presence of the Silane coupling agent. The addition of the Silane clearly improved the interfacial durability so that cohesive fracture of the adhesive could be reliably produced. By avoiding adhesive disbond failures, the full strength of the adhesive can be achieved. Figure 2-21 shows the adhesive regions from the failed specimens that used Option 4 (no chemical treatment) and Option 6 (Silane treatment) processes. In the photo on the left, note the clear presence of the pink adhesive on both halves of the specimen indicating that the adhesive has fractured. In the photo on the right, note the large number of dark regions which are the exposed portions of the steel surface. These are disbond areas where the adhesive separated from the substrate steel material. The diagonal patterns present in both

photos are created by the scrim cloth that is used to carry the film adhesive. It is estimated that the better surface preparation techniques produced joints with less than 1% adhesive failure while the poor surface preparation techniques produced joints that exhibited 50% to 75% adhesive failure.

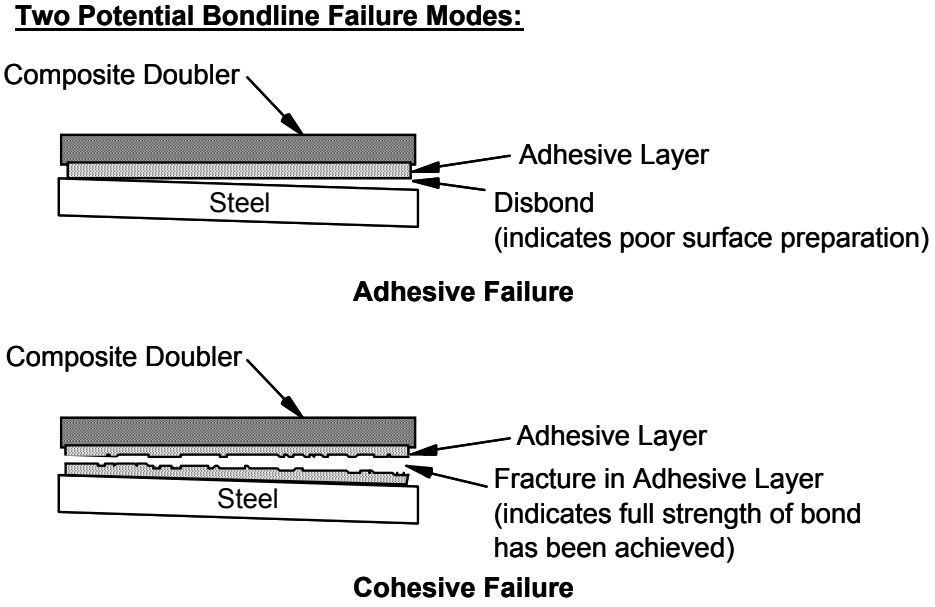

Figure 2-20: The Two Primary Failure Modes in Adhesive Joints

2.3 Final Determination of Optimum Process for Bonding Composites to Steel Structures

The variables studied in this effort relate to the three basic methods of surface treatment for good adhesion: 1) removal of contamination or weak boundary layers such as corrosive scale or oxide layers, 2) changing the surface chemistry, and 3) changing the surface texture. By comparing the hand sanded surfaces with the grit blast family of bonds, it can be seen that the uniformity of the roughness provided by grit blasting improves both the ultimate shear strength and crack mitigation capability of the bond. The use of chemical coupling agents and protective primers are also necessary to optimize the performance of bonded joints in carbon steel structures. Conversely, use of timesaving but marginal methods such as hand sanding plus solvent cleaning produces weak bonds with poor environmental durability. The chemical treatment and primer co-cure process validated in this study eliminates the need for two elevated temperature cure cycles. This minimizes complexity and saves installation time.

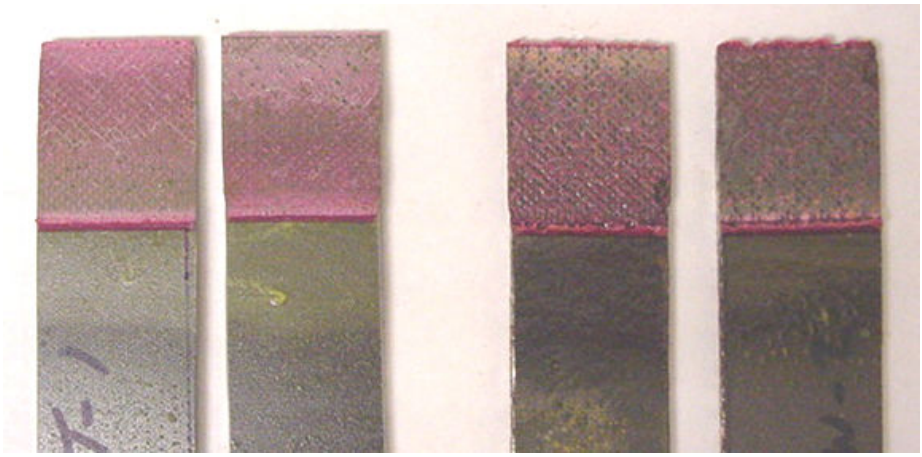

Option 6
Primarily
Cohesive
Fracture

Option 4
Primarily
Adhesive (Disbond)
Failure

A. Macroscopic View of Failure Surfaces

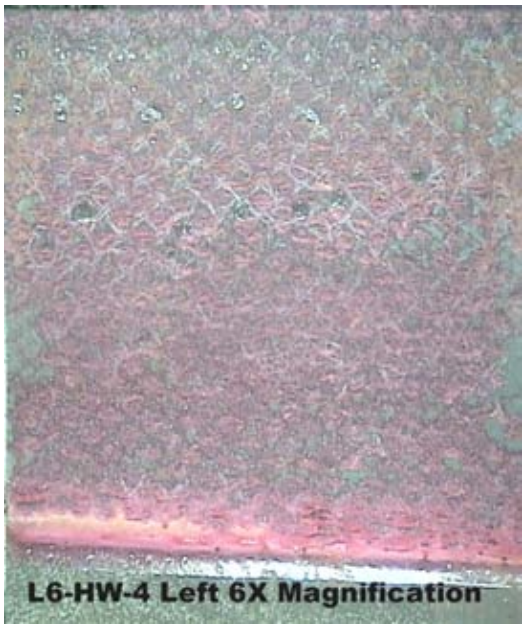

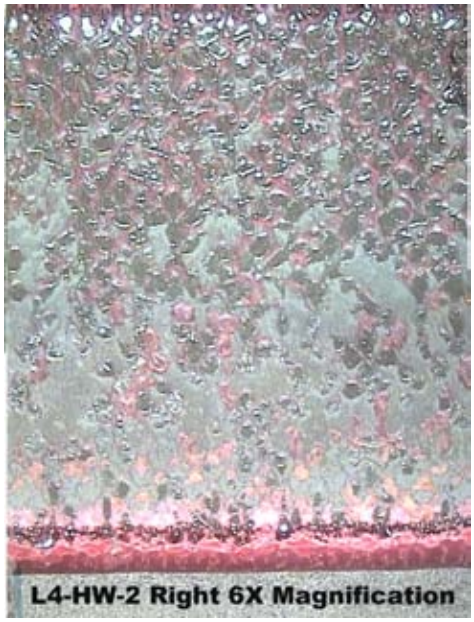

Cohesive Fracture of Adhesive Film
(Option 6 silane treatment)

Adhesive Failure at Interface
(Option 4 no chemical treatment)

B. Microscopic View of Failure Surfaces

Figure 2-21: Photo of Fracture Surface in Lap Shear Specimens

Table 2-3 summarizes the overall capability of each surface preparation process by ranking its relative performance in each of the tests described above. While Option 4 produced the best results for all of the peel stress-oriented tests (wedge and cleavage peel), it produced the poorest numbers in the shear stress-oriented tests (lap shear, shear fatigue). Since shear loading is one of the primary features of these composite repairs, it is a major consideration and sufficient reason for rejecting the Option 4 process. The rankings show that both the grit blast-Sol-Gel-primer and the grit blast-Silane-primer processes produce the best overall results for bond strength and long-term durability. The results were very repeatable with less than 3% variations observed among common test specimens. *The highest ranking across the range of qualification tests was produced by Option 6. For the most part, it is always ranked in the top 3 surface preparation options. When ease of installation and availability of materials are considered, the Silane process (Option 6) becomes the obvious surface preparation of choice for this composite doubler repair program.* Figure 2-22 is a schematic summarizing the Option 6 installation process. The process uses a single heat cycle to simultaneously co-cure the Silane, primer, adhesive film, composite doubler and fiberglass cover ply. As discussed above, there are situations where grit blasting is not desirable or cannot be performed. In such cases, surface sanding is the next best option for producing the necessary surface roughness. Of the three surface sanding processes (Options 9-11), Option 11 produced the best overall results in the various bond tests. Test specimens were also prepared using the Option 11 sand procedure. They were tested in fatigue environments to establish the performance of composite doublers in situations where grit blasting cannot be performed (see Chapter 4).

Test	Rank of Surface Preparation Option									
	1	2	4	5	6	7	8	9	10	11
Wedge Crack Growth										
Room Temp	7	8	1	5	2	6	3	4	10	9
Zero Degree	7	5	1	8	6	4	2	10	9	3
Hot-Wet	5	2	4	8	3	6	1	9	10	7
Lap Ultimate Shear										
Room Temp	3	1	10	9	4	5	7	6	8	2
Zero Degree	2	1	10	5	3	4	7	8	9	6
Hot-Wet	3	2	10	8	1	6	4	7	9	5
Lap Tension Fatigue										
Room Temp	4	1	10	7	2	6	5	8	9	3
Zero Degree	4	5	2	1	3	6	10	7	9	8
Hot-Wet	3	1	10	8	2	6	4	7	9	5
Cleavage Peel - Critical Crack Extension										
Room Temp	7	8	1	6	3	5	2	4	-	-
Zero Degree	4	6	1	7	3	5	2	8	-	-
Hot-Wet	5	4	2	7	3	6	1	8	-	-
Cleavage Peel - Crack Arrest										
Room Temp	7	8	1	6	3	5	2	4	-	-
Zero Degree	5	7	1	6	3	4	2	8	-	-
Hot-Wet	5	4	1	7	3	6	2	8	-	-

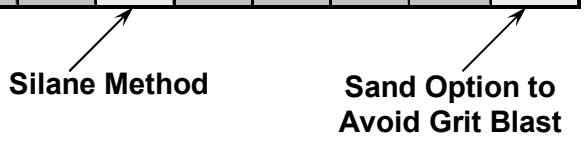

Table 2-3: Summary of Overall Performance of the Surface Preparation Options

Figure 2-23 is a flowchart of the installation steps along with the time required to complete each step. Appendix A contains a photo summary of the surface preparation and composite doubler hot bonding process that was developed for Syncrude carbon steel structures. Appendix B provides a detailed procedure for installing a composite doubler repair on steel structures.

The results presented here provide the first step in applying adhesively bonded composite doublers as an alternative to the fusion fillet welding of steel plates to repair trucks and shovels used in the Syncrude mining and oil recovery operation. By combining these test results with composite doubler research from the aviation industry, it appears that the use of heat-cured epoxy resins and fiber-reinforced composites is feasible for replacing fillet welded plates on carbon steel structures. Composite joints can provide sufficient strength requirements while maintaining needed flexibility and improving durability. The limiting factor in bonded composite repairs will probably be their performance in compression stress fields.

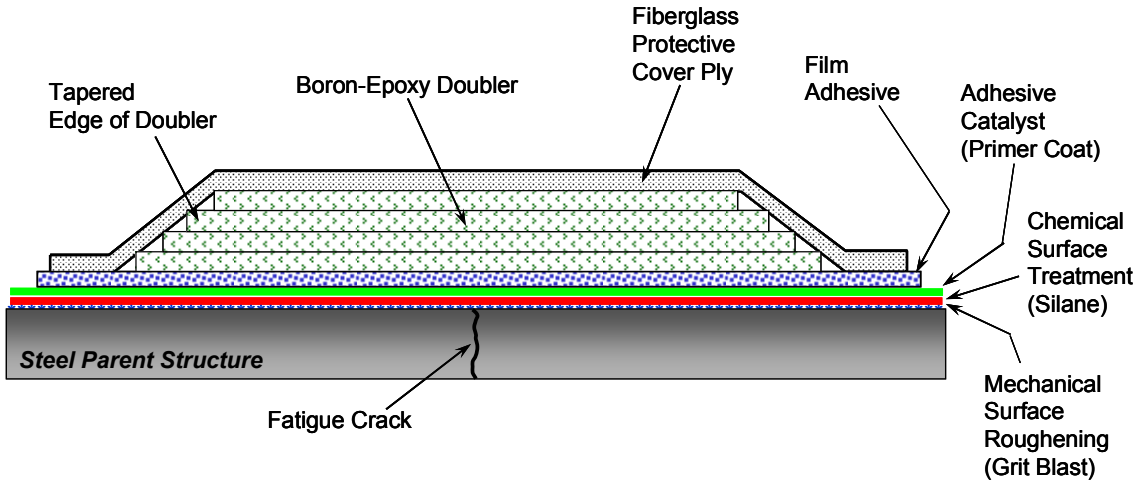

Figure 2-22: Summary of Optimum Composite Doubler Installation Process for Steel Structures

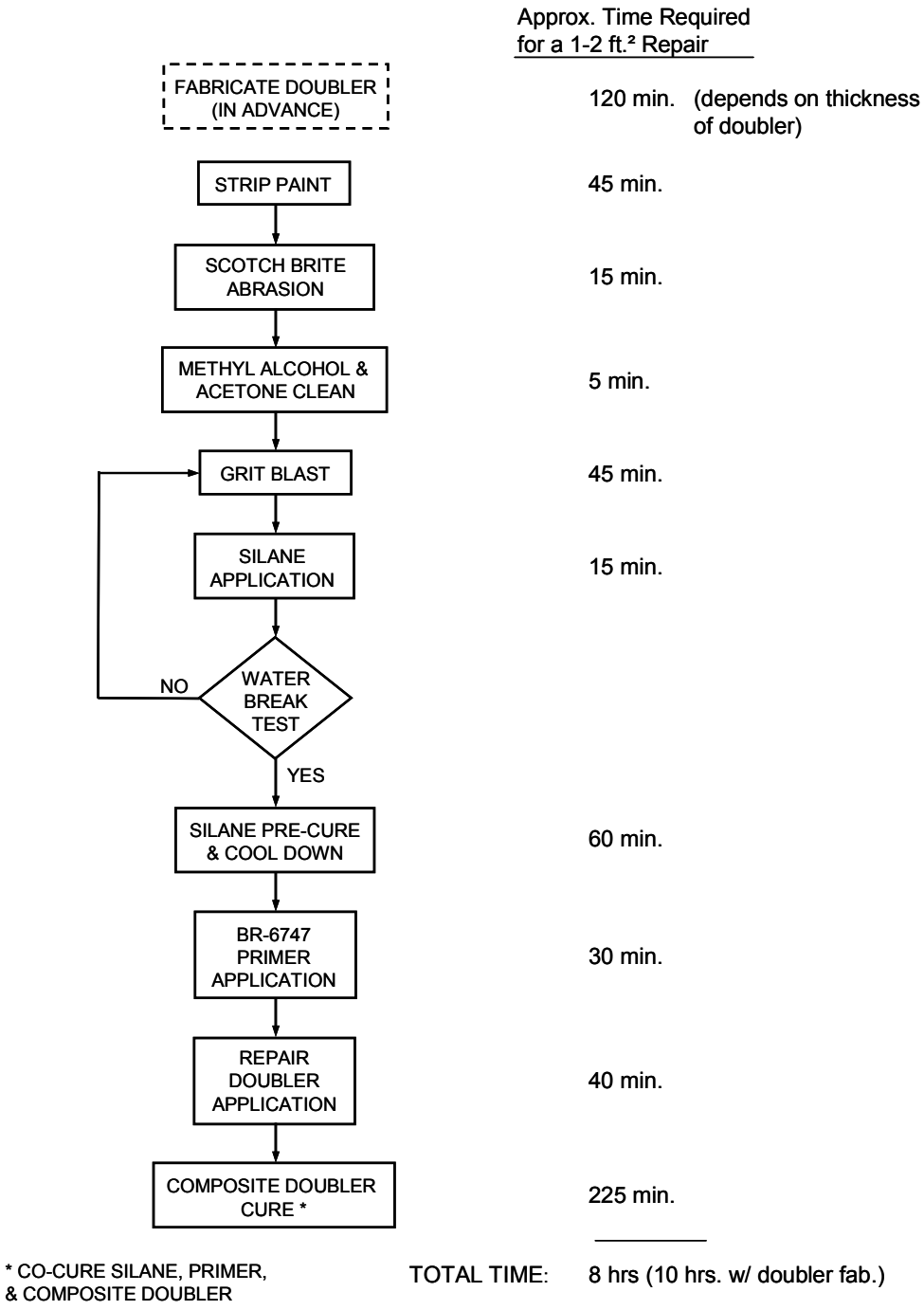

Figure 2-23: Flowchart Summary of Composite Doubler Installation on Steel Structures

2.4 Heat Source/Sink Analysis

One of the key issues in assessing the viability of composite repairs for thick steel structures is the ability to produce sufficient, controlled temperatures in the areas to be repaired. The method of applying the temperature must allow the doubler to be cured within the allowable temperature envelope and avoid any degradation in the surrounding structure or systems. Heating options include the use of traditional rubber/coil heat blankets for composite material cures and/or the use of ceramic heat blankets currently used by Syncrude in its welding process.

With the list of potential repair applications in mind and some idea of the approximate size of the patches, a heat source and heat sink test was conducted on a thick-walled Syncrude structure. Figure 2-24 shows the shovel bucket that was used for this test. The wall of the bucket was approximately 3" thick and the heat sinks included a thicker region immediately adjacent to the zone to be heated and a free edge exposed to open air. So, this portion of the study was attempting to produce proper heat levels in extremely thick steel structures. It was immediately apparent that the conventional 5W heat blankets used in thin-walled aircraft repairs could not provide the heat necessary to produce cure temperatures of 225^{o}F. Discussions with Cooper-MQS Canada indicated that the Cooperheat ceramic blankets and associated control system would have sufficient power and control to produce the desired temperature profile.

The approach involved mounting the Cooperheat flexible ceramic pad heaters around the area to be "repaired" and inducing the temperature in this region using the projection heating method depicted in Figure 2-25. Numerous rings of heat blankets can be placed around the region to be repaired and placed over large flanges, etc. to counteract the heat sinks. Figure 2-26 shows several of the blankets and associated thermocouples being installed around the 18" X 18" repair region. Tack welds were used to secure the heaters and thermocouples. Figure 2-27 shows the final arrangement of ceramic heaters and thermocouples around the test site. The thermocouples around the exposed steel repair region and a close-up of the ceramic heat blankets are shown in Figure 2-28. Figure 2-29 is a photo of the complete assembly with insulation placed over the 7 heat blankets.

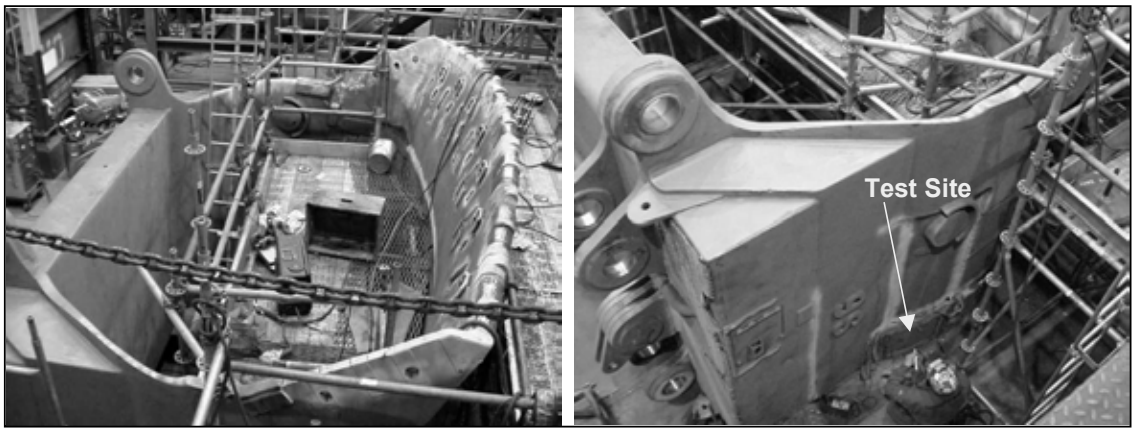

Figure 2-24: View of Shovel Bucket and Heat Source/Sink Test Location

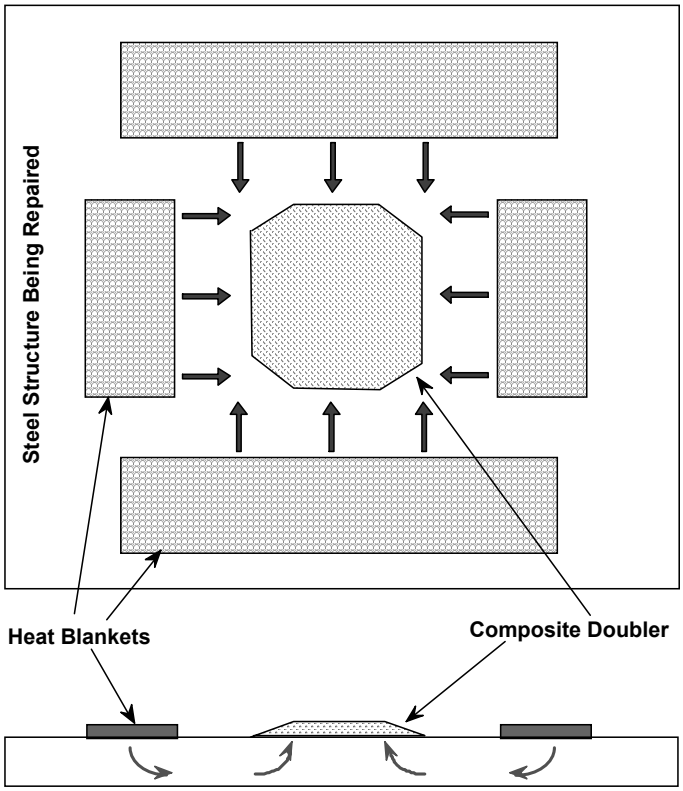

Figure 2-25: Basic Concept of Projection Heating

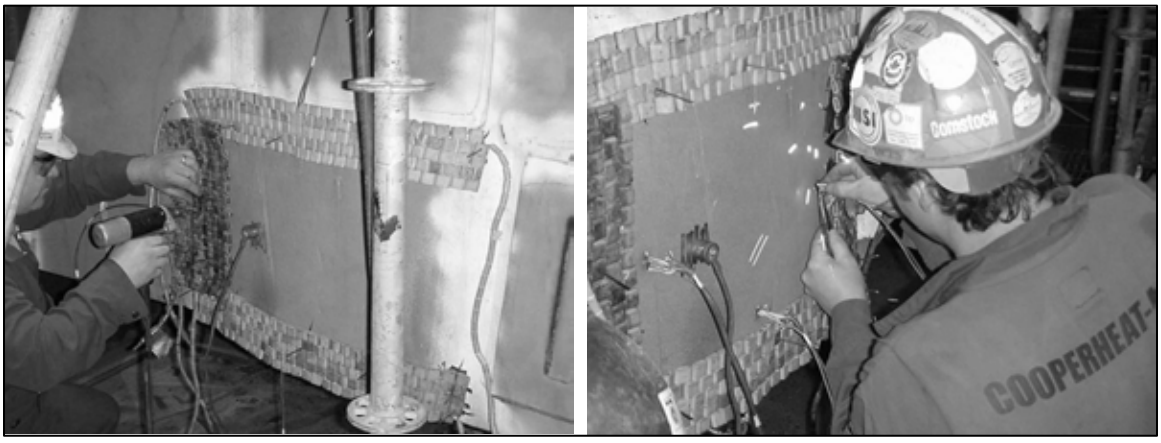

Figure 2-26: Placing and Securing Ceramic Heater Pad and Thermocouples Using Tack Welds

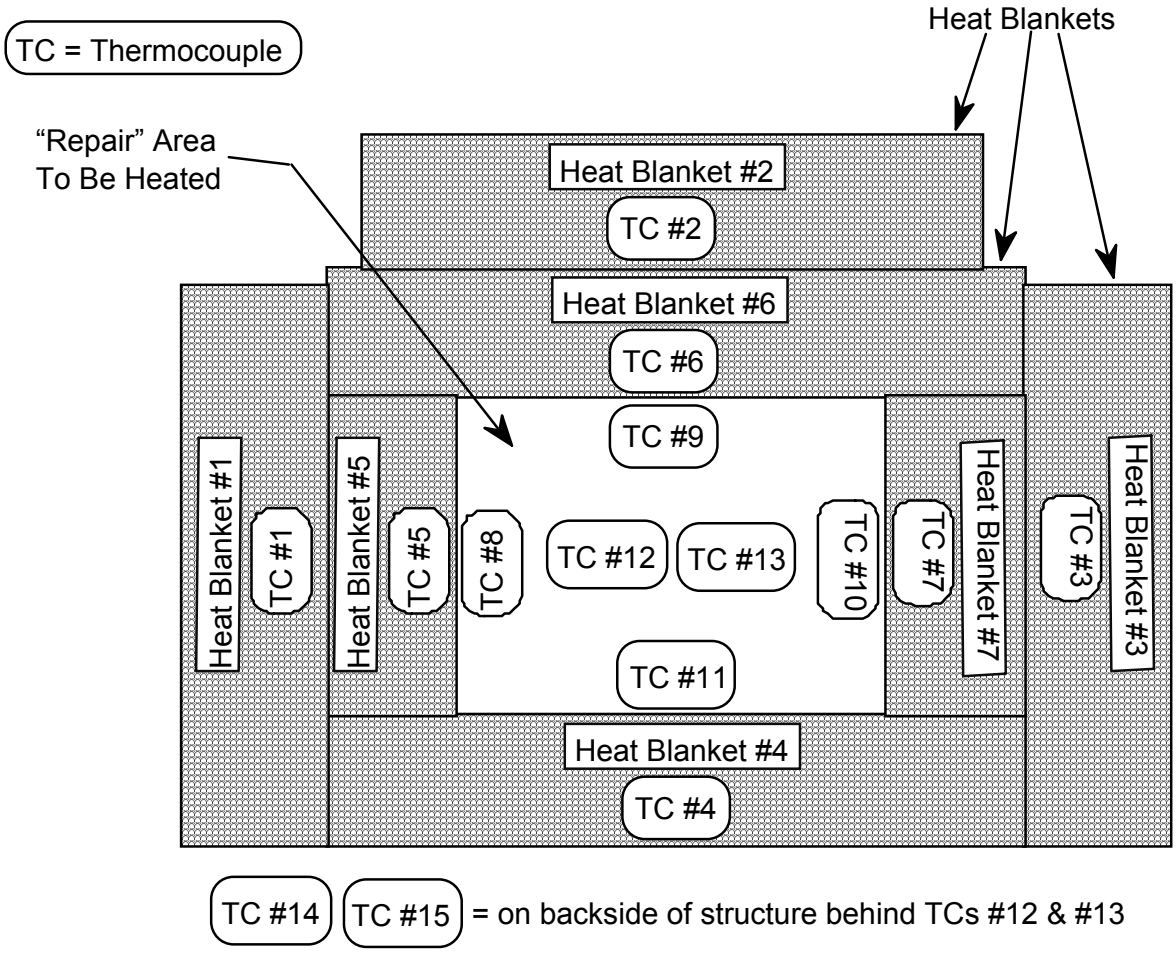

Figure 2-27: Heater Pad Placement Around Perimeter of Area to Be Repaired and Thermocouple Locations Used to Monitor Heating Process

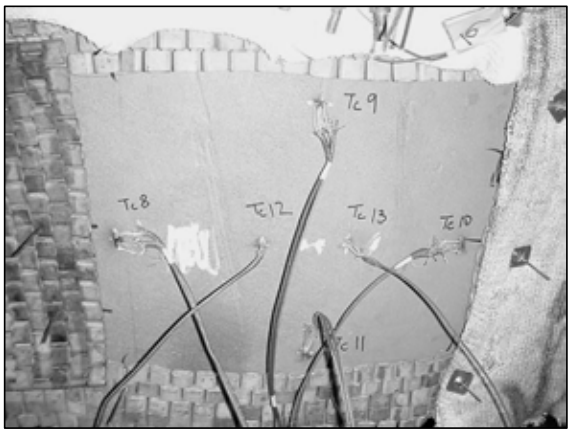

Figure 2-28: Thermocouples Placed Inside "Repair" Region (18" X 18")

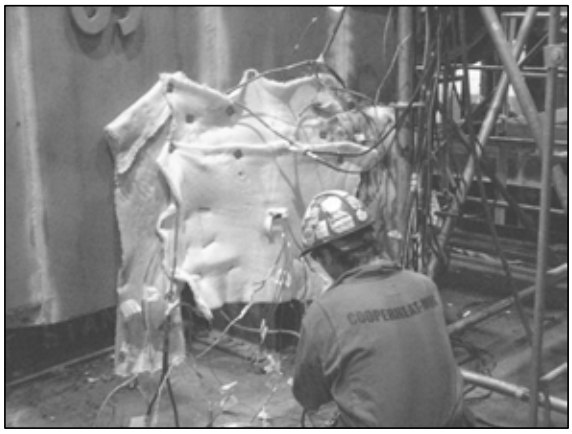

Figure 2-29: Final Assembly with Insulation Placed Over 7 Heater Pads

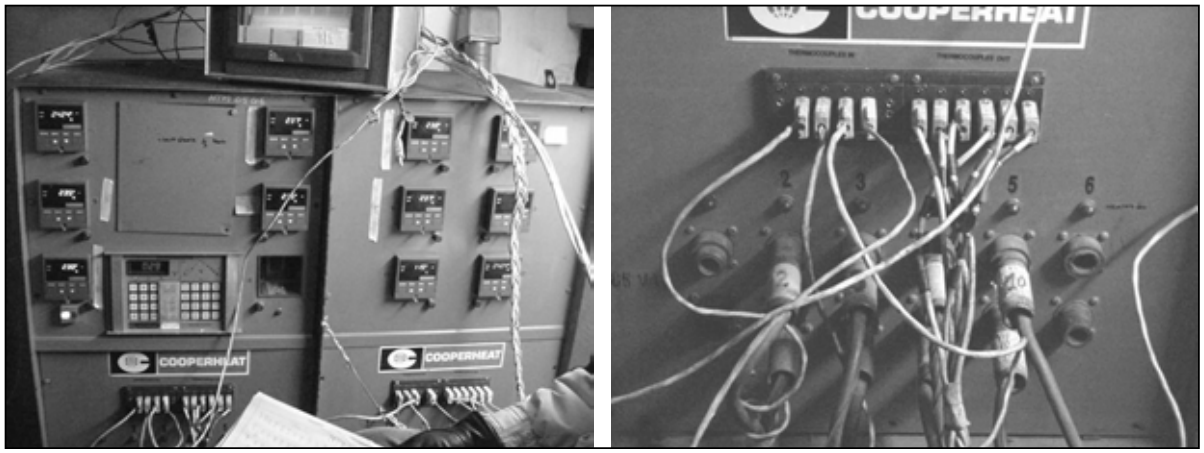

Figure 2-30: Cooperheat Controller Showing Input from Thermocouples, Output to Heater Pads, and Temperature Logging

The Cooperheat control system, shown in Figure 2-30, was programmed to produce a temperature ramp-up rate of 3°F/minute, a temperature hold at 225°F, and a temperature ramp-down of 5°F/minute. Figure 2-31 shows this target temperature profile along with the temperatures from all 15 thermocouples. Thermocouples 1-7 were located under heater pads 1-7, respectively, so they can be interpreted as the driving temperatures for the projection heating process. Note that they match the programmed profile quite well. The remaining thermocouples, #8-15, were inside the perimeter of the heater pads and represent the cure temperatures for a composite doubler. As expected, there is some lag in the temperature ramp-up but the slope gradually improves to the 3°F/minute target. As noted in Fig. 2-31, the set point was adjusted to 240°F to speed up the rise to 225°F. There was some concern that the thermal mass of the structure would cause us to overshoot the 225°F target, however, the temperature in the repair region remained very stable. Once the inner repair region reached the hold temperature (see t= 95 minutes), the temperatures in thermocouples 8-15 remained well within the $\pm$25°F tolerance (min temp. = 222°F; max temp. = 234°F). After the hold temperature was maintained for 20 minutes, the Cooperheat system was shut down. The two data points taken after shut-down showed that the thermal mass does make it difficult to quickly cool the structure. Temperature logs from the strip chart recorder, left on overnight, showed that the structure cooled at about 0.5°F/minute. Although we would like to cool the doubler a little faster than this (cure profile calls for temperature ramp-down of 1-5°F/min), the temperature ramp-down parameter is the least critical aspect of the cure profile. Overall, this was an excellent demonstration of the heating process. While the Cooperheat system shown here may be supplemented by placing rubberized heat blankets over the composite patch itself, there are no other changes needed for this system to properly cure a composite doubler on extremely thick steel structures.

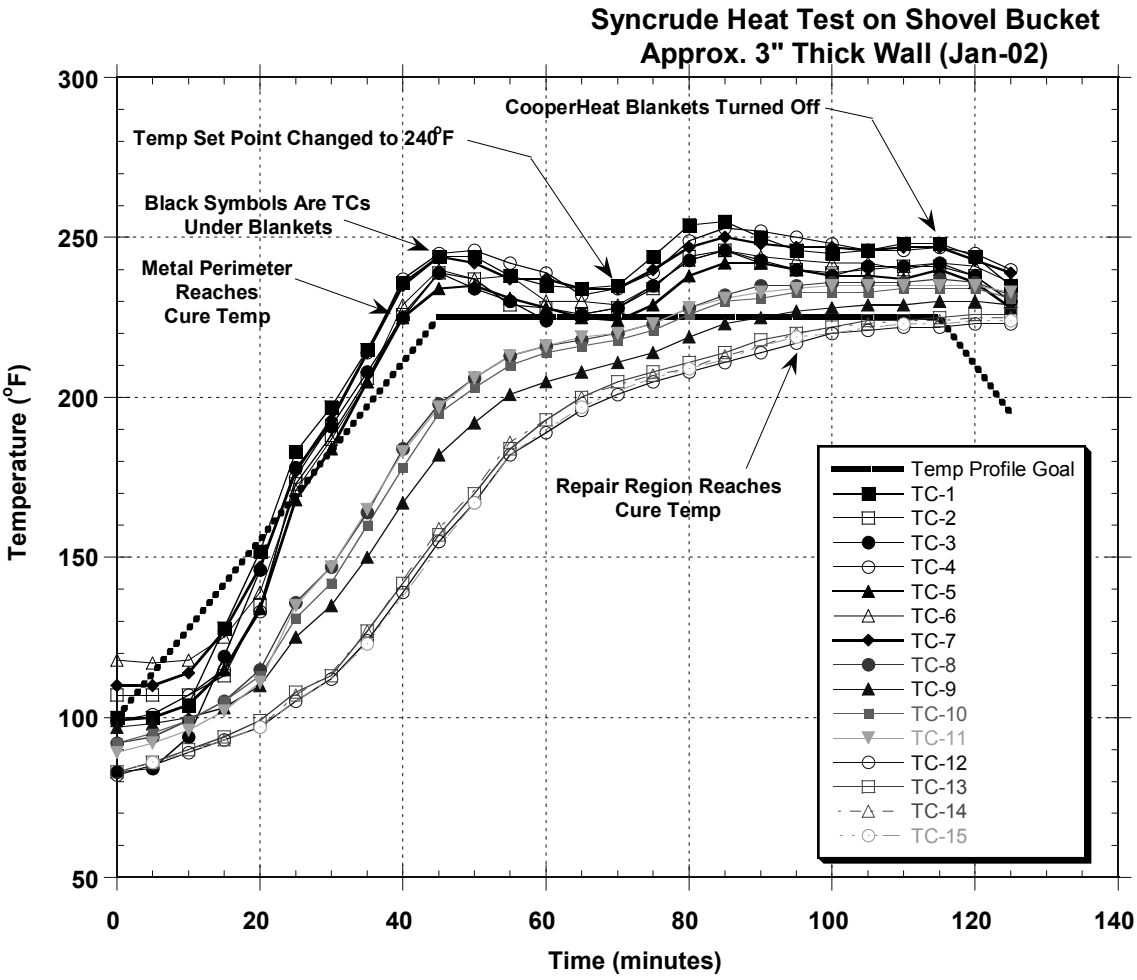

Figure 2-31: Temperature Profile of All Thermocouples with Comparison to Desired Heat/Cure Profile

References

2.1 Brewis, D., "Factors Affecting Bonding of Metals," *Materials and Technology*, Vol. 2, August 1986.

2.2 Bockenheimer, C., Valske, B., and Possart, W., "The Influence of Mechanical Pretreatment on the Polymer Structure of Adhesive Bonds," 5th European Adhesive Conf., September 2000.

2.3 Critchlow, G. and Webb, P., "Chemical Conversion Coatings for Structural Adhesive Bonding of Plain Carbon Steels," *Int'l Journal of Adhesion*, Vol. 20, Aug. 2000.

2.4 Arnott, D., "Bond Durability Performance – The Australian Silane Surface Treatment," Int'l Council of Aero Sciences Congress, September 1998.

2.5 Blohowiak, K., et al., "Bonded Repair Techniques Using Sol-Gel Surface Preparations," DOD/FAA/NASA Conf. on Aging Aircraft, September 1998.

2.6 Clearfield, H., McNamara, D. and Davis, G., "Adherend Surface Preparation for Structural Adhesive Bonding," *Adhesive Bonding*, Cambridge Scientific, 2002.

3.0 COMPOSITE DOUBLER DESIGN GUIDELINES AND VALIDATION FOR REPAIR OF STEEL STRUCTURES

Dennis Roach

Before arriving at a final family of repair designs for the Syncrude shovel boom example or other steel structures, component level testing was completed to study the response of composite doublers on thick steel structure. Fatigue and static tests studied flaw initiation and growth, strain fields, residual strength, ultimate strength, and load transfer. In addition, these tests also established the damage tolerance of composite doubler repairs for a wide variety of applications. Installation and in-service flaws were engineered into critical regions of the repair to determine if and what detrimental effects they have on the repair. The tests evaluated the critical aspects of the repair designs: ply lay-up, ply orientation, patch shape and taper, and the bond layer. The thickness of both the doubler and the parent steel structure were representative of the anticipated field repairs.

Structural Testing Initiative – The purpose of this phase of the study was to assess design options and doubler performance; study flaw initiation and growth, strain fields, residual strength, ultimate strength, and load transfer in realistic composite doubler repairs on carbon steel structure. Fatigue loads were applied to simulate worst-case working environments. NDI & strain gages were used to monitor structural response. Results from a field stress level monitoring activity were used to determine the appropriate test loads.

The component level tests addressed general design and installation issues such as: 1) durability of surface preparation and associated strength of adhesive joint, 2) taper ratios needed to transfer the loads and mitigate crack growth while minimizing the doubler footprint, and 3) required stiffness ratios between the parent structure and the composite patch to produce the desired performance. Configurations with assorted loading and boundary conditions attempted to grow engineered flaws and determine load transfer capabilities of composite doublers in the presence of defects. Specimens were tested in a variety of loading modes (shear, tensile, and bending) and stress intensities were measured around cracks to determine critical bonding parameters. The test specimens were produced using the optimum surface preparation determined in the first segment of this study [see Chapter 2].

Exposure to cold, representing worst-case winter conditions, and heat, representing a weld process in an adjacent area, were included to determine if either if these conditions are detrimental to the composite repair installation. The fatigue tests also provided critical crack growth information so that inspection intervals, if necessary, can be related to the degradation rate of the composite doubler under operational service conditions.

3.1 Doubler Design Guidelines

The primary issues to be addressed include the optimum location, size, shape, and laminate taper for the patches. The major factors that determine the patch design parameters are the stress levels at the repaired flaw, the stress levels in the composite doubler (maximum allowable fiber stresses), and the stress levels in the adhesive layer between the doubler and the metal skin. The

important, fundamental results produced by Jones and Callinan in ref. [3.1, 3.2] are worth reviewing in some detail in order to prepare for the damage tolerance discussions later in this report.

The ref. [3.1] crack repair study used a unidirectional Boron-Epoxy laminate (fiber perpendicular to crack) as a baseline design. The study found that for patches that cover the entire length of the crack, a one ply (0.0057" thick) patch reduces the stress intensity factor to 33.5% of its value for the unpatched crack. Furthermore, the rate of decrease in the stress intensity factor, K_{IP}, as the patch thickness increases was found to be quite low. A six layer patch, for example, produced a K_{IP} value of 19.5% of the unpatched value. Thus, an increase in patch thickness by a factor of 6 only produces an additional 14% reduction in the stress intensity factor. Another important finding of the ref. [3.1] study was that in thin patches, the stresses over the flaw (in both the patch and the adhesive) are critical. However, as the patch thickness is increased, the shear stresses in the adhesive at the edges of the patch footprint become critical and may exceed allowable limits.

The findings summarized above produced a series of design requirements that are necessary to maintaining the structural integrity of a composite doubler repair.

1) Fiber Strain – For a maximum Boron fiber strain of 5,000 με, the stress in the fibers must satisfy

$$\sigma_f \leq 0.005\, E_{11} \qquad (3\text{-}1)$$

where E_{11} is Young's modulus in the direction of the fibers (28.0×10^6 psi). When the fiber stress concentration, K_f, is considered the governing equation for fiber strain becomes

$$\sigma_f = K_f\, \sigma \leq .14 \text{ lb/in}^2 \qquad (3\text{-}2)$$

Thus, if the applied stress, σ, is known the maximum permissible value of K_f and the minimum permissible patch thickness can be determined.

2) Shear Stress in Adhesive – For a maximum allowable adhesive shear stress of 7 KSI and considering the stress concentrations at the crack and at the edge of the patch, the following design equations must be satisfied

$$\tau_{a(c)} = K_{a(c)}\, \sigma \leq 7{,}000 \text{ lb/in}^2 \qquad (3\text{-}3)$$

$$\tau_{a(e)} = K_{a(e)}\, \sigma \leq 7{,}000 \text{ lb/in}^2 \qquad (3\text{-}4)$$

Equations (3-2) and (3-3) can be solved to produce a doubler thickness to satisfy the stress requirements at the crack (for both laminate and adhesive). However, this often produces adhesive stresses at the edge of the doubler that exceed those allowed by eq. (3-4). Ref. [3.1] showed that the adhesive stresses at the edge of the doubler can be reduced to admissible levels

by stepping the thickness of the doubler from one or two plies at the outer perimeter to full thickness over a taper region. The length of the taper region is normally chosen to produce an edge taper ratio (taper depth-to-thickness increase ratio) of 10 to 30. Figure 1-1 shows a typical doubler edge taper used to gradually transfer load from the parent metal skin and reduce the shear stress in the adhesive. An ongoing study at the Sandia Labs AANC regarding the application of composite doublers to DC-10 skin damage encountered this need to balance doubler thickness with an appropriate edge taper [3.3].

Damage Tolerance of Composite Doublers – Inspection requirements (sensitivity and inspection intervals) are driven by Damage Tolerance Analyses (DTA). However, the stack of metal parent material (isotropic), composite lamina (anisotropic), and adhesive layers makes the analysis quite complex and hinders the calculation of an exact DTA. It is difficult to determine the effects of flaw size and the point at which a flaw size/location becomes critical. This is especially true of disbond, delamination, and porosity flaws. Thus, an increased emphasis is placed on quantifying the probability that a flaw of a particular size and location will be detected by a piece of NDT equipment. In addition to this report, detailed discussions on general damage tolerance assessments for structural repairs are presented in references [3.1 – 3.7].

The reference [3.2] observations mirror one of the primary results obtained in the damage tolerance assessment presented in this report: adhesively bonded doublers are extremely damage tolerant to large disbonds and other detrimental conditions such as impact and hot-wet conditioning. These results are quantified in Chapter 4 of this report. If, in fact, disbond and delamination flaws do not grow even under extreme environmental conditions, then an acceptable design should be predicated on the fact that the stresses in the adhesive are kept below a limiting or threshold value. As a result, reference [3.2] introduces an essential design methodology that considers damage tolerance. It uses a fatigue threshold load, P_f, and a fatigue threshold strain, ε_f, below which irreversible damage in the adhesive will not occur. The equations used to determine the threshold load and strain values are as follows:

$$P_f = 2\,(t\,W_f\,ET)^{1/2} \tag{3-5}$$

$$\varepsilon_f = 2\,(t\,W_f\,E/T)^{1/2} \tag{3-6}$$

where,

t = thickness of the adhesive
T = thickness of the adherend (skin)
E = Young's modulus of the skin
W_f = threshold value of the strain energy density of the adhesive

W_f can be determined experimentally [3.1]. Ref. [3.2] also describes the maximum load, P_{max}, that can be carried by a bond in a symmetrical bonded joint as,

$$P_{max} = 2\,(t\,W_c\,ET)^{1/2} \tag{3-7}$$

where W_c is the maximum strain energy density of the adhesive. Thus, composite doubler repair design guidelines are that P_{max} is greater than the ultimate load for the repaired structure and that P_f is greater than the limit load. Ref. [3.2] also points out that these critical design variables are affected by the loading rate. A conservative estimate for P_{max} can be obtained by using the value of the maximum von Mises equivalent stress in the adhesive, σ_e, as measured in high strain rate tests. For AF-163, the adhesive used in this study, $\sigma_e = P_{max}$ = 5,800 psi and the threshold stress σ_{th} = 3,600 psi. This analysis approach clearly shows the importance of the adhesive in determining the overall performance of the bonded repair. Ref. [3.2] goes on to point out the effects of the inelastic strain build-up in the adhesive layer that can accumulate with each load cycle. This hysteresis must be considered when determining the loads and fatigue cycles necessary to reach the maximum strain. Appendix C summarizes the set of basic equations that are used to design a composite doubler repair.

The abilities of nondestructive inspection techniques to meet the flaw detection requirements are presented in Chapter 5. The fundamental result from the NDI study is that a team of NDI techniques can identify flaws well before they reach critical size. Crack detection in the parent steel material can be accomplished using eddy current and X-ray techniques. Also, ultrasonic and thermography methods have been successfully applied to the problem of disbond and delamination detection.

3.2 Sample Application: Repair of Mining Shovel Boom

Load spectra monitoring for the shovel boom was performed in conjunction with the Syncrude fatigue crack management research project [3.8-3.10]. This joint Syncrude-University of Alberta project seeks to understand how cracks form on Syncrude mobile equipment, develop guidelines to predict fatigue crack behavior, and assess which repair techniques are best suited for various conditions. As part of this program a load analysis, load measurement and finite element model were completed for the BE-395E shovel boom. The boom was monitored while in field operating conditions as shown in Figure 3-1. Field monitoring of BE 395B shovel 11-77 was conducted for approximately one week. The field test consisted of controlled operation of the shovel under 'simulated' and normal operating conditions. Strains were measured at two cross-sections along the boom (sections A-A and B-B as shown in Figure 3-2). A total of 32 strain gages were mounted on sections A-A and B-B of the boom as shown in Figures 3-2 and 3-3 [3.9].

The data from the crack management project were used in this repair study to: 1) determine the primary loading and stress fields that lead to fatigue cracking, and 2) quantify the stress field to allow for accurate design and analysis of composite repairs. The hope was that the load monitoring captured both normal and off-design conditions so that true load extremes could be applied in subsequent design validation tests. The gages determined the loads associated with all phases of use including start-up, shut-down, and routine operation. Other environmental information to be determined includes the number of fatigue cycles (i.e. excursions of $\pm$ 80% of operating stresses) incurred during a normal working day. Areas of uniform strain were instrumented to produce clear and reliable data from which finite element models could be

validated. The validated FEMs could then be used to quantify stress risers in the complex geometry regions of the boom.

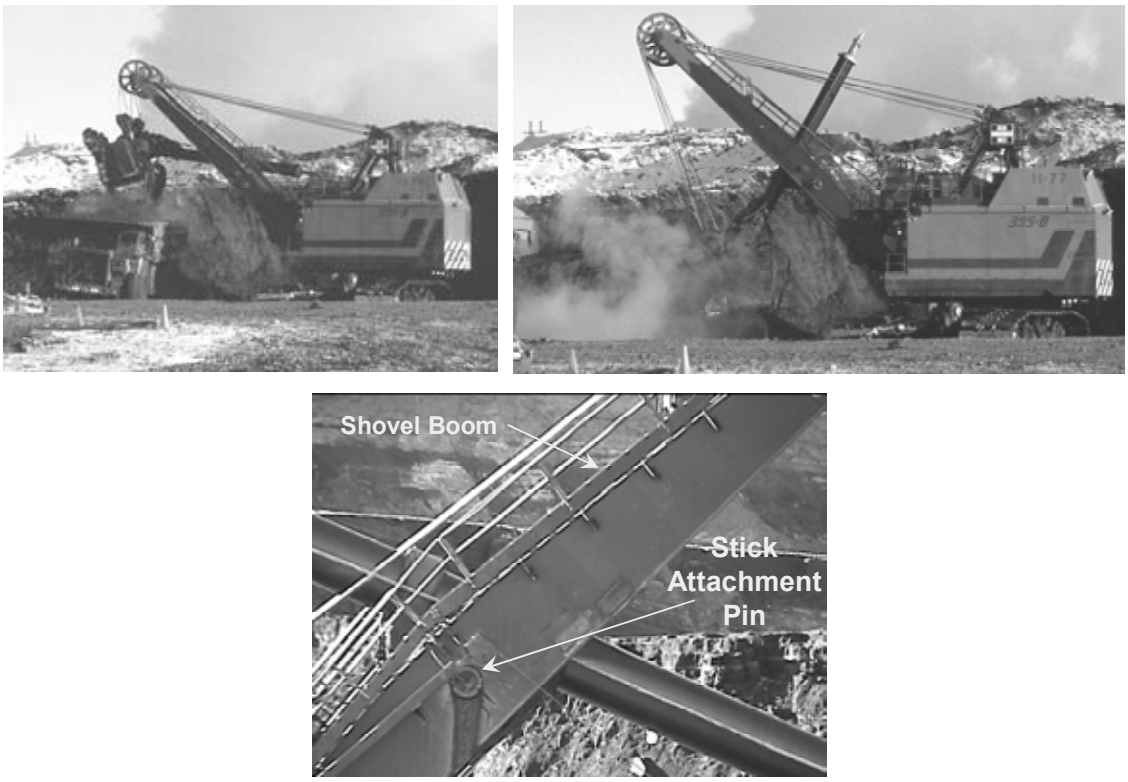

Figure 3-1: Typical Operation of Cable Shovel and Close Up of Boom Being Monitored

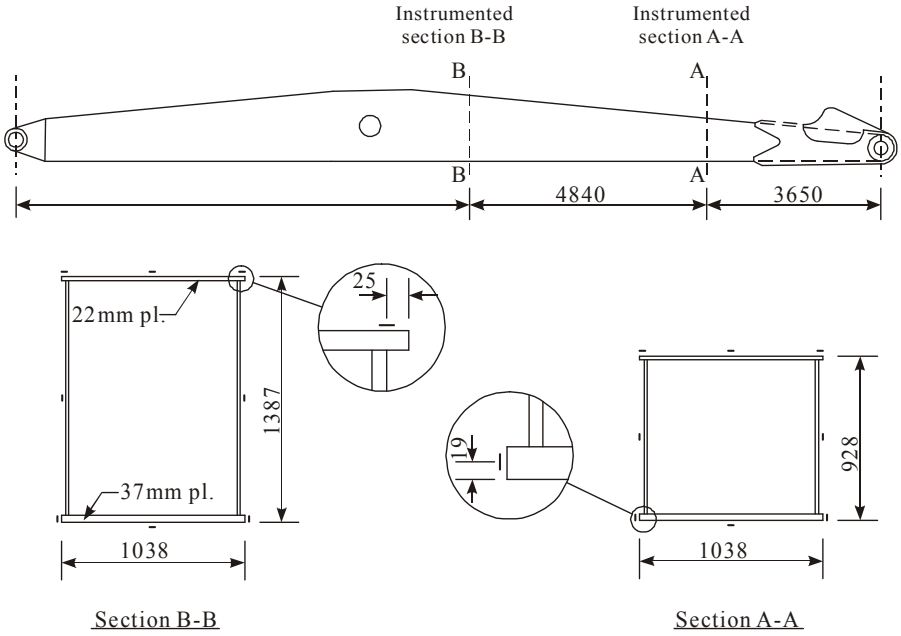

Figure 3-2: Shovel Boom Schematic and Strain Gage Layout Used to Monitor Strain Field

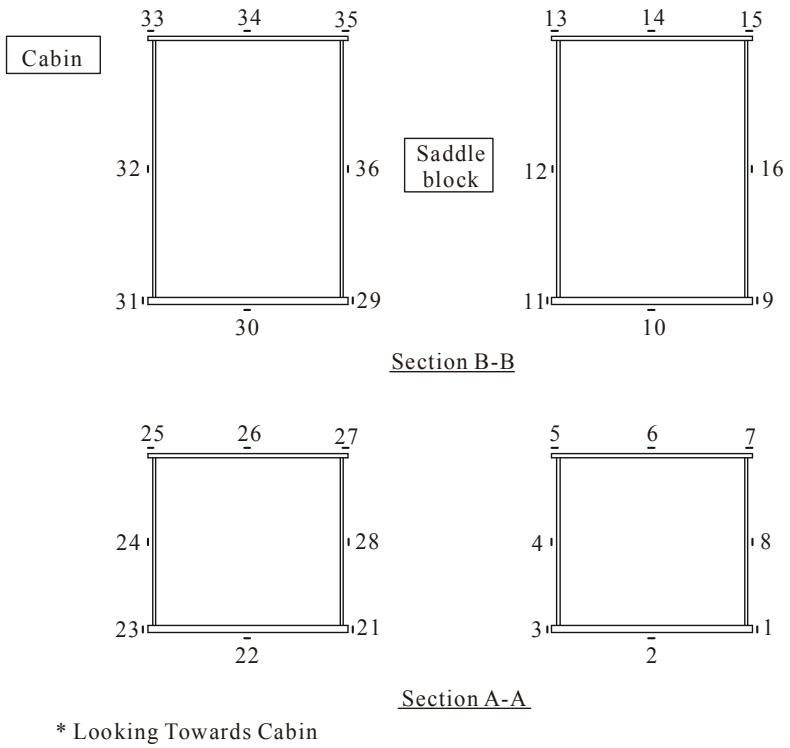

Figure 3-3: Strain Gage Layout and Numbering System Used to Monitor Cable Shovel Booms

The preliminary results from the field measurements and computer model indicated that the loading on the shovel boom was primarily along the longitudinal axis of the boom with very little lateral bending from side to side. In addition, the loading on the bottom section of the boom's box beam is predominately in tension with stress cycles in the range 9.1 ksi - 11.3 ksi (63-78 MPa) with some cycles as high as 14.2 ksi (98 Mpa). It should be noted that these stress ranges do not include any stress concentrations found near the corners, cut-outs, or at the welds.

Overall, the load spectra monitoring and finite element modeling effort produced the following results:

1. Measured ε_{max} = 400 με (σ=12,000 psi); stress risers around stick attachment could double these stress levels.
2. Twisting, and associated variation in stresses from one side of the boom to the other, is considered minimal.
3. Primary loading stems from bending created when shovel retrieves and carries oilsands while cable restrains (lifts) boom at the end. Measured strains indicated no sign of significant out-of-plane or torsional behavior of the boom.
4. Over the monitoring period of approximately one week, the data indicated little variation in the strain spectrum, except for the number of cycles at low stress range 1 ksi (7.5 Mpa) or less. A few hundred cycles a day are applied that reach a stress range of around 10 ksi (70

Mpa) away from regions of stress concentration. Monitoring indicates approximately 1,500 cycles per day or 270,000 cycles every 6 months.

5. A preliminary finite element analysis indicates that these stress ranges can more than double in the regions of high stress concentration. It should also be noted that the data collected to date is representative of summer operating conditions. The variation in strain conditions stemming from winter operating conditions should be investigated.
6. A good correlation between field data and finite element predictions indicates that the finite element model is valid and that the method used to load the finite element model is accurate.

3.2.1 Modeling of Boom Structure on Cable Shovel

Figure 3-4 shows a schematic of the shovel boom that includes the internal diaphragm plates. Stress risers occur at the welds around each of these plates, as well as at the stick-to-boom attachment point, and act as crack initiation points in the boom. The corresponding FEM of the cable shovel boom is shown in Figure 3-5. The boom model was discretized using three-node and four-node shell elements implemented in the commercial software ABAQUS [3.10]. Figures 3-6 and 3-7 contain sample analysis results with typical deformation modes and stress levels present in the boom during operation.

FEM results show only minor differences between the principal stresses and the axial stresses. This indicates that the stresses in the boom are primarily axial stresses. The high stress regions, indicated in red, are in areas where fatigue cracks have been detected in the booms. The maximum equivalent stress is 10.4 ksi (72 Mpa). Further mesh refinement is needed to accurately calculate the local stress concentrations expected at the diaphragm welds. *In order to perform the composite doubler evaluations in a conservative manner, the performance testing conducted in this composite doubler repair study will use minimum stress levels of two to four times the stress levels determined in this crack management program. The applied fatigue test spectrums in the performance tests (see Section 3.2.6) were: 24 ksi, 33 ksi, and 41 ksi.*

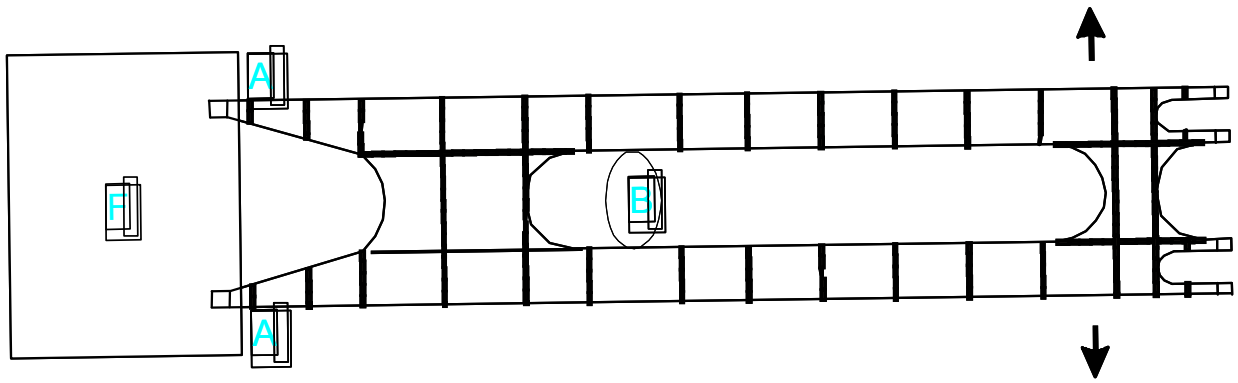

Figure 3-4: Top View of Boom Showing Internal Diaphragm Plates

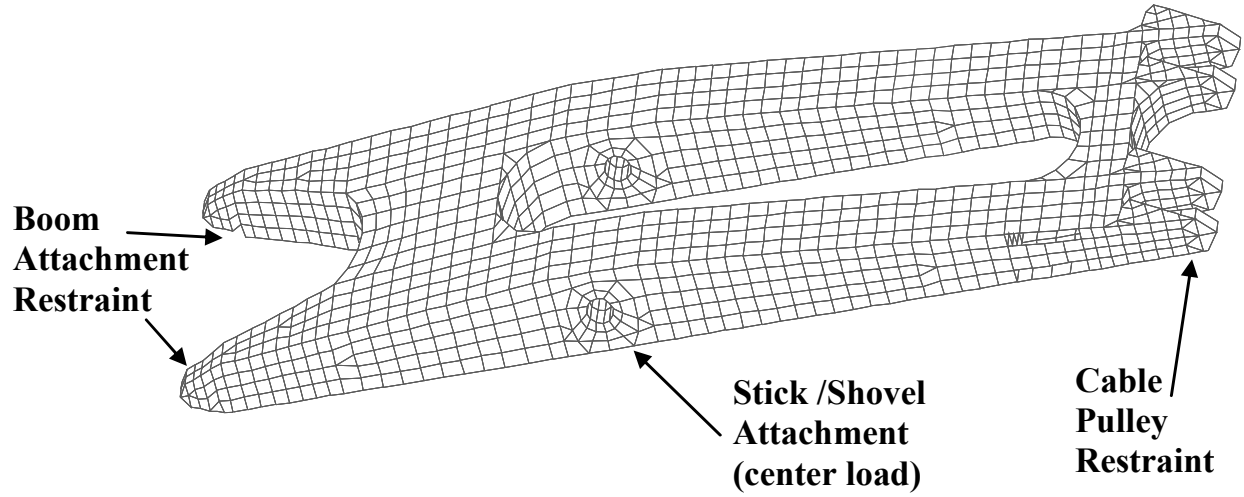

Figure 3-5: Finite Element Model of Cable Shovel Boom

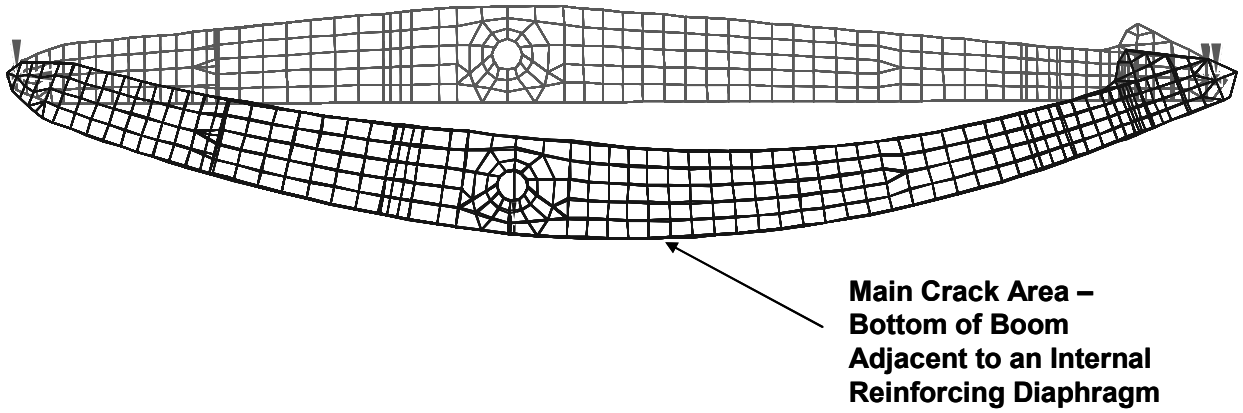

Figure 3-6: Primary Deformation During Operation That Causes Boom Cracks

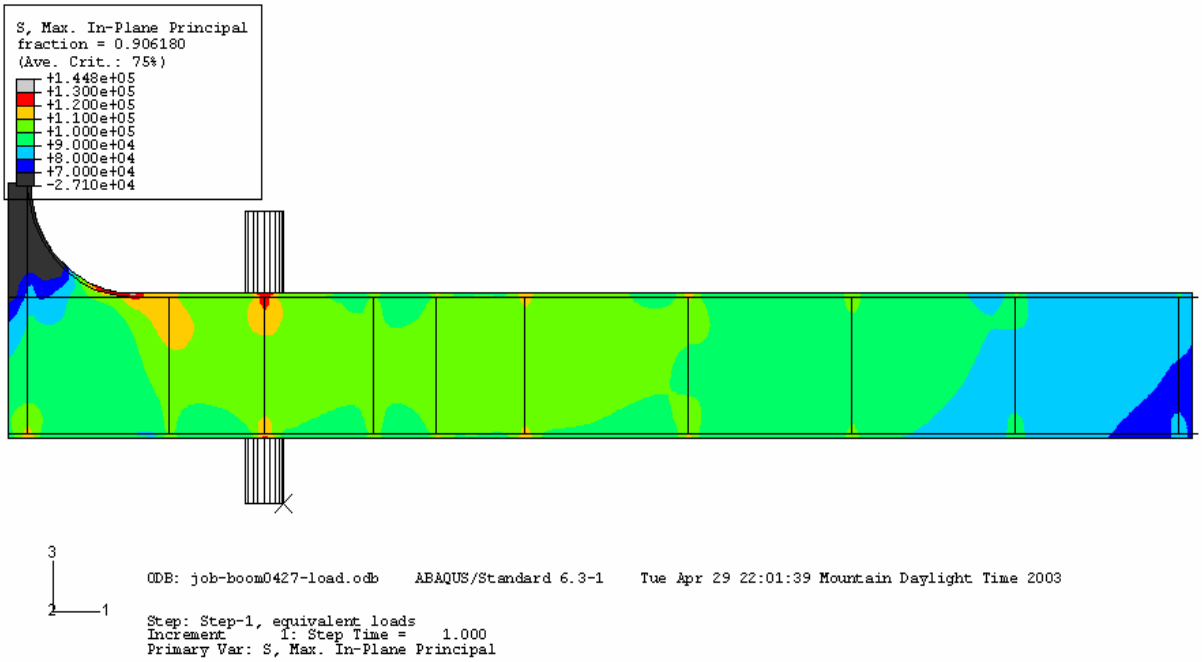

A. Principle Stresses in Bottom Flange

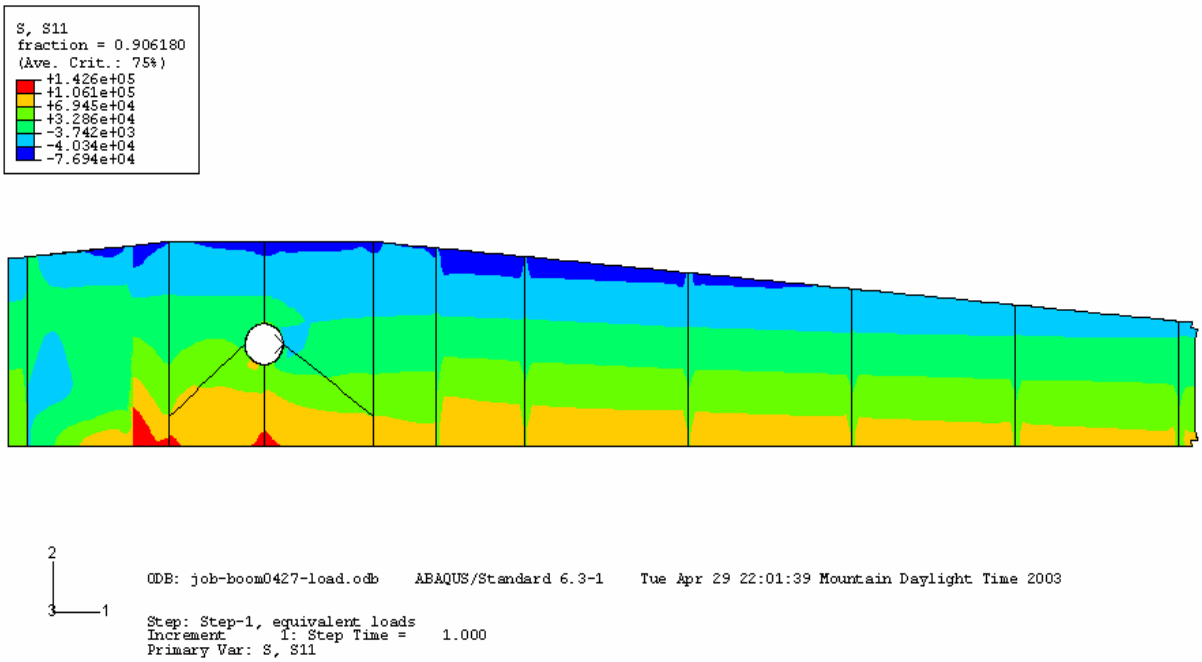

B. Axial Stresses in Inside Web Region

Figure 3-7: Shovel Boom Stresses Calculated by Finite element Model (Note: stresses shown in the legends are twice the stress range in kPa)

3.2.2 Fatigue Properties of Boom Structure

As part of the crack management program, the Univ. of Alberta and Syncrude conducted crack growth rate tests (specimens produced from representative G40.21 350WT steel plate). The results of six crack growth rate tests conducted at two different stress ranges and two different mean stresses are presented in Figure 3-8. The results are presented in terms of crack growth rate (m/cycle) versus stress intensity factor range ($\mathrm{MPa}\sqrt{\mathrm{m}}$).

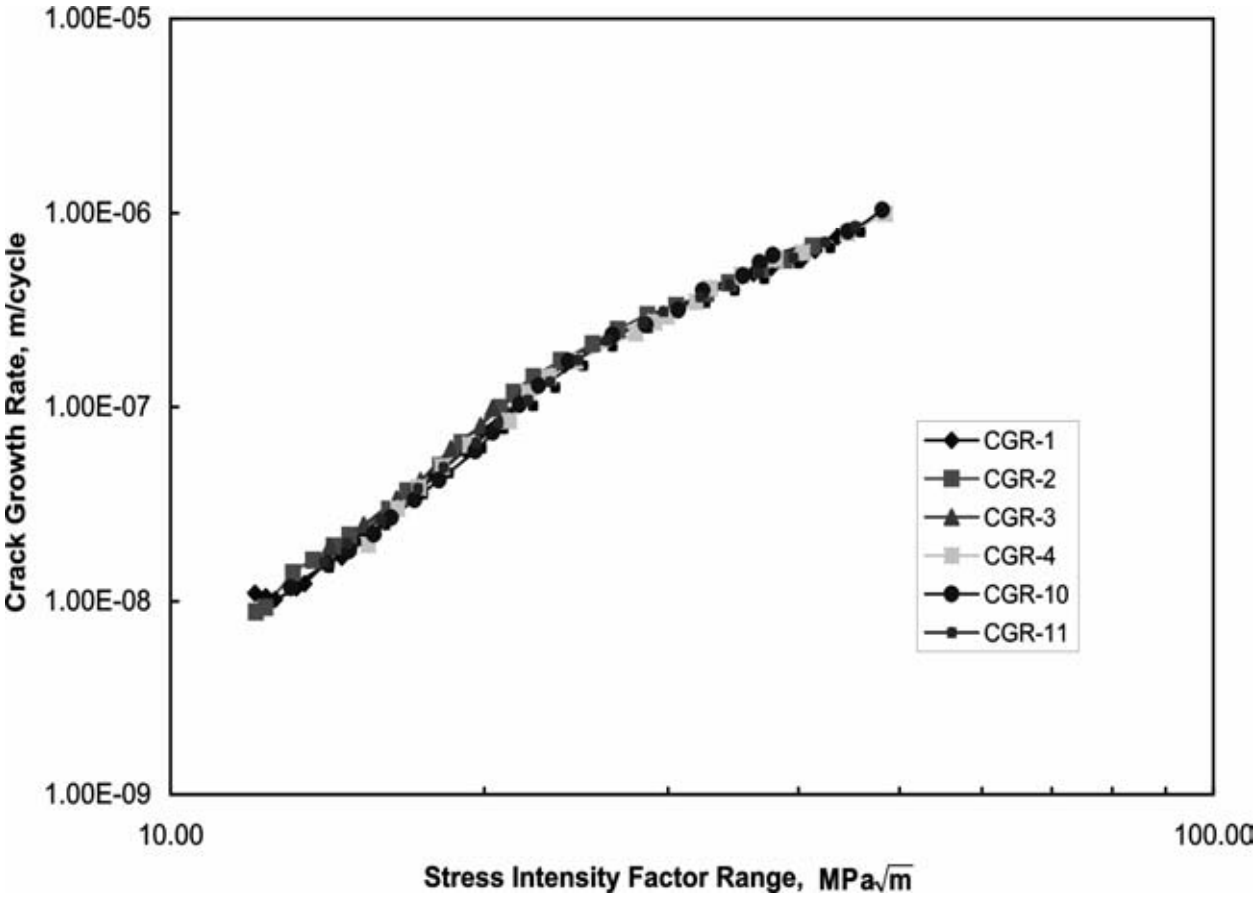

Figure 3-8: Results from Crack Growth Rate Tests on Representative Boom Material

The crack growth rate test results, presented in Figure 3-8 as the log of crack growth rate versus the log of the stress intensity factor range, indicate that the relationship between crack growth rate and stress intensity factor range is almost linear, as expected. A linear regression analysis was used to obtain the crack growth rate equation required to assess the rate of crack propagation in the shovel boom. The resulting crack growth equation takes the following form:

$$\frac{da}{dN} = 1.55\times10^{-12}\ (\Delta K)^{3.59} \qquad (3\text{-}8)$$

where, da/dN is the crack growth rate expressed in m/cycle and ΔK is the stress intensity factor range expressed in $\text{MPa}\sqrt{\text{m}}$. The data in Figure 3-8 indicates that a crack might grow anywhere from 0.1" to 10" during a six month operation period (250,000 cycles) depending on the stress intensity factor associated with its location. These crack growth values provide an important basis of comparison when evaluating the crack mitigation capabilities of composite doublers (see Chapter 4).

3.3 Damage Tolerance and Crack Mitigation of Composite Doubler Repair Method

3.3.1 Fatigue Panels – Damage Tolerance and Crack Growth Testing

Component level testing was conducted to study the response of composite doubler repairs on steel structure. Fatigue and static tests studied flaw initiation and growth, strain fields, residual strength, ultimate strength, and load transfer. These tests were used to help guide repair designs for thick steel applications and to establish the damage tolerance of composite doubler repairs on steel structure. Engineered flaws were implanted in both the parent structure (cracks) and the composite patch (disbonds and delaminations) to determine if and what detrimental effects they will have on the repair.

Fatigue and ultimate strength tests were performed on specimens with crack, disbond, and impact flaws. Environmental conditions representing temperature and humidity exposure were also included in some of the test specimens. The structural tests were used to: 1) assess the potential for interply delaminations and disbonds between the steel and the laminate, and 2) determine the load transfer and crack mitigation capabilities of composite doublers in the presence of severe defects. A series of specimens were subjected to ultimate tension tests in order to determine strength values and failure modes.

The two main potential causes of structural failure in composite doubler installations are cracks in the steel and adhesive disbonds/delaminations. When disbonds or delaminations occur, they may lead to joint failures. By their nature, they occur at an interface and are, therefore, always hidden. A combination of fatigue loads and other environmental weathering effects can combine to initiate these types of flaws. Inspection of the composite doubler for disbonds and delaminations (from fabrication, installation, fatigue, or impact damage) is essential to assuring the successful operation of the doubler over time.

3.3.2 General Fatigue Specimen Description

Figures 3-9 show the tension-tension fatigue test panels that were used to measure the crack mitigation capability of the proposed repair design. Each specimen consisted of a steel "parent" plate, representing the original steel structure, with a bonded composite doubler. The doubler is bonded over a flaw in the steel. The most severe flaw scenario was an unabated fatigue crack with a co-located disbond (i.e. no adhesion between doubler and parent steel plate) as well as two, large disbonds in the critical load transfer region of the doubler perimeter. Fatigue testing an actual 0.875" or 1.25" thick plate, representing the wall thickness on the cable shovel boom, was not feasible. However, a plate that fits into the thick plate category (3/8" th.) was used and

the proper stiffness ratio between the composite doubler and the parent steel was maintained. The stiffness ratio is defined as:

$$R_x = (E_x t_{laminate})_{BE} / (E_x t)_{St} \qquad (3\text{-}9)$$

Where BE represents the Boron-Epoxy laminate properties and St represents the properties of the steel plate. The stiffness ratio should produce adequate stress reduction and crack closure without creating stress concentrations. For the hybrid repair proposed here, the stiffness ratio used was $R_x = 0.3$. Normal stiffness ratios for aircraft repairs with the cracks still present (i.e. not removed by a weld fill process) are on the order of $R_x = 1.0$ to 1.2.

A through-thickness weld repair region was installed in the parent plate before the doubler was installed. This was done by cutting the original plate into two halves and welding them together using the penetration weld profile shown in Figure 3-10. This process was used to simulate the hybrid repair where a composite doubler is placed over a region where a crack has been removed by a welding process. In order to simulate a worst case condition where the weld process fails to completely remove a crack, a fatigue crack was also added to the weld region of the test specimen prior to bonding the doubler in place. The final test specimen configuration is presented in Section 3.3.4.

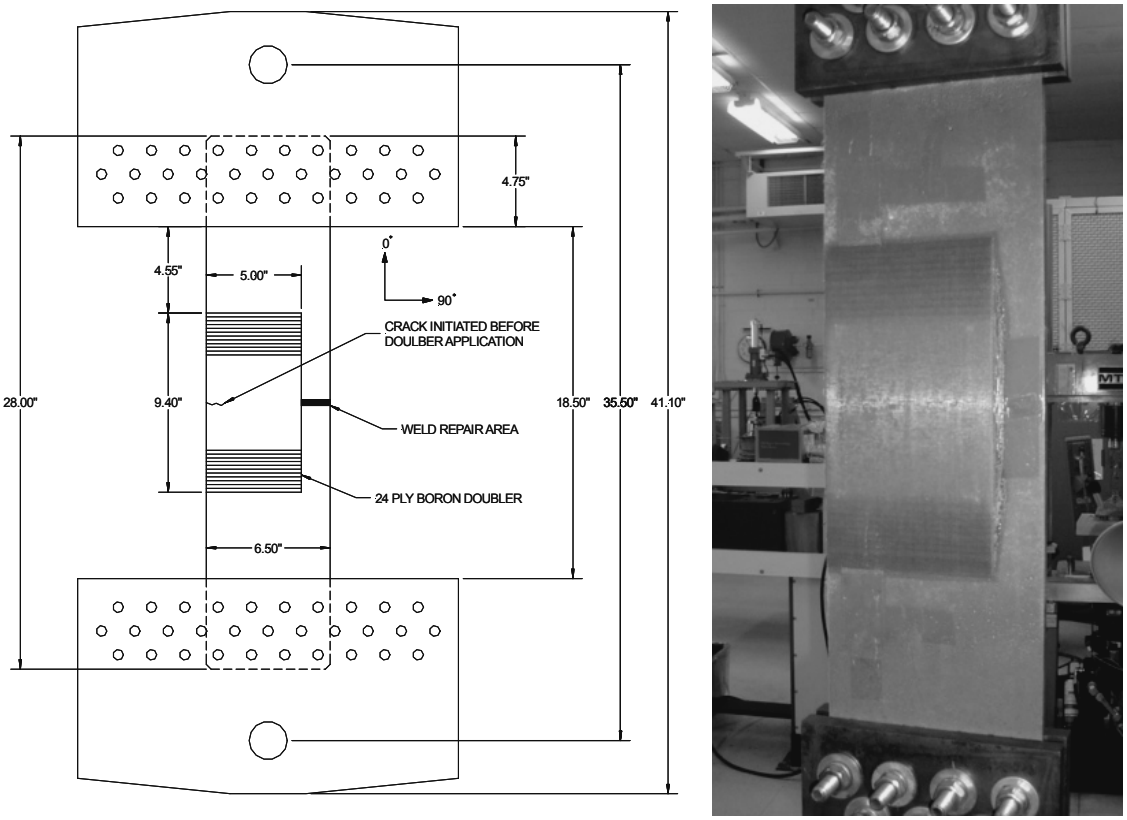

Figure 3-9: Fatigue Test Panel with Composite Repair

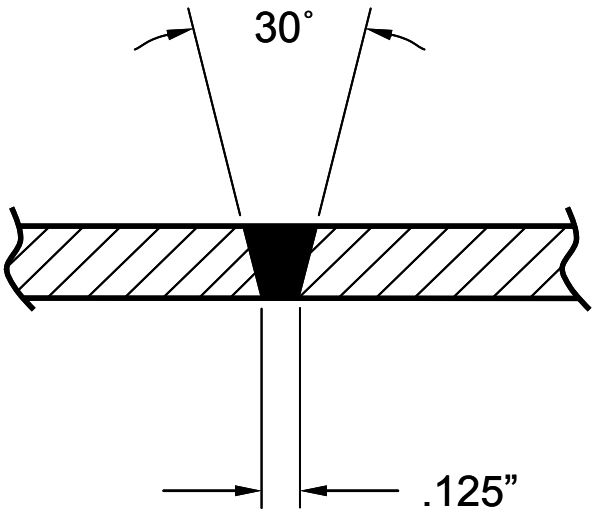

Figure 3-10: Crossection of Through-Thickness Weld Repair Installed Over The Entire Width of Steel Plate

Material - The parent steel plate was ASTM 572-50 material. It was chosen because its chemical make-up closely matches the steel material used in the Syncrude cable shovel boom (Canadian Spec CAN/CSA-G40.21, Grade 50WT). Table 3-1 summarizes the chemical make-up of the CAN/CSA-G40.21 material used in the shovel booms and compares it to the material available for use in this test series. The plate thickness was 0.375”. The Boron-Epoxy material was type 5521/4. The specifications for production of the Boron-Epoxy material was as follows: 1) SAE Aerospace Material Specification (AMS) 3865C for the Boron fiber, and 2) AMS 3867B and AMS 3867/4A specification for the Boron-Epoxy pre-preg tape material. The adhesive material was AF-163, (0.06 PSF) and the primer was Cytec BR6747. All composite doublers were installed using the process determined in Chapter 2 and the procedure listed in Appendix B.

3.3.3 Composite Doubler Design for Tension Test Specimens

The Boron-Epoxy composite doublers were a multi-ply, multi-directional lay-up of 24 plies: [0,0,0,0,45,-45,0,0,0,0,0,-45,0,0,45,0,0,0,0,0,-45,45,0,0,0,0] with the top ply having the same footprint as the first ply that contacts the adhesive layer. Thus, each composite doubler had a nominal post-cure thickness of 0.140” (approximately 0.0057” per ply plus a nominal pre-cure adhesive layer of 0.010”; the post-cure adhesive thickness is approximately 0.006”). The plies were cut to different lengths in the X (tension load) direction in order to taper the thickness of the resulting doubler edges. This produced a more gradual load transfer between the steel and the doubler (i.e. reduces the stress concentration in the bondline around the perimeter). A ply taper ratio of approximately 16:1 was utilized; this results in a reduction in length of 16 times the ply thickness (approximately 0.2” step every 2 plies). The number of plies and fiber orientations produced an extensional stiffness ratio of Boron-Epoxy to steel of 0.3:1 $\{(Et)_{BE} = 0.3\ (Et)_{Steel}\}$. The subsections of 3.3.3 below describe how this doubler design was produced.

Carbon Steel Material Composition Comparisons								
Material Type	**Yield**	**Tensile Strength**	**Carbon**	**Maganese**	**Phosphorous**	**Sulphur**	**Silicon**	**Cb**
CAN/CSA-G40.21, Gr. 50WT	50K	70/95K	.22 max	.80-1.50	.03 max	.04 max	.15/.40	.10 max
ASTM A572 Gr. 50	65K	85K	.23 max	1.35 max	.04 max	.05 max	.40 max	.05 max
ASTM A607, Gr. 50, Class 1	50K	65K	.23 max	1.35 max	.04 max	.04 max	-	0.005
4130 Chromium-Molybdenum Steel	63K	97K	.28/.33	.40/.60	.035 max	.04 max	.15/.35	Cr .80/1.1
ASTM A570 Gr. 50	55K	65K	0.25	1.35	0.035	0.04	-	-
ASTM A569 (ASTM A1011)	38K	52K	0.15	0.60	0.035	0.04	-	Cu .20 min
ASTM A537	50K	70/90K	0.24	.70/1.35	0.035	0.035	.15/.50	-
ASTM A36	36K	58/80K	0.25	-	.04 max	.05 max	.40 max	Cu .20 min
Stainless Steel (316)	30K	75K	0.08	2.00	0.045	0.03	1.0 max	Cr 16.00

Table 3-1: Chemical Composition of Syncrude Cable Shovel Steel and the Steel Used in Performance Test Specimens

Calculation of Laminate-to-Steel Extensional Stiffness Ratio - This section describes the method that was used to arrive at the stiffness parameter, $E_x t$, for composite doublers. The calculations used classical laminated plate theory, along with Boron-Epoxy lamina properties, to arrive at the average cured laminate modulus E_x (where x is the direction of the fatigue load).

The Boron-Epoxy lamina properties at room temperature are:

$$E_{11} = 28.0 \text{ X } 10^6 \text{ psi}$$

$$E_{22} = 2.7 \text{ X } 10^6 \text{ psi}$$

$$G_{12} = 0.8 \text{ X } 10^6 \text{ psi}$$

$$\nu_{12} = 0.21$$

$$t_{ply} = 0.0057 \text{ in.}$$

The average laminate properties are calculated using the individual lamina properties listed above along with the following specific lay-up configuration: 1) 24 plies {[0,0,0,0,45,-45,0,0,0,0,-45,0,0,45,0,0,0,0,-45,45,0,0,0,0]}, and 2) laminate thickness t = 0.14" (24 plies X 0.0058"/ply). The resulting laminate properties were calculated:

$$E_x = 25.2 \text{ X } 10^6 \text{ psi}$$

$$G_{xy} = 3.77 \text{ X } 10^6 \text{ psi}$$

$$\nu_{xy} = 0.32$$

Compared to a 0.375" thick, steel plate, the stiffness ratio is,

$$R_x = (E_x t_{laminate})_{BE} / (E_x t)_{St} \qquad (3\text{-}9)$$

$$= \frac{(25.2 \text{ X } 10^6 \text{ psi})(0.14")}{(30 \text{ X } 10^6 \text{ psi})(0.375")}$$

$$R = 0.31$$

This method was used to arrive at the 0.3 extensional stiffness ratio listed in the composite doubler hybrid design plan (Section 3.3.2). By designing the specimens using the nondimensional stiffness ratio, it is possible to extrapolate these results to various parent structure and composite laminate combinations.

Fatigue Test Specimen Design Features - The composite laminate design was completed using the repair design methodology described in Appendix C. This process was aided by the use of an Excel-based analysis package [3.11] that automates the application of the principles presented in Appendix C. The computer program allows the user to input the parameters listed below and to assess how variations in the design parameters will affect the strain fields in and around the composite repair. Laminate design principles were used to determine the E_x, E_y, ν_{xy}, and G_{xy} for a composite lay-up design. The required number of plies and the transfer length, which defines the overall repair length, were calculated for a one-sided (external) composite repair. An iterative process was then followed whereby specific design parameters were adjusted in an effort to meet general design guidelines. The input data and doubler design results are summarized below.

Design Input Data:

- Parent Plate Thickness = 0.375" th. (ASTM 572)
- Parent Plate Width = 6.5"
- Parent Plate Modulus = 30 X 10^6 psi
- Doubler (Patch) Thickness = 24 plies X 0.0058" = 0.140" th.
- Doubler Length, L_r = 9.4" (constant thickness length = 5"; taper length @ ea. side = 2.2")
- Doubler Width = 5"
- Doubler Width / Parent Width = 76%
- Stacking sequence - wedding cake stacking sequence (largest ply at the steel interface; sequentially smaller footprint plies are stacked on top)
- Parent Plate Length = 9.4" doubler + 4.55" ea. side for load + 4.75" ea. side for grips = 28" long
- Taper Ratio = 16 (0.2" step every 2 plies). When combined with patch thickness, the taper ratio determines the transfer length, β.
- Vacuum bag debulk every 4 plies
- Patch shape = rectangular. The doubler edge tapers will be in the X-direction (axial) only as shown in Figures 3-9 and 3-11. The doubler will have no taper perpendicular to the axial direction (Y-direction across width of boom) because: 1) it is reinforcing the axial

strength of the boom, and 2) it will probably be located along the edge of the box beam plate where full reinforcement strength is needed (i.e. tapered edges do not provide full strength around the perimeter).

- Load constant, N, is related to the full thickness length of the patch. The overlap length, or one half the doubler full thickness length is equal to N times the transfer length β.

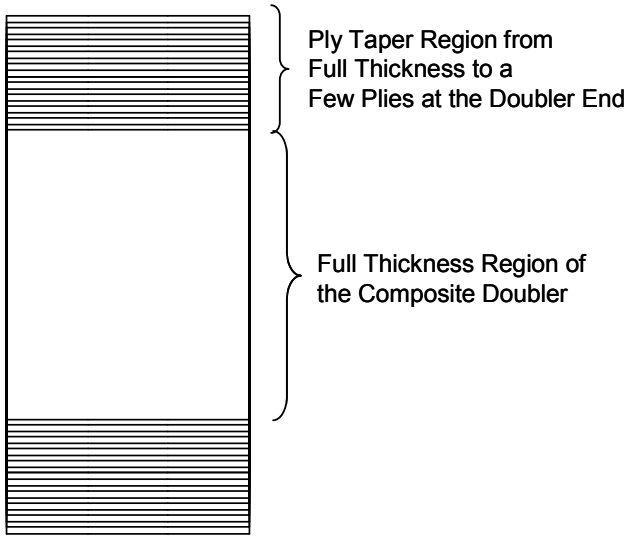

Figure 3-11: Composite Doubler for Tension Beam Repair Has Taper in Axial Direction Only (X-direction) and Most Plies Are Oriented in the Axial Direction

Doubler Design Notes:

- 45^o plies provide better performance in shear loads.
- Use of corner angle (more difficult lay-up) reduces stress riser in steel-doubler interface – no corner angle used in current designs.
- Adding width improves load transfer into doubler and decreases bypass strain.
- Increasing taper ratio reduces peel stresses – in order to minimize the total doubler length, the taper ratio is purposely selected for the lower end (16); desire is to determine if adequate performance is obtained with this design; higher taper ratios will require longer doublers with more material and more heat requirements.
- No side taper at edge of doubler where maximum reinforcement is needed.
- Twisting of boom (shear loads) is considered minimal – primarily tension loads with occasional reverse compression loading during shovel break-through during digs.

Doubler Design Output:

- Doubler Lay-Up = [0,0,0,0,45,-45,0,0,0,0,-45,0,0,45,0,0,0,0,-45,45,0,0,0,0]
- Stiffness Ratio = 0.31
- Effective Doubler Modulus = 25.2 X 10^6 psi

Doubler Design Analysis - Performance Criteria and Trade-Off Study with Design Prototypes - The input parameters listed above where placed in the spreadsheet program and the doubler lay-up, also listed above, was determined. The repair was optimized by varying the number and orientation of the plies, the taper ratio, the load constant, and the patch geometry. Table 3-2 shows one of the iterations where trial values are substituted for existing input parameters.

	Range Tested:	Current Value:	Trial Values
Stiffness Ratio, S	1.1 - 1.6	0.307	**0.307**
Step-off Rate	15.0 - 50.0	20	**16.000**
Patch Width	1.5 - 5.0	5.000	**5.000**
Load Constant, N	4.0 - 12.0	10.000	**5.000**
Adhesive Thickness	1	1	**1.000**
(number of plies)	2		
	3		
Patch shape	Rectangle	1	**1.000**
	30-deg Corner		
	45-deg Corner		
Stacking Sequence	Wedding Cake	1	**1.000**
	Reverse Wedding Cake		

Current Value doubler length = 10.5" (taper length = 2.75" so taper ratio is 20)
Trial Value doubler length = 9.4" (taper length = 2.2" so taper ratio is 16)

Table 3-2: Iteration on Composite Doubler Design by Varying Input Parameters

After each iteration, specific guidelines were reviewed to optimize the repair design. The efficiency of the repair was evaluated by studying the resulting strain ratios for the composite doubler repair installation. Figure 3-12 shows a typical repair under uniaxial loading. Strain locations G1 through G8 pinpoint various regions of the doubler and surrounding parent structure. Table 3-3 defines the strain ratios that are calculated by comparing the strain levels at each of the various points in Figure 3-12. In addition, Table 3-3 lists the goal (design guidelines) for these strain ratios along with a description of the criticality of each strain ratio. The strain ratios listed are in order of importance and the first two items are primary relationships. Therefore, the goal of the iterative design process was to optimize the ratios for the first two or three relationships while producing results that are close to the design goal for the lower few relationships.

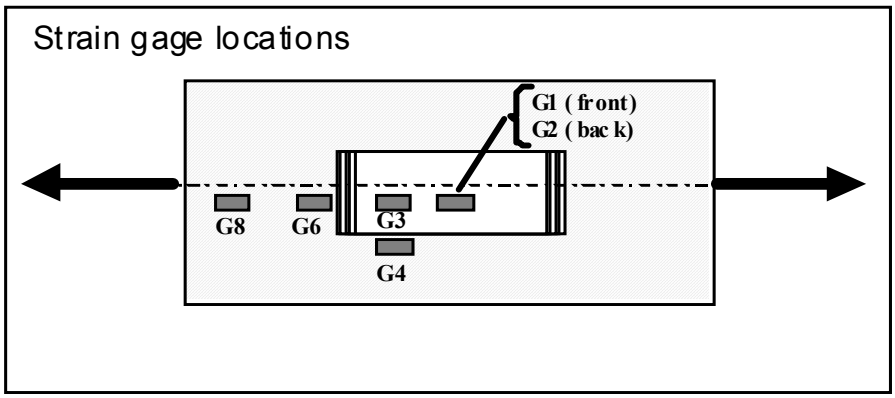

Figure 3-12: Strain Locations for Assessing Composite Doubler Designs

Strain Gage Ratio	Priority	Minimize or Maximize	Goal	Criticality of the Ratio
G2/G8	1	Min	< 0.60	Lower strain ratio prevents crack growth.
G6/G8	2	Min	< 1.15 - 1.30	Lower peel stresses / stress concentration
				at edge of patch
G1/G2	3	Max	> 0.75	Doubler design carries more load than
				underlying aluminum substrate.
G1/G8	4	Max	> 0.70	Relationship of doubler strain above notch
				to far-field steel strain.
G3/G4	5	Max	> 1.30	Doubler design carries more load than
				adjacent steel structure.
G3/G8	6	Max	> 0.70	Relationship of doubler strain in middle
				of doubler to far-field steel strain.
G4/G8	7	Min	< 0.50	Lower steel strain near doubler
				indicates if is carrying more load.

Strain Ratio:	Criteria:
G2/G8	Strain at crack compared to far field strain is most critical ratio to prevent or slow crack propagation by alleviating strain concentration at the crack. Patch width has most effect on G2/G8.
G6/G8	Strain kick in parent metal at end of patch compared to far field strain should be minimized to lessen p stresses at adhesive edge. Requires less stiff, thinner, shorter patch with abrupt taper. N most effecti
G1/G2	Strain on the patch above the notch compared to the strain on the back side of the substrate should be maximum to indicate a patch design efficiently carrying most of the applied load.
G1/G8	Relationship of strain in doubler directly above notch to far field steel strain shows load efficiency
G3/G4	Quarter patch strain on patch to same location on parent
G3/G8	Quarter patch strain to far field
G4/G8	Quarter steel strain or bypass strain to farfield strain

Table 3-3: Performance Criteria for Assessing Viability of Composite Doubler Repairs

Table 3-4 summarizes the results from the final two design iterations. The green-filled boxes indicate that the strain ratio goal was achieved. Note that in the second design scenario - which was the final design selected for the performance tests - the top three goals were met while the lower four goals are very close to the desired numbers. Finally, Table 3-5 summarizes the geometry of the composite doubler design to reveal a 24-ply doubler that is 9.4" long, 5" wide, has a 2.2" long taper region (16:1 ply drop-off rate), and a central, full-thickness length of 5". Figure 3-13 shows the engineering drawing of this repair.

Design Scenario #1

Strain Ratio:	Goal	Current
G2/G8	< 0.60	0.2140
G6/G8	< 1.15 - 1.30	1.3103
G1/G2	> 0.75	1.3147
G1/G8	> 0..70	0.8706
G3/G4	> 1.30	1.3656
G3/G8	> 0.70	0.7906
G4/G8	< 0.50	0.6181

N = 10; W_r = 5, Taper = 2.75 (TR = 20); R_x = 0.336; Off-Angle Plies = $\pm$ 30^o

Design Scenario #2

Strain Ratio:	Goal	Current
G2/G8	< 0.60	0.3764
G6/G8	< 1.15 - 1.30	1.1860
G1/G2	> 0.75	1.0373
G1/G8	> 0..70	0.6690
G3/G4	> 1.30	1.2457
G3/G8	> 0.70	0.6223
G4/G8	< 0.50	0.5910

N = 5, W_r = 5, Taper = 2.2 (TR = 16); R_x = 0.307; Off-Angle Plies = $\pm$ 45^o

Table 3-4: Comparison of Strain Ratio Evaluations Corresponding to User-Supplied Design Trade-Off Adjustments

Patch Design from 'Baker Criteria' sheet:	
No. of plies	24
Transfer Length β (in)	0.4805
Patch Width Wp (in)	5.0000
Constant Thickness Length Lr (in)	5.0000
Step-off Rate of tapered edge	16
Tapered length Lt [each end] (in)	2.2000
Total length Lp (in)	9.4000
Corner Angle (deg)	0
Stacking Sequence	Wedding Cake

Table 3-5: Summary of Final Composite Doubler Design Dimensions

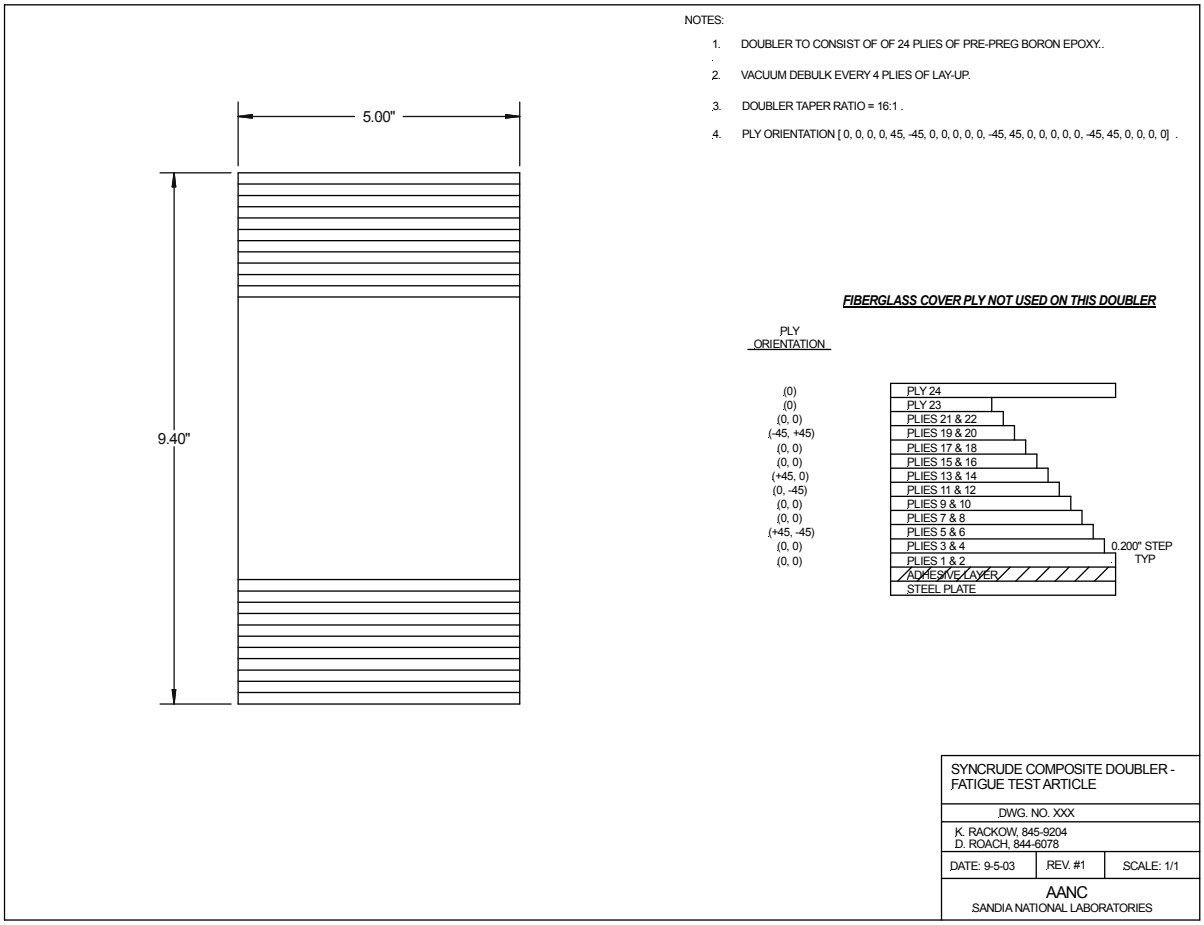

Figure 3-13: Final Composite Doubler Design

3.3.4 Performance Test Specimen Configurations

The specimen configurations that were tested are summarized in Table 3-6. All but seven of the 27 specimens consisted of a steel "parent" plate with a bonded composite doubler. The doubler was bonded over an unabated crack in the steel structure. The other eight specimens contained unrepaired fatigue cracks in the weld region and provided unrepaired baselines to assess composite doubler performance. Tension-tension fatigue and residual strength tests were conducted on these specimens to evaluate: 1) the composite doubler design methodology, 2) the doubler installation process, 3) the damage tolerance of composite repairs, 4) crack mitigation performance, and 5) long-term durability and strength in the presence of severe environments and off-design conditions.

Figures 3-14 and 3-15 show the two basic building blocks for the various test configurations: 1) precracked specimen with optimum composite doubler repair and 2) precracked specimen with a flawed composite doubler repair. The installed flaws consisted of pull tabs in the critical load transfer (tapered edge) region and Teflon inserts placed directly over the crack. Both methods produce disbonds between the composite doubler and the steel structure. Figure 3-16 shows the flaw inserts placed on a steel panel before the application of the composite repair. It also shows two composite doublers being positioned for final curing and bonding to the steel panels. Note the six thermocouples placed around the perimeter of the doubler installations. These provide temperature feedback to the hot bonder to control the cure temperature profile. The fatigue and ultimate strength test specimen configurations are summarized as follows:

- All 27 specimens contained a full penetration weld simulating a crack fill process (see Fig. 3-10)
- Total of 27 specimens: 20 with composite doubler repairs, 7 unrepaired baseline specimens
  1. Weld repair only with re-crack (no composite doubler)
  2. Hybrid repair - weld with re-crack and repaired with optimum composite doubler
  3. Hybrid repair - weld with re-crack and repaired with flawed composite doubler
  4. Hybrid repair - weld with re-crack and repaired with optimum composite doubler; specimen conditioned with hot-wet and/or cold exposure
  5. Hybrid repair - weld with re-crack and repaired with flawed composite doubler; specimen conditioned with hot-wet and/or cold exposure
- Three fatigue stress spectrums: 24 ksi, 33 ksi, 41 ksi; corresponds to amplification of 2, 3, and 4 times the field stress measurements of 10-11 ksi.
- Ultimate (residual strength) failure tests conducted on select panels after fatigue testing.

Generation of Cracks in Steel Parent Material - Prior to installing the composite doublers, fatigue cracks were generated in the weld region of the steel substrate plate. Specimen configurations listed in Table 3-6 with the descriptor "re-crack" were used to simulate welded repairs that subsequently cracked. First, 0.75" length saw cuts were placed in the steel panels to provide starter notches for the fatigue cracks. Second, tension-tension fatigue loads were applied and crack gages with 0.010" resolution were used to monitor 0.25" of actual fatigue crack growth in the specimens. These pre-doubler, crack lengths were recorded and used as the initial crack lengths in the subsequent composite coupon fatigue tests after the composite doubler was

installed. Three different fatigue load spectrums were applied to induce stress levels of 24 ksi, 33 ksi, and 41 ksi. Note that the yield stress level for the ASTM572 material is 50 to 65 ksi.

Specimen No.	Condition	Pristine or Flawed	Stress Spectrum (psi)	Specimen Configuration
SYN-FAT-10	Baseline Unrepaired	N/A	2ksi - 24 ksi	Weld repair only with re-crack (no composite doubler)
SYN-FAT-5	No Conditioning	Pristine	2ksi - 24 ksi	Hybrid weld & composite doubler repair with re-crack
SYN-FAT-9	No Conditioning	Flawed	2ksi - 24 ksi	Hybrid weld & composite doubler repair with re-crack and installation flaws
SYN-FAT-16	Hot-Wet Plus Cold	Pristine	2ksi - 24 ksi	Hybrid weld & composite doubler repair with re-crack
SYN-FAT-18	Hot-Wet Plus Cold	Flawed	2ksi - 24 ksi	Hybrid weld & composite doubler repair with re-crack and installation flaws
SYN-FAT-19	No Conditioning	Pristine	2ksi - 24 ksi	Hybrid weld & composite doubler repair with re-crack
SYN-FAT-21	No Conditioning	Flawed	2ksi - 24 ksi	Hybrid weld & composite doubler repair with re-crack and installation flaws
SYN-FAT-22	No Conditioning	Pristine	2ksi - 24 ksi	Hybrid weld & composite doubler repair with re-crack (SAND surface prep)
SYN-FAT-25	Baseline Unrepaired	N/A	2ksi - 24 ksi	Weld repair only with re-crack (no composite doubler)
SYN-FAT-5A	No Conditioning	Pristine	2ksi - 33 ksi	Hybrid weld & composite doubler repair with re-crack
SYN-FAT-9A	No Conditioning	Flawed	2ksi - 33 ksi	Hybrid weld & composite doubler repair with re-crack and installation flaws
SYN-FAT-14	Hot-Wet	Pristine	2ksi - 33 ksi	Hybrid weld & composite doubler repair with re-crack
SYN-FAT-16A	Hot-Wet Plus Cold	Pristine	2ksi - 33 ksi	Hybrid weld & composite doubler repair with re-crack
SYN-FAT-18A	Hot-Wet Plus Cold	Flawed	2ksi - 33 ksi	Hybrid weld & composite doubler repair with re-crack and installation flaws
SYN-FAT-19A	No Conditioning	Pristine	2ksi - 33 ksi	Hybrid weld & composite doubler repair with re-crack
SYN-FAT-22A	No Conditioning	Pristine	2ksi - 33 ksi	Hybrid weld & composite doubler repair with re-crack (SAND surface prep)
SYN-FAT-24	Baseline Unrepaired	N/A	2ksi - 33 ksi	Weld repair only with re-crack (no composite doubler)
SYN-FAT-26	Baseline Unrepaired	N/A	2ksi - 33 ksi	Weld repair only with re-crack (no composite doubler)

Table 3-6: Specimen Matrix for Composite Doubler Fatigue Panels

Specimen No.	Condition	Pristine or Flawed	Stress Spectrum (psi)	Specimen Configuration
SYN-FAT-3	Baseline Unrepaired	N/A	2ksi -41 ksi	Weld repair only with re-crack (no composite doubler)
SYN-FAT-4	Baseline Unrepaired	N/A	2ksi -41 ksi	Weld repair only with re-crack (no composite doubler)
SYN-FAT-7	No Conditioning	Pristine	2ksi -41 ksi	Hybrid weld & composite doubler repair with re-crack
SYN-FAT-8	No Conditioning	Pristine	2ksi -41 ksi	Hybrid weld & composite doubler repair with re-crack
SYN-FAT-12	No Conditioning	Flawed	2ksi -41 ksi	Hybrid weld & composite doubler repair with re-crack and installation flaws
SYN-FAT-13	No Conditioning	Flawed	2ksi -41 ksi	Hybrid weld & composite doubler repair with re-crack and installation flaws
SYN-FAT-15	Hot-Wet	Pristine	2ksi -41 ksi	Hybrid weld & composite doubler repair with re-crack
SYN-FAT-17	Hot-Wet	Flawed	2ksi -41 ksi	Hybrid weld & composite doubler repair with re-crack and installation flaws
SYN-FAT-20	Baseline Unrepaired	N/A	2ksi -41 ksi	Weld repair only with re-crack (no composite doubler)

Table 3-6 (cont.): Specimen Matrix for Composite Doubler Fatigue Panels

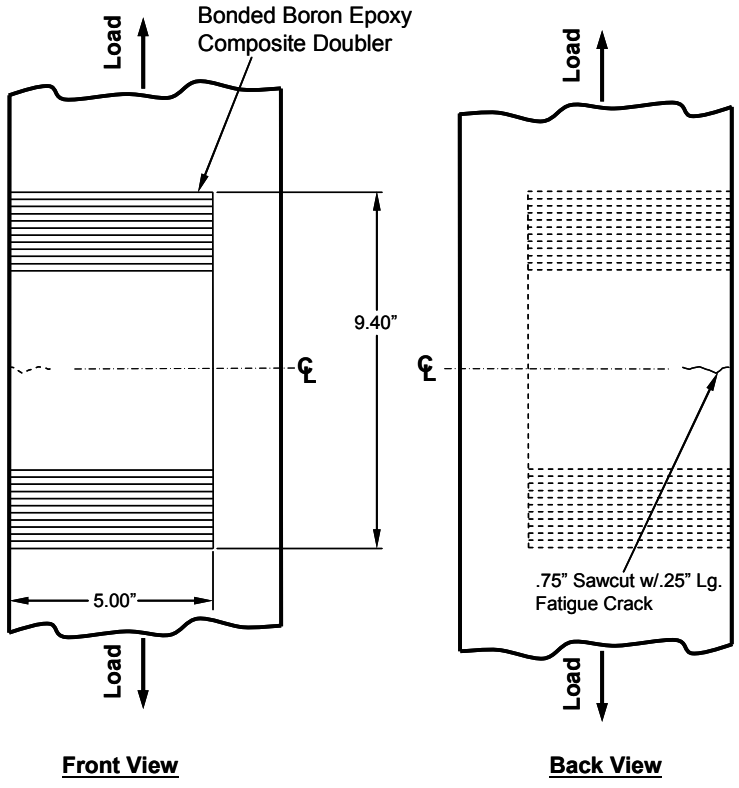

Figure 3-14: Tension-Tension Fatigue Panel with Optimum Composite Doubler Repair

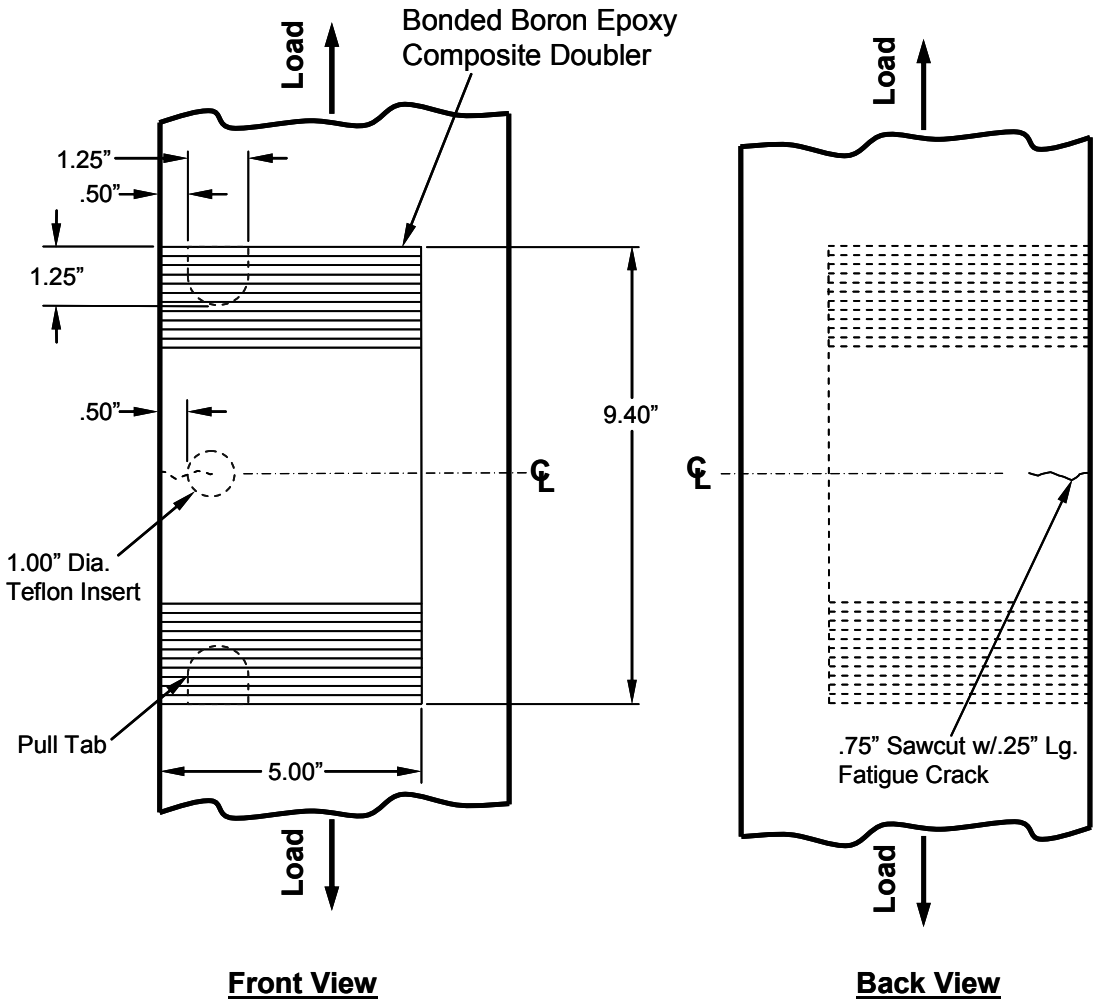

Figure 3-15: Tension-Tension Fatigue Panel with Flawed Composite Doubler Repair Installation

Temperature and Humidity Conditioning – Table 3-6 also indicates the specimens that were subjected to temperature and humidity conditioning. In order to simulate moisture absorption that may occur during field operations, the specimens were placed in an environmental conditioning chamber at 140°F ± 5°F and 97% ± 3% relative humidity. The specimens remained in the chamber for 30 days to provide a period of time sufficient to achieve saturation moisture content. Some of the test specimens were then subjected to temperatures of 0°F to simulate low temperature operating conditions for composite doublers containing high moisture content. Any trapped moisture could freeze and fracture the composite fibers. Figure 3-17 shows a photo of the specimen being inserted into the environmental chamber for hot-wet conditioning and the freezer for 0°F temperature exposure. *Note that this conditioning produces very conservative tests since the normal fiberglass cover plies and epoxy paint coatings, absent in the fatigue test specimens, will almost eliminate moisture absorption in the field.*

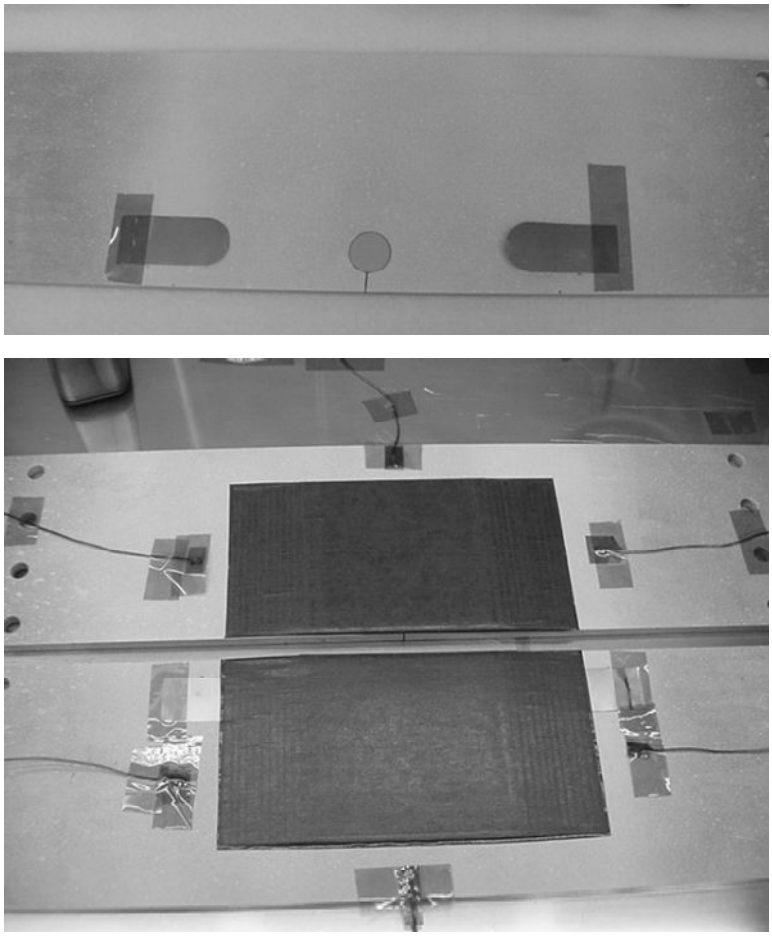

Figure 3-16: Flaw Insert Placement On Steel Surface and Cure of Composite Doublers on Steel Coupons

Figure 3-17: Tension Specimens Being Placed into Environmental Chamber and Freezer for Hot/Wet and Cold Conditioning

3.3.5 Load Spectrums and Instrumentation

The lowest stress level for the fatigue tests (baseline stress levels) was 24 ksi to represent slightly more than two times the stress level measured during field monitoring exercises. This assessed composite doubler repairs in stress riser regions where the stress may be amplified by as much as a factor of two. Additional fatigue tests applied stress levels of 33 ksi (3 times the field stress levels) and 41 ksi (4 times the field stress levels) in order to study performance in high stress environments approaching yield levels. These were extremely conservative tests intended to establish safety factors associated with composite doubler repair technology. All fatigue tests were conducted at a test frequency of 3 – 5 Hz. Several specimens that survived the fatigue tests were subjected to ultimate tension tests in order to determine their ultimate/residual strength and to determine failure modes. During residual strength testing, the load was increased, using displacement mode control, at a continuous rate of 0.05 inch/minute. Failure was defined as the point where the specimen was unable to sustain an increasing load.

Strain Field and Crack Growth Monitoring - Load transfer through the composite doubler, stress reduction around cracks, and stress risers around the defects were monitored using the strain gage layouts shown in Figures 3-18 to 3-22. Some biaxial gages were used to measure both the axial and transverse strains in the anisotropic composite material. [In Figs. 3-18 and 3-19, the first number listed represents the axial gage and the second number represents the lateral gage.] Crack growth gages with a resolution of 0.2" per filament were mounted on the back side of the specimen (steel surface) to measure the sequential growth of the seeded fatigue crack. Strain measurements were acquired before and after the fatigue tests and at select intervals during the fatigue tests. These intervals were determined by crack propagation in the test specimen (i.e. after the crack gage indicated additional crack growth).

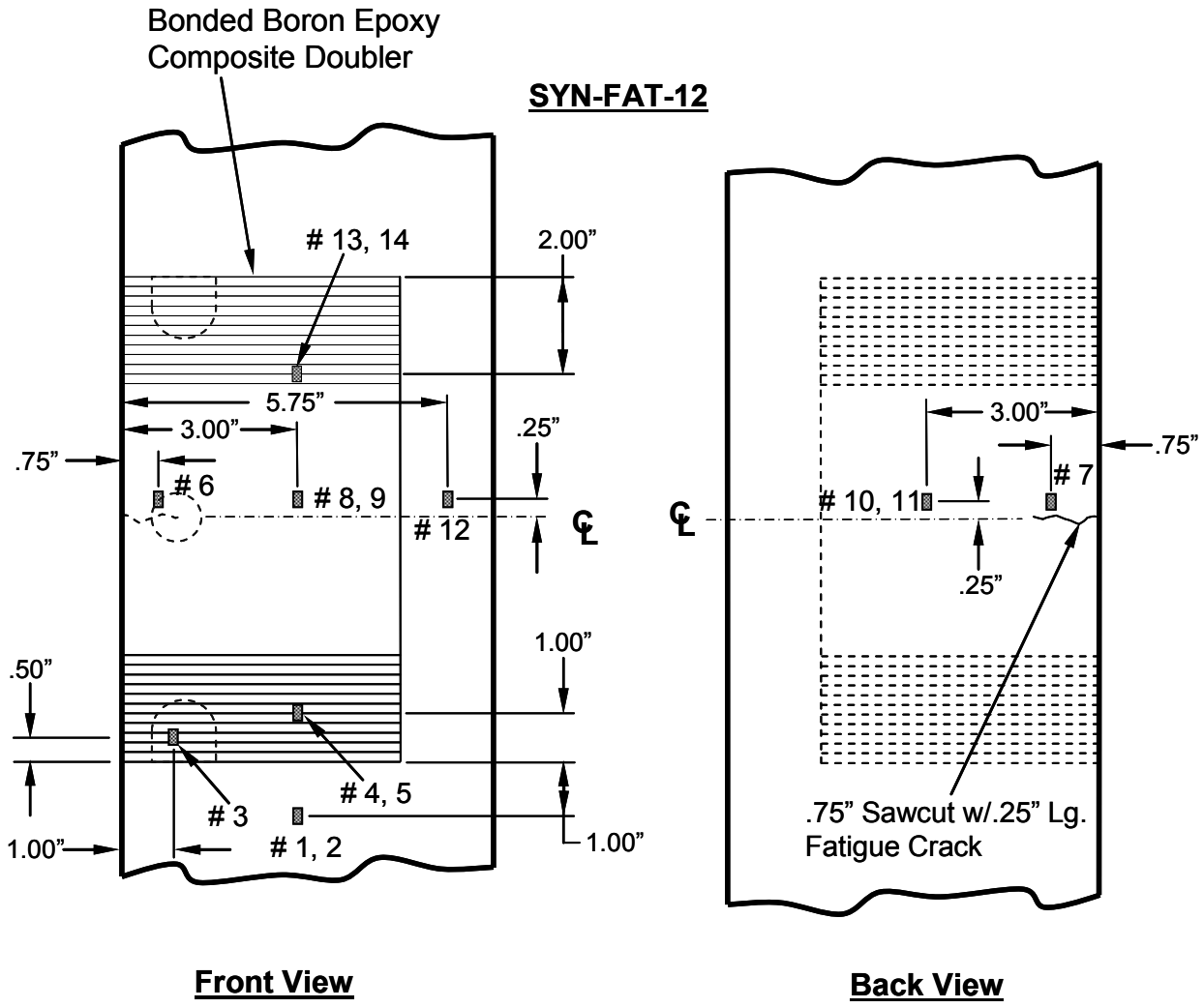

Figure 3-18: Strain Gage Layout on Flawed Composite Repair Installation; Unconditioned Specimen SYN-FAT-12

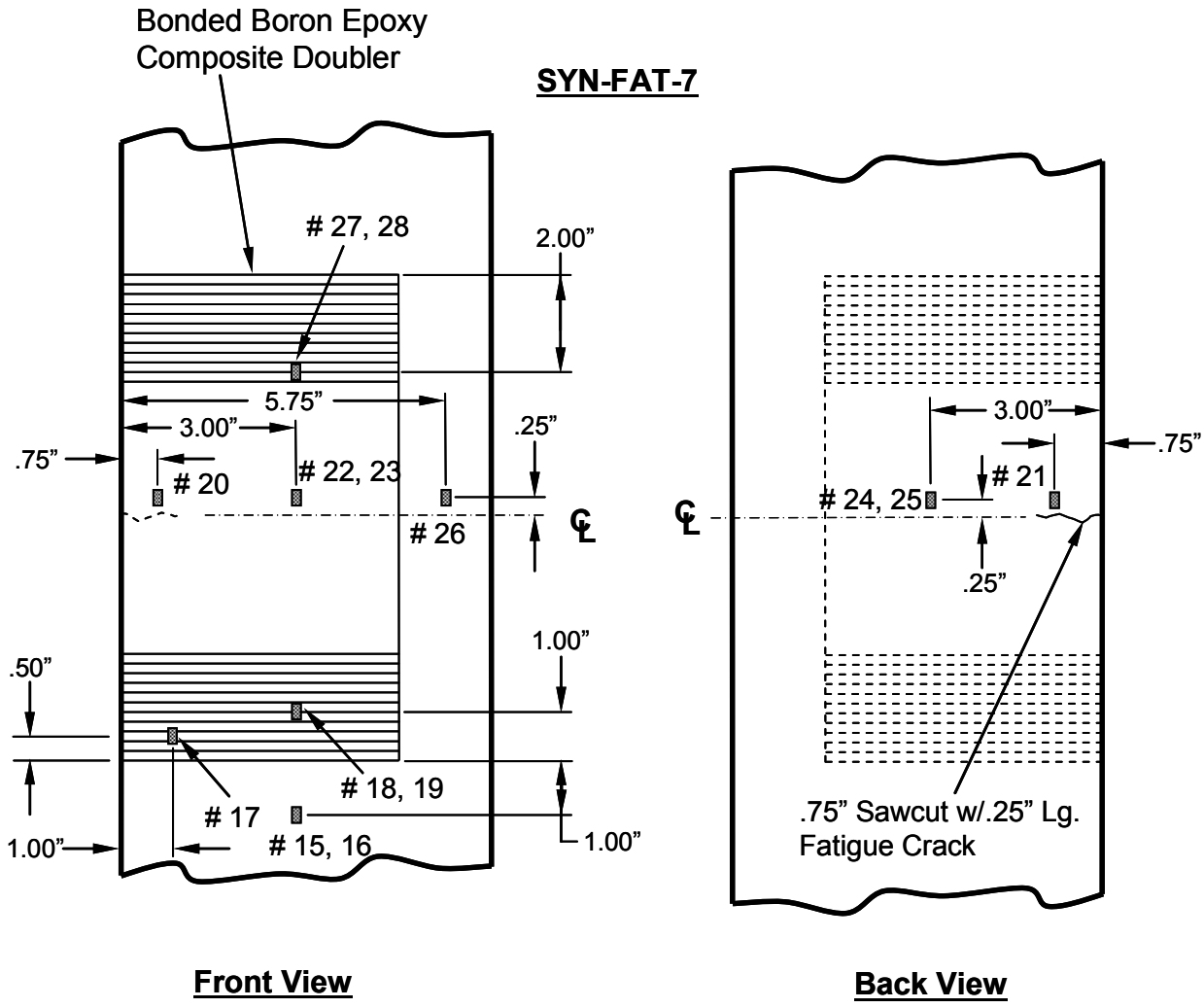

Figure 3-19: Strain Gage Layout on Unflawed Composite Repair Installation; Unconditioned Specimen SYN-FAT-7

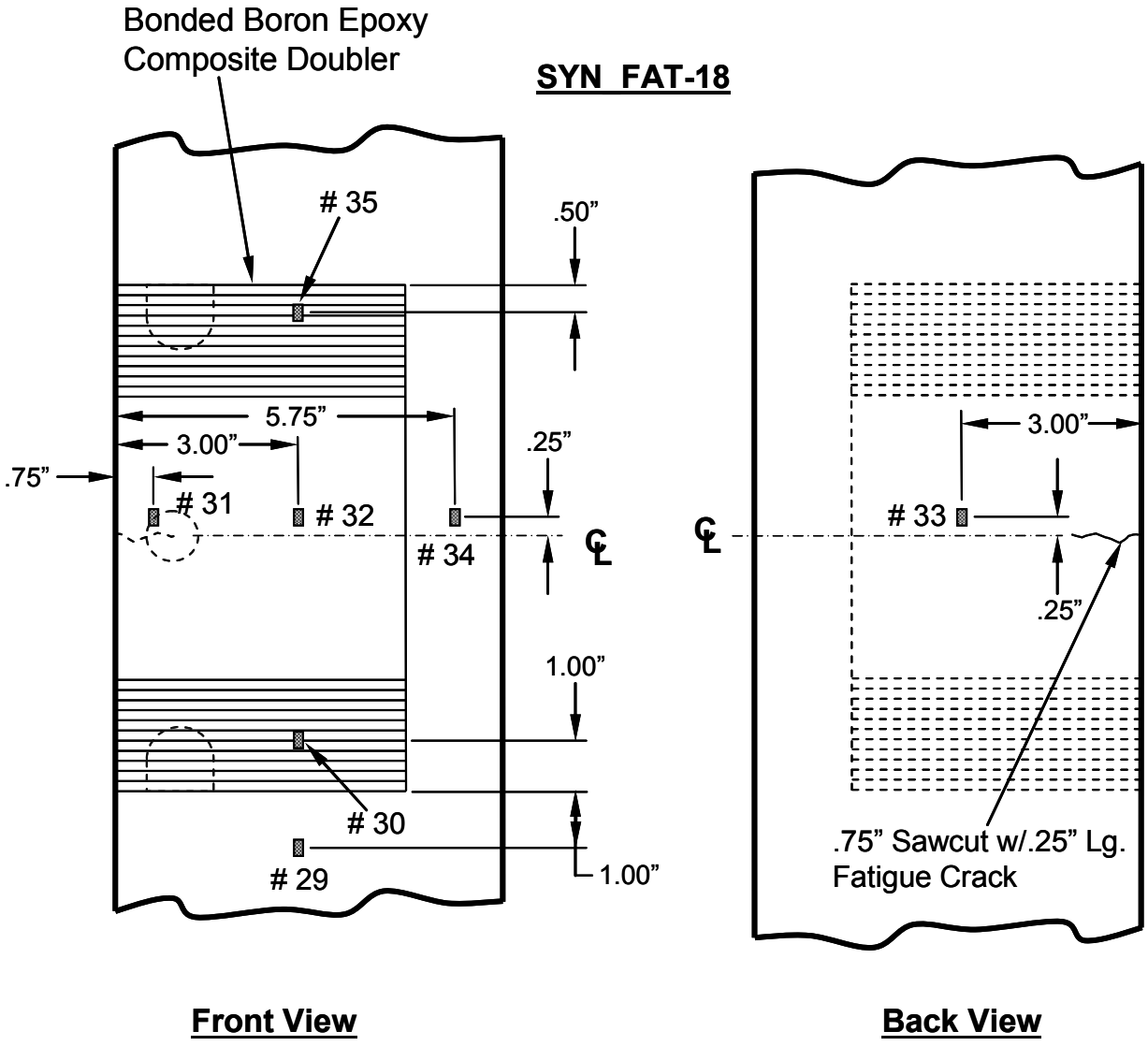

Figure 3-20: Strain Gage Layout on Flawed Composite Repair Installation; Conditioned Specimen SYN-FAT-18

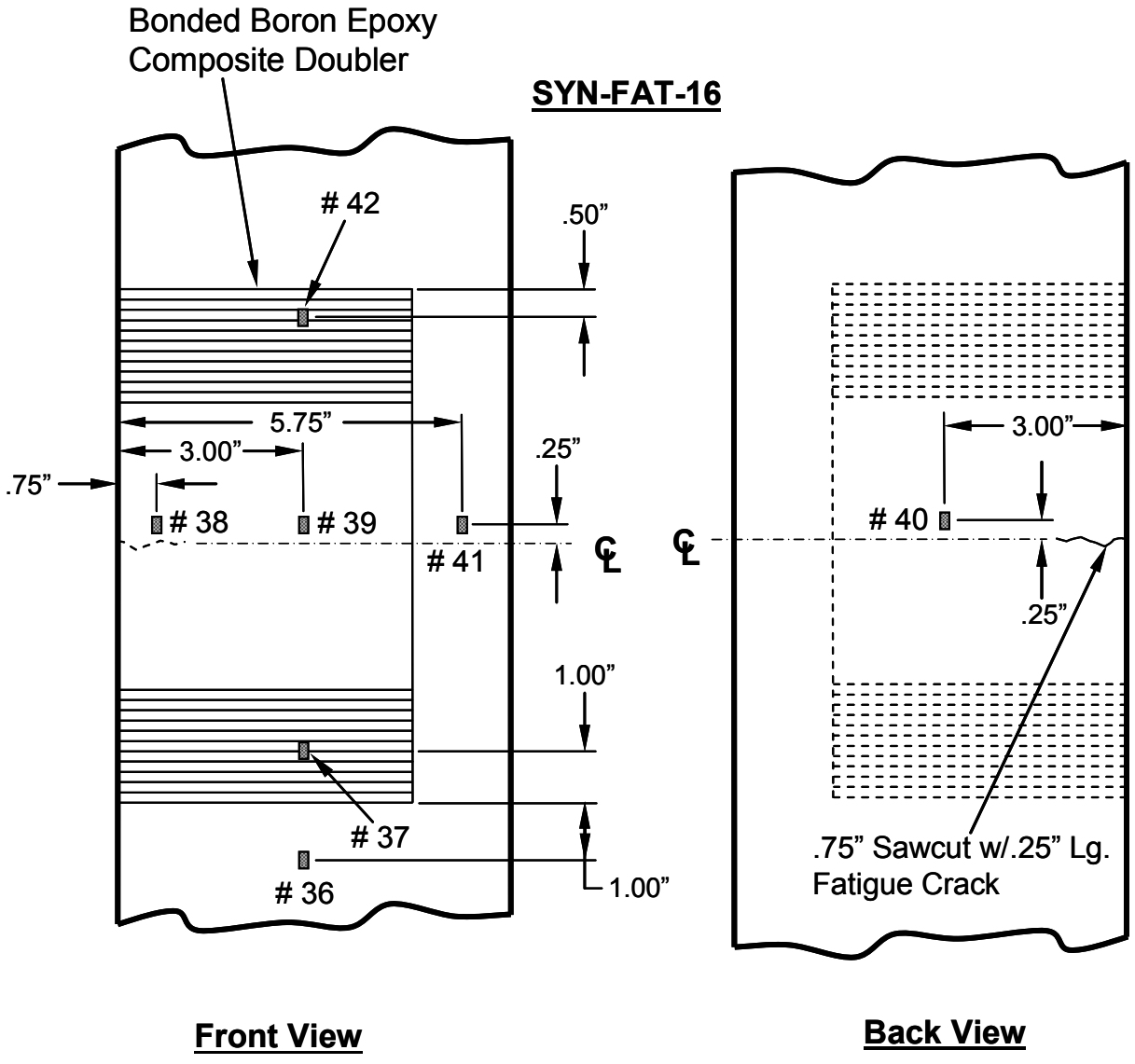

Figure 3-21: Strain Gage Layout on Unflawed Composite Repair Installation; Conditioned Specimen SYN-FAT-16

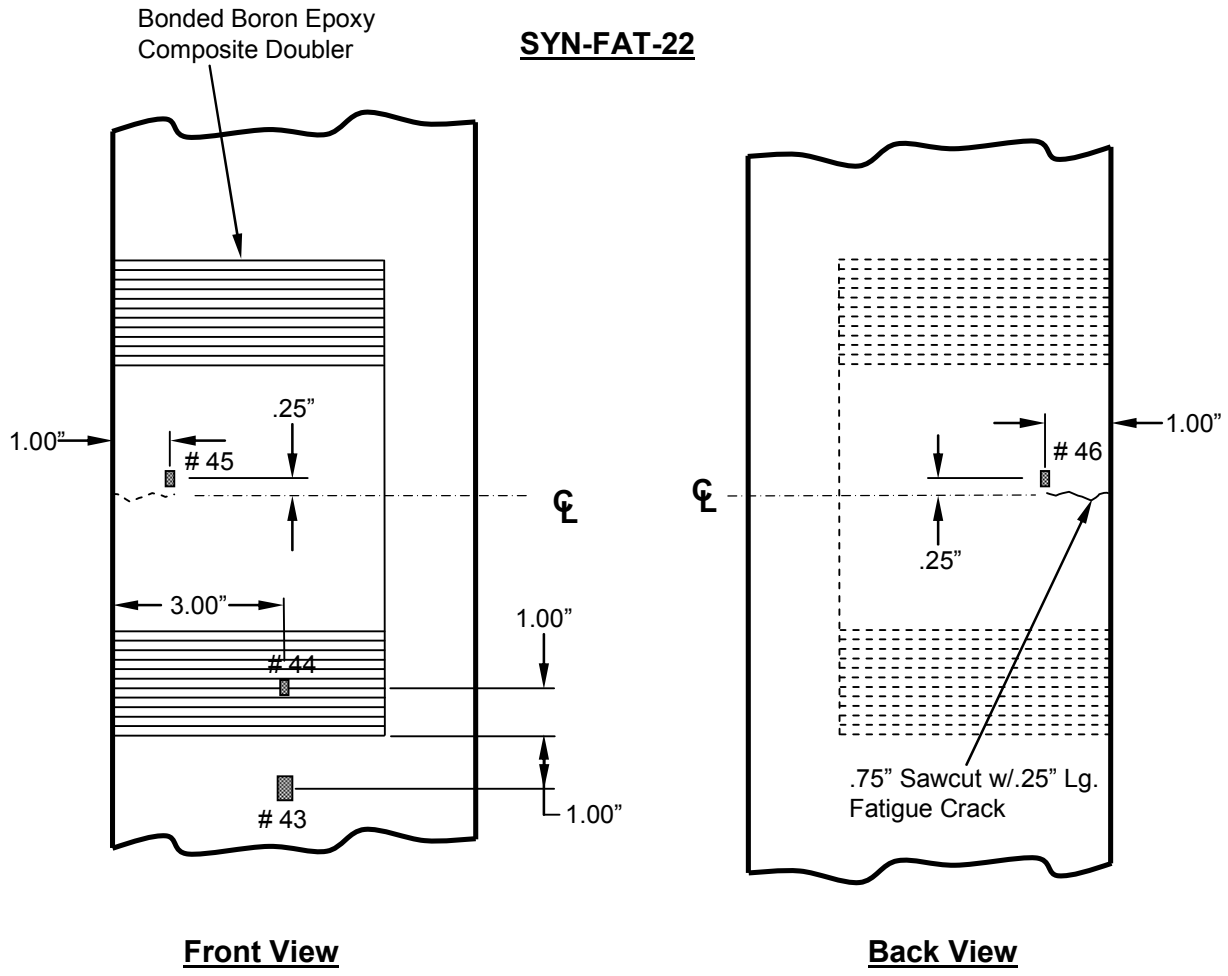

Figure 3-22: Strain Gage Layout on Unflawed Composite Repair Installation; Unconditioned Specimen SYN-FAT-22

References

3.1 Jones, R. and Callinan, R., "A Design Study in Crack Patching," Fibre Science and Technology, Vol. 14, 1981.

3.2 Jones, R., Chiu, C., Paul, J., "Designing for Damage Tolerant Bonded Joints," *Composite Structures*, Vol. 25, 1993.

3.3 Roach, D., "Commercial Application of Composite Doublers for DC-10 Fuselage Repairs," Int'l SAMPE Symposium on Composites in Engineering, May 2001.

3.4 Roach, D.P., and Walkington, P., "Full Scale Structural and NDI Validation Tests on Bonded Composite Doublers for Commercial Aircraft Applications", Sandia National Laboratories/ Dept. of Energy Report No. SAND98-1015 , November 1998.

3.5 Baker, A.A., "Fatigue Studies Related to Certification of Composite Crack Patching for Primary Metallic Aircraft Structure," FAA-NASA Symposium on Continued Airworthiness if Aircraft Structures, Dept. of Transportation Report No. DOT/FAA/AR-97-2,I, July 1997.
3.6 Rice, R., Francini, R., Rahman, S., Rosenfeld, S., Rust, S., Smith, S., and Broek, D., "Effects of Repair on Structural Integrity", Dept. of Transportation Report No. DOT/FAA/CT-93/79, December 1993.
3.7 Chiu, W.K., Rees, D., Chalkley, P., and Jones, R., "Designing for Damage Tolerant Repairs," ARL Aircraft Structures Report 450, August 1992.
3.8 Obaia, K., Radke, C., "Crack Management of Mobile Equipment", Syncrude Canada Ltd., Research Department Progress Report 31 (5) 266-275 (2002).
3.9 Yin, Y., Grondin, G., Obaia, K., "Crack Management of Mobile Equipment," Syncrude Canada Ltd., Research Department Progress Report 31 (7), 2002.
3.10 Yin, Y., Grondin, G., Elwi, A., Obaia, K., "Fatigue Crack Management in Heavy Mining Equipment," Syncrude Canada Ltd., Research Department Progress Report 32 (07), 2003.
3.11 Fiebig, J., "Composite Doubler Design and Optimization Handbook Tool," Warner Robins Air Logistic Center, June 1999.

4.0 PERFORMANCE OF COMPOSITE DOUBLER REPAIR METHOD ON STEEL STRUCTURES

Dennis Roach, Kirk Rackow, and Waylon DeLong

The test results supporting this damage tolerance assessment of composite doublers will be presented in three distinct sections: 1) fatigue test results, 2) strain field measurements (evaluation of load transfer), and 3) residual strength tests. Nondestructive inspections, used to relate the above items to flaw initiation and growth, will be discussed in the section on the fatigue test results. The data presented in this chapter provides a comprehensive evaluation of the effectiveness of composite doublers in reducing crack growth in steel substructure. Fatigue and strength tests were performed on specimens with various combinations of crack and bondline flaws. The flaw sizes, locations, and combinations were engineered to produce extreme worst case conditions. Environmental conditions simulating temperature and humidity exposure are also included in the test specimens (ref. Section 3.2). Twenty-seven specimens representing five different configurations were tested.

Disbond, delamination and crack sizes used in these damage tolerance tests were at least twice the size of those which can be detected by the NDI requirements. Futhermore, the stress spectrums applied in the fatigue tests were 2 to 4 times the stress levels measured in the field. Finally, it should be noted that the cracks were started from free edges so that crack opening during faigue testing was much greater than the displacements that occur in the field. Thus, there is an inherent safety factor built into this crack mitigation and damage tolerance assessment. The composite doubler performance sited here should be conservative.

4.1 Performance Results from Damage Tolerance Tests

Photographs of the damage tolerance test set-up and a close-up view of a composite doubler test coupon are shown in Figure 4-1. Figure 4-2 shows the seeded fatigue crack, generated before the composite repair was installed, and the crack propagating through the crack growth gage during testing. The results from all of the fatigue tests are summarized in Table 4-1 which is broken down into performance for low (24 ksi), medium (33 ksi), and high (41 ksi) stress spectrums. Results from the low stress spectrum tests, which are believed to be the most representative of the maximum stress levels incurred in the field, clearly show the ability of composite doublers to eliminate crack growth when bonded to thick steel structure. The 24 ksi fatigue spectrum specimens are plotted in Figure 4-3. No fatigue crack growth was observed after 251,000 to 331,000 cycles. Nondestructive inspections, conducted after the fatigue tests, also revealed that there was no flaw initiation or growth in the composite laminate or laminate-to-steel bondline (see Section 4.2). These results were achieved in all specimens, even those containing engineered flaws and subjected to hot-wet and cold conditioning. Note that these performance impediments are anticipated to be extreme worst-case scenarios in that the disbonds removed 20% of the critical load transfer region in the doubler and also eliminated local reinforcement directly over the crack.

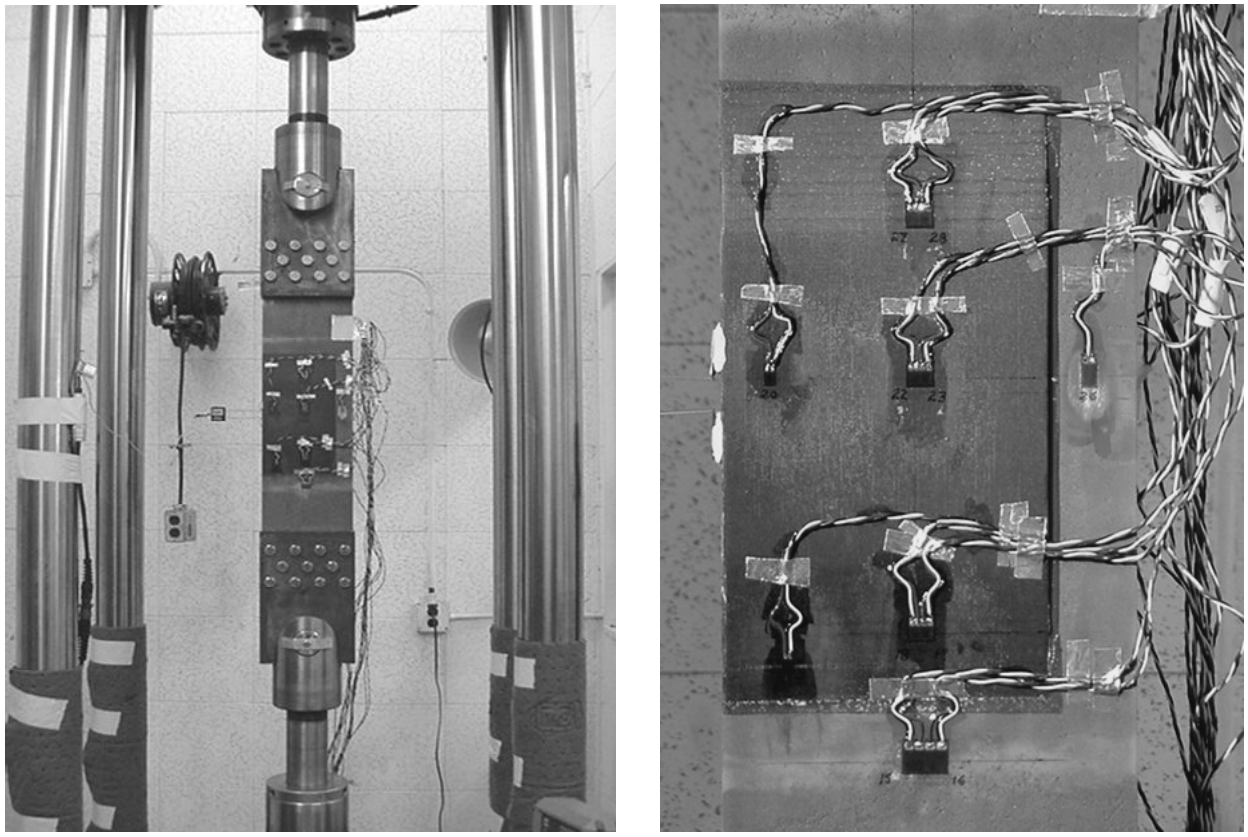

Figure 4-1: Fatigue Test Set-Up of Repaired Steel Coupons and Close-Up View of Strain Gage Layout

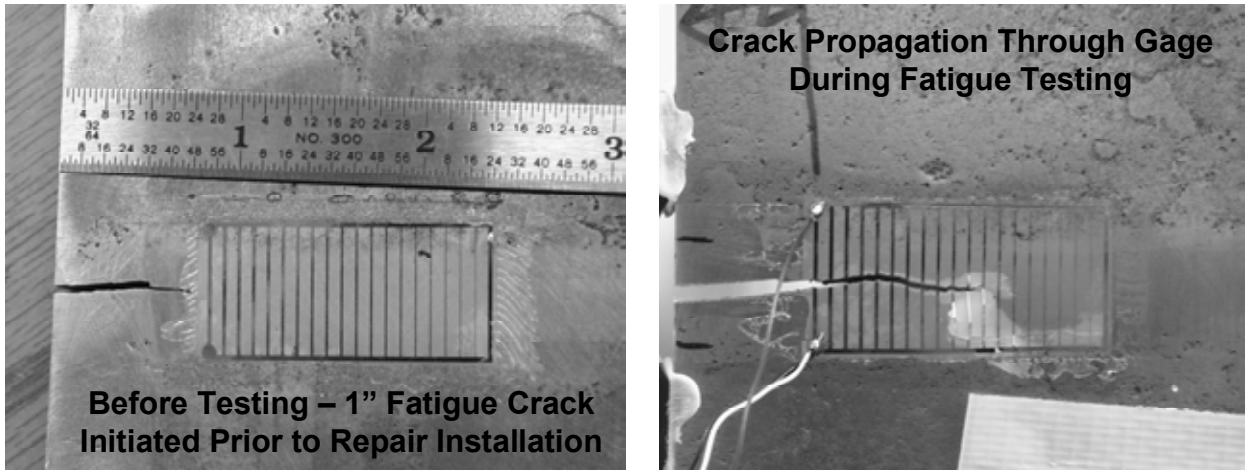

Figure 4-2: Crack Growth Gage on Back of Steel Coupon and Crack Status Before and After Fatigue Testing

Specimen No.	Condition	Pristine or Flawed	Stress Spectrum (psi)	Number of Fatigue Cycles	Total Crack Growth
SYN-FAT-10	Baseline Unrepaired	N/A	2ksi - 24 ksi	129,044	1.44"
SYN-FAT-5	No Conditioning	Pristine	2ksi - 24 ksi	251,011	None
SYN-FAT-9	No Conditioning	Flawed	2ksi - 24 ksi	323,508	None
SYN-FAT-16	Hot-Wet Plus Cold	Pristine	2ksi - 24 ksi	331,384	None
SYN-FAT-18	Hot-Wet Plus Cold	Flawed	2ksi - 24 ksi	325,017	None
SYN-FAT-19	No Conditioning	Pristine	2ksi - 24 ksi	250,000	0.030"
SYN-FAT-21	No Conditioning	Flawed	2ksi - 24 ksi	250,000	0.098"
SYN-FAT-22	No Conditioning	Pristine	2ksi - 24 ksi	250,000	0.030"
SYN-FAT-25	Baseline Unrepaired	N/A	2ksi - 24 ksi	65,000	1.45
SYN-FAT-5A	No Conditioning	Pristine	2ksi - 33 ksi	188,703	0.96"
SYN-FAT-9A	No Conditioning	Flawed	2ksi - 33 ksi	299,017	0.88"
SYN-FAT-14	Hot-Wet	Pristine	2ksi - 33 ksi	628,422	0.80"
SYN-FAT-16A	Hot-Wet Plus Cold	Pristine	2ksi - 33 ksi	208,391	0.64"
SYN-FAT-18A	Hot-Wet Plus Cold	Flawed	2ksi - 33 ksi	241,859	0.96"
SYN-FAT-19A	No Conditioning	Pristine	2ksi - 33 ksi	146,000	0.96"
SYN-FAT-22A	No Conditioning	Pristine	2ksi - 33 ksi	192,000	0.93
SYN-FAT-24	Baseline Unrepaired	N/A	2ksi - 33 ksi	11,033	1.47
SYN-FAT-26	Baseline Unrepaired	N/A	2ksi - 33 ksi	16,000	1.32
SYN-FAT-3	Baseline Unrepaired	N/A	2ksi -41 ksi	12,651	5.50"
SYN-FAT-4	Baseline Unrepaired	N/A	2ksi -41 ksi	9,743	5.50"
SYN-FAT-7	No Conditioning	Pristine	2ksi -41 ksi	109,004	1.355"
SYN-FAT-8	No Conditioning	Pristine	2ksi -41 ksi	110,897	1.525"
SYN-FAT-12	No Conditioning	Flawed	2ksi -41 ksi	86,500	1.42"
SYN-FAT-13	No Conditioning	Flawed	2ksi -41 ksi	70,143	1.47"
SYN-FAT-15	Hot-Wet	Pristine	2ksi -41 ksi	42,399	5.50"
SYN-FAT-17	Hot-Wet	Flawed	2ksi -41 ksi	23,266	1.20"
SYN-FAT-20	Baseline Unrepaired	N/A	2ksi -41 ksi	739	1.58"

Table 4-1: Composite Doubler Crack Mitigation and Damage Tolerance Fatigue Test Summary

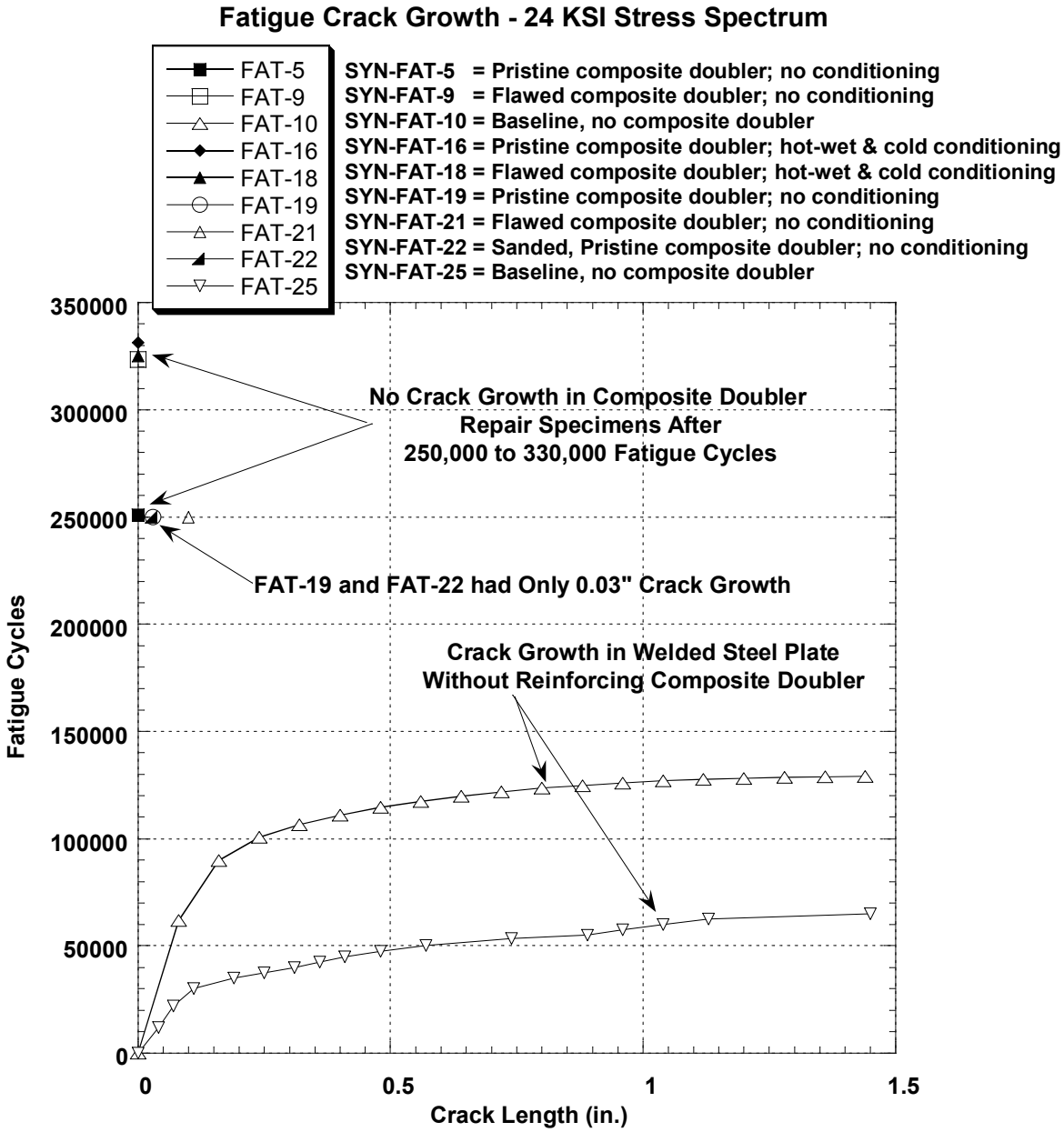

Figure 4-3: Fatigue Crack Growth in Steel Plates With and Without Composite Doubler Repairs; 24 ksi Stress Fatigue Spectrum

Since the initial goal was to survive 250,000 fatigue cycles, most of the tests were stopped at 250,000 cycles and the rest were stopped at the 30% overtest level (325,000 cycles). These same specimens were then tested using the medium stress spectrum (33 ksi). The fatigue cycles accumulated in the 24 ksi stress spectrum were translated into equivalent 33 ksi stress cycles using equation (4-1). Fatigue testing was continued from this point until 1" to 1.5" of crack growth was produced. Calculation of the equivalent number of fatigue cycles at a higher stress spectrum was accomplished using the following equation based on a combination of Miner's Rule and the DOE-B curve.

$$N_{A_{eqv}} = N_{A_1} \left\{ \frac{S_1}{S_2} \right\}^{-4} \qquad (4\text{-}1)$$

Where:

$N_{A_{eqv}}$ = equivalent number of cycles for sample A at the specified stress spectrum

N_{A_1} = number of fatigue cycles applied at stress spectrum #1

S_1 = stress spectrum #1 (24 ksi)

S_2 = stress spectrum #2 (33 ksi)

For the 33 ksi stress spectrum, Table 4-1 indicates that the composite doublers survived 200,000 to 625,000 fatigue cycles before 0.8" to 1.0" of crack growth was produced. The corresponding crack growth plots in Figure 4-4 show that there is more scatter in the medium stress spectrum results. This is primarily due to the fact that the medium stress spectrum induces stress levels in the adhesive layer that approach the ultimate capability of the adhesive. This is especially true in the case of hot-wet conditioned specimens where testing has shown that exposure to hot-wet conditions may reduce the adhesive ultimate strength by as much as 20%. However, the overall performance characteristics indicate that the composite doublers still functioned close to the desired 250,000 fatigue cycle goal despite the heightened stress levels of 3 times those measured in the field. The unrepaired baseline specimens failed at 16,000 cycles or less. Note that these results were achieved with composite doubler specimens, containing worst-case performance impediments of engineered flaws, hot-wet and cold conditioning, and free-edge fatigue cracks.

NDI evaluations and microscopic views of the laminate and steel surfaces revealed that any flaw growth was produced by a cohesive fracture of the adhesive versus the undesirable disbond between the two adherends. This proves that the full strength of the adhesive was achieved and that repair design revisions, not installation process revisions, are needed to improve the fatigue performance in this regime.

Because the highest stress spectrum represents over 4 times those measured in the field, results from the 41 ksi tests can best be viewed by comparing the flaw growth in baseline specimens containing no composite repair to the flaw growth observed after a composite repair was installed. Figure 4-5 shows that specimens SYN-FAT-3, SYN-FAT-4, and SYN-FAT-20 failed completely (5.5" crack growth) after 10,000, 12,000, and 700 fatigue cycles, respectively at this level. The optimum composite doubler repairs (SYN-FAT-7 and SYN-FAT-8 with no engineered flaws, no conditioning) improved on this performance by an order of magnitude by only allowing approximately 1.5" of crack growth in 110,000 cycles. The effects of engineered flaws and hot-wet conditioning were much more pronounced in the 41 ksi stress spectrum. Flawed composite doubler installations allowed 1.5" of crack growth in 70,000 to 90,000 cycles, still an improvement of 7 to 9 times over the unreinforced structure. Performance of the hot-wet conditioned specimens was reduced further by the combination of the high stress levels and the

reduction in the ultimate strength of the adhesive discussed above. In this latter case, the composite doubler repaired specimens still survived 23,000 to 42,000 fatigue cycles – an improvement of 2 to 4 times over the unreinforced steel plate.

Comparison of Grit Blast and Sanding Process for Producing Surface Roughness - Recall that a secondary objective of the performance testing was to assess the composite repair process using alternative installation procedures. Specifically, it was desired to develop a surface sanding process that could replace the grit blast step for producing surface roughness. If successful, the sanding process could then be used in certain instances where the containment of the grit is a concern or the space available to conduct the grit blast is limited. Test specimen SYN-FAT-22 was prepared using machine-applied, 24 grit sand paper (Option 11) in lieu of the grit blast.

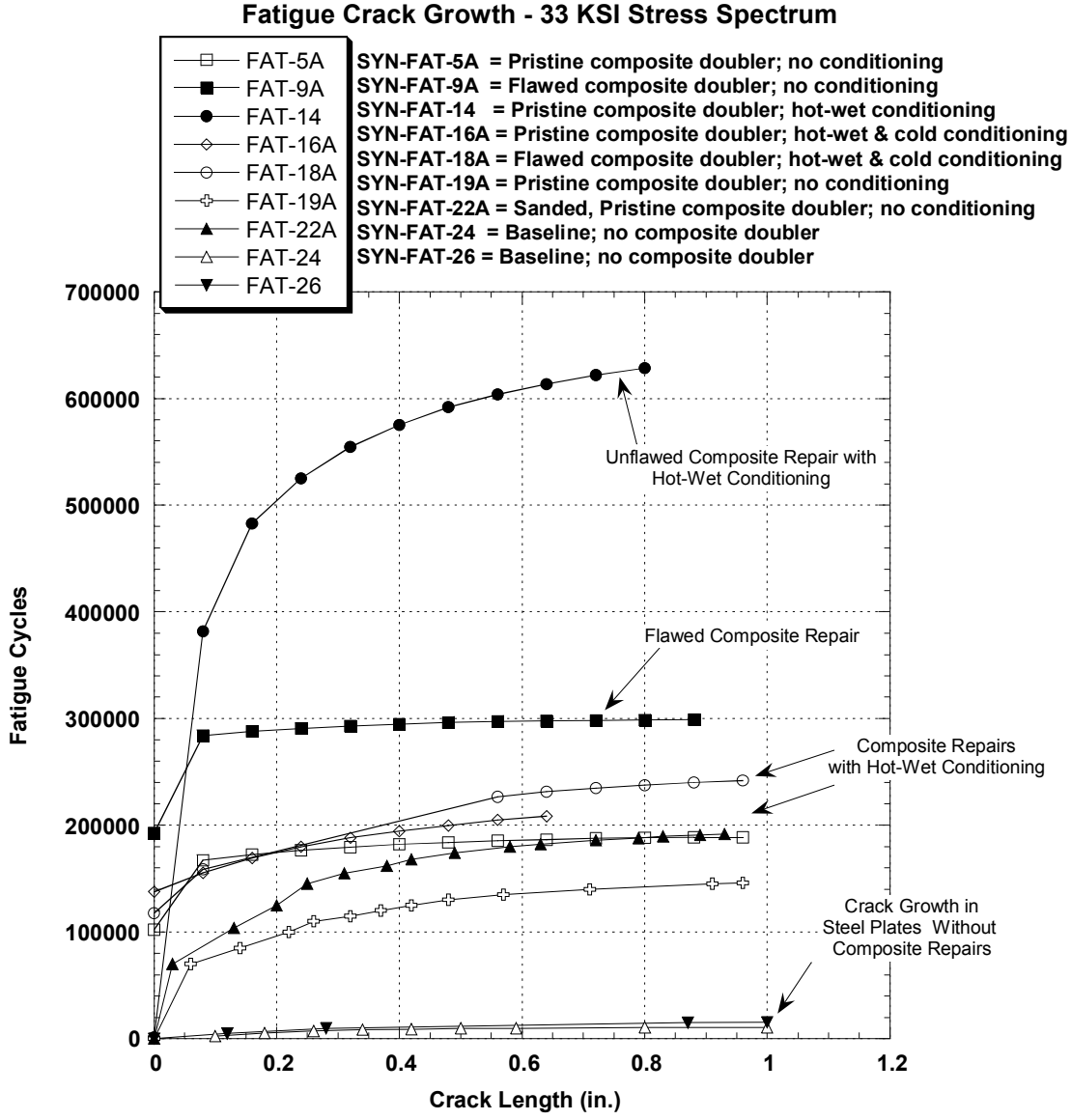

Figure 4-4: Fatigue Crack Growth in Steel Plates With and Without Composite Doubler Repairs; 33 ksi Stress Fatigue Spectrum

Table 4-1 shows that the crack mitigation and durability of SYN-FAT-22 compared well with the grit blast specimens. For the 24 KSI stress spectrum, SYN-FAT-22 only exhibited 0.030" of crack growth after 250,000 fatigue cycles (see Fig. 4-3). When tested in the more extreme 33 KSI spectrum the sanded surface specimen was still comparable with many of the other grit blast specimens, allowing only 0.93" of crack growth in 192,000 cycles (see Fig. 4-4).

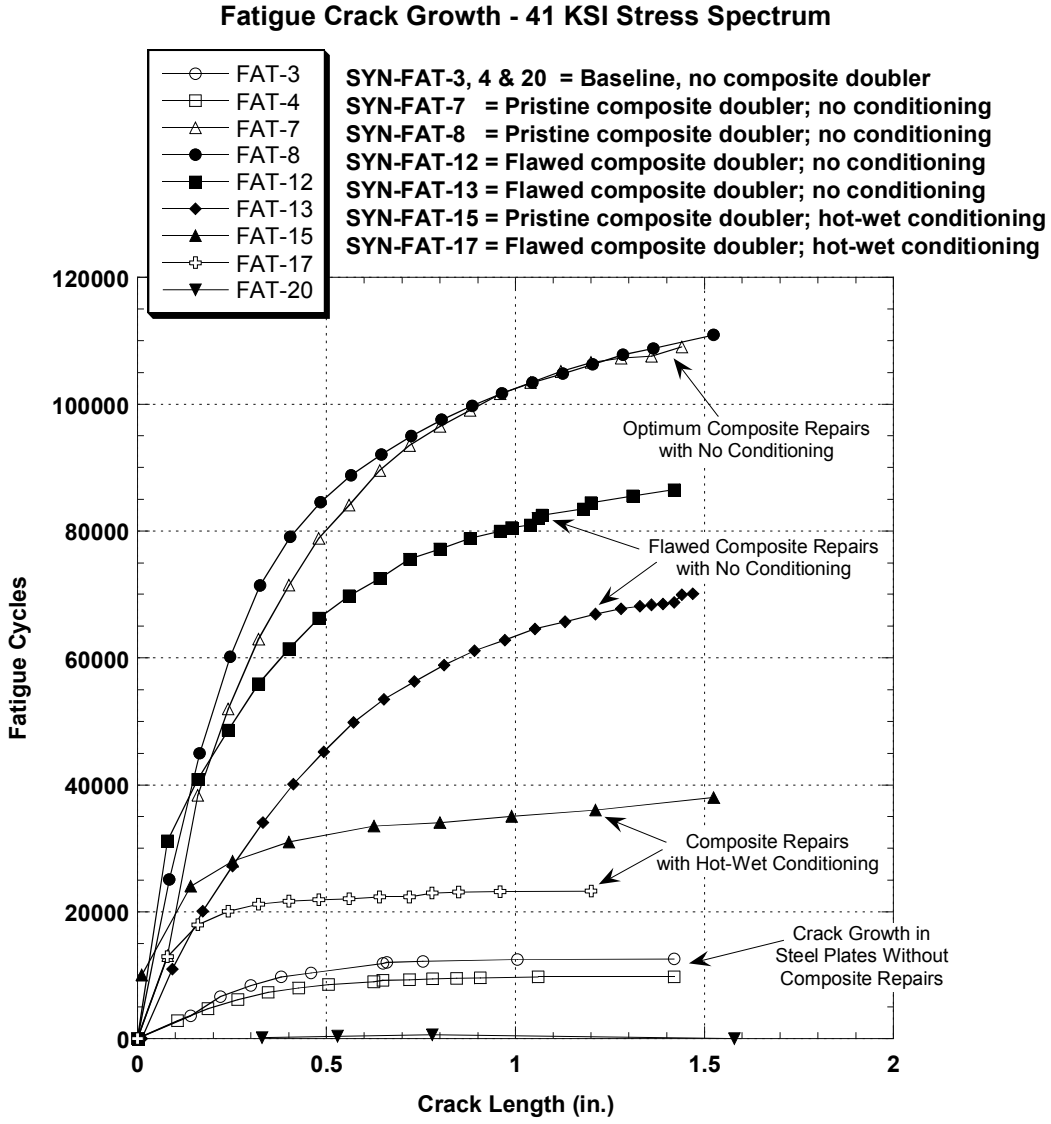

Figure 4-5: Fatigue Crack Growth in Steel Plates With and Without Composite Doubler Repairs; 41 ksi Stress Fatigue Spectrum

If the optimum composite repair – protected sufficiently to minimize or eliminate the effects of environmental conditioning – is used as the final performance metric, the results presented above indicate that the fatigue life of steel structures can be extended by a factor of 10. *Bonded*

composite doubler repairs, if properly installed, can withstand 200,000 to 600,000 fatigue cycles while allowing little or no crack growth in a parent steel structure. If small amounts of crack growth can be tolerated then composite doubler repairs may not need to be revisited until as much as 1,000,000 cycles. Furthermore, if weld repairs are first used to fill the crack and applied in conjunction with composite doublers, the fatigue life could extend another order of magnitude before significant re-cracking occurs. These results are obtained for composite laminate designs that are 30% of the stiffness of the structure being repaired.

4.2 Through-Transmission Ultrasonic Inspection of Fatigue Coupons to Assess Pre- and Post-Fatigue Damage

Through-transmission ultrasonics (TTU) passes a beam of sound energy through a component under test and, rather than interpreting the returned wave as pulse-echo ultrasonics (PE-UT) does, it uses the signals which are transmitted through the test piece. The TTU method requires the use of two transducers, one transmitting the UT wave and one acting as a receiver. Figure 4-6 shows a schematic of a TTU ultrasonic inspection system. The transducers must be accurately aligned with each other on opposite sides of the component under test. Disbonds, delaminations, or porosity in the test piece will prevent all or part of the transmitted sound from reaching the receiver transducer. As in pulse-echo UT, the TTU inspection and data interpretation can be improved through the use of C-scan systems. The C-scan records the echoes from the internal structure of the composite doubler as a function of the position of each reflecting interface within the composite material boundaries. A detailed map of the composite doubler and flaws are shown as a plan view. Both flaw size and position within the plan view are recorded, however, flaw depth is not recorded.

To perform an inspection using TTU, both sides of the test piece must be accessible. A water medium is used to provide the UT coupling. Inspections are performed with the test piece immersed in a water tank or positioned between water jets (UT squirter set-up). When using the immersion method, the part and the transducers are submerged in water. The transducers, which are not normally in contact with the inspection surface, are mounted on fixtures that automatically maintain alignment while scanning the entire test piece.

Because of the efficient UT coupling and the associated ability to optimize the amount of energy introduced to the test piece, automated, laboratory TTU immersion tanks are more accurate and sensitive than fieldable, hand scanning devices. The primary disadvantage is the need for parts to be disassembled and immersed in water in order to be inspected. Since this technique requires the sending-receiving transducer pair to be located in front and back of the structure being inspected, accessibility and deployment issues severely restrict the field application of TTU techniques. The motion of the transducer pair must be linked and water coupling to the structure, through complete immersion of the part or through focused water jets, is necessary. TTU is a very accurate NDI technique and was used to establish the degree of damage present in the fatigue test specimens before and after testing.

These damage tolerance tests assessed the potential for loss-of-adhesion flaws (disbonds and delaminations) to initiate and grow in the composite doubler installation. Disbonds can occur between the composite doubler and the steel skin while delaminations can develop between

adjacent plies of Boron-Epoxy material. It has been shown in related studies that the primary load transfer region, which is critical to the doubler's performance, is around its perimeter [4.1-4.4]. The purpose of the disbonds in configurations SYN-FAT-9, -9A, -12, -13, -17, -18, -18A, and 21 were to demonstrate the capabilities of composite doublers when large disbonds exist in the critical load transfer region, as well as around the cracks which the doublers are intended to arrest. In this manner, severe worst case scenarios could be assessed and quantitative performance numbers could be established.

The damage tolerance fatigue coupons were inspected using through-transmission ultrasonics. Figures 3-15 and 3-16 show the locations of the engineered flaws in the test coupon. Figures 4-7 and 4-8 and 4-10 to 4-13 contain the C-scan results from the TTU inspections conducted before and after fatigue testing. The validation testing revealed ultrasonic resolution and sensitivity for flaw detection less than 1/4" in diameter.

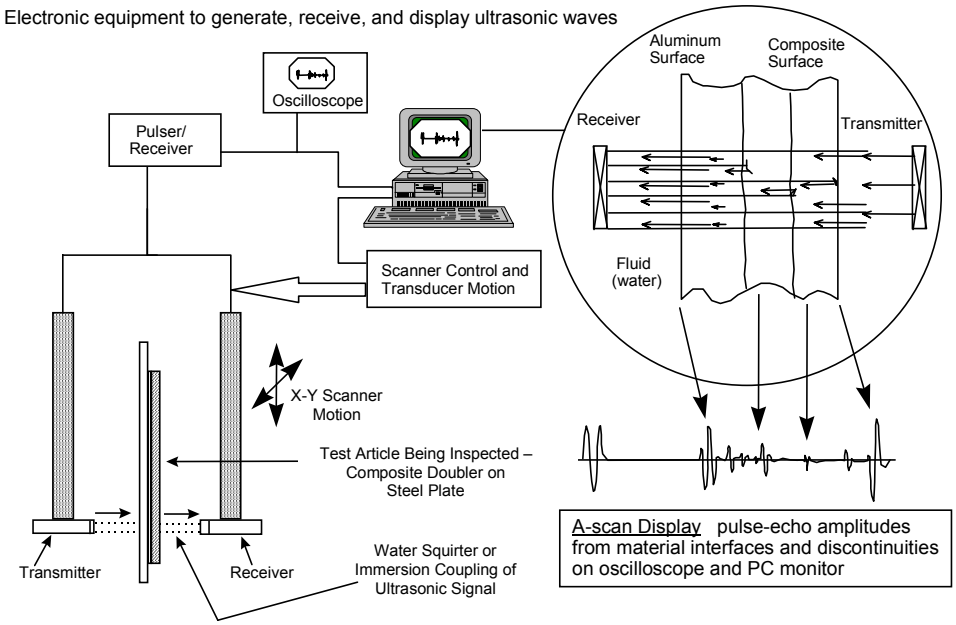

Figure 4-6: Through-Transmission Ultrasonic Test Set-Up

Figure 4-7 shows the C-scan images of several unflawed specimens. The scans show that the repair installations were good and that there weren't any unintentional flaws produced during the curing process. The color schemes in SYN-FAT-8 and SYN-FAT-15 specimens differ from the color palette in specimens SYN-FAT-7 and SYN-FAT-16 because different data acquisition settings were used during these inspections. However, there are no flaws revealed in any of the scans. Figure 4-8 clearly shows the distinct flaw regions identified in the specimens containing the engineered flaws described in Figs. 3-15 and 3-16. The dark regions indicate the three 1" diameter disbonds (pull tabs) placed over the center crack and in the critical, tapered, load-transfer region. Large deviations from the norm and the high signal attenuation levels associated with the flaw regions, makes the repair flaws easily identifiable.

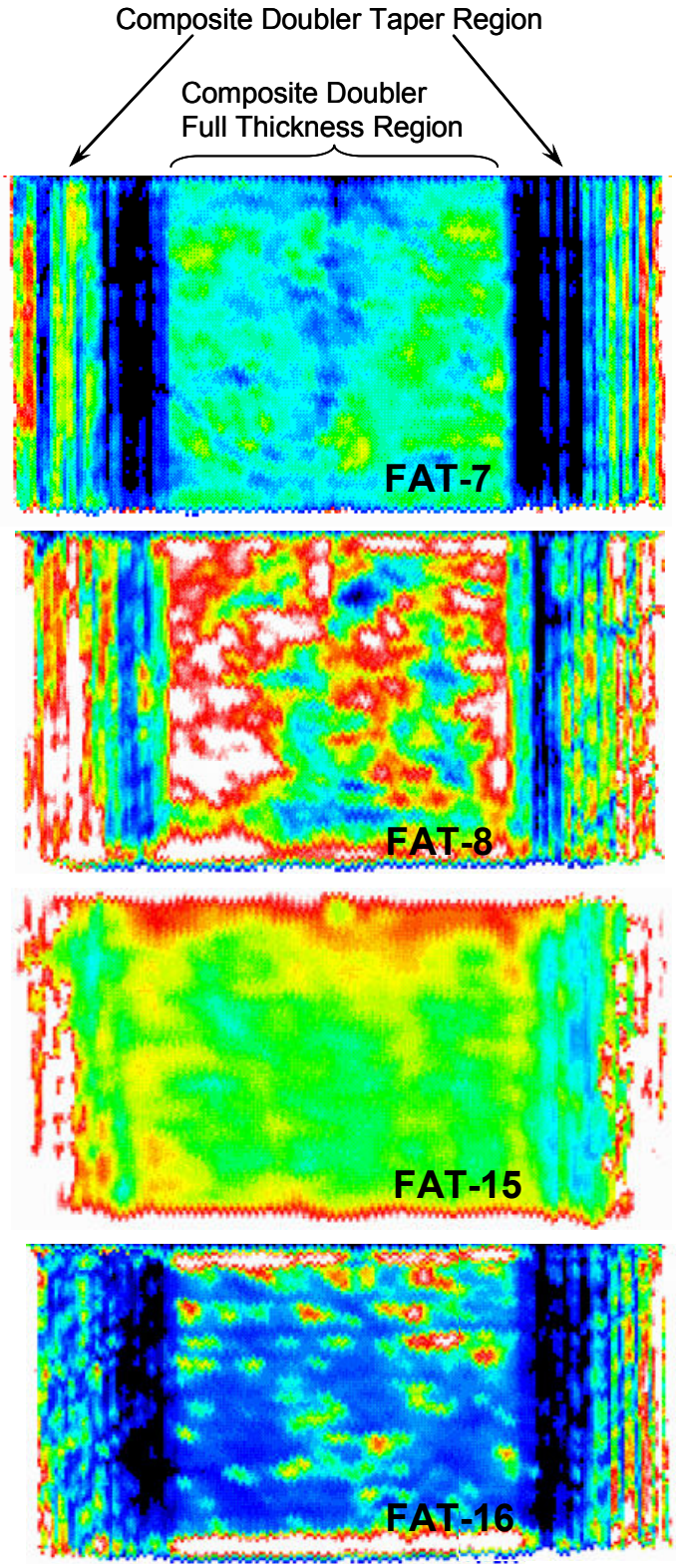

Figure 4-7: Through-Transmission Ultrasonic Images of Unflawed Test Specimens Before Fatigue Testing

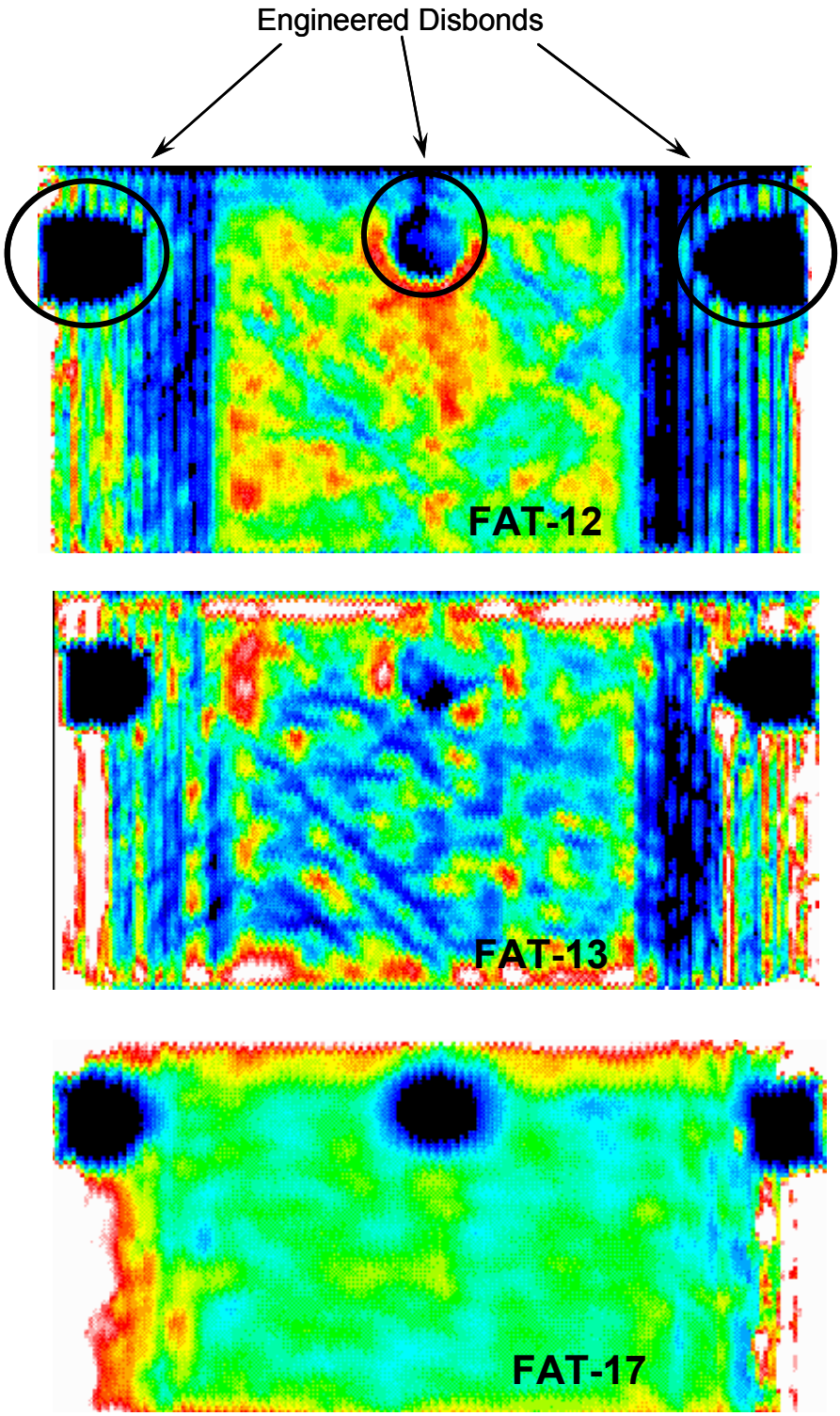

Figure 4-8: Through-Transmission Ultrasonic Images of Flawed Test Specimens Before Fatigue Testing

Views of fatigue cracks at different stages of propagation are shown in Figure 4-9. The upper left photo shows the starter notch and fatigue crack that was induced before the composite repair. This crack has not engaged the crack growth gage yet. The following three photos show the fatigue cracks generated during cyclic testing and the degree of opening associated with a free-edge crack. The lower photo shows that this crack opening gets extreme – approaching 0.5" – as the crack reaches several inches in length and the test loads are increased to ultimate failure levels. These photos highlight the local displacement in the steel around the crack. This local displacement produces one of the primary forms of degradation in the adhesive layer: cohesive fracture. As the crack opens and closes the adhesive will fracture in the area of the propagating crack. This is not a disbond (i.e. the full strength of the adhesive has been achieved) and the fracture zone is confined to the immediate region of the crack.

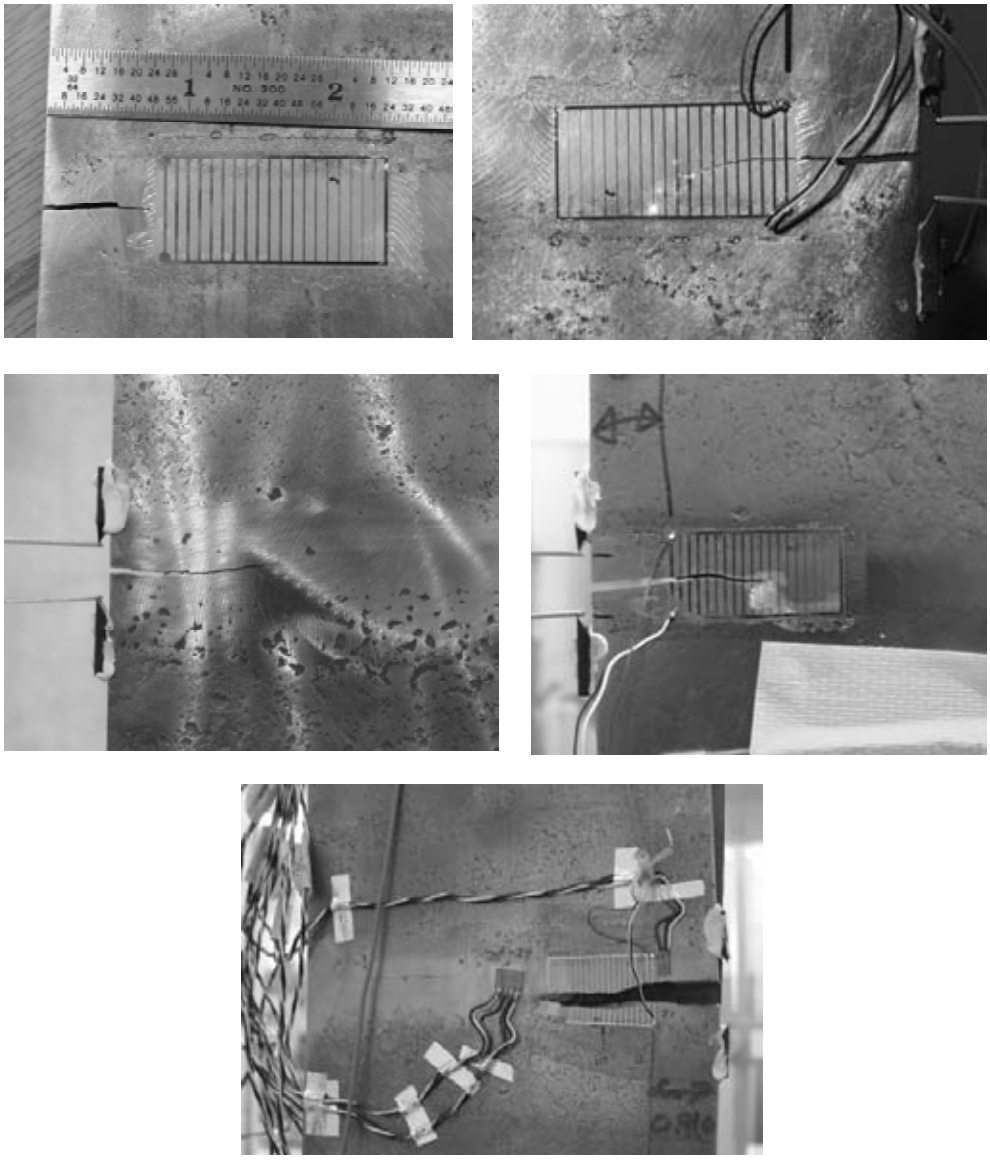

Figure 4-9: Photos of Various Stages of Crack Propagation Showing the Local Opening in the Steel Structure

The effects of this opening and closing phenomenon, and the associated fracture of the adhesive layer, can be seen the Figure 4-10. The C-scan images in Fig. 4-10 compare the flaw profiles before and after fatigue testing of specimen SYN-FAT-13. This specimen was subjected to over 70,000 cycles at the highest stress spectrum of 41 ksi (100,000 lbs.). The primary features of note are: 1) there is no growth in the disbond flaws located in the load transfer region, and 2) the adhesive fracture is confined to the immediate region of the crack with minimal impact on the overall performance of the composite doubler repair.

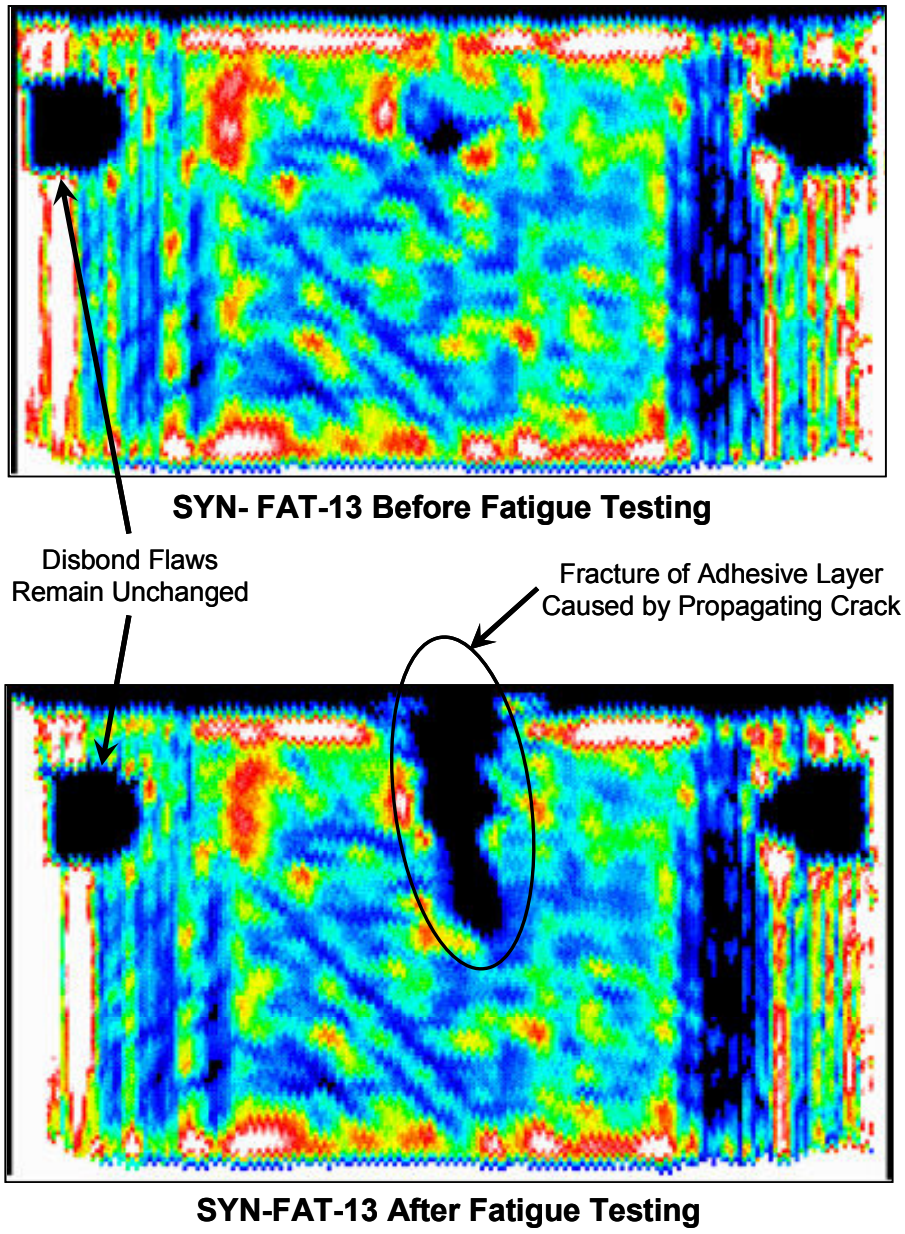

Figure 4-10: Through-Transmission Ultrasonic Images Comparing Flaw Profiles Before and After Fatigue Testing (SYN-FAT-13 flawed specimen); High Stress Spectrum = 41 ksi

Figures 4-11 to 4-13 also show the effects of fatigue loading on composite doubler repairs. Figure 4-11 compares the flaw profiles in specimen SYN-FAT-14 before and after 628,400 fatigue cycles at the medium stress spectrum of 33 ksi (80,000 lbs.). In these scans, the flaws show up as brighter regions. The primary features of note are: 1) the composite doubler survived over 600,000 fatigue cycles without failing, 2) the edge flaws are adhesive fracture regions versus the undesirable disbonds, 3) adhesive was present on both the composite laminate and the steel surface indicating that the failure mode was optimum, cohesive fracture of the adhesive, 4) the medium (33 ksi) and upper (41 ksi) stress spectrums produce adhesive stress levels that approach the ultimate capabilities of the adhesive film (especially for hot-wet conditioned adhesive), and 5) total crack growth was 0.80" so there was very little fracture of the adhesive layer in the vicinity of the propagating crack.

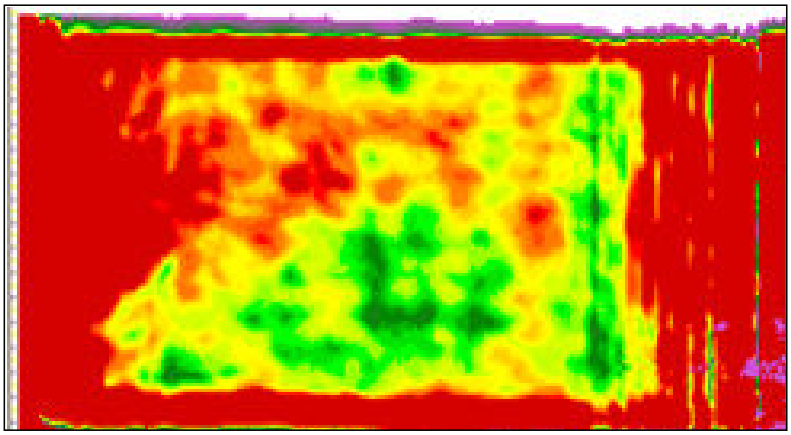

SYN-FAT-14 Before Fatigue Testing

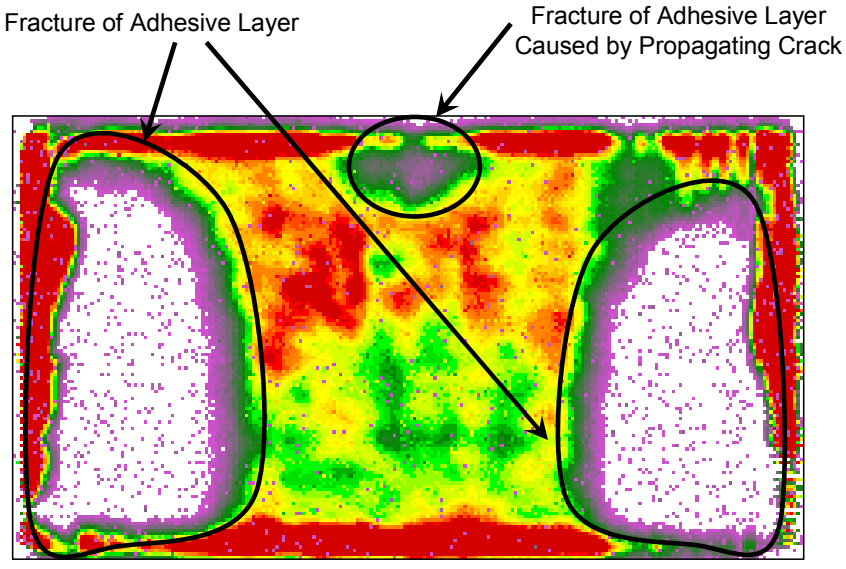

SYN-FAT-14 After 628,400 Fatigue Cycles

Figure 4-11: Through-Transmission Ultrasonic Images Comparing Flaw Profiles Before and After Fatigue Testing (SYN-FAT-14 unflawed specimen with conditioning); Medium Stress Spectrum = 33 ksi

Figure 4-12 compares the flaw profiles in specimen SYN-FAT-18 before and after 325,000 fatigue cycles at the lower stress spectrum of 24 ksi (60,000 lbs.). Again, different data acquisition settings were used in the various inspections so the flaws show up in some scans as dark regions and in other scans as bright regions. In either case, the large deviation from the norm and the high signal attenuation levels associated the flaw regions, makes the repair flaws easily identifiable. The primary features of note are: 1) the composite doubler was subjected to over 325,000 fatigue cycles with no growth in the engineered flaws or initiation of new flaws, and 2) the lower (24 ksi), and probably most realistic, stress spectrum did not produce any flaw growth in the composite doubler repairs or any crack growth in the parent steel after 250,000 to 330,000 fatigue cycles. The latter point is true even in the cases of specimens with seeded flaws and extreme hot-wet and cold conditioning.

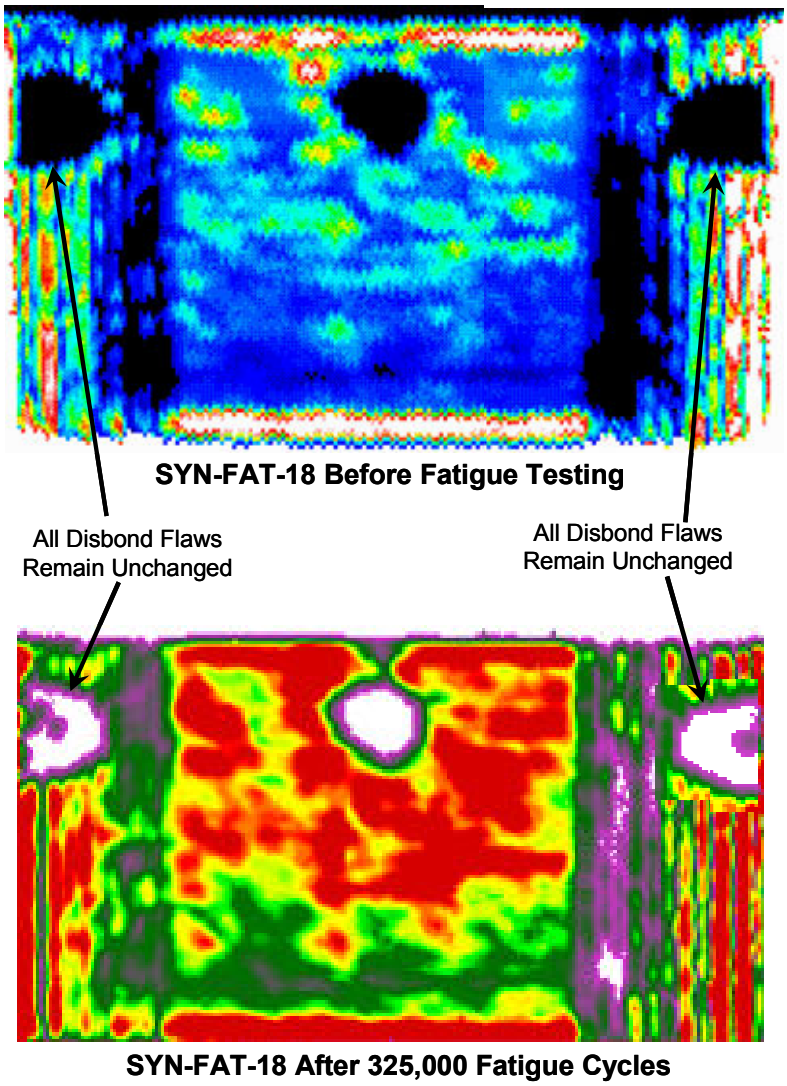

Figure 4-12: Through-Transmission Ultrasonic Images Comparing Flaw Profiles Before and After Fatigue Testing (SYN-FAT-18 flawed specimen with conditioning); Low Stress Spectrum = 24 ksi

Figure 4-13 returns to the higher stress spectrums to look further into the actual stress field limitations of composite doubler repairs. Figure 4-13 shows the flaw profile in specimen SYN-FAT-9A after 299,000 fatigue cycles at the medium stress spectrum of 33 ksi (80,000 lbs.). In this scan, the flaws show up as brighter regions. The primary features of note are: 1) the medium (33 ksi) stress spectrum produces adhesive stress levels that approach the ultimate capabilities of the adhesive film and result in the fracture regions shown, and 2) despite the large fracture regions, the composite doubler was able to function to mitigate the crack growth to under 0.90" after almost 300,000 cycles

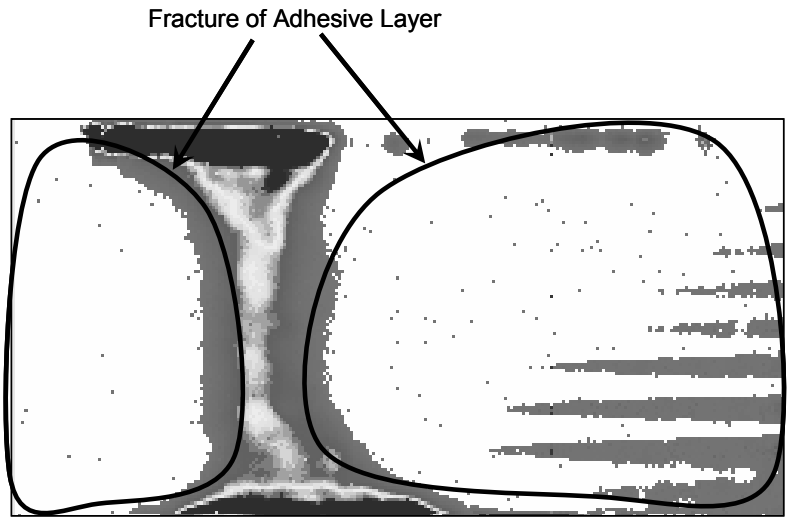

Figure 4-13: Through-Transmission Ultrasonic Image After Fatigue Testing (SYN-FAT-9 flawed specimen with no conditioning); Medium Stress Spectrum = 33 ksi

4.3 Strain Field Measurements

Figures 3-18 to 3-22 show the strain gage layouts that were used to monitor: 1) the load transfer into the composite doublers and, 2) the strain field throughout the composite laminate and steel plate. The stress, strain, and load transfer values presented in this section quantify the doubler performance characteristics discussed above. They provide additional insights into the doubler's ability to: 1) resist crack initiation or mitigate crack growth, and 2) perform acceptably in spite of worst-case installations.

In general, it was observed that all strain responses from the simulated operation stress spectrum were linear. No residual strains were noted when the specimens were unloaded except in the instance where the strain measurement occurred at the fatigue crack. In this latter case, the strain riser associated with the crack caused the strain response to be non-linear (plastic). Subsequent

failure tests (see Section 4.4 below) showed that the strains induced by the fatigue load spectrum were well inside the linear elastic regime for the steel and Boron-Epoxy composite materials.

The maximum doubler strains were found in the load transfer region (taper area) at the ends of the doubler. In all fatigue specimens, the strains monitored in this area were approximately 70% of the total strain in the parent steel plate. This value remained constant over all or most of the fatigue cycles indicating that any bond strength deterioration was minimal and occurred late in the fatigue test cycles. The strain in the steel plate beneath the doubler is reduced in accordance with the strain picked up by the composite doubler. Despite large disbonds which affected approximately 20% of the critical load transfer region, the composite doublers maintained acceptable strain fields in the doubler and steel material. Furthermore, the doublers were able to pick up the strains necessary to accomplishing their intended purpose of strain reduction and crack mitigation in the parent structure. This performance was achieved in spite of collocated flaw scenarios such as disbond flaws and extreme hot/wet conditioning (water absorption/ingress). Note also that these flaws were directly over the cracks which the doublers were intended to arrest.

4.3.1 Strain Field Analysis

A summary of the strain fields in the fatigue test coupons can be seen in the series of curves shown in Figures 4-14 to 4-19. The maximum total axial strain in the steel plate (away from the doubler) was always around 900 με for the 24 ksi stress spectrum (test load P = 60,000 lbs.), 1,100 με for the 33 ksi stress spectrum (test load P = 80,000 lbs.), and 1,500 με for the 41 ksi stress spectrum (test load P = 100,000 lbs.). Axial strains in the steel plate beneath the doubler were approximately 50% to 70% of this maximum value while axial strains in the composite doubler ranged from 50% to 70% of the total strain in the specimen. The lateral strains in each of the specimens were produced by the Poisson effect and agreed well with the theoretical relation:

$$\varepsilon_a = - (\nu \text{ X } \varepsilon_l) \qquad (4\text{-}2)$$

where ν is Poisson's ratio, ε_a represents axial strain and ε_l represents lateral strain. Following is a summary of observations regarding the coupon strain fields from the different configurations tested.

Figures 4-14 and 4-15 show the axial and lateral strain fields measure in specimen SYN-FAT-7 prior to fatigue testing. The strains were produced by the high stress spectrum (41 ksi) and are representative of an unflawed doubler. Strain reduction in the steel plate and the corresponding strain shedding into the composite laminate is evident. The nonlinear response and strain relief around the crack tip (Channel 21) is also evident. Similar information is obtained from Figures 4-16 and 4-17 which plot axial and lateral strains for SYN-FAT-12. These strains were produced by the high stress spectrum (41 ksi) and are representative of a flawed doubler. Note that, for the most part, the strain levels are the same as in the unflawed SYN-FAT-7 specimen. However, strain relief created by the edge disbond is evidenced by the low strain in Channel 3. The higher strains around the center disbond (Channel 6) show that load transfer still occurs through internal

disbonds and proves that flaws in these regions are not critical. Finally, a comparison of strain levels in SYN-FAT-7 and SYN-FAT-12 reveal that the effects of the disbonds are very localized and have very little effect on the overall strain field in the repair.

Figures 4-18 and 4-19 plot the strain values for flawed (SYN-FAT-18) and unflawed (SYN-FAT-16) specimens subjected to the low and medium stress spectrums. Observations similar to those sited above can be made. As expected, the load transfer is shown to be the same at the upper and lower taper regions. Overall, the disbonds appear to have minimal effect on the doubler's ability to transfer load and relieve the parent steel plate.

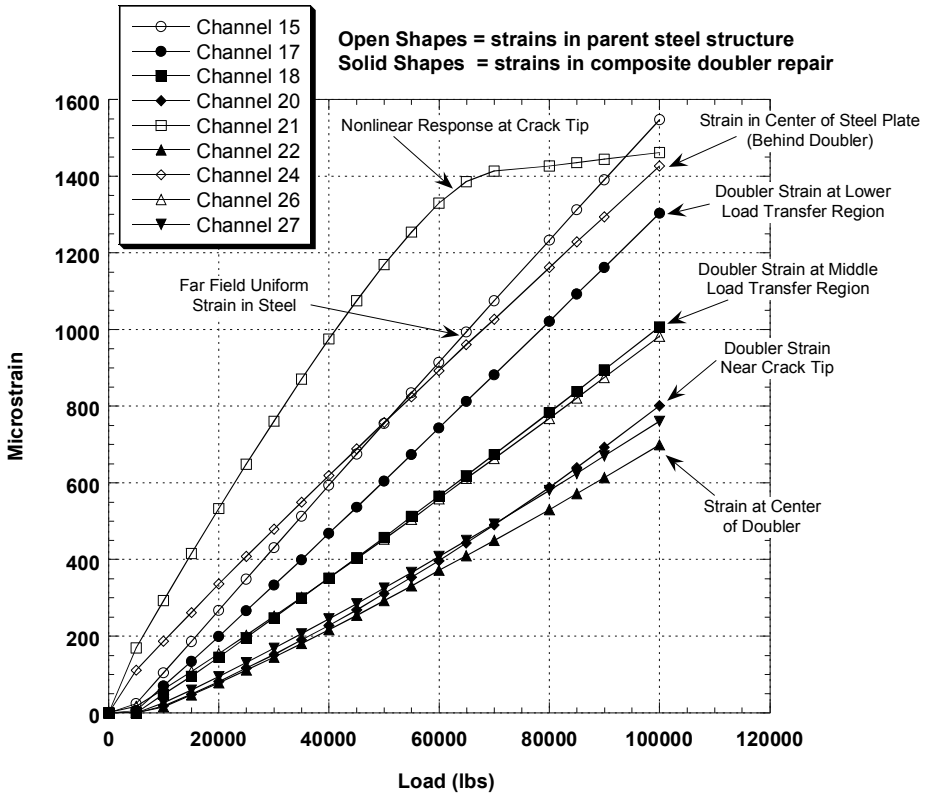

Figure 4-14: Axial Strain Field in Steel and Composite for Configuration SYN-FAT-7 – Pristine Composite Doubler with No Conditioning (ref. strain gage locations shown in Fig. 3-19)

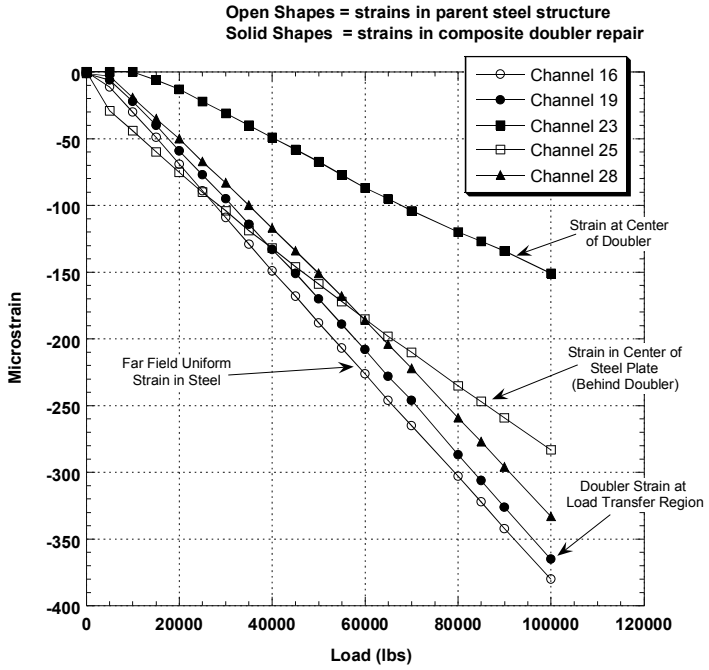

Figure 4-15: Lateral Strain Field in Steel and Composite for Configuration SYN-FAT-7 – Pristine Composite Doubler with No Conditioning (ref. strain gage locations shown in Fig. 3-19)

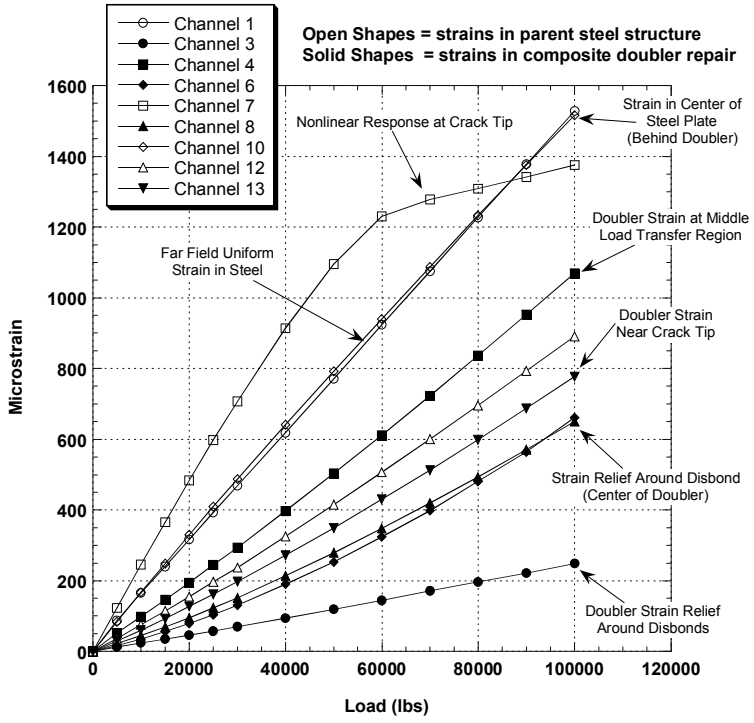

Figure 4-16: Axial Strain Field in Steel and Composite for Configuration SYN-FAT-12 – Flawed Composite Doubler with No Conditioning (ref. strain gage locations shown in Fig. 3-18)

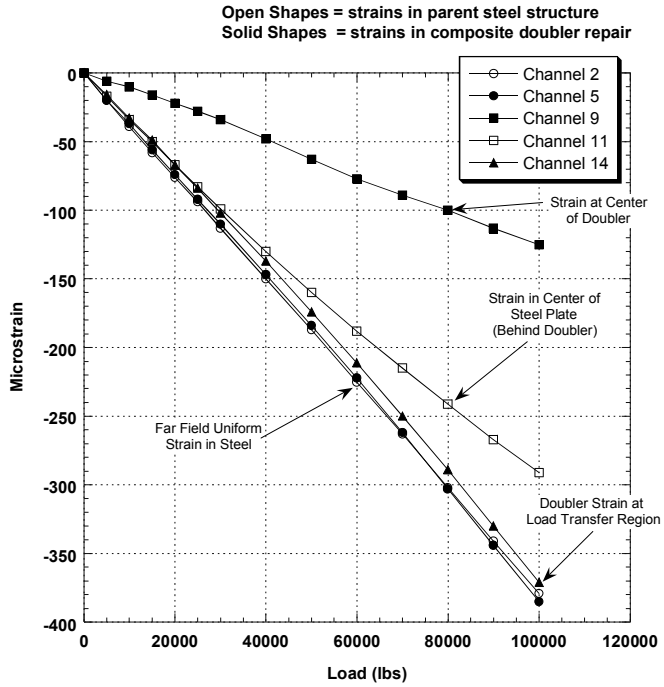

Figure 4-17: Lateral Strain Field in Steel and Composite for Configuration SYN-FAT-12 – Flawed Composite Doubler with No Conditioning (ref. strain gage locations shown in Fig. 3-18)

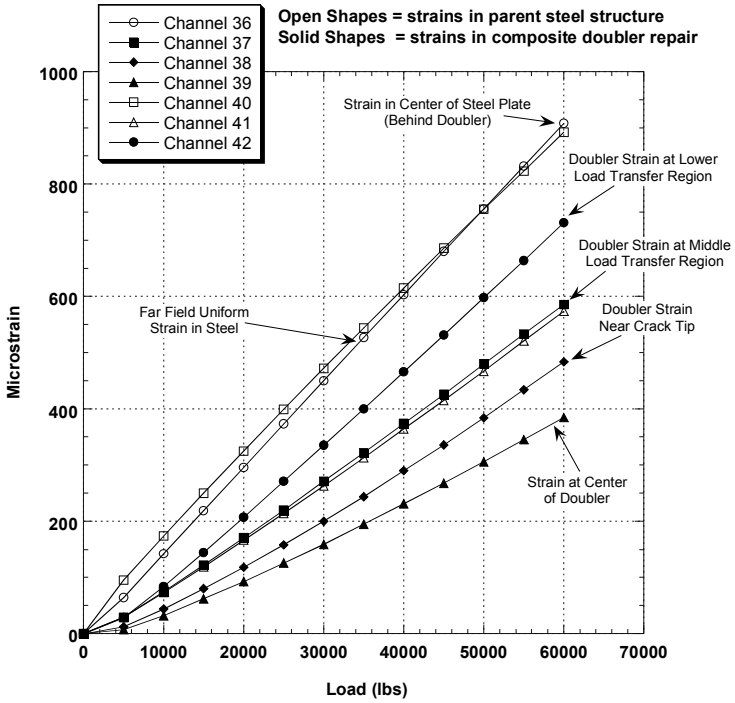

Figure 4-18: Axial Strain Field in Steel and Composite for Configuration SYN-FAT-16 – Pristine Composite Doubler with Hot/Wet & Cold Conditioning (ref. strain gage locations shown in Fig. 3-21)

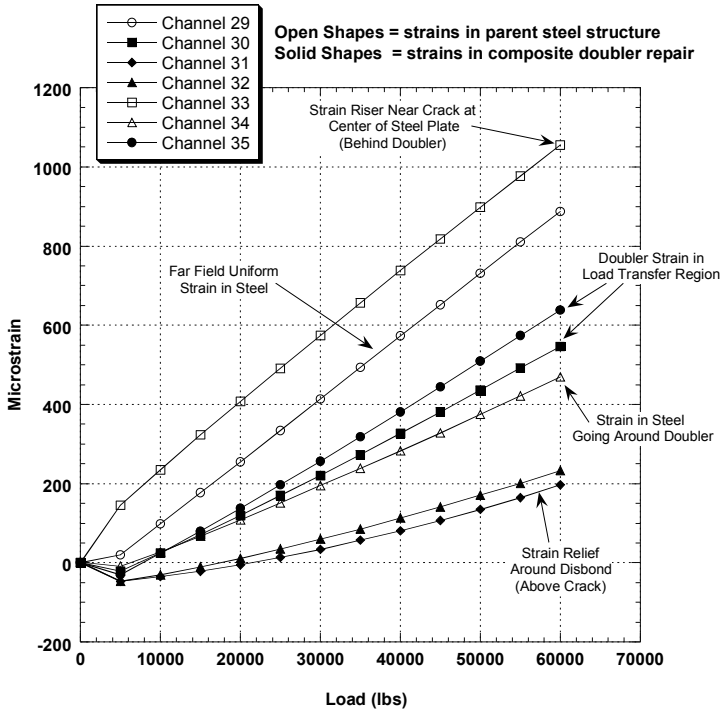

Figure 4-19: Axial Strain Field in Steel and Composite for Configuration SYN-FAT-18 – Flawed Composite Doubler with Hot/Wet & Cold Conditioning (ref. strain gage locations shown in Fig. 3-20)

4.3.2 Stresses in Steel Plate and Composite Doubler

To provide a point of reference for any Boron-Epoxy doubler installation, various stresses sustained by the fatigue test specimens are listed in Table 4-2. Strain data collected from the biaxial (axial and lateral) gages were used to calculate stresses in the composite doubler and parent steel plate. Strains measured by these gages were used to calculate the corresponding membrane stresses through the following equations:

$$\sigma_a = \frac{E}{1-\nu^2}(\varepsilon_a + \nu\varepsilon_l) \tag{4-3}$$

$$\sigma_l = \frac{E}{1-\nu^2}(\varepsilon_l + \nu\varepsilon_a) \tag{4-4}$$

where E is the modulus of elasticity, ν is Poisson's ratio, σ_a is the axial stress in the skin, σ_l is the longitudinal (lateral) stress in the skin, ε_a is the hoop strain, and ε_l is the longitudinal

(lateral) strain. From Mil-Handbook 5, the modulus of elasticity and Poisson's ratio for ASTM 572 steel are: E =26.5 X 10^6 psi and ν =0.26, respectively. As stated in Section 3.3.3, the properties of the Boron-Epoxy laminate are E_x = 25.2 X 10^6 psi, E_y = 2.43 X 10^6 psi and ν = 0.32. In cases where there were no lateral strain gages installed, the Poisson strain levels were calculated using equation (4-2).

Table 4-2 shows that uniform stresses of 24 ksi, 33 ksi, and 41 ksi were achieved in the parent skin for each specimen configuration. Away from the fatigue crack, the maximum stresses in the steel beneath the doubler were roughly 60% of the yield stress for ASTM 572 steel. Figures 4-20 and 4-21 plot the stress data from the uniaxial tests on specimens SYN-FAT-7 and SYN-FAT-12, respectively, for the 41 ksi stress spectrum (100,000 lb. max load). The maximum stresses in the composite doublers occurred at the edge of the doubler (load transfer region) and were between 70% and 80% of the far field stresses in the steel (16 ksi doubler edge stress for the 24 ksi far field stress; 25 ksi doubler edge stress for the 33 ksi far field stress; 33 ksi doubler edge stress for the 41 ksi far field stress). Stress risers near fatigue cracks, which normally amount to two or three times the uniform strain field away from the flaw, were reduced drastically by the composite doubler. The maximum steel stresses immediately adjacent to the fatigue cracks were less than or approximately equal to, the uniform stress field outside the doubler. A comparison of the stresses at zero and after 100,000 to 325,000 fatigue cycles shows that the doublers picked up additional stresses when the fatigue crack growth reduced the load carrying capacity of the parent steel (i.e. stress relief occurred in steel). This is discussed further in Section 4.3.4 "Effects of Multiple Fatigue Lifetimes on Strain Fields."

Specimen No.	Strain Chs.	Max. Load for Stress Spectrum (lbs)	Stress at 0 Cycles (psi)	Fatigue Cycles	Stress After Fatigue (psi)	Total Crack Growth	Location on Test Specimen
SYN-FAT-7 (Unflawed, No Conditioning.)	15, 16	100,000 (41ksi)	41,200	109,004	44,000	1.35"	Steel - Far Field
	17		32,850		40,700		Doubler Edge (upper taper region)
	18, 19		25,000		32,350		Doubler Edge (middle taper region)
	20		20,200		52,000		Doubler Above Crack (full thickness region)
	22, 23		18,300		23,400		Doubler in Front of Crack (full thickness region)
	24, 25		38,450		66,500		Steel - Near Crack Tip
	27, 28		18,400		26,300		Doubler Edge (upper taper region)
SYN-FAT-12 (Flawed, No Conditioning)	1, 2	100,000 (41ksi)	40,650	86,500	44,600	1.42"	Steel - Far Field
	4, 5		26,600		35,250		Doubler Edge (middle taper region)
	8, 9		17,150		22,100		Doubler Above Crack (full thickness region)
	10, 11		41,000		61,850		Steel - Near Crack Tip
	13, 14		18,500		24,000		Doubler Edge (upper taper region)
SYN-FAT-16A (Unflawed, Conditioned, H-W & Cold)	36, ν36	80,000 (33ksi)	32,000	208,391	31,300	.64"	Steel - Far Field
	37, ν37		20,400		21,250		Doubler Edge (middle taper region)
	38, ν38		16,900		22,050		Doubler Above Crack (full thickness region)
	39, ν39		13,400		11,600		Doubler in Front of Crack (full thickness region)
	40, ν40		31,300		38,300		Steel - Near Crack Tip
	42, ν42		24,800		26,600		Doubler Edge (lower taper region)
SYN-FAT-16 (Unflawed, Conditioned, H-W & Cold)	36, ν36	60,000 (24ksi)	24,100	331,384	24,100	None	Steel - Far Field
	37, ν37		14,800		14,500		Doubler Edge (middle taper region)
	38, ν38		12,200		12,700		Doubler Above Crack (full thickness region)
	39, ν39		9,700		9,250		Doubler in Front of Crack (full thickness region)
	40, ν40		23,650		23,650		Steel - Near Crack Tip
	42, ν42		18,400		17,900		Doubler Edge (upper taper region)
SYN-FAT-18 (Flawed, Conditioned, H-W & Cold)	29, ν29	60,000 (24ksi)	23,500	325,017	23,450	None	Steel - Far Field
	30, ν30		13,800		13,300		Doubler Edge (middle taper region)
	31, ν31		5,000		5,000		Doubler Above Crack (full thickness region)
	32, ν32		5,900		5,100		Doubler in Front of Crack (full thickness region)
	33, ν33		28,000		27,950		Steel - Near Crack Tip
	35, ν35		16,100		15,450		Doubler Edge (upper taper region)

Table 4-2: Stresses in Steel Plate and Composite Doubler at Maximum Test Loads

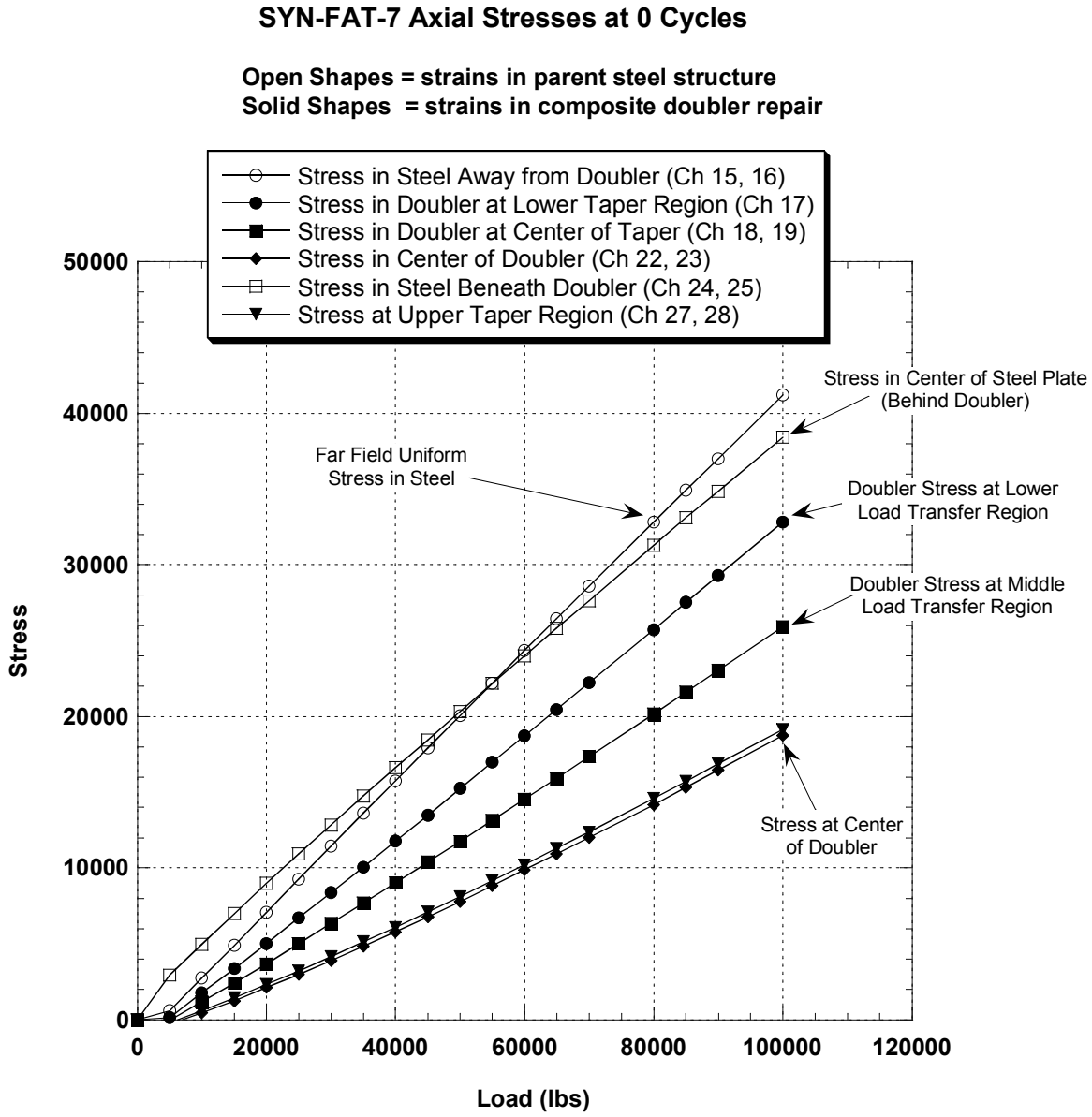

Figure 4-20: Stress Levels in Steel and Composite for Configuration SYN-FAT-7 – Pristine Composite Doubler with No Conditioning; 41 ksi Stress Spectrum

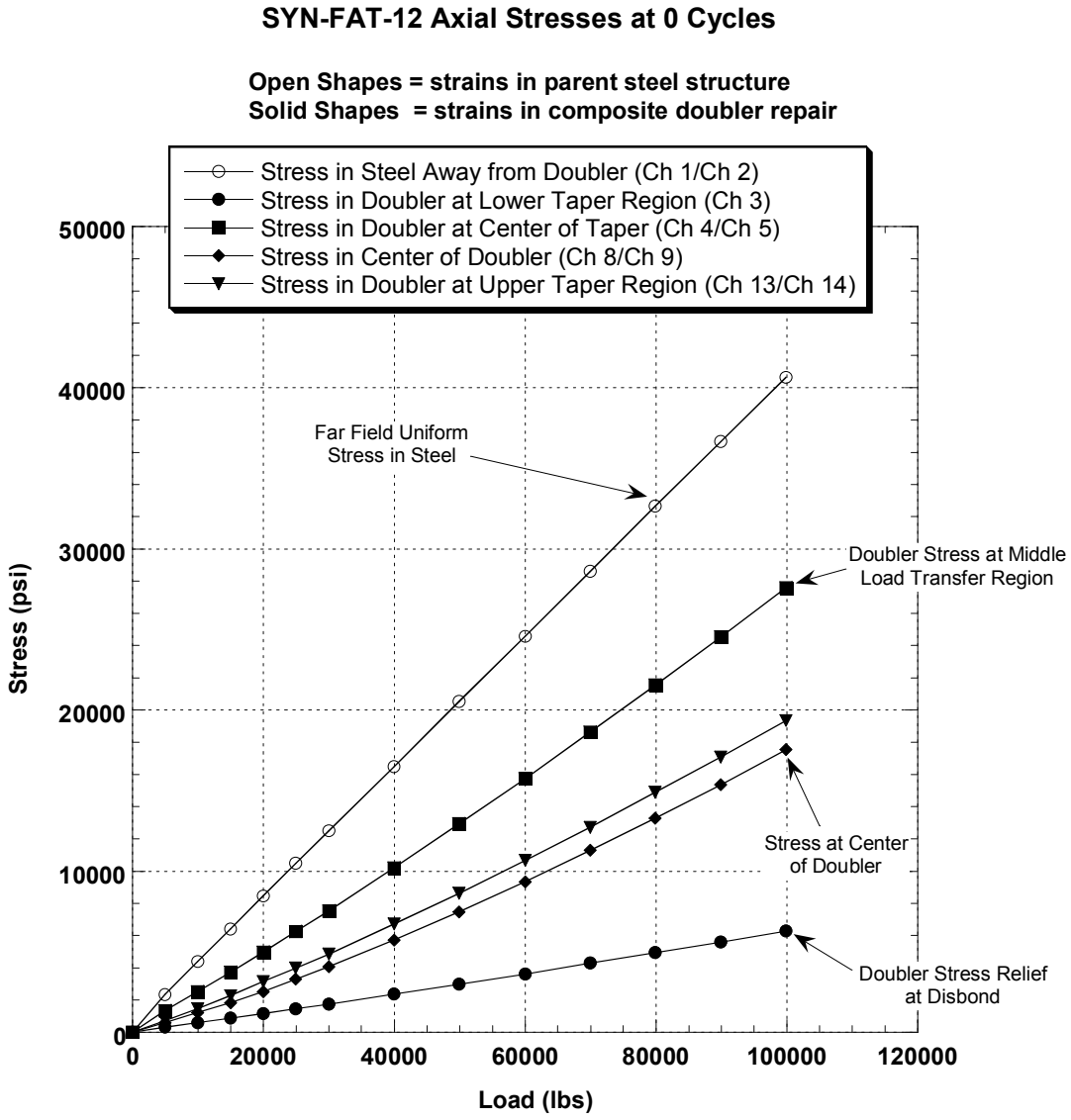

Figure 4-21: Stress Levels in Steel and Composite for Configuration SYN-FAT-12 – Flawed Composite Doubler with No Conditioning; 41 ksi Stress Spectrum

4.3.3 Load Transfer

Plots of percent load transfer were obtained by calculating the ratio between doubler strains and strains in corresponding portions of the steel plate. Figures 4-22 to 4-25 show the resulting load transfer plots for various doubler and steel reference channels $\{\varepsilon_{doubler} / \varepsilon_{steel(ref)}\}$ when subjected to the high and low stress spectrums.

The curves indicate that the load transfer into the doubler - and away from the steel - was similar in all fatigue specimens regardless of the type and degree of damage in the specimen. In the tapered portion of the doubler, the load transfer was consistently in the 40 - 80 % range. In the center, where the doubler reaches its maximum thickness of 24 plies, the load transfer was in the 40 - 60% range.

The array of fatigue specimens ranged from unflawed (optimum installation) to large, co-located flaws (worst-case scenarios) with hot-wet and cold conditioning. Figures 4-22 to 4-25 show the consistency of load transfer values across the full spectrum of specimens despite the large variations in flaw scenarios. Furthermore, these load transfer values remained constant over much of the fatigue testing. This indicates that there was little deterioration in the bond strength over this time. Normal repair methodologies that utilize doubler stiffness ratios of 0.8 to 1.0, would produce load transfer ratios in the 40-60% range [6, 19, 20]. However, since this repair has a lower stiffness ratio of 0.3, the resulting stresses in the doubler are higher as shown in the graphs. This is an acceptable approach as long as the stress levels in the composite laminate and adhesive layer do not approach ultimate levels.

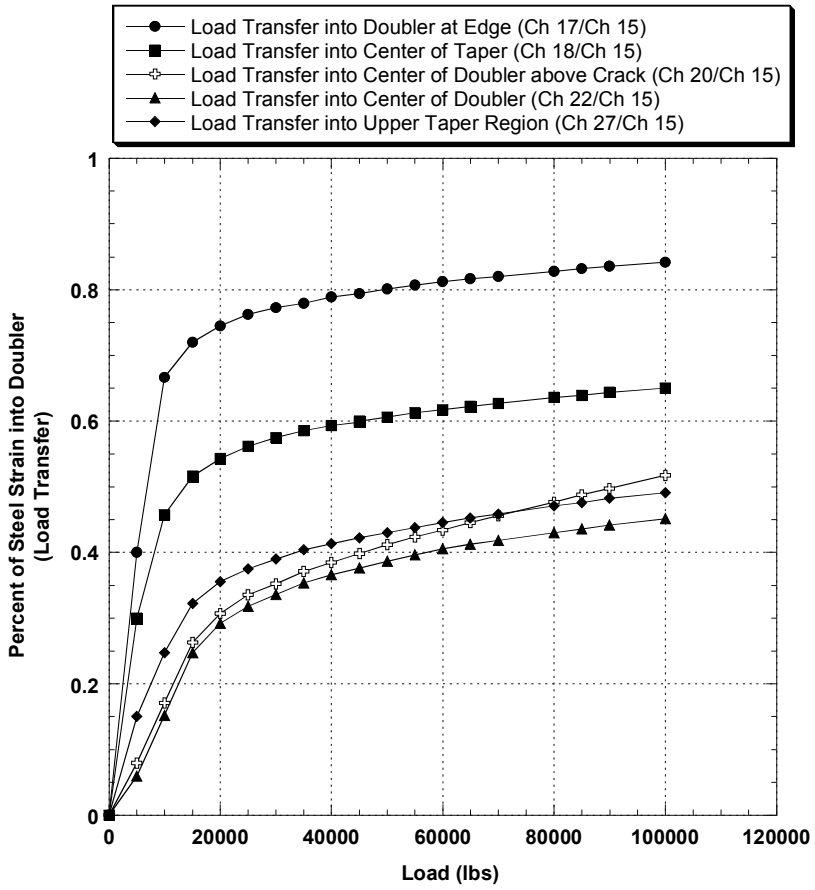

Figure 4-22: Load Transfer in Composite Repair SYN-FAT-7 – Pristine Composite Doubler with No Conditioning; 41 ksi Stress Spectrum

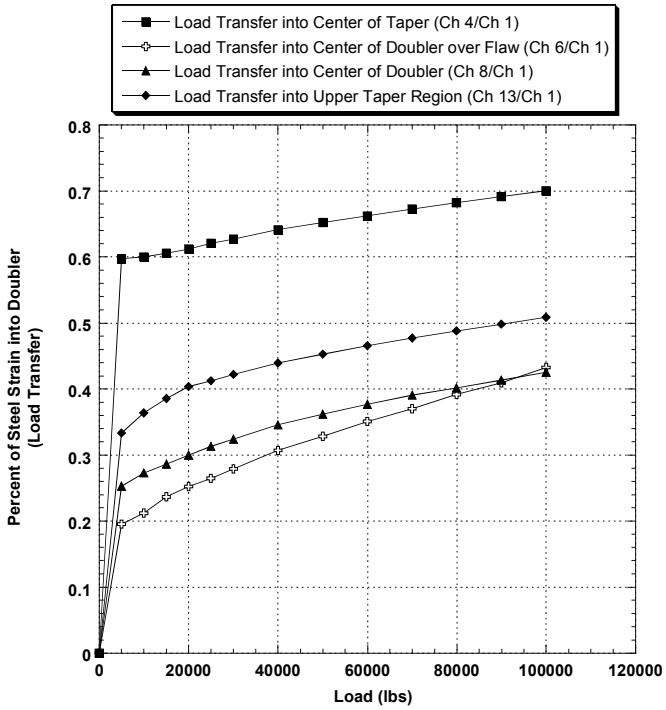

Figure 4-23: Load Transfer in Composite Repair SYN-FAT-12 – Flawed Composite Doubler with No Conditioning; 41 ksi Stress Spectrum

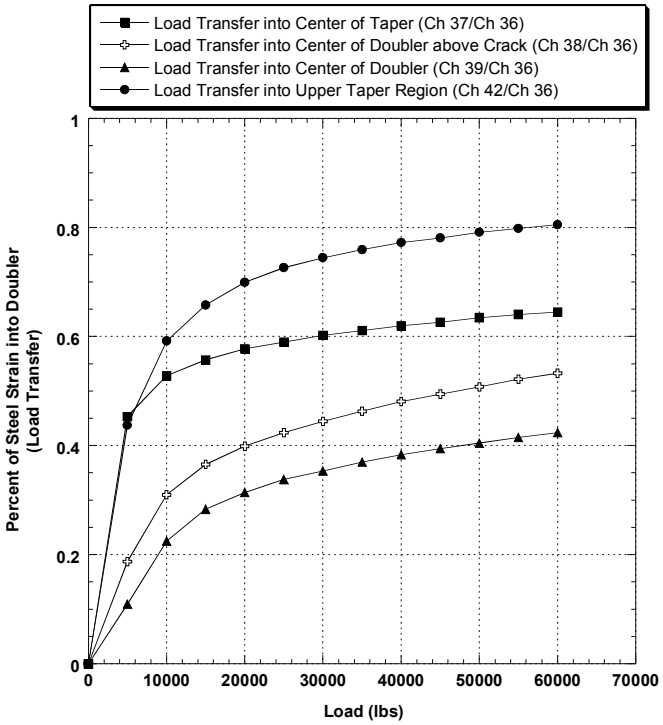

Figure 4-24: Load Transfer in Composite Repair SYN-FAT-16 – Pristine Composite Doubler with Hot-Wet & Cold Conditioning; 24 ksi Stress Spectrum

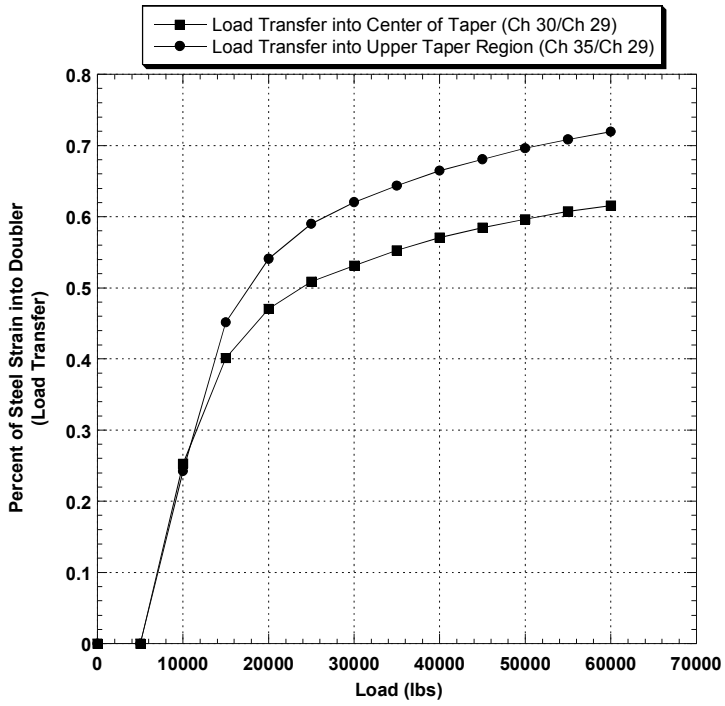

Figure 4-25: Load Transfer in Composite Repair SYN-FAT-18 – Flawed Composite Doubler with Hot-Wet & Cold Conditioning; 24 ksi Stress Spectrum

4.3.4 Effects of Multiple Fatigue Lifetimes on Strain Fields

In each of the fatigue specimens, the vast majority of the strain field remained unchanged over the course of the fatigue tests. Several of the specimen configurations showed no change in strain levels from 0 fatigue cycles to 330,000 fatigue cycles. The only strain changes noted in any of the specimens were caused by crack propagation. In these instances, the composite doublers picked up additional strain as the crack propagated across the steel structure.

No Change in Strain Field - Configurations SYN-FAT-5, -9, -16, and -18 exhibited little or no change in strain field during the course of their fatigue tests. No crack growth was measured during the tests that applied 250,000 to 330,000 cycles. The NDI before-and-after results in Figure 4-12 show that the initial "programmed" flaws in SYN-FAT-18 did not change shape nor did any new flaws develop as a result of the fatigue loads. Quantitatively, the strain gage values acquired before and after fatigue testing substantiate the NDI results. Figure 4-26 plots the strain field for configurations SYN-FAT-16 before and after 331,000 fatigue cycles. The before-and-after plots lie on top of each other demonstrating an unchanged strain field. Similarly, Figure 4-27 shows that the strains in the SYN-FAT-18 were undisturbed by 325,00 fatigue cycles. The corresponding stress entries in Table 4-2 summarize the unchanged stress levels since the stresses in the specimen before and after fatigue cycling are within 5% of each other.

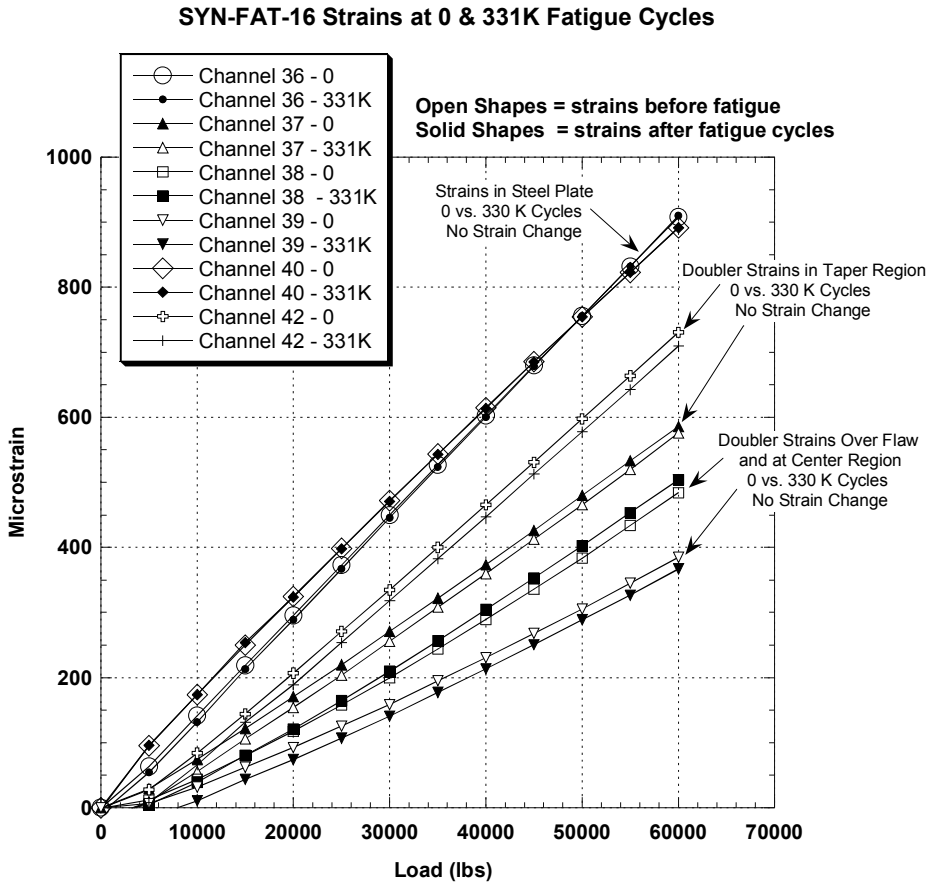

Figure 4-26: Strain Field in SYN-FAT-16 Remains Unchanged Over 330,000 Fatigue Cycles – No Crack Growth or Flaw Growth in Doubler Installation; Pristine Composite Doubler with Hot-Wet & Cold Conditioning; 24 ksi Stress Spectrum

Strain Changes Caused by Fatigue Cracks - In the specimens where crack growth occurred, and especially where the crack grew beyond the perimeters of the implanted disbond flaw, significant strain changes were observed in the immediate area of the propagating crack. The results, however, highlight the ability of the composite doubler to pick up additional load in response to a loss of strength in the parent structure.

The NDI results in Figure 4-10 show how the propagating crack produced a fracture in the adhesive layer in SYN-FAT-13. Similar changes were observed in SYN-FAT-7, -8, -12, -15, -17 and -22 specimens that all experienced crack growth of 1" or more. Once again, the strain gage results quantify and verify the NDI assessments. Although the strains remained constant in the critical load transfer region, Figures 4-28 to 4-34 show that there were several localized changes in the strain fields due to the propagation of the crack through the steel plate.

Channel 20 in Figure 4-28 highlights the increasing load picked up by the composite doubler as the steel crack propagates in SYN-FAT-7. Channel 21 in Figure 4-29 shows the corresponding reduction in steel strain as the crack grows and eliminates the steel's ability to take any load in

this region. At N= 0 cycles, the strains at the center of the doublers amounted to 50% of the total strain in the steel plates. After N = 109,000 cycles and a crack propagation of 1.4", the same strain gages registered 95% of the total strain in the plate. During the fatigue tests, the Channel 21 strains (steel plate adjacent to crack) drop from 90% of total strain to 26% of total strain in plate.

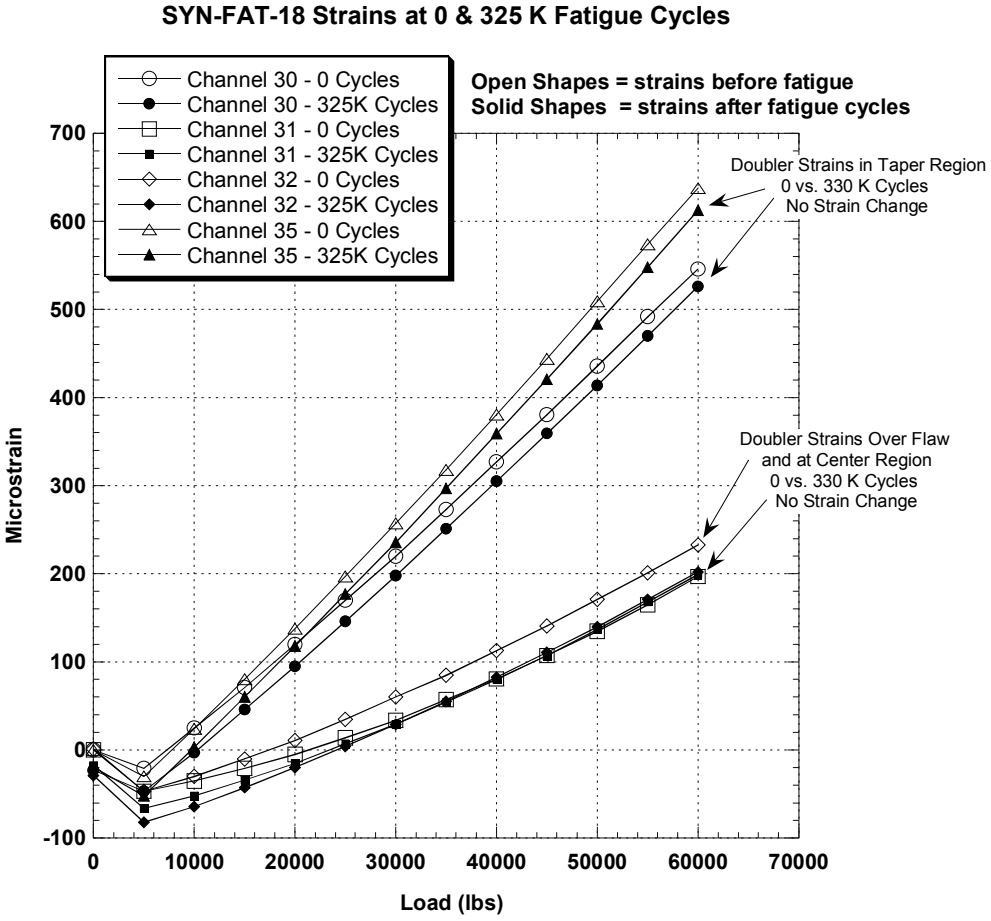

Figure 4-27: Strain Field in SYN-FAT-18 Remains Unchanged Over 325,000 Fatigue Cycles – No Crack Growth or Flaw Growth in Doubler Installation; Flawed Composite Doubler with Hot-Wet & Cold Conditioning; 24 ksi Stress Spectrum

Similarly, Channel 6 in Figure 4-30 shows how the strain in the doubler center region rises significantly after the fatigue loads grew the crack 1.4". At N= 0 cycles, the strains at the center of the doublers amounted to 40% of the total strain in the steel plates. After N = 87,000 cycles and a crack propagation of 1.4", the same strain gages registered 56% of the total strain in the plate. The central portion of the steel plate (Channel 7 in Figure 4-31) shows the associated strain reduction (loss of strength) produced by the crack growth. The curves for N = 0 and N = 208,000 cycles in Figure 4-32 and 4-33 show how the doubler in SYN-FAT-16A picks up more load as the crack propagates and the plate relieves its load (reference Channel 38). These results

quantify the ability of bonded composite doubler repairs to increase its reinforcing value as flaws grow and the parent structure losses its ability to sustain normal working loads.

The stress entries in Table 4-2 quantify the changes in load distribution within the repaired structure. Stress levels in the load transfer (taper) region go up 25% to 40% as the doubler takes on more load. Doubler stress levels in the vicinity of the crack go up 30% to 50%. At the highest stress riser near the crack tip, stress increases of over 100% were measured in the doubler.

It is important to note three items regarding these change in strain fields: 1) the composite doubler was able to meet its design objectives and absorb additional load as required, 2) the effects were localized about the crack (i.e. the strains around the perimeter - especially in the critical load transfer region - remained unchanged), and 3) the change in flaw shape (ref. Fig. 4-10) was caused by a cohesive failure of the adhesive, not a growth in the implanted disbond. This latter point is key because the cohesive failure indicates that the installation was good and that the full strength of the adhesive was achieved. Disbonds, indicated by a lack of adhesive on either the laminate or steel mating surface, are undesirable since they can occur at lower loads

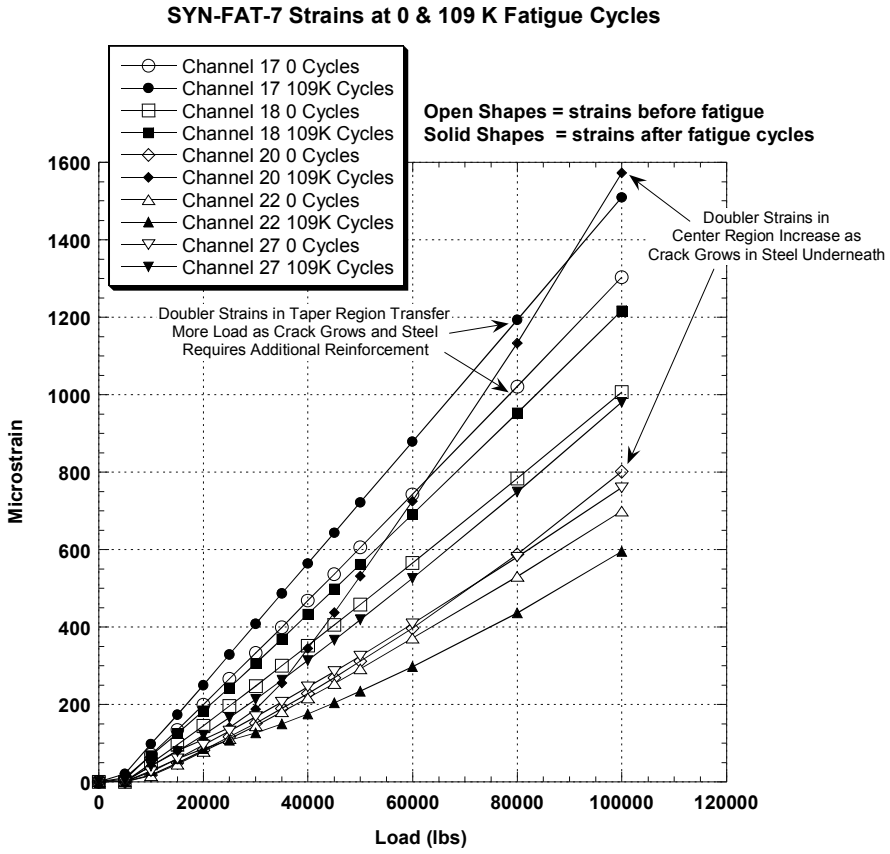

Figure 4-28: Strain Field in SYN-FAT-7 Doubler Undergoes Slight Changes Due to Crack Growth in Steel – No Flaw Growth in Doubler Over 109,000 Fatigue Cycles; Pristine Composite Doubler with No Conditioning; 41 ksi Stress Spectrum

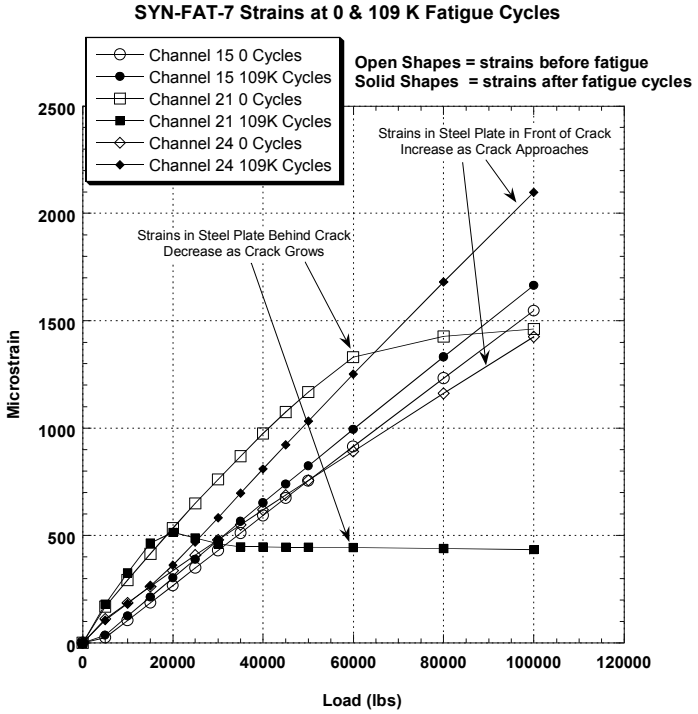

Figure 4-29: Strain Field in SYN-FAT-7 Steel Decreases Due to Crack Growth in Plate and Associated Load Shedding; 41 ksi Stress Spectrum

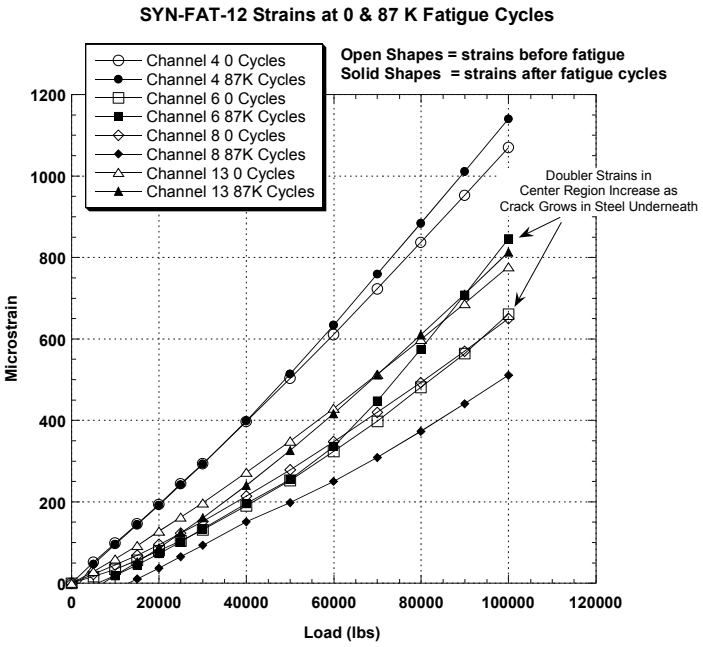

Figure 4-30: Strain Field in SYN-FAT-12 Doubler Undergoes Slight Changes Due to Crack Growth in Steel – No Flaw Growth in Doubler Over 87,000 Fatigue Cycles; Flawed Composite Doubler with No Conditioning; 41 ksi Stress Spectrum

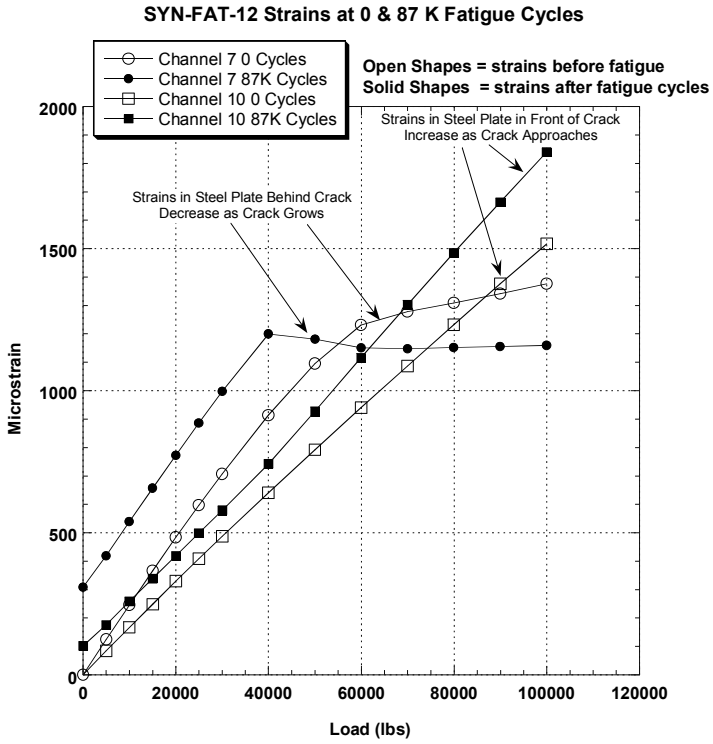

Figure 4-31: Strain Field in SYN-FAT-12 Steel Changes Due to Crack Growth in Plate and Associated Load Shedding; 41 ksi Stress Spectrum

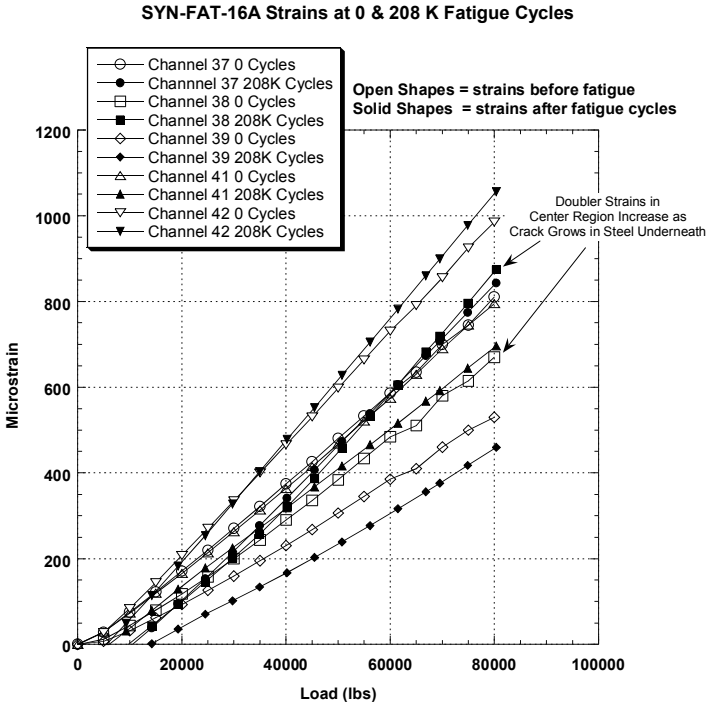

Figure 4-32: Strain Field in SYN-FAT-16A Doubler Undergoes Slight Changes Due to Crack Growth in Steel – No Flaw Growth in Doubler Over 208,000 Fatigue Cycles; Pristine Composite Doubler with Hot-Wet & Cold Conditioning; 33 ksi Stress Spectrum

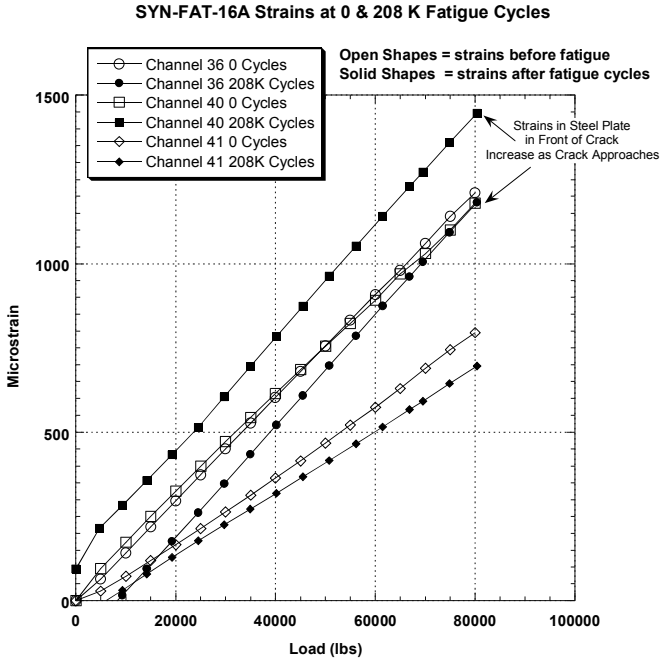

Figure 4-33: Strain Field in SYN-FAT-16A Steel Changes Due to Crack Growth in Plate and Associated Load Shedding - No Flaw Growth in Doubler in 192,000 Fatigue Cycles at 33 ksi Stress Spectrum

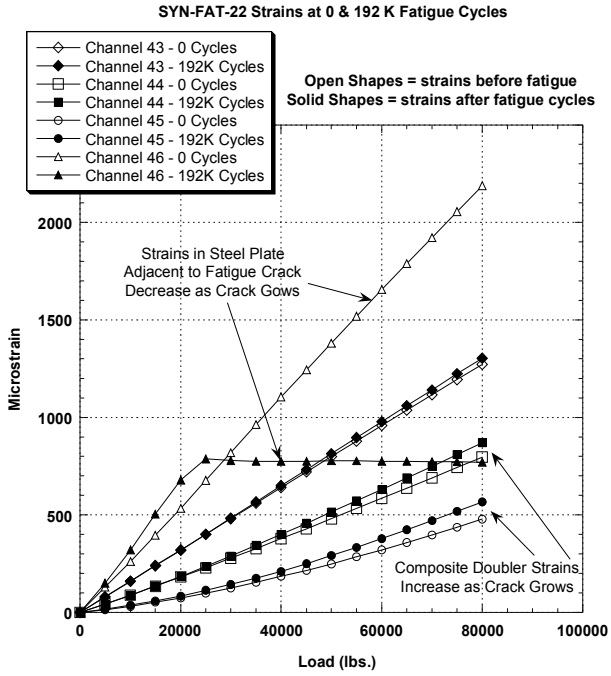

Figure 4-34: Strain Field in SYN-FAT-22A Changes Due to Crack Growth in Plate and Associated Load Shedding into Composite Doubler; 33 ksi Stress Spectrum

Comparison of Grit Blast and Sanding Process for Producing Surface Roughness – Strain readings from these tests could also be used to evaluate the success of the sanding process as a substitute for the grit blast. Strain readings were acquired from test specimen SYN-FAT-22 which was prepared using a sanding procedure for the surface roughening step. The strain gages were placed in the same locations as those installed on the grit blast specimen SYN-FAT-7. Figure 4-35 compares the strain levels from each of these specimens. Almost duplicate strain readings were observed indicating that the sanded specimen produced a similar degree of load transfer and protection to the damaged region.

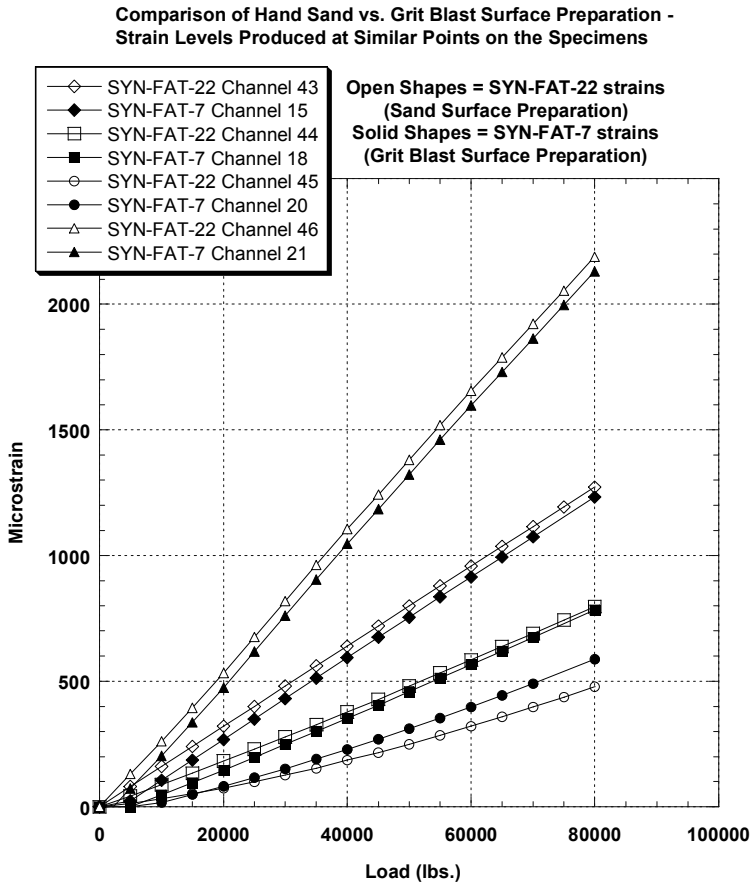

Figure 4-35: Comparison of Strain Levels at Similar Points in Specimens Produced with Different Surface Preparation Methods - Establishes Viability of Surface Sanding Process in Lieu of Grit Blast

4.4 Residual Strength of Damaged Steel Structure with Composite Doubler Repairs

After the fatigue tests were completed, seven of the specimens were subsequently loaded to determine their static residual tensile strength. It is important to note that these were not actually ultimate strength tests since the specimens were tested after flaws were engineered into the specimens and the implanted cracks were grown. By using the maximum load at failure and the

original cross section area at the start of the static residual strength test, the resulting "residual tensile strength" numbers are conservative. In the ultimate/residual strength tests, failure was defined as the point where the specimen was unable to sustain an increasing load. The peak load recorded during each failure test was used to calculate the maximum uniform stresses sustained by the flawed specimens (residual strength). Strain gage data was also used to determine the stress values at various locations in the specimen. These locations included the far-field, uniform stress regions, the load transfer regions in the doubler, and the stress riser regions adjacent to the propagating crack.

All seven specimens – SYN-FAT-7, -8, -11, -12, -13, -16A, and -18A – experienced crack growth during the course of their fatigue tests. Their failure occurred in one of two modes: 1) crack propagation and associated cohesive bond failure through the steel plate, and 2) failure of the composite laminate. In the first failure mode, the doubler separated from the steel plate through a cohesive fracture of the adhesive. Thus, there was no disbond growth and adhesive was found on both the steel and composite laminate. Figure 4-36 shows this failure mode where the adhesive layer fractures in a cohesive mode.

As the load was increased, the steel beneath the doubler and adjacent to the crack began to yield and elongate. The yield zone expanded to include the tapered edge of the doubler as well as the center of the specimen. This caused the steel to sequentially pull away from the doubler which was not yielding or stretching at the same rate as the parent steel. The result was a rolling wave of cohesive failure in the adhesive layer. *There was no disbond growth in the specimen as evidenced by the presence of adhesive on both the steel and mating composite doubler. This indicates that the installation was successful and the full strength of the adhesive was achieved.* During the course of the test it was possible to hear popping sounds corresponding to the fracture of the adhesive. When this cohesive failure (as opposed to adhesive, or disbond, failure) in the adhesive reached the center crack of the coupon, half of the steel plate was left without doubler reinforcement. At that point, the crack in the steel propagated rapidly across the entire width of the test specimen.

The second failure mode occurred when the interlaminar stresses in the composite laminate exceeded the ultimate capability of the material. These interply fractures, such as the one shown in Figure 4-37, always occurred at the interfaces to the 45^{o} plies. This is reasonable since the 45^{o} plies have less strength than 0^{o} plies in the load direction. Figure 4-37 shows that the ply orientation at the failed interface surface is 45^{o}. The fact that either failure mode was possible indicates that the repair design was fairly balanced in its ability to achieve the maximum allowable stress levels in the laminate and the adhesive layer. Figure 4-37 shows the extreme crack growth and crack opening that was withstood by the composite repair before failure occurred.

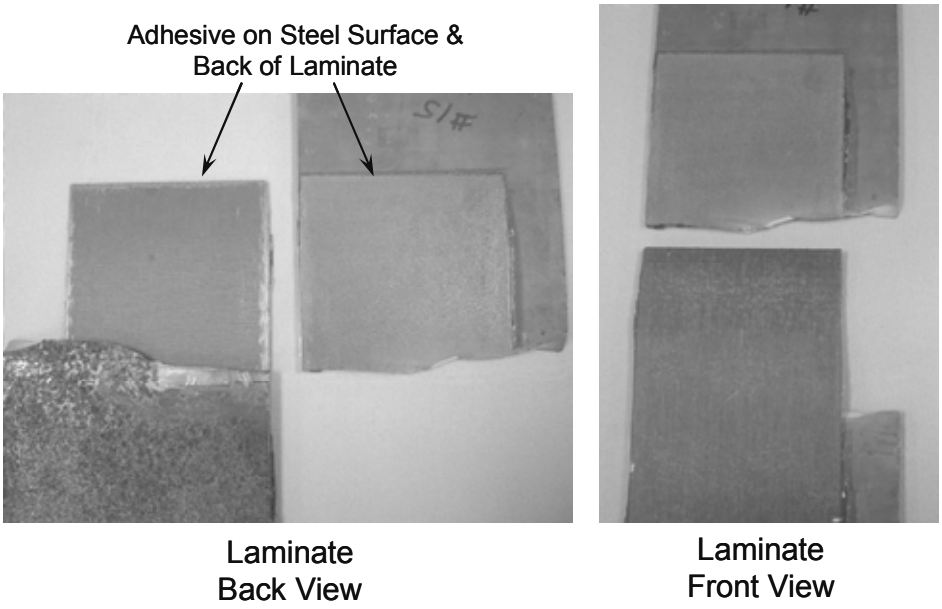

Figure 4-36: View of Repair Specimen After Ultimate Failure; Mode of Failure was Cohesive Fracture of the Adhesive Layer Between the Laminate and the Steel

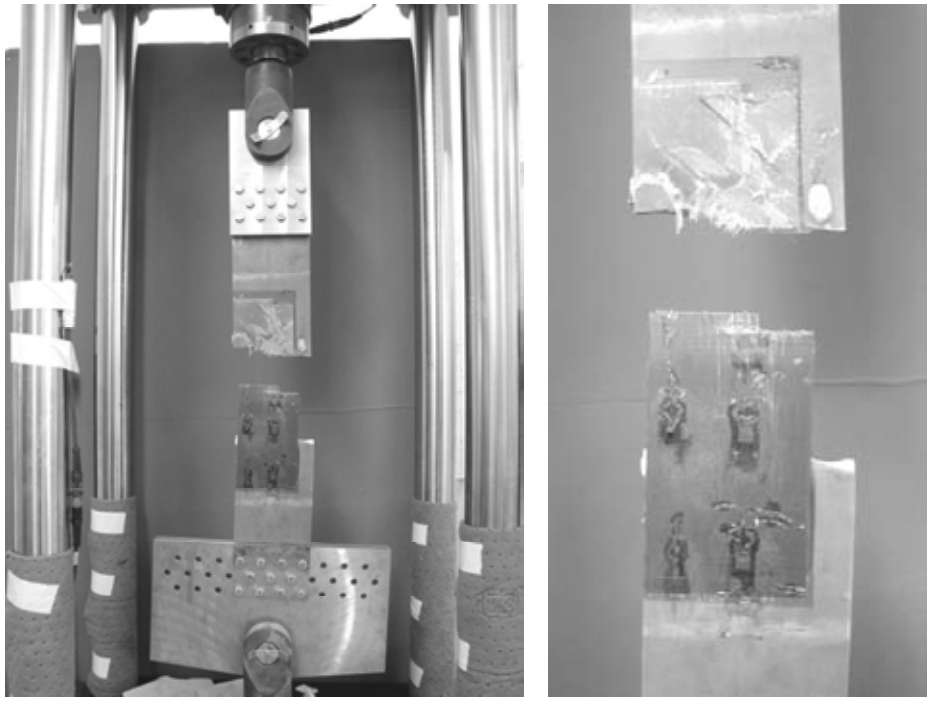

Figure 4-37: View of Repair Specimen After Ultimate Failure; Mode of Failure was Interply Fracture of the Composite Laminate

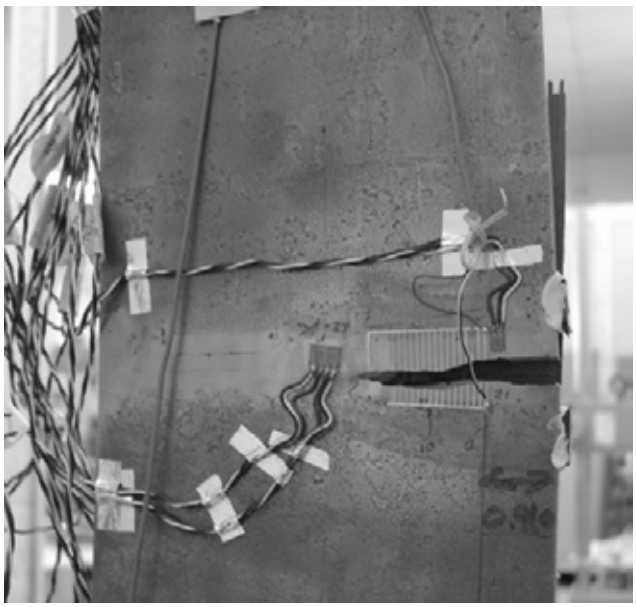

Figure 4-38: Extreme Crack Growth/Opening in Structure Before Doubler Failure Occurred

Figures 4-39 to 4-41 show the stress and strain fields in specimens SYN-FAT-7, -12, and -16A up to failure. The steel plate away from the doubler (Channels 15/16, 1/2, and 36) began to yield at approximately 130,000 to 140,000 lbs. (approximately 50 ksi) while the doubler continued to increase its load. Stresses near the crack increased dramatically. Doubler stresses increased in response to stress relief that occurred in the steel plate behind the crack. *Figures* 4-39 to 4-41 *clearly show a nonlinear response in the composite laminate even though the Boron-Epoxy material alone does not have a plastic regime in its response. This indicates that the composite doubler was able to transmit plastic stresses from the steel structure and that extensive yielding and loading beyond the initial yield level was required to fail the installation.*

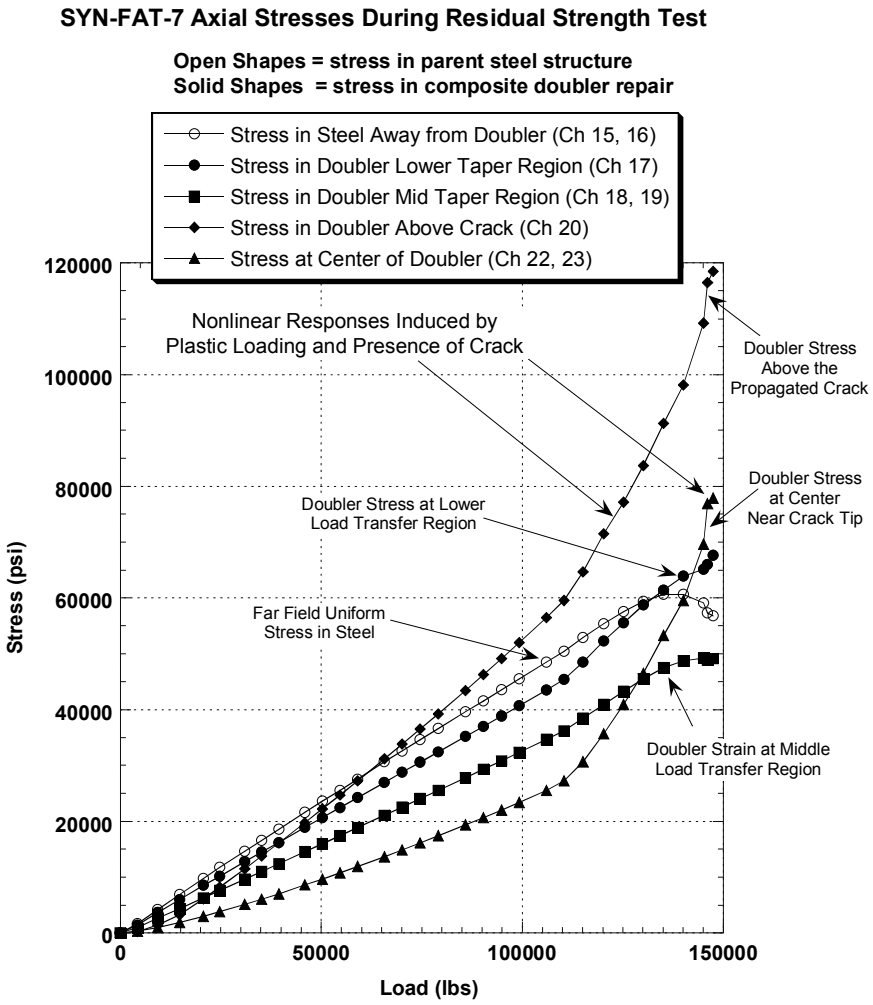

Figure 4-39: Stress Levels in Steel and Composite Doubler During Ultimate/Residual Strength Failure Test of SYN-FAT-7 – Pristine Composite Doubler with No Conditioning

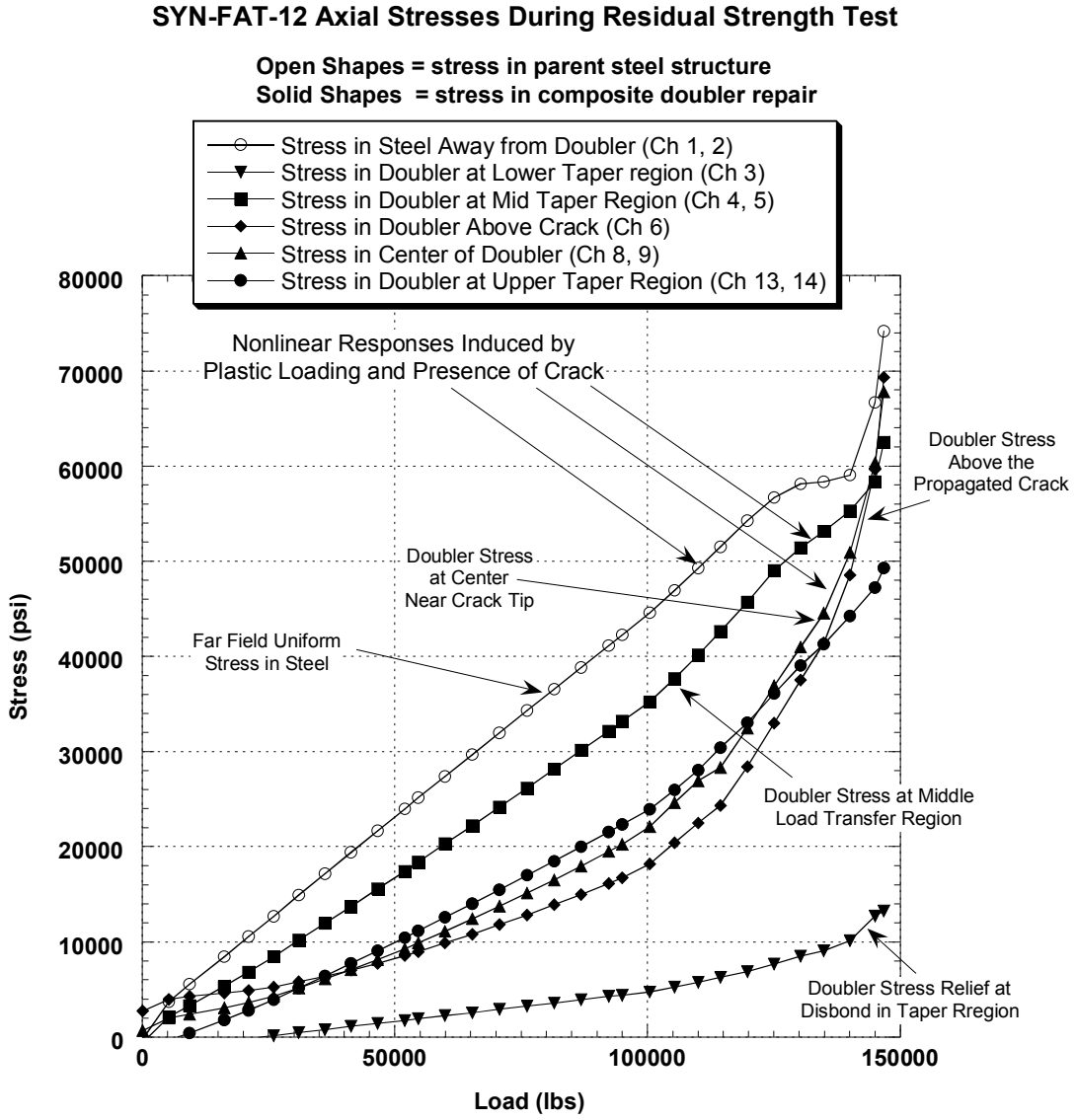

Figure 4-40: Stress Levels in Steel and Composite Doubler During Ultimate/Residual Strength Failure Test of SYN-FAT-12 – Flawed Composite Doubler with No Conditioning

Table 4-3 summarizes the stress levels in the test specimens at the failure load. While yielding in the parent steel was measured at approximately 50 ksi in these tests, the stress levels in the steel and composite laminate went well beyond this yield level. Maximum stresses around the crack tip even exceeded the 65 ksi ultimate strength value measured in failure tests on the welded steel alone. The residual strength values are listed in Table 4-4. The residual strength values in all of the specimens were quite similar despite the large differences in the configurations. The baseline for comparison purposes comes from specimen SYN-FAT-11 which contained a welded region without a composite doubler. Ultimate failure of this specimen occurred at 65 ksi. Failure in all six specimens which contained composite doubler repairs exceeded this value and ranged from 77 ksi to 94 ksi. The average residual strength was 89 ksi. It is worth noting that essentially all

but one of the specimens exceeded the ultimate strength value for the pristine, unwelded steel material (Manufacturer supplied data on ASTM A572 material tested: $\sigma_{ult.}$ = 85,000 psi). Thus, *even in the presence of severe worst case installations (disbonds amounting to 20% of the load transfer region) and extensive damage growth (fatigue cracks extending through 50% of the specimen width), it was seen that the doubler-reinforced plates were able to achieve residual tensile strengths (i.e. post-damage tensile strength) which exceeded the 65 ksi baseline value for this steel material. Thus, the Boron-Epoxy doubler was able to return the parent structure to its original strength and load carrying capability.*

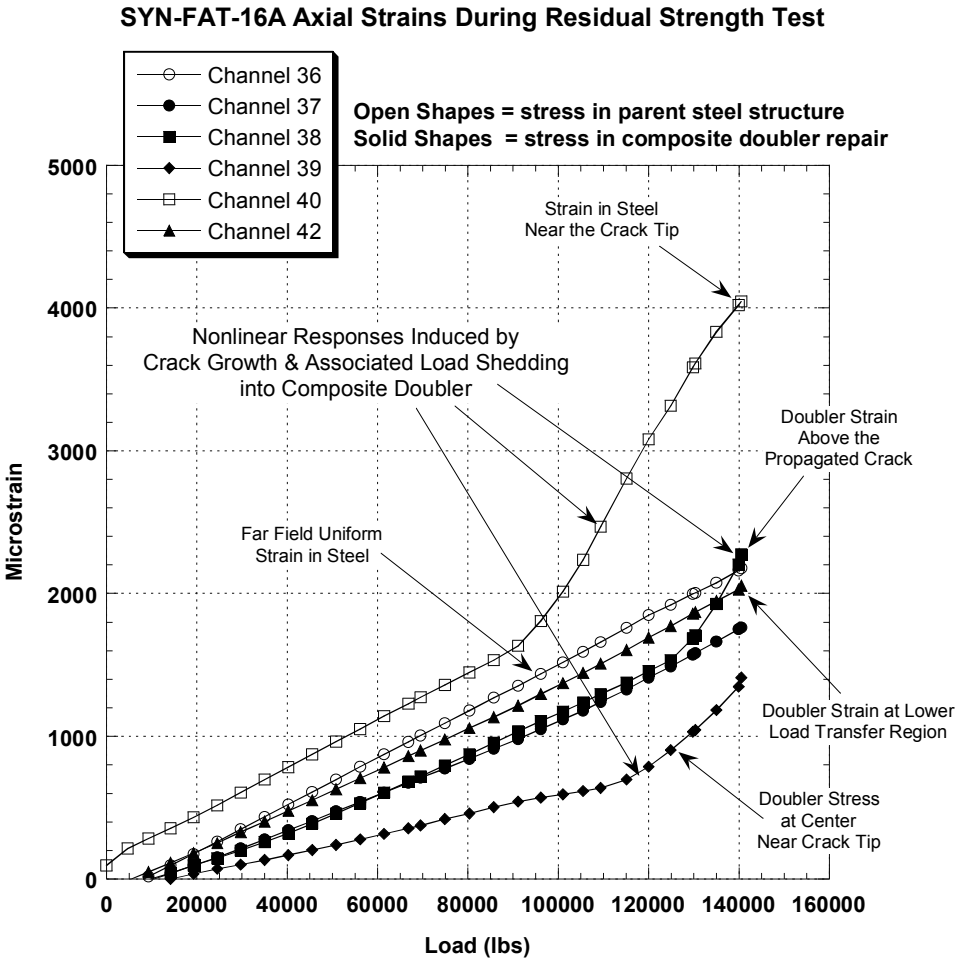

Figure 4-41: Strain Levels in Steel and Composite Doubler During Ultimate/Residual Strength Failure Test of SYN-FAT-16 – Pristine Composite Doubler with Hot-Wet & Cold Conditioning

Specimen No.	Strain Channels	Ultimate Load	Ultimate Stress	Location on Test Specimen
SYN-FAT-7 (pristine composite doubler with no conditioning)	15, 16	147,400	56,788	Steel - Far Field
	17		67,561	Doubler Edge (upper taper region)
	18, 19		49,131	Doubler Edge (middle taper region)
	20		118,465	Doubler Above Crack (full thickness region)
	22, 23		77,907	Doubler in Front of Crack (full thickness region)
	24, 25		161,820	Steel - Near Crack Tip
	27, 28		52,640	Doubler Edge (upper taper region)
SYN-FAT-12 (flawed composite doubler with no conditioning)	1, 2	147,000	74,162	Steel - Far Field
	4, 5		62,491	Doubler Edge (middle taper region)
	6		69,300	Doubler Above Crack (full thickness region)
	8, 9		67,824	Doubler Above Crack (full thickness region)
	10, 11		260,780	Steel - Near Crack Tip
	13, 14		49,275	Doubler Edge (upper taper region)
SYN-FAT-16 (pristine composite doubler with hot-wet & cold conditioning)	36	140,600	57,706	Steel - Far Field
	37		44,402	Doubler Edge (middle taper region)
	38		57,304	Doubler Above Crack (full thickness region)
	40		107,272	Steel - Near Crack Tip
	41		27,321	Steel - Relief Adjacent to Doubler
	42		51,836	Doubler Edge (lower taper region)

Table 4-3: Stresses in Steel Plates and Composite Doublers Produced by the Post-Fatigue Residual Strength Tests

Specimen No.	Configuration	Max. Stress Measured at Failure (psi)	Residual (Ultimate) Tensile Strength (psi) *
SYN-FAT-7	Unflawed composite doubler with no conditioning	161,820	93,970
SYN-FAT-8	Unflawed composite doubler with no conditioning	N/A	93,300
SYN-FAT-11	No composite doubler; Weld repair only	N/A	65,250 Δ
SYN-FAT-12	Flawed composite doubler with no conditioning	260,780	96,100
SYN-FAT-13	Flawed composite doubler with no conditioning	N/A	83,400
SYN-FAT-16A	Unflawed composite doubler with hot-wet & cold conditioning	107,272	77,400
SYN-FAT-18A	Flawed composite doubler with hot-wet & cold conditioning	N/A	86,930

* Manufacturer supplied data on ASTM A572 material tested $\sigma_{ult.}$ = 85,000 psi
Δ Baseline residual strength for comparison with composite doubler repair specimens

Table 4-4: Residual Strength Values from Specimens After Fatigue Tests Have Propagated Cracks (Post-Fatigue Load to Failure)

4.5 Response of Composite Doublers in Extreme Shear and Bending Environments

4.5.1 Three Point Bending Test Description

Objective - The purpose of this test series was to experimentally assess the potential for delaminations and disbonds in a thick composite doubler installation when subjected to extreme bending, compressive, and shear stresses. Bending of the shovel boom, and the associated shear stresses in the adhesive layer, is an important consideration and this test focused on worst case conditions. Three point bending was used to produce high shear stress in doublers and simulate the compression stresses which arise during shovel "break-out" conditions (reverse bending as shovel breaks free from its dig). The loads in this test did not simulate a particular operating condition. Rather, the bending loads were increased until the specimen failed. In this manner, it was possible to assess the design margin and mode of failure associated with high bending and compressive shear strains.

Three Point Bending Test Specimens and Test Set-Up - For this test series, the specimen was a beam comprised of a 24 ply Boron-Epoxy laminate bonded to a steel substrate such that the stiffness ratio between the repair doubler and parent structure was 1:3 (30% patch stiffness). The beam was 20″ long and 1″ wide and the doubler design (ply lay-up) was the same as the one used in the fatigue test specimens described on Section 3.3. Figure 4-42 shows the schematic of the test specimen and Figure 4-43 is a photo of some test specimens. Six similar specimens were tested so that the repair installation could be evaluated at conditions corresponding to minimal environmental effects and for performance after exposure to hot-wet-cold conditioning. The bend specimens did not contain weld regions

ASTM specifications require hot-wet and cold conditioning to run for a minimum of 40 hours with a 50% relative humidity. The bending specimens for this program were subjected to 98% relative humidity (140^{o}F) for 30 days followed by exposure to cold temperatures 0^{o}F for 10 days. Since exposure to the 0^{o}F temperatures came after the hot-wet conditioning, is was possible for any absorbed moisture to freeze, expand, and create local ruptures in the composite material. The extreme nature of this environmental conditioning was further exacerbated by the omission of any fiberglass cover ply, sealant or epoxy paint over the top of the composite doubler repair. Such protective coatings will be installed in an actual field repair and testing has shown that the fiberglass cover ply and epoxy paint should eliminate the detrimental effects of moisture and associated corrosion.

Prior to testing, NDI was applied to each test specimen. Pulse Echo ultrasonics was used to check for any pre-existing flaws which may affect the test results. Upper and lower load rods were used to support the specimen and transfer the load as indicated in Figures 4-42 and 4-44. Figure 4-45 is a photograph of a test specimen during testing in the uniaxial test machine. Strain gages were used to monitor the stress field in the composite and steel substrates during the tests. Figure 4-42 shows the strain gage layouts used on one unconditioned and one environmentally-exposed specimen. During the structural tests, the load was uniformly and continuously increased until structural failure occurred. Failure was defined as an inability to sustain an increasing load (i.e. a “knee” in load vs. displacement curve).

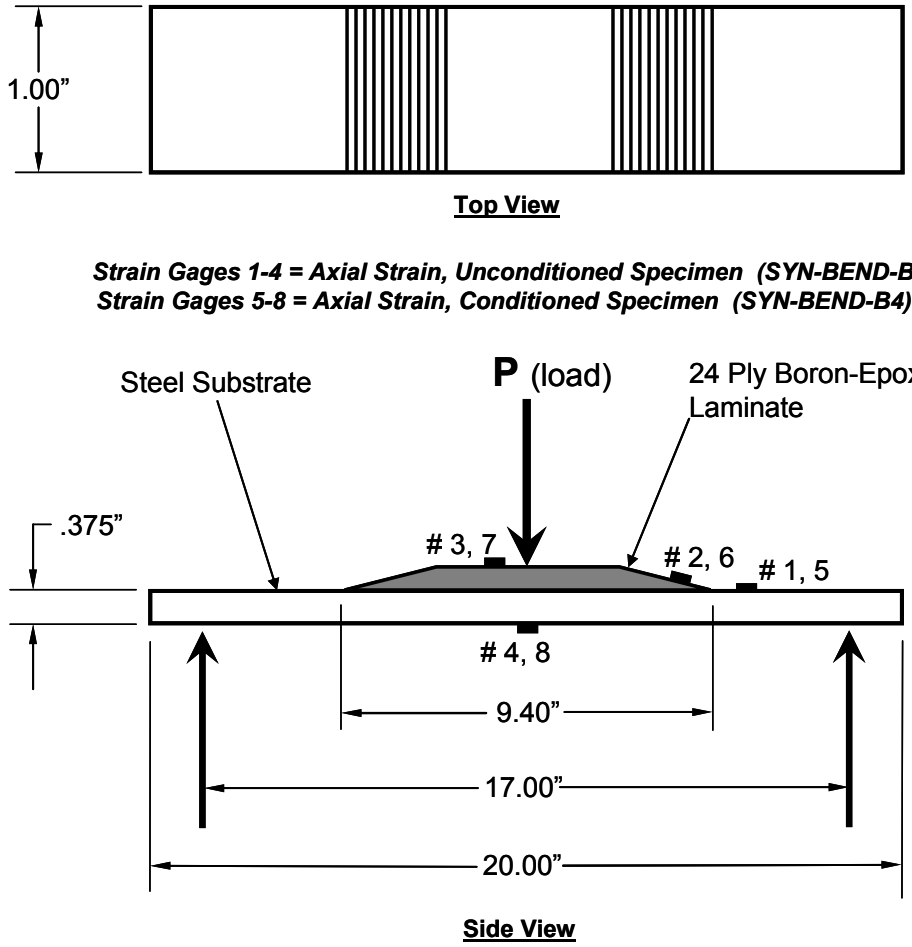

Figure 4-42: Composite Doubler Three-Point Bend Specimens for Evaluating Affects of Extreme Shear and Compressive Stresses; Strain Gage Layout Used to Monitor Stress Fields

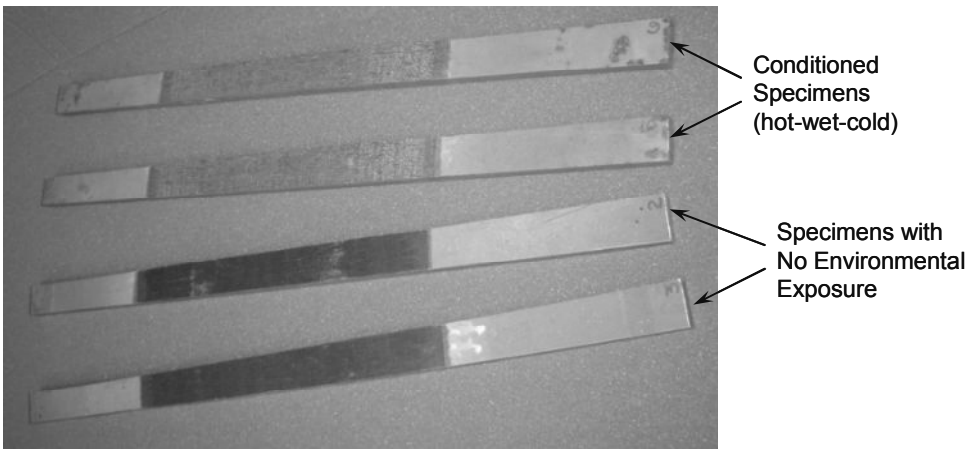

Figure 4-43: Conditioned and Unconditioned Test Specimens for Bending-Shear Tests

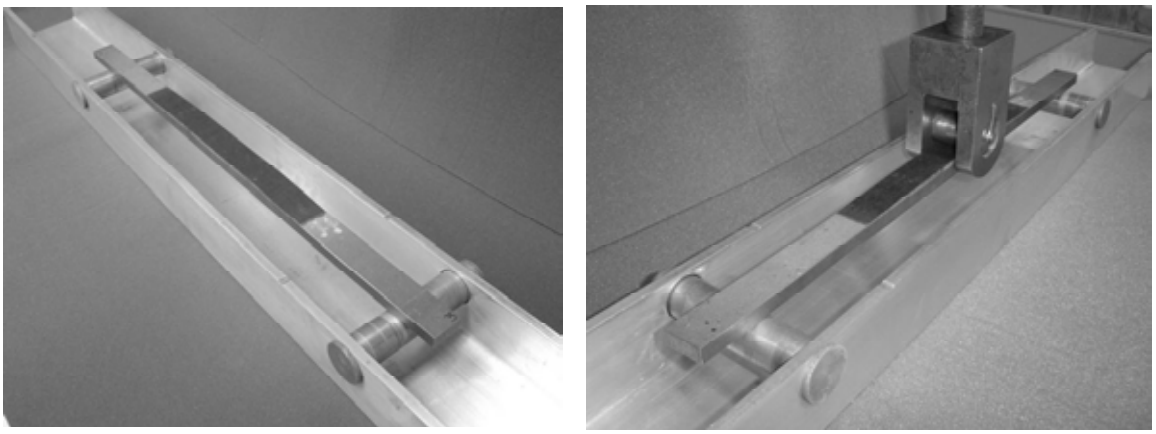

Figure 4-44: Three-Point Bend Specimen in Test Fixture Showing Load Application and Boundary Conditions

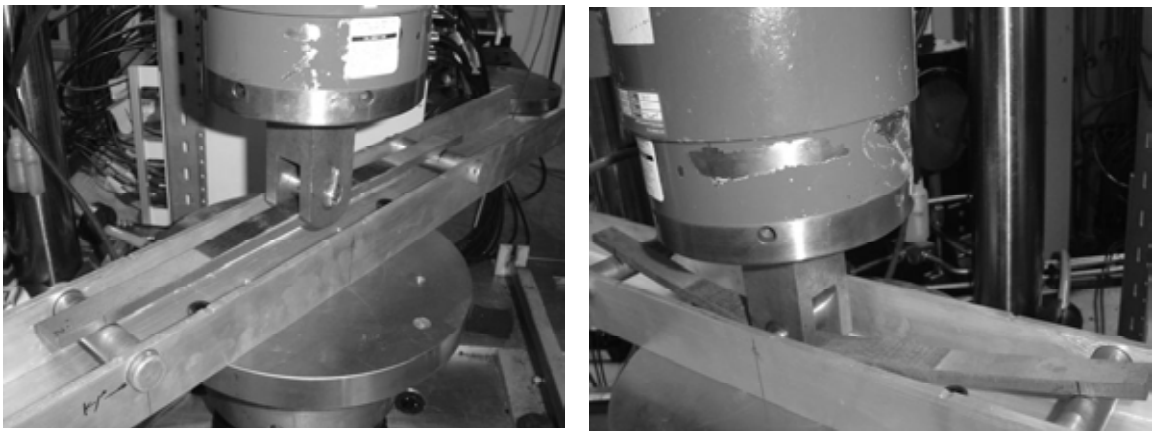

Figure 4-45: Three-Point Bend Specimen During Testing

4.5.2 Three Point Bending Test Results

Pre-test inspections did not reveal any flaws in the test specimens. The maximum moment generated in the test specimen is given by the relation:

$$M_{max} = PL/4 \qquad (4\text{-}5)$$

The stress produced by this moment can be calculated using the following equation:

$$\sigma = M\,y/I \qquad (4\text{-}6)$$

Where:

I = moment of inertia of cross section

M = moment [in.-lbs.]
P = load [lbs.]
L = distance between load supports
y = distance from neutral axis to point of interest
σ = stress [psi]

When the beam is supported at two endpoints and loaded at the midpoint as shown in Figure 4-42 and 4-44, the maximum stress occurs in the outer surface of the test specimen at the midpoint of the beam. This shear stress may be calculated by using equation (4-5) for the midpoint of the specimen L/2:

$$\sigma_{max} = 3PL/2bd^2 \qquad (4\text{-}7)$$

Where:

σ_{max} = stress in outer fibers at midpoint [psi]
b = width of beam [in.]
d = depth of beam [in.]

Figures 4-46 and 4-47 plot the shear stress values calculated from the strains measured during the 3-point bend tests. Strains in the steel at the bottom of the specimen were tensile while strains in the composite laminate on top were approximately equal in magnitude but were compressive. Tests on steel specimens without composite doublers revealed that yielding in the bend specimens occurs at approximately 55 ksi. Figure 4-46 shows that yielding in the bend specimens, and the corresponding nonlinear response in the composite repair, began slightly later at 66 ksi. Strain could not be measured in the exact center of the laminate due to the presence of the load application bar. Gages #3 and #7 were close to the center but due to the high strain gradient in this area, equation (4-7) was also used to make some stress level assessments. Table 4-5 lists the maximum compressive stress levels produced in the composite repair during the tests. Note the decrease in the stress levels achievable in the hot-wet conditioned specimens. Focused testing has shown that the adhesive strength can be reduced by as much as 20% through exposure to hot-wet conditions. This is the approximate difference between maximum compression stresses in the unconditioned and conditioned specimens. Proven, protective measures will be taken in an actual installation to eliminate these degrading effects. In all tests, the maximum stress levels exceeded the normal yield levels of 55 ksi established for this material. Several of the specimens were able to survive compressive stresses that approached the ultimate strength value for the pristine, unwelded steel material (85 ksi). Once again, these results demonstrate that the composite doubler repair method is able to survive extreme compressive stresses and that the parent structure must go into the yield regime in order to fail the repair.

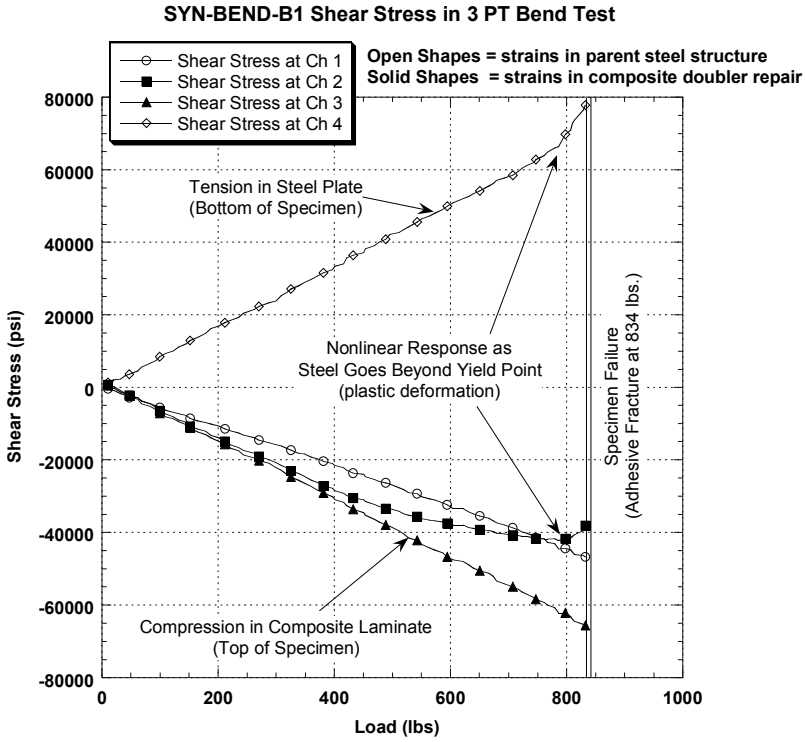

Figure 4-46: Shear Stress in SYN-BEND-B1 During Three Point Bend-to-Failure Tests

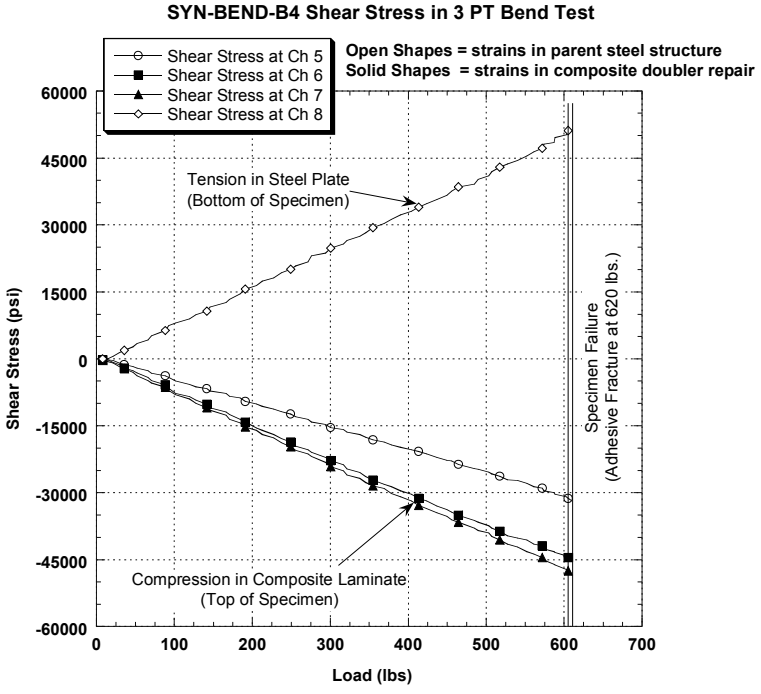

Figure 4-47: Shear Stress in SYN-BEND-B4 During Three Point Bend-to-Failure Tests

Compression Stresses Sustained in 3- Point Bend Specimens			
Specimen No.	**Specimen Configuration**	**Condition**	**Max Compression Stress at Failure (psi)**
SYN-BEND-B1	Doubler Repair	No Conditioning	79,000
SYN-BEND-B2	Doubler Repair	No Conditioning	83,600
SYN-BEND-B3	Doubler Repair	No Conditioning	73,900
SYN-BEND-B4	Doubler Repair	Hot-Wet	58,700
SYN-BEND-B5	Doubler Repair	Hot-Wet	64,800
SYN-BEND-B6	Doubler Repair	Hot-Wet	61,300

Table 4-5: Compression Stress Levels in Composite Doubler Laminates Produced by Bending/Compression Tests

References

4.1 Roach, D., "Development Program to Certify Composite Doubler Repair Technique for Commercial Aircraft," First DoD/FAA/NASA Conference on Aging Aircraft, July 1997.

4.2 Baker, A.A. and Jones, R., *Bonded Repair of Aircraft Structures*, Martinus Nijhoff Pub., The Netherlands, 1988.

4.3 Roach, D., "Damage Tolerance Assessment of Bonded Composite Doubler Repairs for Commercial Aircraft Applications," Sandia National Laboratories/ Dept. of Energy Report No. SAND98-1016 , August 1998.

4.4 Rice, R., Francini, R., Rahman, S., Rosenfeld, S., Rust, S., Smith, S., and Broek, D., "Effects of Repair on Structural Integrity", Dept. of Transportation Report No. DOT/FAA/CT-93/79, December 1993.

5.0 NONDESTRUCTIVE INSPECTION OF COMPOSITE DOUBLER REPAIRS ON CARBON STEEL STRUCTURES

Dennis Roach, Kirk Rackow, and Waylon DeLong

The two main potential causes of structural failure in composite doubler installations are cracks in the steel, disbonds at the adhesive layer, and delaminations between adjacent plies in the doubler. When disbonds or delaminations occur, they may lead to joint failures. By their nature, they occur at an interface and are, therefore, always hidden. A combination of fatigue loads and other environmental weathering effects can combine to initiate these types of flaws. Periodic inspections of the composite doubler for disbonds and delaminations (from fabrication, installation, fatigue, or impact damage) is essential to assuring the successful operation of the doubler over time. The interactions at the bond interface are extremely complex, with the result that the strength of the bond is difficult to predict or measure. Although extensive testing has shown this repair method to be extremely damage tolerant, disbonds in critical regions may compromise the integrity of the structural assembly. Therefore, it is necessary to detect all areas of disbonding or delamination, as directed by DTA, before joint failures can occur. The overall goals of the NDI effort was to: 1) utilize suitable NDI techniques to detect cracks in the parent structure, interply delaminations in the doubler, and steel interface disbonds, and 2) generate an inspection method (equipment and procedures) that can be easily deployed by personnel in the field.

5.1 Damage Tolerance Assessment and Inspection Intervals

Establishing Damage Tolerance - Damage tolerance is the ability of a structure to sustain damage, without catastrophic failure, until such time that the component can be repaired or replaced. In aircraft for example, the U.S. Federal Aviation Requirements specify that the residual strength shall not fall below limit load, P_L, which is the load anticipated to occur once in the life of an aircraft. This establishes the minimum permissible residual strength $\sigma_P = \sigma_L$. To varying degrees, the strength of composite doublers is affected by crack, disbond, and delamination flaws. The residual strength as a function of flaw size can be calculated using fracture mechanics concepts. Figure 5-1 shows a sample residual strength diagram. The residual strength curve is used to relate this minimum permissible residual strength, σ_P, to a maximum permissible flaw size a_P. In the case of the civil structures, field inspection data indicates that many of the structures sited in this report can operate with cracks that are several inches in length. As a result, the goal of this NDI effort was conservatively set to detect cracks of 1" in length which are concealed beneath a composite doubler that may be as thick as 72 plies (0.40" thick). With the damage tolerance assessment presented in section 4.0, the goal for disbond/delamination detection in the composite doublers was set at a size of 0.5" in diameter.

A fracture control plan is needed to safely address any possible flaws which may develop in a structure. Nondestructive inspection is the tool used to implement the fracture control plan. Once the maximum permissible flaw size is determined, the additional information needed to properly apply NDI is the flaw growth versus time or number of cycles. Figure 5-2 contains a flaw growth curve. The first item of note is the total time, or cycles, required to reach a_P. A

second parameter of note is a_d which is the minimum detectable flaw size. A flaw smaller than a_d would likely be undetected and thus, inspections performed in the time frame prior to n_d would be of little value. The time, or number of cycles, associated with the bounding parameters a_d and a_P is set forth by the flaw growth curve and establishes *H(inspection)*. Safety is maintained by providing at least two inspections during *H(inspection)* to ensure flaw detection between a_d and a_P .

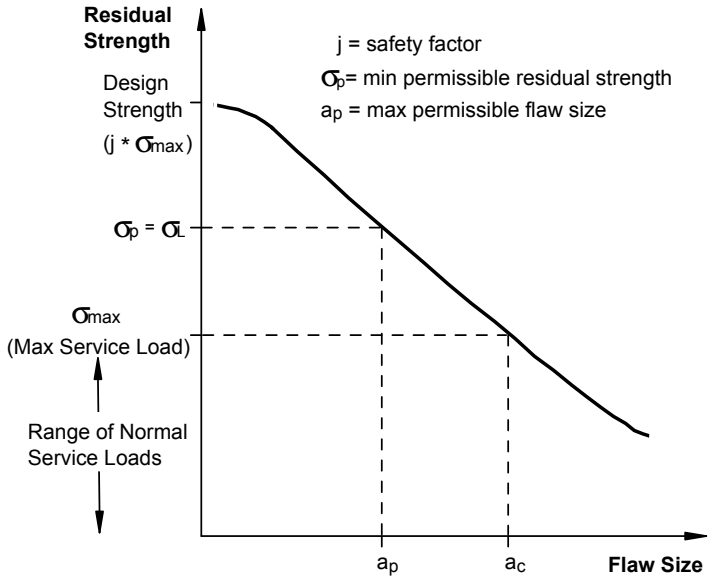

Figure 5-1: Residual Strength Curve

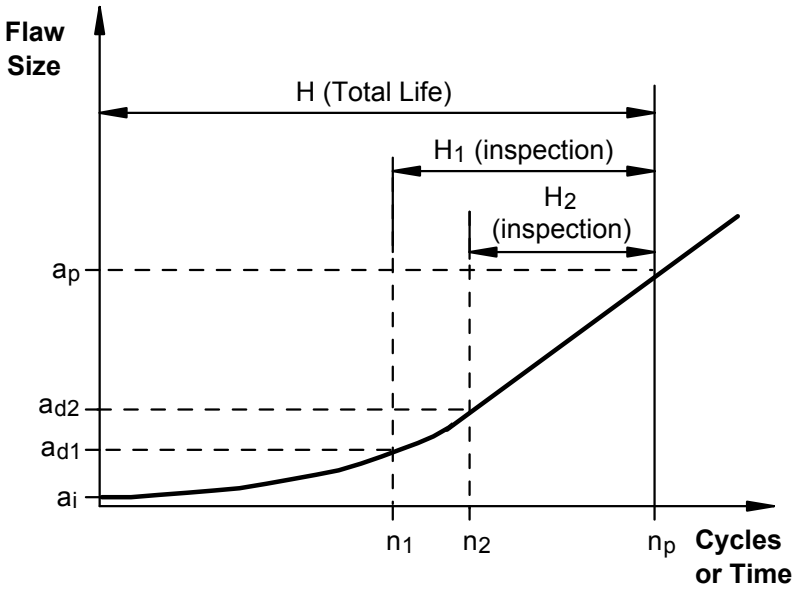

Figure 5-2: Crack Growth Curve Showing Time Available for Fracture Control

Inspection Intervals - An important NDI feature highlighted by Figure 5-2 is the large effect that NDI sensitivity has on the required inspection interval. Two sample flaw detection levels $a_{d\,(1)}$ and $a_{d\,(2)}$ are shown along with their corresponding intervals $n_{d\,(1)}$ and $n_{d\,(2)}$. Because of the gradual slope of the flaw growth curve in this region, it can be seen that the inspection interval $H_1(inspection)$ can be much larger than $H_2(inspection)$ if NDI can produce just a slightly better flaw detection capability. Since the detectable flaw size provides the basis for the inspection interval, it is essential that quantitative measures of flaw detection are performed for each NDI technique applied to the structure of interest. Such quantitative flaw detection measures are presented in the remainder of Chapter 5.

5.2 Quality Assurance Coupons to Ensure Proper Surface Preparation

Before moving into routine in-service inspections, it is first necessary to ensure that the initial installation was completed properly. Towards that end, quality assurance testing has been developed for certifying the initial installation. The primary QA test utilizes a witness coupon. The witness coupon is a steel strip that is bonded to the prepared surface alongside the composite doubler. After curing, the witness strip is pried off with a wedge. If the adhesive is found on both the coupon and the steel structure, then the surface preparation is good. The full strength of the adhesive is assured since the failure mode was cohesive failure (fracture) rather than adhesive failure (disbond). Figure 5-3 depicts this surface preparation QA test and the two potential failure modes.

Nondestructive Inspection - It is now necessary to detect any flaws in the installation. Initially, the status of flaws in the doubler and bondline must be ascertained to accept the installation. Thereafter, the flaw status of the doubler, bondline, and parent material must be periodically measured. Nondestructive inspection provides the last line of defense in this regard. NDI is the only means for determining if the structural integrity of the repair area changes over time.

5.3 Inspections for Cracks in Parent Material Beneath Composite Doubler

In addition to the normal difficulties associated with crack detection in steel structures, the added complexity of inspecting through a composite doubler to assess the structure beneath introduces new impediments. The two NDT inspection techniques commonly used for crack detection were assessed in this study: eddy current and X-ray.

5.3.1 Eddy Current Inspection

Eddy Current (EC) inspection uses the principles of electromagnetic induction to identify or differentiate structural conditions in conductive metals [5.1, 5.2]. In this study, it was applied to numerous bonded composite doubler installations in order to assess the ability of EC to detect cracks in steel plates beneath a composite laminate. The presence of a crack is indicated by changes in the flow of eddy currents in the structure. EC signals are physically monitored using

impedance-plane plots which show the reactive and resistive components of a coil as functions of frequency, conductivity, or permeability.

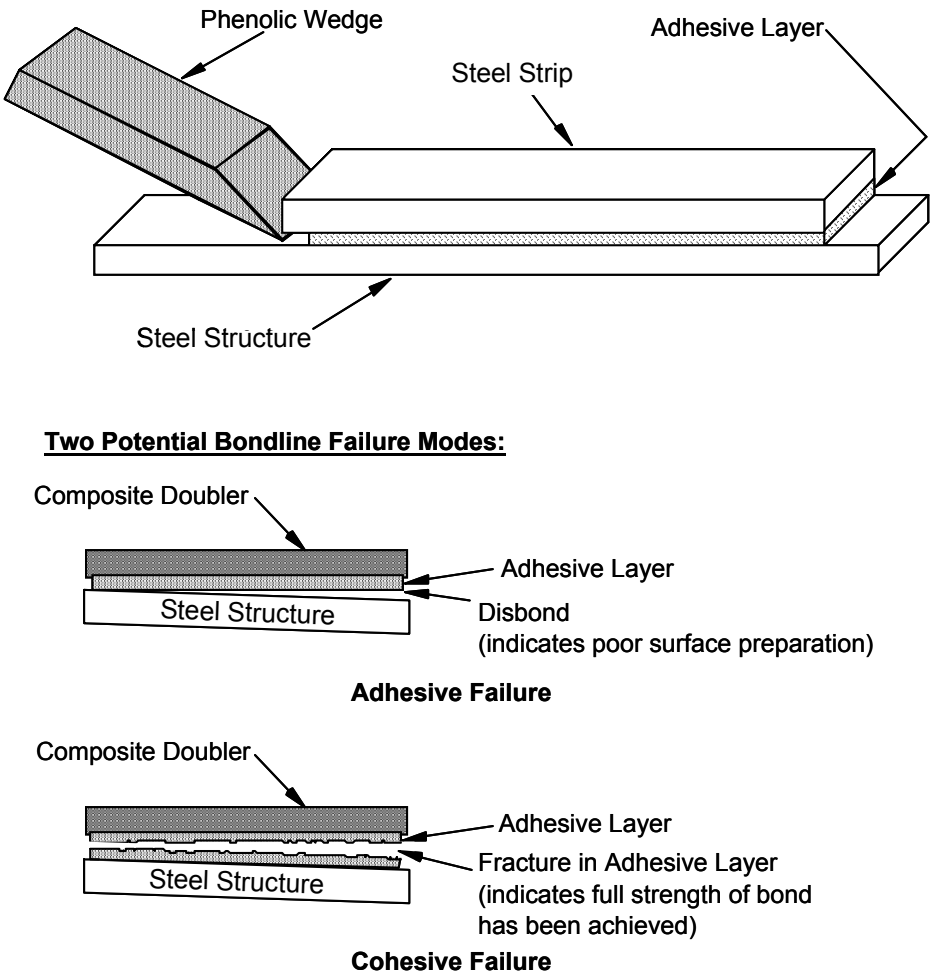

Figure 5-3: Quality Assurance Wedge Test for Surface Preparation

When EC inspections are performed, an electrically conductive material is exposed to an alternating magnetic field that is generated by a coil of wire carrying an alternating current. As a result, eddy currents are induced on and below the surface of the material (see Figure 5-4). These eddy currents, in turn, generate their own magnetic field which opposes the magnetic field of the test coil. Cracks or thickness changes in the structure being inspected influence the flow of eddy currents and change the impedance of the test coil accordingly. EC instruments record these impedance changes and display them in impedance plane plots to aid the flaw detection process.

The depth of penetration of eddy currents is inversely proportional to the product of magnetic permeability, electrical conductivity, and frequency of the inducing currents. Therefore, eddy current tests are most sensitive to discontinuities on the surface next to the coil, which makes

them very effective for detecting fatigue cracks in the near surface. High frequency eddy current (HFEC) is generally considered 100 kHz and above and is used to detect near-surface flaws. Low frequency eddy current (LFEC) is in the 100 Hz to 10 kHz range and is used to penetrate deeper to detect flaws in underlying structure. As the structure to be penetrated gets thicker, a lower EC operating frequency is required to reach the desired depth. However, the detectable flaw size usually becomes larger as the frequency is lowered. Eddy currents deeper in the material are weaker and lag in phase compared to the currents near the surface. By measuring the phase, it is possible to determine whether the defect is near the surface or at the inner wall. Figure 5-5 shows an example of an impedance plane display showing phase and amplitudes of EC signals generated by cracks of varying depths.

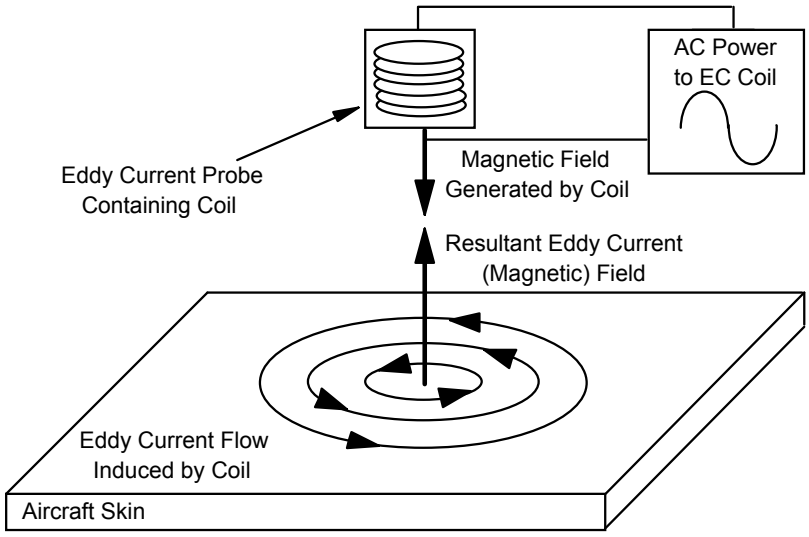

Figure 5-4: Induction of Eddy Currents in Conductive Materials

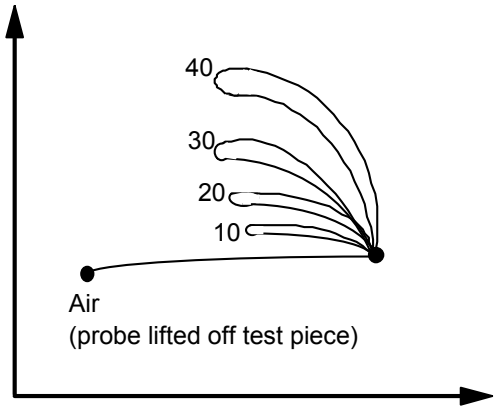

Figure 5-5: Impedance Plane Display Showing Signal Traces for Surface Cracks of Different Depths (shown in mils)

External surface inspections which may key off visible attributes such as fastener locations (normal origin of fatigue cracks) must now be performed blind since the doubler covers the steel surface. Because eddy currents are created using an electromagnetic induction technique, the inspection method does not require direct electrical contact with the part being inspected. The composite doubler, between the EC transducer and the steel being inspected, does, however, create a lift-off effect which changes the EC signal. This lift-off effect can mask important aspects of flaw detection and must be counteracted by careful equipment set-up, use of suitable calibration standards, and experience in EC signal interpretation. Eddy currents are not uniformly distributed throughout the plate; rather, they are densest at the surface immediately beneath the coil (transducer) and become progressively less dense with increasing distance below the surface. Thus, the inspection sensitivity through composite doublers is decreased by the lift-off effects (equal to thickness of doubler) and associated need to inspect below the surface of the EC transducer. Lower frequency probes can be used to produce a greater depth of EC penetration, however, this is accompanied by a loss in sensitivity versus higher frequency probes. Thus, the thicker the doubler, the greater reduction in crack detection sensitivity. Therefore, EC inspection through composite doublers becomes a balance between signal resolution and the frequency required to inspect beneath a particular laminate.

Structured EC testing was performed in this study in an attempt to quantify EC performance through composite doublers. Both sliding and spot probes were used in this inspection series. Both probes are suited for this type of inspection and have the low frequencies needed to penetrate the doubler layer. Figure 5-6 shows several of the cracked steel specimens, with and without composite doublers, which were used in this study. Figure 5-7 shows the Nortec 1000 eddy current device being applied to one of the composite doubler fatigue coupon specimens along with photos of the two EC probes tested.

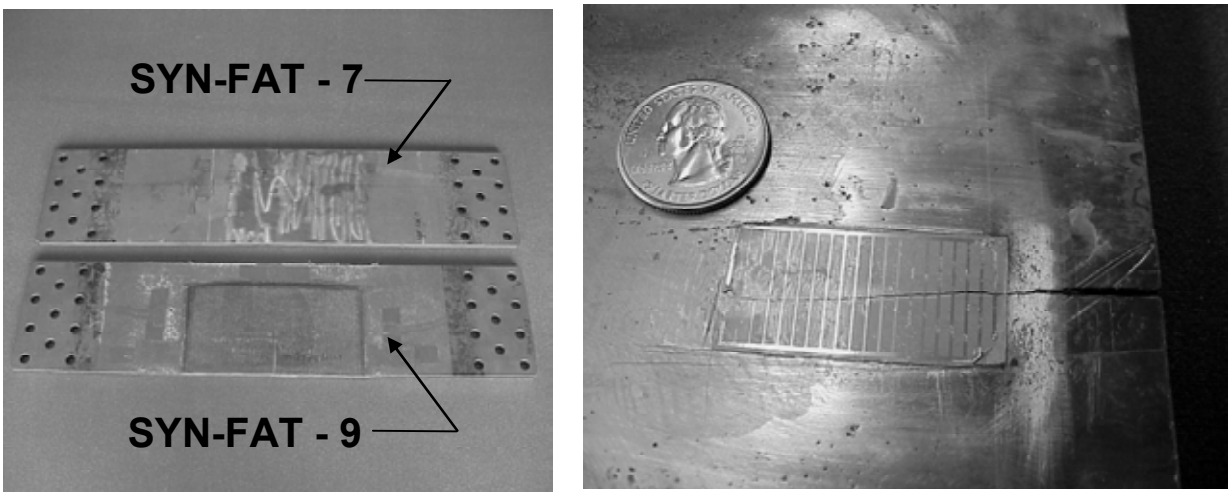

Figure 5-6: Panels Used in EC Validation Tests and Typical Fatigue Crack Propagating Through the Crack Gage on the Back of the Specimens

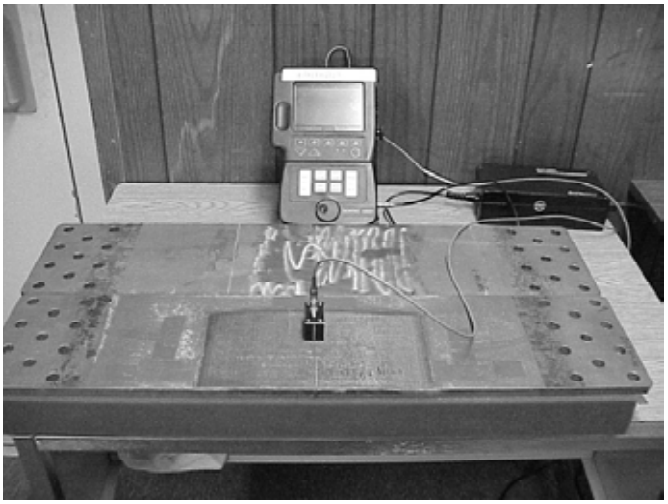

EC Spot Probe

EC Sliding Probe

Figure 5-7: Eddy Current Inspection Set-Up with Nortec 1000 Readout Device Connected to EC Spot probe or EC Sliding Probe

The first test involved placing the EC probes on a composite repair specimen which contained a fatigue crack under the doubler (SYN-FAT-9). This assessed crack detection through a 24 ply (0.144" thick), non-conductive, composite laminate. Spot probe crack detection occurred ¼" before the probe reached the crack tip. In the case of the sliding probe, crack detection occurred after the crack was under the footprint of the probe. Figure 5-8 shows representative EC signals generated in cracked structure located beneath the Boron-Epoxy doublers.

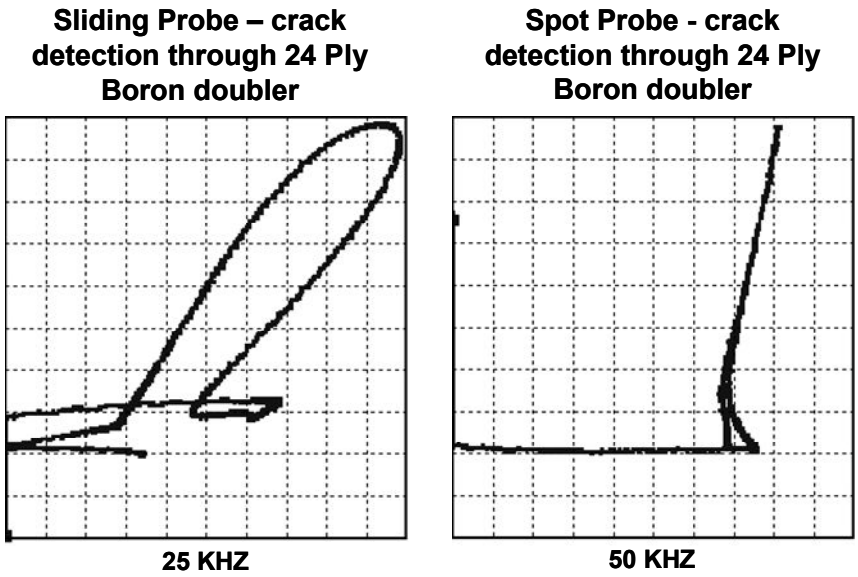

Figure 5-8: Large Signals Produced by EC Sliding and EC Spot Probe Indicating Strong Crack Detection Beneath a 24 Ply Composite Doubler

Figure 5-9 provides the baseline EC signals associated with no crack in the structure. This is essentially the noise associated with the EC probe, the signal acquisition equipment, and the method used to deploy the transducer. Any deviation from this flat line signal can provide a crack indication. From a reliability standpoint, the desired signal-to-noise ratio is at least 2:1. Comparisons between the signals in Figs. 5-8 and 5-9 reveal that the signal-to-noise ratio for crack detection through the 24-ply doublers used in this study is approximately 8:1.

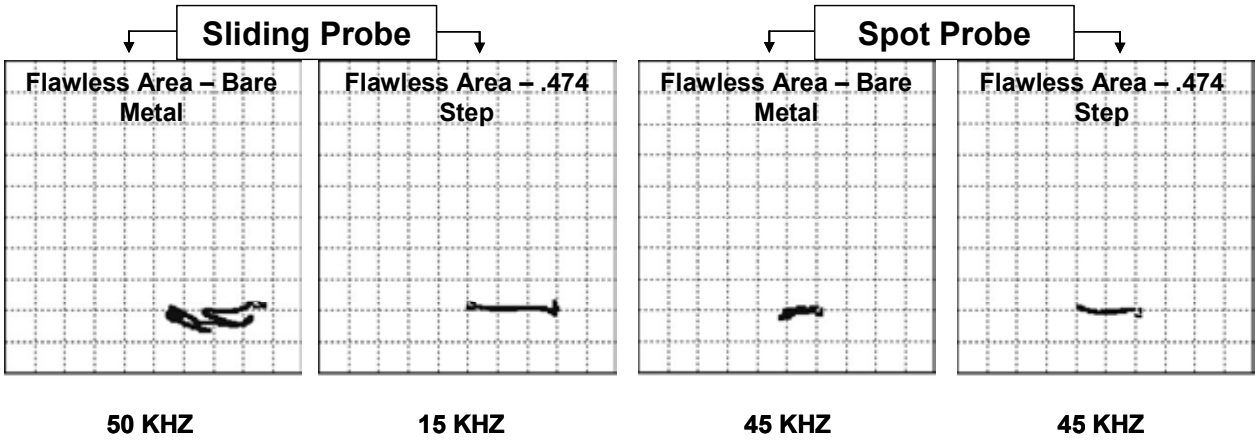

Figure 5-9: Signals Produced by EC Sliding and EC Spot Probe When Inspecting an Unflawed Region

The second test series involved the superposition of a Boron-Epoxy laminate step wedge (see Fig. 5-10) over a cracked steel structure. The purpose of these tests was to assess crack detection beneath composite doublers of different thicknesses. By placing various step thicknesses of the step wedge over a fatigue crack and studying the eddy current response through this thickness, it was possible to determine any limitations in EC crack detection through ultra-thick composite doublers. For these inspections, the Sliding Probe and Spot Probe were placed on top of the step wedge at each thickness (step thicknesses = 0.016", 0.031", 0.093", 0.143", 0.205", 0.251", 0.307", 0.361", and 0.470"). Then the entire unit (step wedge & probe) was slid towards the crack as shown in Figure 5-11. Signal characteristics and locations of detection were monitored and documented.

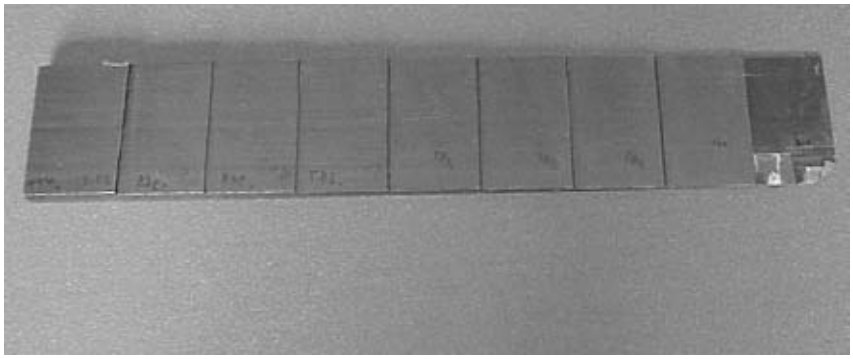

Figure 5-10: Boron-Epoxy Laminate Step Wedge Used to Assess Crack Detection Beneath Composite Doublers of Different Thicknesses

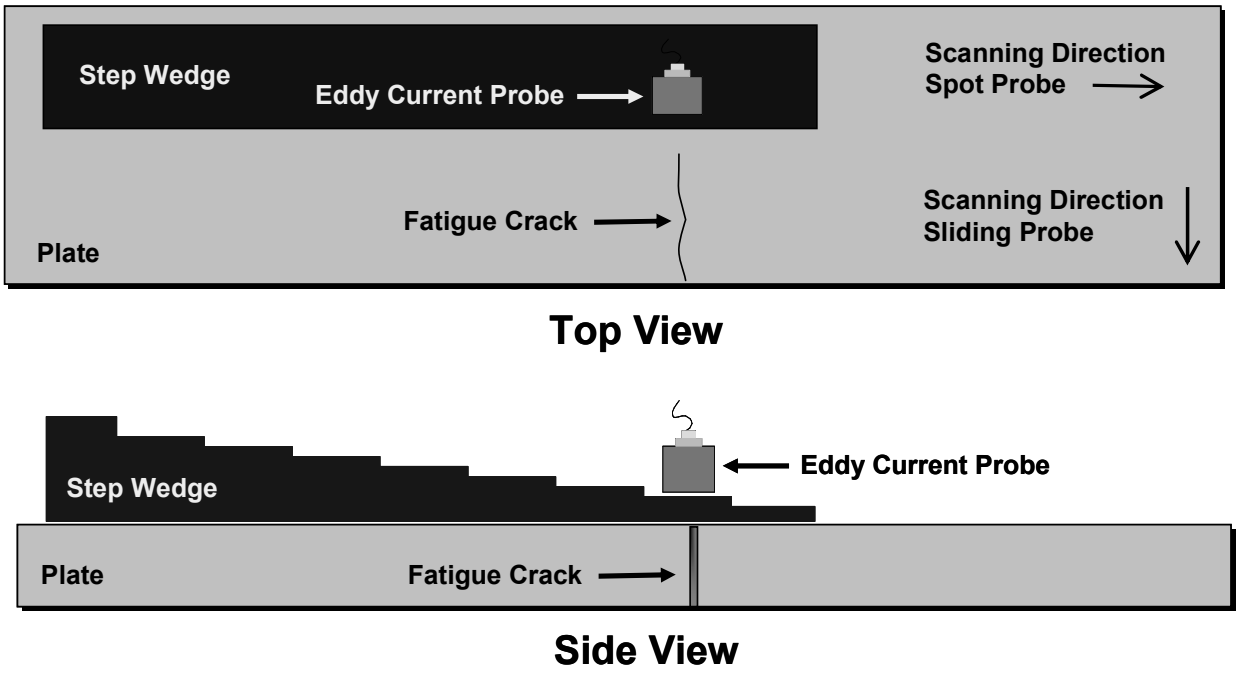

Figure 5-11: Inspection with Sliding and Spot Probes Using Step Wedge Over a Cracked Steel Structure

Figures 5-12 to 5-15 show the eddy current signals corresponding to cracks located beneath increasingly thicker composite laminates. The non-conductive composite laminate serves as a lift-off in the eddy current field and produces a reduction in the signal strength. The results shown in Figures 5-12 and 5-14 correspond to sliding probe and spot probe inspections through the Boron-Epoxy step wedge placed over the 24-ply doubler. As a result, the thickness (lift-off) of the composite laminate ranges from 27 plies (0.160" th.) to 103 plies (0.618" th.). The results shown in Figures 5-13 and 5-15 correspond to sliding probe and spot probe inspections through the step wedge placed over a cracked steel plate with no doubler. As a result, the thickness (lift-off) of the composite laminate for these results ranges from 3 plies (0.016" th.) to 79 plies (0.474" th.). All of the signal plots indicate that crack detection can be reliably achieved through composite doublers. Furthermore, crack detection signals can be obtained through composite doublers in excess of 100 plies and greater than 0.6" thick. For the steel applications identified thus far, it is anticipated that the composite doubler installations will be on the order of 0.3" to 0.5" thick. The eddy current spot probe appears to provide a slightly more repeatable and uniform signal than the sliding probe. The signal-to-noise ratios for the sliding probe ranges from a low of 2:1 to a high of 14:1. The signal-to-noise ratios for the spot probe ranges from a low of 3:1 to a high of 22:1. As discussed above there is some signal loss associated with the placement of the laminate step wedge instead of the more realistic bonding of the laminate. When this unrealistic signal loss is removed, the signal-to-noise ratios for actual composite doublers installations may be twice the values listed here.

It is important to note that because the step wedge was not bonded to the steel plate, highly non-conductive air was located between the wedge and the steel structure. As a result, the signal levels are artificially low. This effect can be quantified by comparing the crack signal from the 0.144" thick bonded doubler (see signal on left side of Figure 5-8) and to the crack signal from a 0.144" step wedge placed on top of a steel crack (see middle-left signal in Figure 5-13). For a common gain and doubler thickness, the difference in eddy current signal strength between a bonded and unbonded (air gap) doubler is approximately a factor of two. Thus, the results presented for the step wedge experiments are conservative and the signal-to-noise ratios may be improved by as much as a factor of two for an actual bonded, composite repair installation.

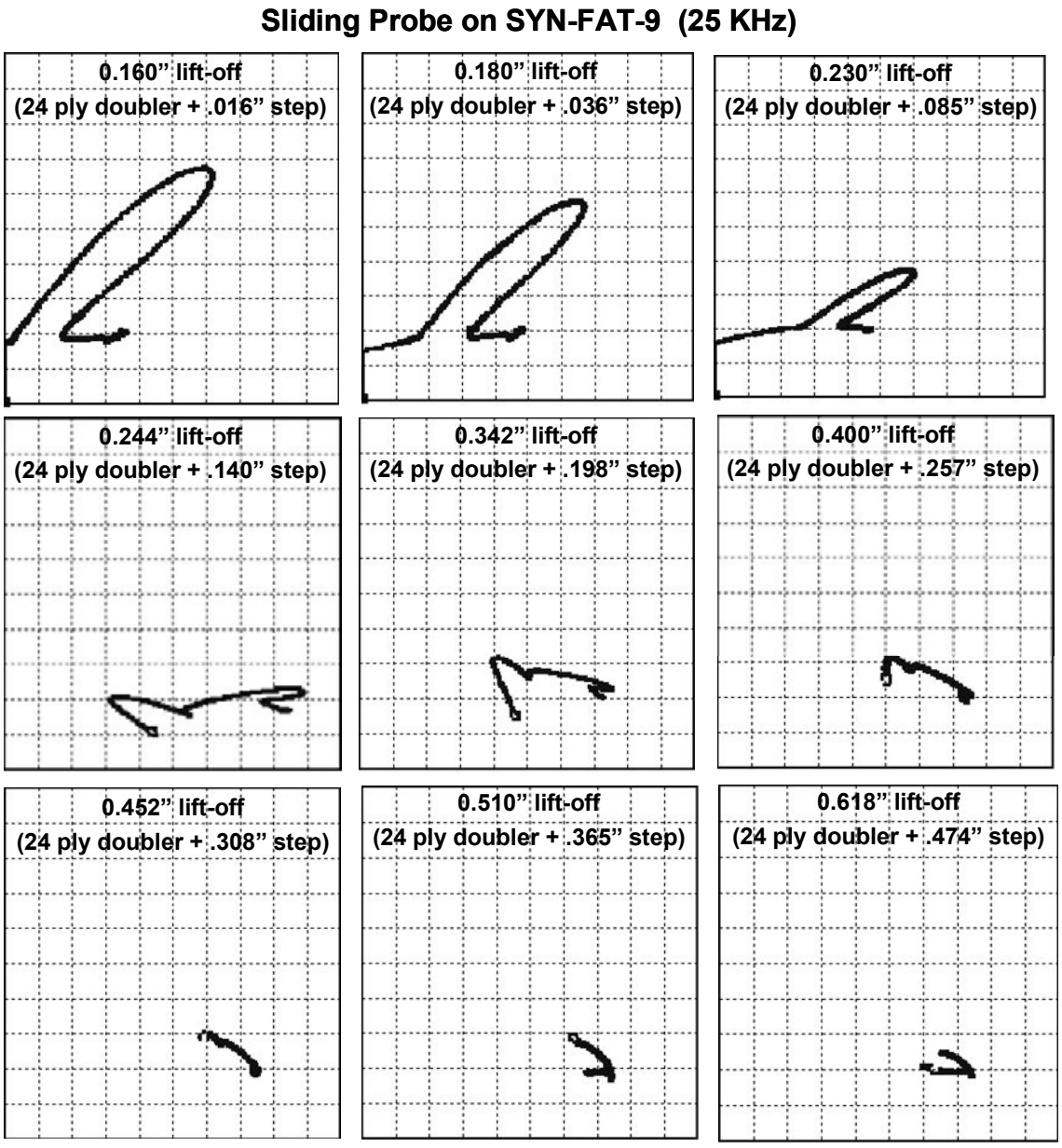

Figure 5-12: EC Signals from Sliding Probe Inspection of Composite Repaired Specimen (SYN-FAT-9) with a Fatigue Crack and Step Wedge Placed Over Laminate

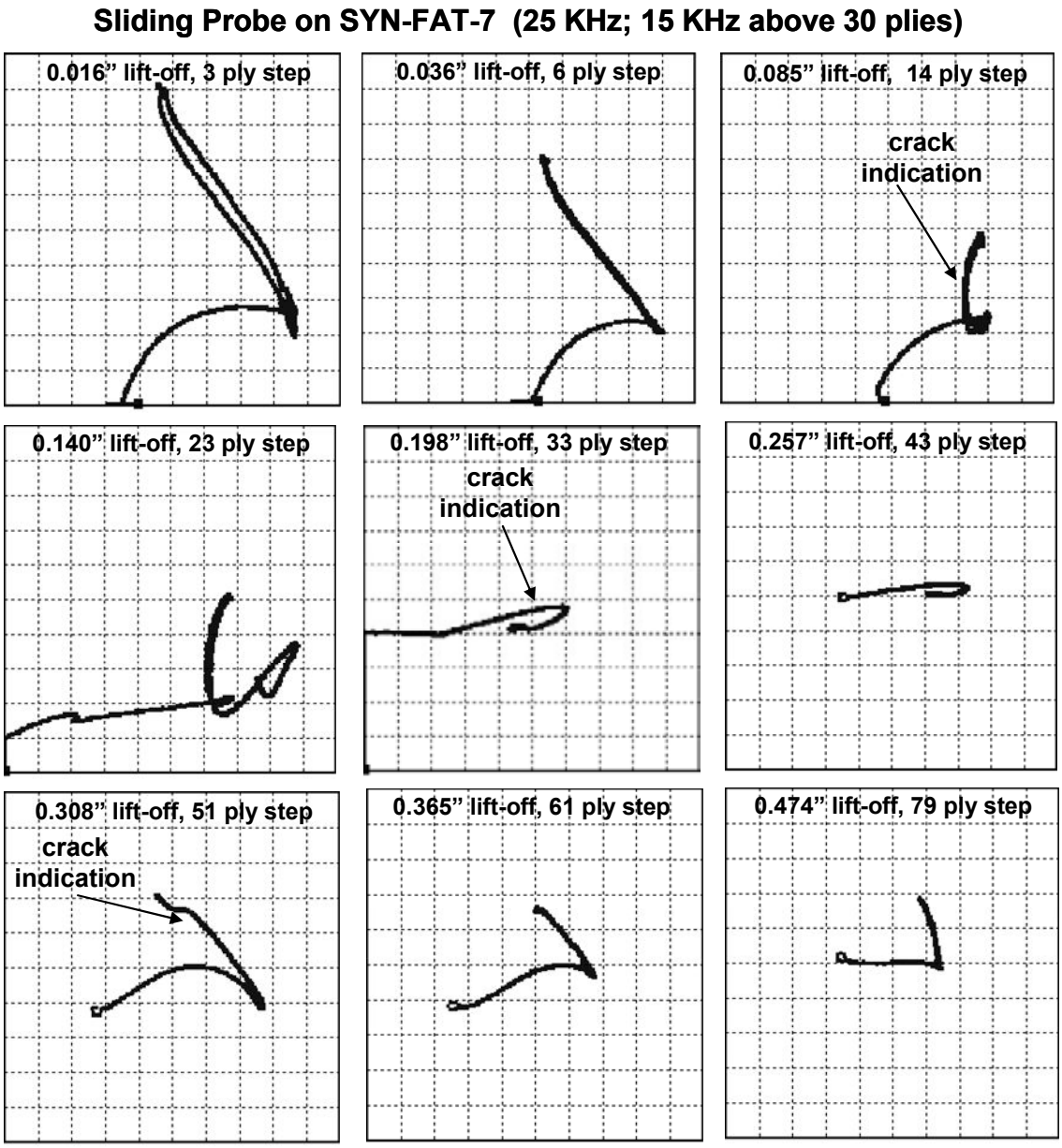

Figure 5-13: EC Signals from Sliding Probe Inspection of Unrepaired Specimen (SYN-FAT-7) with a Fatigue Crack and Step Wedge Placed Over Bare Steel Surface

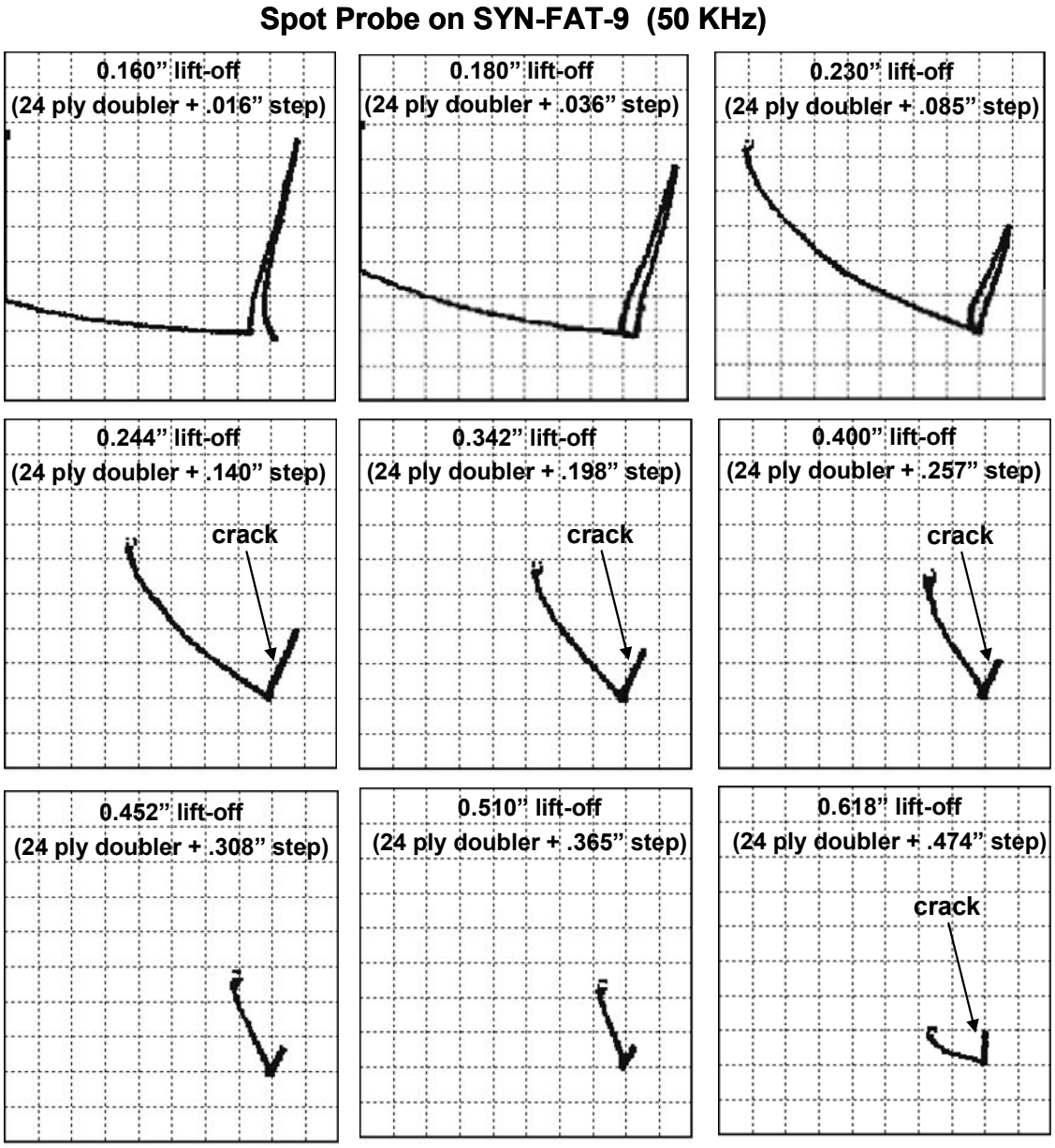

Figure 5-14: EC Signals from Spot Probe Inspection of Composite Repaired Specimen (SYN-FAT-9) with a Fatigue Crack and Step Wedge Placed Over Laminate

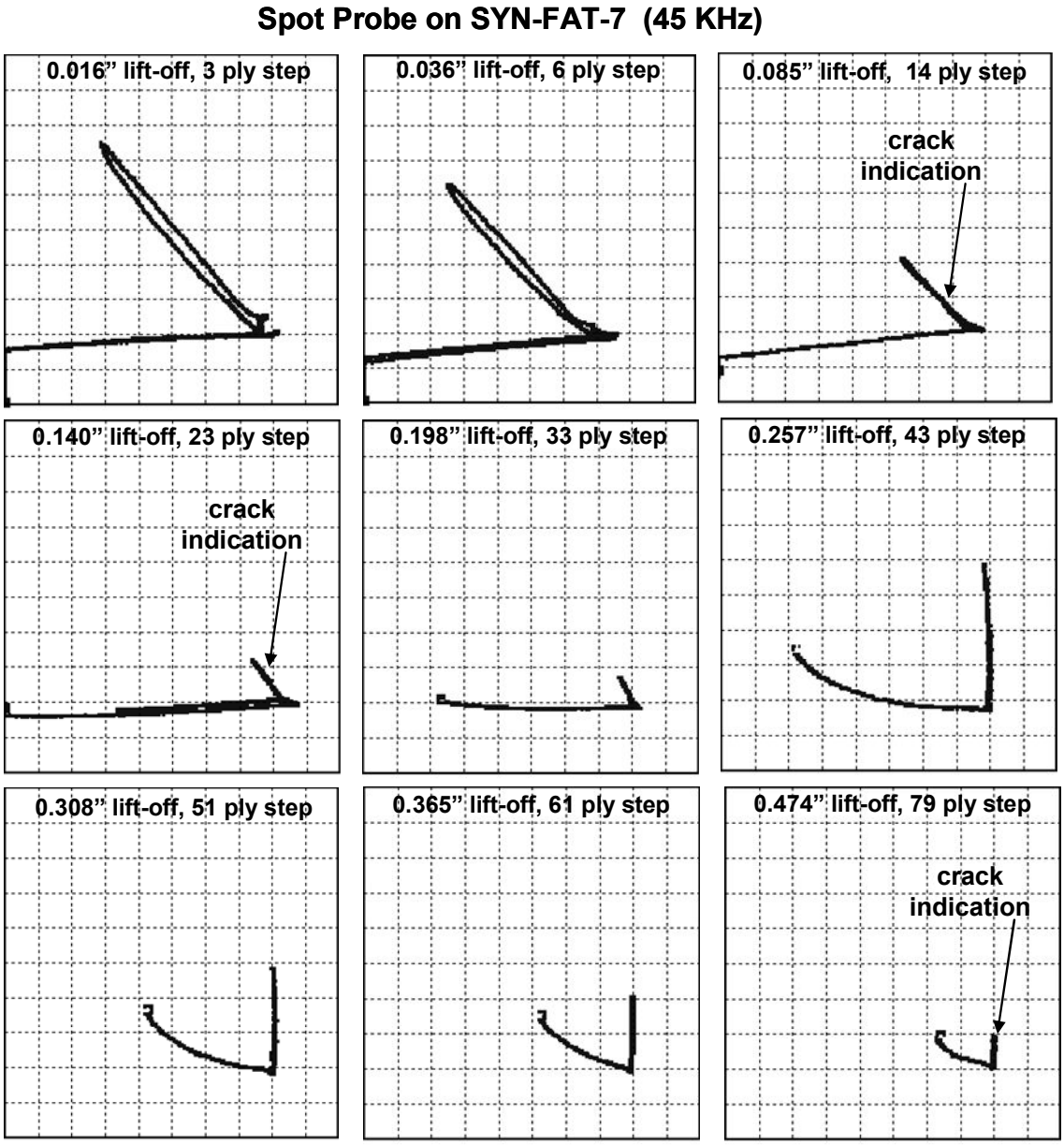

Figure 5-15: EC Signals from Spot Probe Inspection of Unrepaired Specimen (SYN-FAT-7) with a Fatigue Crack and Step Wedge Placed Over Bare Steel Surface

5.3.2 X-Ray Inspection

Radiographic inspection is a nondestructive method of inspecting materials for surface and subsurface discontinuities [5.1]. The method utilizes radiation in the form of either x-rays or gamma rays, which are electromagnetic waves of very short wavelength. The waves penetrate the material and are absorbed depending on the thickness or density of the material being examined. By recording the differences in absorption of the transmitted waves, variations in the material can be detected. Figure 5-16 shows an application of X-radiography in a field

environment. The most common way of measuring X-ray transmission is with film. After exposure and development, the film will become proportionally darker depending on the amount of radiation which reached the film. Areas that are thinner or lower density will allow more radiation to pass through the part. The greater the radiation transmitted through the part, the darker the film will be.

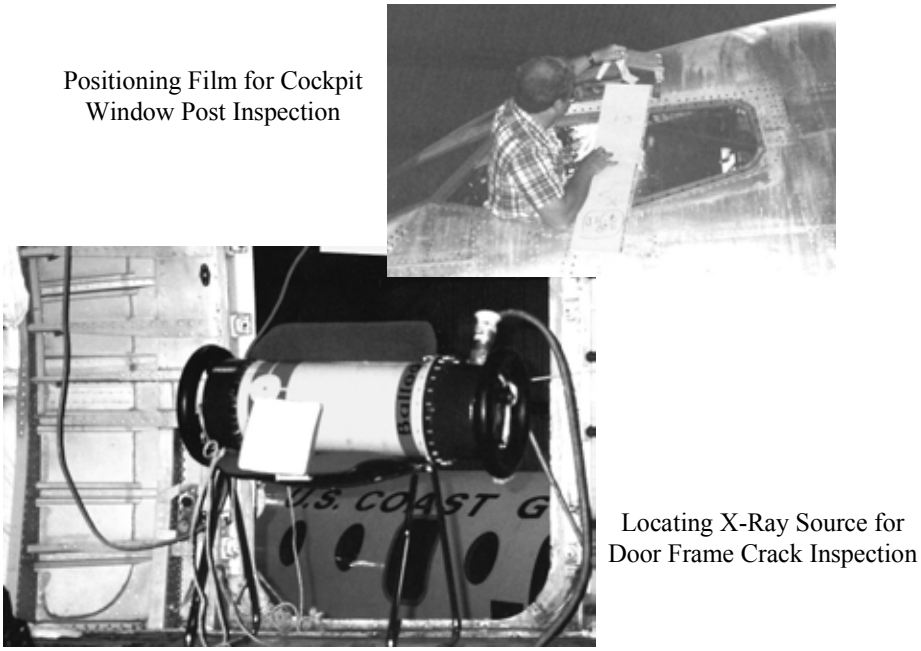

Figure 5-16: Aircraft Fuselage Inspection for Cracks Using X-Ray

Radiographic Sensitivity (Image Quality) - Radiographic sensitivity is a function of two factors. The ability to see a density variation in the film, which is "radiographic contrast" and the ability to detect the image outline which is "radiographic definition." Radiographic contrast is the difference in darkness of two areas of a radiograph. If contrast is high, small defects or density changes will be noticeable. Using lower power will result in higher subject contrast. However, lower power requires longer exposure times to obtain the adequate film density. If the energy level is too low, it will not penetrate the part at all.

Radiographic Definition - This term is defined as the ability to resolve the defect image on the radiograph. It is affected by the geometric factors of the exposure: size of the radiation source (focal spot size), distance from the target/source to the film, and distance from the part to the film. All of these factors contribute to a loss of geometric sharpness and as geometric sharpness decreases, the ability to see small defects decreases.

Image Quality Indicators - Image Quality Indicators (IQI) are used to measure the quality of the exposure and assure that proper sensitivity has been achieved. They measure the definition of the radiograph. By imaging IQI wires of various thicknesses and lengths it is possible to verify the resolution and sensitivity of a radiographic technique/set-up.

Resolution and Sensitivity - Image Production Through Composite Doublers - The discussion above provides some background on X-ray inspections and difficulties associated with its use. All of the issues described above exist regardless of whether or not the X-ray exposure takes place through a composite doubler. The primary question to be addressed in this study was: What is the overall effect of a composite doubler on X-ray inspections of structure beneath the doubler? To answer this question, a study was conducted to: 1) demonstrate that composite doublers do not interfere with the ability to perform X-ray inspections for cracks in steel, and 2) identify proper exposure time and power settings to optimize the sensitivity of the X-ray technique when inspecting through thick doublers.

Several fatigue crack specimens were inspected through a 72 ply composite doubler. To form a basis of comparison, X-rays were also taken without the doubler placed over the cracked specimens. The specimens placed beneath the doubler included 1st layer and 2nd layer fatigue crack panels with crack lengths ranging from 0.05" to 1.0". Radiography was found to be a very effective inspection method to interrogate the interior of the parent material covered by a composite doubler. This technique provides the advantage of a permanent film record. To increase the contrast on the film, the X-ray inspection was performed at low kilovoltage (80 kV). Test results showed the ability to detect cracks less than 1" in length. Fatigue cracks on the order of 0.38" in length were found under 0.41" thick (72 ply) Boron-Epoxy doublers. A sample X-ray result of a crack imaged through a 72 ply composite doubler is shown in Figure 5-17. [Note that significant resolution is lost in translating the X-ray film to a black and white graphic.]

Comparisons with X-rays taken without composite doublers revealed that while the doubler may darken the X-ray image slightly it does not impede the X-ray inspection. Power and exposure times were adjusted in order to restore the desired contract and maintain the specified film density of between 2 and 3. The initial set-up (80 kV, 12 mA, 6 inch source-to-film-distance and 30 second exposure time) on medium speed film produced a film density of 0.98. Increasing the exposure time to 90 seconds produced a film density of 2.64. Image Quality Indicators (IQI), inserted into the field of view, verified the resolution and sensitivity of the radiographic technique. IQI lines with widths of 0.010" and dots with diameters of 0.10" were clearly imaged on the X-ray film. These results showed that X-ray inspections are as effective as before a doubler is installed.

X-ray Results Summary - The X-ray tests performed in this study determined that there are no additional impediments brought on by the presence of composite doublers. X-ray inspections were able to achieve high levels of resolution when inspecting through thick composite doublers and the films were very comparable with films acquired on similar structures without doublers. All difficulties associated with X-ray inspections - shadowing from substructure elements, accessibility, and safety issues - are the same as in structures without composite doublers.

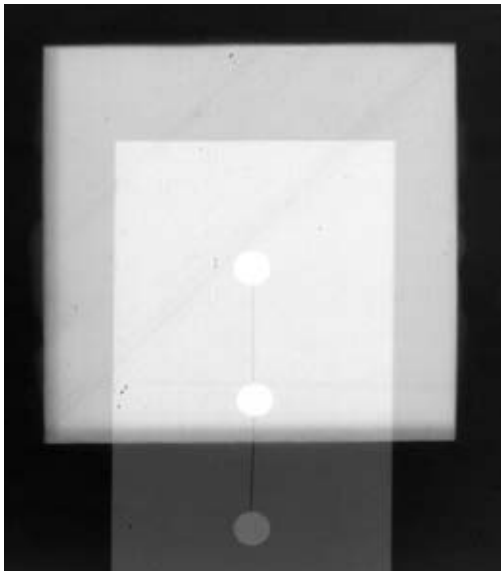

Figure 5-17: Sample X-Ray Image of a Cracked Structure Beneath a 72 Ply Composite Doubler

5.4 Nondestructive Inspection Methods for Patch and Bond Integrity

5.4.1 Pulse-Echo Ultrasonic Inspection

Ultrasonic (UT) inspection is a nondestructive method in which beams of high frequency sound waves are introduced into materials for the detection of surface and subsurface flaws in the material. The sound waves, normally at frequencies between 0.1 and 25 MHz, travel through the material with some attendant loss of energy (attenuation) and are reflected at interfaces. The reflected beam is displayed and then analyzed to define the presence and location of flaws. The degree of reflection depends largely on the physical state of the materials forming the interface. Cracks, delaminations, shrinkage cavities, pores, disbonds, and other discontinuities that produce reflective interfaces can be detected. Complete reflection, partial reflection, scattering, or other detectable effect on the ultrasonic waves can be used as the basis of flaw detection. In addition to wave reflection, other variations in the wave which can be monitored include: time of transit through the test piece, attenuation, and features of the spectral response [5.2 - 5.4].

The principal advantages of UT inspection as compared to other NDI techniques are: 1) superior penetrating power for detection of deep flaws, 2) high sensitivity permitting the detection of extremely small flaws, 3) accuracy in determining size and position of flaws, 4) only one surface needs to be accessible, and 5) portability.

In UT pulse-echo inspections, short bursts of ultrasonic energy are interjected into a test piece at regular intervals of time. In most pulse-echo systems, a single transducer acts alternately as the sending and receiving transducer. The mechanical vibration (ultrasound) is introduced into a test piece through a couplant and travels by wave motion through the test piece at the velocity of

sound, which depends on the material. If the pulses encounter a reflecting surface, some or all of the energy is reflected and monitored by the transducer. The reflected beam, or echo, can be created by any normal (e.g. in multi-layered structures) or abnormal (flaw) interface. Figure 5-18 is a schematic of the pulse-echo technique and the interaction of UT waves with various interfaces within a structure. Sometimes it is advantageous to use separate sending and receiving transducers for pulse-echo inspection. The term pitch-catch is often used in connection with separate sending and receiving transducers.

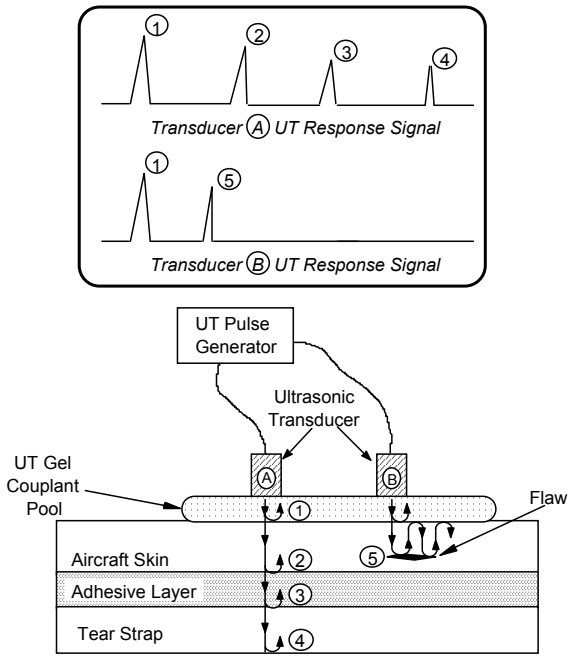

Figure 5-18: Schematic of Pulse-Echo Ultrasonic Inspection and Reflection of UT Waves at Assorted Interfaces

A-Scan Mode - In conventional Pulse-Echo Ultrasonics (PE UT), pulses of high frequency sound waves are introduced into a structure being inspected. A-Scan signals represent the response of the stress waves, in amplitude and time, as they travel through the material. As the waves interact with defects or flaw interfaces within the solid and portions of the pulse's energy are reflected back to the transducer, the flaws are detected, amplified and displayed on a CRT screen. The interaction of the ultrasonic waves with defects and the resulting time vs. amplitude signal produced on the CRT depends on the wave mode, its frequency and the material properties of the structure. Flaw size can be estimated by comparing the amplitude of a discontinuity signal with that of a signal from a discontinuity of known size and shape. Flaw location (depth) is determined from the position of the flaw echo along a calibrated time base. The mechanical vibration (ultrasound) is introduced into the specimen through a couplant and travels by wave motion through the specimen at the velocity of sound. If the pulses encounter a reflecting surface, some or all of the energy is reflected and monitored by the transducer. The reflected beam, or echo, can be created by any normal or abnormal (flaw) interface. Complete reflection,

partial reflection, scattering, or other detectable effects on the ultrasonic waves can be used as the basis of flaw detection.

Figure 5-19 and 5-20 show a Quantum ultrasonic device being used to perform a pitch-catch UT inspection (pulse-echo mode) of a composite doubler bonded to a carbon steel structure. In most pulse-echo systems, a single transducer acts alternately as the sending and receiving transducer. In the pitch-catch inspection mode deployed for this inspection one transducer transmits the UT wave and a second, remotely positioned transducer receives the signal after it travels through the materials being inspected. Figure 5-21 contains a schematic showing the pitch-catch inspection method and the UT wave travel within the structure during this inspection. During testing, the transmitting transducer was placed on top of the composite doubler and the receiving transducer was placed on top of the parent steel material. If the adhesive bond between the two articles is intact, the ultrasonic signal will pass unobstructed to the receiving transducer.

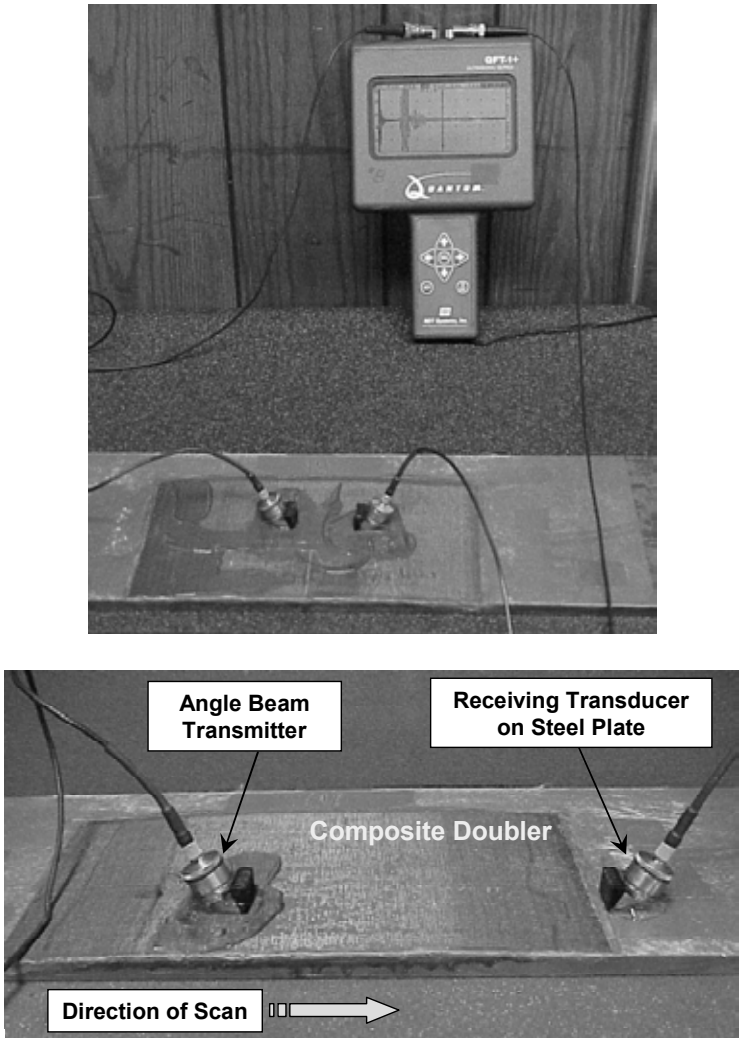

Figure 5-19: Pulse-Echo Ultrasonic Inspection of a Steel Structure with a Composite Doubler Installed

Figure 5-20: Inspector Deploying Pulse-Echo Inspection on Composite Doubler Repair

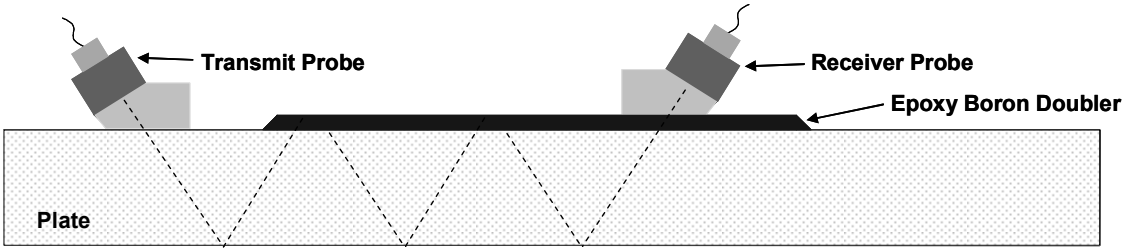

Figure 5-21: Schematic of Ultrasonic Wave Travel in a Pulse Echo, Pitch-Catch Inspection of a Composite Repair Installation

Figure 5-22 contains a series of A-scan signals produced by the pulse-echo inspection of a doubler specimen that contained intentional, engineered flaws at discrete locations. Changes in the A-Scan signal (i.e. lack of reflected signal from steel back wall), caused by the presence of the disbond or interply delamination, are clearly visible. Key portions of the signal in Figure 5-22 are identified to highlight how the A-Scan can be used to detect disbonds and delaminations. The primary items of note are: 1) the unique signature of the amplitude vs. time waveform which allows the user to ascertain the transmission of the ultrasonic pulse through various layers of the test article and which indicate a good bond, and 2) the absence of signature waveforms indicating a disbond. The thickness of the composite doubler does not significantly affect the transmission of the ultrasonic signal so similar flaw detection signals can be produced regardless of the doubler thickness. Another important consideration is that this technique can be deployed quickly. A one square foot region can be inspection in approximately 15 minutes.

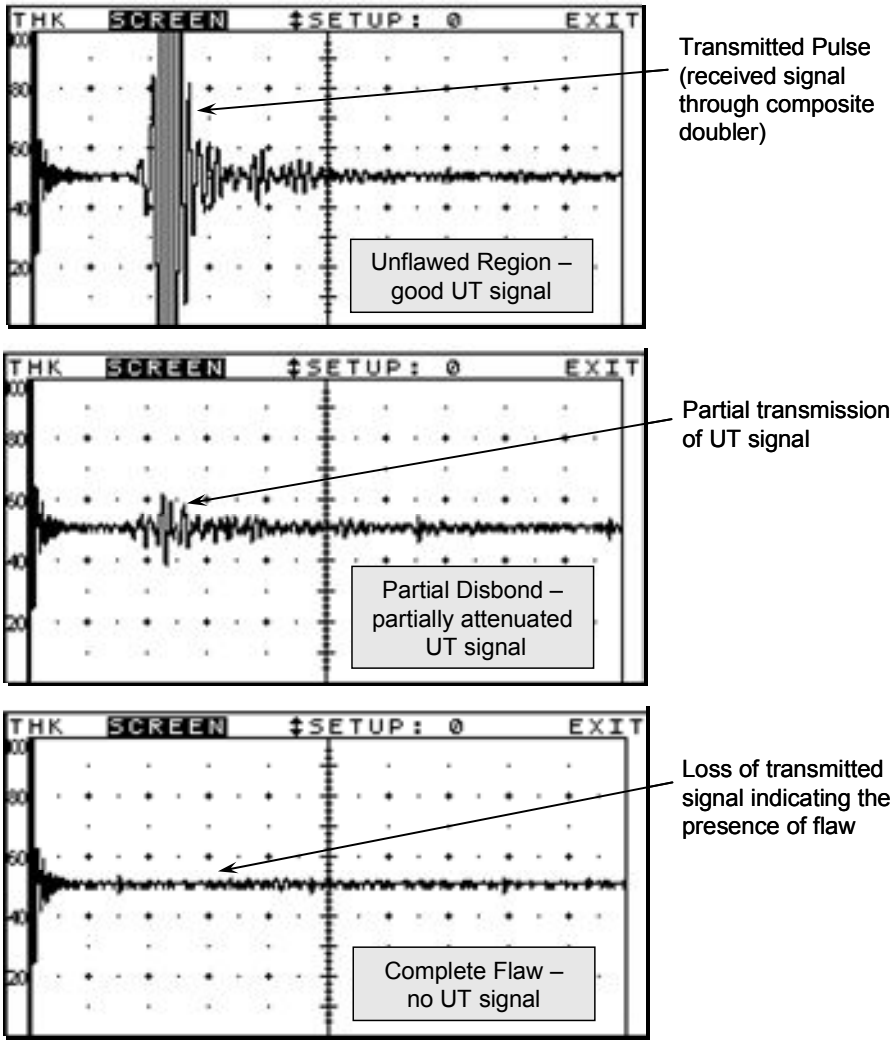

Figure 5-22: A-Scan Waveforms from Bonded and Disbonded Portions of a Composite Doubler Repair

Validation of Pulse-Echo NDI Technique for Disbond and Delamination Detection: Probability of Detection Study - In order to make a valid measurement of the flaw detection capabilities of the pulse-echo ultrasonic inspection method, a Probability of Detection (PoD) study was performed. Flaw detection performance was measured through blind experiments where inspectors had no knowledge of the specimen flaw profiles. A statistically relevant specimen set was used to provide: 1) opportunities for flaw calls over the full range of applicable flaw sizes and locations, and 2) sufficient unflawed sites to assess the Probability of False Alarm (PoFA). Flaw sizes in the test specimens ranged from 0.75" diameter to 0.375" diameter. The results are as follows: 98% of the flaws at or above 0.5" diameter were found. Seventy percent of the flaws less than 0.5" diameter were also found. The NDI techniques worked well with flaw detection including disbond and delamination flaws as small as 1/8" diameter. Damage tolerance thresholds will conservatively require the detection 1" diameter disbond and delamination flaws around the perimeter of the doublers. The inspection intervals for this program can be set up to

allow for at least two inspections and two opportunities to find a flaw before it reaches the maximum allowable size. The outcome of this scenario can be simulated by combining the results from two different inspectors. Such a combination produced the following results: 100% detection of all flaws, even those smaller than 0.25" in diameter, and zero false calls. Overall, the test series described above clearly demonstrated that disbond and delamination flaws on the order of 0.5" to 1.0" in diameter can be reliably detected through thick composite doublers.

C-Scan Mode: Use of Scanning Technology - Disbond and delamination detection can be also be achieved by taking the A-Scan signals and transforming them into a single C-Scan image of the part being inspected. C-Scan technology uses information from single point A-Scan waveforms to produce an area mapping of the inspection surface. These 2-D images are produced by digitizing point-by-point signal variations of an interrogating sensor while it is scanned over a surface. C-Scan area views provide the inspector with easier-to-use and more reliable data with which to recognize flaw patterns. This format provides a quantitative display of signal amplitudes or time-of-flight data obtained over an area. The X-Y position of flaws can be mapped and time-of-flight data can be converted and displayed by image processing-equipment to provide an indication of flaw depth. A variety of PC-based manual and automated scanning devices can provide position information with digitized ultrasonic signals. Specific emphasis can be placed on portions of the UT signal - and highlighted in the color-mapped C-Scan - based on user specified amplitude gates, time-of-flight values and signal waveforms. When addressing scanner system capabilities and limitations, key performance factors include: cost (approximately 10 times the cost of a hand-held UT device), design, portability, deployment, articulation and access to enclosed areas, speed of coverage, accuracy, usability (human factors), and computer hardware/software.

Figure 5-23 shows a C-scan image (based on amplitude) of a thick composite doubler with engineered flaws. The test specimen schematic is also shown to provide doubler lay-up information and the embedded flaws profile. A three-dimensional contour plot is also shown to demonstrate another means of displaying the data and interpreting the results. Disbond and delamination flaws are revealed by continuous and distinct signal loss areas which, depending on the color palette chosen, are either relatively bright or dark compared to the surrounding colors.

The post-fatigue composite repair specimens were inspected using the pulse-echo, pitch-catch method described above. The fatigue-induced fracture of the adhesive was identified by noting the onset of UT signal drop-out. Figure 5-24 shows the adhesive fracture region that was traced out by the hand-deployed inspection alongside a C-scan image produced by an automated scanner device. Note the similarity in the size and shape of the flaw regions.

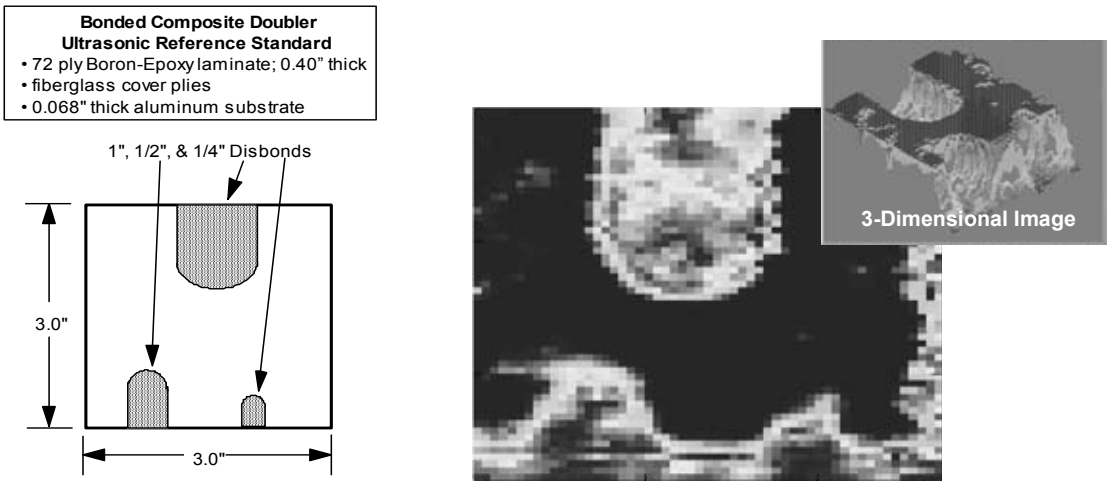

Figure 5-23: C-Scan Image Produced by Selective Gating on the Amplitude of All Signals Received by the Transducer

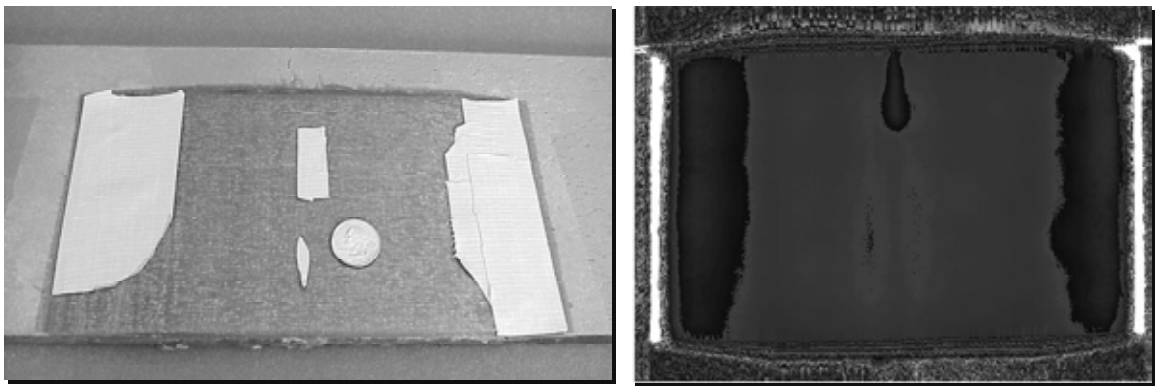

Figure 5-24: Comparison of Hand-Deployed Pitch-Catch UT Inspection with Data Produced by an Automated Scanning Device

5.4.2 Thermographic Inspection

Thermography is a nondestructive inspection method that uses thermal gradients to analyze physical characteristics of a structure, such as internal defects. This is done by converting a thermal gradient into a visible image using a thermally sensitive detector such as an infrared camera or thermally sensitive film materials. The temperature distribution on a structure can be measured optically by the radiation that it produces at infrared wavelengths. Many defects affect the thermal properties of materials. Examples are corrosion, disbonds, cracks, impact damage, panel thinning, and fluid ingress into composite or honeycomb materials. By the judicious application of external heat sources, these defects can be detected by an appropriate infrared survey. In this composite doubler study, a turn-key thermography inspection system, the Thermal Wave Imager (TWI), was used to assess the merits of thermography to detect disbonds and delaminations in composite doublers.

Thermal wave imaging is accomplished using high-power flash lamps, an infrared (IR) video camera, and image processing hardware and software, all of which are controlled by a personal computer. The flashlamps put out a short, high-power pulse of light, which raises the surface temperature of the structure approximately ten degrees when it is absorbed by the surface. This temperature pulse propagates into the material as a thermal wave and gets reflected by any defects which may be present in the material. The resulting temperature distribution is then recorded by the IR camera and displayed on the computer monitor. In practice, the computer actually obtains several images at progressively later times after each flash. This method is particularly useful for imaging and determining the depths of disbonds and delaminations in Boron-Epoxy repair doublers. A photograph of the Thermal Wave Imaging System being applied to an aircraft inspection is shown in Figure 5-25.

Results from Composite Doubler Inspections - Following are results obtained from Thermal Wave Imaging inspections on composite doubler installations which contain engineered flaws. Figure 5-26 shows a schematic of a composite doubler installed on a metal fatigue coupon. The schematic shows the disbond and crack flaws that were placed in the parent plate and composite doubler installation. The series of images produced at different times during the TWI inspection of this test specimen are shown in Figure 5-27.

The early time images following the flash clearly resolve the ply drop-off at the edges of composite patch. Beginning at around 0.68 sec, intentionally placed disbonds between the patch and the metal at the left and right edges (where the patch is thinnest) begin to appear. As time progresses, these disbonds begin to show in thicker and thicker layers of the patch. Between 4 and 8 seconds it is possible to see the circular disbond which was implanted over the crack tip and a "tail" extending downward along the induced fatigue crack. The circular disbond is located 13 plies deep in the doubler installation. The disbond tail is also located between the 13 ply doubler and the skin and is associated with a cohesive fracture of the adhesive layer immediately adjacent to the crack growth.

TWI was applied to another Boron-Epoxy doubler which was installed on a DC-9 fuselage section in the Sandia Labs' Airworthiness Assurance hangar. Figure 5-28 shows a schematic of the 10 ply doubler installation which identifies the size, shape, and location of the embedded flaws. The resultant sequence of images produced by a TWI inspection is shown in Figure 5-29.

(a) Close-Up View of TWI Equipment

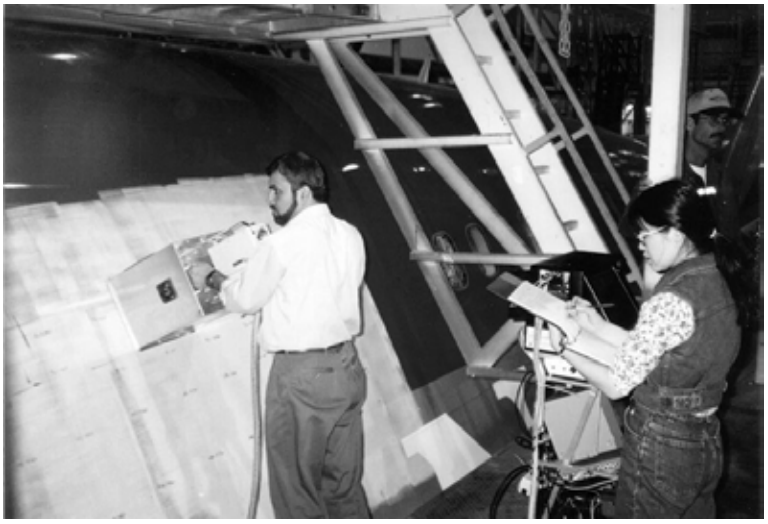

(b) Application of Thermography on 747 Aircraft

Figure 5-25: Thermal Wave Imaging System Inspecting an Aircraft

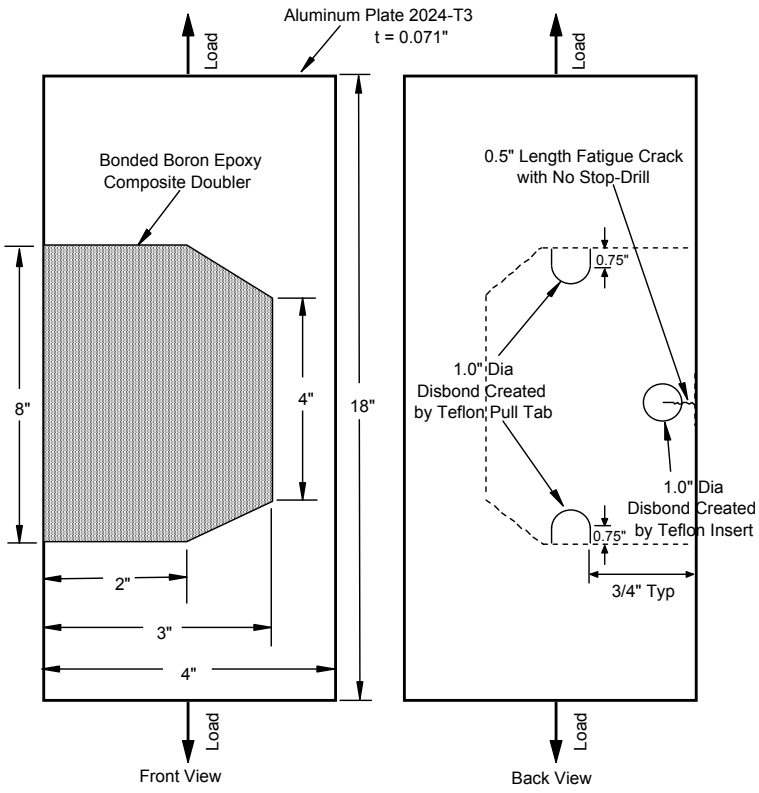

Figure 5-26: Composite Doubler Damage Tolerance Test Coupon with Engineered Flaws

The features seen at early times are defects closest to the outside surface of the patch (note appearance of flaws #1 and #2 in the first few frames). The disbonds, located at the base of the doubler, and the deeper delaminations appear in the later frames corresponding to their delayed effect on the thermal field. All six embedded flaws were identified in the TWI images and flaws smaller than 0.5" in diameter could be detected. Another item of note is that the flaws around the perimeter of the doubler, at its thinnest region, are clearly imaged and do not induce the imaging difficulties.

The advantages of the thermography inspection method include: 1) thermography can be performed without physical contact with the surface, 2) single images can include relatively large areas (1-2 ft^2) allowing for rapid inspections of large surface areas, and 3) two-dimensional image of the inspected surface helps the operator visualize the location and extent of any defect. The primary disadvantages of thermography are: 1) it is often necessary to apply a high-emissivity coating during inspections to obtain an acceptable image; steps have been taken to minimize the labor time associated with this task, 2) damage to layers deep within a structure is more difficult to detect than damage in surface layers because the larger mass of material tends to dissipate the applied heat energy. Penetration inspection experiments have shown that thermography can inspect doublers up to 40 or 50 plies (0.25" to 0.30") thick.

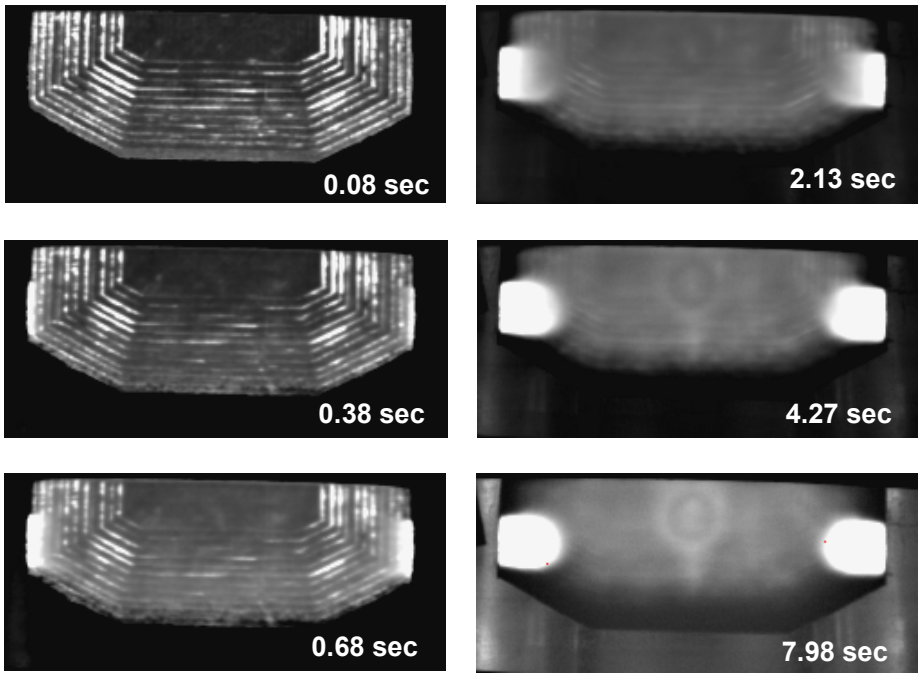

Figure 5-27: Sequence of Thermal Wave Images of Composite Doubler Specimen

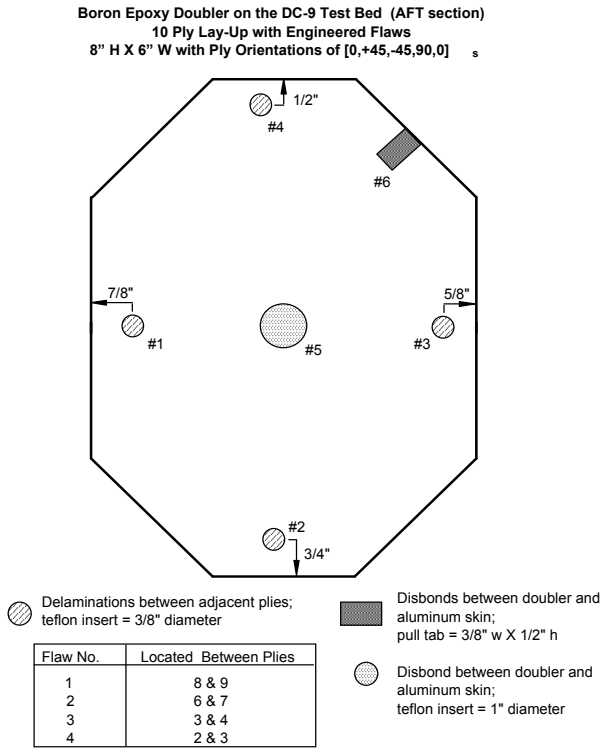

Flaw No.	Located Between Plies
1	8 & 9
2	6 & 7
3	3 & 4
4	2 & 3

Figure 5-28: Composite Doubler Installation on DC-9 Testbed

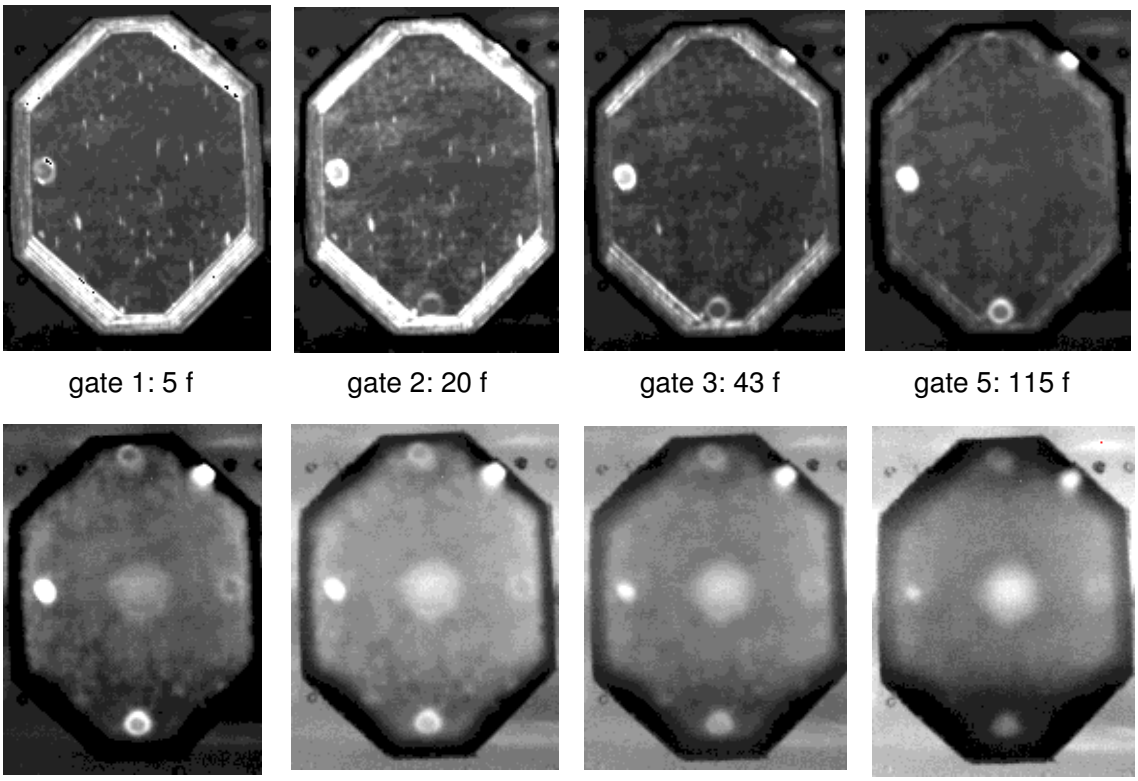

Figure 5-29: Sequence of Thermal Wave Images from DC-9 Composite Doubler Inspection

References

5.1 Metals Handbook Ninth Edition "Volume 17 Nondestructive Evaluation and Quality Control", ASM International, 1989, pp 241 - 246.

5.2 Ansley, G., et. al., "Current Nondestructive Inspection Methods for Aging Aircraft," U.S. Dept. of Transportation, FAA Report No. DOT/FAA/CT-91/5, June 1992.

5.3 Roach, D., Moore, D., and Walkington, P., "Nondestructive Inspection of Bonded Composite Doublers for Aircraft", SPIE Int'l Conf. on NDI of Aging Aircraft, December 1996.

5.4 Roach, D. and Walkington, P., "Development and Validation of Nondestructive Inspection Techniques for Composite Doubler Repairs on Commercial Aircraft", Sandia Report SAND98-1014, May 1998.

6.0 NUMERICAL MODELING AND DESIGN ANALYSIS FOR COMPOSITE DOUBLER REPAIRS

Dave Reedy

Useful methods for analyzing and designing a composite material patch to repair a cracked aluminum aircraft panel have been developed during the past twenty years [6.1, 6.2]. Unfortunately, these methods are not directly applicable to the type of repair considered in this study. Here the parent material is relatively thick and stiff (e.g., 3/8 to 2-inch thick steel) and the patch-to-parent material stiffness ratio is only ~0.3 instead of a value of one or more for a typical aluminum aircraft structure repair. Furthermore, this is a hybrid repair where the crack in the parent material is fill-weld repaired prior to application of the composite patch.

The goal of the present work is to develop a set of simple approximate relations that can be used to design a composite patch for a thick steel plate that contains a crack (with or without an accompanying fill-weld repair). These relations must be simple enough that they can be readily used in a spreadsheet based analysis. This was done by first developing and validating a 2-D finite element analysis of a thick steel plate with a bonded composite material patch that 1) accurately models stress transfer within a patched plate, and 2) predicts material failure including adhesive yielding, recracking of the repaired fill-weld crack, and debonding of the composite patch from the parent material. This finite element analysis capability is then used to guide and validate the approximate design analysis.

6.1 Finite Element Model for Mechanical Loading

6.1.1 Two-Dimension Geometric Model

The geometry of the plane stress model of a tapered boron/epoxy patch bonded to a steel plate is defined by six parameters: h_p h_r, h_t, s_1, s_2, and s_3 (Fig. 6-1). Both the steel plate and the boron/epoxy patch are modeled as isotropic, linear elastic materials (boron/epoxy is actually orthotropic, but test calculations suggest that material's orthotropy does not have a large effect on calculated load transfer). The stiffness of a boron/epoxy patch depends on the particular laminate lay-up that is used (i.e., per cent of plies in 0^o, 90^o, and +/-45^o directions). To provide representative finite element results that can be compared to existing experimental data, this study uses patch properties that have been reported in a previous study: Young's modulus E = 25.2 msi normal to the fill-weld repair, Poisson's ratio ν = 0.32, and tensile strength = 125 ksi (which corresponds to a fiber strain of 0.005) [6.3]. The steel plate is assumed to have properties of a common structural steel: E = 29 msi, ν = 0.30, yield strength σ_y = 50 ksi, and an allowable fatigue stress range of 16 ksi [6.4].

The boron/epoxy patch is connected to the steel plate using zero-thickness cohesive zone elements (CZEs) that have properties that are representative of the epoxy bond. For two-sided repairs, the bottom edge is a symmetry plane and h_p is half the steel thickness. The right hand side of the steel plate is displaced in x-direction with no constraint against out-of-plane bending.

Note that a large deformation analysis is performed in order to include nonlinear bending effects in a one-sided repair.

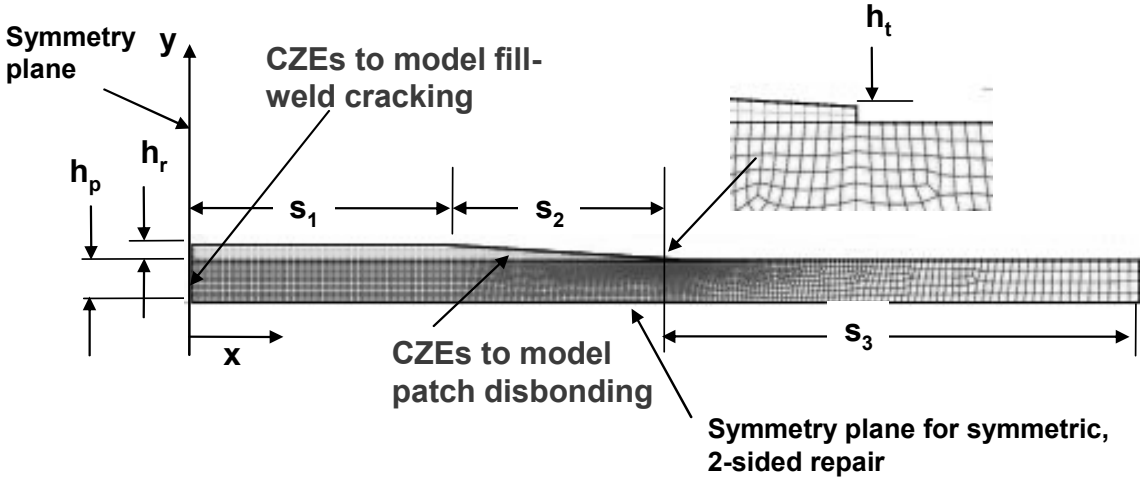

Figure 6-1: Finite Element Model and Key Parameters

6.1.2 Method for Modeling Disbonding in Adhesive Joint

The possibility that the patch debonds from the steel plate was included in the finite element analysis by using a cohesive zone modeling approach. The cohesive zone model is a computationally attractive method for modeling debonding since in this approach debonding is a natural outcome of the solution, and moreover it leads to mesh-independent result since a length scale is embedded within the traction-separation relationship. In the broadest sense, this approach can be thought of as equivalent to using connecting springs between the bonded materials where the springs soften in such a way that the energy of separation is equal to the adhesive's fracture toughness.

The specific cohesive zone model used in this study is similar to that introduced by Tvergaard and Hutchinson [6.5]. Debonding is based on a specified traction-effective separation relationship (Fig. 6-2), where the effective separation λ is

$$\lambda = \sqrt{\left(\frac{\delta_n}{\delta_n^c}\right)^2 + \left(\frac{\delta_t}{\delta_t^c}\right)^2} \tag{6-1}$$

where δ_n and δ_t are the normal and tangential displacement jump across the bond while δ_n^c and δ_t^c are the respective critical values. The normal and tangential interfacial tractions (T_n and T_t, respectively) are defined via the potential

$$\phi(\delta_n, \delta_t) = \delta_n^c \int_0^\lambda \sigma(\lambda')d\lambda' \tag{6-2}$$

with $$T_n = \frac{\partial \phi}{\partial \delta_n} = \frac{\sigma(\lambda)}{\lambda}\frac{\delta_n}{\delta_n^e} \quad \text{and} \quad T_t = \frac{\partial \phi}{\partial \delta_t} = \frac{\sigma(\lambda)}{\lambda}\frac{\delta_n^e}{\delta_t^e}\frac{\delta_t}{\delta_t^e} \tag{6-3}$$

The cohesive zone model has 5 parameters: $\hat{\sigma}$, λ_1, λ_2, δ_n^e, δ_t^e (see Fig. 6-2 for the definition of λ_1 and λ_2). The values of these parameters were chosen so that 1) the cohesive zone element's extensional and shear stiffness match that of the adhesive layer, 2) the separation in shear initiates at the adhesive's shear yield strength, and 3) the separation energy (area under the traction-separation curve) equals the adhesive's fracture toughness.

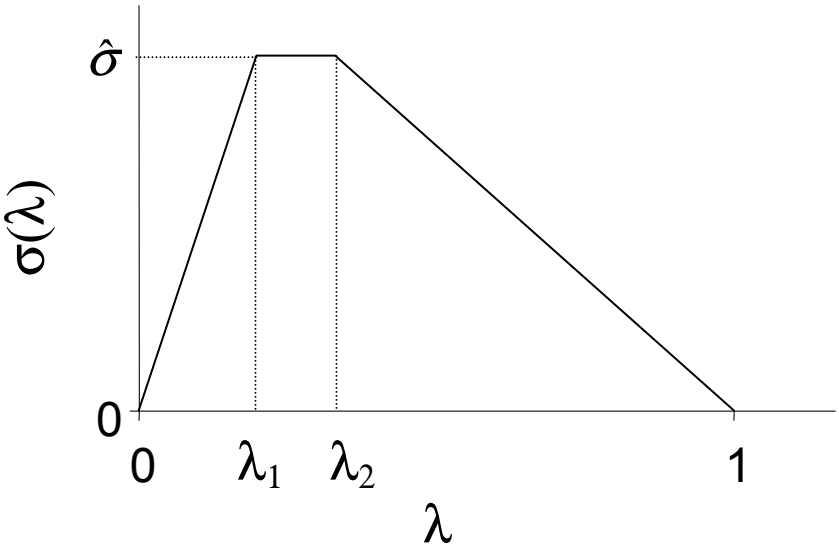

Figure 6-2: Effective Traction-Separation Relationship

The cohesive zone model parameters were determined using published property data for a structural adhesive that has been used to bond composite patches to a steel plate (3M's AF163-2 structural adhesive film) [6.3, 6.6]. The adhesive properties used are adhesive Young's modulus E = 160 ksi, adhesive shear modulus G = 60 ksi, bond thickness h_a = 0.006 in., adhesive shear yield strength τ_y = 5.3 ksi, and adhesive fracture toughness G_c = 8 lb/in. Based upon these values, the derived cohesive zone model parameters are:

$$\hat{\sigma} = 8690 \text{ psi}, \quad \delta_n^e = 0.00161 \text{ in.}, \quad \delta_t^e = 0.00264 \text{ in.}, \quad \lambda_1 = 0.200, \text{ and } \quad \lambda_2 = 0.344 \tag{6-4}$$

6.1.3 Validation of Finite Element Model

In a patched plate, a portion of the load carried by the steel is transferred to the patch, with the maximum load transferred at the center of the patch (x=0 in Fig. 6-1). The patch taper will determine how quickly load is transferred. To be useful, the finite element analysis must be able to accurately determine load transfer as a function of position along the patch. This capability was verified by comparing existing experimental data with calculated finite element results. The

particular test analyzed (SYN-FAT-7) is described in detail in [6.3]. This is a one-sided repair with an axial cross-section like that shown in Fig. 6-1 where h_p = 0.375 in., h_r = 0.140 in., h_t = 0.012 in., s_1 = 2.5 in., s_2 = 2.2 in., and s_3 = 4.5 in. Figure 6-3 compares the measured and calculated strains along the length of the patch (distance x measured from center of patch as shown in Fig. 6-1). These results are for a nominal applied stress of 41 ksi in the steel plate (i.e., at the right hand side in Fig. 6-1). As shown in the plot, the analysis is in good agreement with the test data. A large deflection finite element analysis was performed so as to accurately capture the nonlinear bending effects induced by a one-sided repair. The analysis predicts no adhesive yielding or debonding for these load levels and neither where observed during the test.

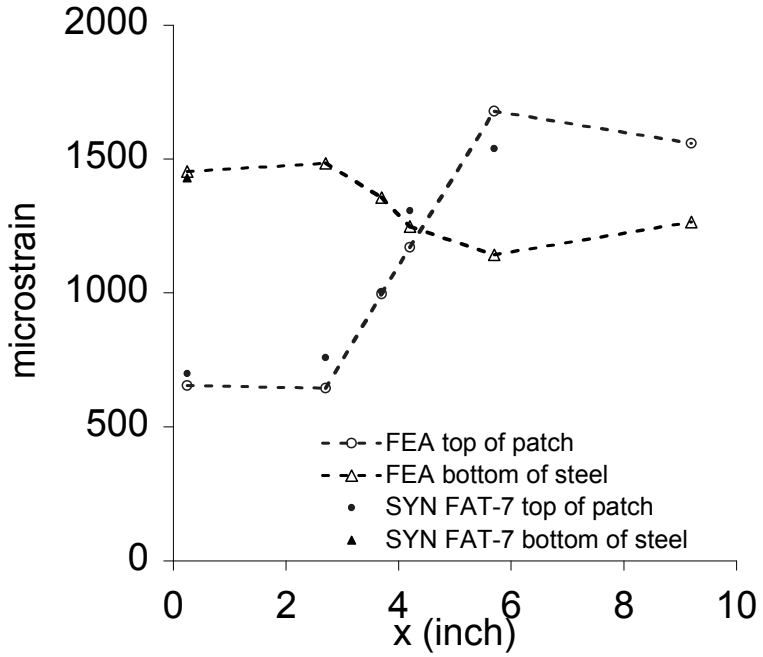

Figure 6-3: Comparison of Measured and Calculated Strains Along the Length of a Boron-Epoxy Patch that is Repairing a Steel Plate
(plate is subjected to a nominal applied stress of 41 ksi (specimen SYN-FAT-7, with axial distance x measured from center of patch, see Chapter 4 for test details)

6.2 Analysis for Patch Design

One of the key design parameters in a composite patch repair is the stiffness ratio. The stiffness ration S, is defined as

$$S = \frac{nE_r h_r}{E_p h_p} \tag{6-5}$$

where n = 1 or 2 for one or two-sided repairs, respectively (note, only considering symmetric, two-sided repairs), E is Young's modulus and h is the material's thickness and the subscripts p

and *r* denote plate and reinforcement patch, respectively. Increasing *S* reduces the stress in the steel by a factor of 1/(1+*S*) (assumes that patch is sufficiently long so as to transfer as much load as is physically possible). In typical aluminum aircraft structure repair, an *S* value of one or more is typical. In the current work, a hybrid repair, where the crack is fill-weld repaired and a composite patch is bonded over the repair with an *S* value of about 0.3, is proposed. It is simply impractical to apply a patch with an *S* value of one to a thick, steel structure. So a hybrid repair approach is proposed. The crack is fill-weld repaired and a patch with a relatively low *S* value of about 0.3 is applied to provide a modest reduction in the stress at the repaired crack (as discussed below, residual stress and bending induced by a one-sided repair are potential complications).

Five composite patch design requirements have been identified. First, a patch must be of adequate length to transfer as much load as is physically possible from the steel to the patch. Second, the adhesive should not yield, thus reducing the possibility of fatigue induced adhesive failure. Third, the patch should not disbond from the steel. Fourth, the patch should not fail. Fifth, and finally, there should be no recracking within the fill-weld crack repair. The analysis and criterion used to address each of these requirements is presented below, but first the approach used to account for the residual stress generated during cooling from an elevated temperature cure is discussed.

6.2.1 Residual Stress

The adhesive shear stress that is generated along the edge of a bonded patch during cool-down from the patch's elevated cure temperature will act opposite of that generated during tensile loading of the patched plate. In theory the elevated temperature induced residual stress will thus increases the level of tensile stress that can be applied before adhesive yielding and patch debonding occurs. Note, however, that at the bond-end the stress state is more severe and complicated than assumed in simple approximate analysis (such as the commonly used shear-lag theory) and the stress is in fact singular within the context of linear elasticity theory when there are geometrically sharp corners [6.7]. Furthermore, there is some experimental evidence that the residual stress generated during cool-down does not mitigate that generated by loading in the region of high stress concentration as found at the end of an adhesive bond. Nonlinear, viscoelastic stress relaxation can occur in regions of intense stress concentrations [6.8]. In contrast, the residual stress generated away from the end of a bond, e.g. at the center of the patch (x = 0, Fig. 6-1), should be predictable by a linear analysis when the stress is well below the epoxy's apparent yield strength. It is therefore a conservative assumption to ignore the mitigating effect of cure stress on bond yielding and patch debonding (which occur at the bond-end), but to include residual stress effects that increase the potentially detrimental tensile stress in the plate at the fill-weld repaired crack (which occurs away from the bond-end). This is the assumption used in this study.

6.2.2 Load Transfer and Patch Length

Shear-lag theory is commonly used to design adhesively bonded patches. A full derivation of classical shear-lag theory for a patch that is adhesively bonded to a plate can be found in [6.1]. Note that classical shear-lag theory does not include 1) patch taper, 2) bending deformation, 3) peel stress at the bond-end, and 4) residual stress. Shear-lag theory can be used to predict how

quickly load is transferred from the steel plate to the reinforcement patch. Shear-lag theory predicts that peak shear occurs at the end of the bond and decays to 5% of the peak value at a distance of $3/\beta$ where

$$\beta = \left(\frac{G_a}{h_a} \left(\frac{1}{E_p h_p} + \frac{1}{E_r h_r} \right) \right)^{1/2} \tag{6-6}$$

Here G is shear modulus, h is thickness, and E is Young's modulus, and the subscripts a, p and r denote adhesive, plate and reinforcement patch. A finite element model that uses cohesive zone elements to represent the adhesive bond (as describe above in Section 6.2) will generate load transfer results similar to those predicted by shear-lag theory. Figure 6-4 compares shear-lag results for adhesive shear stress τ as the bond end (normalized by the peak shear stress τ_{max} found at the bond-end) versus distance from the center of the patch (where distance x is normalized by the characteristic length β, as defined by eq. 6-6). Results are for a symmetric, double-sided repair with no taper so as to be consistent with classical shear-lag assumptions (h_p = 0.1875 in., $h_r = h_t$ = 0.07 in., $L_r = s_1 + s_2$ = 4.7 in., see Fig. 6-1 for the definition of the geometric parameters). The finite element and shear-lag theory results are in excellent agreement when there is no patch taper. Shear stress decays exponentially with distance from the bond-end.

In actual practice, patch edges are usually tapered with a typical taper angle of $<5^o$. This is done to reduce bond-end shear and peel stress. Illustrative results for a symmetric, double sided repair with s_1 = 2.5 in., s_2 = 2.2 in., h_p = 0.1875 in., h_r = 0.07 in. and with h_t = 0.07 in. (no taper) or with h_t = 0.006 in. (tapered) show that patch taper is effective in reducing bond-end stresses. A taper angle of 2.4 degrees significantly reduces peel stress (Fig. 6-5) and also reduces peak shear stress, although significant stress transfer occurs over a longer distance (Fig 6-6). In these plots, adhesive peel stress σ_n and the adhesive shear stress τ are normalized by the nominal applied stress σ^∞ and the distance x from the center of the patch is normalized by the patch length L_r. Stress is transferred from the steel plate to the boron/epoxy patch via shear stress in the adhesive bond. The portion of the bond with significantly elevated shear stress coincides with the distance over which stress transfer occurs. In the case analyzed, stress transfer occurs mostly in the tapered region. In the present study a common estimate for the length of a patch ($2L_r$) needed to ensure that the maximum possible load transfer into the patch will occur is used:

$$2L_r = 6/\beta + \textit{total length of the tapered regions}$$

where $3/\beta$ is the shear-lag estimate for load transfer into a patch with no taper (see section 6.2.2, and note that there are two bond-ends) and any load transfer in the tapered regions is neglected [6.9]. This is a conservative estimate since, as shown above, substantial load transfer can occur in a tapered region.

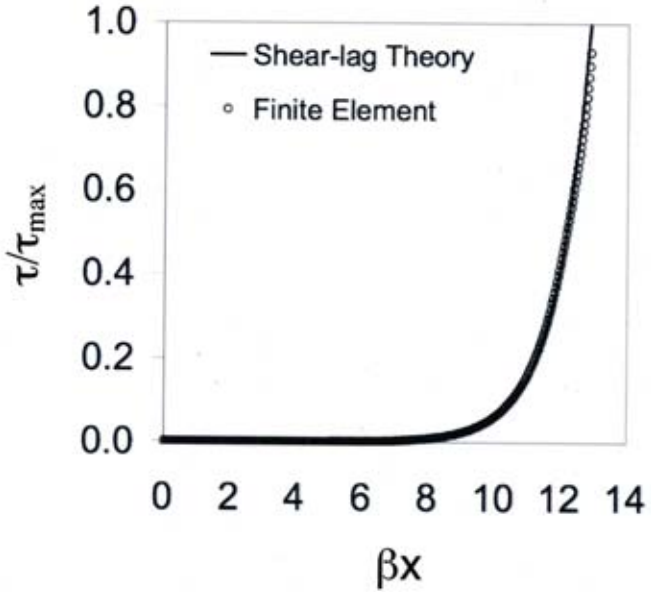

Figure 6-4: Comparison of Shear-Lag and Cohesive Zone Finite Element Predictions for Shear Stress

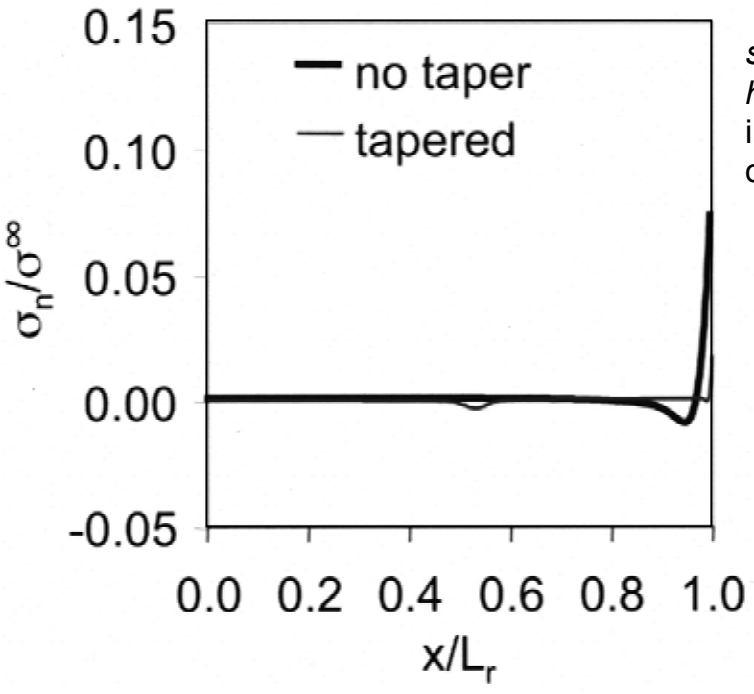

s1=2.5 in., *s2*=2.2 in., *hp*=0.1875 in., *hr*=0.07 in. *ht*=0.07 in. (no taper) or *ht*=0.006 in (tapered)).

Figure 6-5: Comparison of Finite Element Results for Peel Stress when the Patch is Either Tapered or Untapered

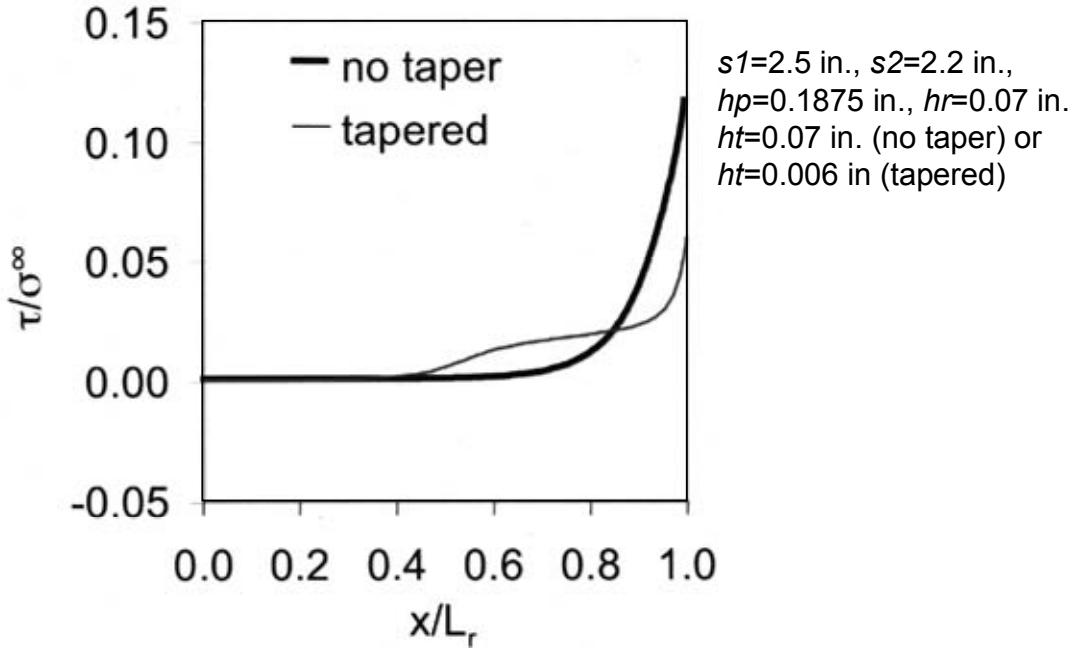

Figure 6-6: Comparison of Finite Element Results for Shear Stress when the Patch is Either Tapered or Untapered

6.2.3 Yielding of the Adhesive Bond

Shear-lag theory can also be used to estimate the applied tensile load at which the adhesive bond will yield in shear at the bond-end. Shear-lag theory predicts a peak shear stress τ_{max} at the bond end of

$$\tau_{\max} = \frac{-\sigma^{\infty} G_a}{\beta h_a E_p} \tag{6-7}$$

where σ^{∞} is the applied nominal tensile stress. Note that this shear-lag result assumes plane stress and is valid for the case of a long bond, i.e., $\beta L_r >> 1$, where $L_r = s_1 + s_2$. As illustrated in Fig. 6-6, shear-lag theory (no taper) provides an upper bound estimate for peak shear stress for the case of a tapered patch. A series of finite element analysis (FEA) calculations were performed for one-sided (one patch with a thickness of 0.14 in.) and two-sided (two patches, each with a thickness of 0.07 in.) repairs. Both tapered and non-tapered patches were considered. In addition, two geometrically similar models were analyzed where all the geometric parameters of one model (except bond thickness) were a factor of 5.33 larger than that of the other model (i.e., increase steel thickness from 0.375 in. to 2.0 in., etc.). The results of these analyses are presented in Table 6-1 where shear-lag and finite element predictions for the nominal applied stress σ^{∞} to initiate bond yielding are listed. As expected, the shear-lag and finite element results are in excellent agreement for two-sided repairs when the patch is not tapered and are also in good agreement for one-sided repairs when there is no patch taper. When the patch is tapered, shear-lag results are rather conservative, underestimating the nominal applied tensile stress to initiate adhesive

yielding by roughly 50% for the taper angle considered. This is expected since the reason for introducing a patch taper is to reduce bond-end stresses and shear-lag theory does not take into account the patch taper. Note that shear-lag theory says that when all geometric parameters (except bond thickness) are scaled by a factor of n, β^1 and τ_{max} both scale by a factor of $\sqrt{n}$. In the present work, the shear-lag estimate for adhesive bond yielding will be used for both tapered and untapered patches to ensure a conservative estimate for τ_{max} and the associated σ^{∞} to initiate bond yielding.

Type of Repair	Patch End	Steel Thickness (in.)	Shear-lag (ksi)	FEA (ksi)	Shear-lag /FEA
2-sided	no taper	0.375	42.1	41.7	1.01
2-sided	no taper	2.000	18.2	18.3	1.00
2-sided	tapered	0.375	42.1	86.4	0.49
2-sided	tapered	2.000	18.2	45.3	0.40
1-sided	no taper	0.375	29.8	32.6	0.91
1-sided	no taper	2.000	12.9	15.2	0.85
1-sided	tapered	0.375	29.8	50.2	0.59
1-sided	tapered	2.000	12.9	26.6	0.48

Table 6-1: Predicted Nominal Applied Stress σ^{∞} to Initiate Bond Yielding

6.2.4 Patch Disbonding

A linear elastic fracture mechanics (LEFM) analysis can be used to provide an estimate for the load that will initiate patch debonding. The model analyzed is essentially the same as that of a cracked-lap shear specimen (Fig. 6-7). Disbonding (crack growth) will initiate from an assumed edge crack when the energy release rate G exceeds the toughness of the adhesive, G_c (i.e., $G > G_c$). The energy release rate G for a cracked-lap shear specimen can be easily determined by a J-integral evaluation and for the case of no taper and a symmetric, two-sided repair [6.10].

$$G = \frac{\sigma^{\infty 2}(h_p/n)}{2E_p}\left(\frac{S}{1+S}\right) \tag{6-8}$$

where n = 1 or 2 for one or two-sided repairs, respectively and S is defined in eq. 6-5. This analytic result can be used to predict the nominal applied stress to initiate patch disbonding by

setting $G = G_c$ in eq. 6-8 and solving for σ^{∞}. Table 6-2 compares the J-integral analytic result to finite element results that use cohesive zone elements to model patch debonding (G_c = 8 lb/in). The analytic J-integral-based results are in excellent agreement with the finite element results for two-sided repairs when the patch is not tapered and are also in good agreement for one-sided repairs provided when there is no patch taper. When the patch is tapered, the analytic J-integral based results are rather conservative, underestimating the nominal applied tensile stress to initiate debonding by roughly 50% for the taper angle considered. Note that the J-integral estimate for debonding indicates than when all geometric parameters (except bond thickness) are scaled by a factor of n, the σ^{∞} to initiate patch debonding scales by a factor of $1/\sqrt{n}$. In the present work, the analytic J-integral estimate for debonding will be used for both tapered and untapered patches to ensure a conservative estimate for the σ^{∞} to initiate patch debonding.

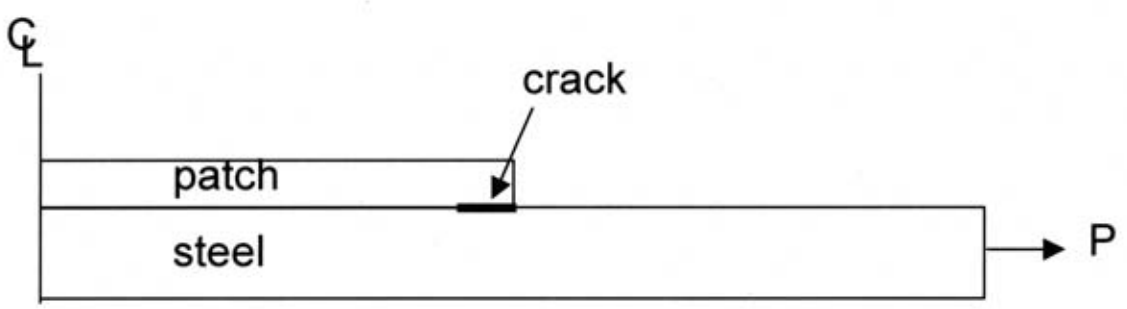

Figure 6-7: Model Used to Analyze Patch Disbonding

6.2.5 Patch Failure and Recracking of the Steel Fill-Weld Repair

Simple estimates for stress levels at the center of a repaired structure (*x=0* in Fig. 6-1) can be derived when the patch, either tapered or untapered, is sufficiently long to ensure maximum possible load transfer. The calculated stress in the boron/epoxy patch and in the steel (at the position of fill-weld repair) can be compared with material strength and fatigue limits to determine allowable load limits. The present work uses design allowables for the fill-weld repaired steel plate that are consistent with the American Welding Society Specifications for Welded Joints in Machinery and Equipment (D14.4) for Class I Joints in carbon and low-allow steels [6.4]. Specifically, the maximum allowable stress equals the ultimate tensile strength of base metal divided by four and the maximum allowable stress range (the algebraic difference between the maximum stress and the minimum stress) is 16 ksi for a fatigue loading of greater than 2×10^6 cycles. It is proposed that the allowable for the boron/epoxy patch be defined in terms of axial fiber strain in the laminate with a conservative criterion of 0.005 for both ultimate and fatigue loadings.

In the following sections, symmetric repairs (or one-sided repairs that are constrained against out-of-plane deformation) are discussed first. Next, unconstrained, one-sided repairs are discussed. Here the analysis is extended so as to incorporate bending induced by an applied load that is not aligned with the neutral axis of the patched plate. Finally, the effect of residual stress generated during cool-down from a high temperature cure is considered. Cool-down induced

residual stress must be included in the analysis since it can introduce potentially detrimental tensile stress acting across the fill-weld repaired crack in the steel plate.

Type of Repair	Patch End	Steel Thickness (in.)	From J-integral (ksi)	FEA (ksi)	J-integral /FEA
2-sided	no taper	0.375	100.5	100.8	1.00
2-sided	no taper	2.000	43.5	43.5	1.00
2-sided	tapered	0.375	100.5	166.8	0.60
2-sided	tapered	2.000	43.5	96.9	0.45
1-sided	no taper	0.375	71.1	74.2	0.96
1-sided	no taper	2.000	30.8	33.6	0.91
1-sided	tapered	0.375	71.1	96.0	0.74
1-sided	tapered	2.000	30.8	54.3	0.57

Table 6-2: Predicted Nominal Applied Stress σ^{∞} to Initiate Patch Disbonding

Symmetric repairs - Based simply on stress equilibrium and strain compatibility, the axial stress (parallel to the direction of loading and perpendicular to the repaired crack) at the center of a structure with a symmetric, two-sided repair is simply

$$\sigma_{po} = \frac{\sigma^{\infty}}{1+S} \quad \text{and} \quad \sigma_{ro} = \frac{E_r}{E_p}\frac{\sigma^{\infty}}{1+S} \tag{6-9}$$

where σ_{po} is the stress at the center of the plate, σ_{ro} is the stress at the center of the patch, and S is defined in eq. 6-5. Here it is assumed that the patch, either tapered or untapered, is sufficiently long as to ensure maximum possible load transfer from the plate to the patch. Note that these stress magnitudes depend only on steel and reinforcement thickness and stiffness ratios.

One-Sided Repairs - A bending moment is generated in a plate with a one-sided repair unless the plate is constrained against bending. Bending is induced by the vertical offset of the loading axis from the neutral axis of the patched plate. This induced bending stress must be added to the axial stress (eq. 6-9). In general, the magnitude of the induced moment can change with applied load since bending deformation will change the offset in the loading and neutral axes. Such

deformation can reduce the induced moment since the two axes will tend to align as load increases. In the present work, a linear analysis, which does not include large deformations, is used. This is considered appropriate because the linear analysis yields upper bound estimates for stress, and furthermore, only modest bending is anticipated in these lightly loaded, thick steel structures that are repaired with a relatively thin patch (S~0.3). For a linear analysis, the induced moment M_i is

$$\mathrm{M_i} = -\sigma^{\infty} \mathrm{h_p y^*} \quad \text{where} \quad y^* = \frac{S(h_p + h_r)}{2(1+S)} \tag{6-10}$$

where M_i is the induced moment and y^* is the distance that the neutral axis lays above the centerline of the plate (see Fig. 6-8 for the sign convention used to define bending and distance from the neutral axis). The bending stress in the plate σ_{pb} and in the patch σ_{rb} is given by

$$\sigma_{pb} = \frac{M_i y E_p}{E_p I_p + E_r I_r} \quad \text{and} \quad \sigma_{rb} = \frac{M_i y E_r}{E_p I_p + E_r I_r} \tag{6-11}$$

where y is distance from the neutral axis and I_p and I_r are the moments of inertia of cross-sectional areas of the plate and the reinforcement patch, respectively, about the neutral axis.

$$I_p = \frac{h_p^3}{12} + h_p y^{*2} \quad \text{and} \quad I_r = \frac{h_r^3}{12} + \frac{h_r (h_p + h_r - 2y^*)^2}{4} \tag{6-12}$$

Table 6-3 compares linear bending theory predictions (eq. 6-11) for maximum tensile stress in the steel (which occurs on the outer surface of the steel) with finite element results that include finite-deformation effects. These results are for a nominal applied tensile stress σ^{∞} of 10 ksi. As anticipated, finite deformation effects for one-sided repairs have only a modest effect. Table 6-3 also confirms that there is no change in the predicted stress when all geometric parameters (except bond thickness) are scaled by a factor of n. It is important to note that a one-sided repair can induce a higher maximum stress in the steel than would exist if there were no patch at all (the average stress in the steel is lower, but the bending-induced stress at the outer surface is higher). The analysis suggests that a one-sided repair may be counterproductive.

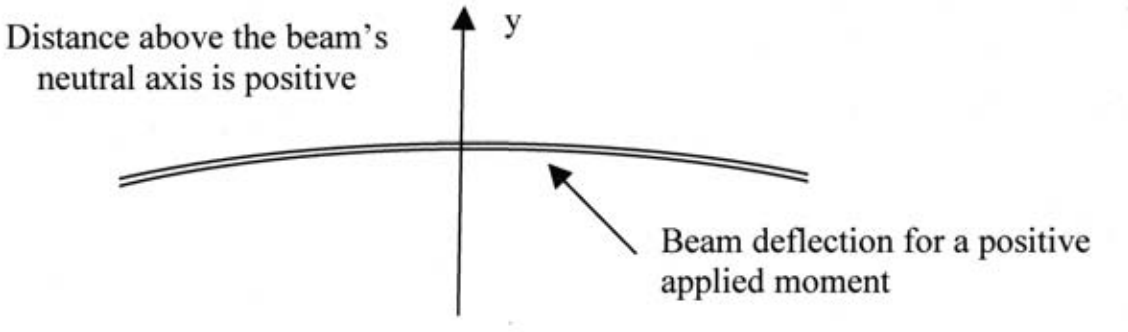

Figure 6-8: Sign Convention for Moment and Distance from the Neutral Axis Used in the Bending Analysis

Type of Repair	Patch End	Steel Thickness (in.)	Analytic Theory (ksi)	FEA (ksi)	Analytic Theory/FEA
2-sided	no taper	0.375	7.6	7.6	1.00
2-sided	no taper	2.000	7.6	7.6	1.00
2-sided	tapered	0.375	7.6	7.6	1.00
2-sided	tapered	2.000	7.6	7.6	1.00
1-sided	no taper	0.375	13.1	11.7	0.90
1-sided	no taper	2.000	13.1	11.7	0.89
1-sided	tapered	0.375	13.1	11.9	0.91
1-sided	tapered	2.000	13.1	11.8	0.90

Table 6-3: Maximum Steel Stress Under Repair When $\sigma^{\infty} = 10$ ksi

Inclusion of Residual Stress - Design calculations for stress in the steel plate should include the residual stress generated during cool-down from the patch/adhesive cure temperature. This is important because a tensile stress that acts across the fill-weld repaired crack is produced. When

there is a two-sided, symmetric repair (or a one-sided repair constrained against bending) the thermal stress in the plate, σ_{po}^{th} and in the reinforcement, σ_{ro}^{th} are

$$\sigma_{po}^{th} = -\sigma_{ro}^{th}\frac{h_r}{h_p} = \frac{-E_p(\alpha_p - \alpha_r)(T - T_c)S}{(1-\nu_r) + (1-\nu_p)S} \tag{6-13}$$

where T is temperature, T_c is the cure temperature, α_p is the coefficient of thermal expansion of the plate, α_r is the coefficient of thermal expansion of the reinforcement patch, ν_p is the Poisson's ratio of the plate, and ν_r is the Poisson's ratio of the reinforcement patch. This result is based simply on stress equilibrium, strain compatibility, and that the patch (either tapered or untapered) is sufficiently large to ensure maximum possible load transfer from the plate to the patch. It also neglects the possibility that the initial heating of the plate is localized to some relatively small region surrounding the patch. Such localized initial heating could generate compressive stress in the steel and thus reduce the tensile stress generated in the steel during cooling from the cure temperature. It seems reasonable to neglect the effect of initial, localized heating since it is difficult to accurately quantify this effect, and furthermore, an analysis that neglects this effect provides an upper bound estimate for the tensile stress that is generated in the steel by cooling from the cure temperature.

The analysis must be augmented for one-sided repairs since a thermal moment is induced in this case. The thermal moment M_{th} is

$$M_{th} = \sigma_p^{th} h_p (h_p + h_r)/2 \tag{6-14}$$

and the induced bending stress in the plate, σ_{pb}^{th}, and the reinforcement, σ_{rb}^{th}, are

$$\sigma_{pb}^{th} = \frac{M_{th} y E_p}{E_p I_p + E_r I_r} \quad \text{and} \quad \sigma_{rb}^{th} = \frac{M_{th} y E_r}{E_p I_p + E_r I_r} \tag{6-15}$$

The maximum stress at the center of the repaired plate is the sum of the in-plane and bending stresses generated by tensile and thermal loading (eqs 6-9, 6-11, 6-13, and 6-15).

$$\sigma_p^{\max} = \sigma_{po} + \sigma_{pb} + \sigma_{po}^{th} + \sigma_{pb}^{th} \tag{6-16}$$

$$\sigma_r^{\max} = \sigma_{ro}^{o} + \sigma_{rb}^{b} + \sigma_{ro}^{th} + \sigma_{rb}^{th} \tag{6-17}$$

The maximum tensile stress in the steel can occur at the interface when there is bending, so stress should be calculated on either side of the interface as well as on the exterior surfaces. Note that the thermal stress at the center of the repaired plated is biaxial, with $\sigma_{xx}^{th} = \sigma_{yy}^{th}$, while that for a unidirectional applied load is nearly uniaxial if the Poisson's ratio of the plate and reinforcement are similar.

Table 6-4 compares the analytic results for stress in the steel (eq. 6-16) with finite element results that include finite-deformation effects. Results for both a one-sided repair (one untapered

0.14 in. thick patch) and a two-sided repair (two untapered, 0.07 in. thick patches) on a 0.375 in. thick steel plate are presented in Table 6-4. Note that 3-D finite element calculations were performed since thermal stress is inherently biaxial. The 3-D mesh was generated by simply translating the 2-D mesh (Fig. 6-1) in the z-direction (see Fig. 6-9, s_1=2.5 in., s_2=2.2 in., s_3=4.5 in., while the half-width is 2 in.). The 3-D analysis used the same steel plate, boron/epoxy reinforcement, and cohesive zone adhesive model parameters as used in 2-D simulations, and a coefficient of thermal expansion of $6.7 \times 10^{6}/^{o}F$ for the steel and $3.0 \times 10^{-6}/^{o}F$ for the boron/epoxy laminate. Table 6-4 shows that the analytic and finite element results are in excellent agreement for two-sided (symmetric) repairs and only differ slightly for one-sided repairs.

Type of Repair	Temp Change ^{o}F	Applied tensile load (ksi)	Analytic Theory: Steel stress at surface (ksi)	Analytic Theory: Steel stress at interface (ksi)	FEA: Steel stress at surface (ksi)	FEA: Steel stress at interface (ksi)
2-sided	-200	0	7.7	7.7	7.6	7.6
2-sided	-200	10	15.2	15.2	15.2	15.2
1-sided	-200	0	-9.7	16.3	-9.9	16.5
1-sided	-200	10	3.4	21.1	4.9	20.4

Table 6-4: Maximum Steel Stress Under the Repair When Thermal Residual Stress is Included

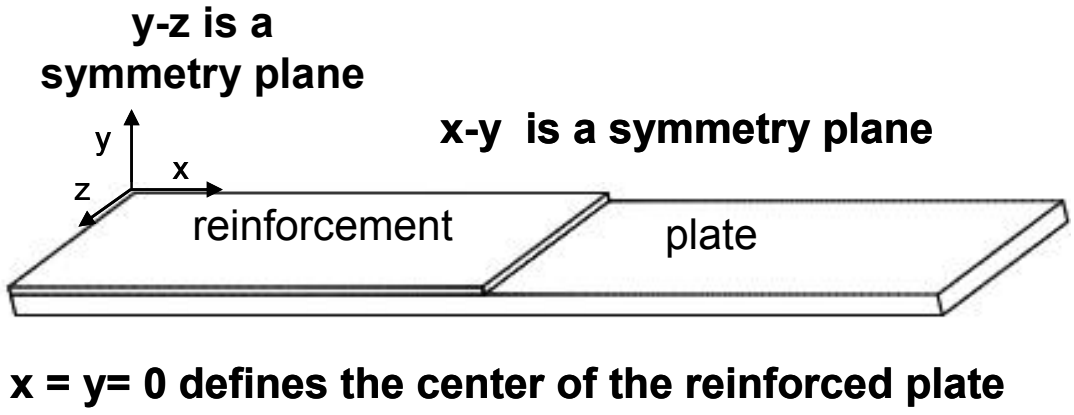

Figure 6-9: Patch Repair Geometry Used in 3D Finite Element Calculations

It is important to note that a 200^{o} F cool-down from the patch/adhesive elevated cure temperature can generate significant levels of tensile residual stress in the fill-weld repaired steel plate. For example in the case of a two-sided repair, the tensile stress generated in the steel plate by a 200^{o} F cool-down is comparable to that induced by a 10 ksi tensile loading. It might be possible to ameliorate this stress by using pre-cured boron/epoxy patches that are then bonded to the steel plate using an epoxy with a lower cure temperature.

6.3 Design Tool

An Excel-based design tool that incorporates the analytic results discussed in Section 6-2 has been developed. Specifically, the design tool includes: 1) patch sizing for maximum load transfer (section 6.2.2), 2) adhesive yielding (section 6.2.3), 3) patch disbonding (section 6.2.4), patch failure (section 6.2.5), and 5) recracking of the repaired fill-weld crack (section 6.2.5). Both one-sided and two-sided repairs are considered and residual stress is included when appropriate (section 6.2.1). The spreadsheet also includes laminate plate theory-based estimates of patch Young's modulus, Poisson's ratio, and coefficient of thermal expansion [6.11]. The user simply inputs the number of plies perpendicular to, parallel to, and at +/- 45^{o} to the fill-weld repaired crack. The laminate is assumed to be balanced (i.e., the number of plies at +45^{o} equals that at -45^{o}) and symmetric about the mid-plane. Such laminates avoid the complications of extension-bending coupling and in-plane extension-shear coupling.

References

6.1 Rose, L.R.F. and C.H. Wang, *Analytical Methods for Designing Composite Repairs*, in *Advances in the Bonded Composite Repair of Metallic Aircraft Structure*, A.A. Baker, L.R.F. Rose, and R. Jones, Editors. 2002, Elsevier: New York. p. 137-175.

6.2 Rose, L.R.F., *Theoretical analysis of crack patching*, in *Bonded Repair of Aircraft Structures*, A.A. Baker and R. Jones, Editors. 1988, Martinus Nijhoff Publishers: Boston. p. 77-106.

6.3 Roach, D.P. and K.A. Rackow, *Development of Bonded Composite Doublers for the Repair of Oil recovery Equipment*. 2005, Sandia National Laboratories.

6.4 *Specification for Welded Joints in Machinery and Equipment (AWS D14.4/D14.4M:2005)*. 2005, American Welding Society: Miami, FL.

6.5 Tvergaard, V. and J.W. Hutchinson, *The influence of plasticity on mixed mode interface toughness.* Journal of the Mechanics and Physics of Solids, 1993. **41**: p. 1119-1135.

6.6 3M, *Scotch-weld Structural Adhesive Film AF163-2 Data Sheet*. 2004.

6.7 Reedy, E.D., Jr., *Strength of Butt and Sharp-Cornered Joints*, in *The Mechanics of Adhesion*, D.A. Dillard and A.V. Pocius, Editors. 2002, Elsevier: New York, NY. p. 145-192.

6.8 Reedy, E.D., Jr. and T.R. Guess, *Butt Joint Strength: Effect of Residual Stress and Stress Relaxation.* Journal of Adhesion Science and Technology, 1996. **10**: p. 33-45.

6.9 Baker, A.A., *Crack patching: experimental studies, practical applications*, in *Bonded Repair of Aircraft Structures*, A.A. Baker and R. Jones, Editors. 1988, Martinus Nijhoff Publishers: Boston. p. 107-173.

6.10 Lai, Y.-H., M.D. Rakestraw, and D.A. Dillard, *The Cracked Lap Shear Specimen Revisited - A Closed From Solution.* International Journal of Solids and Structures, 1996. **33**: p. 1725-1743.
6.11 Jones, R.M., *Mechanics of Composite Materials*. 1999: Taylor and Francis, Inc.

7.0 LIVING INFRASTRUCTURE CONCEPTS PART I: SELF-HEALING COMPOSITES

Scott White, Gina Miller and Dennis Roach

7.1 Self-Healing Composites

Inspired by living systems, self-healing materials autonomically repair minor damage. To accomplish healing, two phases are incorporated into the polymer matrix. The first phase is a microencapsulated healing agent, which when ruptured by an approaching crack releases healing agent into the crack plane via capillary action. Polymerization of the healing agent is triggered by contact with embedded catalyst, effectively healing the material and bonding the crack faces. This triggering mechanism provides site-specific healing similar to biological systems. Repair of damage is accomplished automatically and without human intervention, improving performance and service-life.

For this study the biologically inspired mechanism for healing is consistent with previously demonstrated self-healing polymers [7.1] and occurs in three stages as illustrated in Figure 7-1. Catalyst particles and liquid filled microcapsules are dispersed within the epoxy matrix. During crack propagation embedded microcapsules rupture and deliver the healing agent dicyclopentadiene (DPCD) to the crack plane via capillary action. Upon contact with embedded Grubbs' catalyst, ring-opening-metathesis-polymerization (ROMP) occurs effectively healing the material [7.1]. A unique feature of utilizing Grubbs' catalyst and ROMP polymerization is the use of *living* polymerization, enabling multiple healing events.

Self-healing or crack repair of polymers has been examined considerably in the literature. While some of these methods repair cracks, the healing is not autonomic and requires external intervention [7.2]. Autonomic healing methods have a distinct advantage in applications where repair is difficult and/or expensive to detect and access. Several autonomic healing schemes have been accomplished. Williams and colleagues achieve healing by embedding hollow fibers filled with a healing agent within a composite matrix [7.3]. During a fracture event, the hollow fibers break releasing the healing agent into the crack surface. Another healing technique, developed by White *et al.,* incorporates microencapsulated healing agent and catalyst phases [7.1]. Successful healing was accomplished by incorporating microcapsules and a transition metal catalyst into the polymer matrix. To evaluate healing performance, double cantilever beam specimens were utilized. For an epoxy matrix, recovery of over 90% of the virgin fracture toughness was achieved as illustrated in Figure 7.2.

The two phase system developed by White and co-workers has been applied to several applications including structural composite materials [7.4], fatigue damage [7.5, 7.6, 7.7] and polydimethylsiloxane self-healing systems [7.8]. In epoxies subject to cyclic loading, significant fatigue life extension can be achieved (e.g. Figure 7.3) or even complete crack arrest [7.7]. Toohey *et al.*, achieve multiple healing events by embedding a three-dimensional microvascular network within the substrate and filling these channels with a healing agent [7.9].

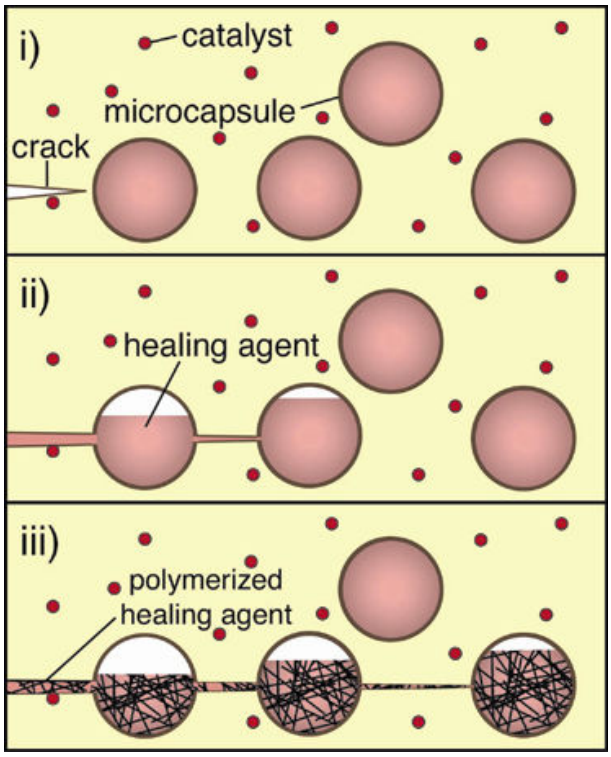

Figure 7-1: Self-Healing Concept Where Microcapsules and Catalyst are Dispersed in a Polymer Matrix

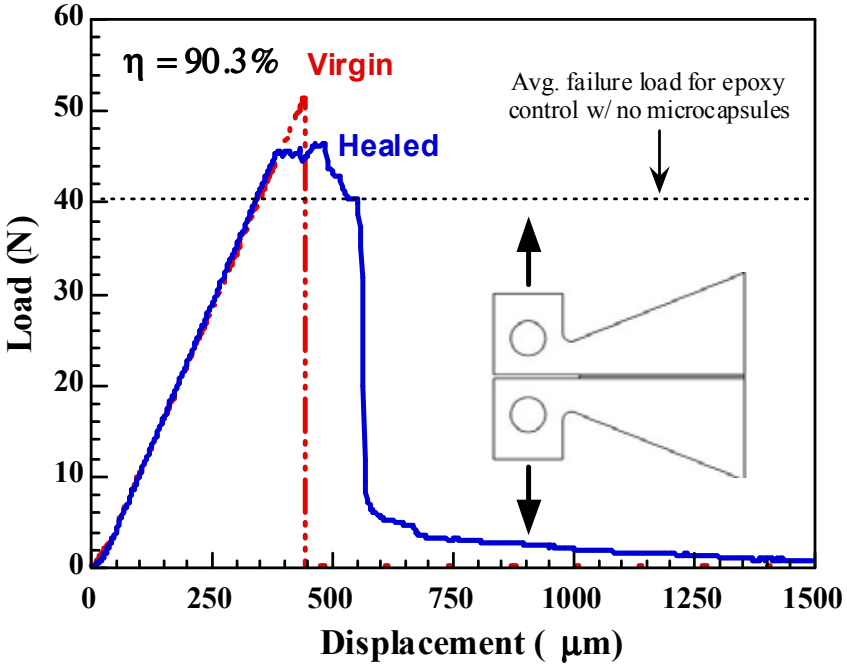

Figure 7-2: Load-Displacement Data for Virgin and Healed Epoxy Fracture Toughness Specimen

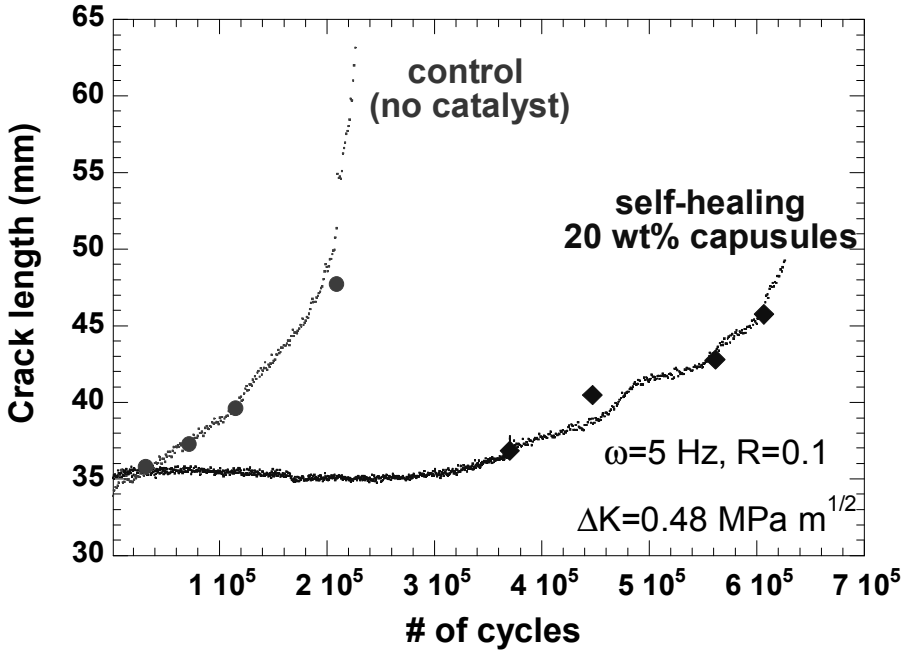

Figure 7-3: Fatigue Crack Length Versus Number of Cycles for Self-Healing and Control Epoxy Samples

7.2 Material System

7.2.1 FM®Adhesive Film

FM®73 adhesive film (Cytec Engineered Materials) was chosen as the matrix for the self-healing adhesive film system. This adhesive is a general purpose aerospace epoxy adhesive film that is suitable for adhesion to both metal and structural composite substrates. FM®73 adhesive film comes in forms both unsupported and supported by either a polyester knit or polyester mat. The unsupported form, FM®73U, was chosen for this study.

7.2.2 EPON™ Resin 828/Ancamine® DETA

The second matrix system used was EPON™ Resin 828/Anacamine® diethylenetriamine (DETA). This epoxy has previously been identified as a self-healing polymer in bulk form [7.1]. EPON™ Resin 828 is a general purpose bisphenol-A epoxide with the chemical structure shown in Table 7-1. The curing agent Ancamine® DETA is a primary amine curing agent with the chemical structure also shown in Table 7.1. The epoxy was mixed with a ratio of 12 pph DETA with 828 resin, and cured for 24 hours at room temperature followed by a 30 °C post-cure for 24 hours.

Component	Chemical Structure	Comments
EPON™ Resin 828	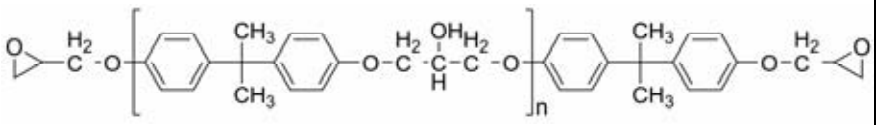	General purpose epoxy resin
Ancamine® DETA	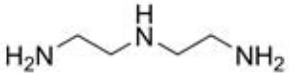	Primary amine curing agent

Table 7-1: EPON™ 828/DETA Matrix Components

7.2.3 Specimen Geometry and Adherends

The width tapered-double cantilevered beam (WTDCB) specimen geometry was chosen for evaluation of healing efficiency because it provides a crack length independent measure of fracture toughness [7.4]. The analysis of this geometry, shown in Figure 7-4, is established by linear elastic fracture mechanics. The mode I energy release rate G_I, is given by,

$$G_I = -\left(\frac{d\Pi}{dA}\right)_{\delta} = \frac{P^2}{2}\frac{dC}{dA}, \tag{7-1}$$

where Π is the potential energy, A is the crack area, P is the load, C is the specimen compliance, and δ is the opening displacement [7.10].

For a width tapered specimen as depicted in Figure 7-4, with a constant taper ratio, k ($k = a/b$) the change in the fracture area, dA, can be given by,

$$dA = b(a)\cdot da = \frac{1}{2}\frac{b(a)}{a}d(a^2) = \frac{1}{2k}d(a^2), \tag{7-2}$$

where a is the crack length and $b(a)$ is the width as a function of crack length [7.11]. Substituting equation (7-2) into (7-1), G becomes,

$$G_I = kP^2\frac{dC}{d(a^2)}. \tag{7-3}$$

For the width tapered specimen geometry, the specimen compliance is given by,

$$C = \frac{\delta}{P} = \frac{12ka^2}{E_{adherend}h_{adherend}^3}, \tag{7-4}$$

where $E_{adherend}$ is the Young's modulus of the adherend and $h_{adherend}$ is the thickness of one adherend. Differentiating equation (7-4) with respect to a^2 and substituting into equation (7-3), the mode I energy release rate for a width tapered double cantilevered beam specimen is expressed as,

$$G_I = \frac{12P^2k^2}{E_{adherend}h_{adherend}^3}. \tag{7-5}$$

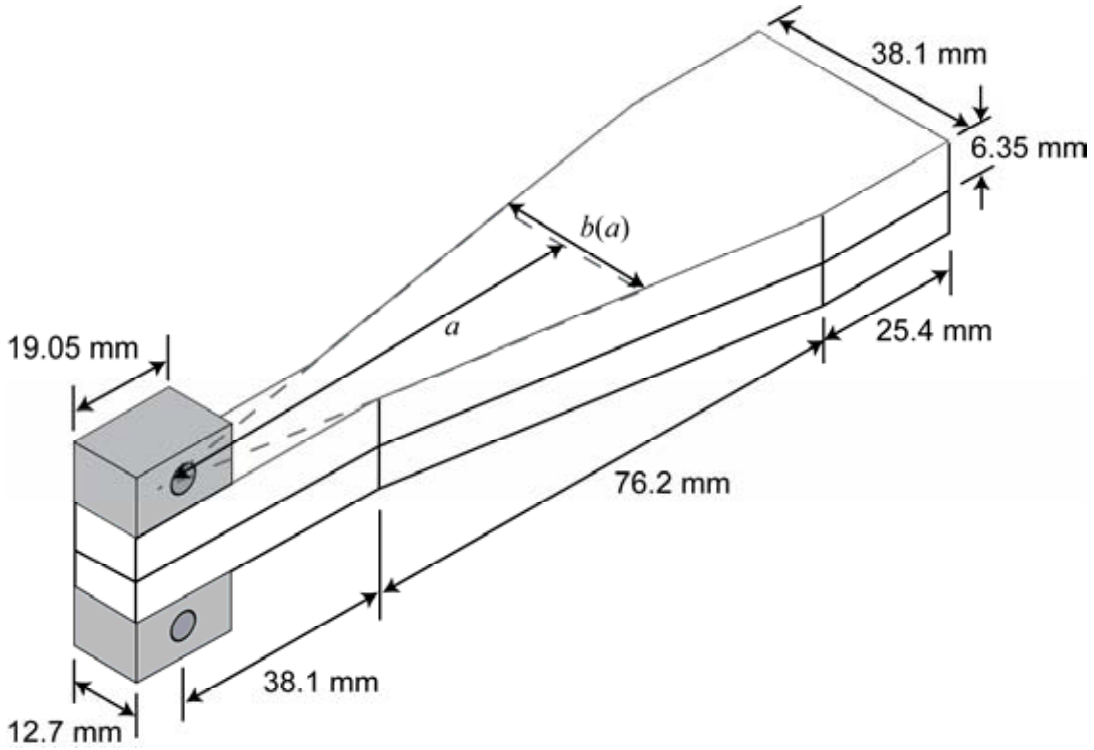

Figure 7-4: Geometry of Width-Tapered Double Cantilevered Beam (WTDCB) Specimen Which Consists of a Thin Layer of Adhesive Film Between Two Steel Adherends

For the experiments reported herein a taper ratio of k=6 was used. Assuming plane strain conditions, the fracture toughness can be derived from the energy release rate by the relation,

$$K_I = \sqrt{\frac{G_I E}{(1-\nu^2)}}, \tag{7-6}$$

where ν is the Poisson's ratio [7.10]. The fracture toughness of the epoxy is desired, so equation (7-6) becomes,

$$K_I = \sqrt{\frac{G_I E}{(1-\nu^2)}} = 2Pk\sqrt{\frac{3E_{adhesive}}{(1-\nu^2)E_{adherend}h_{adherend}^3}}, \quad (7\text{-}7)$$

where $E_{adhesive}$ is the Young's modulus of the adhesive. This formulation assumes a thin adhesive layer that does not significantly contribute to the total specimen thickness (i.e. adhesive thickness negligible compared to adherend thickness).

The healing efficiency is defined as the ratio of healed fracture toughness to virgin fracture toughness. For the WTDCB specimen geometry, this is equal to the ratio of critical loads of the healed to virgin material [7.4],

$$\eta = \sqrt{\frac{G_{IC}^{Healed}}{G_{IC}^{Virgin}}} = \frac{K_{IC}^{Healed}}{K_{IC}^{Virgin}} = \frac{P_C^{Healed}}{P_C^{Virgin}}. \quad (7\text{-}8)$$

For this research, steel adherends were chosen as the substrate material. Adherends were manufactured and were subject to both mechanical and chemical surface preparation as described in Sections 7.3.1 and 7.4.1. The material properties used in data analysis are given in Table 7-2.

Material	E (GPa)	ν
Steel adherend	200	0.33
EPON™828/DETA	2.9	0.33
FM®73	3.0	0.33

Table 7-2: Material Properties

7.2.4 Healing Chemistry

Grubbs' catalyst, a ruthenium based catalyst, initiates a living ring-opening metathesis polymerization with the healing agent DCPD. This polymerization reaction occurs at room temperature and produces a tough crosslinked polymer [7.1]. During a fracture event, the DCPD monomer comes in contact with Grubbs' catalyst and initiates the ROMP reaction shown in Figure 7.5. A scanning electron microscope (SEM) micrograph of Grubbs' catalyst is shown in Figure 7.6.

Microcapsules consist of the healing agent DCPD microencapsulated in a urea-formaldehyde shell [7.12]. Two different types of microcapsules were used throughout this study. *In situ* urea-formaldehyde microcapsules have a shell wall of approximately 160-220 nm thick and were used in self-healing specimens within the EPON 828/DETA matrix. The second type of microcapsules, pre-polymer urea-formaldehyde microcapsules, have a substantially thicker shell wall of approximately 2 μm thick and were used in self-healing specimens consisting of FM®73 epoxy matrix.

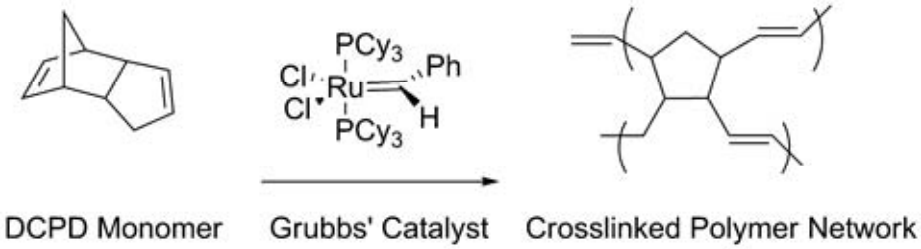

Figure 7-5: Ring-Opening-Metathesis-Polymerization (ROMP) of Healing Agent Dicyclopentadiene DCPD Using Grubbs' First Generation Catalyst

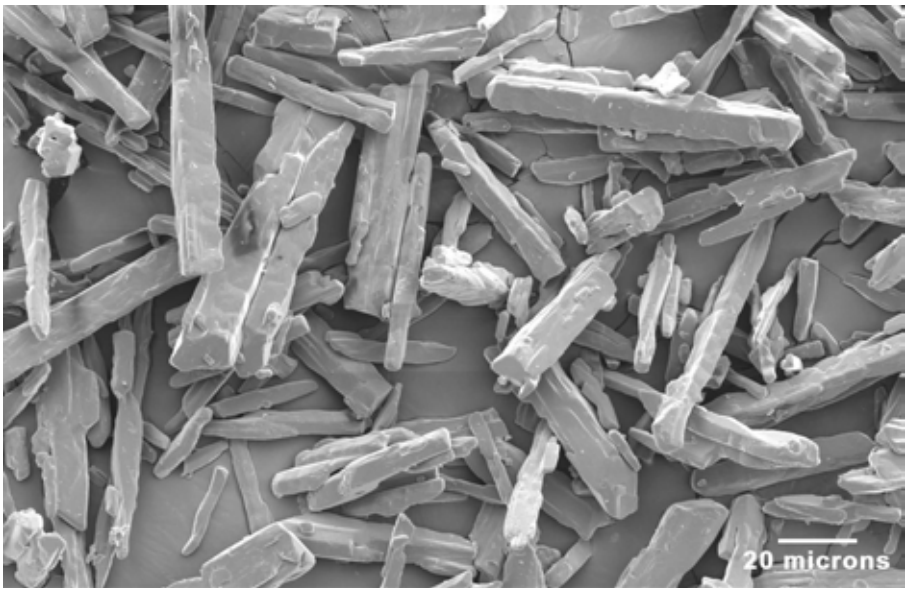

Figure 7-6: SEM Micrograph of As-Received First Generation Grubbs' Catalyst

An image of the microencapsulation setup is shown in Figure 7-7 and the manufacturing procedure for *in situ* urea-formaldehyde microcapsules is outlined in Figure 7-8. To begin the manufacturing process, 2.5wt% poly(ethylene-co-malaic anhydride) is added to water in a beaker. The reaction mixture is placed under a mixer and urea, ammonium chloride, and resorcinol are added to the mixture. Using NaOH the pH of the reaction mixture is adjusted to be between 3.6 and 3.8. Using HCl, the reaction mixture pH is then brought back down to 3.5. One drop of octanol is added to eliminate bubbles. Finally, DCPD and formaldehyde are added to the solution and the temperature is raised to 55°C. During the microencapsulation process, the reaction mixture is stirred, and this rate dictates the microcapsule size. After four hours, microcapsules are washed with water and vacuum filtrated. To complete the manufacturing process they are air dried and sifted. After sifting, microcapsules with a size between 125 μm and 180 μm were saved for use in the self-healing adhesive film.

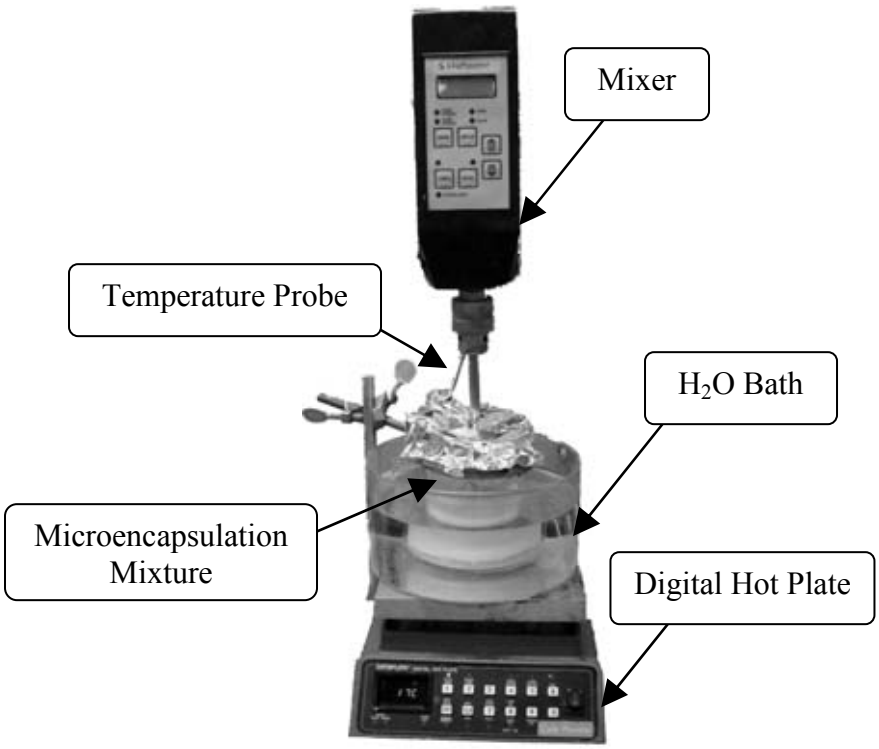

Figure 7-7: Experimental Setup to Manufacture Microcapsules

Pre-polymer microcapsules are manufactured in two steps. The first step is a pre-polymerization of the urea-formaldehyde shell wall. In the second step, the urea-formaldehyde pre-polymer is added to the microencapsulation mixture, where it forms a shell wall around droplets of DCPD. The manufacturing procedure is outlined in Figure 7-9 and the microencapsulation setup is the same as for *in situ* microencapsulation as shown in Figure 7-7.

To begin the microcapsule manufacturing process, 37% formaldehyde solution is added to a beaker, and the pH adjusted to 8.0 using triethanolamine. After placing the beaker in a 70 °C bath, urea is added and stirred until dissolved. The pre-polymer solution remains in the 70 °C bath for 1 hour. In a separate beaker, the encapsulation mixture is formed. To create the encapsulation mixture, 2.5 wt% poly(ethylene-co-malaic anhydride) is added to deionized water. After the pre-polymer solution has remained in the bath for 1 hour, it is quickly added to the encapsulation mixture. The healing agent DCPD is added to the solution. This solution is placed in a water bath under a mixer at the desired stir rate. During the microencapsulation process, the reaction mixture is stirred and the rate dictates the microcapsule size. The bath temperature is set to 35 °C. When the bath temperature reaches 30 °C the pH is adjusted to 2.5 using formic acid. At a bath temperature of 34 °C, 25 ml of warm (~ 30 °C) deionized water is added. Finally, every 15 minutes for one hour an additional 15 ml of warm deionized water is added to the mixture. After stirring for four hours, the microcapsules sit in solution for at least 12 hours. Microcapsules are then vacuum filtrated and washed with water. To complete the manufacturing process they are air dried and sifted. An image of this microencapsulation setup is shown in Figure 7-7. After sifting, microcapsules with a size between 125 μm and 180 μm were saved for use in the self-healing adhesive film.

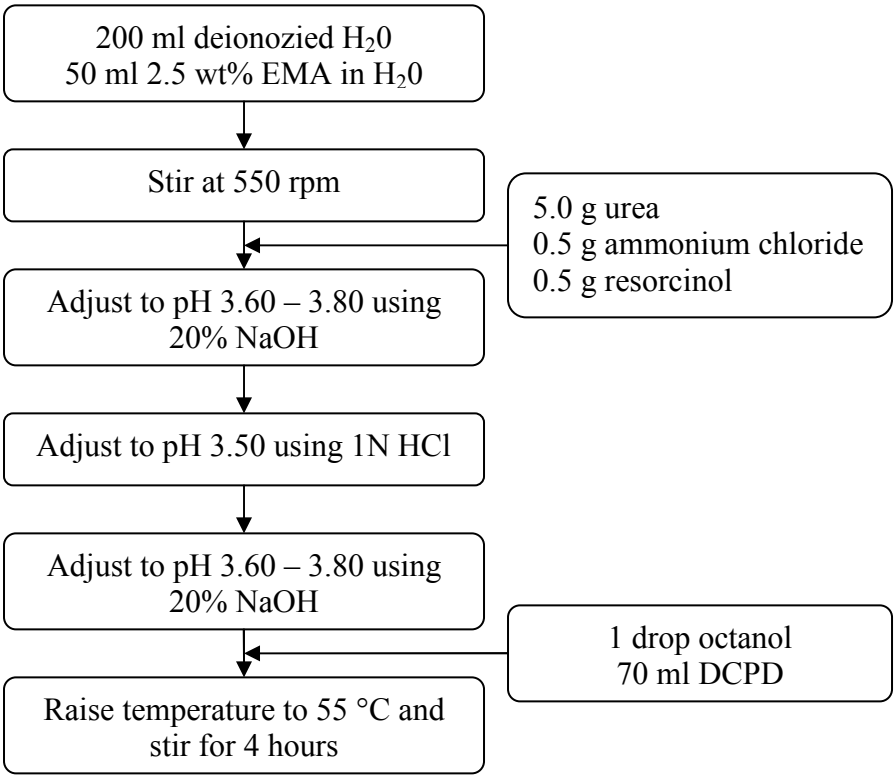

Figure 7-8: *In Situ* Polymerization of DCPD-Filled Urea-Formaldehyde (UF) Microcapsules

An SEM (JEOL 6060LV) was used to examine shell wall thickness and surface morphology of both *in situ* and pre-polymer microcapsules. Microcapsules were mounted with carbon tape on a stage and some microcapsules were ruptured using a razor blade to expose the shell wall for thickness measurements. Samples were sputter-coated with gold-palladium to prevent charging. Scanning electron microscope images of both *in situ* and pre-polymer urea-formaldehyde microcapsules are shown in Figure 7-10 (a) and Figure 7-10 (b) respectively. The contrasting shell wall thicknesses of the thin-walled *in situ* to the thick-walled pre-polymer microcapsules can be distinguished in Figure 7-10 (c) and Figure 7-10 (d). Pre-polymer microcapsules have a thick, and relatively smooth shell wall compared to microcapsules produced by *in situ* polymerization which have a thin shell wall surrounded by a rough outer surface.

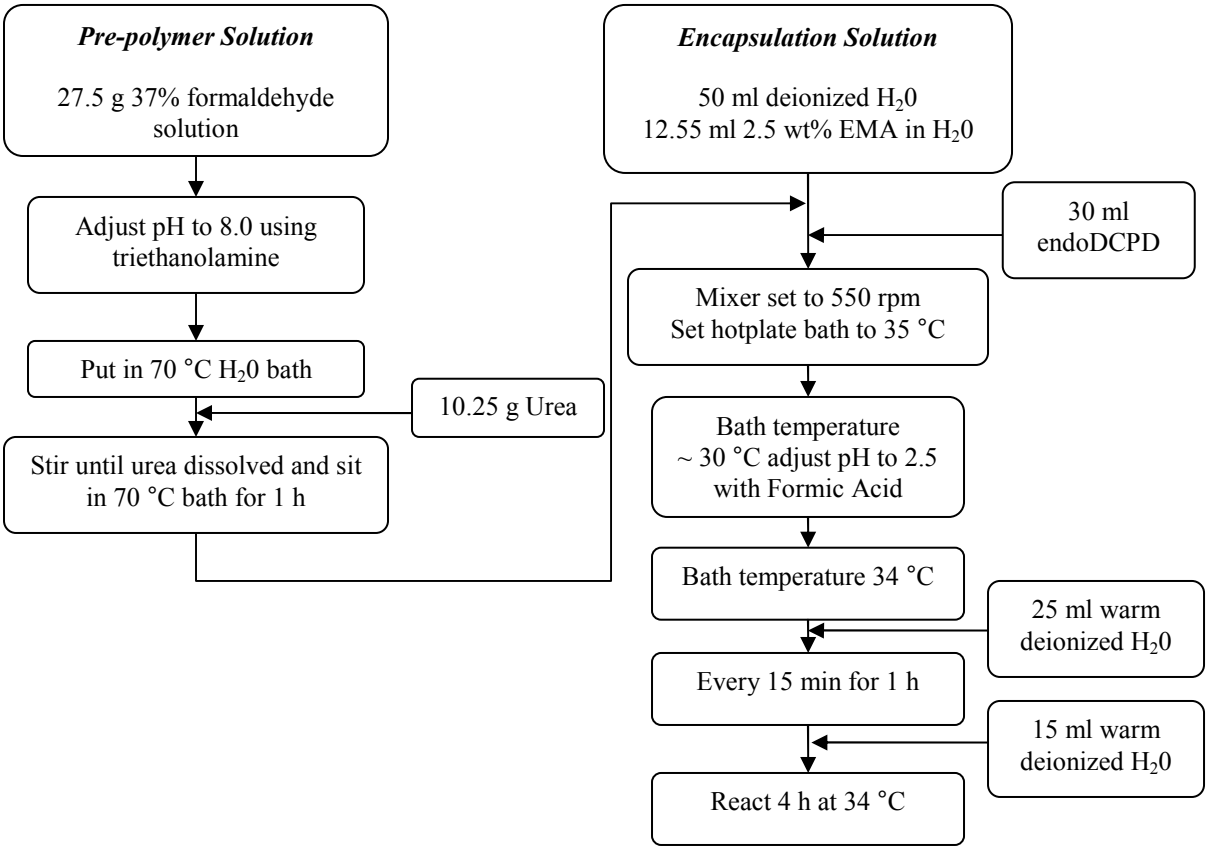

Figure 7-9: Pre-polymer (UF) Microencapsulation of DCPD by Using Interfacial Polymerization

7.3 Quasi-Static Fracture Response of EPON™ 828/DETA Adhesive Film System

7.3.1 Specimen Manufacture and Preparation

Three types of specimens were tested as illustrated in Figure 7-11. Manually injected specimens contained neat EPON 828/DETA epoxy resin and healing occurred via a precatalyzed mixture of *endo*-DCPD and as-received first Generation Grubbs' catalyst injected into the crack plane. Self-activated specimens contained only embedded Grubbs' catalyst and healing occurred via DCPD injected into the crack plane. Fully *in situ* specimens contained both embedded Grubbs' catalyst and microcapsules. For *in situ* specimens, healing occurred as a result of the ROMP reaction between DCPD released from ruptured microcapsules and embedded Grubbs' catalyst.

The steel adherends were both mechanically and chemically treated prior to application of the epoxy. Mechanical sanding using 80 grit sandpaper was carried out followed by manual sanding with a circular motion using 80 grit sandpaper. Following sanding, the samples were rinsed with acetone followed by isopropyl alcohol to remove grit. To chemically prepare the steel surface, a 1 vol% solution of the silane coupling agent (3-glycidyloxypropyl) trimethoxysilane in deionized

water was prepared. Using a squeeze bottle, the mechanically prepared surface was rinsed several times with the silane solution. After drying for 30 minutes the adherends were placed in a 60 ºC oven for 1 hour.

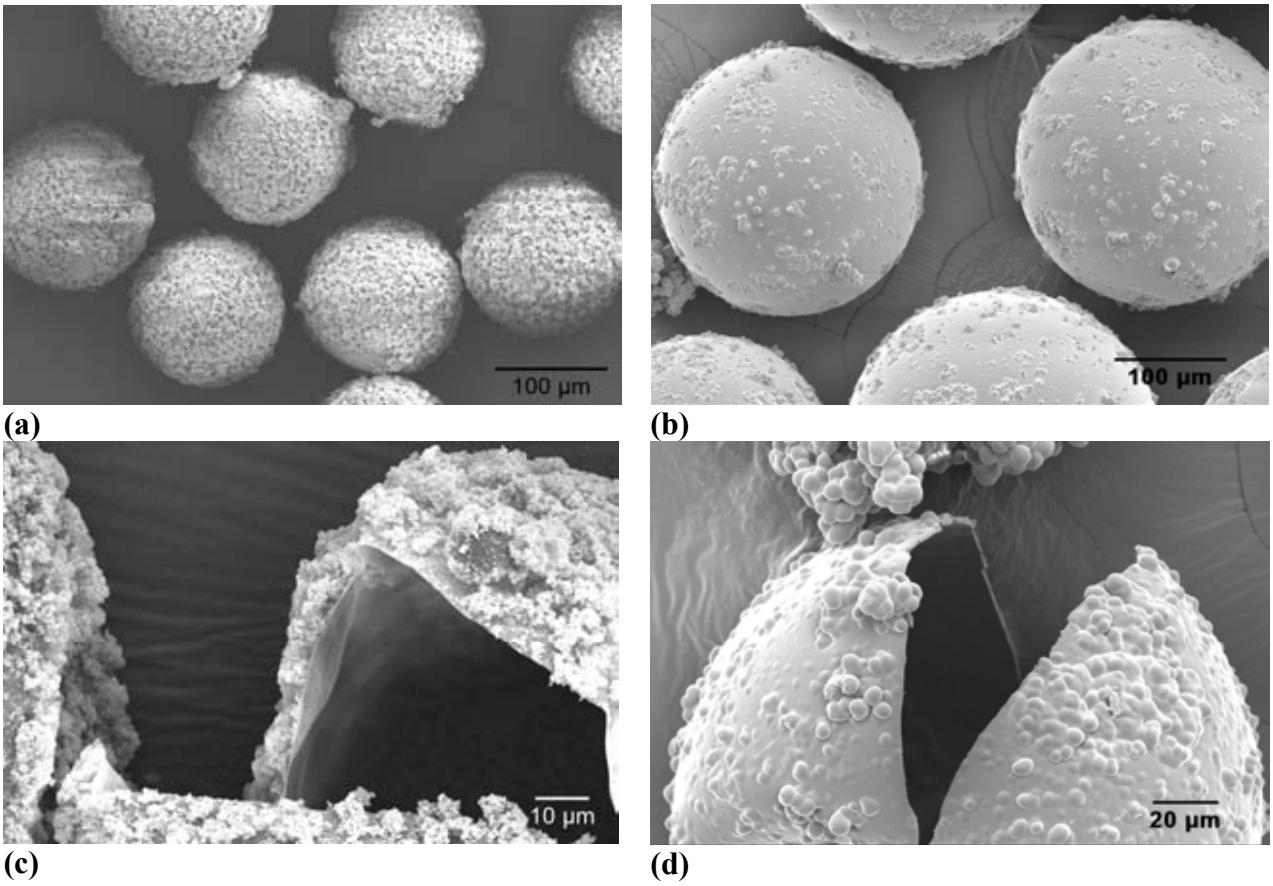

Figure 7-10: SEM Micrographs of (a) *In Situ* UF Microcapsules, (b) Pre-Polymer (UF) Microcapsules, (c) a Ruptured I*n Situ* UF Microcapsule, and (d) a Ruptured Pre-Polymer (UF) Microcapsule.

To prepare the epoxy for samples, EPON™ Resin 828 was mixed with 12 pph Acamine® DETA curing agent. After degassing this mixture, it was poured on each prepared adherend. For self-activated and fully *in situ* specimens, Grubbs' catalyst only or Grubbs' catalyst and microcapsules were mixed into the resin after degassing. The mixture was degassed again for several more minutes to remove entrapped air bubbles. A doctor blade coater was used to evenly spread the epoxy across the adherend surface. A 25 µm thick fluoropolymer release ply was placed between the mating films and serves as a precrack. Samples were cured for 24 hours at room temperature followed by a 30 °C post-cure for 24 hours. After curing, two steel loading blocks with holes for pin loading were attached to the end of each specimen by screws. A photograph of a typical WTDCB specimen with loading blocks attached is shown in Figure 7-12.

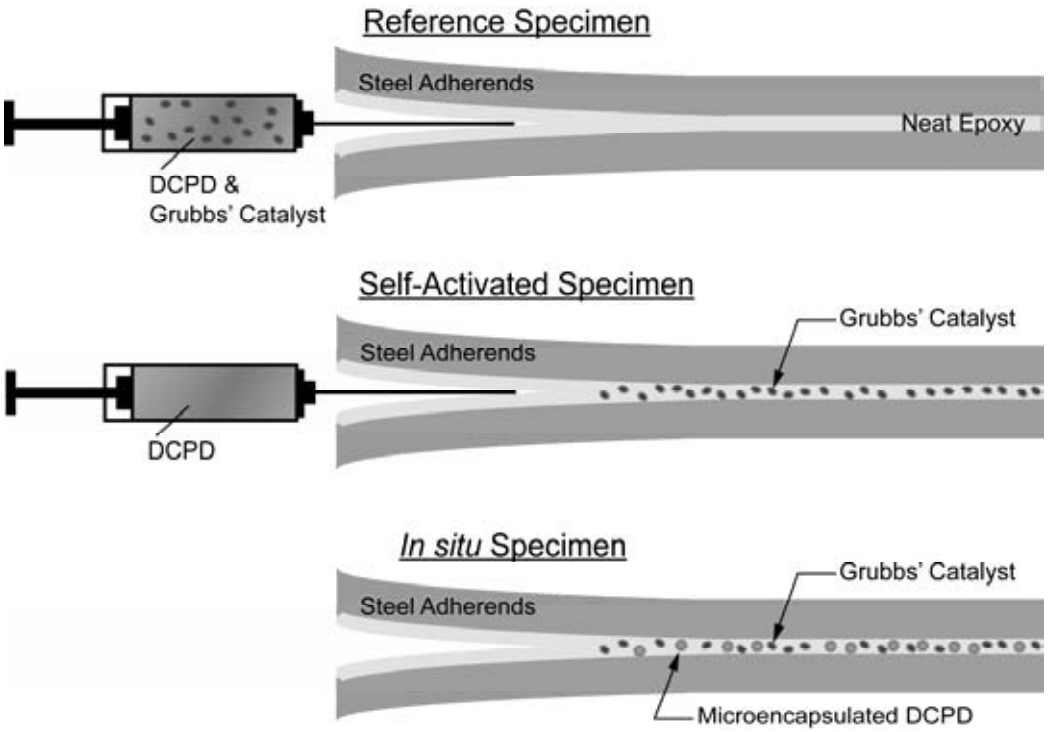

Figure 7-11: Three Types of WTDCB Specimens Used in Experiment

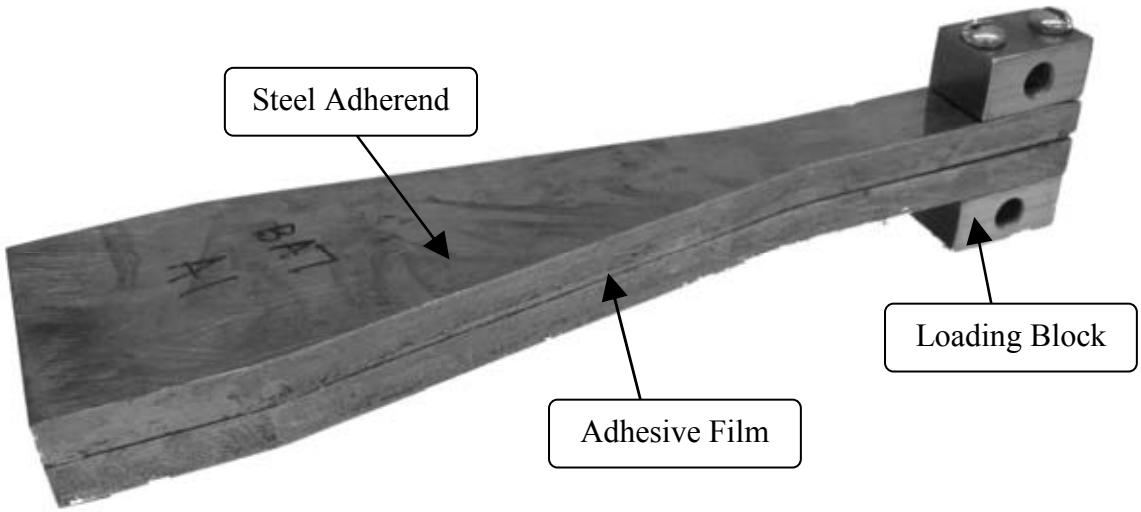

Figure 7-12: WTDCB Specimen with Loading Blocks

7.3.2 Test Procedure

Using a MTS mechanical testing machine, specimens were pin loaded in displacement control at a rate of 10 mm/min until a crosshead displacement of 2 mm was reached. For manually healed specimens, 0.5 ml DCPD was mixed with 2.5 mg Grubbs' catalyst and manually injected into the

crack plane using a syringe. For self-activated samples, 0.5 ml DCPD was manually injected into the crack plane. After injection, the specimens were quickly unloaded at a rate of 15 mm/min. To ensure contact of the two fracture planes, adherends were taped together in several locations. After approximately 24 hours of healing at room temperature the specimens were reloaded to a crosshead displacement of 2 mm at a rate of 10 mm/min and then unloaded at 15 mm/min.

For fully *in situ* samples, specimens were loaded in displacement control at a rate of 10 mm/min until a crack opening displacement of 2 mm was reached. After two seconds the specimens were unloaded at a rate of 15 mm/min. After approximately 24 hours of healing at room temperature, the specimens were tested again.

7.3.3 Results and Discussion

Reference Specimens - Specimens that are manually healed by the injection of premixed DCPD and Grubbs' catalyst are identified as reference specimens. These specimens serve as an experimental control and indicate the maximum amount of healing expected for self-activated and *in situ* specimens. By delivering premixed catalyst and monomer, the variables of complete catalyst and monomer mixing and catalyst survival are removed. The results of reference specimens serve as an upper limit for expected healing efficiency and are used as standard for comparison with self-activated and *in situ* specimens. Figure 7-13 shows a typical load–displacement curve for a reference EPON 828/DETA specimen. The values for the load P in K_{IC} calculations are indicated by black triangles.

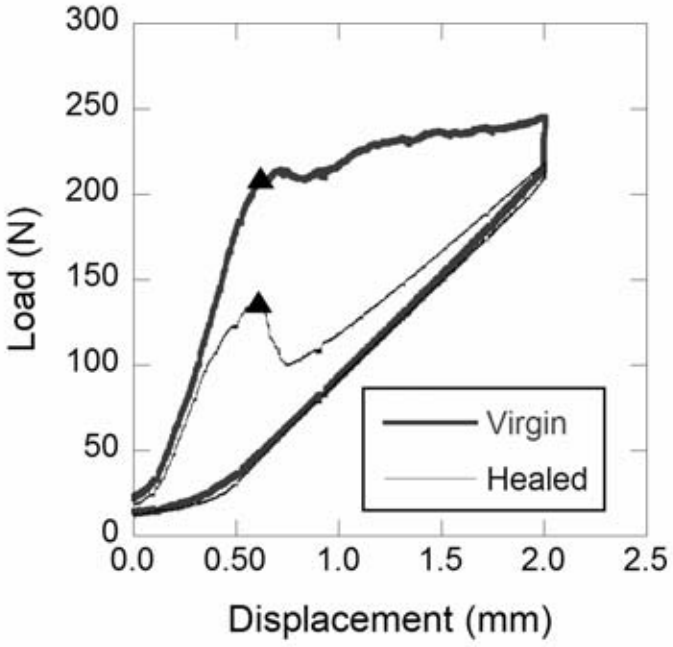

Figure 7-13: Typical Load–Displacement Curve for Reference EPON™ 828/DETA Specimen

In the virgin curve, the specimen shows linear elastic loading until a critical load is reached (~ 210 N) after which controlled and stable crack propagation occurs until the maximum crosshead displacement is reached (δ= 2 mm). At this point the specimen was injected with premixed DCPD and Grubbs' catalyst and then unloaded. Twenty-four hours later, during the healed test, the specimen is reloaded until reaching a critical load about 145 N at which point the crack propagates through the healed region until reaching virgin material again at roughly δ= 0.75 mm crosshead displacement. Continued loading to a crosshead displacement of δ = 2 mm occurs without further crack growth. After the healed test was completed, the specimen was retested and loaded until the crack propagated completely through the sample so that the fracture plane could be imaged.

When examining the fracture surfaces of bonded joints, two failure modes are predominately observed as illustrated in Figure 7-14. Adhesive failure occurs when the failure occurs at the interface between adherend and adhesive. When the failure occurs within the adhesive it is designated cohesive failure. Cohesive failure indicates that the full strength of the adhesive material has been achieved. To examine the fracture surface, photographs were taken of the two adherends as shown in Figure 7-15. Reference specimens of 828/DETA epoxy exhibited primarily adhesive failure as indicated in Figure 7-15. An average healing efficiency η = 67.8 ± 13.8% was obtained for all reference specimen tests.

Figure 7-14: Failure Mechanisms in Adhesives

Self-Activated Specimens - Specimens that are healed by the ROMP reaction of embedded Grubbs' catalyst with injected DCPD are identified as self-activated specimens. These specimens provide evidence of catalyst survival and healing without the variable of monomer delivery. Comparison of self-activated specimens with reference specimens indicates how undergoing the cure cycle and embedding the catalyst affects healing. Figure 7-16 shows a typical load–displacement curve for a self-activated EPON 828/DETA specimen.

As with the reference specimens, these specimens were loaded until a crosshead displacement of δ= 2 mm was attained. At this point, the specimen was injected with 0.5 ml DCPD, and then unloaded at 15 mm/min. The adherends were taped together to ensure contact between fracture surfaces. After 24 hours the specimen was retested to evaluate healing. After the healing test was complete, the specimen was reloaded until the crack propagated completely through the sample for visual imaging of the fracture surface.

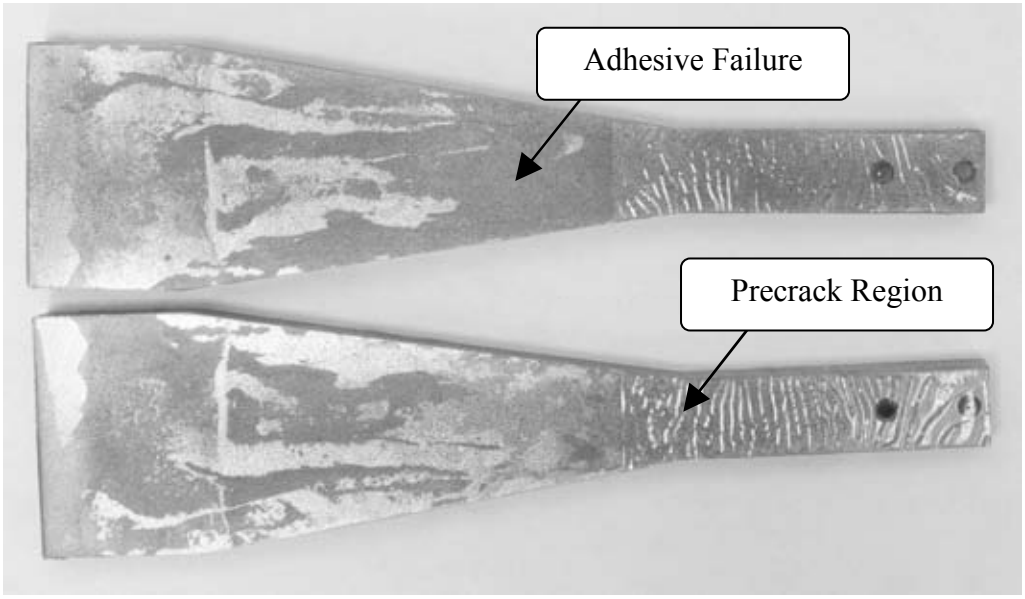

Figure 7-15: Fracture Surface of Neat Reference EPON™ 828/DETA Specimen

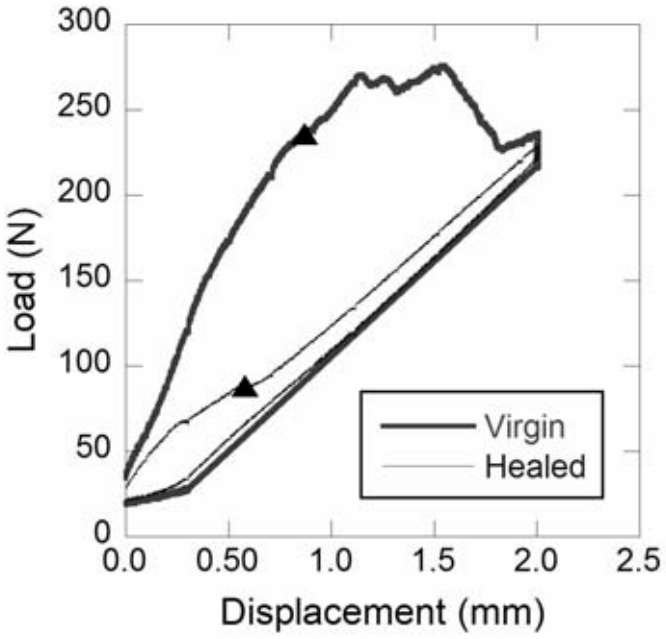

Figure 7-16: Typical Load–Displacement Curve for Self-Activated EPON™ 828/DETA Specimen

A photograph of the fracture surfaces for a typical self-activated sample is shown in 7-17. Similarly to the fracture surfaces of neat reference specimens, predominately adhesive failure was observed. The average healing efficiency for all self-activated specimen tests yields, η =

44.4 ± 9.1%. The decrease in healing efficiency in self-activated specimens compared to reference specimens is attributed to partial deactivation of the catalyst.

Figure 7-17: Fracture Surface of Self-Activated EPON™ 828/DETA Specimen

In-Situ Healing Specimens - Specimens that contain both embedded Grubbs' catalyst and embedded microcapsules are designated *in-situ* specimens. Fully contained, *in situ* specimens represent the completely integrated system for autonomic repair in adhesive film. The fully *in situ* system contained 2.5 wt% embedded Grubbs' catalyst, 15 wt% microcapsules manufactured by *in situ* polymerization, and 1 wt% silane coupling agent. A load – displacement curve for a fully integrated *in situ* specimen is shown in Figure 7-18.

As with reference and self-activated specimens, these specimens were loaded at 10 mm/min until reaching a set crosshead displacement of δ = 2 mm. Afterwards, the specimen was unloaded at a 15 mm/min, taped to ensure the closure of the fracture plane, and then allowed to heal at room temperature for 24 h. The healed specimens were reloaded to a crosshead displacement of δ= 2 mm, unloaded, then reloaded to complete failure in order to image the fracture planes.

In Figure 7-19, a typical fracture surface for a fully *in situ* self-healing specimen is shown. Unlike reference and self-activated specimens, *in situ* specimens showed regions of cohesive failure. During crack propagation stick-slip failure behavior was observed (as shown in Figure 7-18) in *in situ* specimens. The regions of unstable, "slip" failure correspond with regions of cohesive failure on the fracture surface. The average healing efficiency for all *in situ* specimen tests yields, η = 56.5 ± 21.0%.

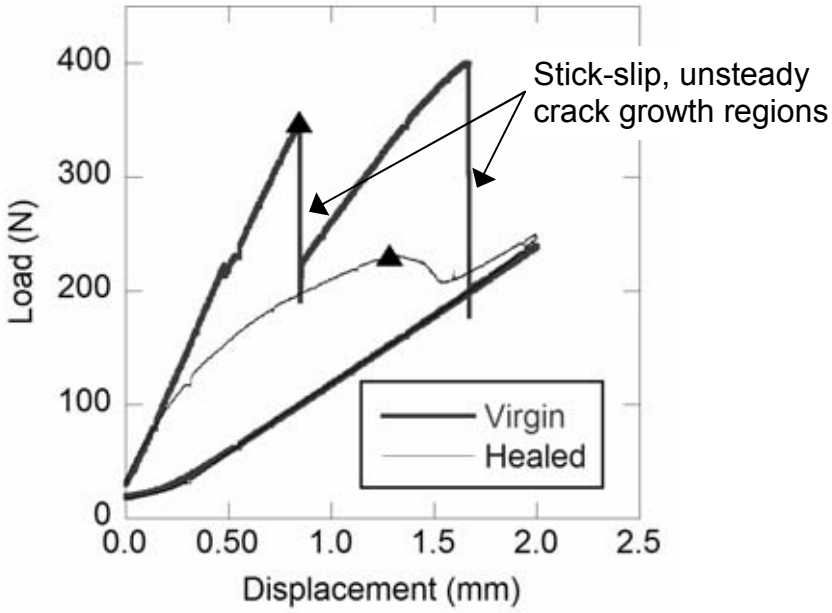

Figure 7-18: Typical Load–Displacement Curve for In-Situ EPON™ 828/DETA specimen

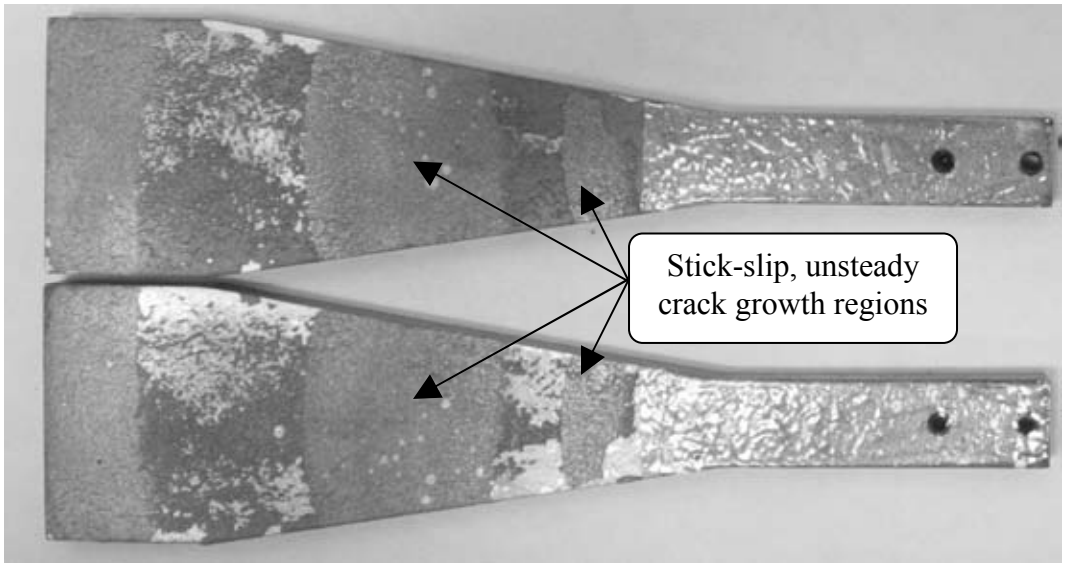

Figure 7-19: Fracture Surface of I*n-Situ* EPON™ 828/DETA Specimen

A summary of WTDCB test results for the EPON™ 828/DETA adhesive system is shown in Table 7-3. Many *in situ* specimens achieved higher healing efficiencies than neat reference and self-activated specimens. This is attributed to the regions of cohesive failure observed in *in situ* specimens. The healed polyDCPD exhibits better adhesion to the rough EPON™ 828/DETA

fracture surface in cohesive failure regions, than to steel as observed in neat reference and self-activated specimens. The virgin fracture toughness increased with addition of microcapsules in the *in situ* specimen.

Sample Type	# of Samples	Fracture Toughness (MPa $m^{1/2}$)		Healing Efficiency (%)
		Virgin	Healed	
Reference Control	6	1.01 ± 0.11	0.68 ± 0.08	67.8 ± 13.8
Self-Activated Control	5	1.08 ± 0.22	0.47 ± 0.11	44.4 ± 9.1
In Situ Self-Healing	9	1.80 ± 0.11	1.01 ± 0.37	56.5 ± 21.0

Table 7-3: Summary of EPON™ 828/DETA Quasi-Static Fracture Test Results

7.4 Quasi-Static Fracture Response of FM®73 Adhesive Film System

7.4.1 Specimen Manufacture and Preparation

As with the EPON 828/DETA matrix system, three types of specimens with an FM®73 adhesive film matrix were tested. These specimens - reference, self-activated and *in situ* - are illustrated in Figure 7-11. FM®73 is the film adhesive used for the bonded composite doubler repairs so these results are more indicative of the healing to be achieved in composite patch repairs on steel structures.

The steel adherends were both mechanically and chemically treated prior to application of the adhesive film. Mechanical sanding using 80 grit sandpaper was carried out followed by manual sanding with a circular motion using 80 grit sandpaper. Following sanding, the adherends were blown with compressed air to remove grit. To chemically prepare the steel surface, a 1% volume solution of the silane coupling agent (3-glycidyloxypropyl)trimethoxysilane in deionized water was prepared. Using a squeeze bottle, the mechanically prepared surface was rinsed several times with the silane solution. After drying for 30 minutes, the adherends were placed in a 60 ºC oven for 1 hour.

To manufacture manually injected specimens, a layer of FM®73 adhesive film was placed on each prepared adherend. EPON™ 828 resin (0.7 ml) was mixed with 1% weight silane coupling agent and spread on each prepared adherend. In fully self-healing samples, EPON™ 828 resin serves as a carrier for microcapsules and accordingly neat EPON™ 828 resin is included in the manually injected control specimens. A 25 μm thick fluoropolymer release ply was placed between the mating films and served as a precrack. Once lay-up was complete, the samples were cured in a programmable oven according to the cure cycle shown in Figure 7-20. During the cure cycle, the temperature ramps from room temperature to 102 – 110 °C (215 – 230 °F) and dwells at that temperature for 3 hours before returning back to room temperature.

For self-activated specimens, a layer of FM®73 adhesive film was placed on each prepared adherend. Grubbs catalyst at 5% weight was deposited on the adhesive film surface and distributed as evenly as possible using a razor blade. As with manually injected reference

specimens, EPON™ 828 resin (0.7 ml) was mixed with 1% weight silane coupling agent and spread on each prepared adherend. A 25 μm thick fluoropolymer release ply was placed between the mating films and served as a precrack. Once lay-up was complete, the samples were cured according the cure cycle shown in Figure 7-20.

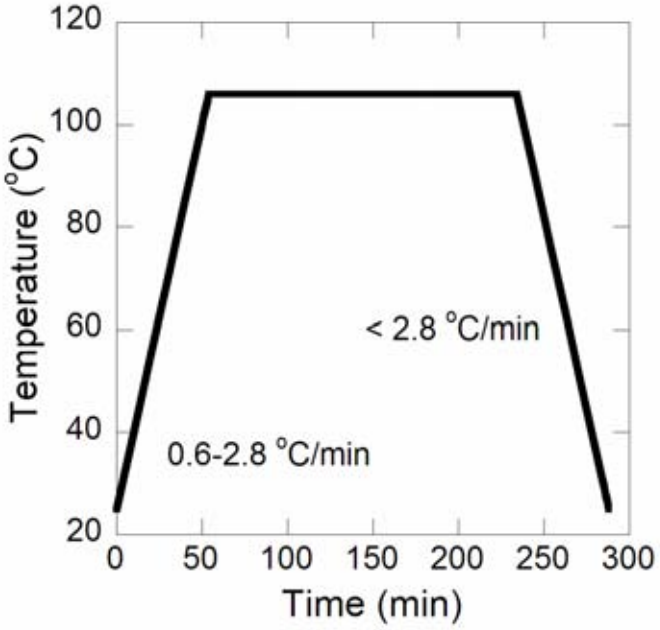

Figure 7-20: Cure Cycle of Adhesive Film for FM®73 Specimens

To prepare the adherends for *in situ* specimens, the surface was treated with a silane coupling agent, as previously described. A layer of FM®73 adhesive film was placed directly on each prepared adherend. Grubbs' catalyst (5 wt%) was deposited on the adhesive film surface as described for the self-activated specimens. Pre-polymer microcapsules at 15% weight were mixed with 1% weight silane and 0.7 ml EPON 828 resin. This paste was spread across the adhesive film surface. A 25 μm micron thick fluropolymer release ply was placed between the mating films to serve as a precrack. Samples were then cured in a programmable oven according to the thermal profile in Figure 7-20.

7.4.2 Test Procedure

Specimens were loaded in displacement control at a rate of 5 mm/min until a crack opening displacement δ= 5 mm was reached. For manually healed specimens, 0.5 ml of DCPD was mixed with 2.5 mg of Grubbs' catalyst and manually injected into the crack plane using a syringe. For self-activated samples, 0.5 ml DCPD was manually injected into the crack plane. After injection, the specimens were unloaded quickly at a rate of 15 mm/min and the adherends taped together to ensure contact of the fracture surfaces. After 24 hours of healing at room temperature specimens were retested to evaluate healing efficiency.

In situ specimens were tested according to the same procedure as control and self-activated specimens; however no catalyst or healing agent were injected into the crack plane. The

specimens were loaded to a crack opening displacement of 5 mm and after two seconds the specimens were unloaded. After 24 hours of healing at room temperature the specimens were tested again.

7.4.3 Results and Discussion

Reference specimens are healed by manually injecting premixed DCPD and Grubbs' catalyst. These specimens serve as an experimental control and indicate the maximum amount of healing expected for self-activated and *in situ* specimens. Reference samples have the advantage of removing variables of complete catalyst and monomer mixing, and catalyst survival by delivering premixed catalyst and monomer. A typical load-displacement plot for a reference sample of FM®73 and EPON™ 828 resin is shown in Figure 7-21.

In the virgin curve, the specimen is loaded and the crack propagates until the maximum crosshead displacement of 5 mm is reached. At this point the specimen is injected with premixed DCPD and Grubbs' catalyst and then unloaded. Twenty-four hours later, during the healed test, the specimen is reloaded and the crack propagates through the healed region until continuing to propagate through virgin material. After loading to the same maximum displacement, the sample is unloaded. After healing, the specimen was retested and loaded until the crack propagated completely through the sample. The fracture surfaces were examined, and Figure 7-22 shows the two adherends for the results in figure 7-21. The failure was primarily adhesive as indicated in Figure 7-22 so much of the specimen bond strength was lost due to these extensive disbonds. The average healing efficiency for all reference specimen yields, η = 18.7 ± 3.8%.

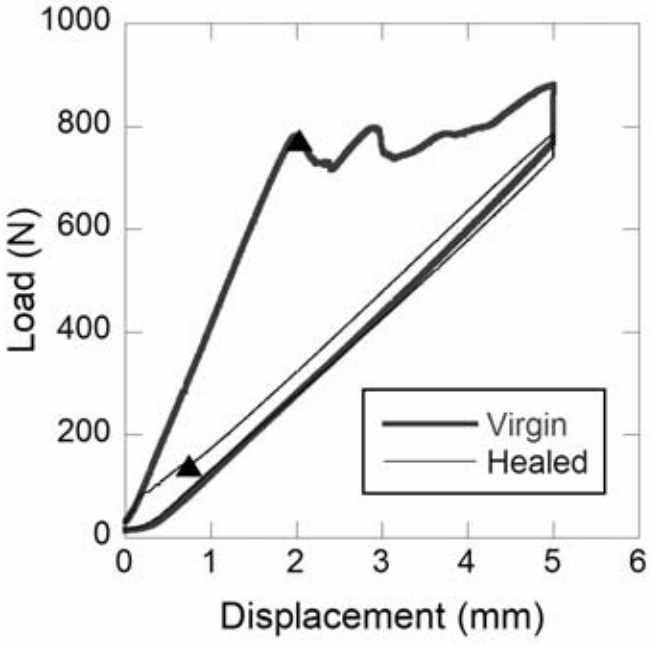

Figure 7-21: Load-Displacement Curve for Reference FM®73 Specimen

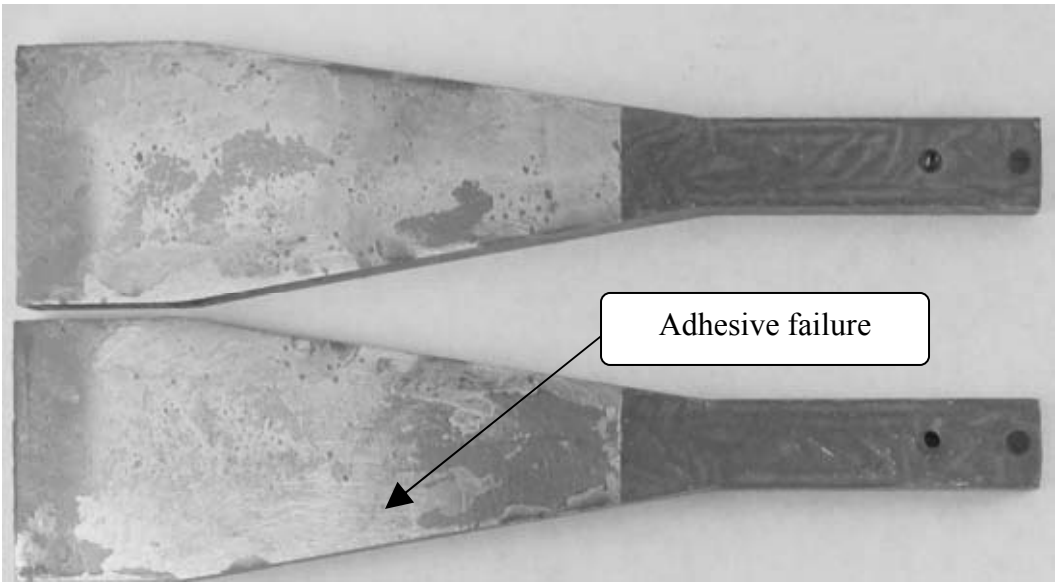

Figure 7-22: Fracture Surface of a Reference FM®73 Adhesive Specimen

Self-activated specimens contain only embedded Grubbs' catalyst, and are healed by the injection of DCPD into the crack surface. These samples remove the variable of monomer delivery and provide evidence of catalyst survival. A typical load-displacement plot for a self-activated FM®73 is shown in Figure 7-23.

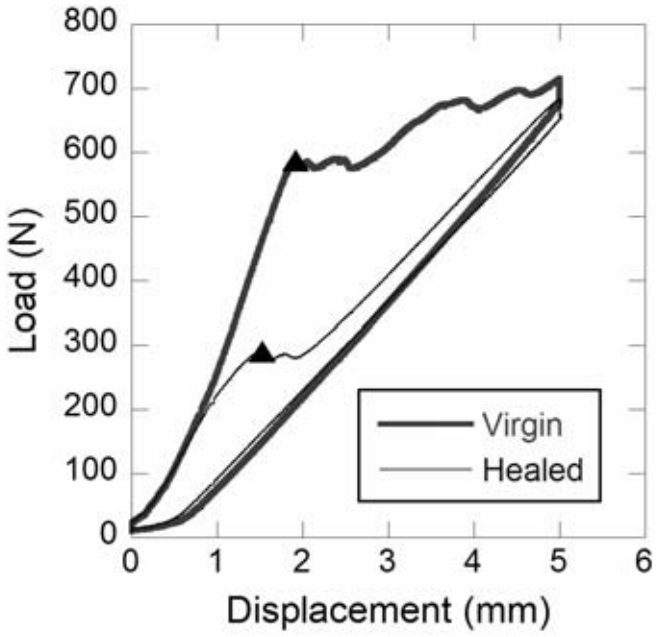

Figure 7-23: Load-Displacement Curve for Self-Activated FM®73 Specimen

These specimens were loaded to the same crosshead displacement of 5 mm as with reference specimens. At the maximum opening displacement the specimens were injected with DCPD only and then unloaded. Adherends were taped together to ensure good contact between fracture surfaces. After 24 hours the specimens were retested to evaluate healing. After healing, the specimen was reloaded until failure to examine the fracture surface. The fracture surfaces for the results plotted in Figure 7-23 are shown in Figure 7-24. As indicated in the Fig. 7-24, both adhesive and cohesive failure was observed. This shows better overall adhesion in the bondline than exhibited in the FM®73 reference specimens. The average healing efficiency for all self-activated tests yields, $\eta = 53.1 \pm 5.4\%$.

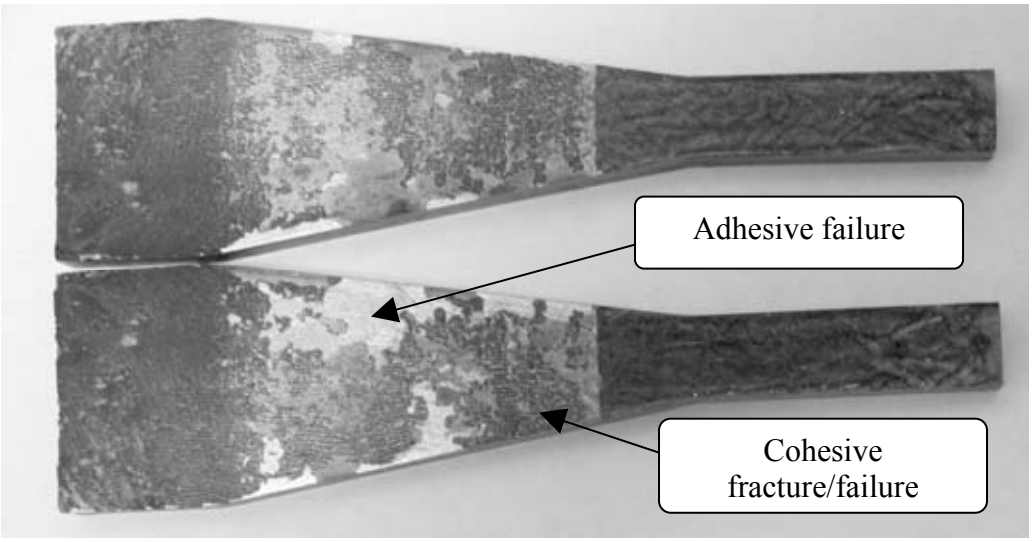

Figure 7-24: Fracture Surface of a Self-Activated FM®73 Adhesive Specimen

The fully integrated self-healing system was evaluated using *in situ* specimens which contain both embedded microcapsules and catalyst. The fully *in situ* system contained 5% weight embedded Grubbs' catalyst, 15% weight microcapsules manufactured by pre-polymer microencapsulation and 1% weight silane coupling agent. A load-displacement plot for a fully integrated *in situ* FM®73 specimen is shown in Figure 7-25.

As with reference and self-activated specimens, *in situ* specimens were loaded until a crosshead displacement of 5 mm was reached. Once this displacement was reached, the specimen was unloaded and allowed to heal for 24 hours. After the healing process was completed, the specimen was reloaded until the crack propagated completely through the sample.

A typical fracture surface for an *in situ* FM®73 film sample is shown in Figure 7-26. The fracture surfaces of *in situ* samples showed almost completely cohesive failure in the bondline. The fracture surface for an *in situ* self-healing sample was more closely examined using scanning electron microscopy. To prepare the sample, the adhesive film was removed from the steel adherend using a razor blade. Using carbon tape the film was mounted on a stage and sputter-coated using gold-palladium to prevent charging. An SEM micrograph of the fracture surface is shown in Figure 7-27. Microcapsules and healed polyDCPD film are visible and labeled.

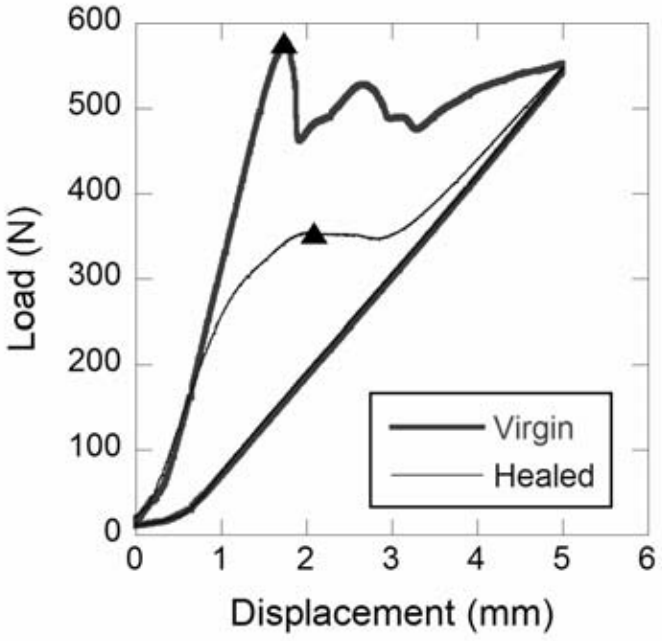

Figure7-25: Load-Displacement Curve for a Fully In-Situ Healing FM®73 Specimen

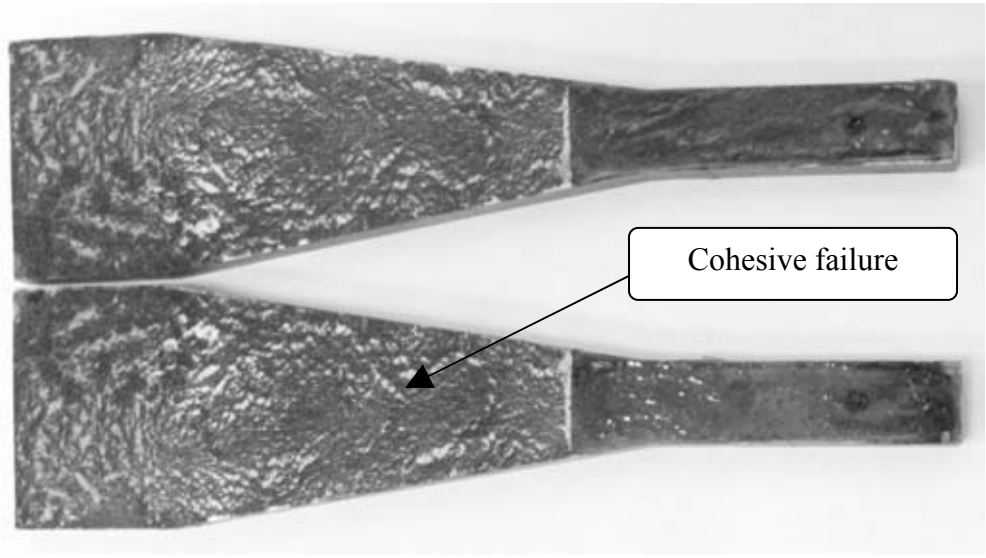

Figure 7-26: Fracture Surface of I*n-Situ* FM®73 Adhesive Specimen

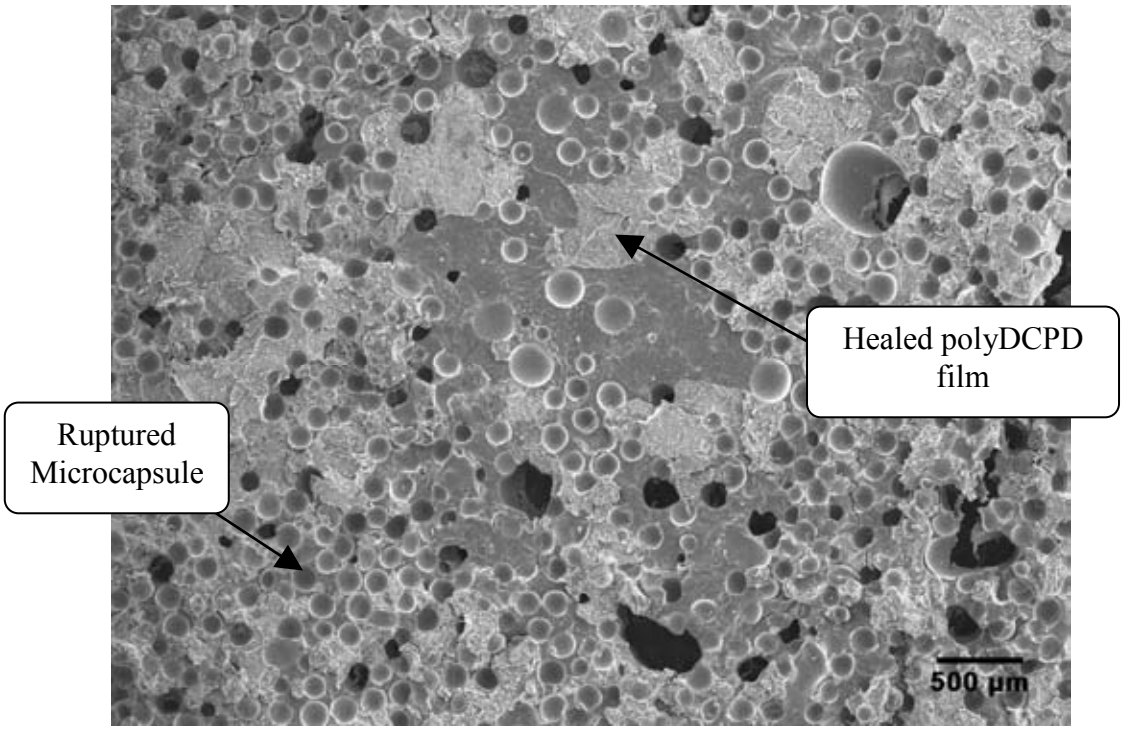

Figure 7-27: Fracture Surface of Healed In-Situ FM®73 Specimen

A summary of healing results for FM®73 samples is listed in Table 7-4. *In situ* samples achieved an average healing efficiency, η = 56.5 ± 9.2%. Overall, *in situ* and self-activated specimens achieved higher healing efficiencies than neat reference specimens. The incorporation of healing components reduced the virgin fracture toughness, but increased the healed fracture toughness resulting in increased healing efficiencies compared with reference control specimens. The failure morphology of self-activated and *in situ* specimens differed significantly from reference specimens as the addition of Grubbs' catalyst and microcapsules promotes cohesive vs. adhesive failure and increases the efficiency of mechanical triggering of the self-healing functionality.

Sample Type	# of Samples	Fracture Toughness (MPa $m^{1/2}$)		Healing Efficiency (%)
		Virgin	Healed	
Reference Control	6	3.88 ± 0.69	0.72 ± 0.16	18.7 ± 3.8
Self-Activated Control	6	3.66 ± 0.29	1.94 ± 0.23	54.1 ± 5.4
In situ Self-Healing	9	3.12 ± 0.27	1.75 ± 0.24	56.5 ± 9.2

Table 7-4: Summary of FM®73 Sample Types and Healing Efficiencies

7.5 Fatigue Response of FM®73 Adhesive Film System

7.5.1 Specimen Manufacture and Preparation

For fatigue experiments, specimens were prepared in the same manner as for static fracture testing. As previously described in section 7.4.1, specimens were sanded to mechanically prepare the surface. Following the mechanical surface preparation, the steel surface was treated with the silane coupling agent as previously described. After specimen lay-up, samples were cured in a programmable oven according to the cure cycle illustrated in Figure 7-20. Both reference FM®73 adhesive film and fully *in situ* fatigue specimens were manufactured and tested.

7.5.2 Test procedure

To study the fatigue crack propagation behavior of the adhesive film, experiments were performed on WTDCB specimens under load control. As previously described, the WTDCB geometry provides a crack length independent relationship between the energy release rate and load. During testing, a haversine waveform was applied at a load ratio $(R=P_{min}/P_{max})$ of 0.1 and a frequency of 2 Hz. The minimum and maximum loading was 25 N and 250 N respectively. Specimen compliance was monitored throughout the test and used to evaluate crack growth.

7.5.3 Results and Discussion

Reference control and fully *in situ* specimen were tested in fatigue. Specimens were cycled until complete failure was achieved as shown in Figure 7-28. The neat control specimen exhibited monotonic crack growth throughout the fatigue test and failed within 170,000 cycles. In stark contrast, the fully in situ self-healing sample initially shows the same crack growth rate, but then slows dramatically, again accelerates between about 100,000-200,000 cycles, then slows again and nearly arrests. Some small growth of the crack is continuing above 200,000 cycles of fatigue. The in situ self-healed specimen survived 514,000 cycles of loading, an increase of over 200% in fatigue life over the control specimen for identical loading conditions. During fatigue testing, crack propagation ruptured the microcapsules releasing the healing agent into the crack plane where it polymerizes upon contact with the embedded catalyst. The polymerized healing agent provided a crack tip shielding mechanism to extend the fatigue life of the host resin. Further research is required to optimize the FM®73 adhesive system for fatigue loading conditions and to identify loading regimes and deployment scenarios were fatigue crack growth is fully arrested.

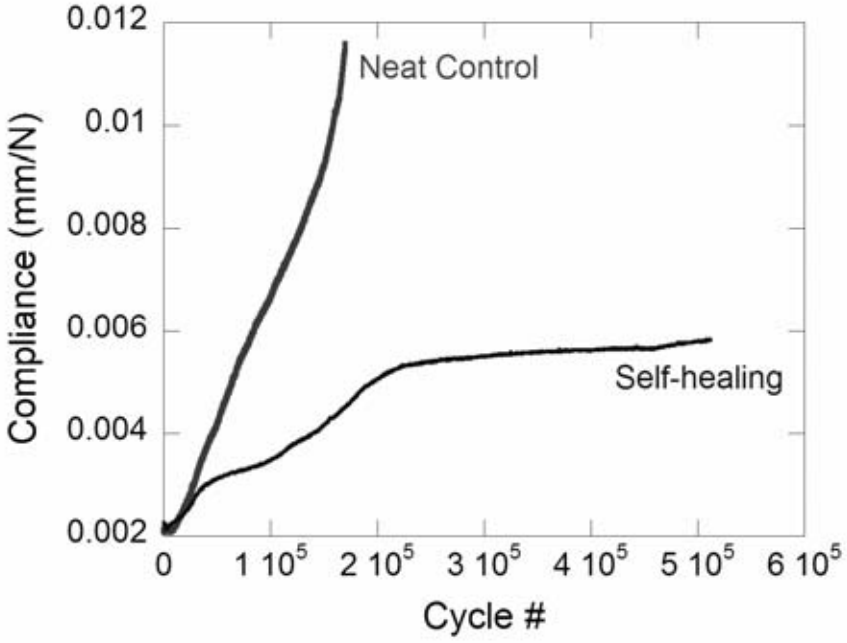

Figure 7-28: Compliance Versus Cycle Number for Neat Control and In-Situ Self-Healing Specimens

7.6 Conclusions & Recommendations

New epoxy adhesives have been developed with the ability to autonomically repair damage. These adhesives show promise for extending service life of composite laminate repairs of metallic structures. The ratio of healed and virgin fracture toughness, or the healing efficiency, was evaluated for WTDCB specimens. Two self-healing adhesives, EPON™ 828/DETA and the commercially available FM®73 were developed. Steel was chosen as the adherend material. For each adhesive system, three types of sample were studied. Reference samples contained neat epoxy and were healed by the manual injection of pre-catalyzed catalyst and monomer. Self-activated specimens contained embedded catalyst and were healed by the manual injection of monomer into the crack face. Finally, *in situ* specimens contained both embedded catalyst and embedded monomer and are representative of the fully incorporated system. For both adhesive systems healing efficiencies of over 50% were achieved for the fully incorporated *in situ* system. In addition to quasi-static fracture studies, the FM®73 adhesive system was studied in fatigue. The *in situ* self-healing system showed a fatigue-life extension of over 200% compared to the neat reference specimen.

With the successful demonstration of the transition of self-healing functionality from laboratory resins (828/DETA) to commercial resin adhesives (FM®73), there are a number of technical

challenges that remain. From a manufacturing perspective the integration of self-healing components (catalyst and microcapsules) into the adhesive resin should be seamless and part of the initial resin film formulation. This task will require partnership and collaboration with an adhesive supplier to accomplish. Secondly, a better method to protect the catalyst in the harsh environment of the base resin and the cure cycle must be found. Some portion of the catalyst is deactivated upon exposure to unreacted amines in the uncured adhesive resin and further deactivation can occur upon exposure to elevated temperatures. Nevertheless, high levels of recovery of fracture toughness was achieved by overcompensating with relatively large concentrations of the catalyst phase (5 wt%). Thirdly, the focus of all mechanical assessment in this study has been mode-I fracture toughness. In practice, mixed-mode conditions would be expected and both mode-II and mixed-mode testing conditions should be explored in terms of self-healing recovery. Finally, in the preliminary fatigue experiments it was possible to demonstrate the potential of self-healing adhesives to prolong fatigue life. A much more thorough study of this effect is warranted in which the effect of issues such as loading frequency, loading magnitude, temperature, and load ratio are fully explored.

References

7.1 White, S. R., N. R. Sottos, P. H. Geubelle, J. S. Moore, M. R. Kessler, S. R. Sriram, E. N. Brown, and S. Viswanathan. 2001. Autonomic healing of polymer composites. *Nature* 409(6822): 794–797.

7.2 Chen, X., F. Wudl, A. Mal, S. Hongbin, S. R. Nutt. 2003. New thermally remendable highly cross-linked polymeric materials. *Macromolecules*. 36: 1802–1807.

7.3 Williams, G., R. Trask, I. Bond. 2007. A self-healing carbon fibre reinforced polymer for aerospace applications. *Composites Part A: Applied Science and Manufacturing.* 38(6): 1525–1532.

7.4 Kessler, M. R., N. R. Sottos, S. R. White. 2003. Self-healing structural composite materials. *Composites Part A: Applied Science and Manufacturing*. 34(8): 743–753.

7.5 Brown, E. N., S. R. White, N. R. Sottos, 2005a. Retardation and repair of fatigue cracks in a microcapsule toughened epoxy composite - Part 1: Manual infiltration. *Composites Science and Technology*. Special Anniversary Issue. 65: 2466–2473.

7.6 Brown, E. N., S. R. White, N. R. Sottos, 2005b. Retardation and repair of fatigue cracks in a microcapsule toughened epoxy composite - Part 2: In situ self-healing", *Composites Science and Technology*. Special Anniversary Issue. 65: 2474–2480.

7.7 Jones, A. S., J. D. Rule, J. S. Moore, N. R. Sottos, S. R. White. 2007. Life extension of self-healing polymers with rapidly growing fatigue cracks. *Journal of the Royal Society Interface*. 4(13): 395–403.

7.8 Cho, S. H., H. M. Andersson, S. R. White, N. R. Sottos, P. V. Braun. 2006. Polydimethylsiloxane-based self-healing materials, *Advanced Materials*. 18: 997–1000.

7.9 Toohey, K.S, N. R. Sottos, J. A. Lewis, J. S. Moore, S. R. White. 2007. Self-healing materials with microvascular networks. *Nature Materials* online. June 10, 2007.

7.10 Kanninen, M. F., C. H. Popelar. 1985. *Advanced Fracture Mechanics*, Oxford: Oxford University Press, 37-42, 158-164.

7.11 Kessler, M. R. 2002. Characterization and performance of a self-healing composite material. Doctor of Philosophy thesis, Department of Theoretical and Applied Mechanics, University of Illinois at Urbana-Champaign.
7.12 Brown, E. N., M. R. Kessler, N. R. Sottos, S. R. White. 2003. In situ poly(urea-formaldehyde) microencapsulation of dicyclopentadiene. *Journal of Microencapsulation*. 20(6): 719–730.

8.0 LIVING INFRASTRUCTURE CONCEPTS PART II: SMART STRUCURES – IN-SITU, DISTRIBUTED HEALTH MONITORING SENSORS

Dennis Roach, Kirk Rackow, and Tony DeLong

8.1 Smart Structures vs. Nondestructive Inspection

The costs associated with the increasing maintenance and surveillance needs of aging structures are rising. The application of distributed sensor systems can reduce these costs by allowing condition-based maintenance practices to be substituted for the current time-based maintenance approach. Through the use of in-situ sensors, it is possible to quickly, routinely, and remotely monitor the integrity of a structure in service [8.1]. This requires the use of reliable structural health monitoring systems that can automatically process data, assess structural condition, and signal the need for human intervention. Prevention of unexpected flaw growth and structural failure can be improved if on-board health monitoring systems exist that could continuously assess structural integrity. Such systems would be able to detect incipient damage before catastrophic failures occurs.

A "smart structure" is one which is sufficiently instrumented so that the data can be synthesized to form an accurate real-time picture of the state of the structure in all its critical aspects. In this case, the absence of disbonds and delaminations indicates that the doubler is able to perform its duty. The absence of cracks indicates that the structure is able to safely continue to operate. The current state of nondestructive inspection – as described in Chapter 5 – involves the manual application of ultrasonic and eddy current NDI methods. While the data presented in this report indicates that manual inspections provide a reliable health monitoring approach, less labor intensive and more frequent structural assessments can be performed via distributed sensor systems. Such health monitoring systems utilize a network of leave-in-place sensors that can assess a structure on a frequent, or even continuous, basis. By positioning sensors along the critical regions of the doubler and surrounding steel structure, as shown in Figure 8-1, it is possible to detect the onset or growth of cracks and disbonds in real time.

Nondestructive Inspection (NDI) – examination of a material to determine geometry, damage, or composition by using technology that does not affect its future usefulness.

- Involves a high degree of human interaction
- Local, focused inspections
- Requires access to area of interest
- Time-based monitoring - applied at predetermined intervals
- Portable and applied to numerous areas.

Structural Health Monitoring (SHM) – "Smart Structures;" use of NDI principles coupled with in-situ sensing to allow for rapid, remote, and even real-time condition assessments; goal is to reduce operational costs and increase life of structures.

- Allows for greater vigilance in key areas – address damage tolerance needs

- Overcomes accessibility limitations, complex geometries, depth of hidden damage
- Eliminates costly and potentially damaging disassembly
- Minimizes human factors with automated sensor deployment and data analysis
- Supports adoption of condition-based maintenance.

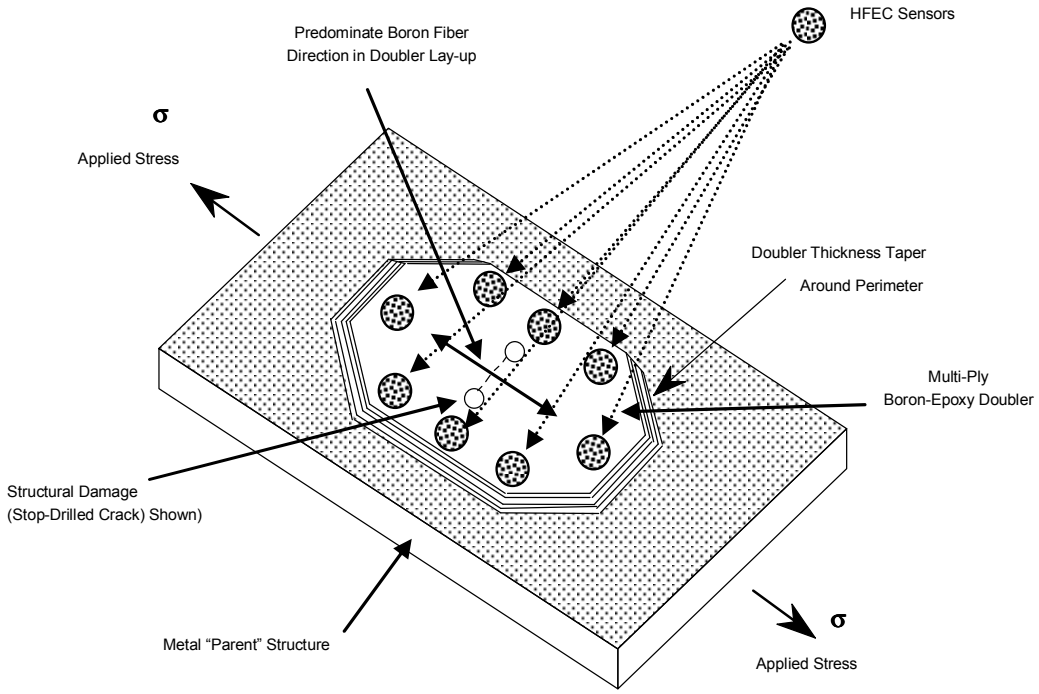

Figure 8-1: Distributed Sensor System to Continuously Monitor the Health of Composite Doubler Repairs and the Parent Steel Structure

8.2 Use and Advantages of In-Situ Structural Health Monitoring

Prevention of unexpected flaw growth and structural failure could be improved if on-board health monitoring systems exist that could continuously assess structural integrity [8.2-8.4]. Reliable, structural health monitoring systems can automatically process real-time data, assess structural condition, and signal the need for human intervention. Such systems would be able to detect incipient damage before catastrophic failures occur. The replacement of our present-day manual inspections with automatic health monitoring would substantially reduce the associated life-cycle costs. Structural Health Monitoring (SHM) systems using distributed sensor networks will allow for condition-based maintenance practices to be substituted for the current time-based maintenance approach. Other advantages of on-board distributed sensor systems are that they can eliminate costly, and potentially damaging, disassembly, improve sensitivity by producing optimum placement of sensors with minimized human factors concerns in deployment, and decrease maintenance costs by eliminating more time-consuming manual inspections. This chapter focuses on developments in mountable and embedded sensors for monitoring composite structures (composite doublers) and how they can be integrated into such a Structural Health Monitoring (SHM) system to guide condition-based maintenance activities.

Whether the sensor network is hardwired to an accessible location within the structure or monitored in a remote, wireless fashion, the sensors can be interrogated easily and often, even in a real-time mode. It is anticipated that the sensors will most likely be examined at discrete intervals; probably at normal maintenance checks. The important item to note is that the ease of monitoring an entire network of distributed sensors means that structural health assessments can occur more often, allowing operators to be even more vigilant with respect to flaw onset. Figure 8-2 depicts a sensor network deployed on an aircraft to monitor critical sites over the entire structure.

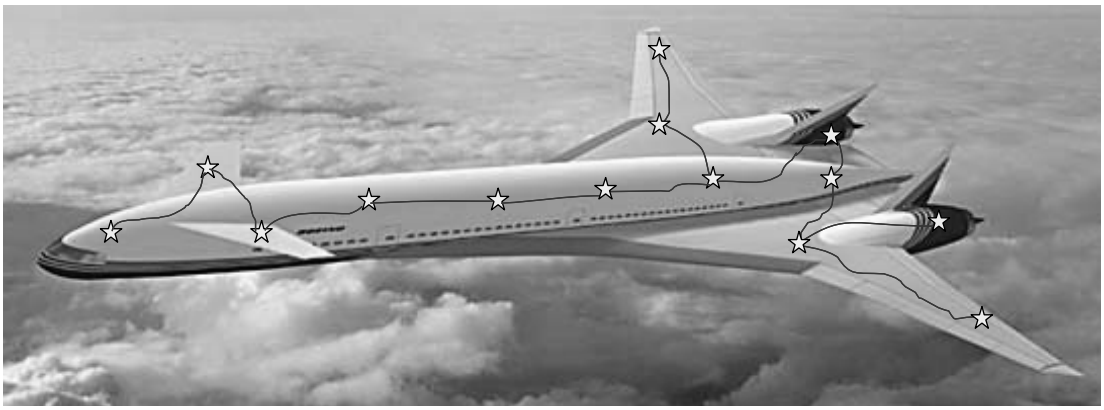

Figure 8-2: Depiction of Distributed Network of Sensors to Monitor Structural Health

Multi-site fatigue damage, hidden cracks in hard-to-reach locations, disbonded joints, erosion, impact, and corrosion are among the major flaws encountered in today's extensive array of aging structures and mechanical assemblies. Furthermore, the extreme damage tolerance and high strength-to-weight ratio of composites have motivated designers to expand the role of advanced materials in industrial structures. These developments, coupled with new and unexpected phenomena, have placed greater demands on the application of advanced nondestructive inspection (NDI) and health monitoring techniques. In addition, innovative deployment methods must be employed to overcome a myriad of inspection impediments stemming from accessibility limitations, complex geometries, and the location and depth of hidden damage. Recent requests for real-time monitoring of structures have produced a niche for active sensor systems.

In addition to mature MEMS devices such as acoustic emission sensors, accelerometers, strain gages, and pressure sensors, recent advances in micro sensors have produced miniature eddy current, ultrasonic, piezoelectric, fiber optic, and other devices that lend themselves more directly to damage detection. Technology exists to co-locate the processing electronics with in-situ sensor networks to produce real-time transmission of data and real–time diagnostics of structural health. When combined in a systems approach that includes sensors to monitor electronics, hydraulics, and avionics, it is possible to produce a prognostic health management architecture that can assist in maintenance scheduling and tracking. This chapter focuses on developments and testing of mountable sensors and how they can be integrated into such a health management system. Specific example applications will be discussed along with issues that must be addressed to realistically deploy leave-in-place sensors. Successful field testing will be

presented to quantify the performance of real-time, health monitoring systems and to highlight their use in guiding condition-based maintenance activities.

The costs associated with the increasing maintenance and surveillance needs of our aging infrastructure are rising at an unexpected rate. The application of distributed sensor systems may reduce these costs by allowing condition-based maintenance practices to be substituted for the current time-based maintenance approach. In the near future, it may be possible to quickly, routinely, and remotely monitor the integrity of a structure in service. A series of expected maintenance functions will already be defined, however, they will only be carried out as their need is established by the health monitoring system [8.3, 8.4].

8.3 Comparative Vacuum Monitoring

Comparative Vacuum Monitoring (CVM) has been developed on the principle that a small volume maintained at a low vacuum is extremely sensitive to any ingress of air [8.5]. Figure 8-3 shows top-view and side-view schematics of the self-adhesive, elastomeric sensors with fine channels on the adhesive face along with a sensor being tested in a lap joint panel. When the sensors are adhered to the structure under test, the fine channels and the structure itself form a manifold of galleries alternately at low vacuum and atmospheric pressure. When a crack develops, it forms a leakage path between the atmospheric and vacuum galleries, producing a measurable change in the vacuum level. This change is detected by the CVM monitoring system shown in Figure 8-4. Embedded sensors may be formed using a load bearing elastomer. This material is able to withstand the high loading stresses that result during the riveting process.

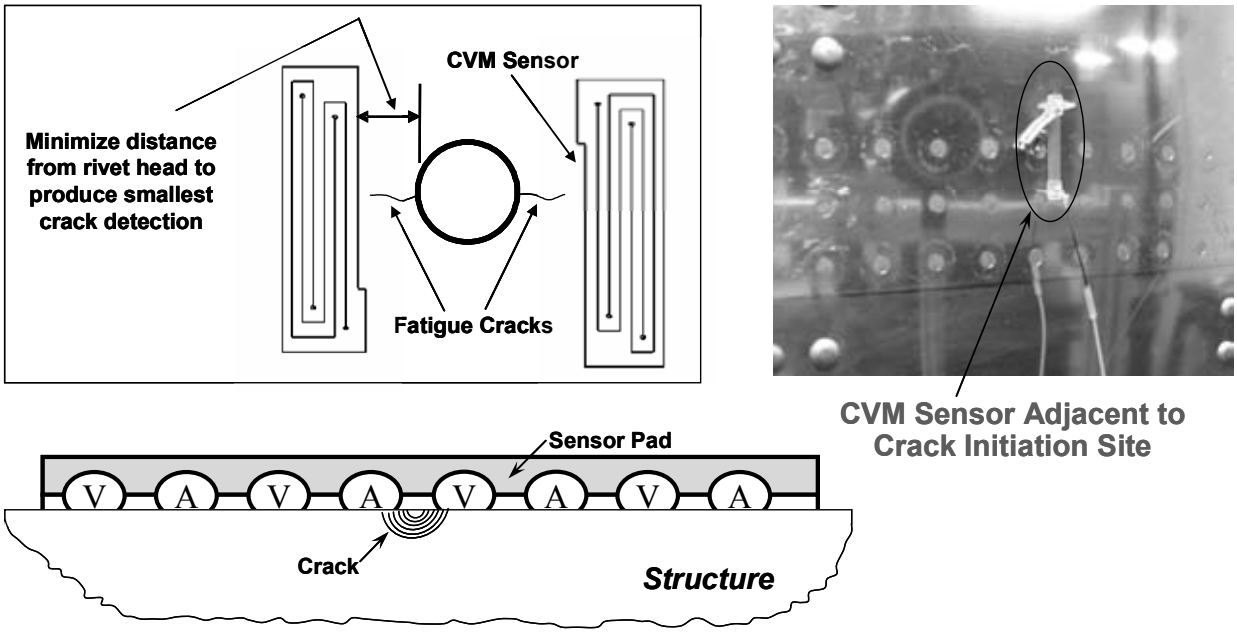

Figure 8-3: Schematics Depicting Operation of CVM Sensor and Polymer Sensor Mounted on Outer Surface of a Riveted Lap Joint

These sensors can be attached to a structure in areas where crack growth is known to occur. On a pre-established engineering interval, a reading will be taken from an easily accessible point on the aircraft. Each time a reading is taken, the system performs a self-test. This inherent fail-safe property ensures the sensor is attached to the structure and working properly. Since the sensor physics is based on pressure measurements, there is no electrical excitation involved. This can be important in areas where electrical signals can create interference (near avionics) or where electrical connections may pose a hazard (fuel tanks).

Figure 8-4 also shows sample CVM sensors mounted on aircraft structure as part of a performance validation effort. A series of 26 sensors have been mounted on structure in four different DC-9, 757, and 767 aircraft in the Northwest Airlines and Delta Air Lines fleet. Some of the sensors were installed over two years ago. Periodic testing was used to study the long-term operation of the sensors in actual operating environments. This environmental durability study compliments the laboratory flaw detection testing described below as part of an overall CVM certification effort.

Sandia Labs, in conjunction with Boeing, Northwest Airlines, Delta Airlines, Structural Monitoring Systems, the University of Arizona, and the FAA, completed validation testing on the CVM system in an effort to adopt Comparative Vacuum Monitoring as a standard NDI practice [8.5, 8.6]. Fatigue tests were completed on simulated aircraft panels to grow cracks in riveted specimens (see Fig. 8-3) while the vacuum pressure within the various sensor galleries were simultaneously recorded. The fatigue crack was propagated until it engaged, and fractured, one of the vacuum galleries such that crack detection was achieved (sensor indicates the presence of a crack by its inability to maintain a vacuum). In order to properly consider the effects of crack closure in an unloaded condition (i.e. during sensor monitoring), a crack was deemed to be detected when a permanent alarm was produced and the CVM sensor did not maintain a vacuum even if the fatigue stress was reduced to zero.

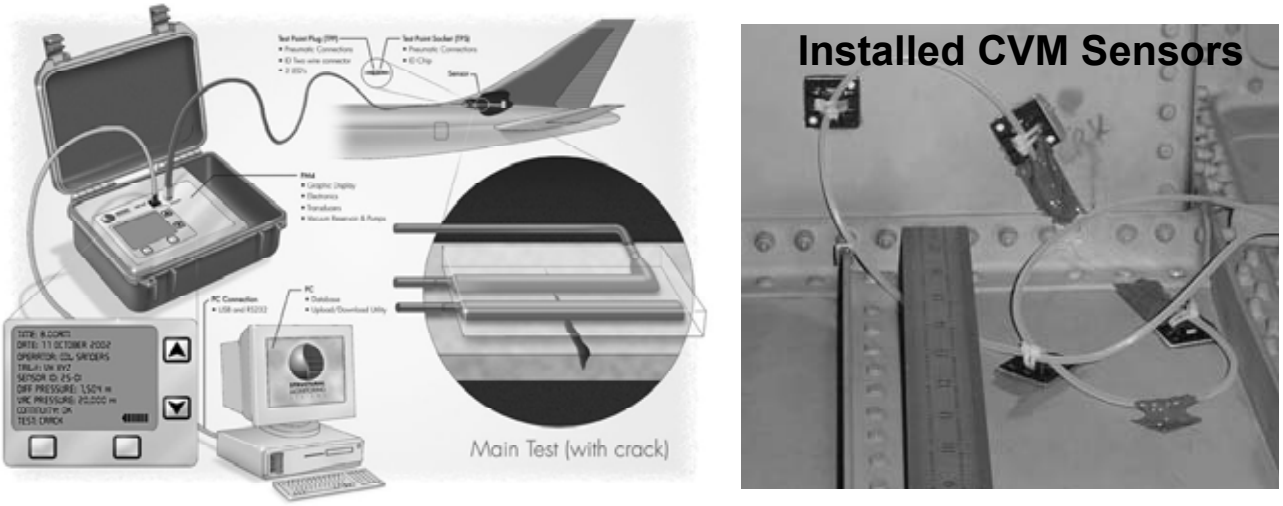

Figure 8-4: Crack Detection Via CVM System and Aircraft Test Installations of Sensors

8.3.1 CVM Validation – Data Analysis Using One-Sided Tolerance Intervals

The CVM sensor is based on the principle that a steady state vacuum, maintained within a small volume, is sensitive to any leakage. A crack in the material beneath the sensor will allow leakage resulting in detection. The data analyzed here consists of cracks that were fatigued cycled in various metal specimens with the direction of growth aligned with the CVM mounted sensors. The data captured is that of the flaw length at the time for which the CVM provided sustainable detection. Thus, the specific flaw would not be considered detectable prior to reaching the stated length, but is considered to continue to be detectable upon further growth. With these assumptions there exists a distribution on the flaw lengths at which detection is first made. In this context, the probability of detection for a given flaw length is just the proportion of the flaws that have a detectable length less than that given length. That is, the reliability analysis becomes one of characterizing the distribution of flaw lengths and the cumulative distribution function is analogous to a Probability of Detection (POD) curve. Assuming that the distribution of flaws is such that the logarithm of the lengths has a Gaussian distribution, we calculate a one sided tolerance bound for various percentile flaw sizes. To do this it is necessary to find factors $K_{n,\gamma,\alpha}$ such that the probability γ is such that at least a proportion $(1-\alpha)$ of the distribution will be less than $X - K_{n,\gamma,\alpha}$ where X and S are estimators of the mean and the standard deviation computed from a random sample of size n. The data captured is the crack length at CVM detection. From the reliability analysis a cumulative distribution function is produced to provide the maximum likelihood estimation (POD). This stems from the one-sided tolerance bound for the flaw of interest using the equation:

$$\text{POD}_{\text{95\% Confidence}} = X + (K_{n,0.95,\alpha})(S) \qquad (8\text{-}1)$$

Where,

X = Mean of detection lengths
K = Probability factor (~ sample size, confidence level desired)
S = Standard deviation of detection lengths
n = Sample size
1- α = Detection level

8.3.2 CVM Performance Testing on Thin Aluminum Structures

This test program produced a statistically-relevant set of crack detection levels for 0.040" and 0.100" thick panels in both the bare and primed configurations. Figure 8-5 shows the fatigue test set-up used to grow cracks and a close-up photo of the CVM sensors monitoring cracks initiating from a center hole. Figure 8-6 shows a photo of a fatigue crack as it engages the first vacuum gallery of a CVM sensor. The pressure rise, corresponding to a rupture in the gallery and a leakage path to atmospheric pressure, is shown on the right side of Figure 8-6. The large increase in the pressure corresponds to crack detection. In actual field measurements, the plot shown in Figure 8-7 would be produced. One signal (lower curve) corresponds to vacuum levels produced when there is no crack indication and the other signal (upper curve) occurs when a

vacuum is not achievable. This latter signal is produced when the CVM detects a crack. Such a curve with a pressure level of at least 300 Pa must be produced when the structure is unloaded.

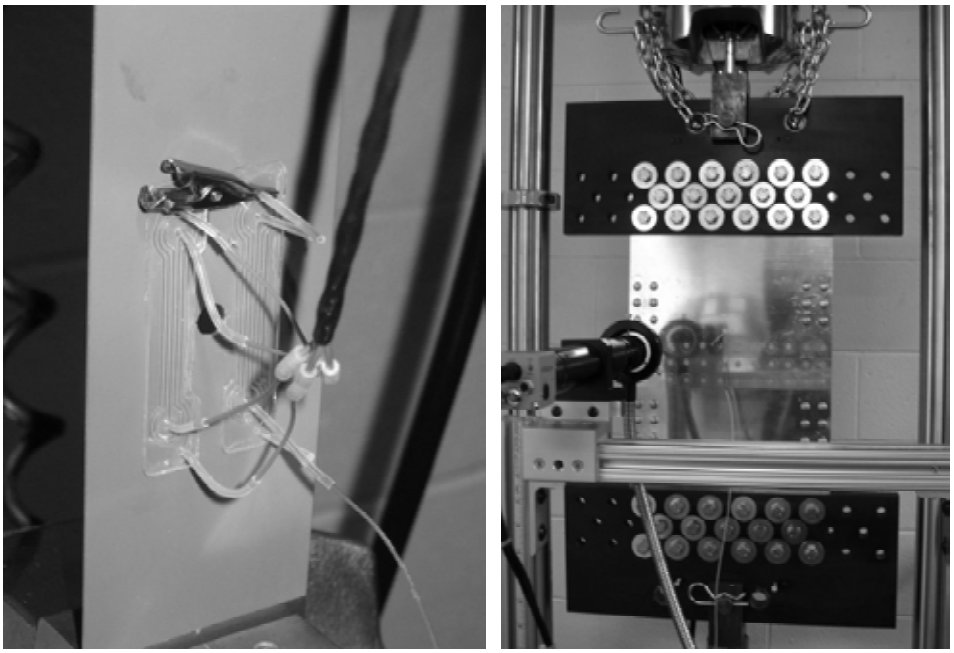

Figure 8-5: CVM Sensors Monitoring Crack Growth on Aluminum Test Specimens

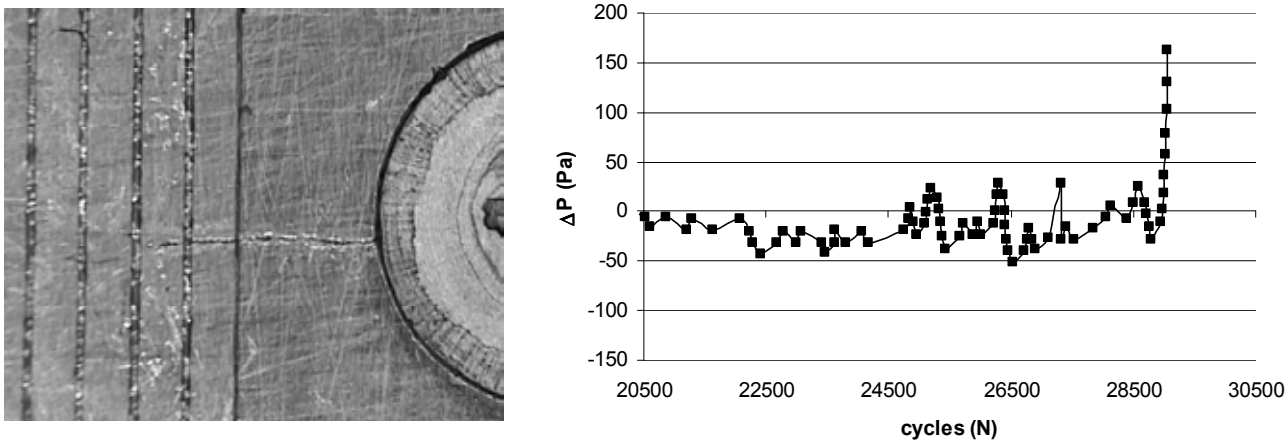

**Figure 8-6: Fatigue Crack Crossing Into CVM Galleries;
Differential Pressure Shown as a Function of Cycle Number
(Pressure Increase Caused by Crack Reaching a Gallery is Clearly Indicated)**

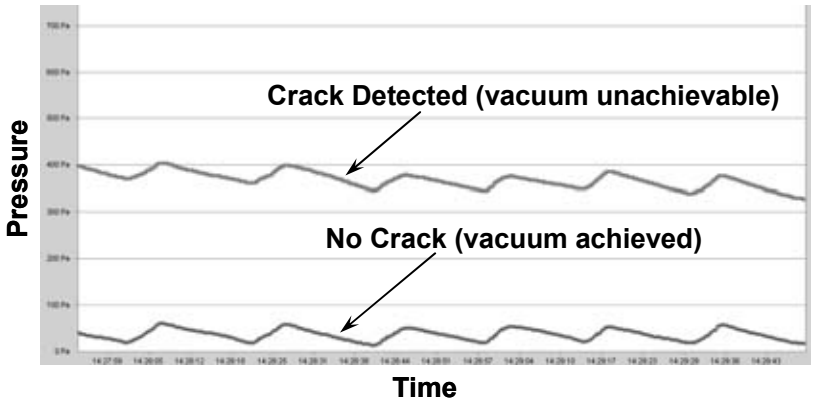

Figure 8-7: Typical Pressure vs. Time Plots from CVM Sensors Indicating 'No Crack' and 'Crack Detection'

Results to date have revealed crack detection lengths – permanent alarm after the fatigue crack engages the CVM sensor – for the bare and primed 0.040" thick panels. Tables 8-1 and 8-2 summarize some of the results. Table 8-2 lists CVM crack detection results for 0.040" thick aluminum plate in both a coated (primer) and uncoated condition. Crack detection lengths ranged from 0.002" to 0.020" in length. Fatigue tests have shown that pressure levels in excess of 300 Pa were measured during fatigue testing however, the compressive residual stresses at the tip of a fatigue crack could allow a vacuum to be produced when the specimen was unloaded. The numbers presented in Tables 8-1 and 8-2 correspond to *permanent* alarm levels for cracks engaging CVM sensors and the structure in an unloaded condition.

The 90% POD level for crack detection on 0.1" thick aluminum - calculated from equation (8-1) – is also listed in Table 8-1. Due to the limited number of data points, the reliability calculations induce a penalty by increasing the magnitude of the K (probability) factor. As a result, the overall POD value (95% confidence level) for CVM crack detection in 0.100" thick aluminum skin is 0.023". This POD curve is plotted in Figure 8-8. As the number of data points increases, the K value will decrease and the POD numbers could also decrease. In this particular instance, it was desired to achieve crack detection before the crack reached 0.100" in length so this goal was achieved. Table 8-3 summarizes the 90% POD levels (95% confidence level) for CVM crack detection for the array of thin-walled aluminum plates tested.

CVM Crack Detection on 0.100" th. Aluminum Plate					
Panel	Fastener Crack Site	Number of Fatigue Cycles	Crack Length at CVM Detection (growth after install in inches)	PM-4 Read-out (Pasm)	PM-4 Indicate Crack (Y or N)
1	1-L	3505	0.007	2123	Y
1	1-R	3205	0.007	1938	Y
1	2-L	5350	0.010	2251	Y
1	2-R	5550	0.011	1954	Y
1	3-L	6650	0.009	4526	Y
1	3-R	7099	0.016	7099	Y
2	1-L	3100	0.011	1786	Y
2	1-R	3400	0.014	1707	Y
2	2-L	5300	0.005	2383	Y
2	2-R	5300	0.016	2204	Y
3	1-L	4475	0.019	1790	Y
3	1-R	4825	0.013	1904	Y
3	2-L	7025	0.008	2100	Y
3	2-R	7878	0.010	4302	Y

90% POD Level	False Calls
0.023"	0

Table 8-1: CVM Crack Detection Values from 0.100” Aluminum Plate

Unpainted 0.040" th. Skin			0.040" Skin with Primer Coating		
Panel Number	Fastener Crack Site	Crack Length at CVM Detection (growth after install in inches)	Panel Number	Fastener Crack Site	Crack Length at CVM Detection (growth after install in inches)
4017	8R	0.003	4018	5R	0.002
4017	6R	0.030	4018	6R	0.007
4017	5R	0.007	4018	7R	0.010
4017	7R	0.002	4018	5R(2)	0.009
4011	7R	0.009	4018	6L	0.005
4011	7L	0.005			
4014	7R	0.004			
4015	7L	0.002			

Table 8-2: Cracks Lengths Detected by CVM Sensors on 0.040” Thick Skins

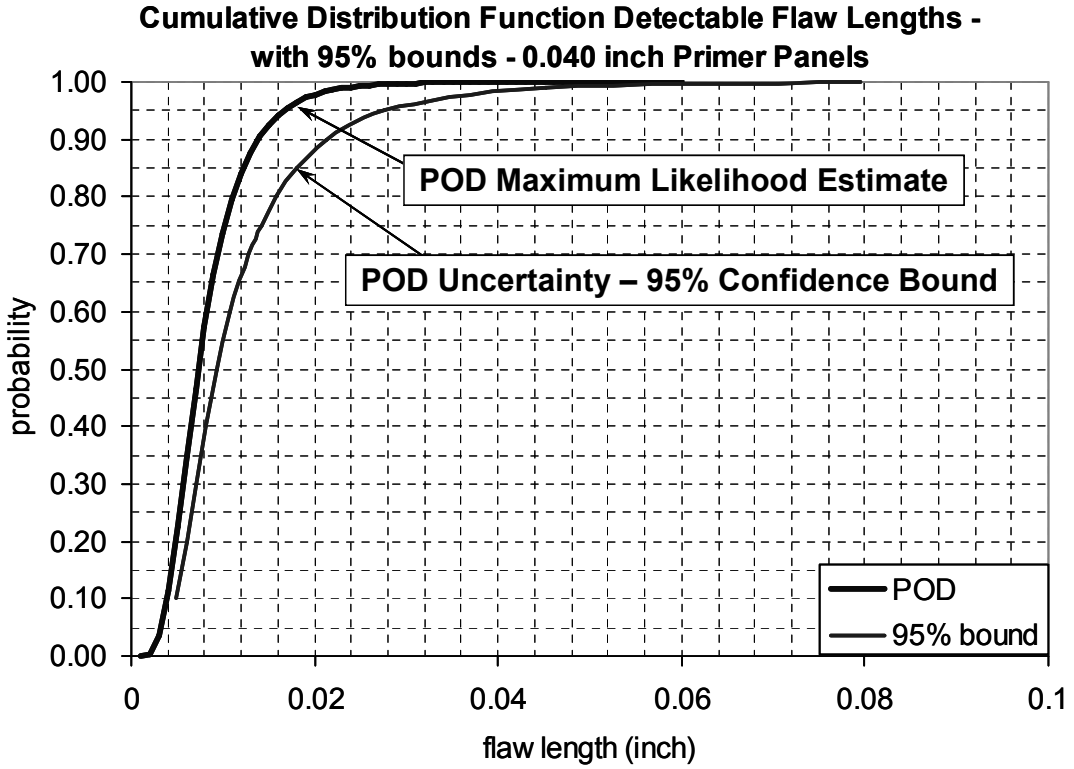

Figure 8-8: Typical Probability of Crack Detection Curves Generated by CVM Data and Data Analysis Using One-Sided Tolerance Intervals

Material	Thickness	Coating	90% POD for Crack Detection
2024-T3	0.040"	bare	0.049"
2024-T3	0.040"	primer	0.021"
2024-T3	0.071"	primer	0.042"
2024-T3	0.100"	bare	0.272"
2024-T3	0.100"	primer	0.090"
7075-T6	0.040"	primer	0.026"
7075-T6	0.071"	primer	0.033"
7075-T6	0.100"	primer	0.023"

Table 8-3: Summary of Raw Crack POD Levels for CVM Deployed on Different Materials, Surface Coatings, and Plate Thicknesses

8.3.3 CVM Performance on Thick Steel Structures

The results sited above are valuable for thin-walled structures such as those used in aircraft, automotive, and some pipeline construction. However, many civil structures use thick steel members. Earlier studies revealed that the thickness of the plate can affect CVM performance so a second round of tests looked at CVM crack detection in thick-walled structures. It should be noted that aircraft use thinner materials and have crack detection requirements of 0.050" to 0.100" in length. Civil structures contain thicker materials and have higher safety factors. Thus, these structures can tolerate longer cracks and their crack detection requirements are in the range of 0.5" to 1" in length. CVM sensors can be fabricated with different gallery sizes in order to accommodate various sensitivity requirements.

Figure 8-9 shows the installation of a CVM sensor on a 0.375" thick steel (ASTM 572) plate. The seeded fatigue crack along the edge of the specimen is visible. These test specimens were then exposed to tension-tension fatigue tests in order to propagate the crack into the CVM sensor. Figures 8-10 and 8-11 show the overall test set-up along with the equipment used to monitor the CVM sensors.

Compressive stresses around the tip of a fatigue crack create a tight tip when the load is removed. As a result, the initial engagement of a crack with a CVM sensor may induce a high pressure reading (crack detection) when the structure is under load; however, the compressive residual stresses at the tip of a fatigue crack could allow a vacuum to be produced when the specimen was unloaded. Therefore, crack detection can be achieved much earlier if the sensors can be monitored while the structure is in use. In the case of real-time monitoring for the steel plate test series, CVM crack detection results for the unloaded and loaded steel structure are summarized in Tables 8-4 and 8-5, respectively.

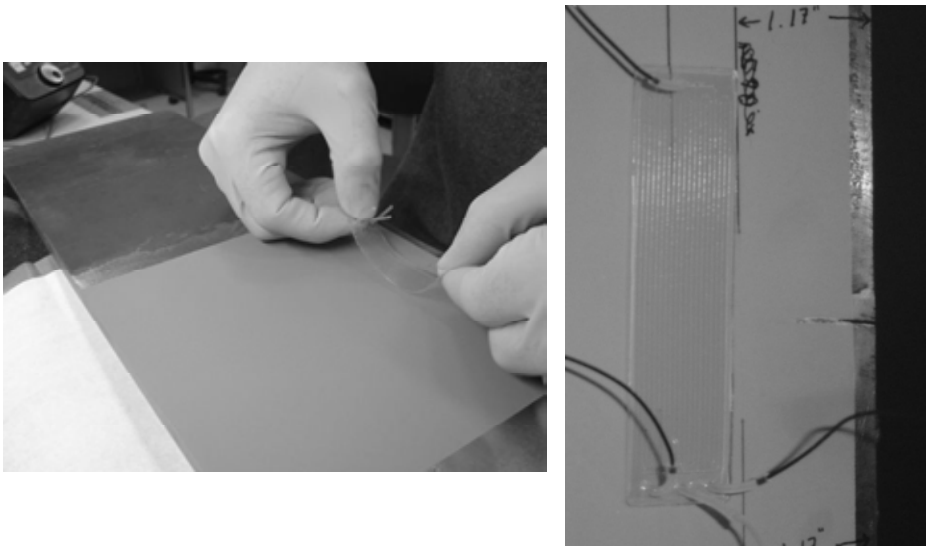

Figure 8-9: Installation of CVM Sensor on Primed Steel Surface and Close-Up of Fatigue Crack Approaching Sensor

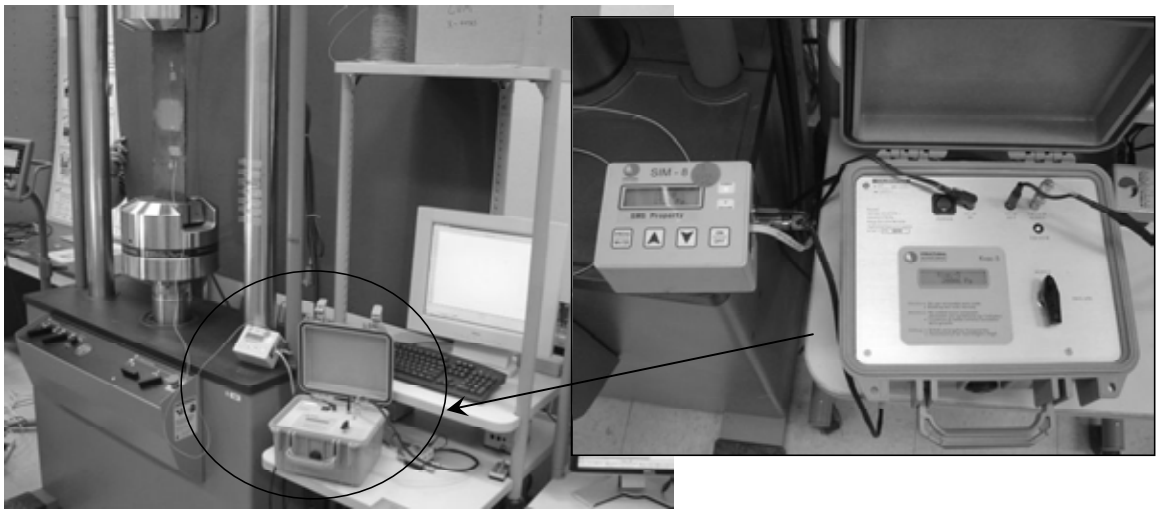

Figure 8-10: Overall Set-Up for Monitoring Crack Growth with CVM Sensor System and Close-Up of Sensor Interrogation Equipment

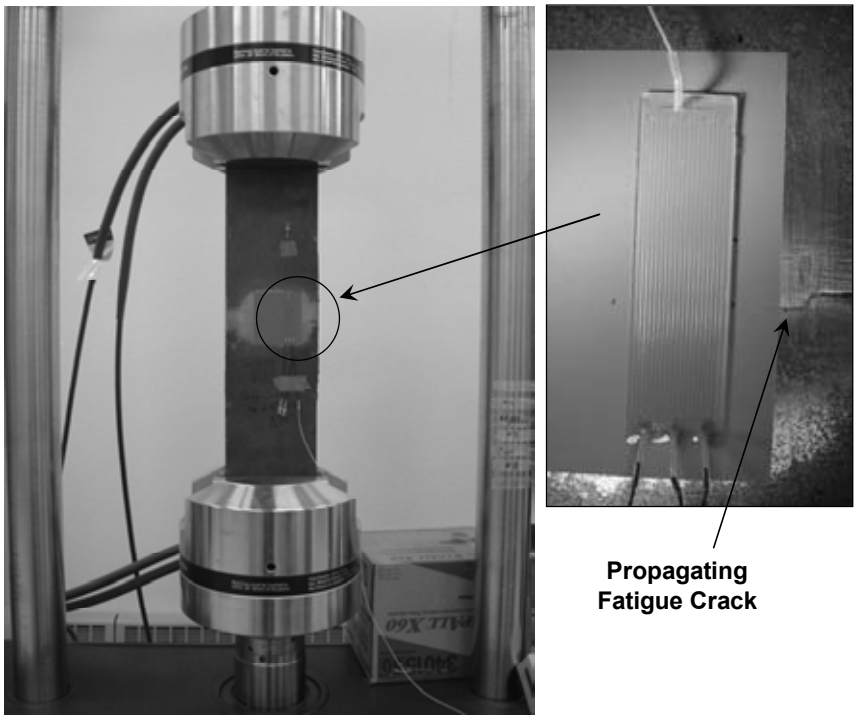

Figure 8-11: Fatigue Test of Steel Specimen to Propagate Crack into CVM Sensor (inset)

CVM Set-Up					CVM Crack Detection with No Load			
Test Specimen	Sensor	Initial Crack Length (in.)	Initial Sensor Location [Distance from Specimen Edge] (in.)	Baseline CVM Pressure Reading [No Crack Engagement Condition] (Pa)	Cycles at Permanent CVM Crack Detection [No Load]	CVM Pressure Reading at Crack Detection [No Load] (Pa)	Total Crack Length at Permanent CVM Crack Detection [No Load] (in.)	Crack Growth for CVM Crack Detection [Engagement with CVM Sensor] (in.)
SYN FAT 24	1	1.10	1.10	1,580	7,626	5,300	1.48	0.380
SYN FAT 24	2	1.48	1.52	1,435	9,797	10,710	1.60	0.080
SYN FAT 24	3	1.90	1.92	1,460	10,768	19,693	2.02	0.100
SYN FAT 19	4	1.17	1.22	1,488	135,000	2,900	1.54	0.315
SYN FAT 19	5	1.55	1.63	1,500	143,358	2,300	1.81	0.175
SYN FAT 19	6	1.81	1.87	1,500	146,000	4,950	1.93	0.060
SYN FAT 22	7	0.94	1.15	1,740	180,000	2,580	1.48	0.330
SYN FAT 22	8	1.48	1.53	1,363	188,500	2,580	1.70	0.170
SYN FAT 22	9	1.70	1.76	1,530	192,000	3,427	1.83	0.075
SYN FAT 21	10	1.00	1.09	1,510	84,000	3,000	1.50	0.410
SYN FAT 21	11	1.50	1.53	1,433	91,500	2,500	1.81	0.275
SYN FAT 23	12	1.45	1.50	1,457	5,000	2,500	1.81	0.310
SYN FAT 23	13	1.81	1.84	1,570	8,500	2,400	1.98	0.135

Table 8-4: Permanent (No Load) Crack Detection Produced by CVM Sensors on Steel Plate

CVM Set-Up					CVM Crack Detection with No Load			
Test Specimen	Sensor	Initial Crack Length (in.)	Initial Sensor Location [Distance from Specimen Edge] (in.)	Baseline CVM Pressure Reading [No Crack Engagement Condition] (Pa)	Cycles at Initial CVM Crack Detection [Under Load]	CVM Pressure Reading at Crack Detection [Under Load] (Pa)	Total Crack Length at Initial CVM Crack Detection [Under Load] (in.)	Crack Growth for CVM Crack Detection [Engagement with CVM Sensor] (in.)
SYN FAT 24	1	1.10	1.10	1,580	2,137	16,500	1.15	0.050
SYN FAT 24	2	1.48	1.52	1,435	9,451	19,600	1.57	0.050
SYN FAT 24	3	1.90	1.92	1,460	10,698	12,250	1.99	0.070
SYN FAT 19	4	1.17	1.22	1,488	115,000	11,610	1.29	0.065
SYN FAT 19	5	1.55	1.63	1,500	139,843	17,000	1.68	0.050
SYN FAT 19	6	1.81	1.87	1,500	145,800	19,000	1.92	0.045
SYN FAT 22	7	0.94	1.15	1,740	150,839	7,000	1.20	0.050
SYN FAT 22	8	1.48	1.53	1,363	184,412	17,800	1.59	0.060
SYN FAT 22	9	1.70	1.76	1,530	191,315	17,000	1.80	0.045
SYN FAT 21	10	1.00	1.09	1,510	44,800	3,000	1.15	0.060
SYN FAT 21	11	1.50	1.53	1,433	88,100	19,000	1.60	0.070
SYN FAT 23	12	1.45	1.50	1,457	2,000	11,000	1.56	0.060
SYN FAT 23	13	1.81	1.84	1,570	6,400	20,000	1.88	0.040

Table 8-5: Initial (Under Load) Crack Detection Produced by CVM Sensors on Steel Plate

For the loaded structure, CVM crack detection occurred when the fatigue cracks ranged from 0.040" to 0.070" in length (Table 8-5). This would correspond to the ability of the CVM sensor to monitor cracks in real-time while the structure is in use. For the unloaded condition, CVM crack detection occurred when the fatigue cracks ranged from 0.060" to 0.380" in length (Table

8-4). Note that the data spread is much larger for this condition due to the varying state of the compressive stresses at the end of the fatigue crack. However, regardless of whether the sensor monitoring is completed during a loaded or unloaded condition, the results indicate that CVM sensors could reliably detect fatigue cracks well before they reach 0.5" in length.

8.4 Piezoelectric Transducers (PZT)

Prime candidates for sensors based on active-material principles utilize thin piezoelectric wafers of 0.125"-0.25" diameter with thicknesses of 0.010" - 0.030". They can be easily attached to existing aging structures without changing the local and global structural dynamics. PZT sensors can also be embedded inside composite structures to closely monitor for internal flaws. These sensors can act as both transmitters and receptors. As transmitters, piezoelectric sensors generate elastic waves in the surrounding material. As receptors, they receive elastic waves and transform them into electric signals. It is conceivable to imagine arrays of active-sensors, in which each element would take, in turn, the role of transmitter and receptor, and thus scan large structural areas using ultrasonic waves [8.8]. The structural interrogation strategies using active piezoelectric sensors are two fold:

(a) For local area detection, the electro-mechanical (E/M) impedance method is applied to detect changes in the point wise structural impedance resulting from the presence and propagation of structural damage.
(b) For large area detection, wave propagation techniques using Lamb and Love waves methods are used to identify zones in the monitored area that have undergone changes in their structural integrity.

In the high-frequency E/M impedance approach, pattern recognition methods are used to compare impedance signatures taken at various time intervals and to identify damage presence and progression from the change in these signatures. In the Lamb/Love waves approach, the acousto-ultrasonic methods identifying changes in transmission velocity, phase, and additional reflections generated from the damage site are used. Both approaches can benefit from the addition of artificial intelligence neural network algorithms that can extract damage features based on a learning process.

Mountable PZT Networks and Lamb Wave Interrogation Methods - This structural health monitoring approach uses a built-in network of piezoelectric transducers embedded in a think dielectric carrier film. The SHM system included the PZT network connected to portable, diagnostic hardware and software developed by Acellent Technologies, Inc. The system performs in-situ monitoring, data collection, signal processing, and real-time data interpretation to produce a two-dimensional image of the structure being interrogated. The Acellent software instructs the actuators to generate pre-selected diagnostic signals and transmit them to neighboring sensors. Multiple diagnostic wave types can be generated including 3-peak, 5-peak, and 10-peak narrow band frequency waveforms, chirp, random, and user defined excitations. The software links each sensor with its neighbors to form a web, or network, covering the structure. The system then collects the total set of responses from each of the sensor sets as each PZT takes its turn as the actuator. Changes in the Lamb waves generated within the structure are used in concert with triangulation methods to detect the presence of structural anomalies and to determine the size and location of the flaws.

Damage Identification through Elastic Wave Propagation - The wave propagation approach uses the pitch-catch method for detecting damage in a structure. Acousto-ultrasonic methods are used to identify changes in wave transmission. Figure 8-12 shows some of the wave motion from sensors (1) and (9) when they are used as the source of excitation for the structure. The mechanical vibration is introduced into the structure by the PZT element and travels by wave motion through the test piece at the velocity of sound, which depends on the material. If the pulses encounter a reflecting surface, some or all of the energy is reflected and monitored by adjacent PZT sensors in the network. The reflected beam, or echo, can be created by any normal (e.g. in multi-layered structures) or abnormal (flaw) interface. Figure 8-12 highlights the interaction of the UT waves with a flaw within the structure. The degree of reflection depends largely on the physical state of the materials forming the interface. Cracks, delaminations, shrinkage cavities, pores, disbonds, and other discontinuities that produce reflective interfaces can be detected. Complete reflection, partial reflection, scattering, or other detectable effects on the ultrasonic waves can be used as the basis for flaw detection.

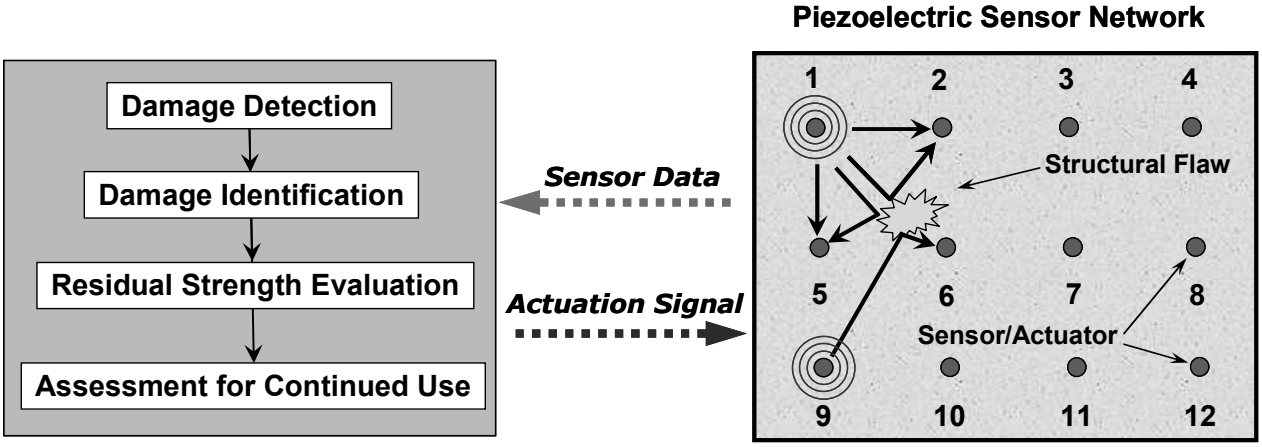

Figure 8-12: Flaw Detection Using the Wave Propagation Method

Validation Testing of PZT Sensor Network - In the first test series, Piezoelectric Transducers (PZT) were built by embedding PZT materials in a thin dielectric carrier film. The spacing of the active PZT elements and the shape of the film were determined by the need to monitor local and global damage in the composite laminate and steel substructure. The PZT sensor network was laid out in custom configurations to detect damage in critical regions and provide an image of the structure in the area of the sensor network. The network of PZT sensors was deployed to assess bonded joints and crack growth in a composite doubler repair installation. Figures 8-13 and 8-14 show schematics and photos of the Boron-Epoxy laminate repair on a metal parent structure along with the set of PZTs distributed over the structure to be monitored. Note that the network of sensors/actuators is embedded in a custom polyamide film to allow for accurate placement of the network and eliminating the need for each sensor to be installed individually. The test specimen, containing engineered disbonds and a central crack, was subjected to constant-amplitude fatigue loads with maximum stresses in excess of 80% of yield levels for the ASTM A36 steel plate (thickness = 0.188"). A time-varying electrical signal was input to the actuators/sensors. This caused a propagating stress wave to emanate from the actuator and travel

through the material for detection by the neighboring sensors. These signals were then compared with previously recorded baseline test signals to identify the location and extent of damage or other structural anomaly.

Similar to conventional ultrasonic testing, the PZT data analysis can include one or more of the following measurements: time of wave transit (or delay), path length, frequency, phase angle, amplitude, and angle of wave deflection (reflection and refraction). In this test series, the pitch-catch method studied the transmission of sound waves as they traveled from each actuator to all other receiving sensors. The sum total of received beams were then analyzed to define the presence and location of flaws. In order to optimize flaw detection, a series of excitation frequencies were used: 50 KHz, 200 KHz, 350 KHz, and 500 KHz. Overall test results revealed that disbond flaws were most strongly detected with the lower, 50 KHz excitation while the crack growth was monitored best with the highest, 500 KHz excitation. Figure 8-15 shows raw PZT response data produced during the Lamb wave interrogation method. Signal attenuations, corresponding to disbonds between the laminate and parent skin, are apparent. When all of the signals are analyzed with the Acellent imaging software and flaw locations are determined by using the time base and triangulation methods, a two dimensional image of the disbond flaws was produced. Figure 8-16 shows the engineered disbonds in the test specimen along with the image produced by the PZT sensor network. Note that both disbond flaws were clearly imaged even though one is a weak bond produced by a mold release agent and one is a complete disbond produced by a Teflon insert.

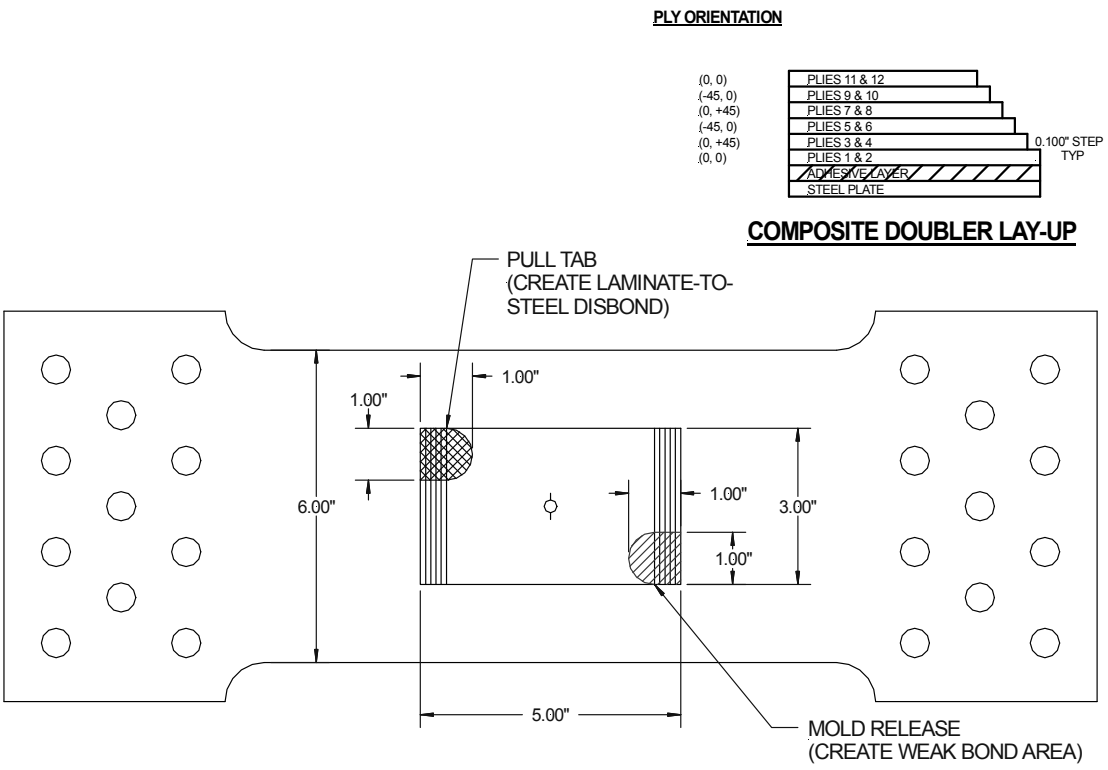

Figure 8-13: Composite Doubler Repair Test Coupon with Disbond and Fatigue Crack Flaws for Evaluation of PZT and Fiber Optic Sensors

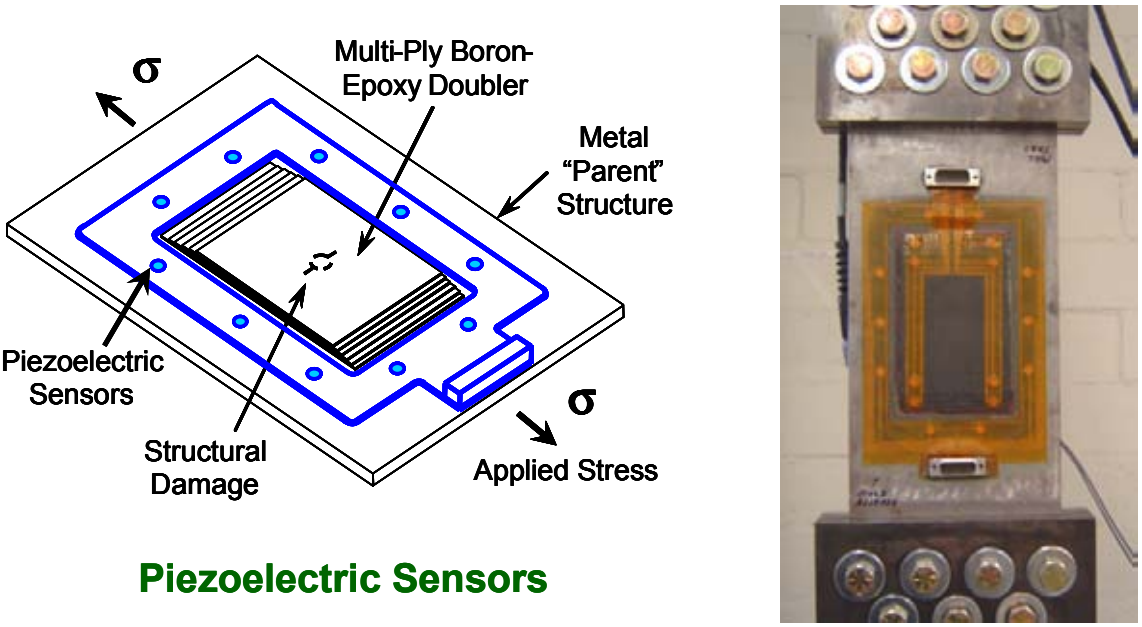

Figure 8-14: Set of Piezoelectric Sensors Used to Monitor Crack Growth and Disbonds in a Composite Doubler Bonded to a Metal Plate

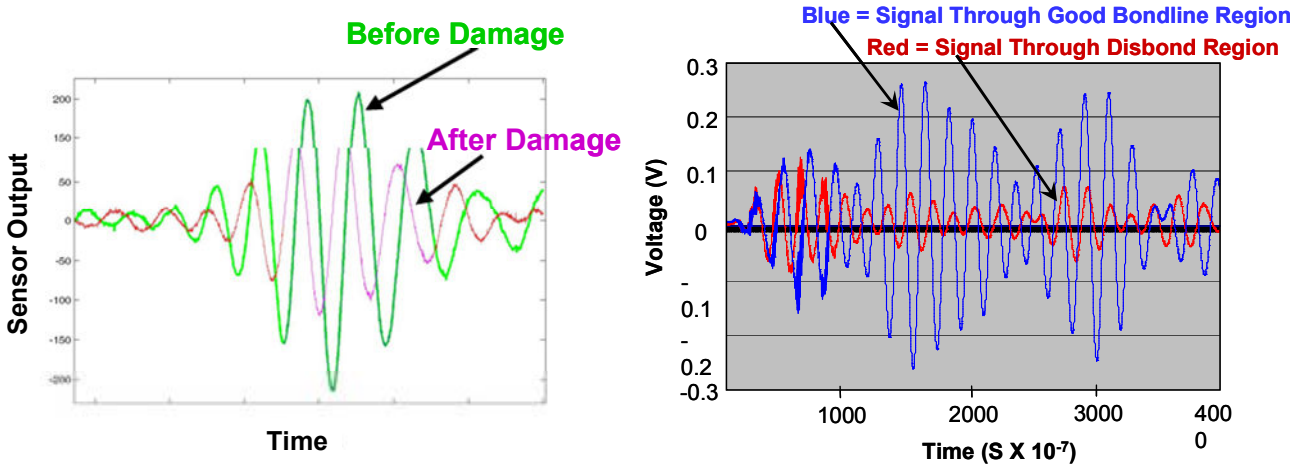

Figure 8-15: Sample Signals Observed by PZTs During 50 KHz Lamb Wave Interrogation Showing the Attenuation Corresponding to Disbonds in the Structure

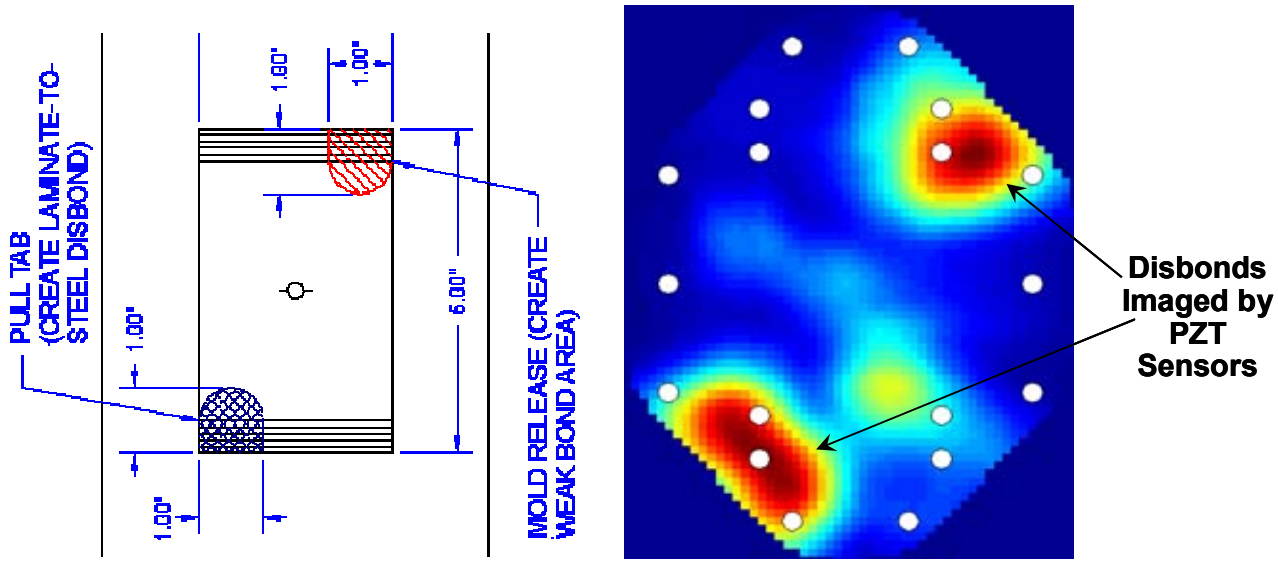

Figure 8-16: Color-Coded Image of Disbond Flaws Produced by the PZT Sensor Network

Crack detection and growth was monitored using the same approach. PZT data was acquired at discrete intervals during the crack growth process. In addition, eddy current and microscopic inspections were conducted to measure the crack lengths at each cycle count. Figure 8-17 shows PZT response signals before and after crack growth occurred into the sensor path. A set of images produced by the PZT network are shown in Figure 8-18. The crack growth (two fatigue cracks emanating from a central hole) can be clearly seen. The PZT crack growth data was analyzed further to produce crack length predictions. The data analysis software contains an algorithm that allows for system learning. After inputting several crack lengths to match with the PZT data at discrete fatigue intervals, it was possible for the system to predict all subsequent crack lengths using the PZT data alone. Table 8-6 compares the crack lengths predicted by the PZT sensor network with the crack lengths determined from eddy current and microscopic measurements. The PZT predictions were all within 5% of the actual crack lengths for data taken at max load (34 kips) and, for the most part, within 10% of actual values for PZT data taken in the unloaded condition.

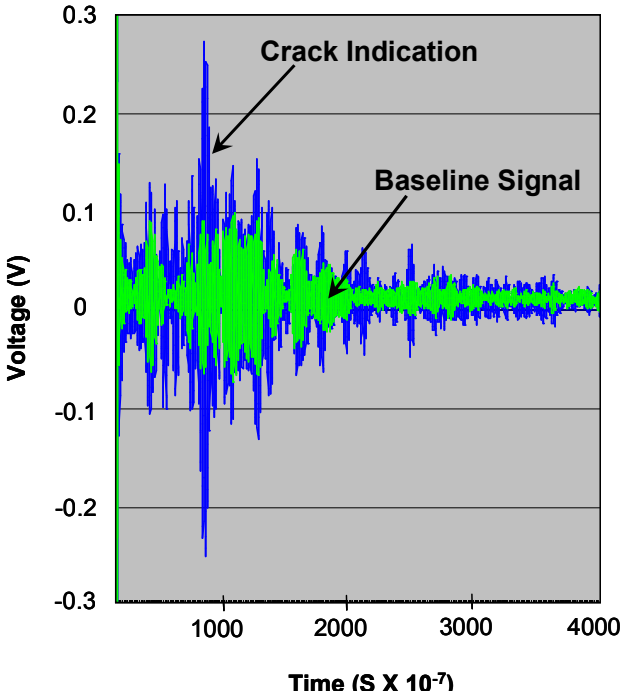

Figure 8-17: Sample PZT Signals Showing the Indication of a Fatigue Crack with a 500KHz Excitation

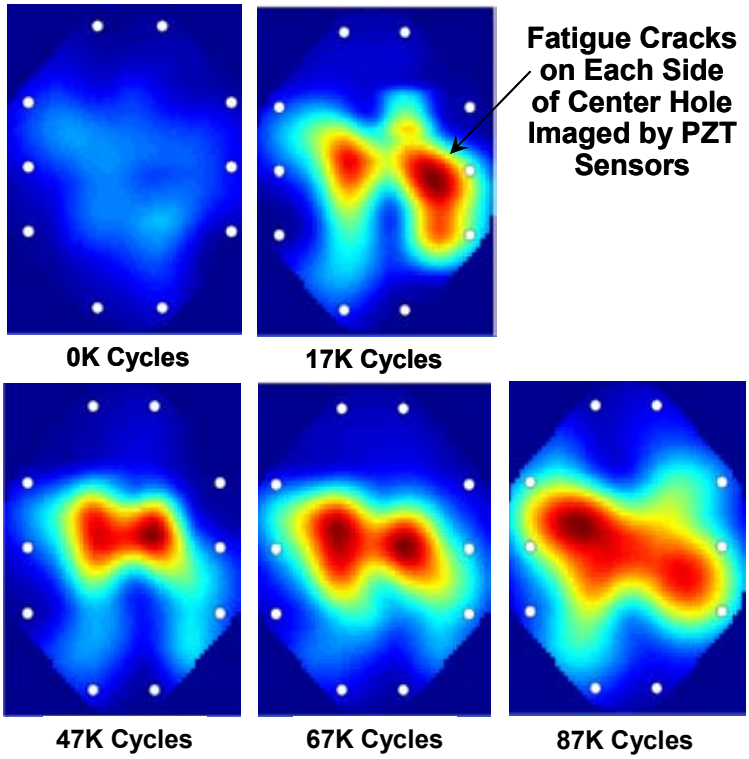

Figure 8-18: Color-Coded PZT Images Showing Crack Growth

Composite Doubler with PZT Health Monitoring			
Fatigue Cycles	**Measured Total Crack Length**	**Estimated Crack Length from PZT Sensor Data (0 lbs. load)**	**Estimated Crack Length from PZT Sensor Data (34 kips load)**
Specimen 1 - Unflawed Composite Doubler			
0	0.00		
26,218	0.32	PZT Learning Data	PZT Learning Data
47,000	0.70	PZT Learning Data	PZT Learning Data
67,000	1.50	1.274	1.385
87,000	2.44	1.956	2.367
Specimen 2 - Composite Doubler with Disbond Flaws			
0	0.00		
19252	0.16	PZT Learning Data	PZT Learning Data
29274	0.32	PZT Learning Data	PZT Learning Data
38064	0.48	PZT Learning Data	PZT Learning Data
51576	0.80	PZT Learning Data	PZT Learning Data
60438	1.08	0.981	1.099
66439	1.34	1.35	1.349
76444	1.76	1.567	1.762
82446	2.02	1.909	2.08

Table 8-6: Comparison of Crack Lengths Predicted by PZT Sensors with Actual Crack Lengths Measured Using Eddy Current and Microscopic Methods

PZT Evaluations on Steel Specimens with Edge Cracks – Similar tests were conducted using a custom array of PZT sensors to monitor a 0.375" thick ASTM 572 steel plate. The test specimen and PZT network are shown in Figure 8-19 and 8-20. This specimen is the same as the general composite doubler performance specimens described in Chapter 4. While assessing the crack mitigation capabilities and durability of the composite repair, it was possible to determine the crack and disbond detection capability of the PZT system. The three engineered disbond flaws and the center fatigue crack placed in the specimen prior to repair are indicated in Figs. 8-19 and 8-20. Disbond flaws were placed in each end of the patch-to-steel bondline at the critical load transfer region and a third disbond was placed over the fatigue crack to degrade the patch protection around the crack. These flaws were added to: 1) determine the damage tolerance of composite doubler repairs in poor installation conditions, and 2) study the ability of sensor networks to detect and accurately track flaw growth.

Figures 8-21 and 8-22 show the installation process used to place the PZT network on the structure. A two-part epoxy was used to bond the PZT film to the steel and it was cured at 140^{o}F while applying vacuum pressure to the film. Since the PZT transducers must act as excitation sources, as well as signal receivers, it is necessary for them to be bonded to the structure they are monitoring. When the PZTs are driven with a voltage, they expand and contract at the driving frequencies. The strong bond allows the PZTs to transfer this strain energy into the structure which results in the generation of the Lamb waves described above.

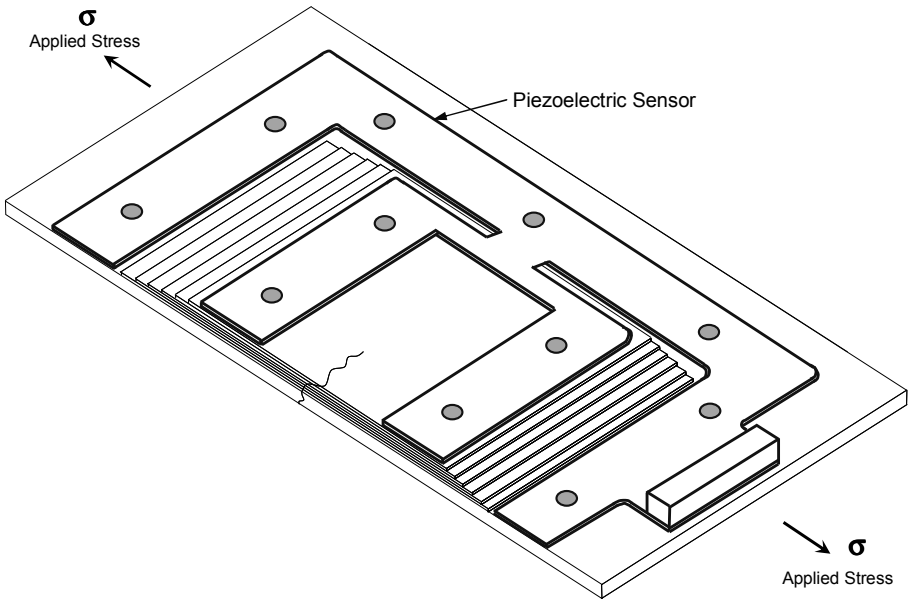

Figure 8-19: General Layout of PZT Network Over and Around Composite Doubler Repair for Edge Doubler Test Series 2

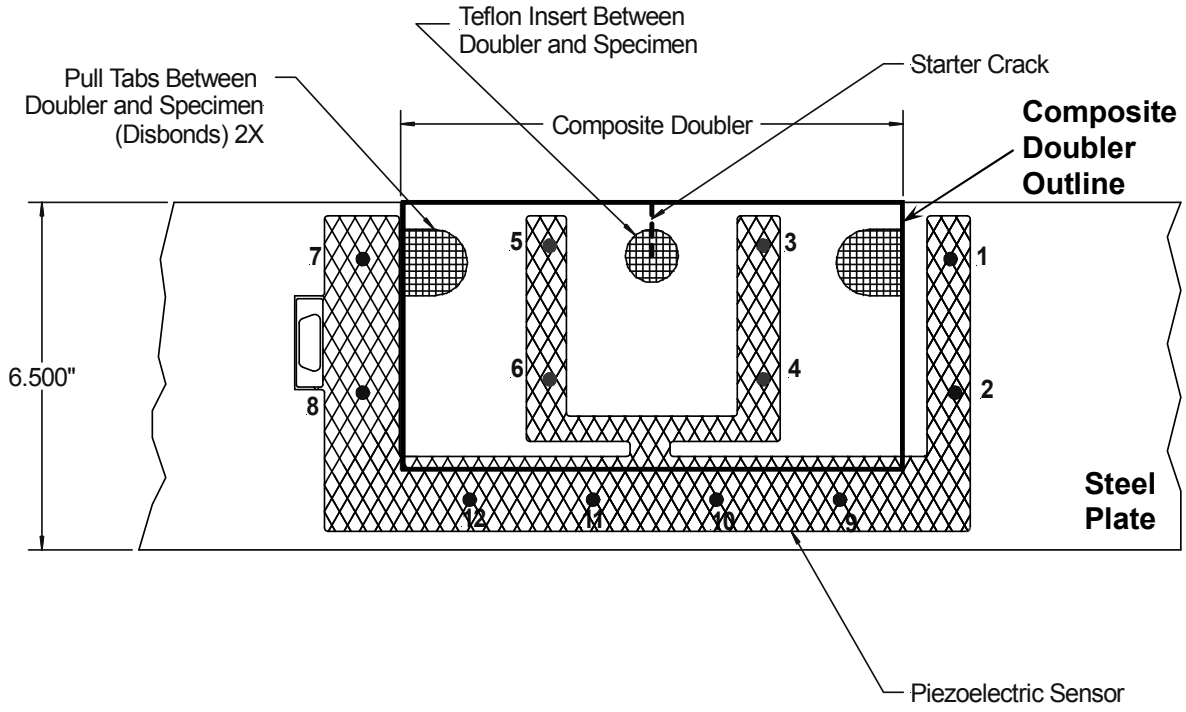

Figure 8-20: Layout of PZT Sensor Network Relative to Composite Doubler and Engineered Flaws

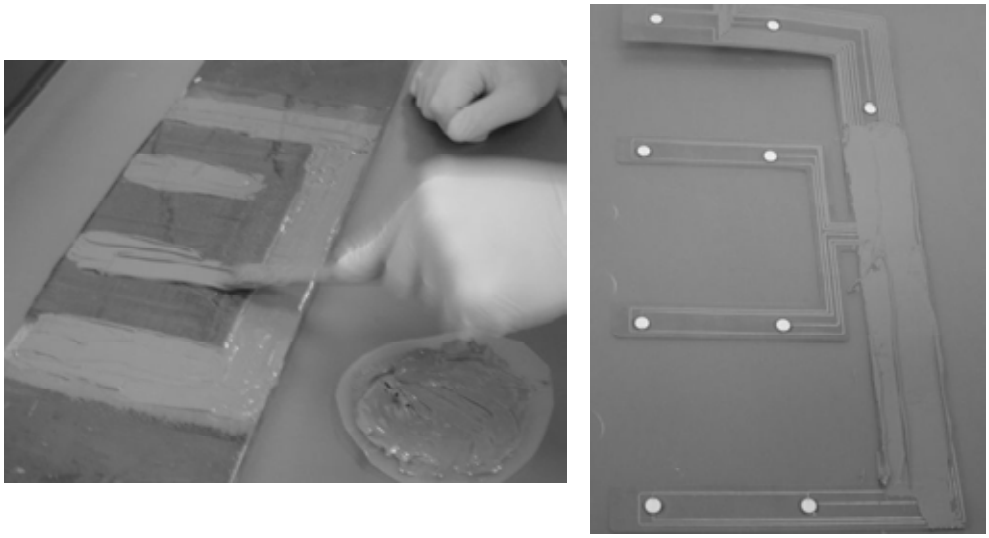

Figure 8-21: Installation of PZT Sensor Film - Application of EA9394 Epoxy to the Test Specimen and Sensor Array

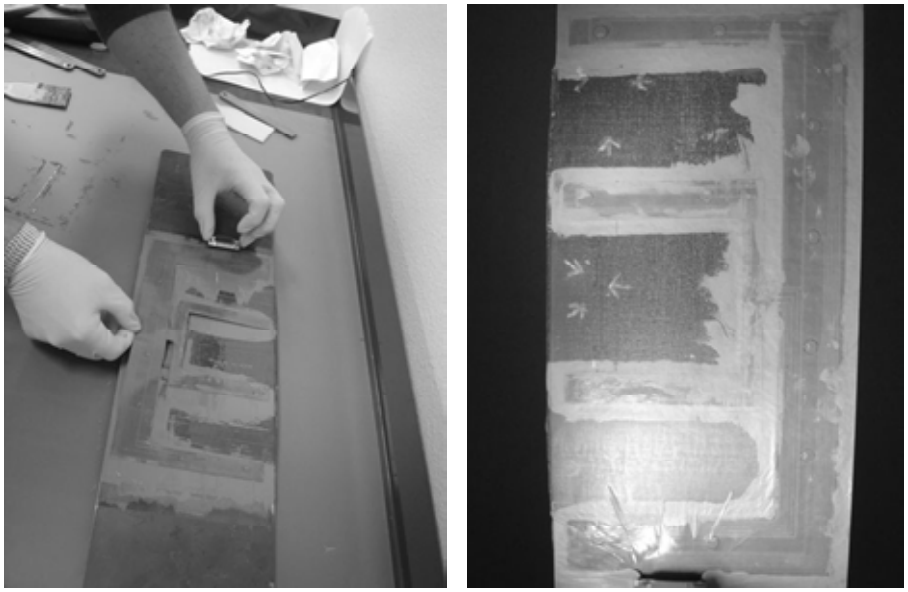

Figure 8-22: Application of Sensors to Specimen and View of the PZTs After the Bonding Process

Figure 8-23: Steel Plate with Composite Doubler, Engineered Flaws, and PZT Sensor Network Undergoing Fatigue Tests

Figure 8-23 shows the repaired test specimen in the fatigue test machine with the PZT network installed over the composite doubler. Note in Fig. 8-19 that there are essentially two concentric sets of inner and outer PZT sensors (7 PZTs on the outer loop and 4 PZTs on the inner loop). This was used to evaluate the maximum PZT spacing that could be deployed while still obtaining the desired flaw detection sensitivity. In the realm of structural health monitoring, it is desirable to accurately interrogate large areas without having to use an extensive number of sensors. With the PZT network shown in Fig. 8-19, it was possible to set up a series of different sensor-receiver paths and to independently determine the flaw detection capability of each of these paths. Figure 8-24 shows the various paths that were set up to study flaw detection versus sensor spatial resolution. The "All-to-All" path set uses every sensor as a transmitter (exciter) and receiver while the "In-to-In" path set uses only the inner four PZT sensors. Similarly, the "In-to-Out" path set looks at the wave travel from each inner PZT to each outer PZT and the "Out-to-Out" path set uses only the sensors in the furthest outer loop. It can be seen that different path sets will emphasize different area coverage and provide a different density of coverage.

Figures 8-25 and 8-26 show the detection of the three engineered disbonds that were imaged by the PZT network. The optimum images are shown here as produced by the densest "All-to-All" PZT path set. While flaw detection could be achieved with the other path sets, they were not as accurate in flaw placement – as calculated using the signal triangulation method described above – or in relative flaw sizing. Obviously, the "In-to-In" path set was not able to image the outer, edge disbonds since this data set did not involve wave travel through the outer disbond regions and thus, did not include any information from these flaws.

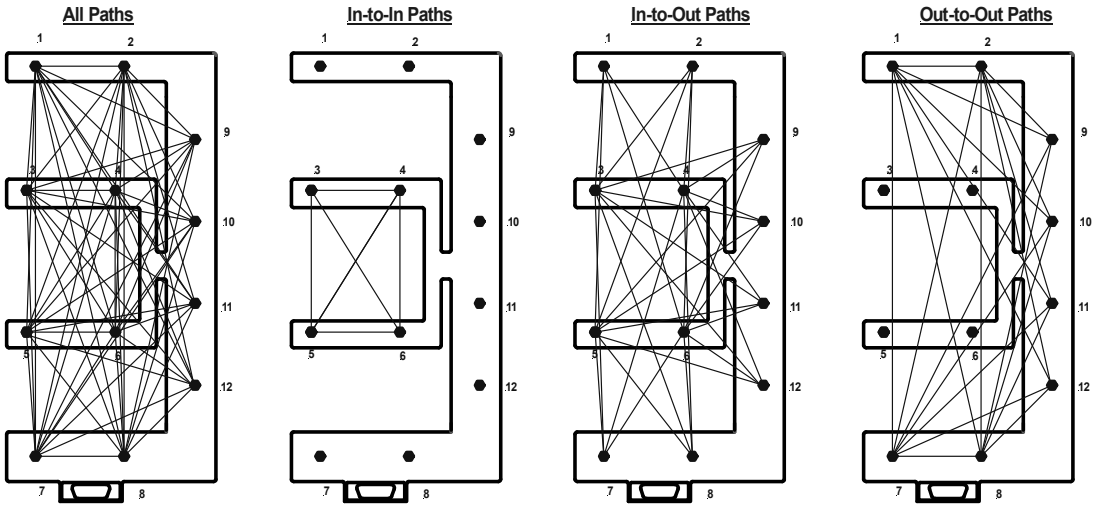

Figure 8-24: PZT Sensor-Receiver Paths Used for Data Analysis

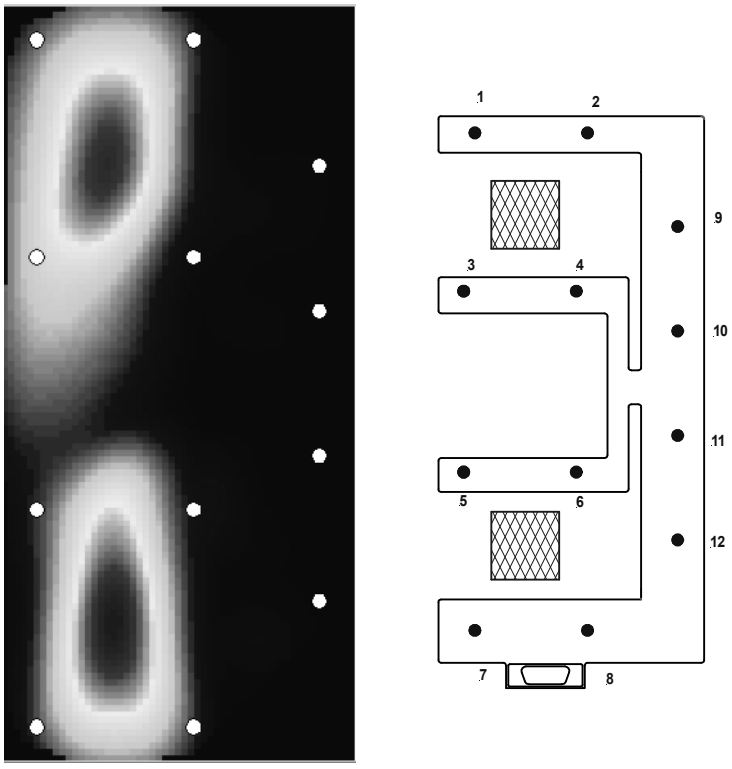

Figure 8-25: Disbond Detection with General Location of Edge Disbonds Shown

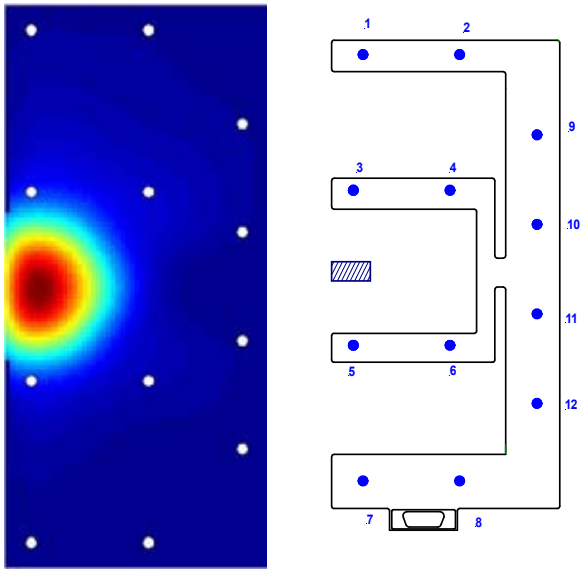

Figure 8-26: Disbond Detection with General Location of Central Disbond Shown

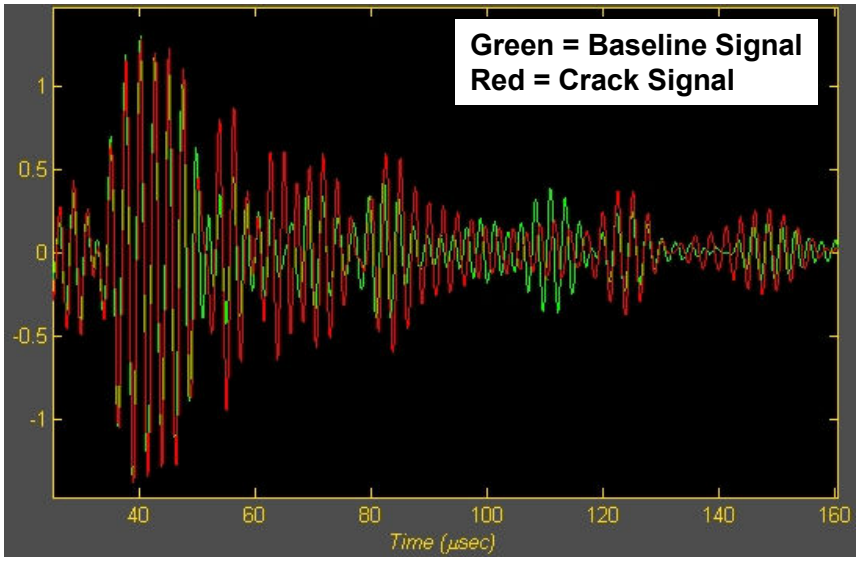

Figure 8-27: Changes in PZT Signals Produced by Crack Growth

Crack detection and growth was monitored using the same set of PZT paths. PZT data was acquired at discrete intervals during the crack growth process. Eddy current and microscopic inspections were also conducted to measure the crack lengths at each cycle count. The variation in PZT signal, for the same path, before and after crack growth is highlighted in Figure 8-27. This data is then used to construct a two-dimensional image of the crack within the PZT

network. Figure 8-28 shows the set of images produced by the PZT sensors at various crack lengths. Note the corresponding number of fatigue cycles and crack lengths associated with each measurement. These optimum images were produced by the "All-to-All" path set. Some level of crack detection was achieved using the next densest "In-to-Out" path set but the images were not as clear. The "Out-to-Out" path set did not encounter the crack region sufficiently to properly image the crack while the "In-to-In" path set produced a sparsely populated data set that was unable to detect the fatigue crack.

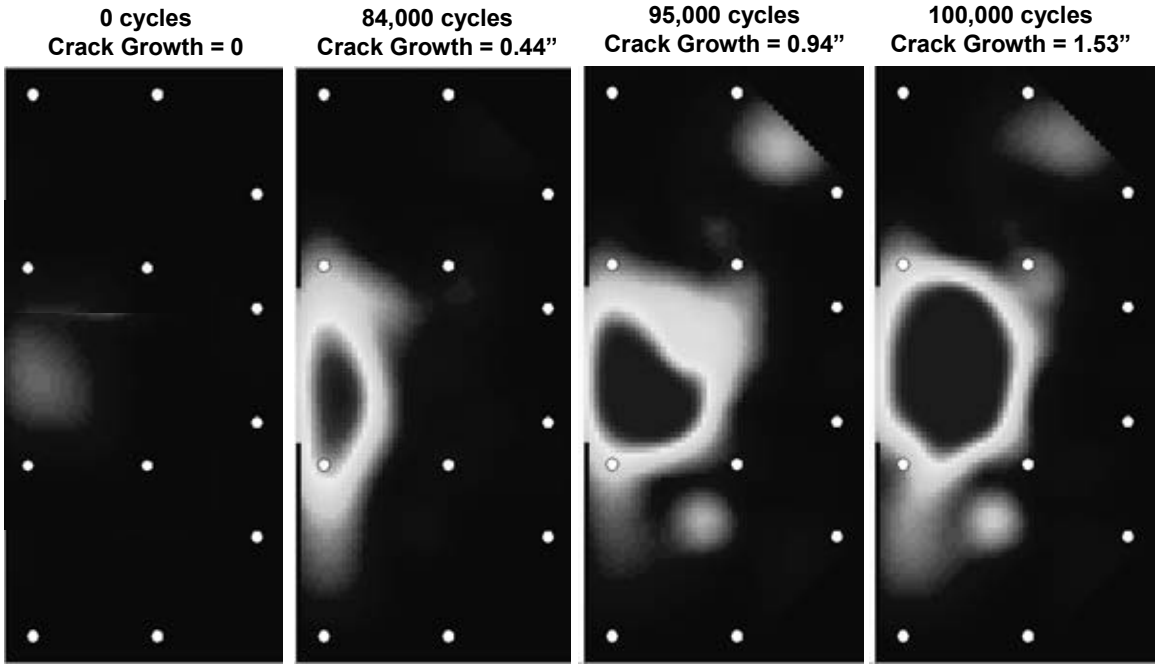

Figure 8-28: Series of Images Produced from PZT Data Corresponding to Different Crack Lengths

8.5 Fiber Optic Sensors

Rapid growth in the optoelectronics and telecommunications industries has resulted in the evolution of highly-sensitive fiber optic sensors. Fiber optic (FO) sensors have been developed for a wide variety of applications including the measurement of rotation, acceleration, vibration, strain, temperature, pressure, electric and magnetic fields, moisture, and humidity. Fiber optic sensors are light weight, low profile (typically 145 microns in diameter with a polyimide coating), are corrosion resistant, and multiple sensors are easily multiplexed into a single fiber. These factors make them ideal for embedding in or surface mounting on composite and metallic structures without affecting structural performance. Other advantages of fiber optic sensors include their high sensitivity, wide bandwidth, EMI resistance, low power requirements, and environmental ruggedness. Fiber optic sensors can also be configured to monitor crack growth and corrosion in civil and aerospace structures [8.9-8.11]. Omni-directional fiber optic sensors can be used to measure large strains (up to 150% strain), small displacements (10 μm range), and

crack growth in any material. The major disadvantages include their high cost, mechanical frailty (during handling stage) and unfamiliarity to the end user. The introduction of low-cost laser diodes, the alternative use of LEDs as light sources, and the development of inexpensive, single mode optical fibers have greatly reduced the costs associated with deploying FO sensors.

Information about the environment to which a fiber optic is exposed can be inferred by analyzing the guided light transmitted through the optical filaments. In this approach the entire length of the fiber acts as a continuous sensor. The fiber can be mounted in a serpentine path or fiber optic tentacles can be created to provide full coverage over a large area of concern. The presence of a crack can be determined by monitoring changes in the magnitude and phase of the returned light in the fiber. Optical time domain reflectometry can then be applied to determine the exact location of the crack. Fiber optic sensors can also aid in the detection of structural corrosion. Sacrificial corrosion sensors can be mounted on the end face of the fiber optic. These sensors are designed to corrode at the same rate as the parent material to which they are mounted. Degradation in these sensors, and thus the parent structure, can be calibrated to changes in the intensity of the reflected light within the fiber optics. Further refinements in the packaging, attachment and monitoring hardware are needed to allow fiber optic crack and corrosion sensors to be rapidly deployed in structural health monitoring applications.

Optical Fibers as Uniaxial Sensors - Fiber optics work on the principle that light can be guided by an interface between materials of different indices of refraction. The components of a fiber optic line consist of a core with a higher index of refraction surrounded by a cladding with a lower index of refraction. The fiber is made mostly of silicone dioxide (SiO_2), with the core containing germanium dopants. The dopants in the core create a differential in the index of refraction between the core and the cladding. These differences in the index of refraction in the core and the cladding cause light to be guided through the core. To better protect the fiber, a Polyimide coating around the cladding is used. Fiber optic sensors (core and cladding) are 80 μm - 120μm in diameter which is about the size of a human hair. With the protective coating added, the fiber is approximately 125 - 150 μm in diameter.

If a short wavelength light is used to illuminate the core region of the fiber, the core material is rearranged to produce an increase in the index of refraction in that region. A quartz phase mask can be used, as in Figure 8-29, to image an interference pattern through the side of the optical fiber. This results in a localized periodic index of refraction modulation along the length of the optical fiber (sensor grating). A typical sensor grating consists of thousands of grating lines with approximately 0.5 micron spacing. The mask shown in Figure 8-29 controls the laser exposure to induce a customized interference pattern on the optical core. This fiber grating can then be used to measure strain since axial stretching or compression of the fiber will change the grating period and, thus, the peak wavelength reflected back from the sensor. When the fiber grating is illuminated by a broadband light source or a tunable laser source the fiber grating will reflect a narrow band of light corresponding to its period. The reflected light will be centered in a narrow band at the Bragg wavelength according to the relationship:

$$\lambda_B = 2n_e\Lambda \qquad (8\text{-}2)$$

where n_e is the effective index of refraction at the core of the fiber and Λ is the grating line spacing. Measuring the shift in wavelength of light reflected back from the grating can thus be used to determine strain or temperature changes. If strain is applied to the Fiber Bragg Grating, the resonant reflected wavelength λ_B will shift by an amount $\Delta\lambda_B$ given by:

$$\Delta\lambda_B / \lambda_B = (1-P_\varepsilon)\varepsilon \qquad (8\text{-}3)$$

where P_ε is the photoelestic constant for the fiber core. By tracking $\Delta\lambda_B$ it is possible to accurately measure strain levels in the structure.

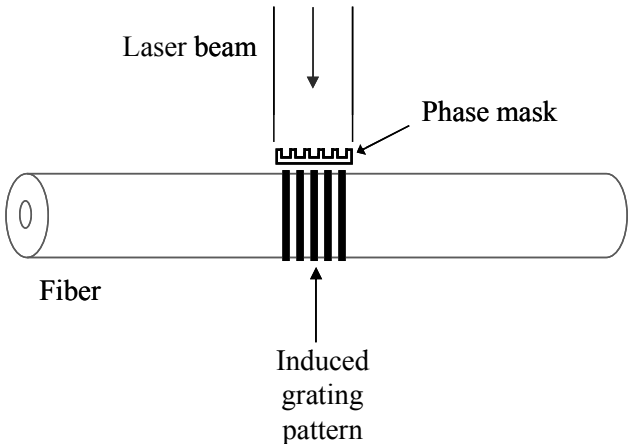

Figure 8-29: Process to Install a Fiber Grating onto an Optical Fiber Using a Short Wavelength Laser in Combination with a Phase Mask

Fiber-Optic Bragg Gratings consist of index of refraction discontinuities intentionally placed in the core of an optical fiber with periodic spacing. Several Bragg gratings can be implemented into a single fiber with multiple different grating values to form a distributed sensing network. A broadband light source is injected into the fiber and the absorption spectrum is measured using a monochromator or similar instrument. The transmission spectrum will have regions of missing energy that correspond to the grating period. Thus, a stress measurement can be performed by observing the wavelength shift while distorting the periodicity of the grating via application of stress. Thus, the Bragg approach provides both strain magnitude and strain position measurements. These can be calibrated to provide information on structural flaws. Fiber breakage, corresponding to crack growth in the structure can also be easily observed. Innovative multi-axis fiber grating sensors have been produced with both extensional and lateral strain sensitivity. This approach may allow strategic measurement of multidimensional strain fields to be used to track the onset of damage in composite repairs.

Multi-Parameter Fiber Grating Strain Sensors – A method of generating multiple fiber gratings capable of measuring multi-directional strain is to write a fiber grating into a special type of fiber called polarization maintaining or birefringent fiber [8.10-8.11]. The birefringence (difference in index in refraction depending on the polarization state of light) in the fiber is created with a built in residual stress introduced during the fiber draw (manufacture). This stress results in a slight

change in the index of refraction along two mutually orthogonal directions (termed the polarization axes). This creates two spectral peaks for each optical grating written into the optical fiber, one associated with each polarization axis. By measuring the wavelength of these peaks it is possible to generate two equations in two unknowns effectively allowing two environmental parameters (in this case, two strain tensors) to be monitored.

For this type of fiber grating strain sensor, a single fiber grating results in two distinct spectral peaks. These peaks correspond to each of the polarization axes of the polarization preserving fiber, which differ slightly in index of refraction. Figure 8-30 illustrates a multi-axis grating written onto polarization preserving fiber, which is subject to uniform transverse loading. In this case, the two spectral reflection peaks, corresponding to the effective fiber gratings along each birefringent (polarization) axis, will move apart or together uniformly providing a means to measure transverse strain. This results in the two major spectral peaks moving apart or together. Each of the two spectral peaks maintains its original unloaded profile.

Figure 8-31 shows how changes in the spectral output from birefringent fiber gratings can be used to measure both axial and transverse strain. When the fiber is loaded transversely, the relative index of refraction of the polarization axes of the fiber changes and the net result is that the difference in wavelength between the spectral peaks changes as well (peak-to-peak separation changes). When the fiber is strained axially, the fiber elongates or compresses, changing the fiber grating spectral period. As a result the output spectrum shifts to longer or shorter wavelengths, respectively.

Measuring the Complex Grating Reflection Profile with a Scanning Laser Interferometer – Traditionally, fiber grating strain measurements are made with high reflectivity fiber gratings, which allow detailed information about the spectral peaks to be accessed directly via illuminating the fiber gratings with broadband light sources and then recording the reflected grating spectrum with an optical spectrum analyzer. By peak-fitting the spectrum and applying wavelength-to-strain conversion coefficients it is possible to obtain strain values. Multiplexing large numbers of high reflectivity fiber gratings can be limited by shading effects wherein gratings with nearby wavelengths are permitted to operate in the same wavelength space such that their spectra may become confused.

An approach to conducting high density multiplexing while avoiding shading effects is to use Optical Frequency Domain Reflectometry (OFDR) to characterize low reflectivity fiber grating strain sensors [8.9, 8.12]. This method employs a tunable light that is used to scan a low-reflectivity fiber grating. A Fourier transform of the detector signals will give the locations of each fiber-grating sensor. With the knowledge of the sensor locations, the detector signal can be passed through narrow band frequency filters in order to separate out spectral information from individual grating sensors, even if the sensors occupy the same wavelength space. The OFDR approach was used in the tests described below to interrogate the FBG sensors and calculate the axial and transverse strains as a function of grating position along the fiber.

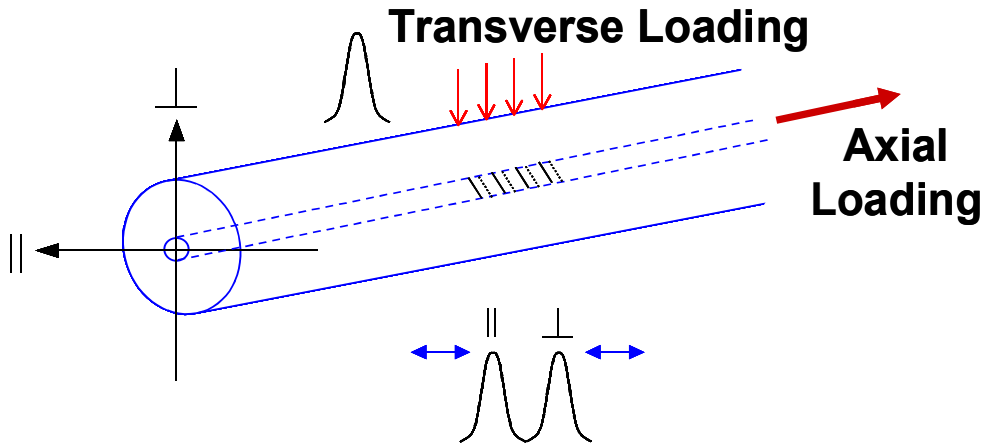

Figure 8-30: Loading and Effects of Strain on Multi-Axis Sensor

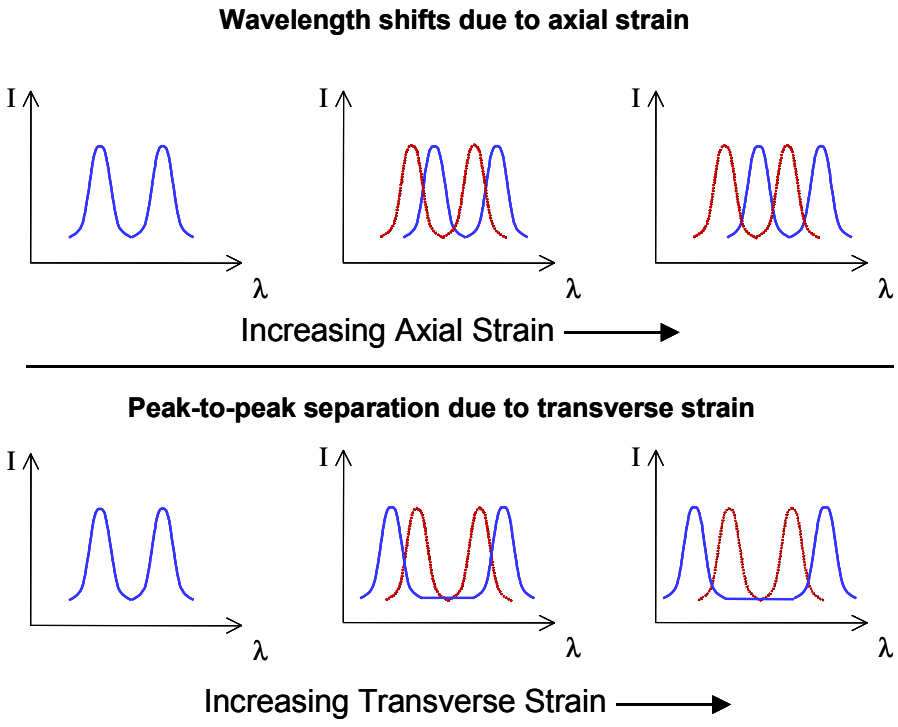

Figure 8-31: Change in Spectral Reflection of a Multi-Axis Fiber Grating Strain Sensor When Subjected to Axial and Transverse Loads

Use of Fiber Optic Strain Measurements to Monitor Cracks and Disbonds - The sensors consisted of long chirped Fiber Bragg gratings (FBG) in polarization maintaining fiber. For chirped gratings, the line width function varies linearly with grating length. Thus, for a chirped grating, the wavelength of light which is reflected from the grating is a function of grating position. This allows the FBG to have an extremely long gage length such that strain gradients over long distances of the fiber can be measured. A scanning laser interferometer was used to readout the grating period as a function of grating position. Both strain along the fiber axis and the differential transverse strain could be deduced from the grating period.

FOBG sensor systems were installed on two composite doubler repair specimens similar to the ones shown in Figure 8-13 and 8-14. The sensors encompass the entire perimeter region of the doubler so that they are able to detect the onset of any flaws within the footprint of the repair. The test specimens were cycled in tension to grow cracks and disbonds while the sensors were monitored. To implant disbonds, a Teflon insert was placed in the bond line at one location and a mold release agent was applied in a controlled region to produce a weak bond in another location. Figure 8-32 shows the overall design of the instrumented test specimen and placement of the FBG sensors within the bondline between the composite laminate repair and the parent metal structure. The objectives of the tests were to: 1) show that these sensors could be successfully installed into the specimen bond line and survive the cure process, 2) demonstrate that the distributed strain profile along the gratings could be measured, and 3) prove that the distributed axial and transverse differential strain profiles could be used to track the presence and location of flaws. The test article was subjected to extreme fatigue loads (peak loads = 80% of yield) to rapidly grow fatigue cracks from notches placed in each side of a center hole in the metal.

A series of 110 mm long FBG were embedded into the bond lines between the metal panel and the boron fiber composite doublers. Gratings A and C were routed between the plate and adhesive across the doubler end (and across the Teflon insert), while gratings B and D were routed in a parabolic path roughly parallel to the long axis of the doubler. The optical fiber was taped down to the steel surface prior to the application of the adhesive and the doubler and survived the high temperature (225^{o}F) and vacuum bag process used to bond the composite doubler to the metal plate. The gratings were purposely oriented so that the polarization axes of the fiber were oriented at 45 degrees to the plane of the metal panel as shown in Figure 8-33. This orientation gave the sensor sensitivity to changes in shear in the bond line between the doubler and the panel.

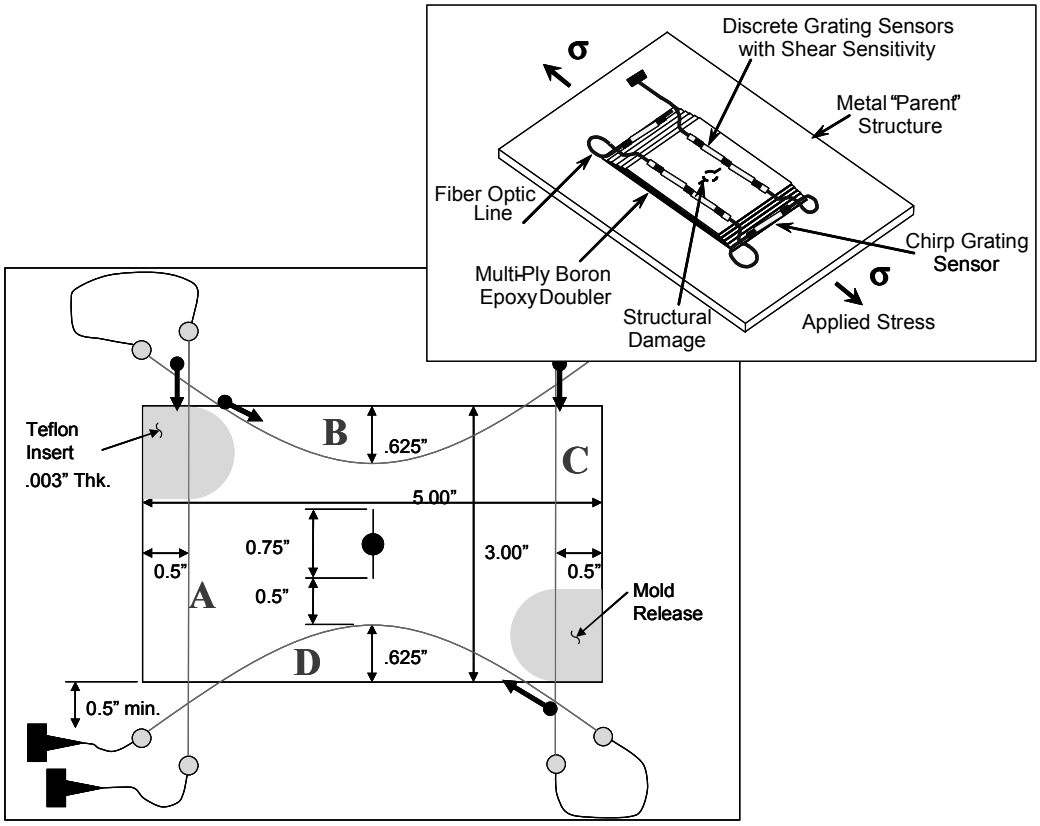

Figure 8-32: Fiber Bragg Grating Sensor Layout and Engineered Flaws in Bonded Composite Repair Test Specimens

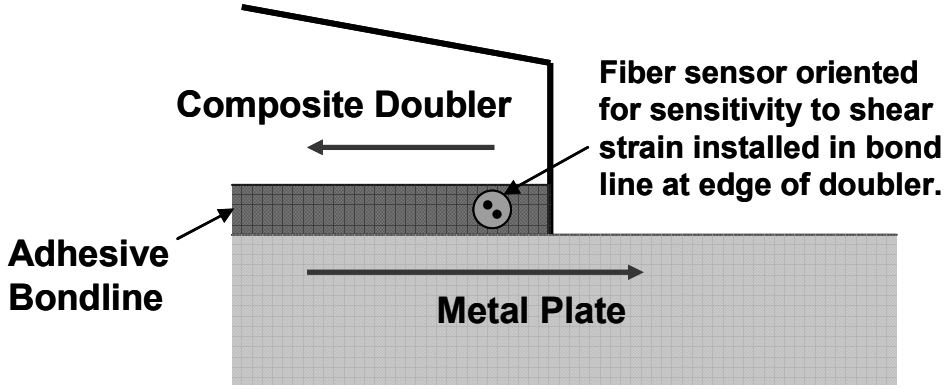

Figure 8-33: FBG Sensor Embedded in Adhesive Layer with Polarization Axis of Grating A Oriented for Maximum Sensitivity to Bondline Shear Strain

Figure 8-34 shows a close-up of the FBG sensors, and associated end connectors, as they enter and exit the bondline of the test specimen. Typical data acquisition equipment used to monitor the FBG sensors is also pictured. During the course of the structural tests, the cyclic loading was

periodically paused to allow the grating sensors to be interrogated. At these intervals, crack lengths were measured using eddy current and optical magnification methods. The presence of disbonds was monitored using hand-held ultrasonic pulse-echo inspections. Strain gage readings were acquired for comparison to FO strain measurements and to monitor the overall performance of the composite doubler repair.

Figure 8-34: Fiber Optic Sensors in Adhesive Bondline and FO Monitoring Equipment

Figure 8-35 contains sample results from the FBG sensors (sensors B & D) as they monitored fatigue crack growth. Both plots show the strain distribution along the sensors as a crack tip approaches. The plot on the left shows the strain levels produced by the crack when there was no load on test specimen 1. Specimen 1 contained a central crack but no disbond flaws. Note that the strain levels are close to 0 με in regions away from the cracks in the center of the plate. The plot on the right shows the strain levels along the axis of sensor B when specimen 2 was loaded to its maximum tension load of 34,000 lbs. A similar strain profile is observed, however, the strain levels produced away from the center cracks is now 1000 με. Normal stress-strain calculations determined that the maximum strain in the plate at 34,000 lbs. load was 1000 με. In addition, strain gage readings in the uniform strain region away from the cracks were between 950 με and 1020 με. Data such as this demonstrated the accuracy of the strain levels obtained from the FBG sensors.

As the cycle number increased and the crack propagated further out from the center of the panel, the strain near the center position of the grating started to rise dramatically. At 63,000 and 67,000 cycles the strain at the 45 mm point in Sensor B (right side plot) finally falls to 0 as the crack passes through the fiber and relieves the strain in that portion of the sensor. Although the FBG sensors were 0.5" or further away from the crack tip, significant and localized strain changes were observed near the center of the sensors with less than 0.100" crack growth.

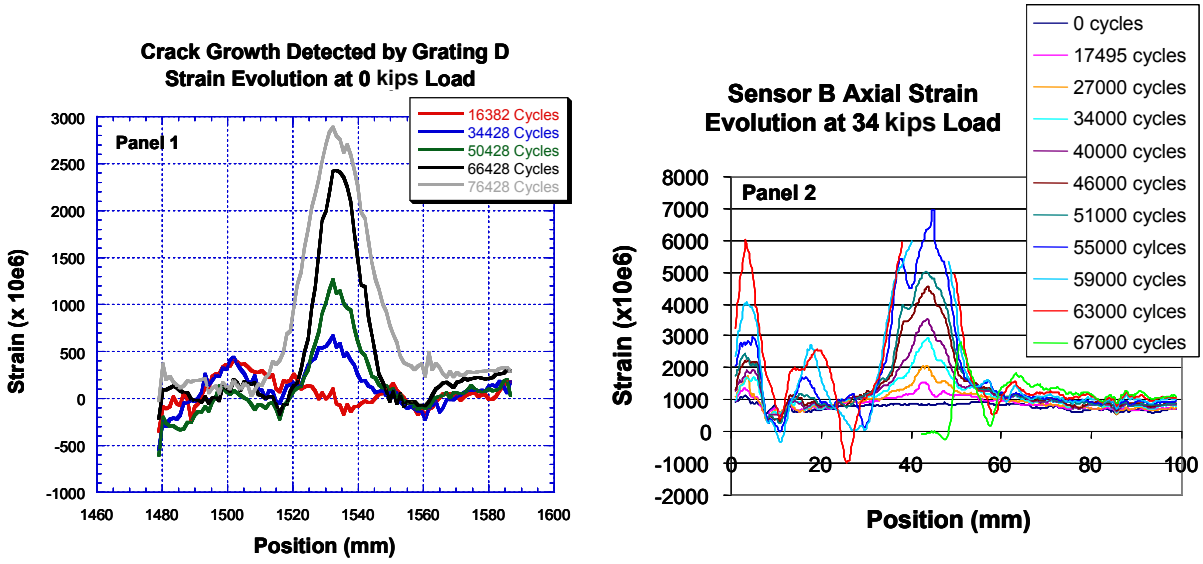

Figure 8-35: Strain Distribution Along Sensors *B* and *D* Determine Strain Levels in the Specimen and Indicate Crack Growth During Fatigue Testing

Sensors A and C were used to interrogate the bondline along the edge of the test specimens. As shown in Figure 8-32, these edges contain the tapered portion of the doubler and are critical, high shear strain areas because the majority of the load transfer into the composite repair occurs here. As a result, it is important to monitor the taper region for disbonds. Since the fibers containing sensors A and C run across the width of the bondline (perpendicular to the direction of load), the shear strain component provided the best measure for identifying disbonds. Figure 8-36 shows the shear strain distribution along sensor A while the specimen was under load.

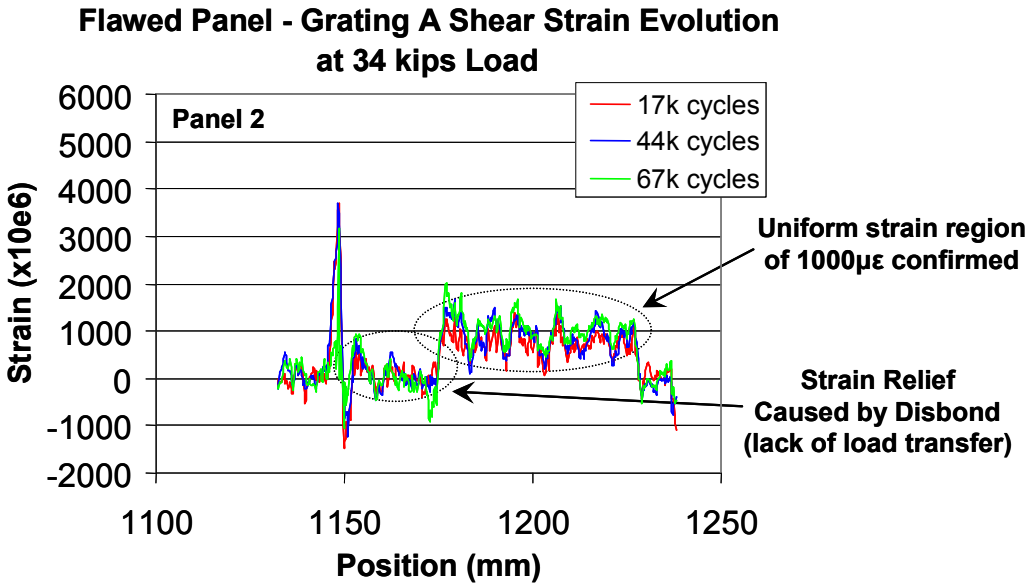

Figure 8-36: Shear Strain Levels Monitored by Sensor *A* Indicating the Presence of a Disbond

Note the 1000 με level across most of the taper region (from 1185 mm to 1235 mm where the bond line is intact). As observed in the sensor B data above, the maximum strain of 1000 με in the direction of the load is confirmed by sensor A. However, in the region of the disbond produced by the Teflon insert, the shear strains are almost 0 indicating the presence of an extreme strain relief (i.e. disbond eliminates load transfer into doubler in this region). This plot indicates that the disbond extends from the 1160 mm position to the 1185 mm position correctly predicting the size of the one inch (25 mm) Teflon insert.

8.6 Mountable Eddy Current Sensor for In-Situ Health Monitoring

As part of this LDRD effort, a wireless, integrated, mountable, battery-operated, non-contact eddy current sensor was developed by Sandia Labs to provide the same accuracy as the large, manually-applied NDI equipment discussed in Chapter 5. Chapter 9 describes the design, operation and validation of this leave-in-place eddy current sensor for crack detection. This sensor was initially developed to allow for crack detection in the parent metal material beneath composite doubler repairs. However, the sensor can be mounted on a wide array of structures for general surface and subsurface crack detection. It can produce a strong enough magnetic field to produce deep crack detection for inspecting second and third layers in complex joints or for detecting cracks hidden beneath non-conducting layers and coatings.

Chapter 9 contains detailed schematics and design drawings of the EC sensor. Figure 8-37 shows a photo of the two coil sensor inspecting for cracks beneath a composite doubler. The use of a rectangular planar coil, coupled with embedded processing, conditioning electronics, and wireless communications provides a stand-alone solution to perform accurate, remote, in-situ, real-time, non-contact, structural health monitoring.

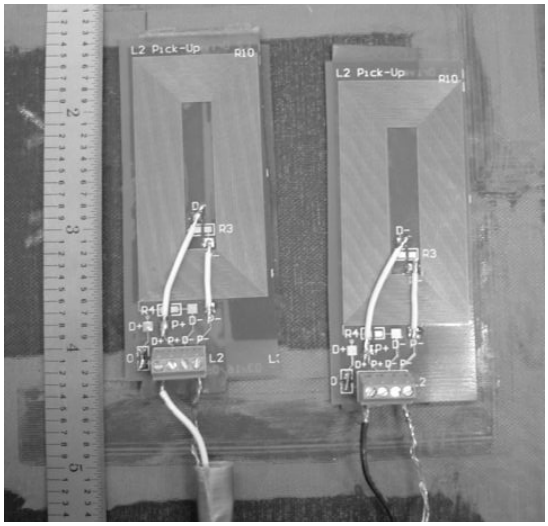

Figure 8-37: Dual/Differential Coil Version of Sandia Eddy Current Sensor for Surface and Subsurface Crack Detection (In-Situ Health Monitoring Methodology)

Quantification of Crack Detection Sensitivity – A series of crack detection tests were completed in order to quantify the crack detection performance of this mountable, EC sensor. In order to construct a good basis of comparison to known crack detection results, the inspection data generated by the EC sensor were compared with results obtained using conventional inspection methods. The EC pencil probe and spot probe methods were deployed along with optical measurements. The EC pencil probe (higher frequency NDI) is intended for surface crack detection. The pencil probe and optical inspections were applied to the metal side of the test specimens described in Chapter 4 and pictured in Figures 3-9, 3-14, 4-1, 8-19, and 8-38. This is not the normal inspection surface but these measurements provided the greatest accuracy and were used as the "referee" for comparison purposes. The EC spot probe and the EC sensor, both with greater depth-of-penetration capabilities - were applied through the composite doubler in the inspection scenario expected in the field.

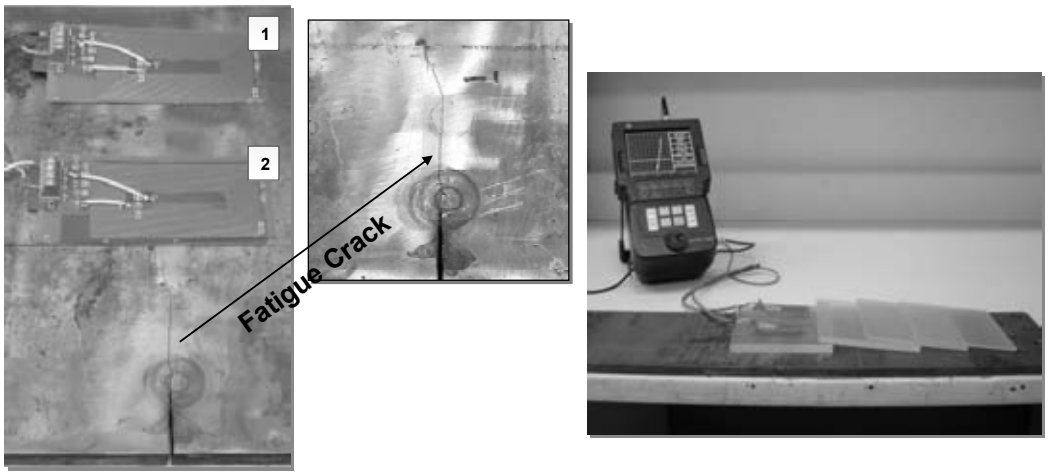

Figure 8-38: Mountable EC Sensor Applied to Bare Steel Side and Composite Doubler Side of the Fatigue Crack Test Specimen

Optical Microscope – crack on steel side of specimen imaged at 24X magnification with load on the test specimen to open crack tip; resolution of 0.0005"; used as referee for determining the actual crack length.

Eddy Current Pencil Probe – higher frequency with less penetrating power but smaller diameter for better small crack resolution; applied to steel surface directly (non-doubler side of test specimen).

Eddy Current Spot Probe – larger coil producing lower frequencies for deeper penetration; truly represents capability in the field for inspections on repaired structure; inspections conducted through composite doubler which produces lift-off, thus requiring lower frequency.

Mountable EC Sensor - larger coil producing lower frequencies for deeper penetration; truly represents capability in the field for inspections on repaired structure; inspections conducted through composite doubler which produces lift-off, thus requiring lower frequency.

Figure 8-38 shows the orientation of the two coil sensor relative to the fatigue crack. The coil labeled number 1 is the reference coil and it remains stationary in a known unflawed area. The coil labeled number 2 is used to detect the crack in a differential set-up that compares the signals from the unflawed (coil #1) and flawed (coil #2) regions. This comparison ensures that the signal generated by the presence of a crack is significantly different than the signals generated in the unflawed region. Good signal-to-noise levels are needed to avoid false calls. Figure 8-38 also shows the sensor inspecting for cracks beneath various thicknesses of lift-off. In addition to the composite doubler, Lucite Test Blocks, ranging in thickness from 0.135" th. to 0.905" th., were placed beneath the EC sensor. This produced additional lift-off effects which evaluated the penetration power and sensitivity of the EC sensor though extreme lift-off scenarios (ref. Chapter 5 for discussion on crack detection through various thicknesses of non-conductive lift-off).

The graphs in Figure 8-39 to 8-41 provides summary results of the direct comparison between the Sandia-developed EC sensor and the conventional hand-held transducers often used to conduct manual inspections. A photo comparing the EC spot probe, pencil probe, and mountable sensor is provided in Figure 8-42. Figures 8-43 and 8-44 show each of the EC transducers being deployed to detect fatigue cracks beneath the composite doubler. The EC signal graphs clearly illustrate that the EC sensor can provide significant response even when subjected to the impediment of large lift-offs. Conversely, the spot probe faltered because it could not maintain its sensitivity while trying to interrogate a structure beneath thick lift-off layers. The pencil EC probe pictured in Figure 8-42 can interrogate with only high frequencies so it was not able to produce any useable inspection signal in these tests. Of equal importance to this comparison is that the hand-deployed probes cannot be permanently mounted to produce in-situ, and potentially real-time, health monitoring.

Inspection performance results for the final sensor design are shown in Figures 8-40 and 8-41. These impedance plots show the overall sensitivity of the mountable sensor as it detects cracks located through increasingly thick lift-off layers up to 0.98" thick. Note that these plots also include the signals produced by the sensor when placed in an unflawed region. Such signals from unflawed regions correspond to the noise in the sensor so it is desirable for the sensor to produce extremely small signals in unflawed regions. By comparing the signal levels at cracked and uncracked regions, it is possible to assess the sensitivity of the EC sensor using signal-to-noise (S-N) levels. Normally, flaw calls can be made if S-N values exceed 3 (S-N ratio of 3:1). The results in Figs. 8-40 and 8-41 show that even through extreme lift-off conditions (inspection impediment), the sensor produced an S-N level of 15:1 even for the most extreme case of the 0.9" thick lift-off.

The final assessment of the EC sensor quantified its ability to not only detect a fatigue crack but to accurately determine its length. Figure 8-43 shows how the EC pencil probe was applied to the exposed metal side of the test specimen. The optical microscope was also used on the side with the exposed fatigue crack. As mentioned above, this is not the normal inspection surface but these measurements provided the greatest accuracy and were used as the "referee" for comparison purposes. The EC spot probe and the EC sensor, both with greater depth-of-penetration capabilities - were applied through the composite doubler in the inspection scenario expected in the field (see Figs. 8-43 and 8-44).

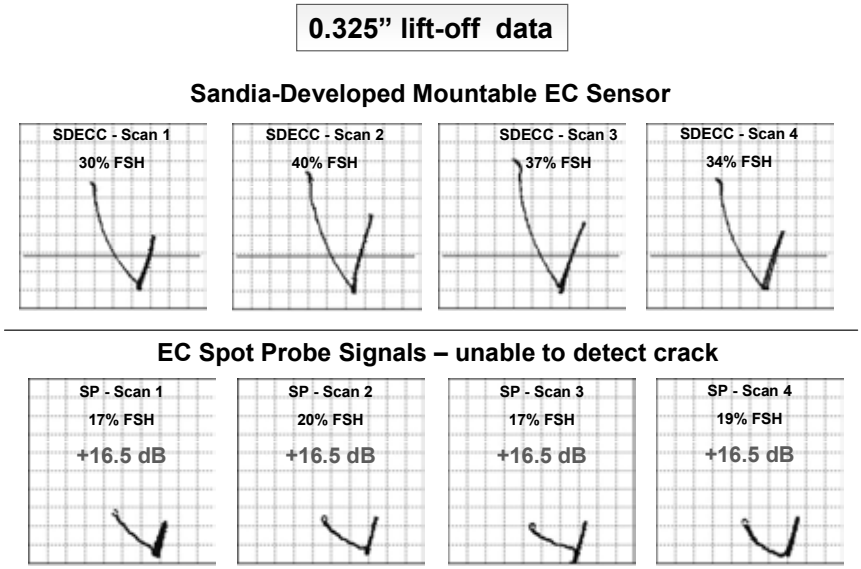

Figure 8-39: Comparison of Eddy Current Signals Generated by Conventional EC Spot Probe and Signals produced by the Sandia EC Sensor

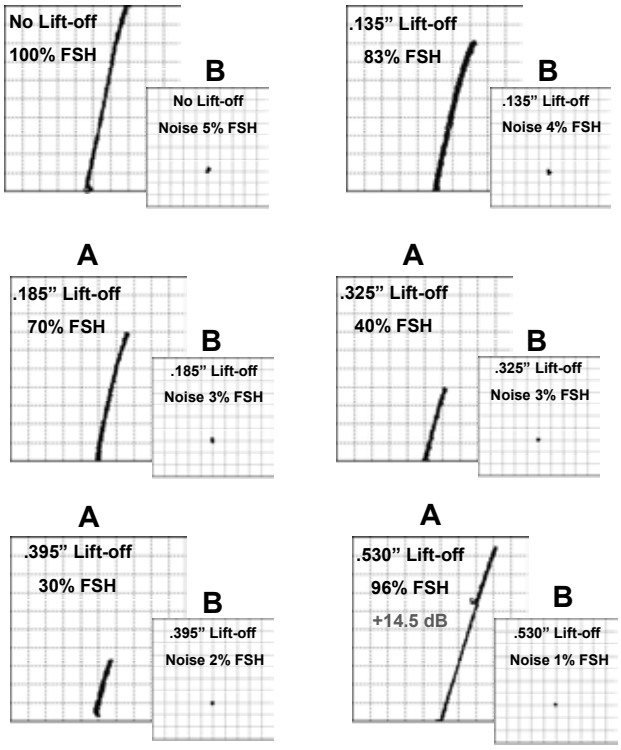

A = Sensor Response to Crack (flaw signal)
B = Sensor Response at Uncracked Region (signal noise)

Figure 8-40: Crack Detection Performance of Sandia Mountable Eddy Current Sensor for Lift-Off Layers Up Through 0.5” Thick

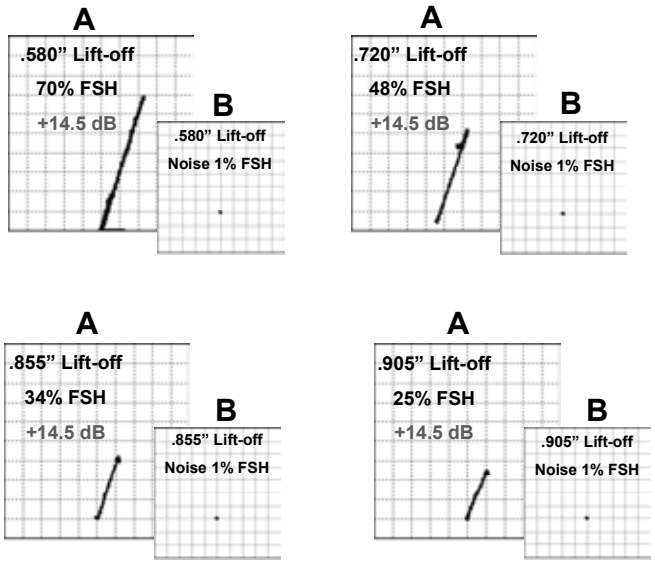

A = Sensor Response to Crack (flaw signal)
B = Sensor Response at Uncracked Region (signal noise)

Figure 8-41: Crack Detection Performance of Mountable Eddy Current Sensor for Lift-Off Layers Up Through 0.9" Thick

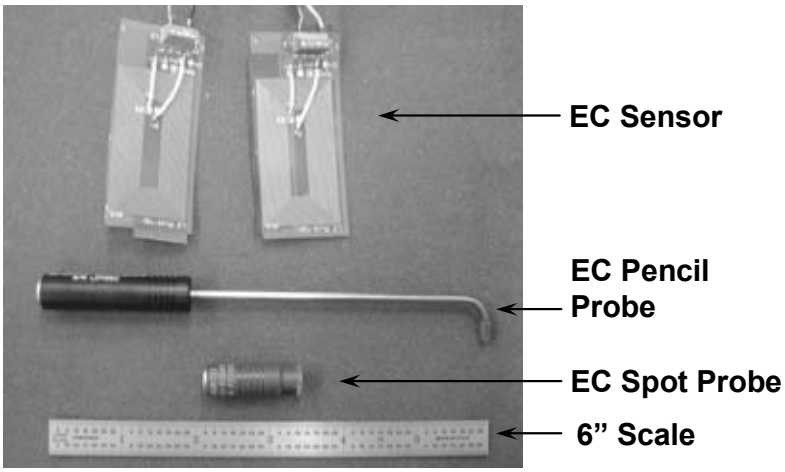

Figure 8-42: Hand-Held and Mountable Eddy Current Transducers Used to Track Crack Growth

Tables 8-7 and 8-8 compare the crack lengths as determined by the various methods described above while Figure 8-45 plots the crack length predictions for each of the four methods. The Sandia EC Sensor was able to accurately track the crack length even when inspecting through the composite doubler. The maximum deviation from the referee measurements was less than 4%.

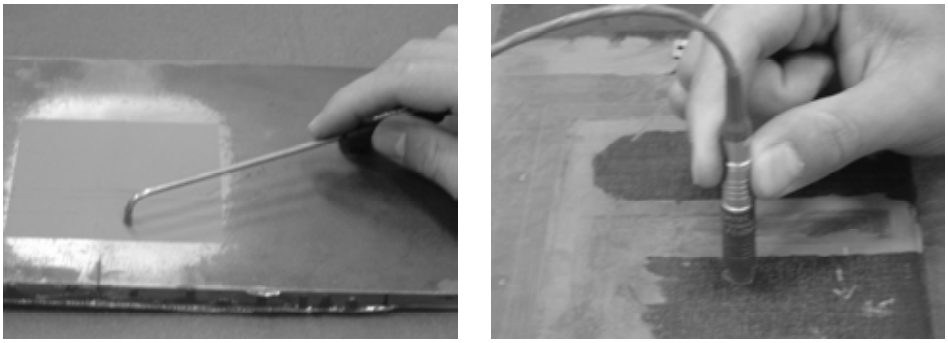

Figure 8-43: Deployment of EC Pencil Probe (Steel Side) and EC Spot Probe (Composite Doubler Side) on Fatigue Crack Specimen

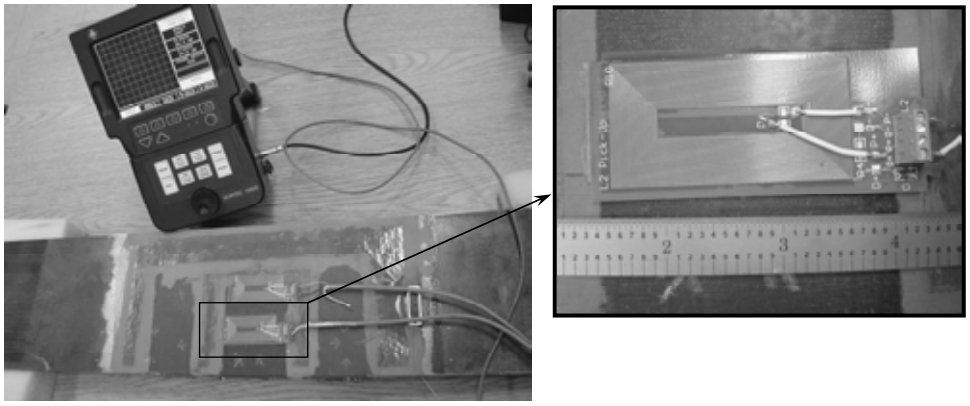

Figure 8-44: Deployment of EC Sensor on Composite Doubler Side of Fatigue Crack Specimen

SYN-FAT-21 Specimen				
No. of Cycles	Crack Length (Optical - Microscope)	Crack Length (Eddy Current Pencil Probe)	Crack Length (Eddy Current Spot Probe)	Crack Length (Eddy Current Mountable Sensor)
0	1.000	1.063	1.063	1.000
73000	1.200	-	1.240	1.250
81000	1.410	-	1.400	1.410
84000	1.495	1.500	1.480	1.510
87700	1.600	-	1.630	1.650
91500	1.805	1.800	1.840	1.825
96500	2.130	2.130	-	-
97200	2.200	2.195	2.045	2.020
99000	2.400	2.390	2.550	2.450
100200	2.590	2.590	2.750	2.620

Table 8-7: Comparison of Crack Lengths Measured by Different Methods on SYN-FAT 21 Specimen

SYN-FAT-23 Specimen				
No. of Cycles	Crack Length (Optical - Microscope)	Crack Length (Eddy Current Pencil Probe)	Crack Length (Eddy Current Spot Probe)	Crack Length (Eddy Current Mountable Sensor)
0	1.45	1.45	1.41	1.48
5000	1.81	1.81	1.75	1.85
8500	1.975	1.97	1.92	1.93

Table 8-8: Comparison of Crack Lengths Measured by Four Different Transducers Showing Ability of Mountable EC Sensor to Accurately Track Crack Growth

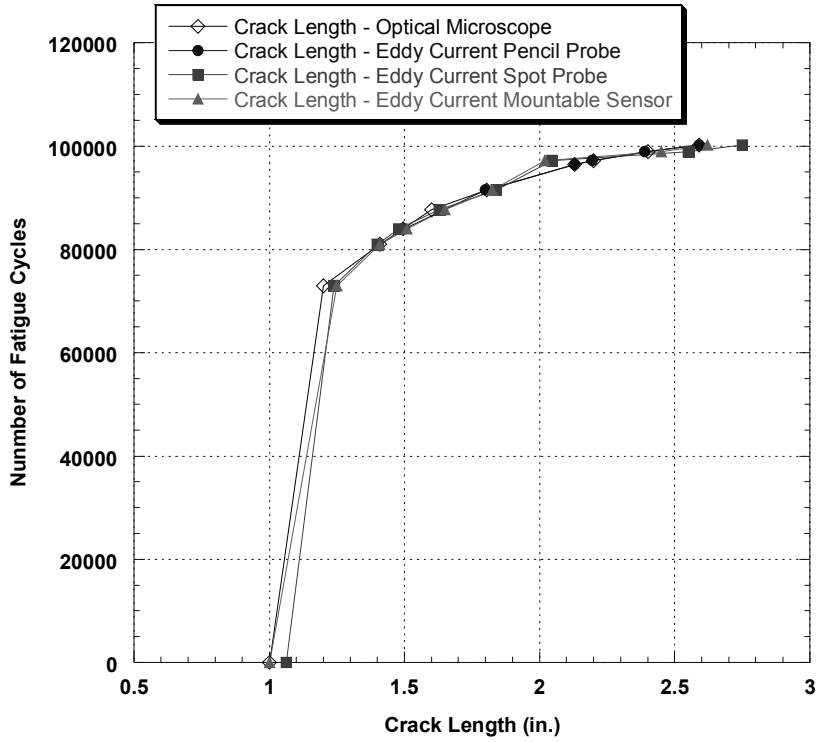

Figure 8-45: Comparison of Crack Lengths Measured by Four Different Methods
(a) Microscopic Measurement (referee)
(b) Conventional Eddy Pencil Probe (referee)
(c) Conventional Eddy Current Spot Probe
(d) Eddy Current In-Situ Sensor

8.7 Deployment of Health Monitoring Sensor Networks

Distributed sensor networks can be deployed in any of the three approaches listed below. These options are listed in the order of increasing complexity, however, less labor is required to monitor the systems as they become more complex.

1. *In-Situ Sensors Only* – The sensors are the only items permanently installed on the structure. At the desired inspection intervals, power, signal conditioning, and data acquisition electronics are manually transported to the structure to be monitored. The sensors are linked to the monitoring electronics via an electrical connector and flaw detection is completed by an inspector at the site.
2. *Sensor Network with In-Situ Data Acquisition* – In this system, miniature, packaged electronics is also placed in-situ with the sensor network. The electronics contains the necessary power, memory and programmable circuitry for automated data logging. The data is periodically downloaded to a laptop through manual hook-ups at the site.
3. *Sensor Network with Real-Time Data Transmission to a Remote Site* – This approach is similar to item #2 with the addition of a telemetry system that allows for continuous, wireless transmission of data to a web site. The web site can be programmed to interrogate critical aspects of the data and use pre-set thresholds to provide continuous green light/red light information regarding the health of the structure. The web site can even be programmed to automatically send an e-mail to operation personnel if the condition monitoring process indicates the need for repairs or other maintenance.

The latter approach allows for true condition-based maintenance in lieu of maintenance checks based on time of operation. A series of expected maintenance functions will already be defined, however, they will only be carried out as their need is established by the health monitoring system. The use of condition-based maintenance coupled with continuous on-line structural integrity monitoring could significantly reduce the cost of inspection, maintenance, and repair.

References

8.1 Roach, D., "Health Monitoring of Aircraft Structures Using Distributed Sensor Systems," DoD/NASA/FAA Aging Aircraft Conference, March 2006.

8.2 Bartkowicz, T. J., Kim, H. M., Zimmerman, D. C., Weaver-Smith, S. (1996) "Autonomous Structural Health Monitoring System: A Demonstration", *Proceedings of the AIAA/ASME Structures, Structural Dynamics, and Materials Conference*, April 1996.

8.3 Beral, B., Speckman, H., "Structural Health Monitoring for Aircraft Structures: A Challenge for System Developers and Aircraft Manufacturers," 4th International Workshop on Structural Health Monitoring, September 2003.

8.4 Roach, D., "*Use of Distributed Sensor Systems to Monitor Structural Integrity in Real-Time*," Quality, Reliability, and Maintenance in Engineering, Professional Engineering Publishing Ltd., Oxford, UK, 2004.

8.5 Roach, D, Kollgaard, J, and Emery, S., “Application and Certification of Comparative Vacuum Monitoring Sensors for In-Situ Crack Detection,” Air Transport Assoc. Nondestructive Testing Forum, October 2006.
8.6 Wheatley, G., Kollgaard, J., Register, J., Zaidi, M, “Comparative Vacuum Monitoring as an Alternate Means of Compliance,” FAA/NASA/DOD Aging Aircraft Conference, September 2003.
8.7 Giurgiutiu, V., Redmond, J., Roach, D., and Rackow, K, "Active Sensors for Health Monitoring of Aging Aerospace Structures," *International Journal of Condition Monitoring and Diagnostics Engineering*, February 2001.
8.8 Kumar, A., Roach, D., Hannum, R., and, “In-Situ Monitoring of the Integrity of Bonded Repair Patches on Civil Infrastructures,” SPIE Smart Structures and Materials Symposium, February 2006.
8.9 Roach, D., Wanser, K., and Griffiths, R., "Application of Fiber Optics to Health Monitoring of Aircraft,” Advanced Aerospace Materials and Processes Conference, June 1994.
8.10 E. Udd, W.L. Schulz, J.M. Seim, E. Haugse, A. Trego, P.E. Johnson, T.E. Bennett, D.V. Nelson, A. Makino, “Multidimensional Strain Field Measurements using Fiber Optic Grating Sensors”, SPIE Proceedings, Vol. 3986, p. 254, 2000.
8.11 M. Froggatt and J. Moore, "Distributed Measurement of Static Strain in an Optical Fiber with Multiple Bragg gratings at Nominally Equal Wavelengths", Applied Optics, Vol. 37, p. 1741, 1998.
8.12 Udd, E., Kreger, S., Calvert, S., Kunzler, M., and Davol, K., “Usage of Multi-Axis Fiber Grating Strain Sensors to Support Nondestructive Evaluation of Composite Parts and Adhesive Bond Lines,” 4th International Workshop on Structural Health Monitoring, September 2003.

9.0 DEVELOPMENT OF A LEAVE-IN-PLACE EDDY CURRENT SENSOR

Steve Yepez, Dennis Roach, Kirk Rackow, and Tony DeLong

Eddy current sensing is an effective, low-cost, low-complexity method to detect flaws in steel structures. There are many commercial solutions available ranging from handheld devices to larger fixtures containing an array of eddy current sensors to permit varying styles of inspection. However, these systems are well not suited for extensive remote field operation to support structural health monitoring; their size and cost make it an expensive liability to place several units to inspect a structure. Additionally, these devices are not meant to operate remotely. They cannot operate off battery power for extended periods of time, do not store information locally, and do not tend to have a wireless interface for remote data retrival.

Additionally, the sensors themselves must be modified to operate under the constraints produced by the device under inspection. In many cases, there will not be direct contact with the structure; there may be a non-conductive or conductive barrier that shields and strengthens the structure. In other situations, the structure needs to be inspected at a junction or other complex geometry that requires a coil to "wrap" around the joint. It may also be necessary to install conformal coils that can be attached over uneven or curved surfaces.

An enhanced impedance analysis device was designed to work with the planar coils to monitor the health of a metallic (conductive) structure. This impedance analysis device incorporates several features ranging from adaptive update rates to wireless data access. These features permit the unit to operate in remote conditions for extended periods without any direct contact.

By using planar coils on extremely thin PCB or flexible plastic, it was possible to develop a sensor and sensor system that is capable of inspecting a 4 inch lateral area through a lift off of one inch. This capability, when combined with the developed impedance analysis device, permits the remote inspection of a bridge or other structure over a period of several months without any direct interaction. It is anticipated that the device will yield significant inspection labor savings without sacrificing fidelity, and still manage to provide relevant data to determine the structure's integrity. In fact, the remote operation and data logging capabilities allow for more frequent structural interrogation. This chapter describes the sensor design and the sensor system that was developed to permit in-situ, remote, and even real-time structural health monitoring [patent pending].

9.1 Eddy Current Background

Eddy Current (EC) sensors use the principles of electromagnetic induction to identify or differentiate structural conditions in conductive metals. The presence of a crack is indicated by changes in the flow of eddy currents in the skin. When EC inspections are performed, an electrically conductive material is exposed to an alternating magnetic field that is generated by a coil of wire carrying an alternating current. As a result, eddy currents are induced on and below

the surface of the material as shown in the Figure 9-1. These eddy currents, in turn, generate their own magnetic field which opposes the magnetic field of the test coil. Cracks or thickness changes in the structure under inspection influence the flow of eddy currents and change the impedance of the test coil accordingly.

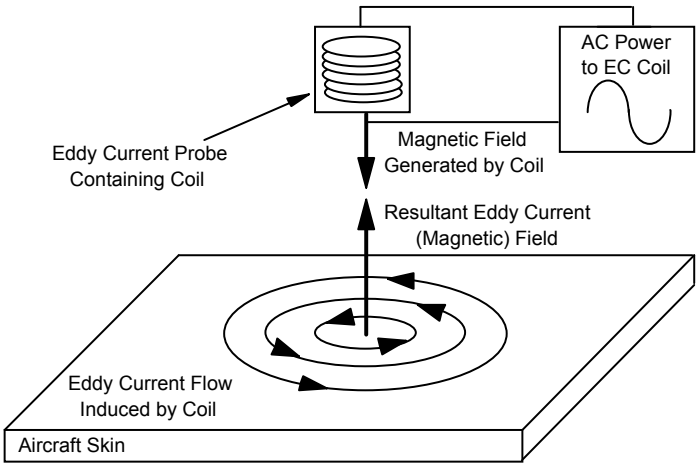

Figure 9-1: Induction of Eddy Currents in Conductive Materials

9.1.1 Impedance Plane Plots

The presence of a crack is indicated by changes in the flow of eddy currents in the skin. EC signals are physically monitored using impedance-plane plots which show the reactive and resistive components of a coil as functions of frequency, conductivity, or permeability. EC instruments record these impedance changes and display them in impedance plane plots to aid the flaw detection process.

When working with eddy currents, the impedance plane plots provide useful insight to the operation of the sensor. The plot in Figure 9-2 shows that the impedance of the coil is complex: in that it contains a real, or resistive component that represents the energy lost as heat in the structure (x-axis), and an imaginary, or reactive component that represents the energy storage of the coil (y-axis). To normalize the data, firstly the resistance at infinite lift-off is subtracted from the resistive component, and secondly, both the resistive and reactive components are divided by the reactive component [9.1]. This generates a curve that starts at a purely reactive response at infinite lift-off, experiences a resistive affect as the coil moves closer to the structure and terminates at the origin where the induced eddy currents completely cancel out the currents in the coil. As can be seen, the resistive component first grows as energy is lost to heat, but then drops off as the majority of energy is transferred directly into the structure.

The response of the coil can also be normalized by the coil radius, the frequency of operation, and the conductivity and permeability of the structure. These normalizations permit objective comparisons of various NDI techniques. Again referring to Figure 9-2, it is illustrated that the response of the coil moves from the upper left, along the curve, and towards the origin as a

function of these factors. Hence a user can adjust the operating point of a sensor by adjusting one of these parameters.

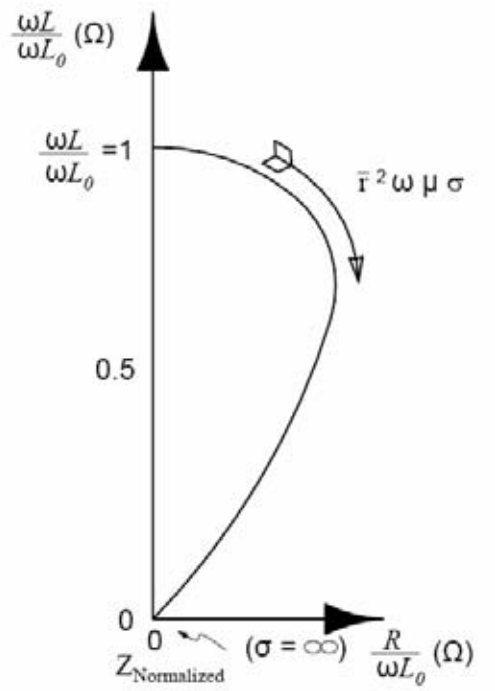

Figure 9-2: Normalized Impedance Plane ($\bar{r}^2 \omega \sigma \mu_0$)

9.1.2 Skin Effect

The depth of penetration of eddy currents is inversely proportional to the product of magnetic permeability, electrical conductivity, and frequency of the inducing currents. High frequency eddy current (HFEC) currents, above 100 kHz, are most sensitive to discontinuities on the surface next to the coil and are used to detect near-surface flaws. Low frequency eddy current (LFEC), ranging from 100 Hz to 10 kHz, are used to penetrate the structure to detect flaws deep within underlying structure. By measuring the phase, it is possible to determine the depth of the defect.

Figure 9-3 shows an example of an impedance plane display showing phase and amplitudes of EC signals generated by cracks of varying depths. Unlike Figure 9-2, this plot illustrates a rotated response so that the lift-off axis is oriented horizontally rather than vertically. Also the inspector may amplify the response and place the apex of the operating region in the lower right-hand corner. This operating region represents a point along the curve in Figure 9-2. The graphs of Figure 9-4 demonstrate how the magnitude and phase response of the coil behave with increasing depth.

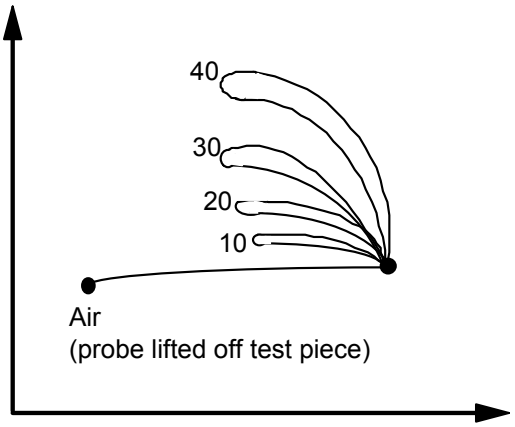

Figure 9-3: Impedance Plane Traces for Surface Cracks of Various Depths

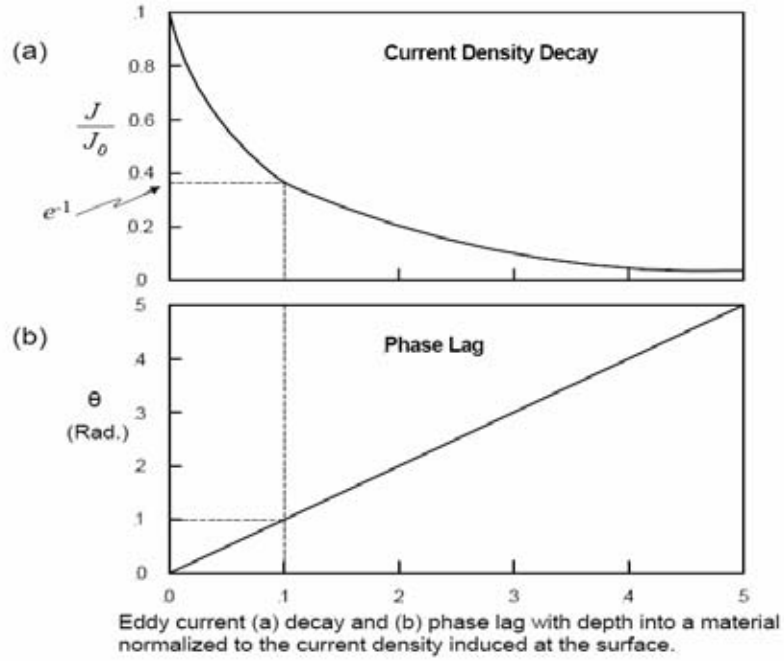

Figure 9-4: Graph of Signal Magnitude and Phase as Function of Depth

9.1.3 Lift-Off Effect

The lift-off, or the distance between the sensor and the structure of interest, also impacts the sensitivity of the EC sensor. A gap introduced by air, or any non-conductive medium, decreases the coupling ratio between the coil and the structure. Eventually, the displacement becomes

large enough that the coil can no longer "sense" the structure. The graph in Figure 9-5 illustrates this point. The user operates on the outermost curve when in direct contact with the structure. As lift-off increases, the curve moves closer to the upper left corner of the graph representing no object present. It is desirable to operate in the outermost curves to obtain the best sensitivity to impedance changes. As a side bar, Figure 9-5 also illustrates the lift-off curves that converge on the normalized infinite lift-off point of (0,1). It is this curve that inspectors rotate so that it is oriented along the x-axis. This rotation is done so that the user can maximize the sensitivity of the sensor in the y-axis where a crack response will be drawn, while minimizing the lift-off and wobble effects that occur in the x-axis.

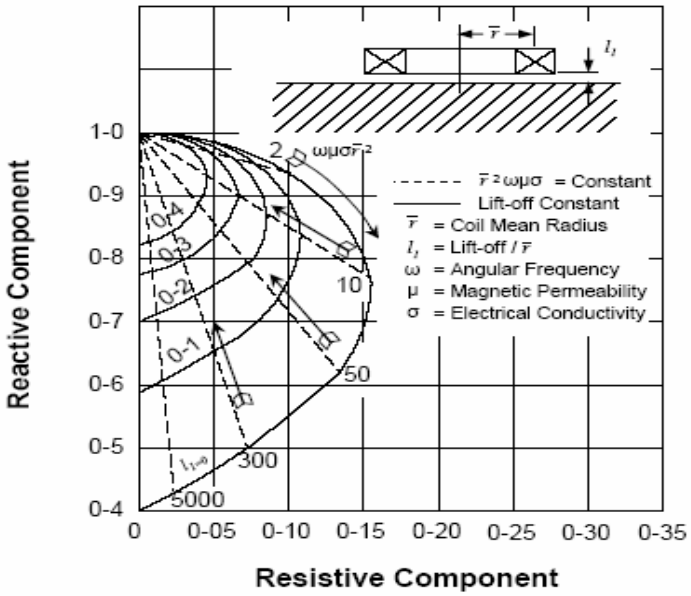

Figure 9-5: Illustration of Lift-off Impact on Impedance Plane Plots

9.2 Sensor Design Concepts

To meet the demands for remote, structural health monitoring, the sensor needs to have the following features and capabilities:

- Low cost
- Consistent Reproduction
- Conformal Placement
- Custom Configuration
- Large Coverage Area
- Noise Reduction (good signal-to-noise ratio)
- Non-Contact Penetration
- System Integration

In some cases, these capabilities can be incorporated directly into the coil design. For some features, a combination of hardware and software must be produced to provide the desired sensor system design.

9.2.1 Fabrication Benefits

Low-cost, conformal and consistent reproduction benefits are achieved by fabricating coils on a very thin (5 mils) circuit material (FR4, Kapton, polymide). Many fabrication houses can generate coils with 5 mil trace widths and spacing for a reasonable cost. The trade off is that the traces have higher resistances than magnetic wire and therefore the coils have a low quality factor. However, the poor quality factor can be overcome by designing the proper detection circuitry. Ultimately, this approach also tends to be less expensive than purchasing custom wound coils that will still satisfy the lift-off requirements. The alternative of interconnecting several of these large pancake coils (see Figure 9-6) to span the same coverage area of a single planar rectangular coil on thin film would be expensive and require individual compensation since each custom wound coil would exhibit different impedance characteristics.

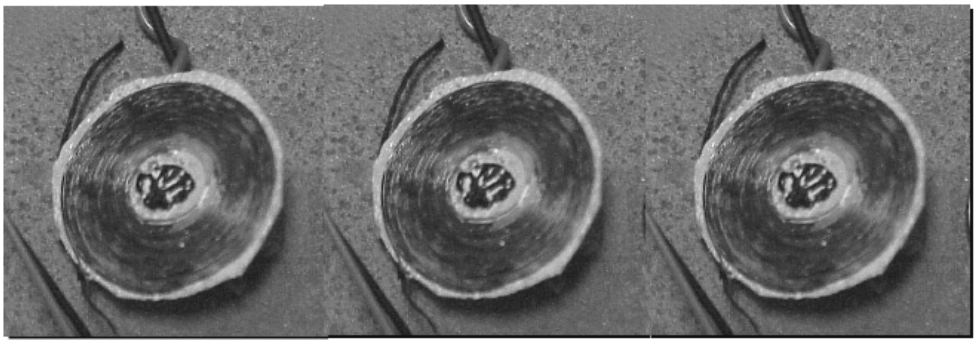

Figure 9-6: Sensor Array Using Custom Wound Coils

9.2.2 Noise Reduction

Perhaps one of the most important benefits from planar coils is that a large coverage area eliminates the need for manual or automated scanning of the structure. Scanning techniques can introduce noise into the measurement that is generated by slight changes in the orientation of the probe as it moves over the surface of the structure. The noise introduced by the wobble is often significant because the system is typically configured to operate at large gain settings to amplify any defects. The amplified wobble is viewed as a large circle around the operating point of the device.

Consider the example provided by Figure 9-7. Because a fixed coil would not trace out the crack and lift-off lines, these graphs are inaccurate, but they still provide a method to visualize the difference between a fixed coil versus a scanning coil. In these illustrations, the vertical line represents the crack and the horizontal line represents lift-off. The apex of these lines represents the operating point of the system. The image on the left side illustrates the response of a flaw

with little noise. In this case, the lines are clean and it easy to determine that a crack is present. One could determine the presence of a crack by expanding the first quadrant containing the apex.

The image on the right side depicts more noise in the signal; the lines are not straight and one must examine the behavior two or three quadrants from the vertex to determine the presence of a crack.

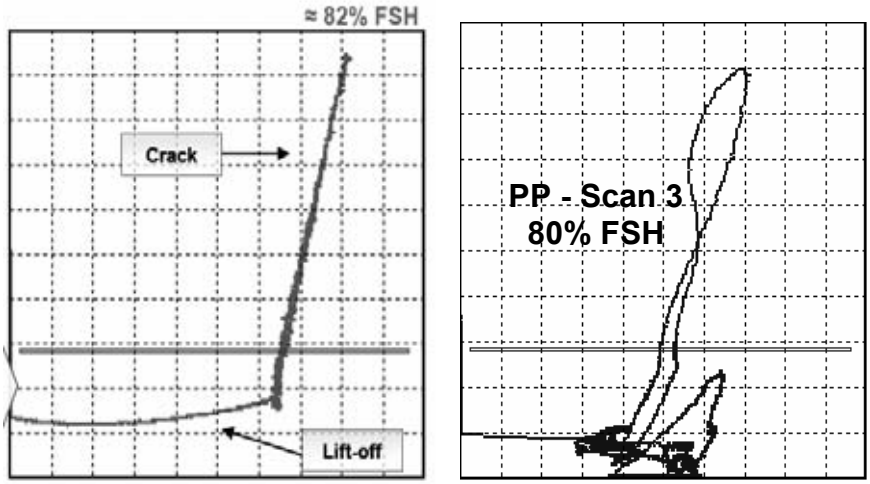

Figure 9-7: Examples of Crack Detection Using a) Fixed Coil, b) Scanning Probe

Having a cleaner signal can allow in-situ sensors to produce better flaw detection (i.e. earlier detection and with more reliability). A planar coil can be used to inspect the same area without movement; any changes in the signal are due to changes in the environmental conditions or from changes in the structures impedance. The result is a much smaller noise footprint around the operating point. The increased sensitivity permits earlier crack detection (see Figure 9-8). This can provide significant cost savings if the damage can be detected early and repaired while it is small and benign.

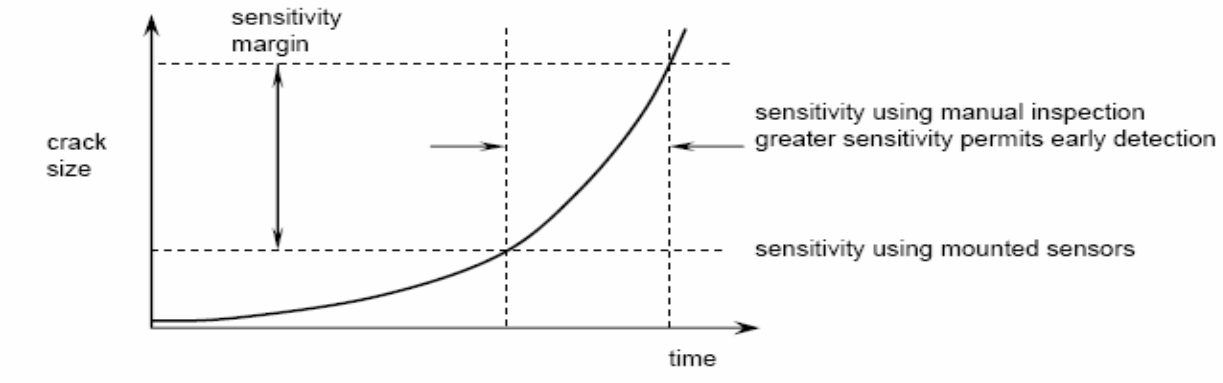

Figure 9-8: Noise Reduction Improves Flaw Detection Sensitivity

9.2.3 Sensor Configuration Considerations

Ultimately, the design of the coil is determined by the inspection requirements. Accessibility, spatial resolution, conformance, as well as the inspection interval are some of the relevant factors. The crack detection system was initially designed to monitor a repaired crack that was reinforced with a composite doubler. However, the sensor system serves the more general use for detecting any surface or subsurface crack growth that develops in a structure. To ensure that the sensor doesn't miss a propagating crack, the system was required to inspect a 4 inch wide region. Figure 9-9 below illustrates an example bridge crack that was repaired and inspected by the system (see Chapter 10).

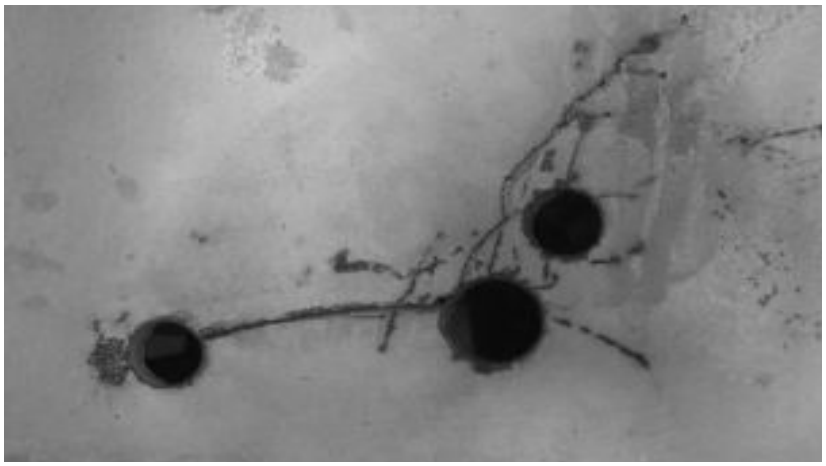

Figure 9-9: Fatigue Cracks and Stop Drilled Holes That Were Repaired and Monitored

The coil geometry was driven by the constraints outlined below:

- keep the design simple
- not necessary to provide spatial resolution
- the crack growth axis can be determined over a set region
- must over-come a lift-off of at least 0.5" as a result of the composite doubler.

Benefits of a Rectangular Geometry - An important aspect of the rectangular coil design is that the strength of the magnetic field is independent of the length when it is much longer than its width. Since the length of the coil dominates the width of the coil, the magnetic field density along the lengthwise axis of the coil becomes a function of the coil's width. Hence a uniform magnetic field is developed among most of the coils length that can be approximated by 2 infinite wires with currents flowing in opposite directions (see Figure 9-10) [9.2].

A large effective coverage is beneficial because the only the orientation, not the location and path of incipient cracks is known. The rectangular coil provides uniaxial crack detection. Figure 9-11 demonstrates how the length of the coil is oriented in parallel to the strain axis and perpendicular to the anticipated crack axis of the repaired structure. New cracks will intercept the coil and impede the flow of the eddy currents in the material directly below the coil thus allowing the sensor to detect the cracks.

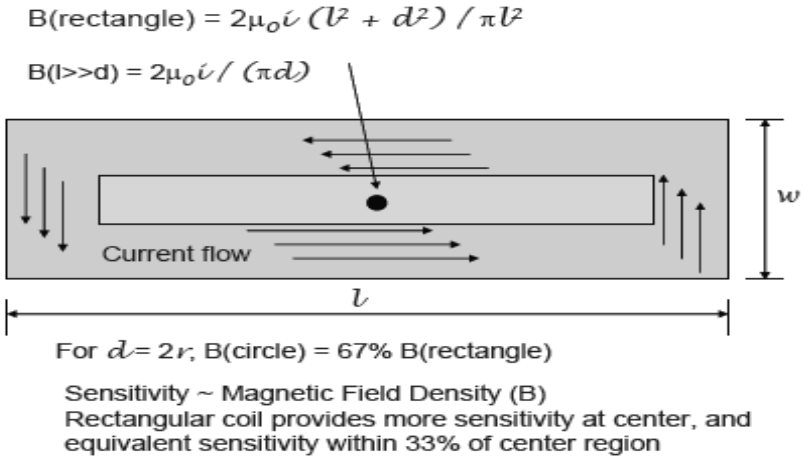

Figure 9-10: Magnetic Field Distribution of a Rectangular Coil

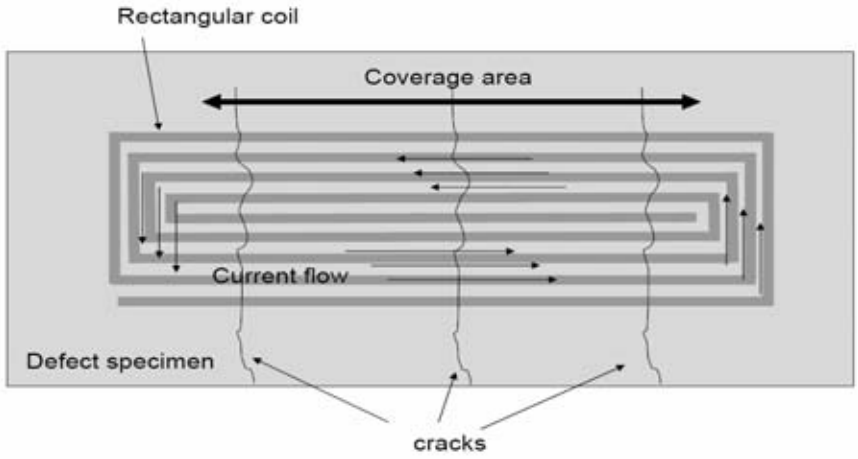

Figure 9-11: Crack Propagation to Intercept Coil Along Effective Region

Custom Coil Configurations - One benefit from the use of planar coils is the relative ease to modify the coil design to conform to a variety of geometries and provide coverage for a range of structures. This flexibility can be useful in applications where the structure dimensions prohibit a retangular form factor, where the crack growth characteristic is deterministic, or where there is a desired inspection area. For example, a serpentine coil configuration can be used to examine a row of fasteners. There are a variety of ways to implement the serpentine design to achieve good coverage, while still considering the manufacturing aspects of the coil design. Figure 9-12 illustrates some serpentine coil examples. A rectangular coil layout in the sensor can also be used to detect cracks that may grow radially from a particular stress point in the structure (see Figure 9-13). However, it may be better to design a coil with other geometries to improve detection and this can be achieved using the sensor design described here.

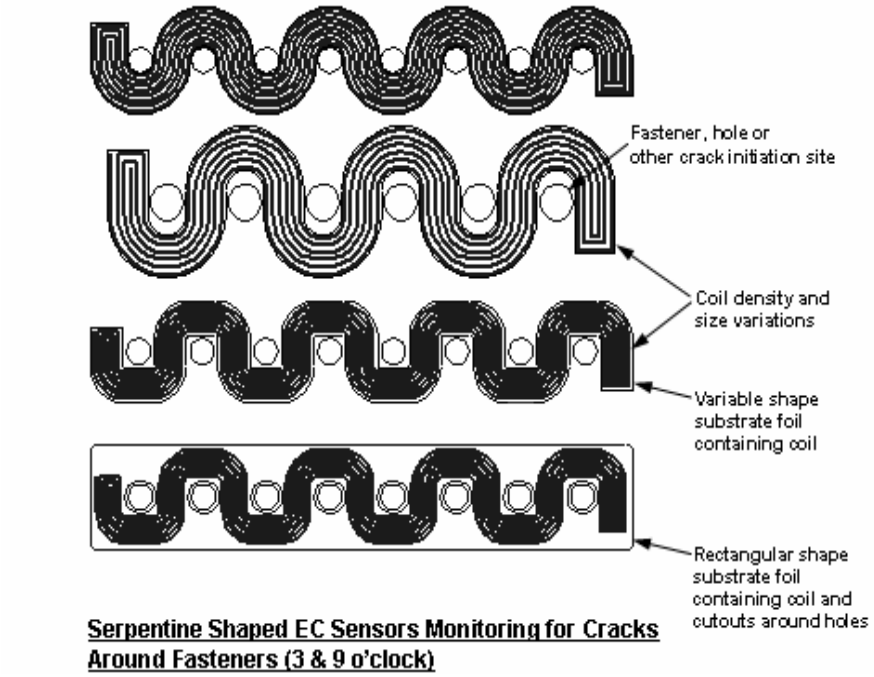

Figure 9-12: Example of Serpentine Coil Designs to Examine Fasteners for Longitudinal Cracks

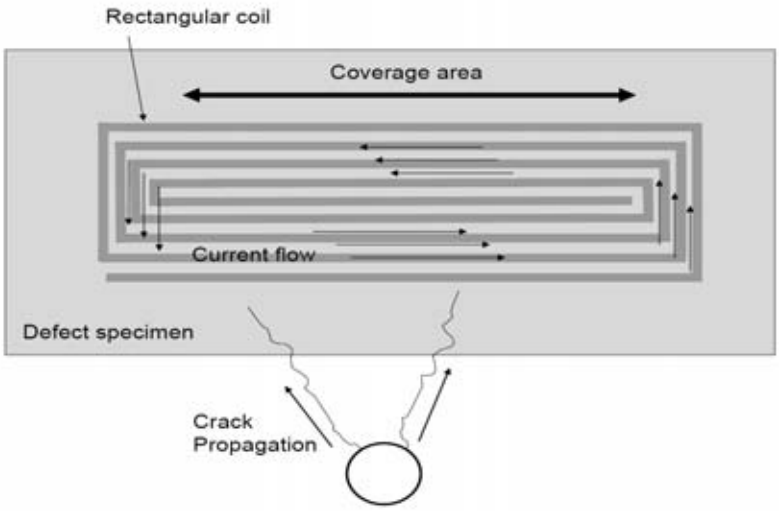

Figure 9-13: Radial Crack Growth Monitored with a Rectangular Coil

Some examples, shown in figure 9-14 below, indicate how the coil can be configured to provide varying degrees of coverage if the crack orientation is deterministic. The blue region in the figure indicates the effective coverage area and the central black shape represents the crack origin. The leftmost, U-shaped figure would provide more than 180 degrees of coverage for

cracks. This coil design would be effective for surrounding a joint. The middle, V-shaped, figure would provide effective coverage in either direction and would be useful for cracks that have a tight growth region. The right-most, C-shaped coil could be used to surround a cylindrical joint or fastener. Figure 9-15 illustrates how a modified rectangular coil can be designed to monitor the entire perimeter of a beam joint by wrapping the coil along the edges at the intersection of the two structures.

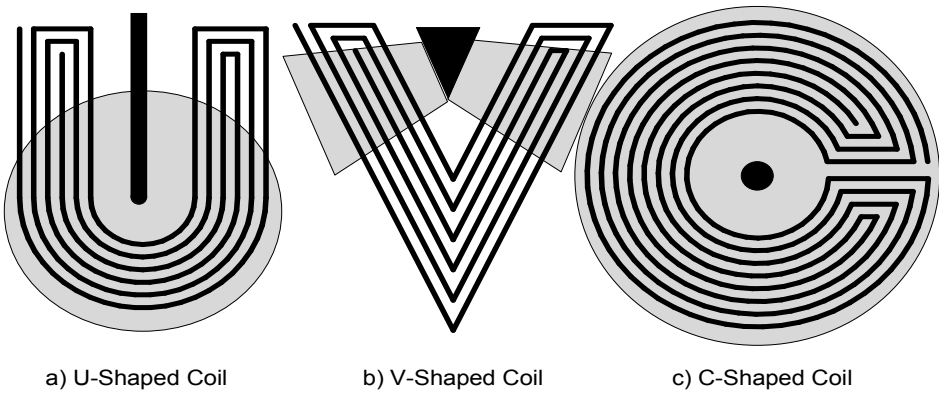

Figure 9-14: Optional, Custom Coil Geometries to Detect Crack Growth in Various Geometries

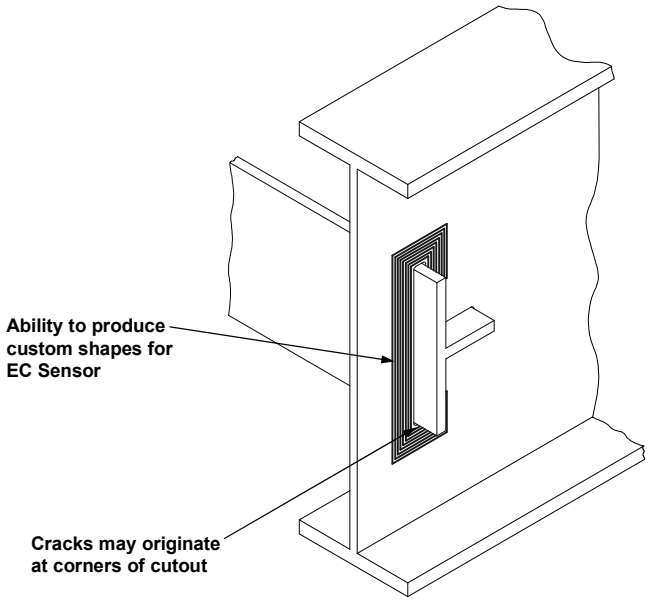

Figure 9-15: Customized Rectangular Coil for Beam Joint Inspection

Coil Array Configurations - Additionally, a thin film solution could employ a series of sectors or concentric regions to form an array of sensors to track the growth of a crack such as depicted in Figure 9-16. This configuration would allow the user to localize the crack and aid in determining its cause, its propagation direction, and its length.

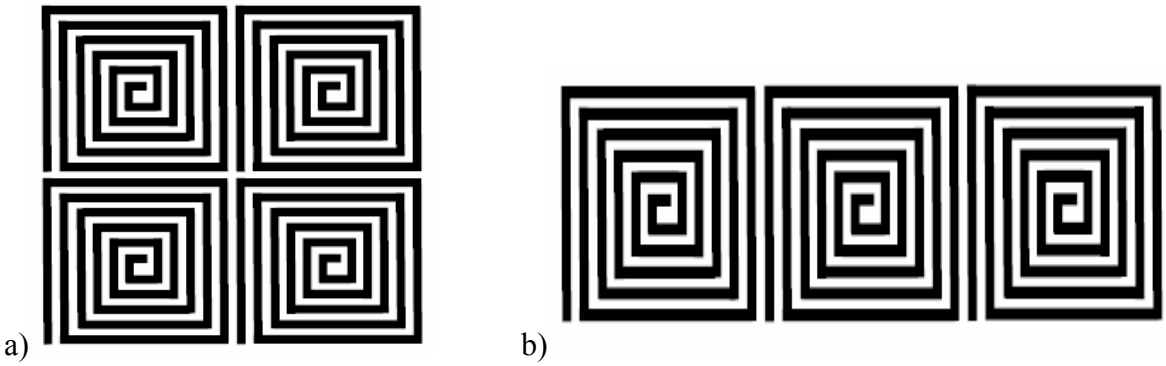

Figure 9-16: Example of Planar Sensor Arrays

The quadrature coil configuration (Figure 9-16a) can determine the quadrant where the crack started. Figure 9-16b illustrates a cascaded coil design to monitor a crack as it grows horizontally. Furthermore, a combination of a rectangular coil followed by rows of smaller square coils can detect and localize the crack. Figure 9-17 illustrates a sensor array to monitor the opposite side of a beam interface. The sensor array is multiplexed to determine impedance changes among adjacent sensors or against a designated reference sensor to determine the relative position of the incipient damage.

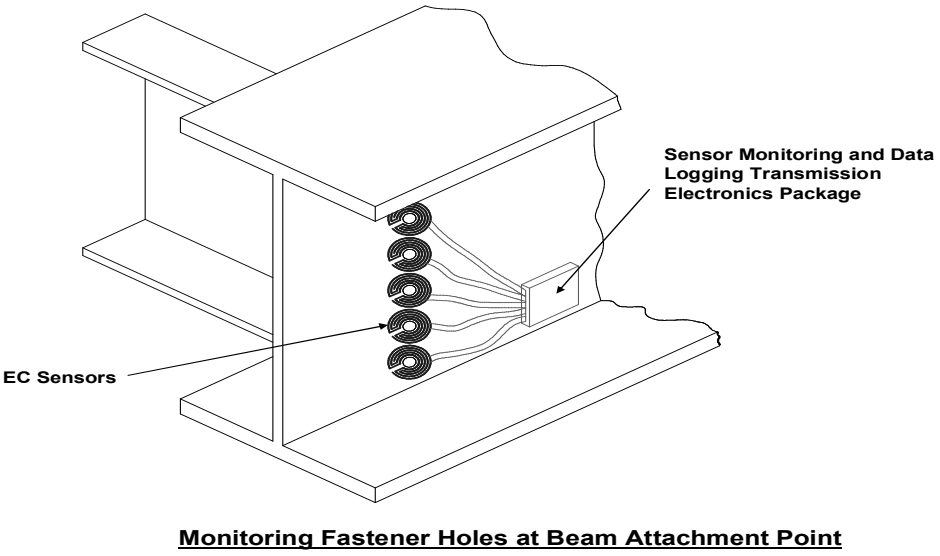

Figure 9-17: Sensor Array Configuration for Beam Interface

9.2.4 Non-Contact Detection

Often the structures are not directly accessible; they can be covered with protection layers (i.e., foam, rubber, coatings, etc) or strengthened by another structure (a conductive plate or composite panel). To be a useful SHM component, the EC sensor must penetrate either/both non-conductive or conductive gaps between the planar coils and the structure. Figure 9-18 illustrates the separation generated by a composite doubler that is installed over the repaired structure. The doubler prevents direct contact with the structure and the EC coil sensor is placed on top of the doubler.

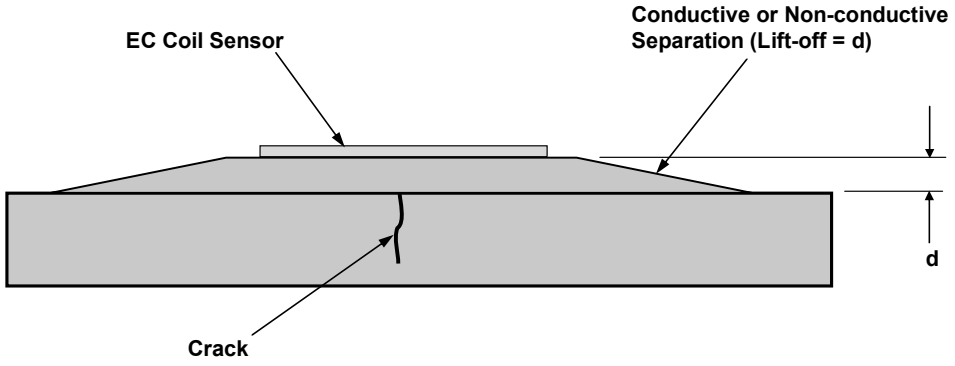

Deep Penetration of Magnetic Field for Subsurface Crack Detection
Coil Designed to Accommodate Max Lift-off (d) Expected

Figure 9-18: Illustration of Separation (Lift-Off) Between Sensor and Structure Being Inspected

Unlike ultrasonics that rely on strong adhesion and coupling with the device under test, eddy current sensing can tolerate weak adhesion and lift-off with the structure. Eddy currents are created using an electromagnetic induction technique to generate currents in the magnetic material under inspection. Thus, the sensor must be in proximity to the structure being monitored but it need not be bonded or in intimate contact with the surface/layer of interest.

Non-Conductive Gap (Lift-Off) - Although non-conductive materials between the EC sensor and the structure do not alter the magnetic fields, the magnetic field degrades as a function of distance. It is the weakened magnetic field that penetrates the structure's surface and generates the eddy currents used for crack detection. As depicted in the figure 9-19, the density of the magnetic field is determined by the magnetic flux of the coil. The field strength drops off by the cube of the distance from the coil. A way to expand the coil's range is to configure the radius near the value of the anticipated displacement. By setting the displacement equal to the coil radius, the magnetic field strength falls off linearly with the radius.

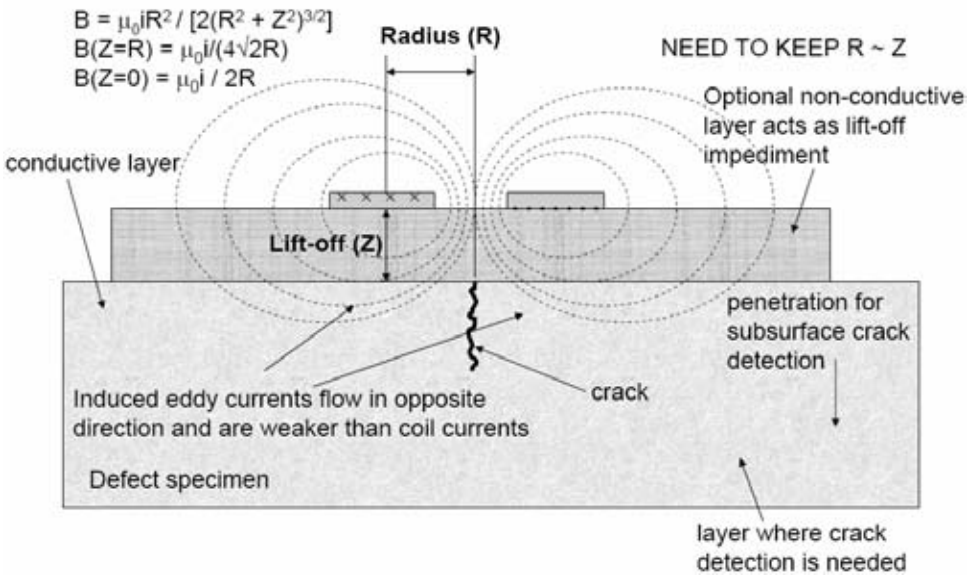

Figure 9-19: Magnetic Flux Density for Non-Conductive Gaps

Using Equation 9-1 for the magnetic field density as a function of lift-off distance, it follows that the coil's sensitivity is essentially flat beyond 1X the radius.

$$B = \frac{\mu_0 i R^2}{2\left(R^2 + Z^2\right)^{3/2}}, B(R = Z) = \frac{\mu_0 i}{4\sqrt{2}R} \qquad (9\text{-}1)$$

where, B = magnetic field density, R = coil radius, Z = distance from coil to depth of interest, μ_0 = normalized magnetic permeability constant for the material, and i = current. Ideally, the coil should be designed with a radius set to 2X the displacement, although aggressive designs can use smaller ratios [9.3]. Figure 9-20 shows how the resistance, inductance and Q of the coil change with proximity. In the graph, the proximity is normalized by the coil radius (x-axis), and the response (y-axis) is in units (L in μH, R in ohms, and Q is unitless).

This phenomenon can also be illustrated using the normalized impedance curves in Figure 9-21. The dashed lines show how the sensor response drifts from the operating point on the outer impedance curve when the sensor is in direct contact with the structure, towards the (0,1) origin where the sensor is operating in free space. The concentric rings within the outer impedance curve represent a revised impedance curve that corresponds to a normalized liftoff as a percentage of the coil's radius. It can be seen that the sensitivity of the coil falls off as the operating point moves inward towards the (0,1) free space operating point.

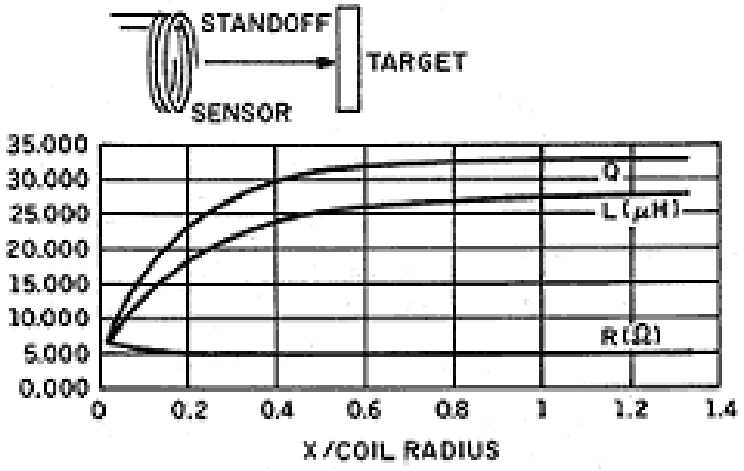

Figure 9-20: Proximity of Sensor Coil as a Function of Radius

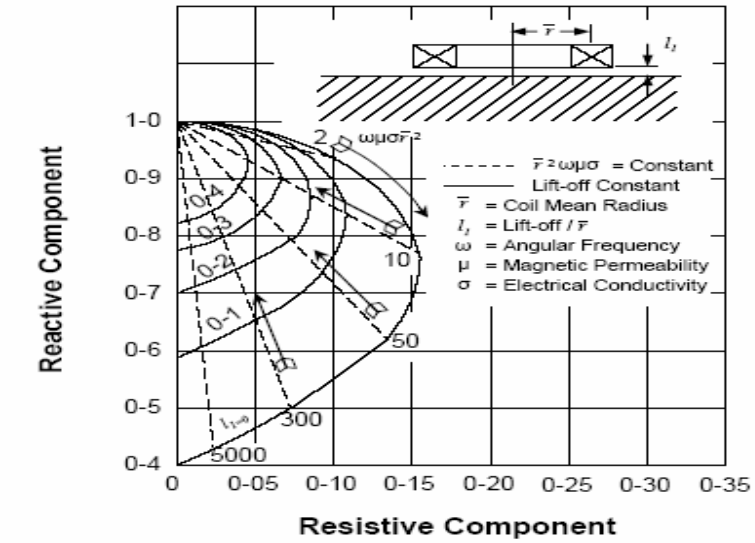

Figure 9-21: Lift-Off Normalized Impedance Curves (x/coil mean radius)

Again, a rectangular design with a width proportional to the lift-off will allow it to perform effectively. In these cases, the magnetic fields generated by a standard spot probe or pencil probe may have a difficult time reaching the material (see Chapter 8).

Conductive Gap (Penetration) - In the case of conductive structures, the proposed coil can operate in sufficiently low frequencies to penetrate through a structure of reasonable thickness and still produce eddy currents in the structure of interest. The depth of penetration is determined by the skin effect and is inversely proportional to the conductivity of the material and the frequency of the current flow. Also, as mentioned in the background section, the phase lag of the coil response can be measured to determine the depth of the signal and confirm that the defect is located in the structure.

$$\delta = \sqrt{\frac{2}{\omega\mu\sigma}} \qquad (9\text{-}2)$$

where δ = depth of field penetration, $\omega = 2\pi f$ and f is the frequency of excitation in the coil, σ = conductivity of the material, $\mu = (\mu_0 \text{ X } \mu_r)$ and μ_0 is the permeability constant and μ_r is the relative permeability of the material. Nevertheless, it is a common mistake to confuse the skin effect phenomenon with proximity. The skin effect only determines the penetration of the eddy current within the structure as a function of frequency and the material's conductivity. As illustrated in Figure 9-22, the drive electronics in the proposed solution can lower the coil's operating frequency to "push" the eddy currents deeper into the structure in order to locate sub-surface defects and to ascertain whether a crack has gone completely through a structure.

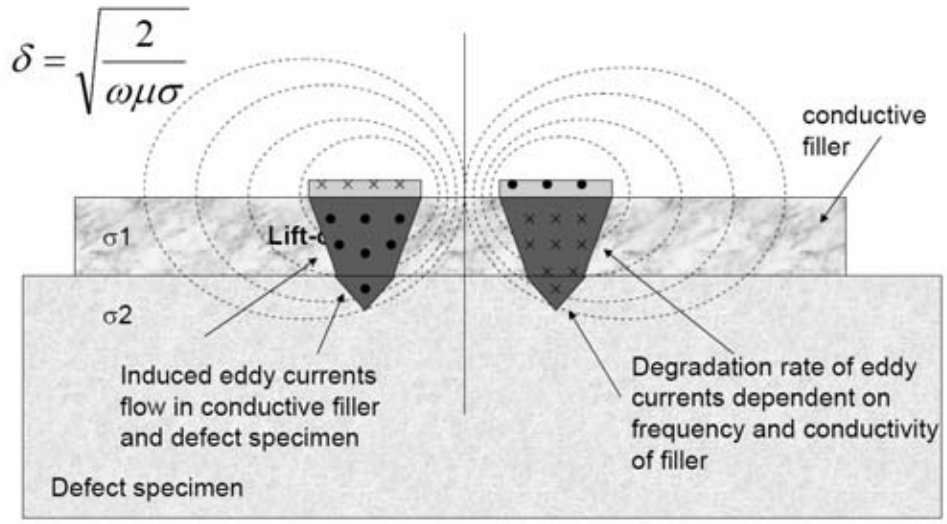

Figure 9-22: Impact of a Conductive Filler on Eddy Currents in the Structure

9. 3 Sensor Coil Parameters

In additional to the requirements and other considerations described previously, several other factors played a role in determining the dimensions and properties of the coil design. This section describes the models employed to design the coil.

9.3.1 Steel Specimen Properties

The specimen selected to represent the general steel structures and validate the sensor is comprised of INCONEL Alloy HX, a nickel-chromium-iron-molybdenum alloy with outstanding strength and oxidation resistance at temperatures to 220^0F. Table 9-1 provides some electrical properties of the steel specimen [9.4].

Electrical Properties			
Electrical Resistivity	0.000116 ohm-cm	0.000116 ohm-cm	
Magnetic Permeability	1.011	1.011	at 200 oersted (15.9 kA/m)

Table 9-1: Electrical Properties of INCONEL Specimen

9.3.2 Coil Trace Properties

The materials used to design the coil also factor into the response of the coil. The ounces of copper pour used to make the traces impact the AC resistance of the traces and the quality factor of the coil. The ratio of the trace width versus the trace thickness can impact current flow ($thickness_{cu} = 1.378*OZ_{cu}$ mils). The pitch, or spacing between traces, and the distance between traces impact the coil's inductance. The derivation is driven by the skin effect within the copper trace. In theory, a larger inductance will generate a larger magnetic field. The inductance is proportional to the square of the number of turns and layers of coils. However, one must try to minimize the length of the coil in order to minimize its resistance ($\sigma_{cu} = 58$ MS/m).

9.3.3 Substrate Properties

Adding layers increases the interlayer capacitance and reduces the self resonant frequency of the coil. The best trade off is achieved by using a turns-to-layers ratio of one. The dielectric coefficient of the circuit materials determines the interlayer capacitance. The values for common materials are captured in Table 9-2.

Material	Thinnest Core	Max Copper	Dieletric Coefficient
Flex(Kapton)	0.001"	2 oz	3.2 – 3.5
FR-4	0.004"	2 oz	4.25 - 4.7
Polyimide	0.005"	2 oz	4.0 – 4.6

Table 9-2: Material Thickness and Dielectric Coefficients

9.3.4 Coil Dimension Properties

As mentioned previously, a rectangular coil provides an effective coverage along its length if the length is excessively larger than its width. Under these conditions, the inductance at the center of the coil is independent of the coils length and is determined by its width. The width of the coil is selected by the amount of lift-off experienced by the coil. Again a ratio of 1:1 between lift-off and coil radius is desirable. The inductance of planar rectangular coils can be modeled using equivalent area ratios of circular coils [9.5, 9.6]. However, problems arise in trying to meet all the constraints. Fortunately, there are equations for single layer rectangular coils that can be combined with multi-layer coil designs to determine workable parameters [9.7, 9.8]. Additionally, one must consider the width to thickness ratio of the trace to correctly determine

the AC resistance of the coil. It turns out that the skin depth generates non-linear behaviors when the estimated depth is larger than the corresponding dimension [9.9].

9.3.5 EC Sensor Coil Parameters

Using this information described in Section 9.3, a rectangular coil design was selected. The coil is oriented with the long edge spanning orthogonal to the crack axis. The length, "A" provides the effective coverage area. Table 9-3 and Figure 9-23 identify the coil dimensions. Although, subsequent revisions to the model have yielded better performance, the coils provide a good signal response for the designed lift-off.

Dimension	Description	Value
A	Inner Coil length	1782 mils
B	External Coil length	2073 mils
C	Inner Coil Width	198 mils
D	External Coil Width	1068 mils
E	Trace Width	8 mils
F	Spacing Width	8 mils

Table 9-3: EC Sensor Coil Parameters

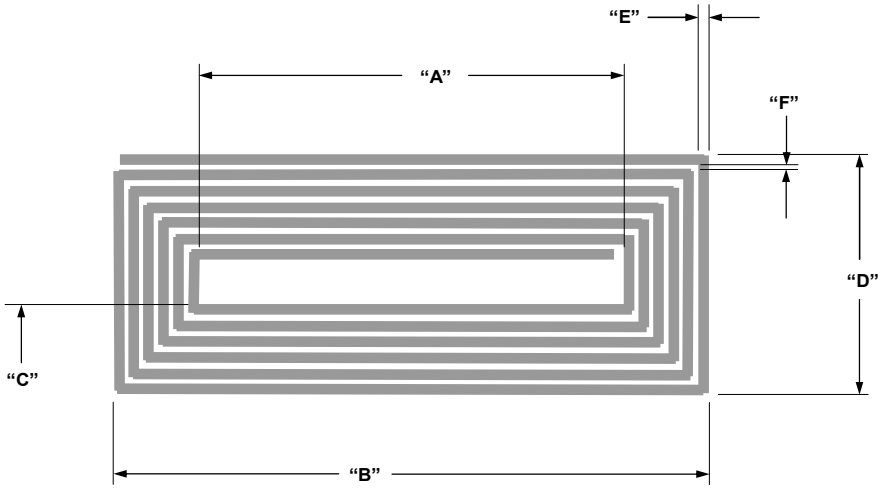

Figure 9-23: EC Sensor Coil Parameters

The fabricated coils, shown in Figure 9-24, are two layers with the electrical properties and coil characteristics listed in Table 9-4 (measured with the HP4194A Impedance/Gain-Phase analyzer).

Variable	Model Value	Actual Value
L	261.6 uH	263 uH
C	26.4 pF	339 pF
R	20.4 ohm	34.8 ohm
SRF	1.9 MHz	533 kHz
Layers	2	2

Table 9-4: EC Sensor Coil Electrical Characteristics

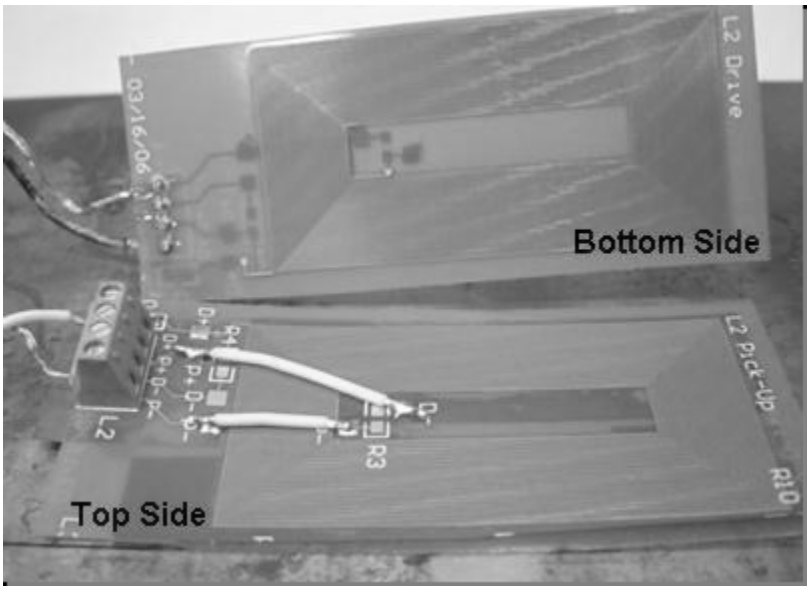

Figure 9-24: Fabricated and Validated Coils in PCB for EC Sensor

9.4 Eddy Current Sensor Performance Testing

An extensive array of validation testing was completed on this sensor to quantify its ability to detect both surface and subsurface fatigue cracks. With the emphasis on sensor use in concert with composite doubler repairs, much of the testing revolved around crack detection through various lift-off thicknesses (one form of subsurface crack detection) corresponding to the presence of the composite doubler between the EC sensor and the metal surface to be inspected. Chapter 8 provides the primary discussion on the sensitivity and reliability performance of the EC sensor. However, some results are sited here for completeness.

Figure 9-7(a) shows one sample signal generated by this mountable, EC sensor when it encounters a crack. It should be noted that in normal operation, the EC sensor is mounted to the surface it is monitoring. Thus, in a real-life scenario the fatigue crack grows until it engages the sensor. For the validation tests, the sensor was placed on top of the surface (composite doubler or other metallic surface) as shown in Figure 9-25 and moved toward the fatigue crack in the underlying metal plate.

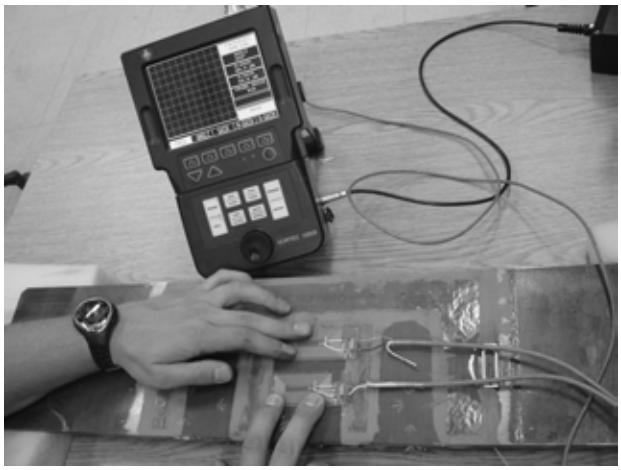

Figure 9-25: Performance Testing of Eddy Current Sensor

One aspect of the testing looked at the degree to which the crack needed to engage the sensor – intersection of the coil over the crack tip as shown in Fig. 9-11 - in order for the sensor to record a positive detection. The level of engagement necessary depended on the design of the sensor coil. If the sensor was designed to detect deep, subsurface cracks (large lift-off), then the crack-to-coil engagement was greater. If the sensor was designed for surface crack detection (sensor mounted directly on steel structure) or small amounts of lift-off, then the crack-to-coil engagement was quite small. The smaller, high frequency coils used for surface or near-surface crack detection could detect cracks when they were as much as 0.020" *away* from the coil (*before* engaging the coil). Worst-case conditions required the crack to engage the coil by approximately 0.020". This is an important consideration when sensors are needed in tight locations that require small crack detection. For the larger coils needed for lower frequencies and deep subsurface crack detection (up to 0.5" lift-off), it was necessary for the crack to overlap the coil by approximately 0.25". In such instances of subsurface structures or structures beneath a repair, it is expected that the "allowable" crack growth before detection will be much longer than an unprotected surface crack.

The second phase of the performance testing studied crack detection through various levels of lift-off. In these evaluations, the sensor signal generated by the presence of a crack was compared to the sensor signal generated when it interrogated an unflawed region (noise). The resulting crack signal-to-noise levels were calculated to establish the sensitivity of the sensor while also determining its ability to eliminate false calls (i.e. false positive indications in uncracked regions). Sufficient tests were conducted on a wide range of specimens in order to assess the overall repeatability and reliability of the sensor function. Figure 9-26 shows two sample signals produced by the EC sensor when it engaged a crack beneath 0.580" and 0.905" lift-offs. Large signal excursions were observed despite lift-off levels approaching 1". In addition, low noise levels produced by this sensor – corresponding to the sensor signal at an unflawed site - were also observed. Normal inspection procedures require signal-to-noise (S-N) values greater than 2 or 3 in order for an inspector to make a flaw call. The results in Figure 9-

25 show that even through extreme lift-off conditions, the sensor produced a S-N level in excess of 10 for the 0.9” lift-off and greater than 35 for the 0.58” lift-off.

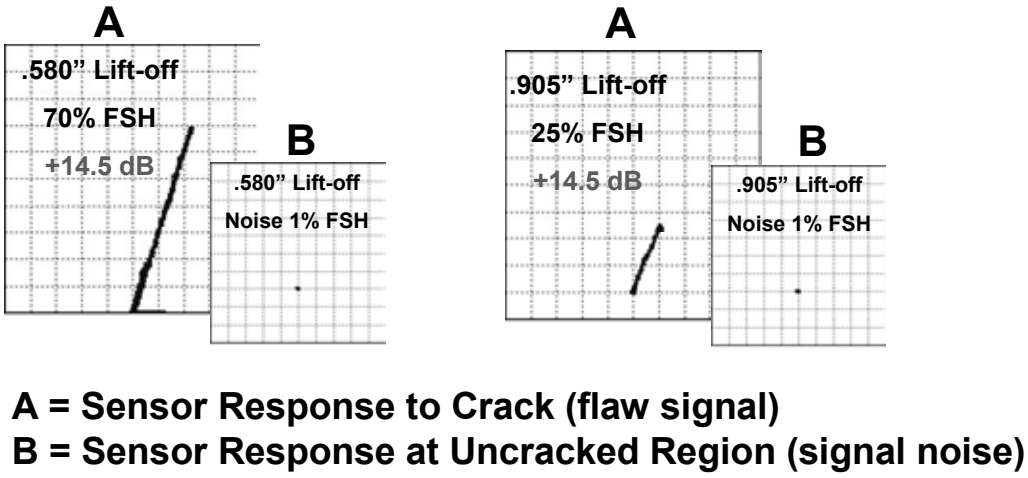

Figure 9-26: Subsurface Crack Detection Signals Produced by Sandia Labs Eddy Current Sensor Inspecting Through Extremely Thick Surface Layers

9.5 Eddy Current Sensor System Components

With the coil design completed, the team focused on developing the system electronics required to provide a remote, monitoring system. Figure 9-27 illustrates the system components. The coil is driven by an impedance integrated circuit that contains both a digital-to-analog converter and an analog-to-digital converter. The coil is placed in either an LC resonant circuit or in an auto-balance bridge configuration to detect changes in the coil’s impedance. The digitized samples are homo-dyned with the same oscillator used to drive the coil. This approach has great noise immunity properties. The resultant complex samples are either stored in non-volatile memory or transmitted wirelessly to a host computer using the ZigBee (802.15) protocol. At the PC, a graphical user interface (GUI) plots the result and allows the user to analyze the performance of the system over a period of time. Automated alarms can also be included in the GUI program to aid in flaw signal interpretation. The system is comprised of a combination of custom and commercial off-the-shelf (COTS) devices. In particular, the system uses a ZigBee PC dongle from Integration to connect with the Freescale MC1324 Integrated MCU and ZigBee transceiver [9.10]. A graphical user interface, written in python for portability, can operate on several OS platforms.

Figure 9-28 shows a more detailed layout of the sensor electronics. The system will operate from a set of rechargeable AA batteries. A MCU (Microchip PIC 4550 USB microcontroller) is used to control the ZIC (Analog Devices AD5933 Impedance IC [9.11]) and store the results in serial EEPROM memory. Future designs could replace the PIC with a Freescale MC13124 MCU containing a 2.4 GHz transceiver. An on-board charger could recharge the batteries when powered directly from a 6VDC port. The components can operate at either 5V or 3.3V levels. A

higher voltage allows the device to drive the coil with higher currents, whereas the lower voltage would extend battery life. The hardware is also designed to support a network of sensors, using the auto-balance bridge design, from a single controller device.

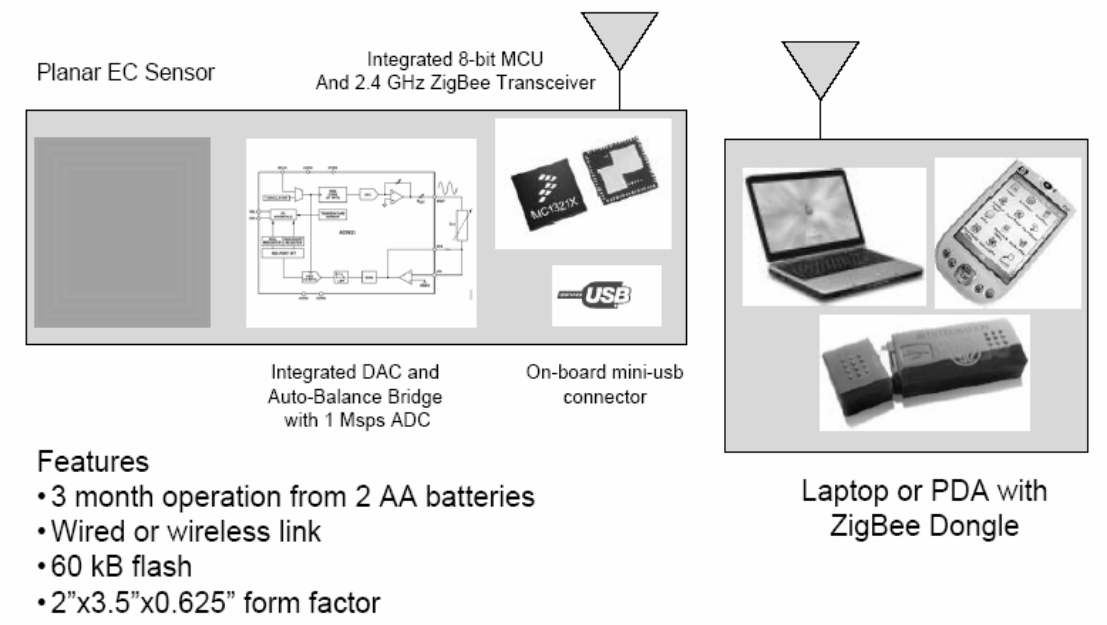

Figure 9-27: Sensor System Components Overview

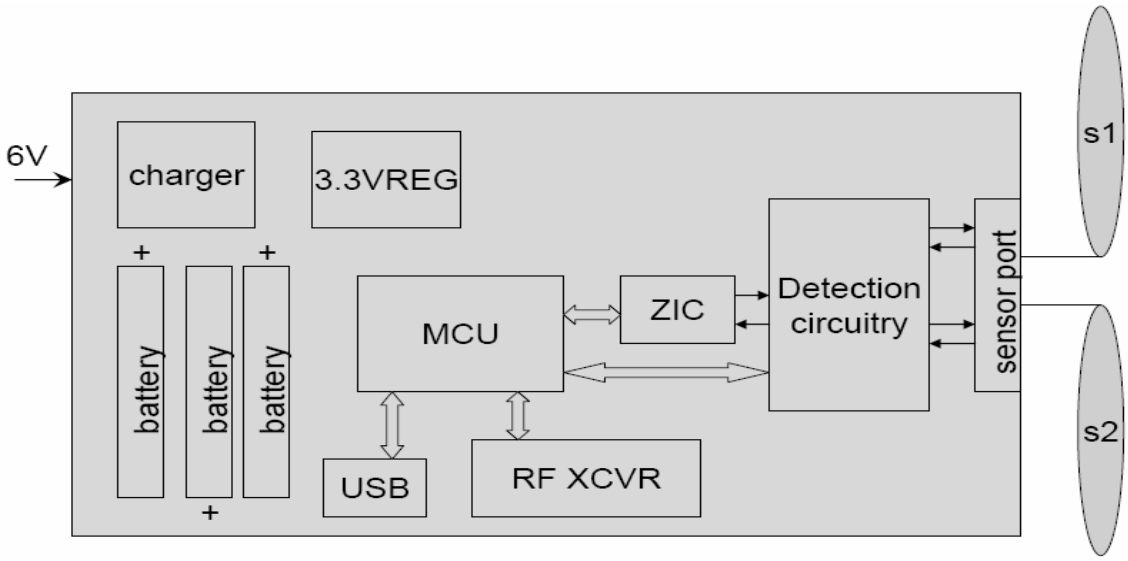

Figure 9-28: Detailed Sensor System Layout

Successive hardware iterations can reduce the footprint and incorporate the detection electronics directly onto the sensor if desired. Depending on the number of sensors employed, the wireless aspects could also be added to the electronics to create autonomous sensor devices.

9.6 Detection Circuitry

The system contains two detection circuits and two calibration circuits to facilitate analysis. A combination of multiplexers and de-multiplexers are used to switch between measurement modes. This flexibility will allow comparing and cross-referencing the various measurements to facilitate crack detection.

Figure 9-29 shows four information transfer signals between the sensor and detectors. The 5V signal is provided to support buffering at the coil in configurations using long cables to connect the sensor to the detector. However, only 3 wires are necessary, the drive signal, a return, and a sense signal. The sense signal is provided to improve measurement accuracy because it will behave like a high impedance input.

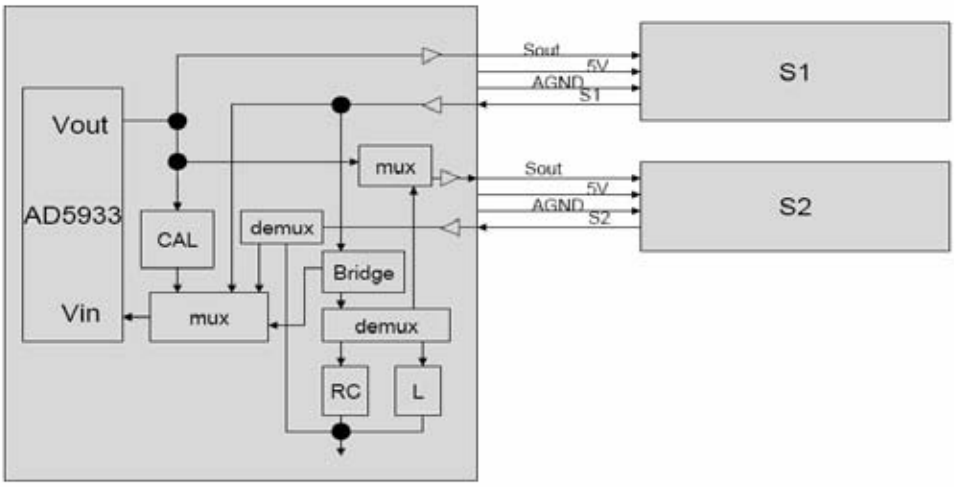

Figure 9-29: Detection Circuit Details

9.6.1 Auto Balance Bridge Detector

The auto-balance bridge circuit uses a reference and a test coil. An instrument amplifier is used to detect changes in impedance between the two coils. Again, the differential output is sampled by the impedance analyzer and converted into complex components. The auto-balance bridge has a wide impedance measurement range, high accuracy and is widely used (see Table 9-5). It uses a simple, single-element bridge, as shown in Figure 9-30, which consists of an oscillator, the unknown impedance, an operational amplifier, and a feedback resistor. The output of the bridge circuit is sampled and mixed with the input signal to produce a signal centered near DC. The circuit seeks to measure the voltage ratio required to balance the current flowing through the unknown impedance with current flowing through the feedback resistor. The circuit also measures the phase shift between the measured voltage and the source voltage. With a known magnitude and phase, the real (resistive) and imaginary (reactive) components of the unknown impedance can be determined.

Technology	Advantage	Disadvantage	Frequency range	Application
Auto-Balancing-Bridge	Most accurate Wide impedance measurement range Wide frequency coverage	Limited frequency coverage	5 Hz–40 MHz	All impedance measurement applications in LF (4194A, etc.)
I-V	Grounded device measurement Probing measurement	Limited frequency and impedance measurement range	10 kHz–100 MHz	In-circuit impedance measurement (4194A + 41941A, etc.)
RF I-V	Accurate impedance measurement through the GHz range Grounded device measurement	Limited frequency coverage	1 MHz–1.8 GHz	Components and materials measurement in RF (4291B, etc.)
Network analysis	Very broad frequency coverage (LF through microwave)	Impedance measurement range is limited to values close to the characteristic impedance of the analyzer.	≥ 10 kHz	Components and materials measurement (8753E, E5100, etc.)

Table 9-5: Comparison of Impedance Measurement Techniques

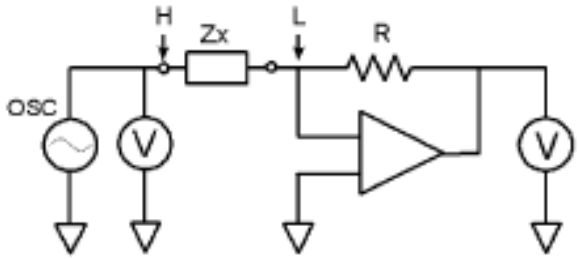

Figure 9-30: Auto-Balance Bridge Circuit

The sensor detector uses a similar bridge amplifier with modifications to linearize the output, improve gain accuracy, and reduce loading from the feedback resistor and op-amp bias current [9.12]. The design in Figure 9-31 uses an op-amp to generate a virtual ground between the impedance elements in the primary branch and a second non-inverting op-amp that measures the voltage at the node of the impedance elements of the secondary branch. The RC impedance in the secondary branch offsets the LR impedance of the coil in the primary branch. This design uses a dual arm bridges and replaces the C1, R3 branch with a test coil. Measurements taken in the bridge configuration are performed at a single frequency.

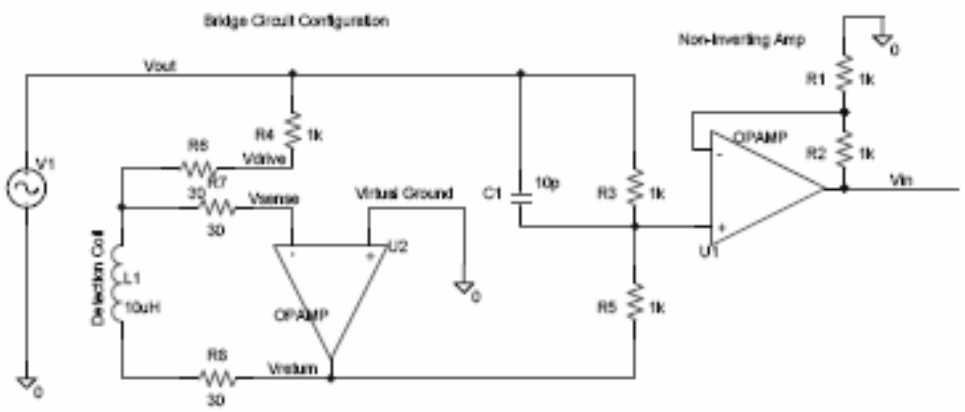

Figure 9-31: Single Arm Bridge in EC Sensor Detector

9.6.2 LC Resonance Detector

The sensor detection circuit can also measure changes in impedance using an LC resonant circuit. Changes in the resonant frequency of the circuit can be determined by adjusting the frequency that generates a zero phase angle. The impedance IC uses a 24-bit register to control the oscillator frequency and can detect 0.1 hertz changes in the resonant frequency. In the resonant mode, the resonant frequency of the circuit is determined by the value of the inductance, assuming that the capacitance is fixed. To locate the resonance, the software must sweep through the frequencies and determine the zero-crossing of the phase (see Figure 9-32). This frequency corresponds to the peak magnitude of the signal. Additionally, the system will attempt to locate the bandwidth of the resonance by identifying the -3 dB (peak/sqrt(2)) frequencies.

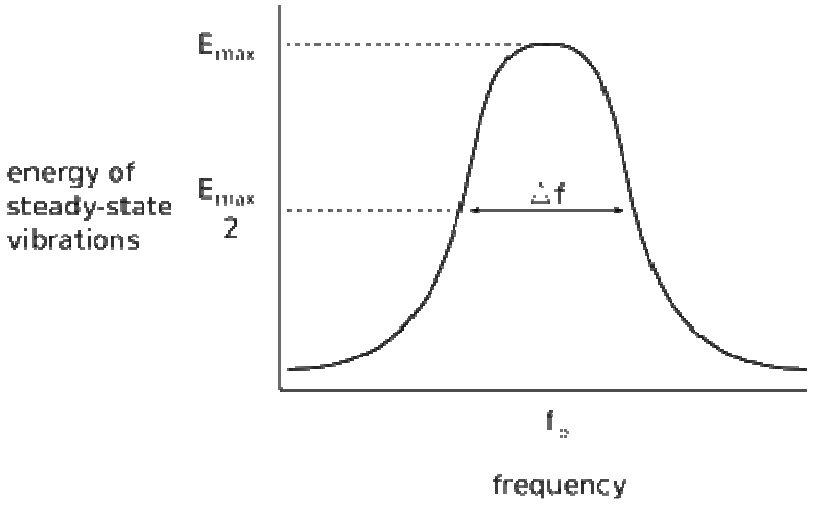

Figure 9-32: Resonant Mode Response

The information stored in memory is the resonant frequency, the peak magnitude, and the start and stop frequencies for the bandwidth. Since the phase is zero at resonance, only the real component needs to be stored.

9.6.3 Calibration Mode

Finally, the detection circuit also contains calibration components to compensate for drift and adjust for offset and gain errors in the system. There are two calibration configurations: a) a purely resistive device with low temperature coefficient, and b) a LCR device that mimics the ideal coil response. Measurements in these modes are taken at a predetermined frequency.

9.7 Impedance Analyzer Description

The Analog Devices AD5933 is responsible for driving the coil and measuring its response [9.13]. This Impedance Integrated Circuit (ZIC) integrates a DAC, ADC, gain stages, and other components necessary for accurate measurements (see Figure 9-33). The device can measure impedances ranging from 100 Ohms to 10 MOhm using frequencies up to 100 kHz. The ZIC is controlled using the I2C serial protocol. A set of registers are used to control the start frequency, frequency step size, number of steps, settling time, and averaging to support either a frequency sweep or repeat measurements at a single frequency.

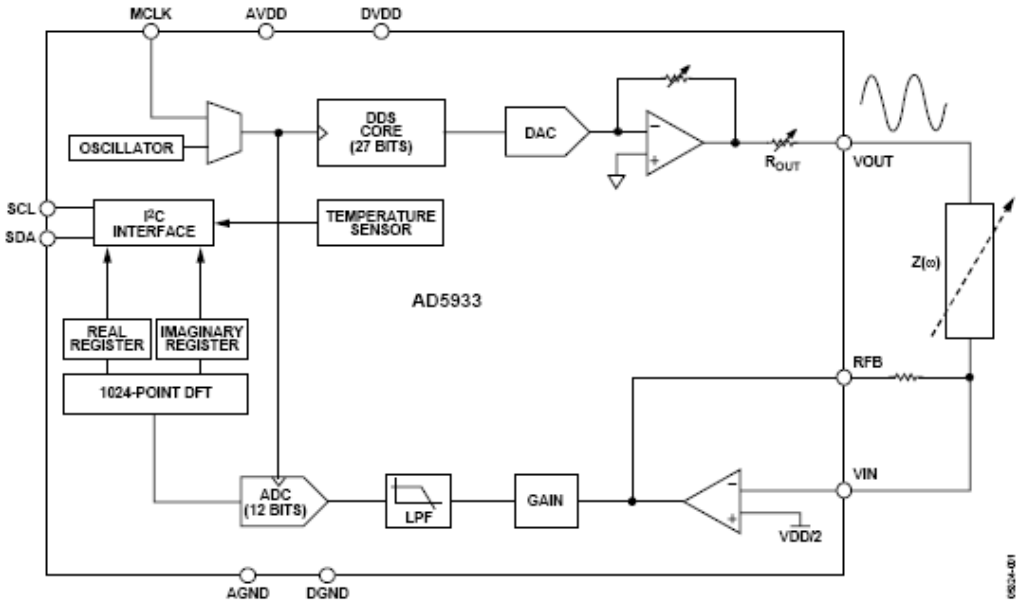

Figure 9-33: Functional Block Diagram of Impedance IC

A 27-bit phase accumulator direct digital synthesis (DDS) core provides the output excitation signal at a specified frequency determined by a 24-bit register. The user can select among 4 output gain and offset settings to drive the impedance. On the receiver, the input is offset to a single sided amplifier and programmable gain stage where it is low pass filtered for anti-aliasing

and digitized with a 12-bit analog-to-digital converter (ADC). The ADC clock is driven by the same oscillator used to drive the DDS to ensure coherence between the input and output. Once digitized, the samples are fed into a 1024 Discrete Fourier Transform stage to generate a complex impedance value. The ZIC also contains a temperature sensor to determine necessary adjustments to the impedance based on temperature.

9.8 Microcontroller Description

A microcontroller is used to configure the ZIC, configure the detection circuitry, make impedance measurements, retrieve the impedance results, and store the impedance. The results are stored in a non-volatile serial EEPROM with a temperature measurement, where it can be retrieved later for additional analysis. The flow of activities and features programmed into the operation of the sensor monitoring hardware is shown in Figure 9-34.

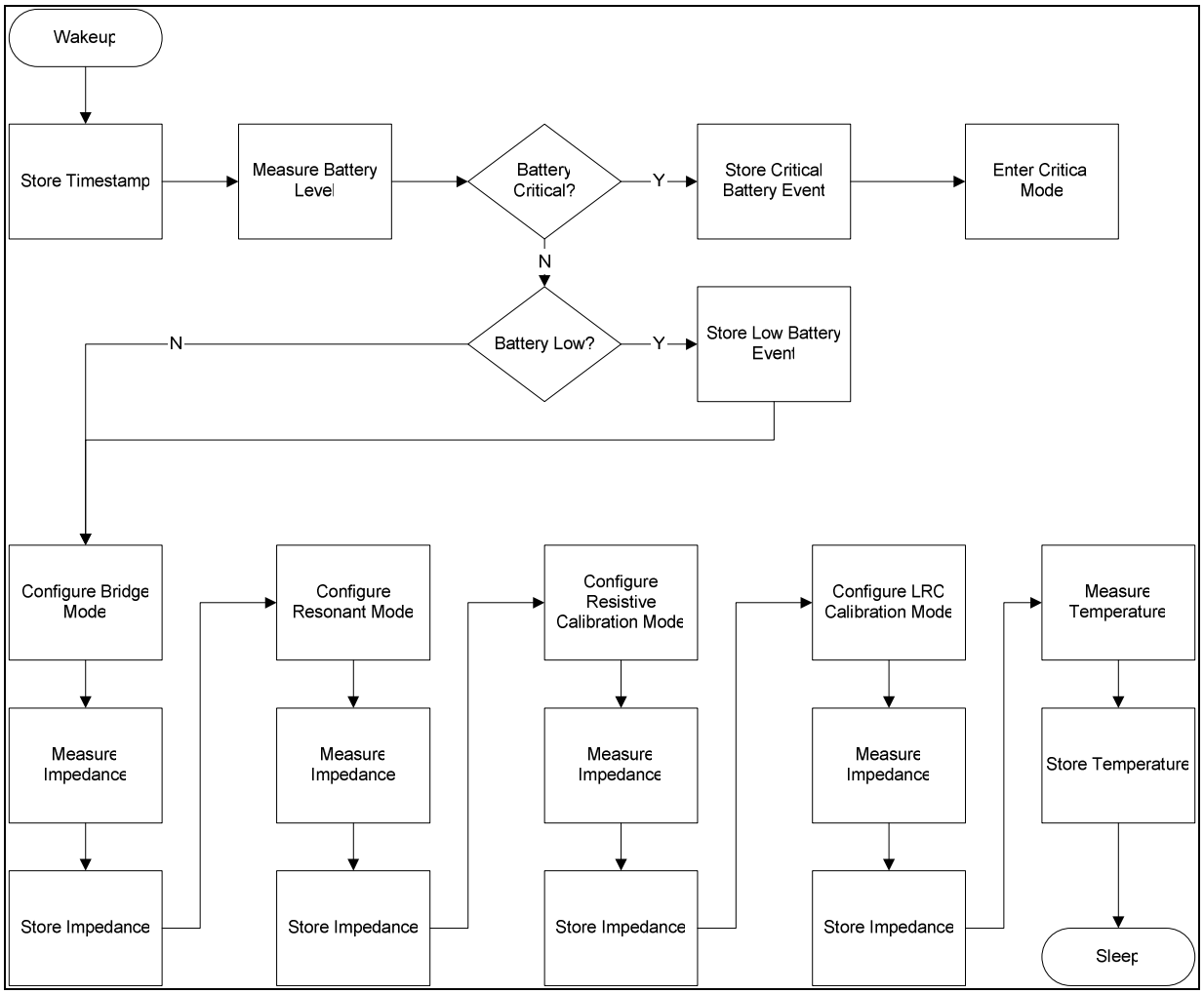

Figure 9-34: Software Flowchart Describing Sensor System Function

An external real-time-clock (RTC) is used to wake up the system at pre-selected interrogation intervals to make measurements. Upon wake-up, the MCU stores the timestamp and measures the battery level to determine if it is critical. If the battery has been depleted, the system enters a critical state where it minimizes activities and stops taking additional measurements. If the battery is not critical, but low, the system will record the event, and proceed with data acquisition. The system rotates between the two measurement and two calibration modes, each time configuring the ZIC and storing the result in the external serial EEPROM. After completing the impedance measurements, the MCU requests a temperature measurement from the ZIC and stores it in EEPROM, before reconfiguring the RTC and going back to sleep.

9.9 Graphical User Interface

A graphical user interface (GUI) was developed to enable interactive operation with the system. The GUI allows the user to control the ZIC directly and plot the results at a fixed update rate of 10 Hz. The GUI is comprised of a series of tabs to manage the display and the ZIC. The interactive mode of operation assumes that the Impedance device is tethered to a PC where commands and responses can be exchanged and visualized. For the interactive mode, a graphical user interface (GUI) was developed using a tabbed windowed approach where a set of tabs is used to configure the device and the other tab is used to display the results from the impedance device.

The display screen can illustrate up to 3 different traces. This information is displayed in either complex or frequency domain format, depending on the type of measurement. Impedance analyzers display information from balance detection circuits in complex data form indicating the reactive and resistive impedance components generated by the coil (see Figure 9-35).

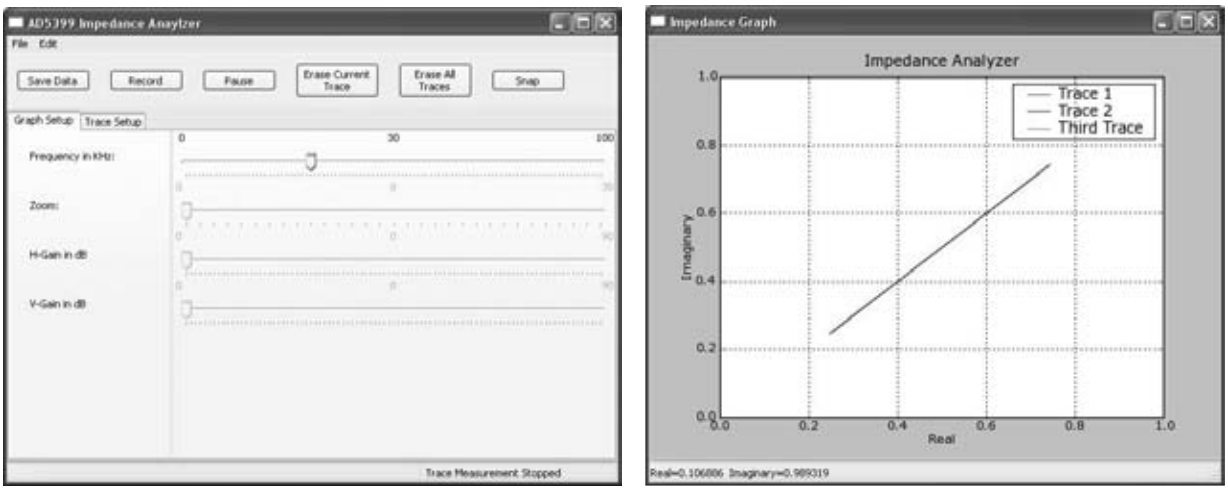

Figure 9-35: Impedance Analyzer GUI for EC Sensor System

In this mode, the user has the ability to rotate the origin of the axis to correspond to a horizontal lift-off and move the operating point into the lower right-hand corner of the display to be consistent with existing impedance analysis displays.

9.10 Packaging

The assembled system consists of the sensor, detection electronics, the communications, and the MCU. At the onset of the program, the team focused on developing an integrated solution that could be packaged into the sensor. One initial solution is depicted in Figure 9-36 where the sensor, inserted on the bottom, would co-exist with the electronics on the top. The sensors would work independently and communicate with a hub to provide inspection results. To provide coverage for any large application, an array of sensors can be distributed in the critical regions.

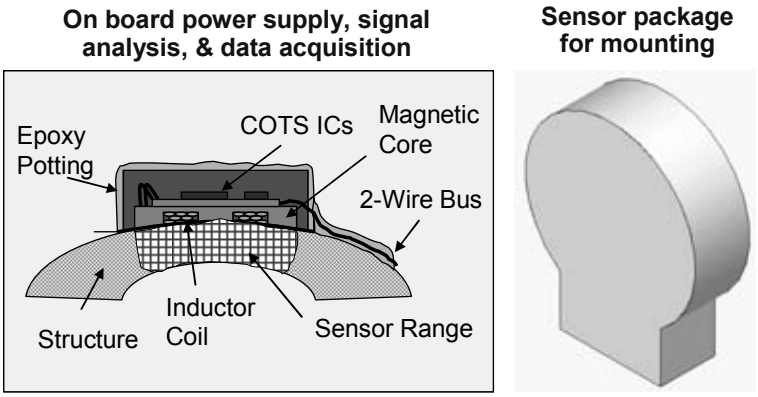

Figure 9-36: Sample of Packaging Approach for EC Sensor with Electronics

Figure 9-37 provides an illustration of the sensor, the electronics and the transceiver development path in two, more elegant, packages. The solution on the left side of Fig. 9-37 shows the sensor and electronics packaged on a single substrate. If a reduction in overall footprint is necessary then a stacked package, as depicted on the right side of Fig. 9-37 can be deployed. The advantage of having the coil directly integrated with the PCB is that simplified manufacturing can reduce assembly costs and part count.

Conversely, the electronics package can be contained in a remote package and then tethered to each of the sensors it controls/monitors as shown in Fig. 9-17. As an example of this more adaptable sensor system Figure 9-38 the first-generation packaging of the integrated sensor system electronics. It combines the electronics to support multiple differential or single-ended sensors. The sensors attach through screw terminals at the end of the case. Programming ports are provided for the PIC4550 microcontroller. The detection circuitry uses a series of multiplexers to select from two measurement and two calibration modes.

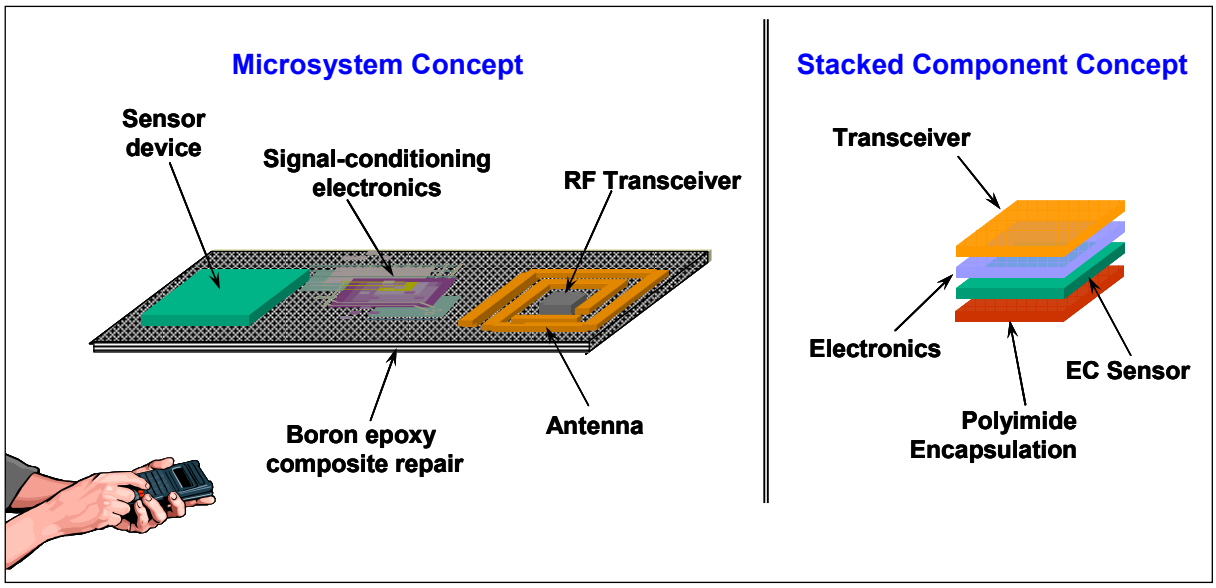

Figure 9-37: EC Sensor and Control Electronics Packaging

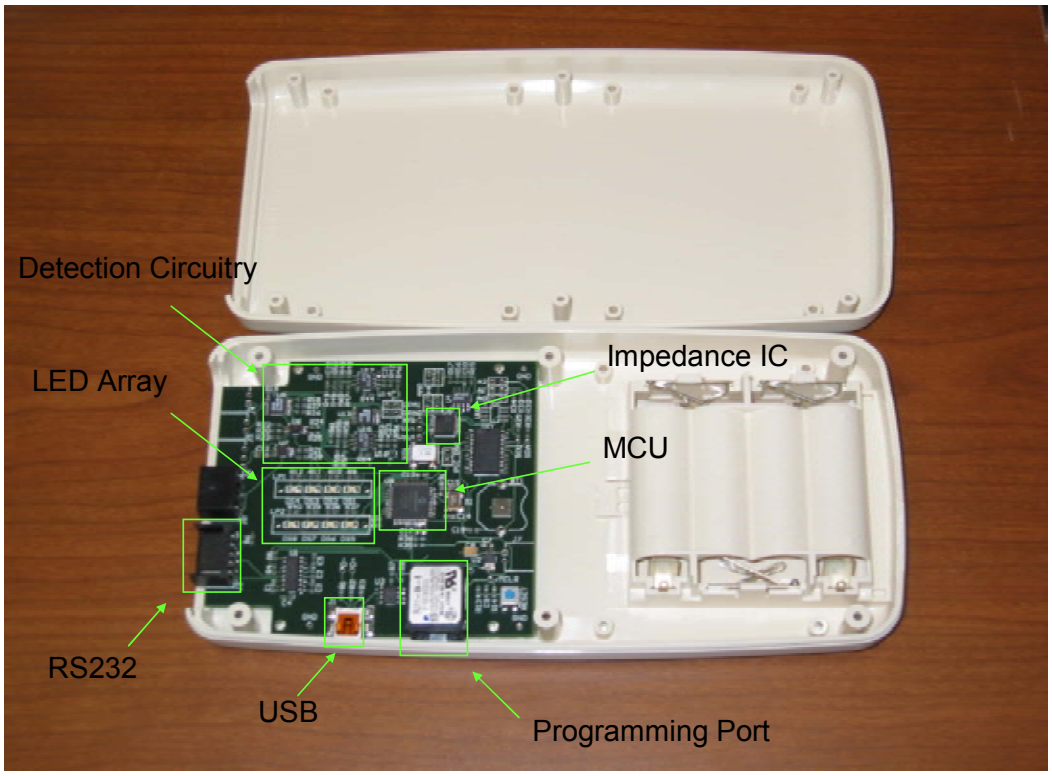

Figure 9-38: Sandia Labs Eddy Current Sensor System Package Containing All Electronics and Power Supply for an Array of Remotely Located Sensors

An LED array is included to provide visual indicators for system status. The MCU can communicate directly with a PC using either USB or RS232 interfaces [9.14]. Additionally, an extern RF modem can be directly connected to the system to provide a wireless PC link. When combined with the XBee Xtender RF Bridge, the system can be accessed from a range of 40 miles (see Figure 9-39). The system can operate from a bank of 4 AA rechargeable batteries that permit the system to operate for a period from 3 to 6 months using a configuration of daily measurements and bi-weekly wireless downloads at pre-scheduled intervals.

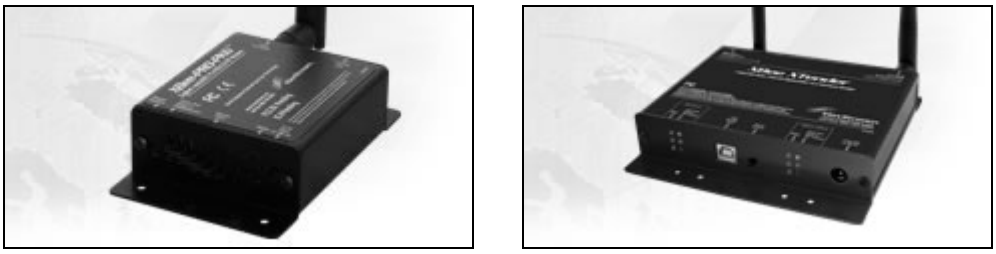

Figure 9-39: Maxstream ZigBee RF Modem and Xtender RF Bridge

9.11 Next Steps in Evolution of Eddy Current Sensor System

Along with the detection circuit and the software to measure impedance changes, the system would benefit from the incorporation of additional features to enhance operations.

Temperature Compensation - Temperature can be incorporated into the software to eliminate indirect deviations. The impedance of the structure and components will change with temperature daily and seasonally. The impedance rate changes caused by temperature should behave with a periodicity whereas crack onset and growth will be non-linear. By calibrating the system against known impedances and correlating them against temperature, these effects can be filtered.

Self-Calibration - Through the use of self-calibration, it is possible to compensate for any drift and offsets in the measurements and provide even greater accuracy.

Data Storage – Storing all data can allow users to filter historical data and possibly better assess trends and data deviations. The software can filter historical information and apply compensation to improve sensitivity and identify significant events.Also local storage allows the device to operate independently for long intervals between data uploads.

Scalable Scanning Frequencies - Scalable scanning frequencies can be used to gage depth of damage and overcome conductive displacement.

Adaptable Measurement Intervals - In the stages before a crack develops, the system will encounter infrequent relevevant impedance changes. However, as the crack develops and grows, the incidence of interesting events should increase. The system can use the information on the variance in impedance measurements to scale the measurement intervals as indicated in Figure 9-

40. Thus, a growing flaw can be monitored more frequently and flaw growth information can be more accurately acquired.

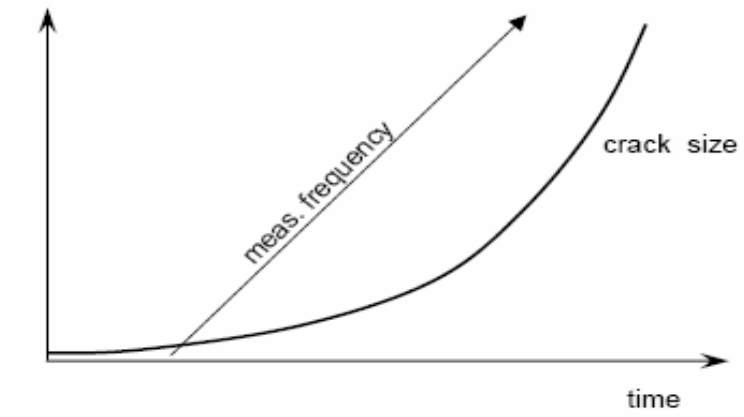

Figure 9-40: Example of Adaptable Measurement Frequency

Remote, Real-Time Monitoring and Event Alarms - The direct integration of detection algorithms and the definition of regions for event logging can be used to initiate external communications. These may be audible alarms or highlighted data signals sent to web sites.

References

9.1 P Shull. Nondestructive Evaluation, Marcel Decker, Inc., 2002.

9.2 D. Halliday and R. Resnick, Physics, 3rd Edition, Part II", John Wiley & Sons, pp. 746-805, 1986.

9.3 Roach, "Designing and Building an Eddy Current Position Sensor," *Sensors Journal*, September, 1998.

9.4 MatWeb Special Metals INCONEL® ALLOY HX. http://www.matweb.com/search/SpecificMaterial.asp?bassnum=NINC52

9.5 H. Wheeler, "Simple Inductance Formulas for Radio Coils," Proceedings of the IRE, Vol. 16, 1928.

9.6 S. Mohan, M. Hershenson, S. Boyd, T. Lee, "Simple Accurate Expressions for Planar Spiral Inductances," IEEE Journal of Solid-State Circuits, Vol. 34, 1999

9.7 A. Balakrishan, W. Palmer, W. Joines, T. Wilson, "Inductance of Planar Rectangular-Spiral Strip Conductors for Low-Profile Inductors," PESC, Vol. 2, 1992.

9.8 H. M. Greenhouse, "Design o f Planar Rectangular Microelectronic Inductors," IEEE Transactions on Parts, Hybrids, and Packaging, Vol. PHP-10, June 1974.

9.9 F. Burkett, "Designs for Thin Film Inductors." Proceedings of the 1971 Electronics Components Conference, 1971.

9.10 MC13211/212/213 ZigBee™ - Compliant Platform – 2.4 GHz Low Power Transceiver for the IEEE® 802.15.4 Standard plus Microcontroller, Freescale Semiconductor, Inc. 2007.

9.11 PIC18F2455/2550/4455/4550 Data Sheet, Microchip Technology, Inc. 2007.

9.12 W. Kester, “Practical Design Techniques for Sensor Signal Conditioning,” Analog Devices, Inc., 1999.
9.13 Analog Devices AD5933 1 MSPS, 12-Bit Impedance Converter, Network Analyzer.
9.14 Freescale MC1321x System In Package 2.4GHz RF Transceiver and 8-bit MCU.

10.0 FIELD APPLICATION: REPAIR OF INTERSTATE 10 HIGHWAY BRIDGE

Dennis Roach, Kirk Rackow, and Waylon DeLong

10.1 Introduction to Bridge Repair Application

Recent failures of aircraft and civil structures have compelled the engineering community to take a fresh look at the fail-safe, safe-life, and damage tolerance design philosophies. Moreover, in the wake of the August 2008 interstate bridge collapse in Minneapolis, a wide range of concerns have arisen over bridges and other civil structures that are being used beyond their initial design lifetime. These concerns are heightened by the fact that many of these structures undergo minimal, and possibly inadequate, inspections. The effect of structural aging and the dangerous combination of fatigue, corrosion, and other environmentally-induced deterioration is now being reassessed. The end result of these assessments has been a greater emphasis on the application of sophisticated rehabilitation and repair technology along with improved health monitoring approaches.

This extensive study demonstrated the feasibility of applying composite repairs to steel structures such as mining trucks, oil recovery equipment, buildings, and bridges. With the foundation provided by this LDRD effort in place, the focus turned to producing a field demonstration of bonded composite repair technology on a civil structure. This chapter presents the application of high-modulus, fiber-reinforced polymer (FRP) composite patches to repair a steel bridge on New Mexico Interstate-10 highway. This bridge experienced fatigue crack growth in one of its steel I-beams at a joint between the I-beam and a cross-bracing diaphragm. All aspects of the bridge repair were coordinated with the New Mexico Department of Transportation (NMDOT).

Steel bridges are susceptible to fatigue cracking caused by numerous cycles of heavy, live loading. Steel superstructure bridges built during the interstate construction boom of the 1950's and 1960's are reaching or surpassing their initial design lifetime. Also, the future magnitude and frequency of loading on interstate highways were underestimated and this produced additional, unanticipated fatigue scenarios. Depending on their level of maintenance, some bridges are showing visible signs of deterioration. Presently, state departments of transportation are being forced to detour permit loads around such structures to limit the magnitude of loading while attempting to replace a large numbers of these structures that have all reached retirement age at the same time. This situation has placed even greater demands on efficient, effective, and safe permanent repair and reinforcement methods.

The use of bonded composite doublers has the potential to overcome difficulties associated with current bridge repair techniques. Instead of installing bolted steel splice plates or performing welds to implement a repair or completely replacing cracked steel superstructure members, it is possible to bond a single FRP composite doubler to a cracked steel component. Current techniques for strengthening steel structures have several drawbacks including: 1) requirement for heavy materials, 2) section loss using bolted steel splice plates, 3) the addition of new crack initiation sites to install fastened repairs, 4) poor fatigue performance in welded repairs, 5) lack of weld quality guarantee, and 6) the need for maintenance due to continued corrosion attack or

crack growth. The use of composite doublers, which do not have brittle fracture problems such as those inherent in welds, helps extend a structure's fatigue life and reduce service downtime.

10.2 Assessing Fatigue Cracks and Repair Needs

The first phase of this repair demonstration included a site visit to view the bridge structure and assess a number of repair design and installation issues. Figures 10-1 through 10-3 show the Interstate 10 bridge and highlight the bridge construction around the damaged region. The goals of the initial site visit were to:

- Measure all structure geometry
- Measure the profile of the fatigue cracks
- Conduct a fit check on the preliminary repair doubler designs
- Perform strain field monitoring to support the final repair design effort
- Assess critical surface preparation and installation steps
  - Ability to grit blast the steel surface
  - Proper sizing of field compressor
  - Ability to draw vacuum over all heat blanket regions
- Complete a heat source/sink analysis to determine:
  - Ability to raise temperatures to 225^{o}F in the repair region
  - Check proposed heat blanket & vacuum bag arrangement
  - Check function of high amperage (30 A) power cables
  - Proper power supply from field generators (2)
- Coordinate logistics with NMDOT– overall preparation for final repair installation.

Figure 10-1: I-10 Bridge at Avenida de Messilla in Las Cruces, NM (Westbound Lanes); Damaged Area is Indicated in the I-Beam Directly Under Westbound Traffic

Figure 10-2: Close-Up View of I-10 bridge Showing Example of Live Loading and Interior I-Beam Containing the Fatigue Cracks

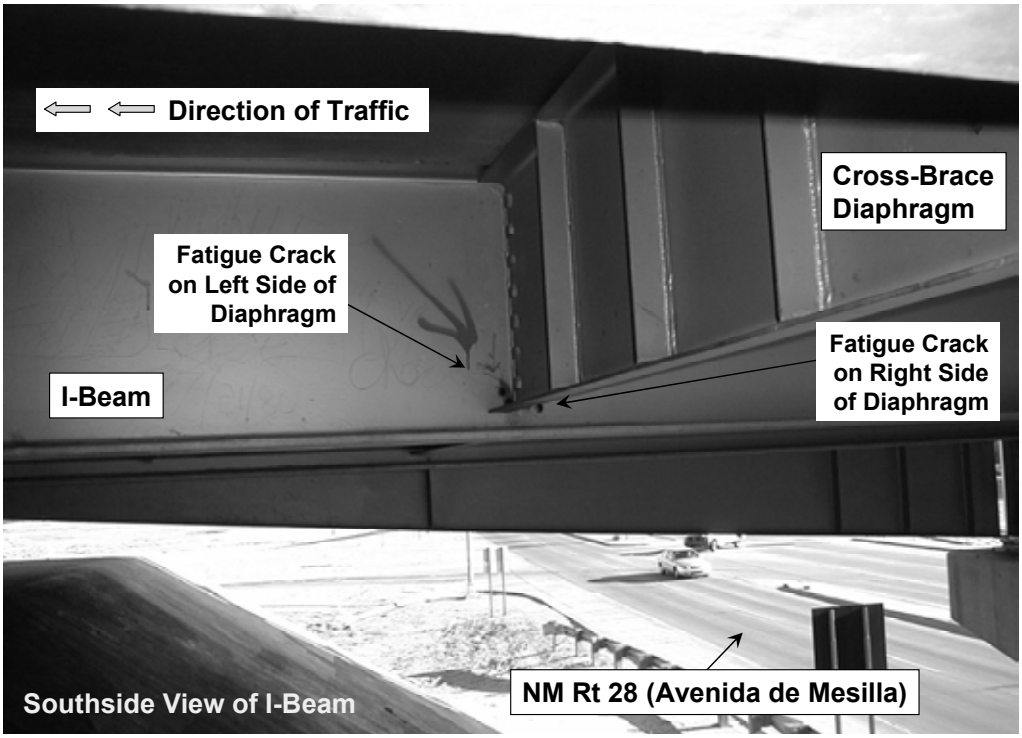

Figure 10-3: View of Damaged I-Beam and Bridge Construction in the Vicinity of the Fatigue Cracks

Figures 10-4 through 10-9 contain a series of photos and schematics to provide a complete description of the fatigue cracks and all steel members surrounding the damaged region. The I-beam to be repaired was 0.5" thick. The set of fatigue cracks covered an area that was approximately 5" L X 4.5" H. In addition to the damaged I-beam, the staggered position of the cross-brace diaphragms are highlighted. The large holes visible in the web of the I-beam are

stop-drills that were added in an attempt to arrest the growth of the fatigue cracks. Figures 10-6 through 10-9 show that the stop-drill method was not successful and that the fatigue cracks continued to propagate.

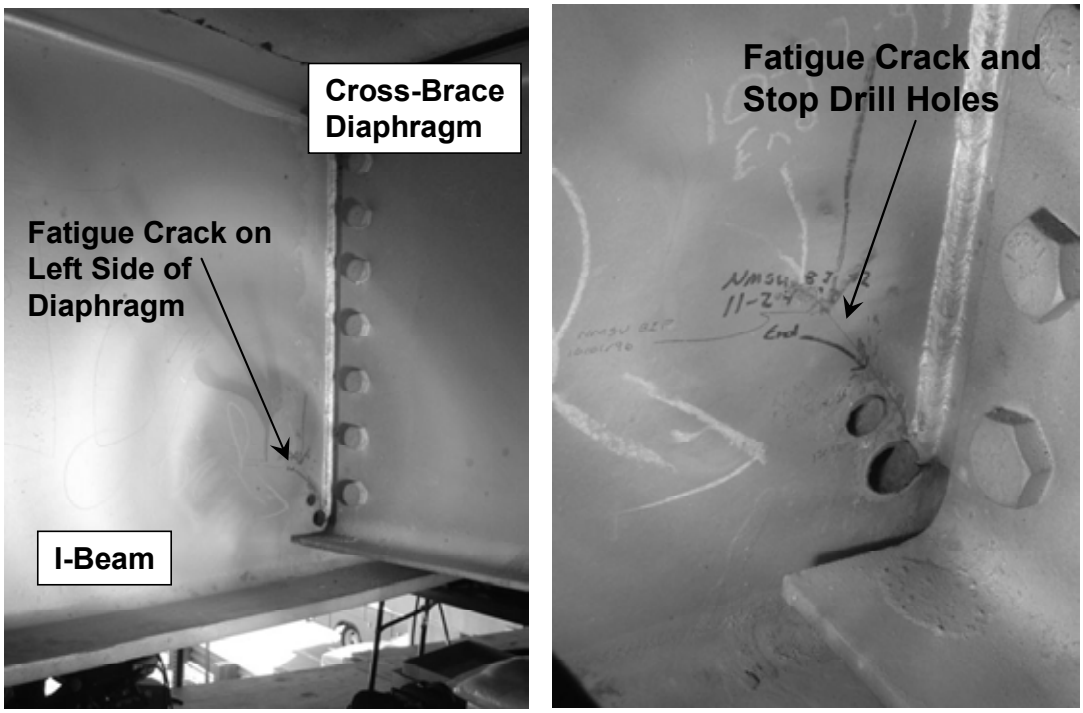

Figure 10-4: View of Segment of Fatigue Cracks on West Side of Diaphragm as Viewed from the Southside of the I-Beam; Unsuccessful Attempts at Arresting Crack with Stop-Drill Holes Can Be Seen

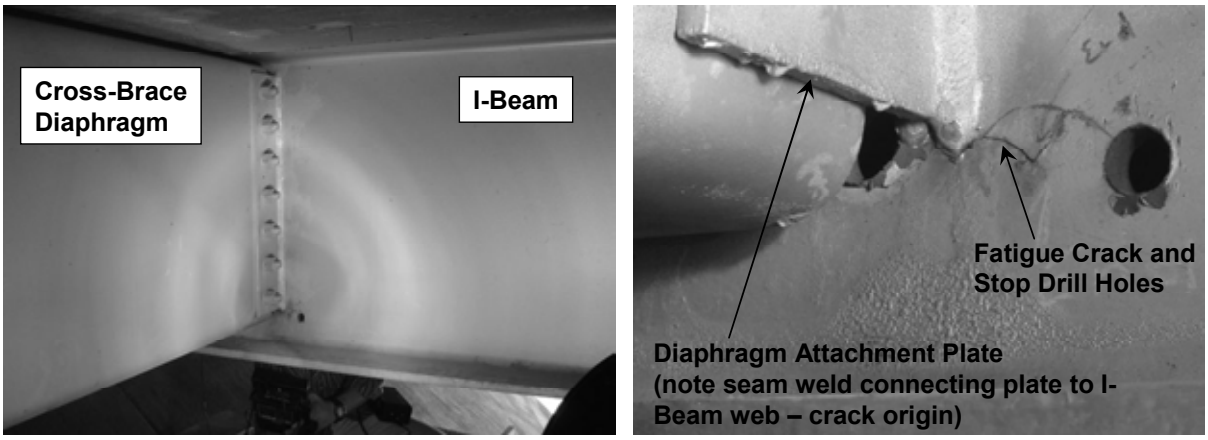

Figure 10-5: View of Segment of Fatigue Cracks on East Side of Diaphragm as Viewed from the Southside of the I-Beam

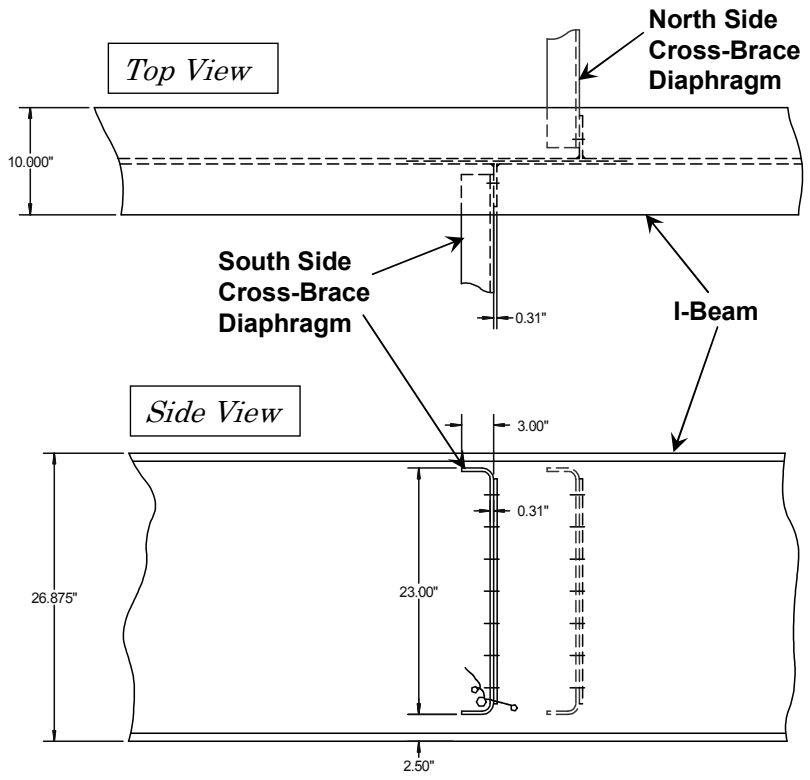

Figure 10-6: Side View and Top View of I-Beam Showing the Staggered Position of the Cross-Brace Diaphragms

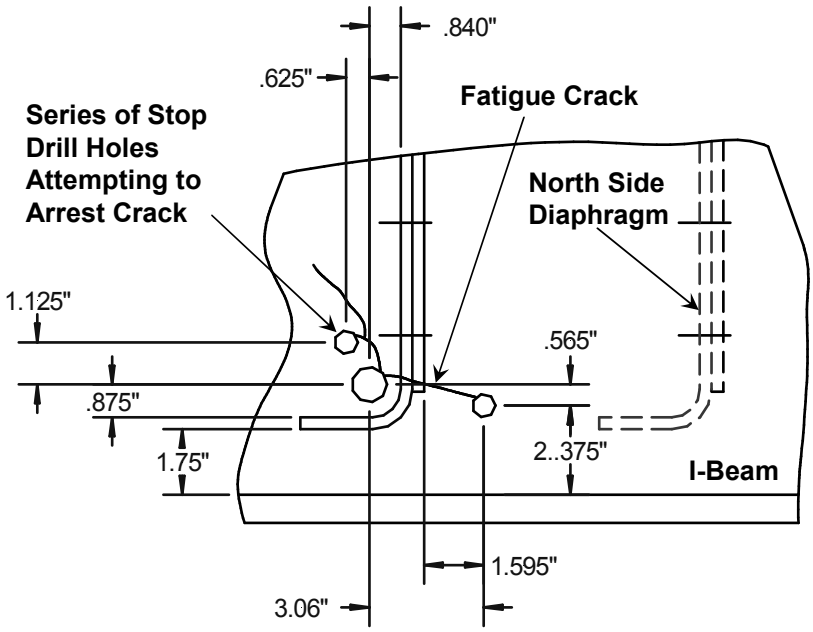

Figure 10-7: Close-Up View of the Fatigue Cracks and Stop-Drill Holes Showing Their Location Relative to the North and South Side Diaphragms

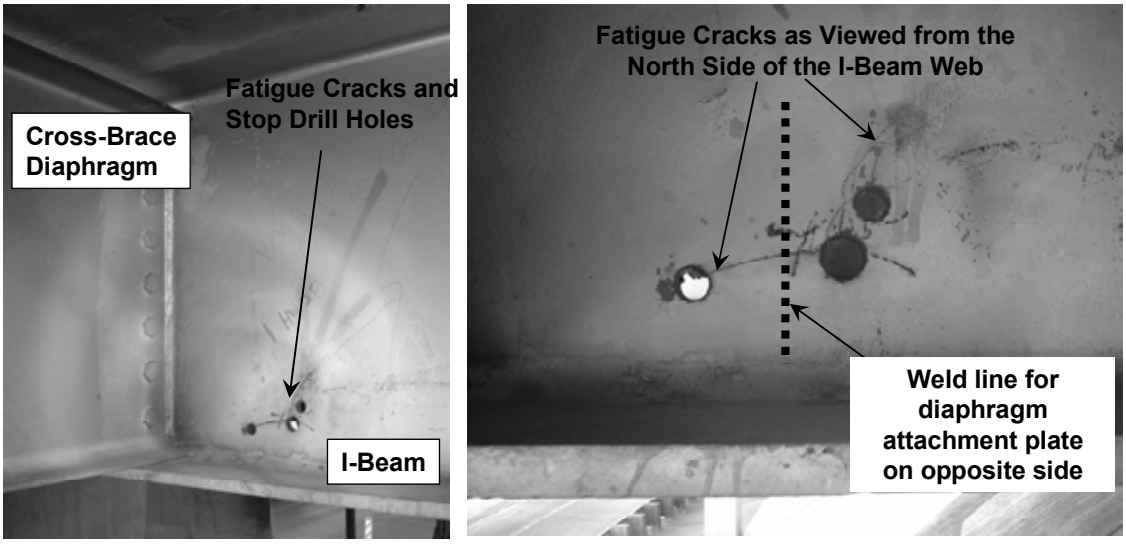

Figure 10-8: View of Segment of Fatigue Cracks and Stop-Drill Holes as Viewed from the Northside of the I-Beam

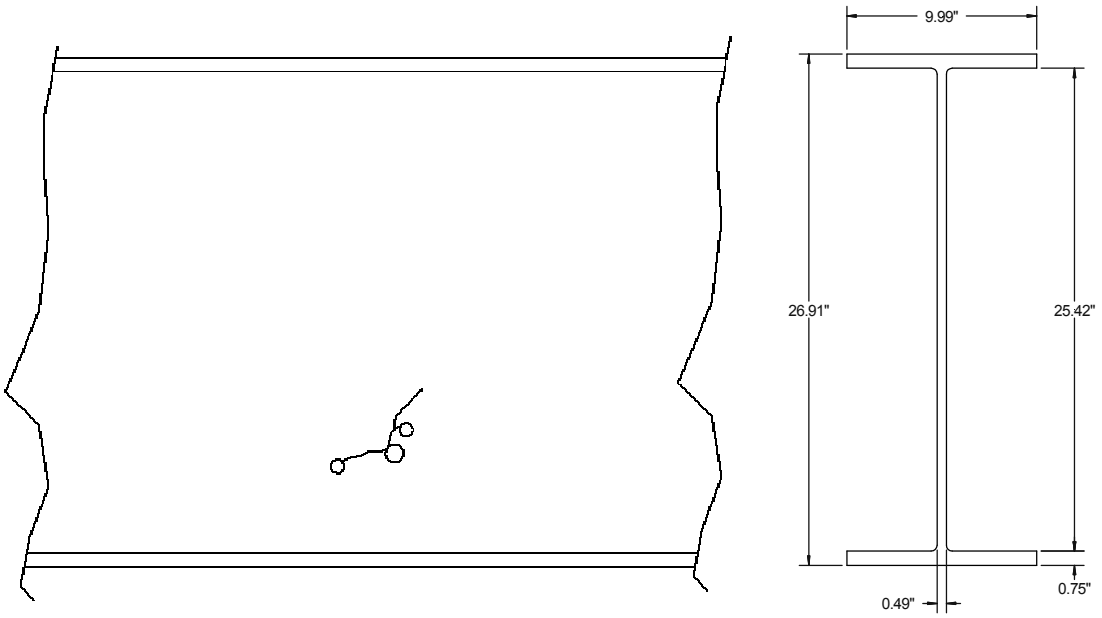

Figure 10-9: Schematic of Fatigue Cracks and Stop-Drill Holes as Viewed from the Northside of the I-Beam

Eddy current inspections – as shown in Figure 10-10 – were used to determine the path of the fatigue cracks and establish the tip of the cracks which were not visible to the human eye. Figure 10-11 shows the cracks highlighted with a black marker.

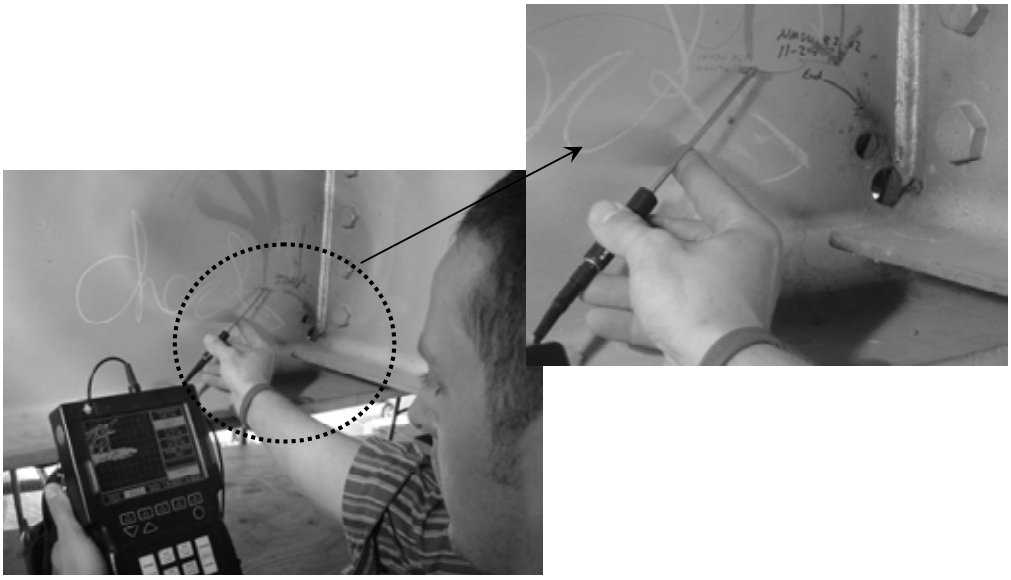

Figure 10-10: Eddy Current Inspection Used to Trace the Path of the Fatigue Cracks

Figure 10-11: Propagation Path of Fatigue Cracks on the North & South Side of the I-Beam

10.3 Stress Field Monitoring

After recording the geometry of all structural members and the profile of the fatigue cracks, field measurements were taken to determine the strain field in the vicinity of the damage. A set of 16 strain gages were used to monitor the strain risers around the crack tips and holes, as well as the uniform far-field strains. Figure 10-12 shows the locations of the five biaxial and two Rosette strain gages installed to determine the axial (I-beam span), shear and Principal stress in the I-beam web. Figures 10-13 and 10-14 show the gage installation, close-up of the gages, and equipment used to monitor the strains during static and dynamic loading. In order to produce extreme loading conditions – so that the composite doubler could be properly and conservatively designed – a combined load of a stationary dump truck and moving semi-truck was placed over the damaged region. Figure 10-5 shows the dump truck provided by NMDOT. It was loaded with dirt to provide a total weight of 53,120 lbs. The dump truck was slowly moved over the damaged beam until a maximum strain reading was obtained. Then, the normal traffic flow in the adjacent passing lane was used to produce the additional loads. Dynamic, peak strain measurements were taken when semi-trucks crossed the bridge traveling at approximately 50 mph. Strain readings were acquired for numerous semi-truck crossings in order to record maximum strain levels corresponding to a fully loaded semi-truck.

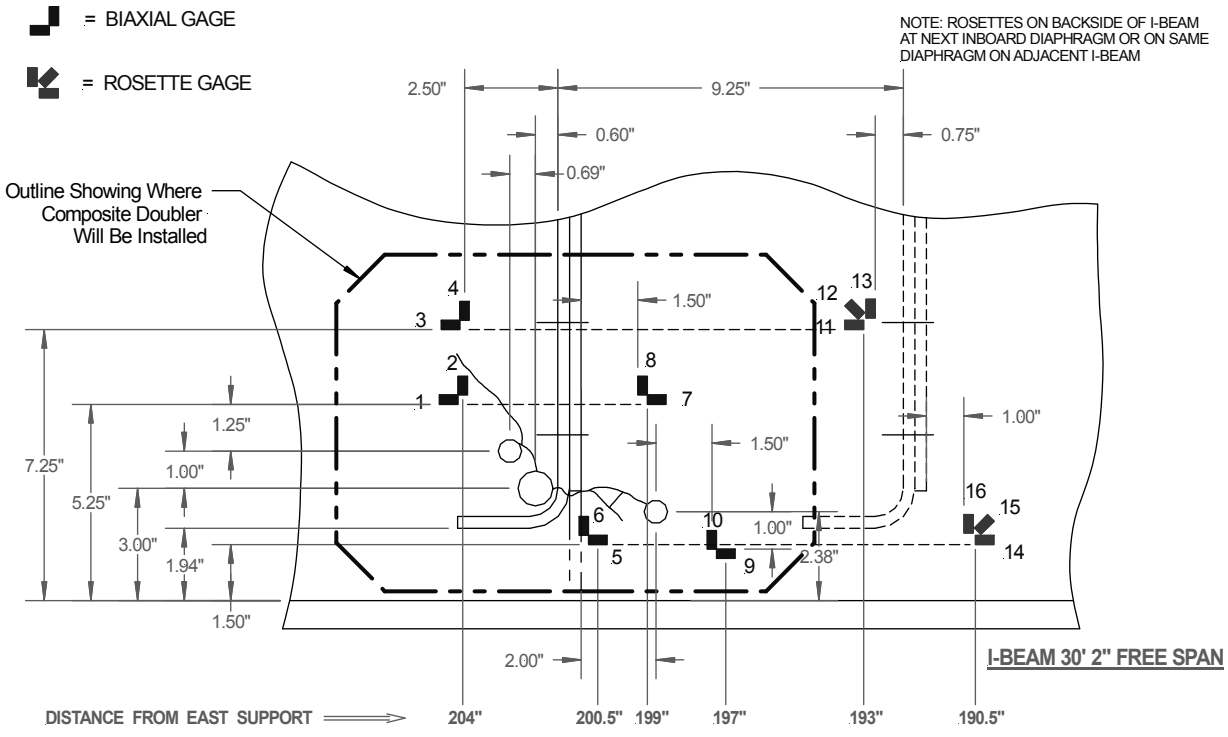

Figure 10-12: Strain Gage Layout to Monitor Strain Field Prior to Installation of Composite Doubler Repair (Doubler Location Shown for Reference)

Figure 10-13: Installation of Strain Gages in Vicinity of Fatigue Cracks

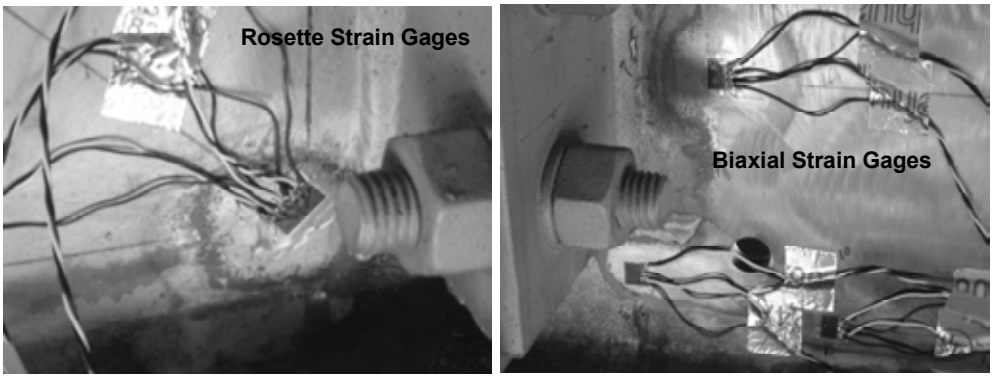

Figure 10-14: Sample Strain Gage Locations

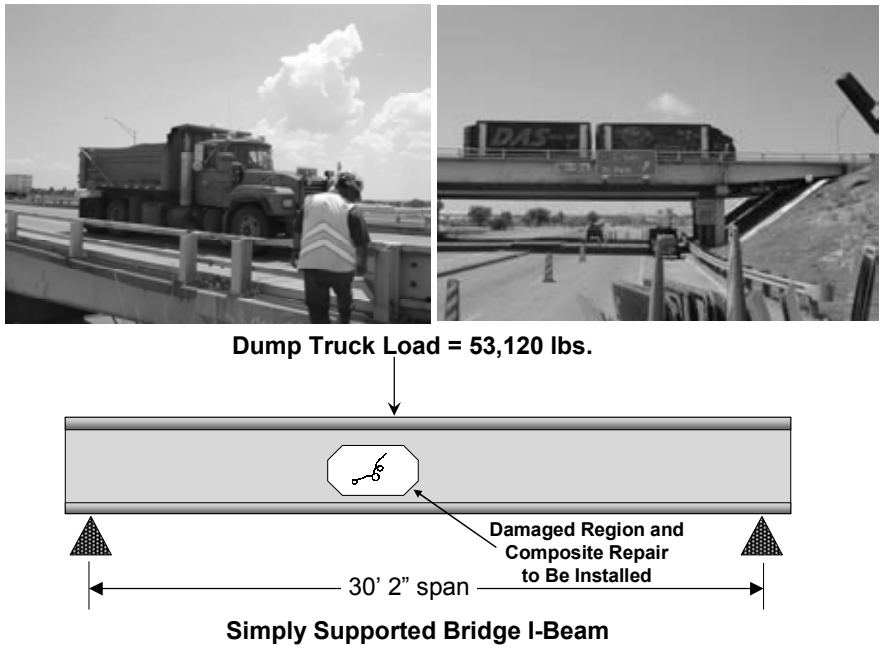

Figure 10-15: Application of Extreme Bridge Loads Using Dump Truck and Semi-Truck

The longitudinal and lateral strains recorded at each of the locations shown in Figure 10-12 are plotted in Figures 10-16 and 10-17, respectively. Peak strains were magnified by a factor of two to three due to the presence of the fatigue cracks.

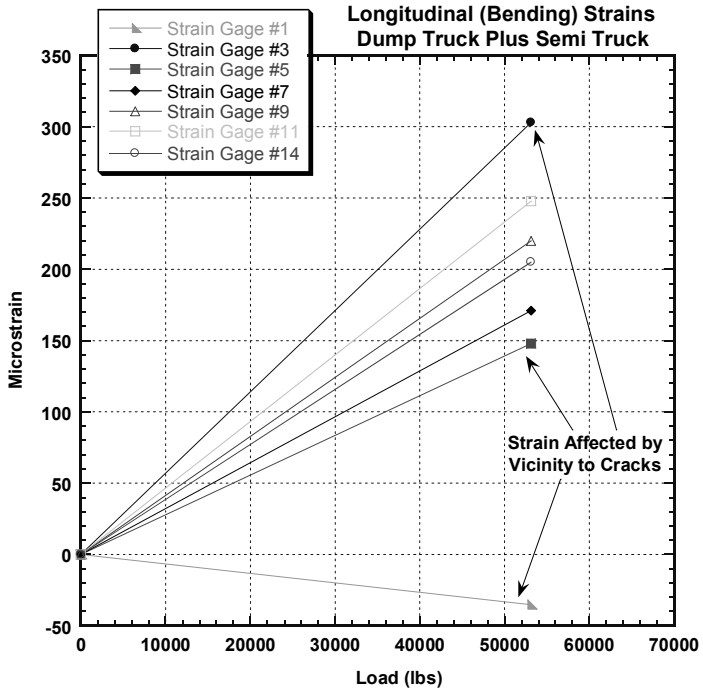

Figure 10-16: Longitudinal Strains in I-Beam Web Around Damaged Region

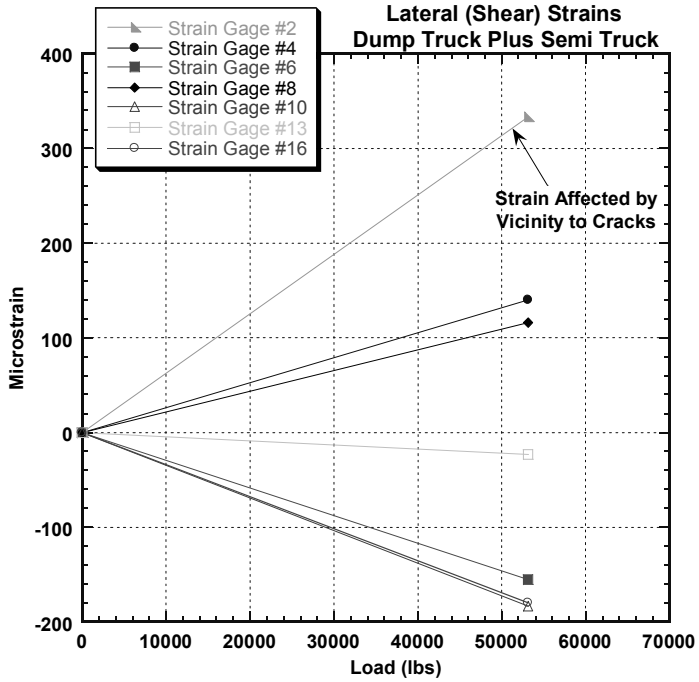

Figure 10-17: Lateral Strains in I-Beam Web Around Damaged Region

Stress Field Analysis - Strain data collected from the biaxial (axial and lateral) gages were used to calculate membrane stresses in parent steel plate. Strains measured by these gages were used to calculate the corresponding membrane stresses through the following equations:

$$\sigma_a = \frac{E}{1-\nu^2}(\varepsilon_a + \nu\varepsilon_l) \tag{10-1}$$

$$\sigma_l = \frac{E}{1-\nu^2}(\varepsilon_l + \nu\varepsilon_a) \tag{10-2}$$

where E is the modulus of elasticity, ν is Poisson's ratio, σ_a is the axial stress in the skin, σ_l is the longitudinal (lateral) stress in the skin, ε_a is the hoop strain, and ε_l is the longitudinal (lateral) strain.

The principal stresses were determined from strain data obtained from the Rosette strain gages. In these three-element rectangular rosettes, gages are located at 0^o, 45^o, and 90^o orientations corresponding to strains ε_1, ε_2, and ε_3, as shown in Figure 10-18. From these individual strains, the maximum and minimum principal stresses can be calculated using the following equations:

$$\sigma_{\max} = \frac{E(\varepsilon_1 + \varepsilon_3)}{2(1-\nu)} + \frac{E}{\sqrt{2}(1+\nu)}\left[(\varepsilon_1 - \varepsilon_2)^2 + (\varepsilon_2 - \varepsilon_3)^2\right]^{1/2} \tag{10-3}$$

$$\sigma_{\min} = \frac{E(\varepsilon_1 + \varepsilon_3)}{2(1-\nu)} - \frac{E}{\sqrt{2}(1+\nu)}\left[(\varepsilon_1 - \varepsilon_2)^2 + (\varepsilon_2 - \varepsilon_3)^2\right]^{1/2} \tag{10-4}$$

The orientation of the maximum principal stress σ_{max} is defined by the angle θ (see Figure 10-18) which is determined from:

$$\tan 2\theta = \frac{2\varepsilon_2 - \varepsilon_1 - \varepsilon_3}{\varepsilon_1 - \varepsilon_3} \tag{10-5}$$

A principal angle of 0◦ would correspond to pure longitudinal stress along the X axis while a principal angle of 90◦ would correspond to pure lateral (shear) stress in the I-beam web.

Figures 10-19 and 10-20 plot the calculated stresses. Maximum stress levels ranged from 11,000 to 12,000 psi. These are similar to the stress levels observed in the Syncrude shovel boom discussed in Chapter 3. Principal stress levels away from the damaged region reached a maximum value of 8,000 psi and were determined to be in the longitudinal direction.

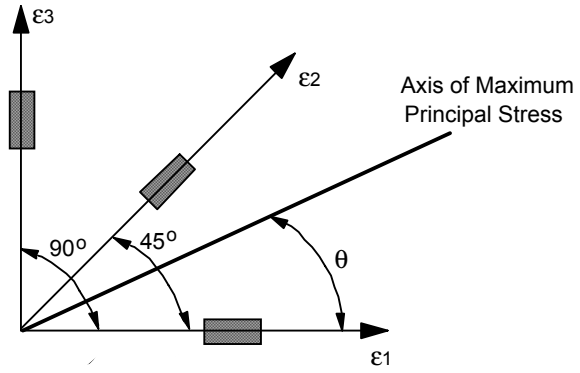

Figure 10-18: Principal Stress Measurements from Strain Components Measured by Rectangular Strain Gage Rosette

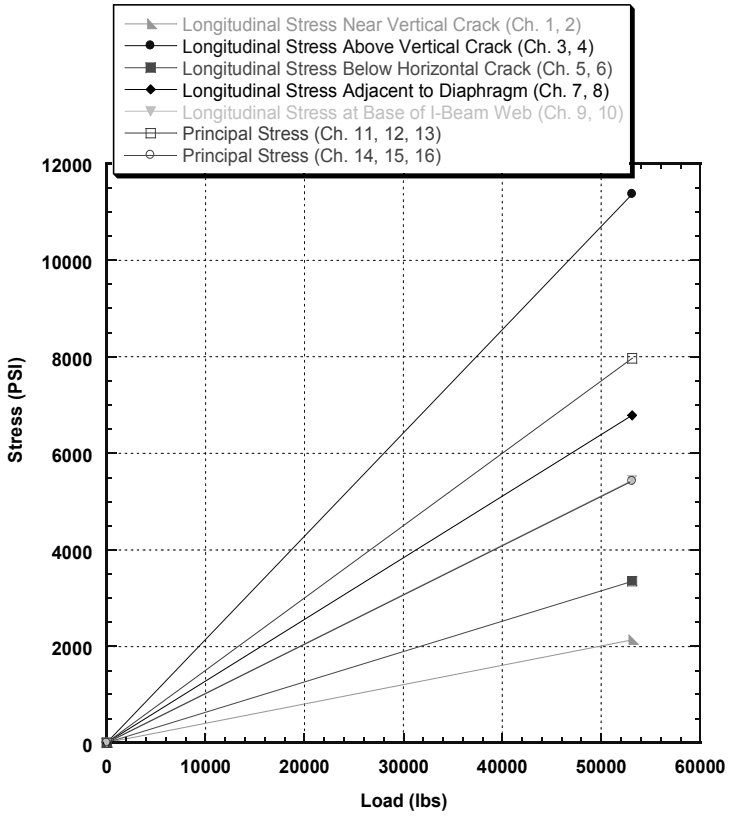

Figure 10-19: Longitudinal Stress in I-Beam Web Generated by Combined Load of Stationary Dump Truck Directly Over I-Beam (Inside Lane) and Moving Semi Truck in the Passing Lane

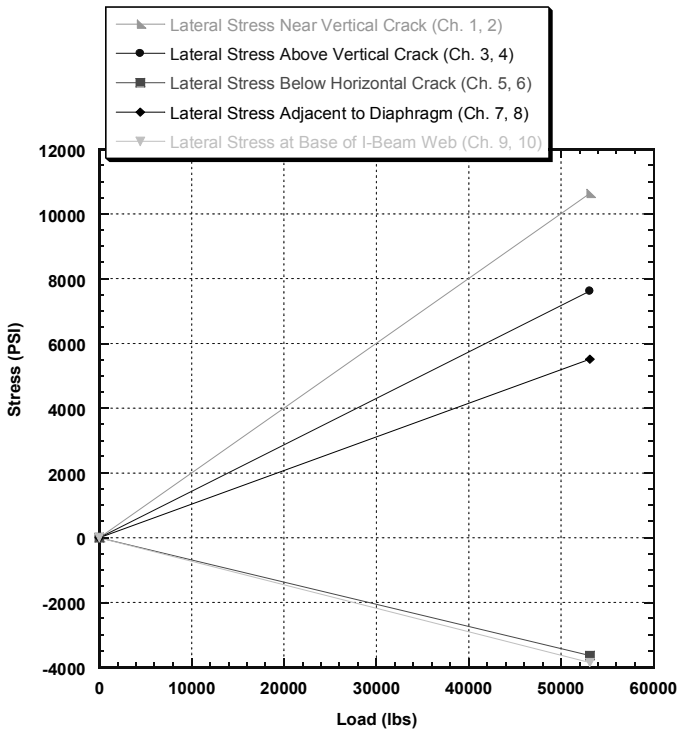

Figure 10-20: Lateral (Shear) Stress in I-Beam Web Generated by Combined Load of Stationary Dump Truck Directly Over I-Beam (Inside Lane) and Moving Semi Truck in the Passing Lane

10.4 Heat Source-Sink Assessment

A critical element in producing field repairs of this nature is the ability to produce sufficient temperatures in the structure to complete the hot-bonding process. As the steel structure becomes thicker higher energy levels are needed to heat the structure to the desired maximum cure temperature of 225^{o}F. Flanges, structural attachments, and other heat sinks that can remove heat from the repair area exacerbate this problem.

Preliminary tests were conducted to determine if the number, size, power, and arrangement of heat blankets were sufficient to provide the necessary composite doubler cure profile. Figures 10-21 through 10-23 show the arrangement of the trial heat blankets and the locations of the thermocouples used to monitor the temperature. In order to minimize the detrimental effects of the major heat sinks, heat lamps were used to warm the bottom flange of the I-beam and the web area immediately adjacent to the repair region.

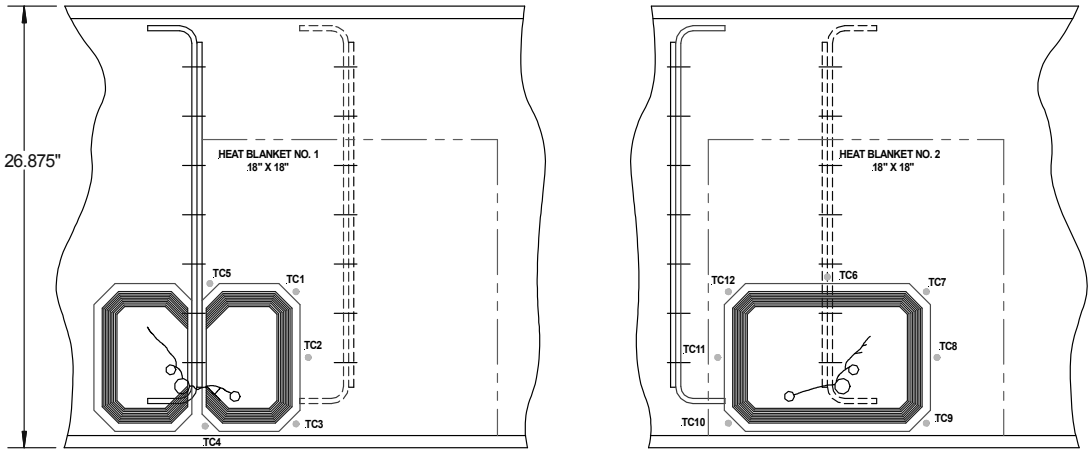

Figure 10-21: Thermocouple Placement for Initial Check on Ability to Produce Proper Temperature Profile for Composite Doubler Cure and Hot Bonding Process (Location of Composite Doublers Shown for Reference Only)

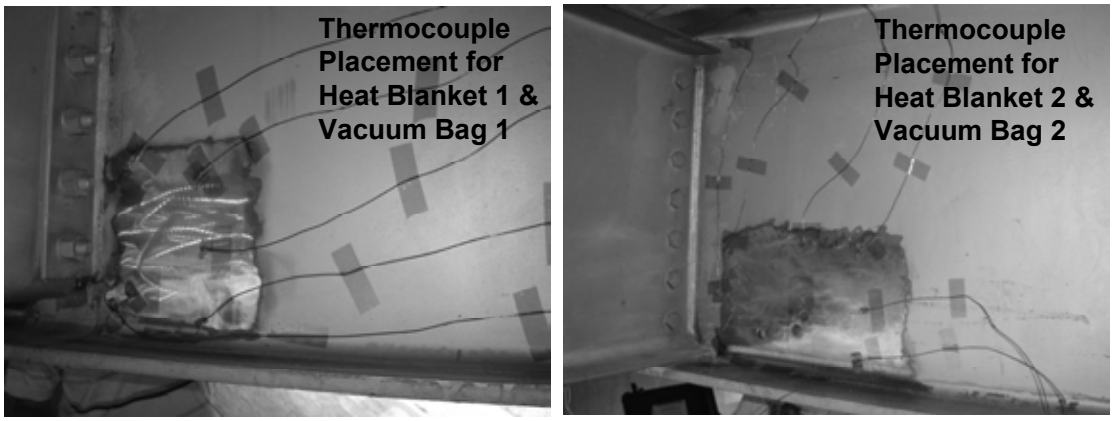

Figure 10-22: Thermocouples Installed in Damaged Area to Be Heated

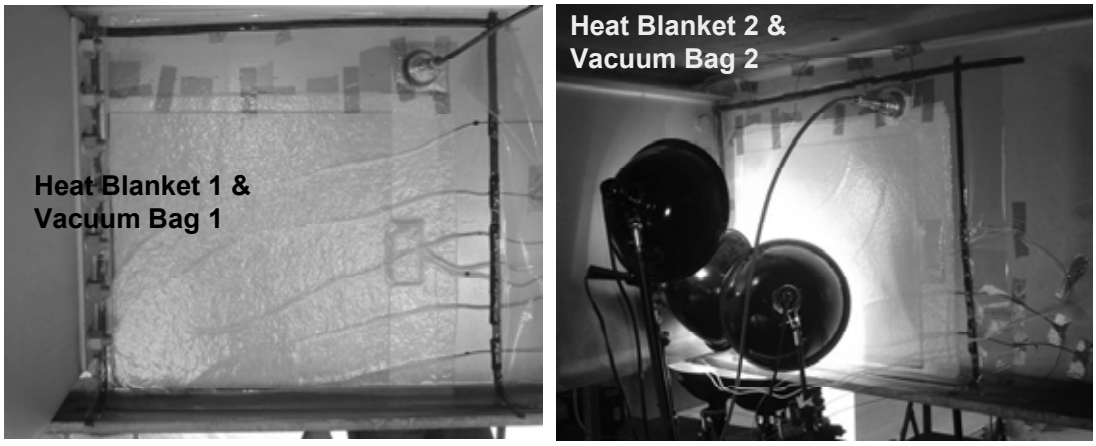

Figure 10-23: Heat Blankets, Vacuum Bags, and Insulation in Area Being Heated

Figure 10-24 shows the resultant temperatures produced in the steel and the desired cure profile for the composite repair. Even though only two heat blankets were used – compared to the five heat blankets planned for the actual repair installation – the temperatures produced were sufficiently close to the desired set points. The delay in reaching the maximum cure temperature of 225°F was slightly longer than desired; however, the additional heat blankets would be more than enough to drive the temperatures in the I-beam to match the cure profile (see Section 10.6)

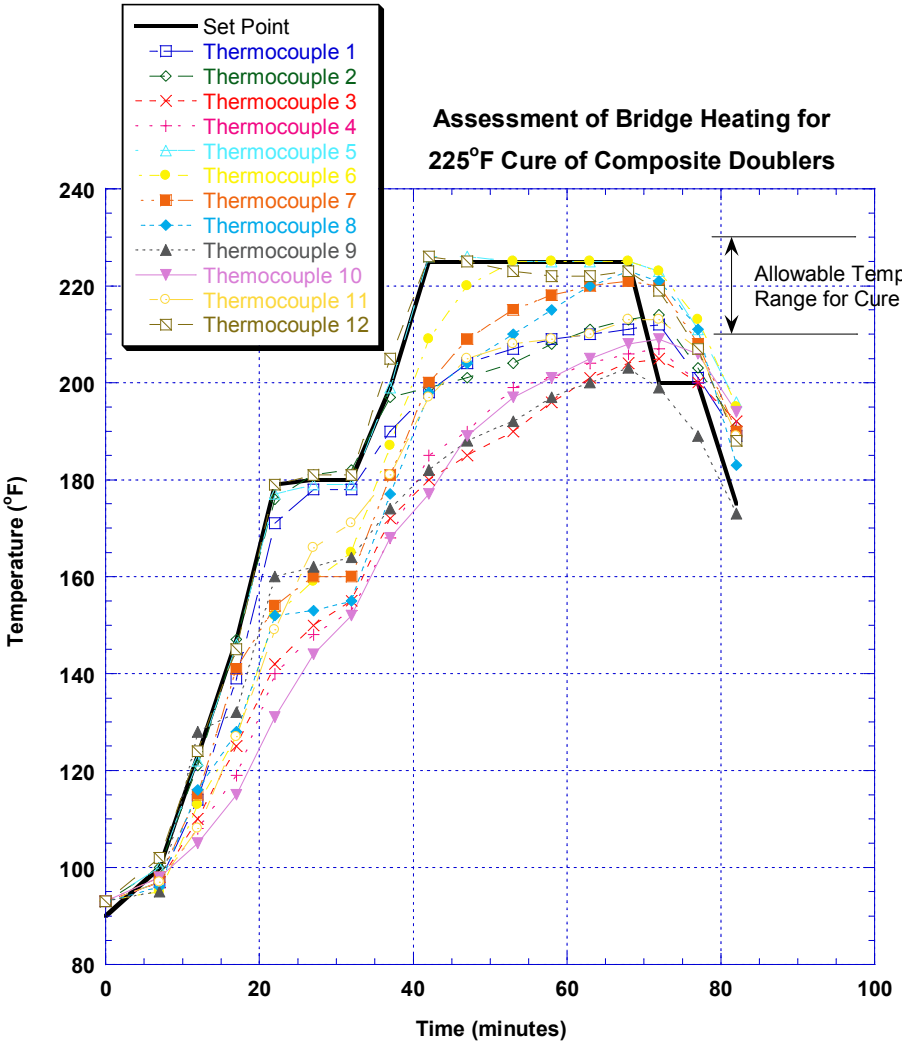

Figure 10-24: Heat Sink Assessment – Application of Vacuum and Heat Blankets with Full Field Temperature Check

10.5 Composite Doubler Repair Design

It was determined that the optimal composite doubler repair would be part of an overall repair method that also includes a weld process. Cracks in structures should first undergo a material removal (gouge) and replacement (weld) process. This is currently the final step in the repair procedure. However, in most instances, fatigue cracks reappear in the weld fill areas.

Composite doublers placed over the weld will produce a true hybrid repair where the heat affected zones or unintentional weld porosity pockets are reinforced to avoid subsequent re-cracking along the weld site. This is a superior repair with a significantly extended fatigue life. *Note that the outstanding crack mitigation results presented in Chapter 3 were produced using specimens containing 1" L edge fatigue cracks. Since the composite doubler repair process proposed here should only have small weld porosity pockets to act as crack nucleation sites, it will perform substantially better.*

Figure 10-25 shows the bridge configuration with all lateral diaphragm beams in place. It also shows the proposed three doubler approach to repair the fatigue cracks that propagated on both sides of the south side diaphragm. It was determined that sufficient lateral stability was provided by adjacent bridge diaphragms and that the two diaphragms shown in Fig. 10-25 could be removed. This allowed for better access to the damaged area, a more complete weld process, and an optimal, two-sided, symmetric composite doubler repair as shown in Figure 10-26.

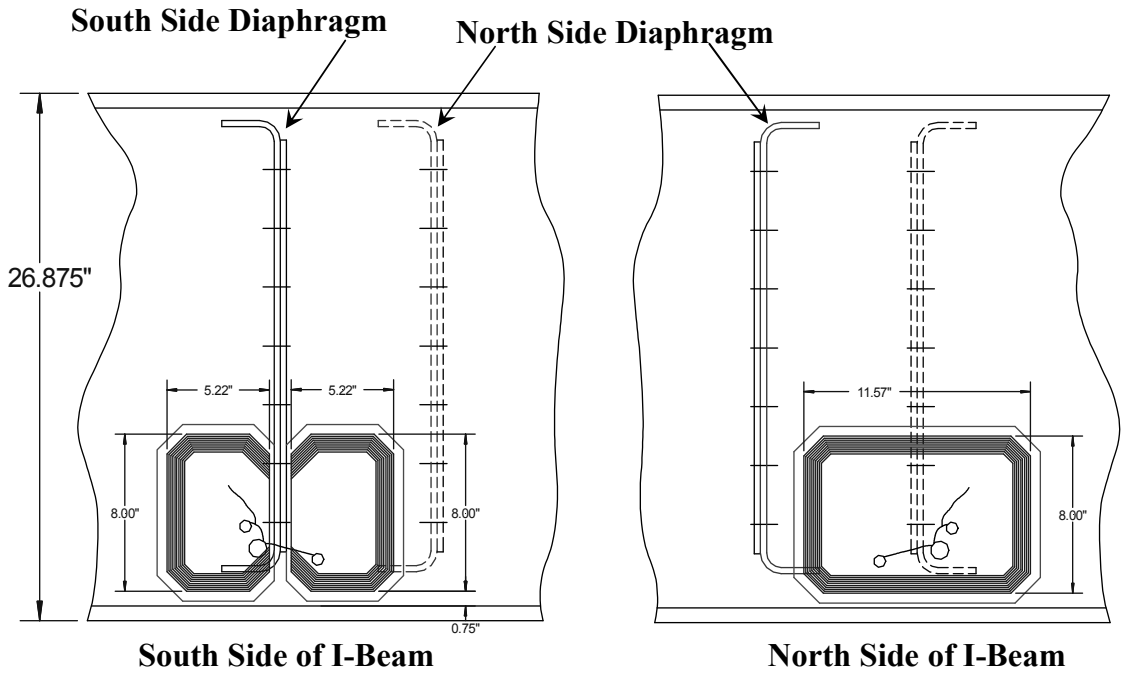

Figure 10-25: Preliminary Composite Doubler Repair Design Based on Bridge Configuration with South Side Cross-Brace Diaphragm Left in Place

The composite doublers used to repair the bridge were designed using the repair methodology described in Appendix C and the analysis software presented in Section 3.3. Because of the similarity in stress levels (~ 12 ksi), many of the design tenets used for the mining equipment discussed in Ch. 3, could be applied here. Laminate design principles were used to determine the E_x, E_y, ν_{xy}, and G_{xy} for a composite lay-up design. The required number of plies and the transfer length, which defines the overall repair length, were calculated for a one-sided (external) composite repair. An iterative process was then followed whereby specific design parameters

were adjusted in an effort to meet general design guidelines. Since the bridge repair was actually a two-sided, symmetric repair, the input value for the parent plate thickness was half the actual thickness to produce a design for a single composite doubler. The input data and doubler design results are summarized below:

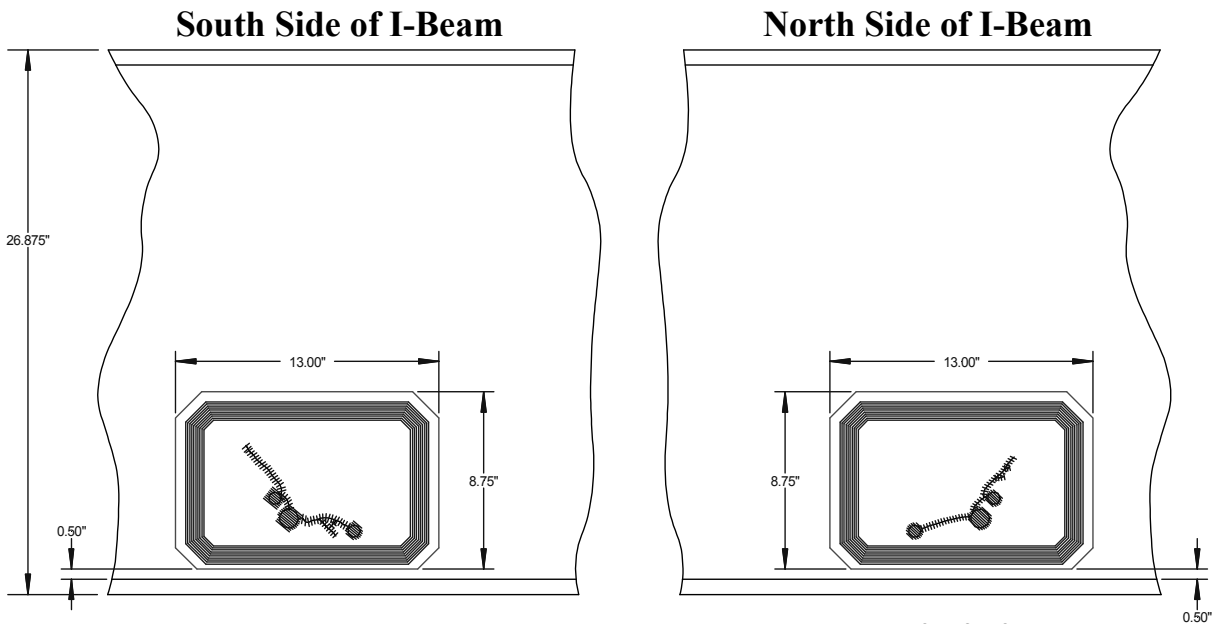

Figure 10-26: Final Composite Doubler Repair Design Based on Bridge Configuration After Removal of the Cross-Brace Diaphragms

Design Input Data:

- Parent Plate Thickness = 0.25" th. (ASTM A36)
- Parent Plate Modulus = 29 X 10^6 psi
- Doubler (Patch) Thickness = 32 plies X 0.00544" = 0.175" th.
- Doubler Length, L_r = 12" (full thickness length = 7"; taper length @ ea. side = 2.5")
- Doubler Width = 8"
- Stacking sequence - wedding cake stacking sequence (largest ply at the steel interface; sequentially smaller footprint plies are stacked on top)
- Taper Ratio = 15 (as shown in Fig. 10-27). When combined with patch thickness, the taper ratio determines the transfer length, $\beta = 0.4$.
- Vacuum bag debulk every 4 plies
- Corner angle = 45^o
- Patch shape = octagon.
- Load constant, N = 8, is related to the full thickness length of the patch. The overlap length, or one half the doubler full thickness length is equal to N times the transfer length β.

Doubler Design Notes:

- 45^o plies provide better performance in shear loads.
- Use of corner angle (more difficult lay-up) reduces stress riser in steel-doubler interface – no corner angle used in current designs.
- Adding width improves load transfer into doubler and decreases bypass strain.
- Increasing taper ratio reduces peel stresses.
- No side taper at edge of doubler where maximum reinforcement is needed.

Doubler Design Output:

- Doubler Lay-Up (32 plies) = $[0,0,45,-45,90,0,0,+45,-45,90,0,0,45,-45,90,0]_s$
- Stiffness Ratio = 0.40
- Effective Doubler Modulus E_x, = 21.3 X 10^6 psi ; E_y = 12.9 X 10^6 psi

The input parameters listed above where used to calculate the doubler lay-up and the final composite doubler design shown in Figure 10-27. The repair was optimized by varying the number and orientation of the plies, the taper ratio, the load constant, and the patch geometry. Table 10-1 shows one of the iterations where trial values are substituted for existing input parameters.

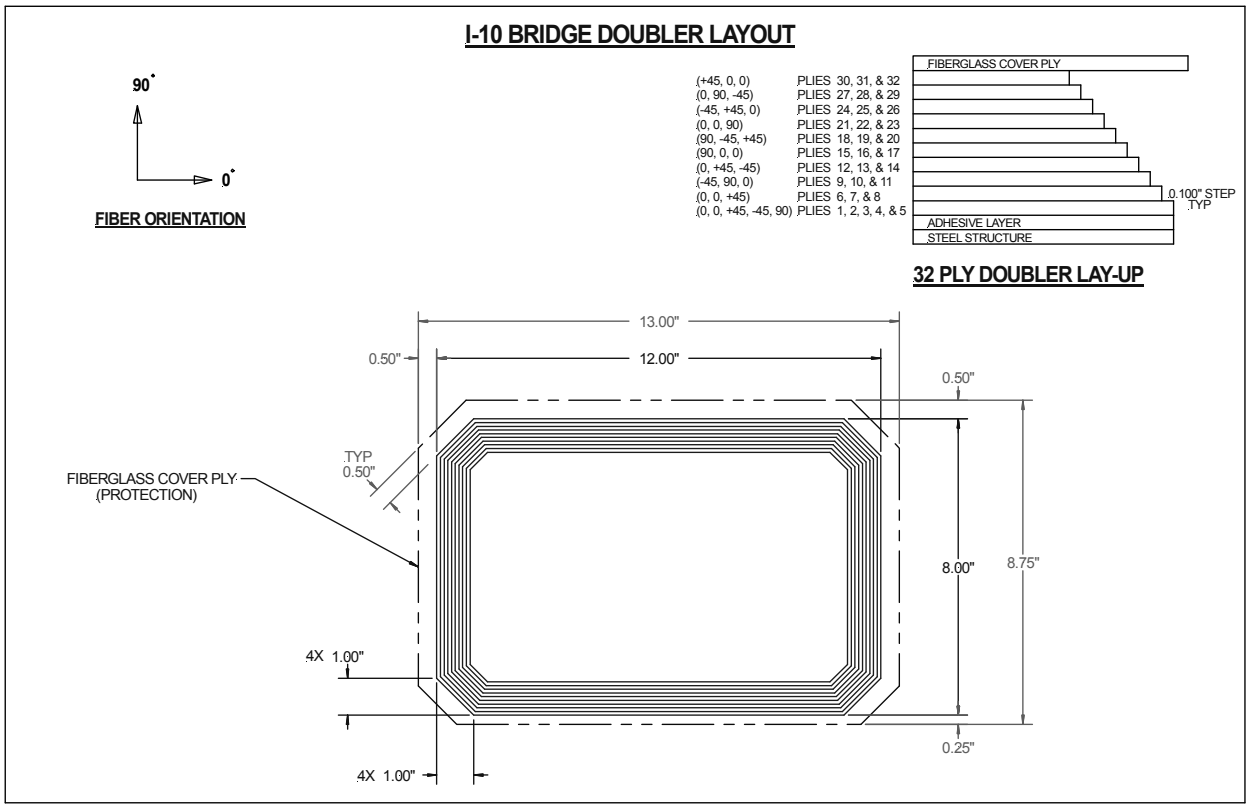

Figure 10-27: Final Composite Doubler Designs for Bridge Repair After Removal of Diaphragms

	Range Tested:	Current Value:	Trial Values
Stiffness Ratio, S	1.1 - 1.6	0.338	**0.400**
Step-off Rate	15.0 - 50.0	15	**10.000**
Patch Width	1.5 - 5.0	8.000	**6.000**
Load Constant, N	4.0 - 12.0	11.000	**8.000**
Adhesive Thickness	1	1	**1.000**
(number of plies)	2		
	3		
Patch shape	Rectangle		
	30-deg Corner		**1.000**
	45-deg Corner	1	
Stacking Sequence	Wedding Cake	1	**1.000**
	Reverse Wedding Cake		

Table 10-1: Iteration on Bridge Composite Doubler Design by Varying Input Parameters

After each iteration, specific guidelines were reviewed to optimize the repair design. The efficiency of the repair was evaluated by studying the resulting strain ratios for the composite doubler repair installation. Figure 10-28 shows a typical repair under uniaxial loading. Strain locations G1 through G8 pinpoint various regions of the doubler and surrounding parent structure. Table 10-2 defines the strain ratios that are calculated by comparing the strain levels at each of the various points in Figure 10-28. In addition, Table10-2 lists the goal (design guidelines) for these strain ratios along with a description of the criticality of each strain ratio. The strain ratios listed are in order of importance and the first two items are primary relationships. Therefore, the goal of the iterative design process was to optimize the ratios for the first two or three relationships while producing results that are close to the design goal for the lower few relationships.

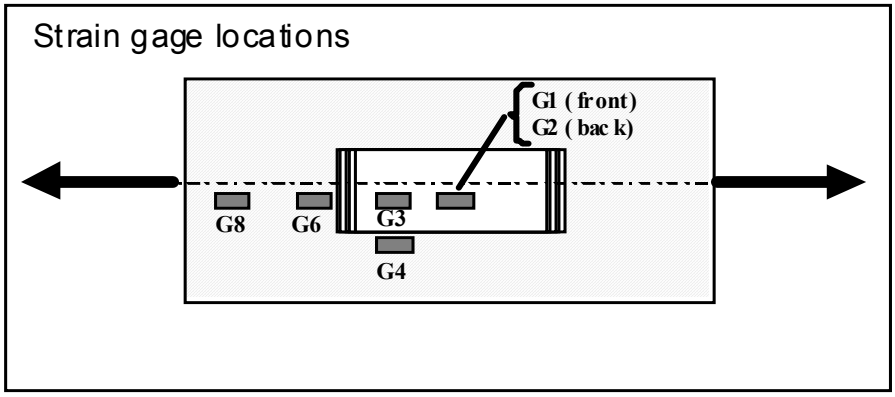

Figure 10-28: Strain Locations for Assessing Composite Doubler Designs

Strain Gage Ratio	Priority	Minimize or Maximize	Goal	Criticality of the Ratio
G2/G8	1	Min	< 0.60	Lower strain ratio prevents crack growth.
G6/G8	2	Min	< 1.15 - 1.30	Lower peel stresses / stress concentration
				at edge of patch
G1/G2	3	Max	> 0.75	Doubler design carries more load than
				underlying aluminum substrate.
G1/G8	4	Max	> 0.70	Relationship of doubler strain above notch
				to far-field aluminum strain
G3/G4	5	Max	> 1.30	Doubler design carries more load than
				adjacent aluminum structure.
G3/G8	6	Max	> 0.70	Relationship of doubler strain in middle
				of doubler to far-field aluminum strain
G4/G8	7	Min	< 0.50	Lower aluminum strain near doubler
				indicates if is carrying more load.

Strain Ratio:	Criteria:
G2/G8	Strain at crack compared to far field strain is most critical ratio to prevent or slow crack propagation by alleviating strain concentration at the crack. Patch width has most effect on G2/G8.
G6/G8	Strain kick in parent metal at end of patch compared to far field strain should be minimized to lessen peel stresses at adhesive edge. Requires less stiff, thinner, shorter patch with abrupt taper. N most effective.
G1/G2	Strain on the patch above the notch compared to the strain on the back side of the substrate should be a maximum to indicate a patch design efficiently carrying most of the applied load.
G1/G8	Relationship of strain in doubler directly above notch to far field alu steel strain ows load efficiency
G3/G4	Quarter patch strain on patch to same location on parent
G3/G8	Quarter patch strain to far field
G4/G8	Quarter al steel strain bypass strain to farfield strain

Table 10-2: Performance Criteria for Assessing Viability of Composite Doubler Repairs

Table 10-3 summarizes the results from the final two design iterations. The green-filled boxes indicate that the strain ratio goal was achieved. Note that in the second design scenario - which was the final design selected for the bridge repair – all design goals were met. Figure 10-27 shows the final engineering drawing used to fabricate the two 32-ply doublers for the bridge repair. Note the addition of a fiberglass cover ply over the boron-epoxy laminate. It is used to provide mechanical (impact) protection, moisture resistance, and ultraviolet (UV) protection. Ultraviolet rays from the sun will break down an epoxy resin system over time and result in boron fiber loss. Figure 10-29 shows a mylar template of the doubler being placed over the damaged region on the bridge to ensure a proper fit and to study vacuum bag and heat blanket layouts.

Strain Ratio:	Goal	Current	Trial
G2/G8	< 0.60	0.2191	0.3657
G6/G8	< 1.15 - 1.30	1.3245	1.2435
G1/G2	> 0.75	1.4745	1.2907
G1/G8	> 0..70	1.0030	0.8848
G3/G4	> 1.30	3.0142	2.9189
G3/G8	> 0.70	1.0902	0.9832
G4/G8	< 0.50	0.2659	0.2367

Table 10-3: Comparison of Strain Ratio Evaluations Corresponding to User-Supplied Design Trade-Off Adjustments

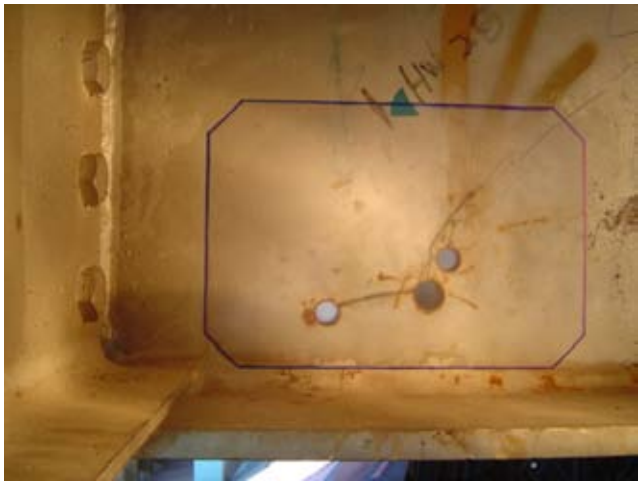

Figure 10-29: Fit Check for Composite Doubler Repair Using Mylar Film

10.6 Composite Repair Installation and Strain Field Monitoring

The composite doubler installation process followed the steps pictured in Appendix A and described in Appendix B. Figures 10-30 through 10-33 and 10-36 through 10-40 provide a summary of the major bridge repair steps. They include: 1) paint removal and coarse sanding to remove oxide layers, 2) grit blasting to produce a proper and uniform surface roughness, 3) application of silane and primer to enhance the chemical bond, 4) placement of the composite doubler and adhesive film over the region to be repaired, and 5) application of controlled heat to cure the boron-epoxy doubler and the adhesive. The arrangement of the three vacuum bags, five heat blankets, and sixteen thermocouples are shown in Figure 10-34. Figure 10-35 is a schematic depicting the feedback loops for control of the heat blankets and vacuum bags.

Figure 10-30: Sanding to Remove Paint and Excess Scale/Oxide

Figure 10-31: Grit Blasting Steel Surface to Produce Optimum Surface Roughness

Figure 10-32: Application of Silane Mixture to Grit Blasted Surface and Use of Heat Lamps to Cure Silane

Figure 10-33: Masked Repair Area and Application of Primer to Chemically Enhance Bond

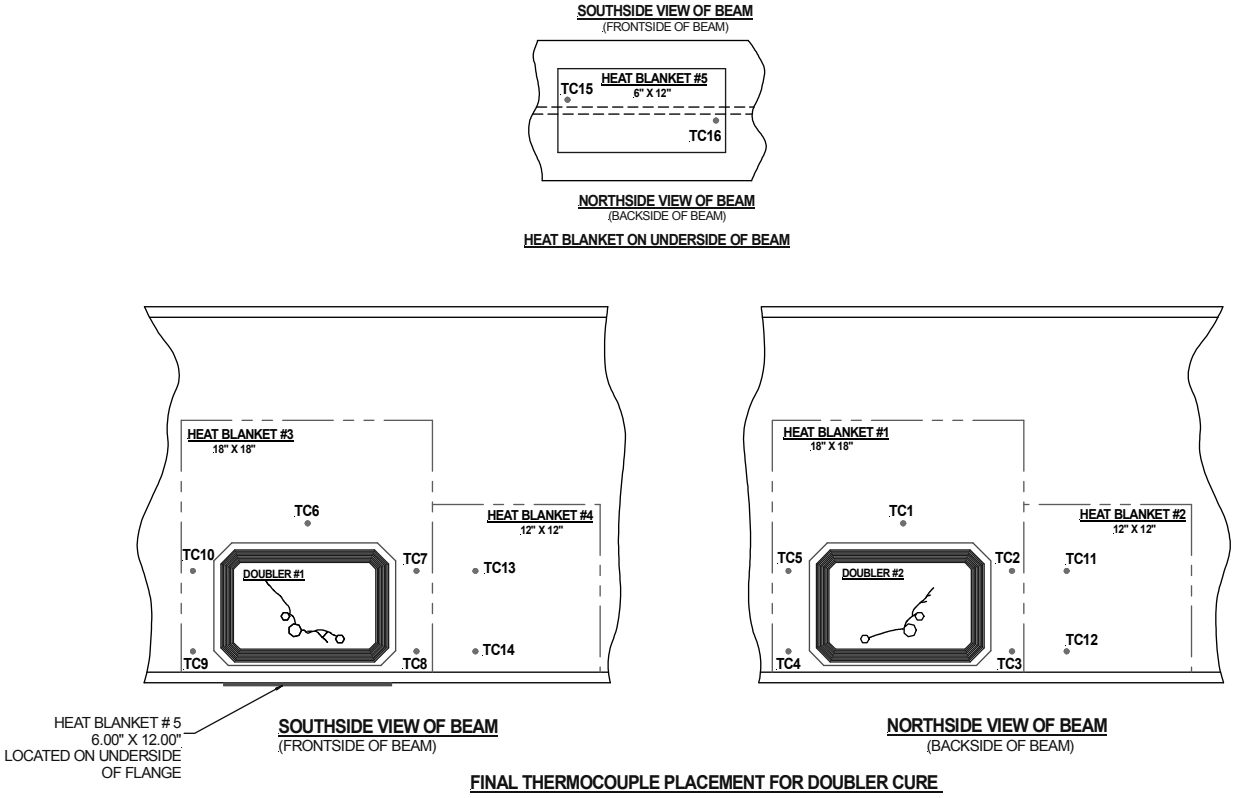

Figure 10-34: Arrangement of the Sixteen Thermocouples and Five Heat Blankets for Installing the Composite Doubler Repairs

I-10 BRIDGE DOUBLER APPLICATION FINAL SET-UP (POWER, HEAT, AND VACUUM)

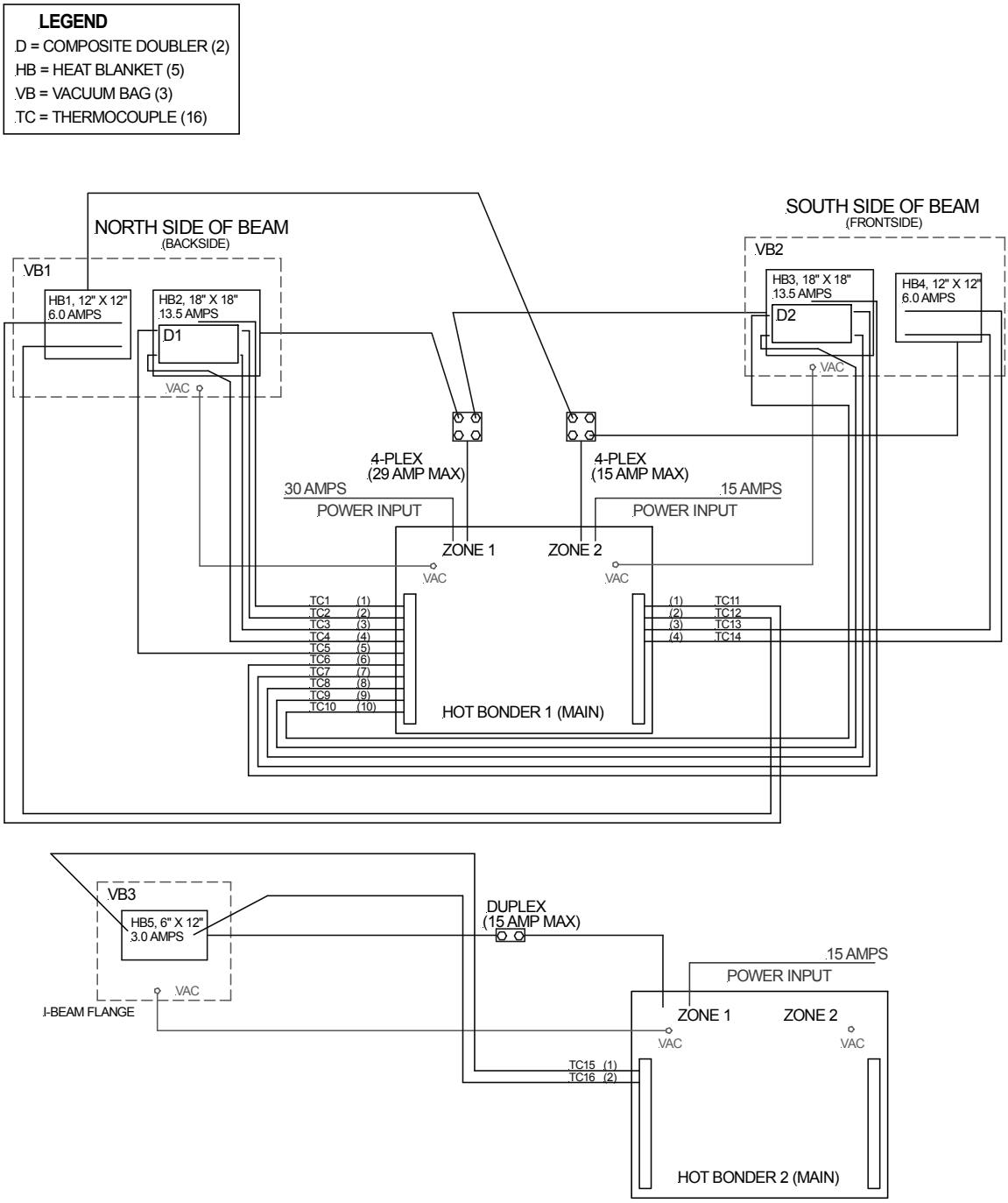

Figure 10-35: Schematic Showing Control of Heat Blankets and Vacuum Bags for Curing Composite Doublers

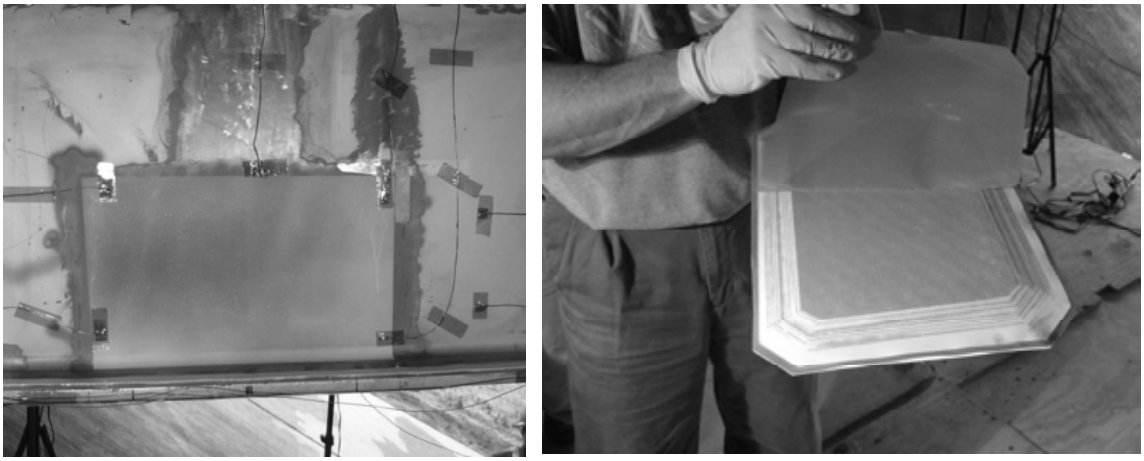

Figure 10-36: Thermocouple Placement Around Primed Repair Region and Boron-Epoxy Composite Doubler Prior to Placement on I-Beam

Figure 10-37: Adding Adhesive Layer to Composite Patch and Placing Patch in Repair Area

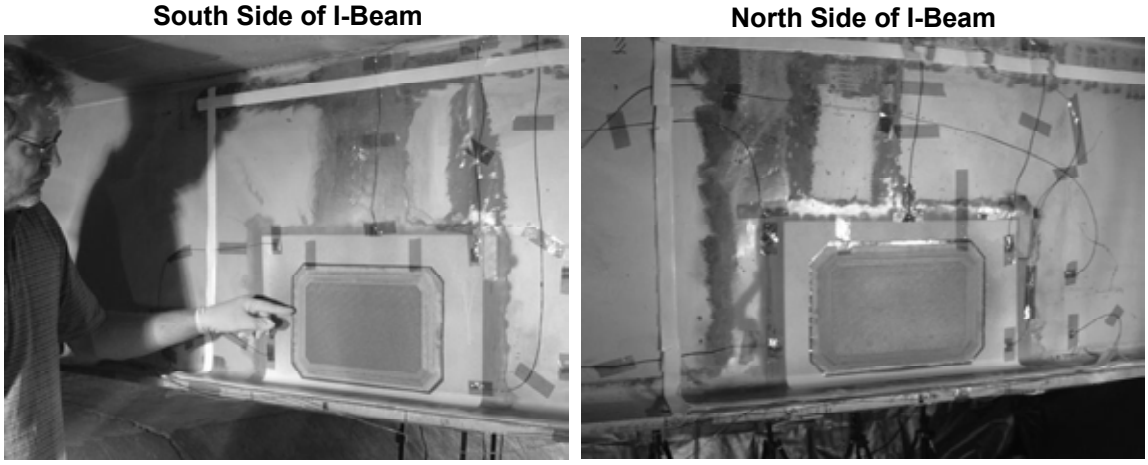

Figure 10-38: Composite Doublers Placed on Each Side of the Cracked I-Beam

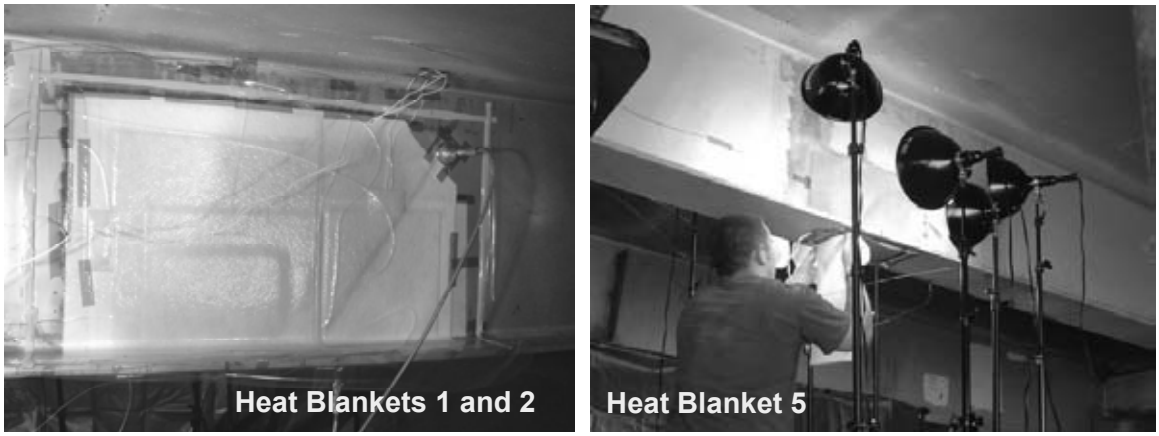

Figure 10-39: Vacuum Bag Set-Up on I-Beam Sides and Installation of Heat Blanket and Vacuum Bag on the Bottom I-Beam Flange to Control Heat Sink

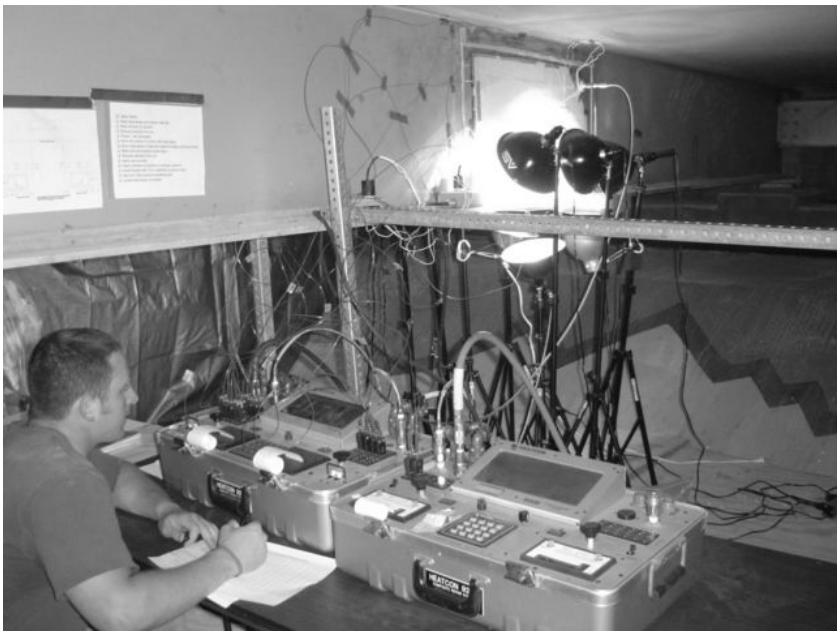

Figure 10-40: Monitoring Pressure and Temperature During the Three Hour Cure Process; Hot Bonder Control Units Shown in Foreground

The temperatures produced by this heat blanket layout at each of the thermocouple locations is plotted in Figure 10-41. The array of heat blankets over the composite doublers and in the adjacent regions were able to adequately control the temperatures and closely follow the desired cure profile. The completed composite doubler repairs are shown in Figure 10-42 prior to the application of a protective paint. The uniform resin flow absorbed by the bleeder cloths placed over the doublers during the vacuum/heat process also indicated that a good cure was achieved.

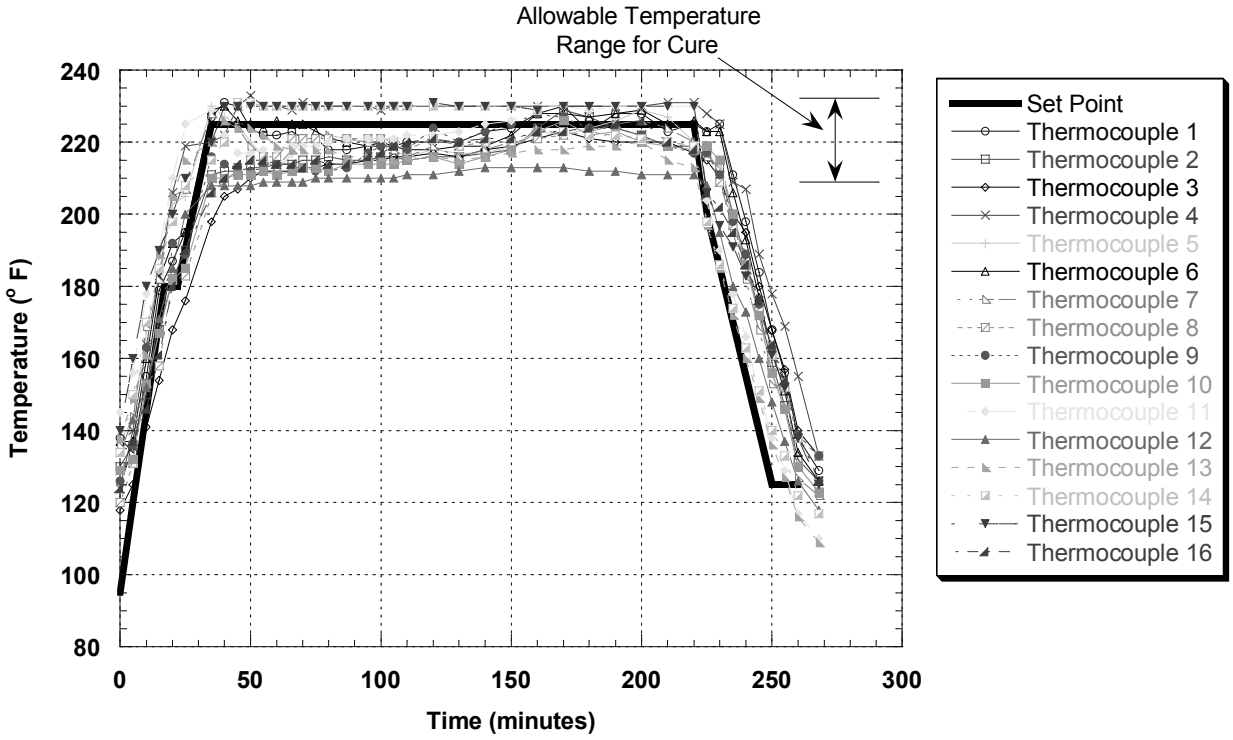

Figure 10-41: Comparison of Optimum Cure Profile and Temperatures Achieved in the Bridge I-Beam During Composite Doubler Installation

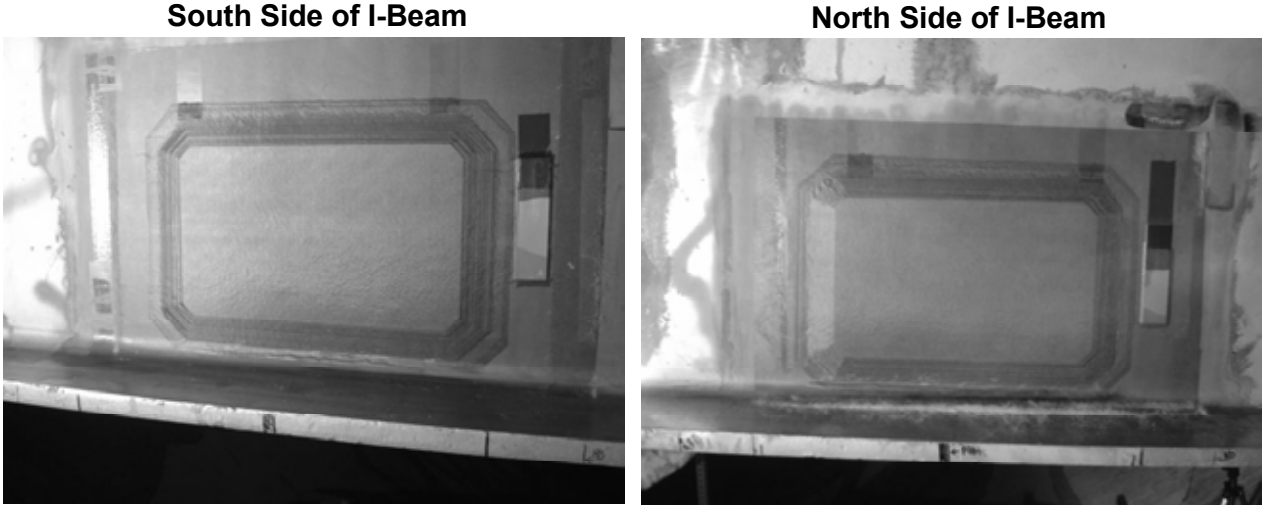

Figure 10-42: Composite Doublers After Hot Bonding Process; Witness Coupons Used for Quality Assurance are Shown Next to Repair Patches

Beside the doublers in Fig. 10-42 are the witness coupons that are used for quality control purposes. A plastic wedge is used to pry these witness coupons away from the aluminum skin at the bondline as shown in Figure 10-43. A successful wedge test result is where adhesive material appears on both the metal substrate and the witness coupon. Note the presence of the pink adhesive on both the witness coupon and the parent aluminum skin in Fig. 10-43. This signifies a good installation and assures that the adhesive layer will fracture at high strains (cohesive failure) rather than disbonding (adhesive failure). Such cohesive failure indicates that the full strength of the adhesive is achieved at the bond line rather than lesser strengths associated with adhesive failure modes.

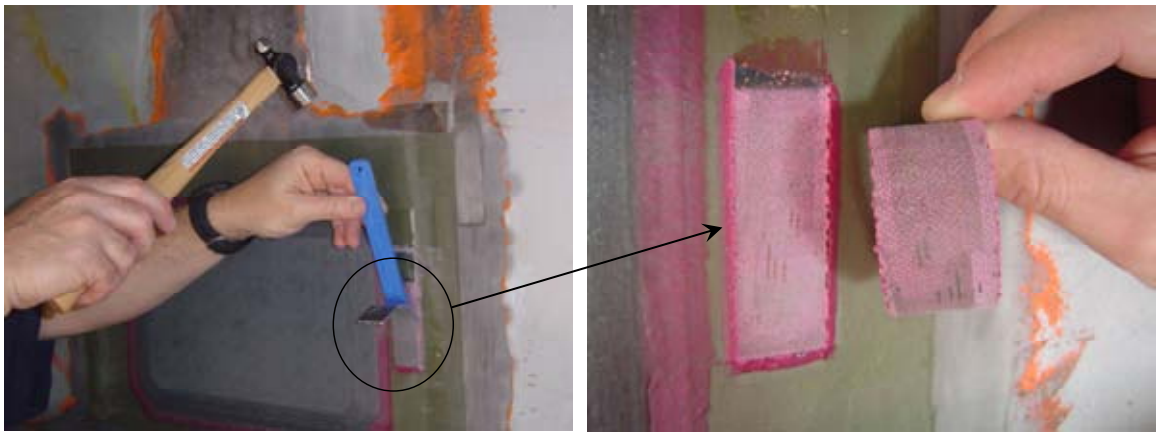

Figure 10-43: Removal of Witness Coupons to Demonstrate that Proper Surface Preparation was Achieved

A post-repair strain mapping was conducted after the composite doubler installation to compare strain fields before and after repairing the bridge cracks. Figure 10-44 shows the strain gage layout and the general location of the fatigue cracks underneath. The sixteen gages were placed in approximately the same location as during the pre-repair strain field monitoring. Figures 10-45 and 10-46 show the strain gage installation and monitoring equipment, as well as close-ups of biaxial and Rosette gages.

The same load scenario described in Section 10.3 was used to induce a combined load of a stationary dump truck and moving semi-truck over the repaired region. Dynamic, peak strain measurements were taken when semi-trucks crossed the bridge traveling at approximately 50 mph. Strain readings were acquired for numerous semi-truck crossings in order to record maximum strain levels corresponding to a fully loaded semi-truck. The longitudinal and lateral strains recorded at each of the locations shown in Figure 10-44 are plotted in Figures 10-47 and 10-48, respectively. The stress risers associated with the cracks were eliminated. The lateral strains were reduced to essentially zero. The larger longitudinal strains were reduced to less than half the values recorded during the pre-repair visit.

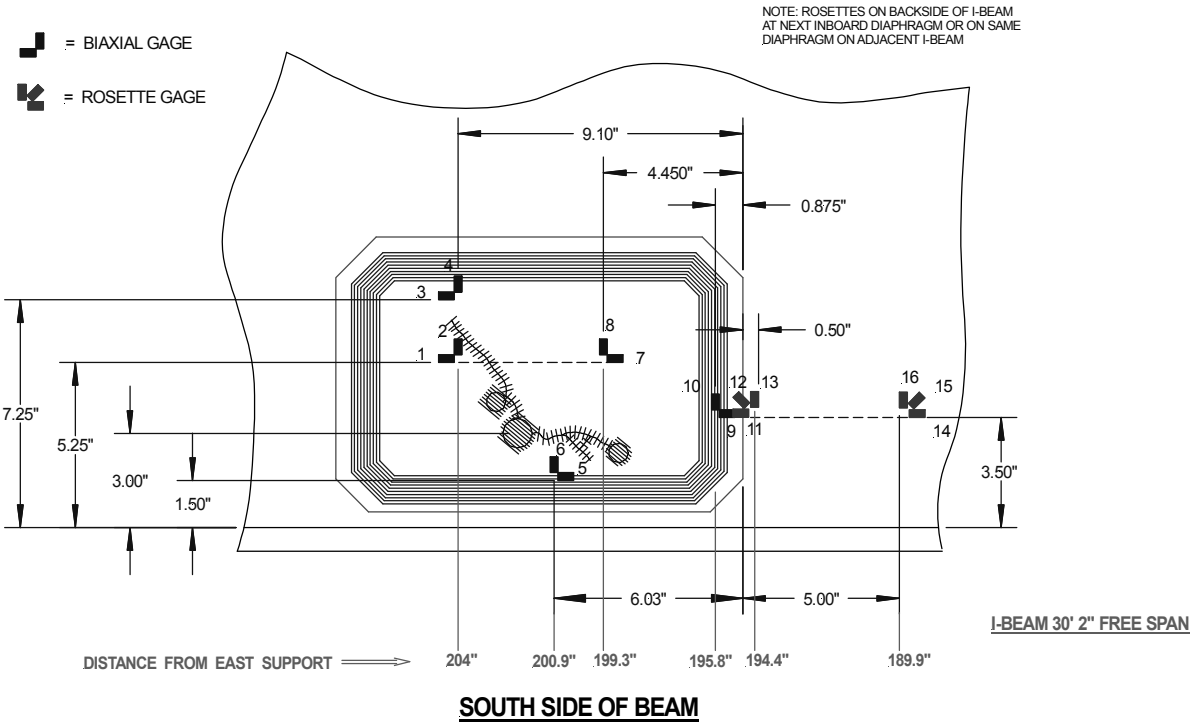

Figure 10-44: Strain Gage Locations Used to Monitor the Strain Field After Composite Doubler Repair

Figure 10-45: Strain Gage Installation and Overall View of Composite Doubler Repair Location with Strain Logging Equipment

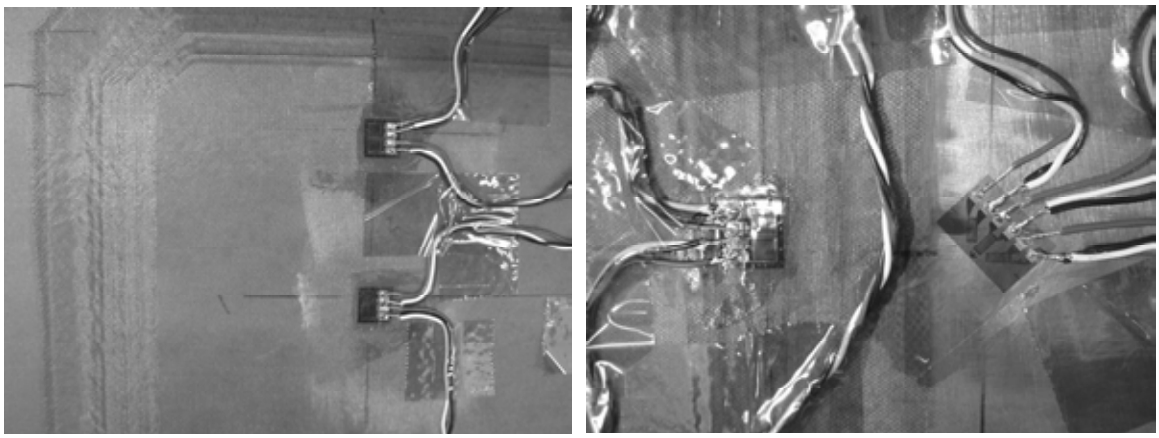

Figure 10-46: Biaxial Strain Gages Mounted on Composite Patch and Rosette Gage on Steel I-Beam Adjacent to Patch

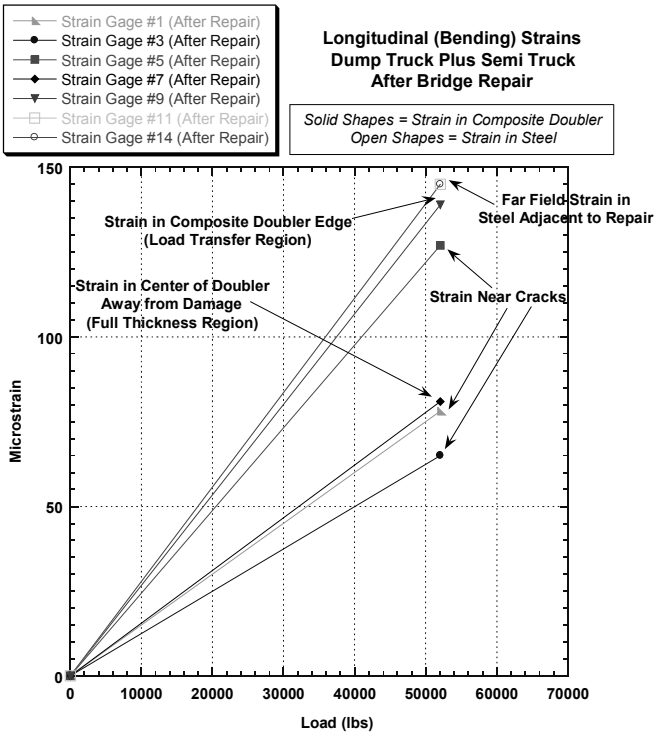

Figure 10-47: Longitudinal Strains in I-Beam Web Generated by Combined Load of Stationary Dump Truck Directly Over I-Beam (Inside Lane) and Moving Semi Truck in the Passing Lane AFTER Repair

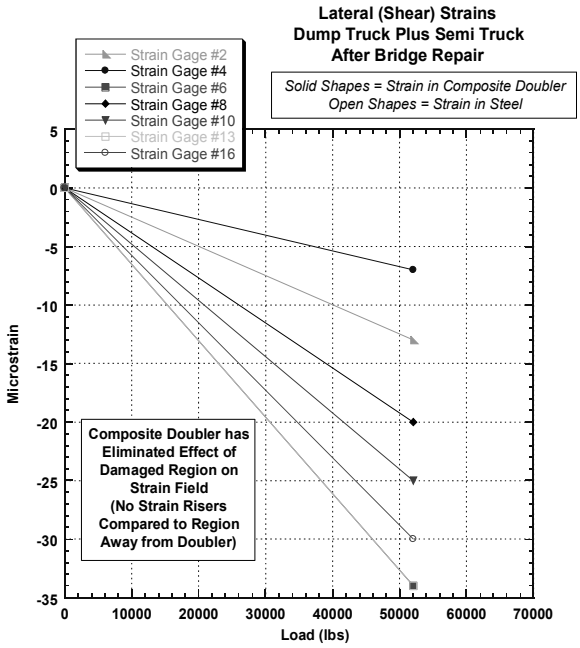

Figure 10-48: Lateral (Shear) Strains in I-Beam Web Generated by Combined Load of Stationary Dump Truck Directly Over I-Beam (Inside Lane) and Moving Semi Truck in the Passing Lane AFTER Repair

Stress Field Analysis - Strain data collected from the biaxial (axial and lateral) gages were used to calculate membrane stresses in parent steel plate using equations 10-1 and 10-2. The principal stresses were determined from strain data obtained from the Rosette strain gages and equations 10-3 and 10-4. The calculated longitudinal and lateral stress levels are plotted in Figures 10-49 and 10-50 respectively. Maximum longitudinal stress levels ranged from 4,000 to 4,500 psi. Principal stress levels away from the damaged region reached a maximum value of 4,600 psi and were determined to be in the longitudinal direction. The lateral stress levels were reduced significantly. Load transfer into the doubler was approximately 50% which agrees with normal repair design principles. Table 10-4 compares the stress levels observed in the I-beam web before and after the installation of the composite doubler repairs. Decreases in the longitudinal stresses ranged from 20% to 80% with the largest reductions occurring in the highest (stress riser) areas. Slight longitudinal stress level increases were observed in the lowest stressed regions. The end result is that the stress field is much more uniform. Also, the stresses in the steel immediately adjacent to the repair patches was not increased as would happen if the patch stiffness was too large. The large lateral stresses, produced primarily by the presence of the fatigue cracks, were reduced more than 90% by the composite doubler patches.

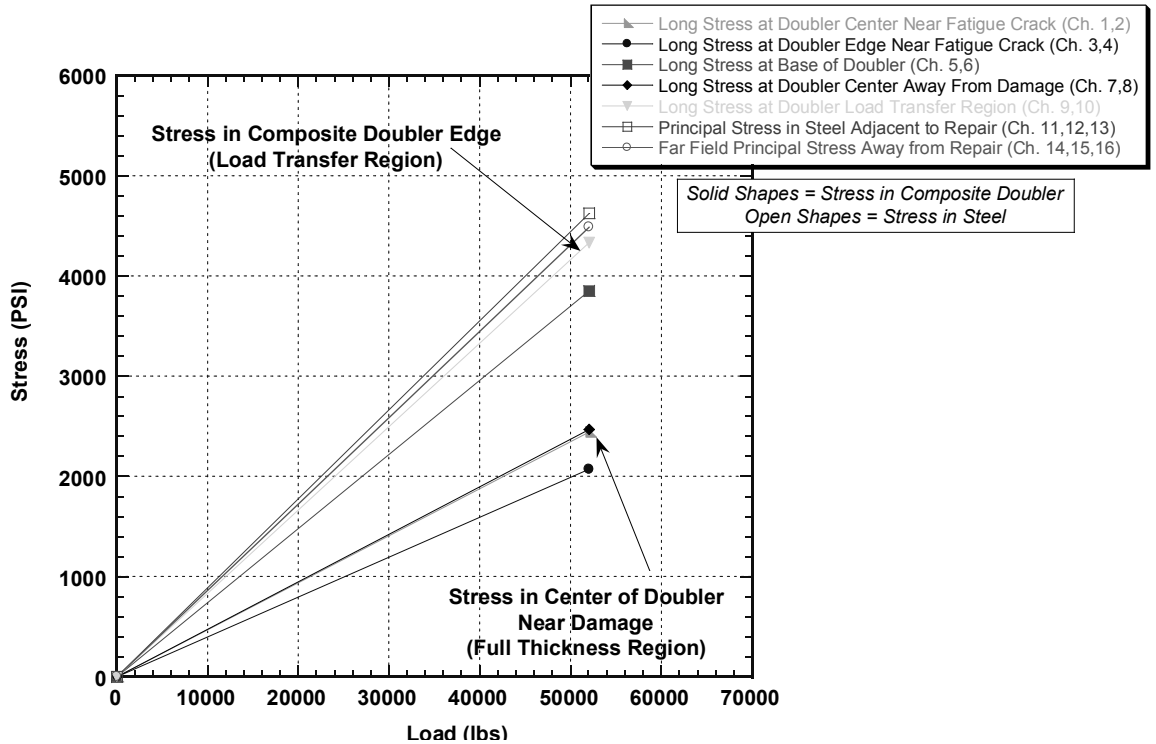

Figure 10-49: Longitudinal Stresses in I-Beam Web Generated by Combined Load of Stationary Dump Truck Directly Over I-Beam (Inside Lane) and Moving Semi Truck in the Passing Lane AFTER Repair

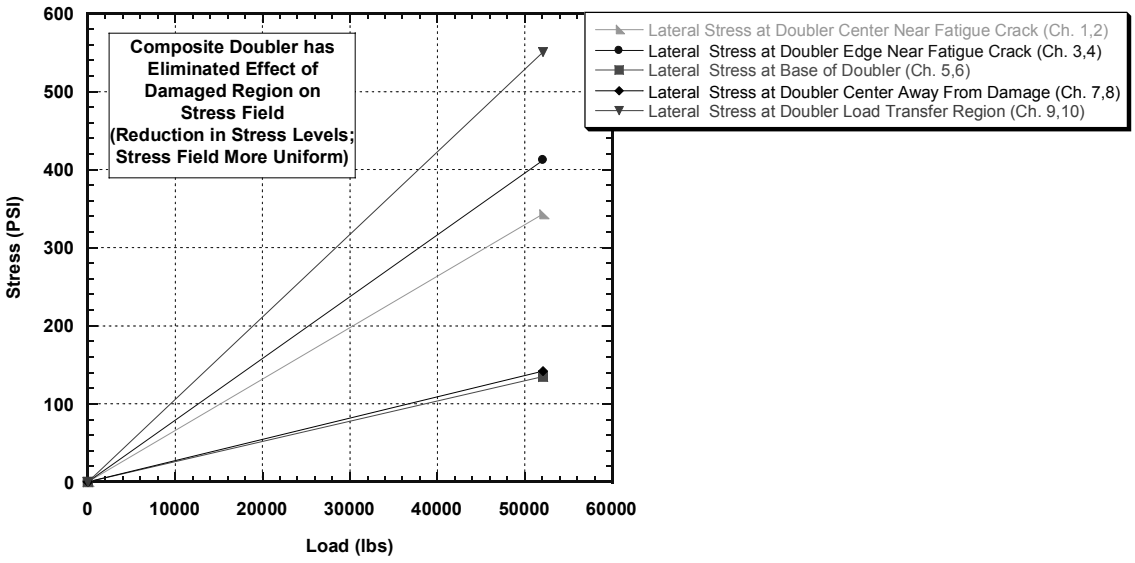

Figure 10-50: Lateral (Shear) Stresses in I-Beam Web Generated by Combined Load of Stationary Dump Truck Directly Over I-Beam (Inside Lane) and Moving Semi Truck in the Passing Lane AFTER Repair

Longitudinal Stresses			
Stress Direction & Strain Gage Description	**Max Stress Level Before Composite Doubler Repairs (psi)**	**Max Stress Level After Composite Doubler Repair (psi)**	**Percent Reduction in Stress**
Longitudinal Stress - Biaxial (Ch. 1,2)	2,139	2,442	-14%
Longitudinal Stress - Biaxial (Ch. 3,4)	11,373	2,073	82%
Longitudinal Stress - Biaxial (Ch. 5,6)	3,346	3,850	-15%
Longitudinal Stress - Biaxial (Ch. 7,8)	6,784	2,472	64%
Longitudinal Stress - Biaxial (Ch. 9,10)	5,442	4,334	20%
Principal Stress - Rosette (Ch. 11,12,13)	7,966	4,624	42%
Principal Stress - Rosette (Ch. 14,15,16)	5,482	4,489	18%

Lateral Stresses			
Stress Direction & Strain Gage Description	**Max Stress Level Before Composite Doubler Repairs (psi)**	**Max Stress Level After Composite Doubler Repair (psi)**	**Percent Reduction in Stress**
Lateral Stress – Biaxial (Ch. 1,2)	10,631	342	97%
Lateral Stress – Biaxial (Ch. 3,4)	7,612	412	95%
Lateral Stress – Biaxial (Ch. 5,6)	3,646	135	96%
Lateral Stress – Biaxial (Ch. 7,8)	5,515	142	97%
Lateral Stress – Biaxial (Ch. 9,10)	3,857	550	86%

Table 10-4: Comparison of Stress Levels in Bridge I-Beam Before and After Composite Doubler Repair

CONCLUSIONS

This Sandia Lab Directed Research and Development (LDRD) program concludes a study into the application of composite patches and associated health monitoring to repair and refurbish thick steel structures typically used in civil and military structures. Instead of riveting multiple metal plates or using welding processes to facilitate a repair, it is possible to bond a single composite doubler to the damaged structure. The use of fiber reinforced polymer (FRP) materials, which do not have brittle fracture problems such as those inherent in welds, can help extend the structure's fatigue life and reduce equipment downtime. Applications include such diverse structures as: buildings, bridges, railroad cars, trucks and other heavy machinery, steel power and communication towers, pipelines, factories, mining equipment, ships, tanks and other military vehicles. Extreme fatigue, temperature, erosive, and corrosive environments induce an array of structural damage. Current techniques for strengthening steel structures have several drawbacks including requiring heavy equipment for installation, poor fatigue performance, heat affected zones around welds, and the need for ongoing maintenance due to continued corrosion attack and crack growth. The current weld repair techniques for these structures provide a fatigue life that is inferior to that of the original plate. Subsequent re-cracking must be revisited on a regular basis. Mechanically fastened repairs involve the addition of new holes with associated stress risers and new crack initiation sites. In addition, the time and labor involved to attach such repairs can be prohibitive.

The use of bonded composite doublers has the potential to overcome the difficulties associated with current repair techniques and the ability to be applied where there are currently no rehabilitation options. It has proven to be cost-effective with minimal disruption to the users of the structure. This study has shown that bonded composite repairs have crack mitigation capabilities that are superior to bolted and welded repairs. Composite doublers offer enhanced safety through improved fatigue life and corrosion resistance. The engineering advantages include: 1) elimination of fastener holes or weld stress risers that produce new crack initiation sites, 2) superior flaw growth mitigation, 3) high strength-to-weight ratio, 4) high durability, 5) ability to tailor strength to meet anisotropy needs thus eliminating the undesirable stiffening of a structure in directions other than those required, 6) corrosion resistance, and 7) formability to complex contours. The economic advantages include rapid repair installations that reduce downtime and do not require future maintenance.

The engineering activities in this program investigated design, analysis, fatigue performance, installation, health monitoring, and adaptive healing issues. This program demonstrated the successful application of composite doubler repairs on steel structure by successfully establishing that:

1. Composite doubler repair technology is viable for steel structures within both civil and military arenas.
2. Composite doublers are able to withstand extensive damage and non-optimum installations while improving fatigue life and ultimate strength.

3. Continuous health monitoring is possible with the necessary sensitivity and minimal need for human involvement in the SHM process.
4. Self healing concepts are feasible within working structures and can help enhance the integrity and safety of composite structures.

This LDRD also contained the self healing, smart structure, and modeling/simulation elements needed to pursue living infrastructure concepts. It produced new science related to distributed and continuous Structural Health Monitoring (SHM), the use of adaptive structures, and the intelligent application of advanced materials to provide a valuable tool for a wide range of critical steel structures. The sensing technology developed under this LDRD allows for continuous in-service monitoring of structures and mechanical assemblies. These sensors can be applied in retrofit applications in which reinforcements are added to an infrastructural asset, such as an aircraft, bridge, or vessel. They can also help ensure safe and effective operation of structures by allowing preventive health monitoring strategies to be implemented across a wide range of industries.

Composite Doubler Installation Process - In order to optimize surface preparation, the basic mechanisms of adhesion for structural adhesive bonding were considered: mechanical interlocking and chemically-enhanced bonding between the polymer and the adherend surface. Eight different processes were evaluated for bonding composite materials to steel structures. Wedge (crack growth), lap shear (fatigue and ultimate strength), and peel tests were completed on pristine and worst-case, environmentally-conditioned specimens to arrive at an optimum process for installing composite repairs. A field installation-friendly process was established that uses grit blasting, Silane chemical, and steel primer to produce a strong and durable bonded joint. In addition to being robust, the selected installation process is also inexpensive and uses readily available equipment and chemicals. Methods and equipment necessary for high-temperature and vacuum bag cures in the field were proven.

Crack Mitigation and Damage Tolerance - One of the primary concerns surrounding composite doubler technology pertains to long-term survivability, especially in the presence of non-optimum installations. This test program demonstrated the extreme damage tolerance capabilities of bonded composite doublers. The fatigue and strength tests quantified the structural response and crack abatement capabilities of Boron-Epoxy doublers in the presence of worst case flaw scenarios. The engineered flaws included cracks in the parent material and disbonds in the adhesive layer between the composite laminate and the steel structure. Environmental conditions representing temperature and humidity exposure were also included in the coupon tests. Stress, fatigue, and ultimate strength tests established the viability of composite doubler repairs to reinforce steel structures and minimize/eliminate the effects of cracks, corrosion or other flaws. As part of the performance testing, the repair designs were varied to quantify the relative importance of specific composite laminate features. Large strains immediately adjacent to the doubler flaws emphasize the fact that relatively large disbond or delamination flaws (up to 1" diameter) in the composite doubler have only localized effects on strain and minimal effect on the overall doubler performance (i.e. undesirable strain relief over a disbond but favorable load transfer immediately next to disbond). This study used flaws that were twice as large as the detectable limit to demonstrate the ability of composite doublers to tolerate potential damage. Similarly, the crack mitigation capabilities of Boron-Epoxy doublers

were evaluated using crack sizes which exceeded the inspection threshold. The damage tolerance tests presented in this document looked at crack growth beneath doublers of up to 5".

Fatigue Performance - Fatigue and ultimate strength tests evaluated the overall effect of composite doublers on stress intensity, crack growth, and strength characteristics of steel structure. The structural tests: 1) assessed the potential for interply delaminations and disbonds between the steel and the laminate, and 2) determined the load transfer and crack mitigation capabilities of composite doublers in the presence of severe defects. If the optimum composite repair – protected sufficiently to minimize or eliminate the effects of environmental conditioning – is used as the final performance metric, the results indicate that the fatigue life of steel structures can be extended by a factor of 2 to 10 through the use of composite patches. For worst case conditions of 1" long edge cracks beneath the repair, bonded composite doubler repairs, can extend fatigue life by factors of 20 to 60 while allowing little or no crack growth in a parent steel structure. If small amounts of crack growth can be tolerated then composite doubler repairs may not need to be revisited until as much as 1,000,000 cycles (100X fatigue life increase). Furthermore, if weld repairs are first used to fill the crack and applied in conjunction with composite doublers, the fatigue life could extend another order of magnitude before significant re-cracking occurs. Finally, the presence of the composite doubler may reduce stress levels below crack onset and growth conditions such that the flaw is completely arrested. These results were obtained for composite laminate designs that are 30% of the stiffness of the structure being repaired. If additional crack mitigation is desired, stiffer repair patches can be used. These results were also obtained in the presence of extreme worst-case conditions including disbonds that removed 20% of the critical load transfer region in the doubler and also eliminated local reinforcement directly over the crack. It should be noted that the results sited here are conservative since they were produced using stress spectrums that were up to three times as large as those measured in the field.

Stress/Strain Fields - Strain field analyses for expected stress environments showed that the large disbonds, in excess of those which will be detected by NDI, and Boron-Epoxy water absorption had minimal affect on the performance of the adhesive layer. The maximum doubler strains were found in the load transfer region around the perimeter (taper region) of the doubler. In all five doubler configurations, the strains monitored in this area were 50% - 80% of the total strain in the steel plate. For the normal stress spectrum, this value remained constant over four fatigue lifetimes indicating that there was no deterioration in the bond strength. During crack propagation, the stresses in the doubler increased to pick up the loads released by the plate. Data acquired during failure tests showed that the composite doubler was able to absorb stresses in the plastic regime and that extensive yielding of the steel was required to fail the installation. Also, stress risers, normally observed around flaws, were minimized by the doubler.

Residual Strength - Post-fatigue load-to-failure tests produced residual strength values for the composite-steel specimens. Even in the presence of severe worst case installations and extensive damage growth (fatigue cracks extending through 50% of the specimen width), it was seen that the doubler-reinforced plates were able to achieve residual tensile strengths (i.e. post-damage tensile strength) which exceeded the 65 ksi baseline value for this steel material. Thus, the Boron-Epoxy doubler was able to return the parent structure to its original strength and load carrying capability.

Nondestructive Inspection - Nondestructive inspection techniques were developed to adequately monitor the health of the patch and the parent structure. Ultrasonic methods can be used to reliably detect disbonds in a composite doubler repair well before the flaw reaches critical size. Pulse-Echo ultrasonics can be easily implemented in the field using hand held inspection devices. Anomalies in A-Scan signals can be used to detect disbond and delamination flaws. The ultrasonic method developed in this study was shown to work well in mapping out flaw shapes and delineating the flaw edges. Even in the thick laminates needed for these repairs, pulse-echo UT is able to repetitively detect disbond flaws as small as 0.25" in diameter. Furthermore, the technique is able to map out a changing flaw profile - a cohesive failure in the adhesive caused by the crack propagating through the steel - during fatigue testing of the composite doubler. Crack detection in the parent steel material can be accomplished using conventional eddy current and X-ray techniques. Crack signals from the parent steel can be obtained through composite doublers in excess of 150 plies and greater than 0.9” thick.

Structural Health Monitoring (SHM) - The effect of structural aging and the dangerous combination of fatigue and corrosion, coupled with recent failures in civil structures, has produced a greater emphasis on the application of sophisticated health monitoring systems. The costs associated with the increasing maintenance and surveillance needs of aging structures are rising. This program showed how the application of distributed sensor systems can reduce these costs and enhance safety by allowing condition-based maintenance practices to be substituted for the current time-based maintenance approach. Through the use of in-situ sensors, it is possible to quickly, routinely, and remotely monitor the integrity of a structure in service. This requires the use of reliable structural health monitoring systems that can automatically process data, assess structural condition, and signal the need for human intervention. Prevention of unexpected flaw growth and structural failure can be improved if on-board health monitoring systems exist that could frequently, or even continuously, assess structural integrity. Such systems would be able to detect incipient damage before catastrophic failures occurs. In addition, corrective repairs initiated by early detection of structural damage are more cost effective since they reduce the need for subsequent major repairs.

Local sensors, such as the ones described in this report, can be used to directly detect the onset of crack, corrosion, or disbond flaws. Global SHM, achieved through the use of sensor networks, can be used to assess overall performance (or deviations from optimum performance) of large structures such as bridges and buildings. The ease of monitoring an entire network of distributed sensors means that structural health assessments can occur more often, allowing operators to be even more vigilant with respect to flaw onset. A “smart structure” is one which is sufficiently instrumented so that the data can be synthesized to form an accurate real-time picture of the state of the structure in all its critical aspects. The absence of cracks or corrosion indicates that a structure is able to safely continue to operate. Similarly, the absence of disbonds and delaminations indicates that a composite doubler is able to perform its function.

This study developed and explored several on-board structural health monitoring sensors and proved that distributed, autonomous health monitoring systems can be applied to reliably detect incipient damage. The SHM portion of this effort developed an eddy current (EC) microsensor that can be permanently mounted on a structure to detect crack onset and growth. The EC sensor

was designed with sufficient penetration power to detect deeply embedded, or subsurface, fatigue cracks. Other sensor approaches studied were: Comparative Vacuum Monitoring sensors, fiber-optic sensors, and piezoelectric sensors embedded within or mounted on the surface of the composite material. Because of the basic lamination concept that builds a structure from multiple composite plies, continuous fiber structural composites naturally lend themselves to embedded sensors that can monitor the structural response in real-time. Continuous or segmented fiber optic sensors were deployed to detect cracks in the steel structure beneath the composite repair and to measure the stresses in the composite doubler after it is placed into service. Irregular changes in the stress field can be used to indicate both crack onset in the steel structure and delaminations or disbands in the composite repair.

Self Healing in the Composite Laminate Repair – Self-healing of composite and adhesive (bondline) materials was accomplished by incorporating a microencapsulated healing agent and a catalytic chemical trigger within a polymer matrix. Damage in the form of a bond dislocation serves as the triggering mechanism for self-healing. The approaching dislocation ruptures the embedded microcapsules, releasing a healing agent into the crack plane through capillary action. Polymerization of the healing agent is triggered by contact with the embedded catalyst, bonding the crack faces. Employing this self-healing research concept, this segment of the LDRD developed self-healing bond lines suitable for bonded repair of metallic structures. Repair of damage is accomplished automatically and without human intervention, improving performance and service-life. The most critical issue for the adhesive fabrication task was to identify the processing window for compaction pressure in which the microcapsules remain structurally intact throughout cure while ensuring full compaction of the laminate stack. Healing efficiencies of over 50% were achieved for the fully incorporated, in-situ healing system. In addition to quasi-static fracture studies, the FM®73 adhesive system was studied in fatigue. The in-situ self-healing system showed a fatigue-life extension of over 200% compared to the reference specimens without healing.

Numerical Modeling - Numerical modeling was used to: 1) produce an understanding of the critical elements of this technology and 2) develop design guidelines with an associated software package to aid the design process. In order to arrive at the necessary insights into service performance plus life and degradation evaluations, a modeling effort to compliment the smart structure approach was required. Composite doubler design and analysis was conducted via finite element analyses. The effects captured in the patch region included the anisotropic response of the composite patch, the gradual load transfer between the parent steel and patch materials over the patch taper region, the residual stresses resulting from the thermal strain mismatch between the patch and parent materials, and out-of-plane bending arising from shifting of the bending neutral axis in the patch area. The two-dimensional finite element analysis also predicted material failure including adhesive yielding, recracking of the repaired fill-weld crack, and disbonding of the composite patch from the parent material. Degraded adhesive properties were modeled in various sub-regions in order to investigate the effects of contamination, imperfect curing, and the presence of flaws. This work developed a set of simple approximate relations that can be used to design a composite patch for a thick steel plate that contains a crack (with or without an accompanying fill-weld repair).

Accomplishments Overview - In summary, an in-depth performance assessment of composite doublers for repair of steel structures was completed. The results presented in this report proved that composite doublers can be installed on steel structures to produce a superior repair with extended fatigue life. The goal of this project was to establish bonded composite doublers as a reliable and cost-effective structural repair method for steel structures and to develop adequate real-time health monitoring to ensure the long-term integrity of such structures with minimal need for human intervention. The use of composite doublers, which do not have brittle fracture problems such as those inherent in welds, along with in-situ structural health monitoring will help extend the structure's fatigue life, enhance safety and reduce the equipment downtime. This LDRD consisted of four related research elements that produced the following milestones: 1) defining design parameters, performance requirements and processes to ensure reliable repair installations, 2) developing sensor systems to accommodate in-situ health monitoring of structures, 3) proving self-healing concepts for composite materials and bonded joints, and 4) elegant use of numerical modeling to guide composite repair designs.

Deployment of FRP materials and bonded joints requires proper design, suitable surface preparation methods, and adequate surveillance to ensure structural integrity. This study developed and proved an optimum field installation process using specific mechanical and chemical surface preparation techniques coupled with unique, in-situ heating methods. In addition, a comprehensive performance assessment of composite doubler repairs was completed to establish the feasibility of this technology for large, steel structures. Damage tolerance, durability, crack mitigation, and ultimate strength tests were performed to quantify the capabilities of composite doubler repairs and to provide insights into the critical laminate design parameters. Design philosophies were evolved to accommodate materials of different moduli, ductility, and failure modes. Installation of ultra-large composite doublers for large steel structure applications was studied. Nondestructive inspection and in-situ Structural health Monitoring methods were developed to adequately monitor the integrity of the patch and the parent structure. The evolution of this technology into smart, living structures that can both detect and repair damage is a tremendous enhancement. The accompanying sensor technology offers the potential for real-time, automatic health monitoring that will be critical for implementing self-healing techniques. Self-healing functionality expands the useful lifetime of polymeric components while incorporating a mechanism to provide increased safety associated with the repair of metallic structures. By encompassing all "cradle-to-grave" tasks - including design, analysis, installation, structural integrity and inspection - this study firmly established the capabilities of composite doubler repairs and introduced technology to incorporate self-monitoring and self-healing concepts.

For more information contact:

Dennis Roach
Sandia National Laboratories
P.O. Box 5800 MS-0615
Albuquerque, NM 87185
dproach@sandia.gov
(505)844-6078

APPENDIX A

Photo Summary of Laminate Fabrication and Installation Process for Bonding Composite Doublers on Carbon Steel Structures

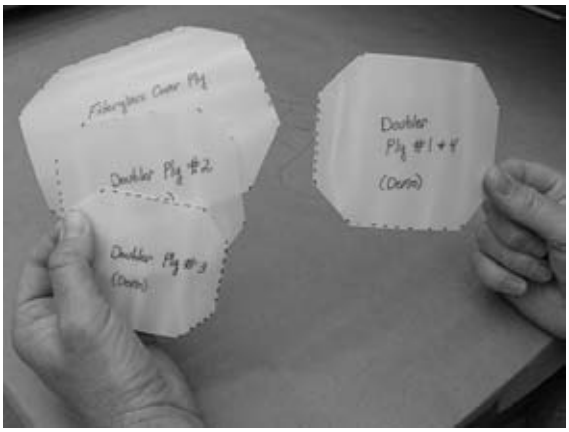

Figure A-1: Mylar templates for B-E Plies, Adhesive and Fiberglass Cover Ply

Figure A-2: Cut Roll of B-E Tape into Doubler Plies

Figure A-3: Use Template for Proper Sizing and Ply Orientation

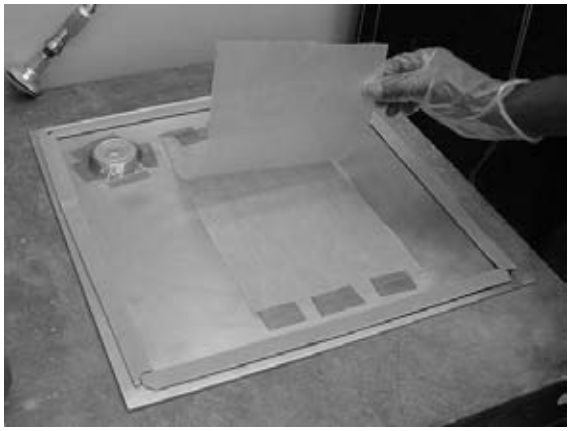

Figure A-4: Sandwich of Armalon Release Fabric on Doubler Debulk Tool

Figure A-5: Lay Up B-E plies in Proper Stack (1st ply goes face down)

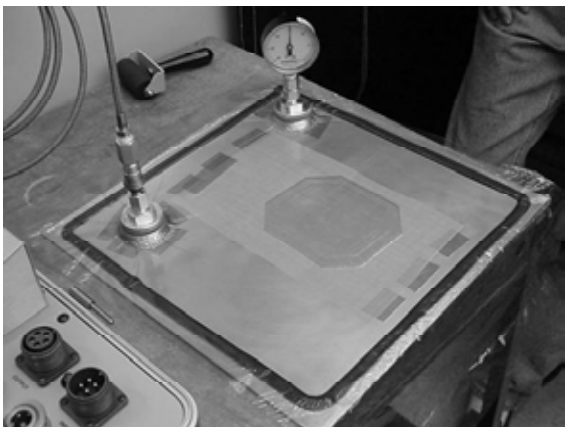

Figure A-6: Vacuum Bag Debulk of Doubler Every Four Plies

Figure A-7: Coarse Scotchbrite Grind to Remove Excess Scale/Oxide

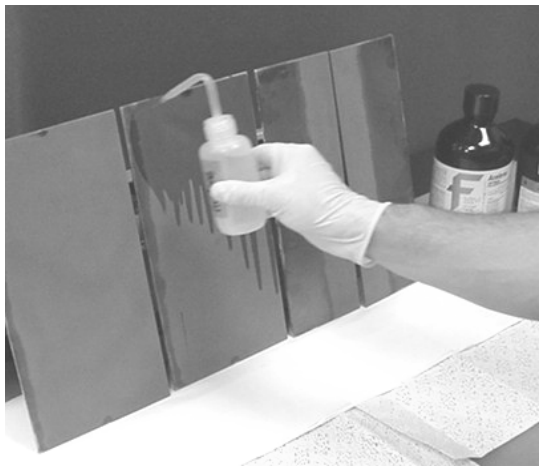

Figure A-8: Degrease with Acetone Followed by Methyl Alcohol

Figure A-9: Grit Blast Device Uses 50 µm Aluminum Oxide Grit

Figure A-10: Grit Blast Steel Surface

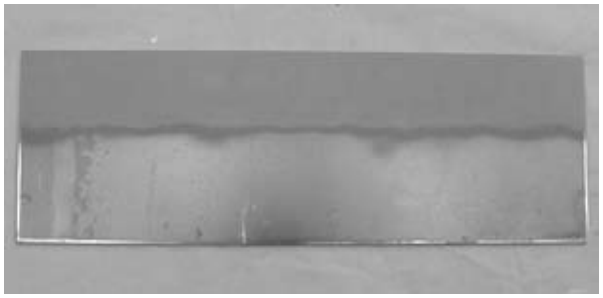

Figure A-11: Grit Blast Surface Along Top

Figure A-12: Mix Silane Solution (99:1 ratio of distilled water to Silane)

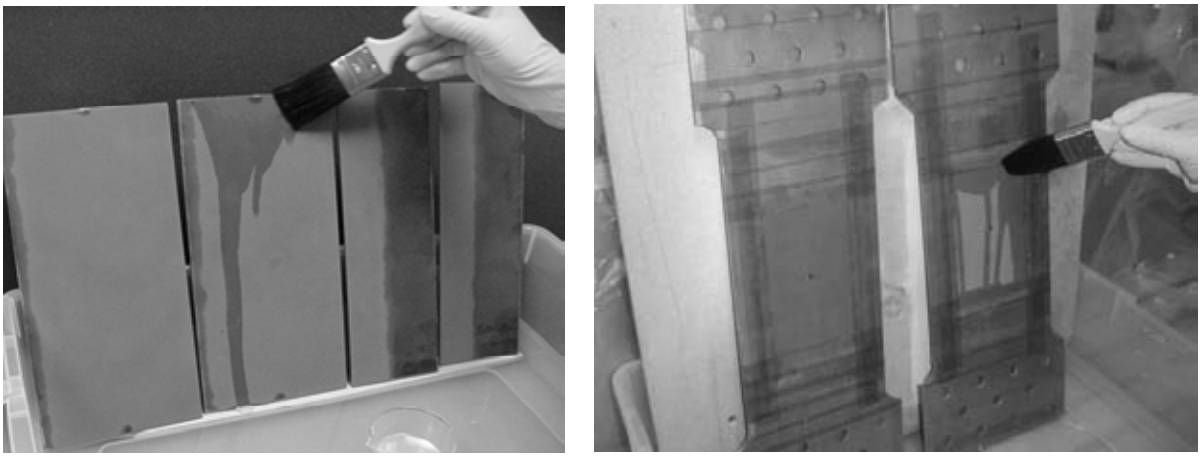

Figure A-13: Brush-On Application of Silane Mixture to Steel Surface

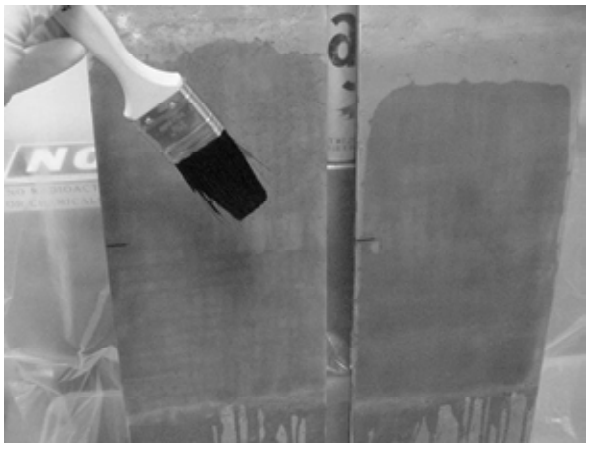

Figure A-14: Wet Surface with Silane Solution for Ten Minutes

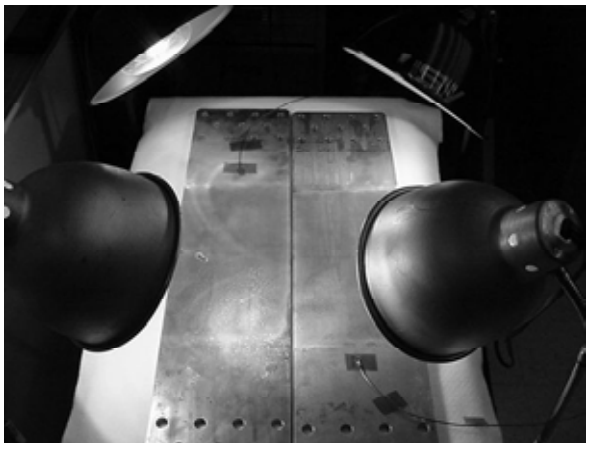

Figure A-15: Drive Off Silane Moisture (Pre-Cure) Using Heat Lamps

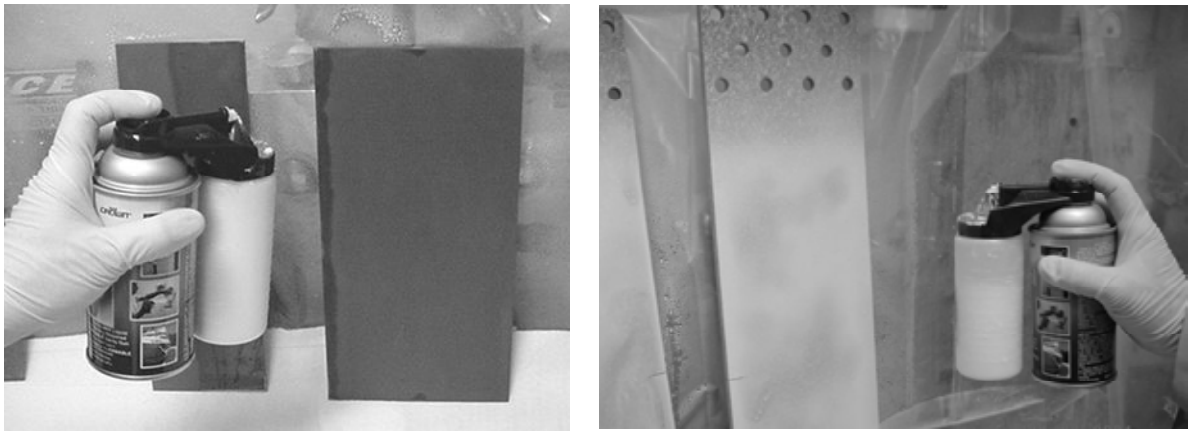

Figure A-16: Spray BR6747 Primer on Steel Surface

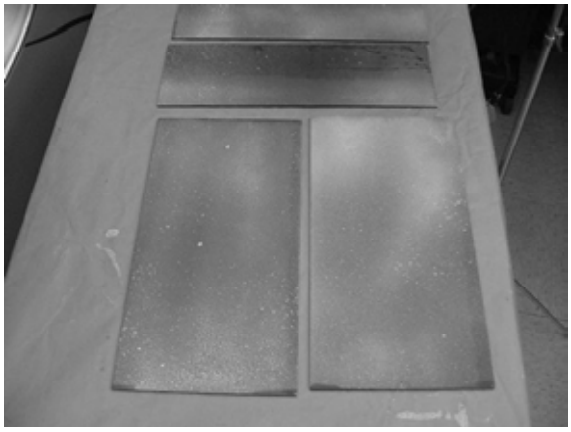

Figure A-17: Drive Off Primer Moisture Using Heat Lamps

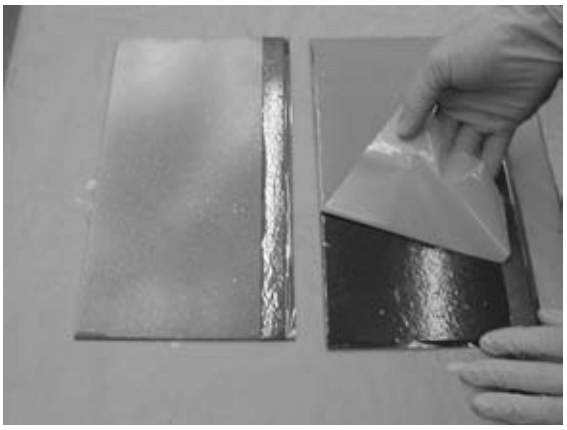

Figure A-18: Apply Adhesive Film to Composite Doubler Laminate

Figure A-19: Cut Two Witness Coupons from Steel Plate and Prepare Surface for Bonding Process

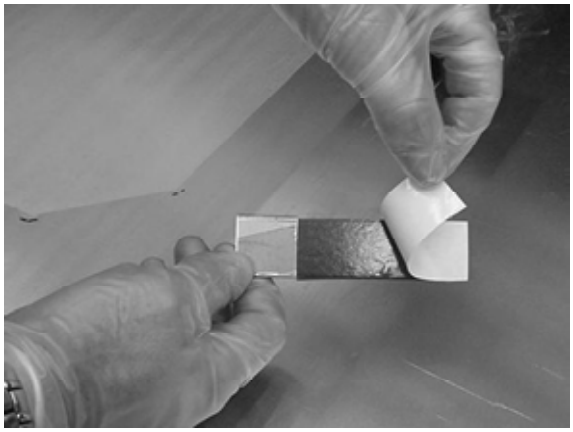

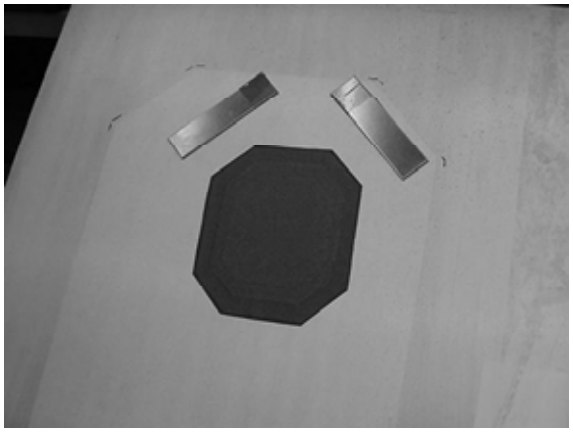

Figure A-20: Place Adhesive Strip on Back of Witness Coupons and Place Doubler and Witness Strips on Prepared Surface

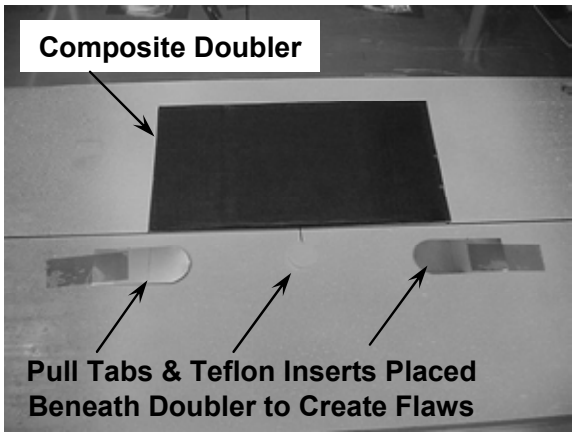

Figure A-21: Place Doubler on Prepared Steel Surface

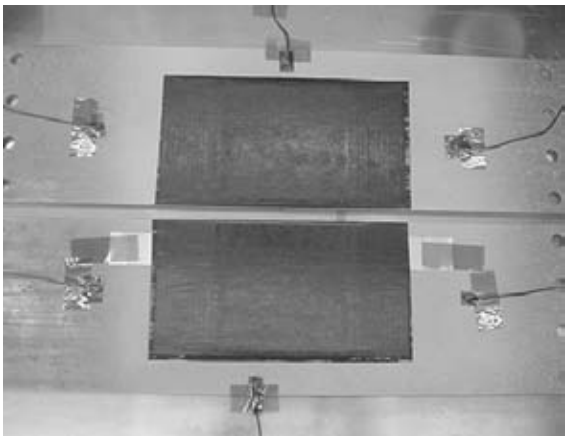

Figure A-22: Two Composite Doublers in Place; Six Thermocouples Placed To Control Cure Temperatures

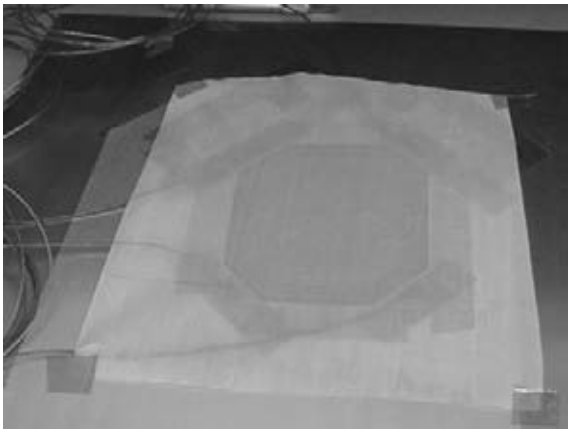

Figure A-23: Place Armalon Release Fabric

Figure A-24: Place Multiple Plies of Bleeder Cloth

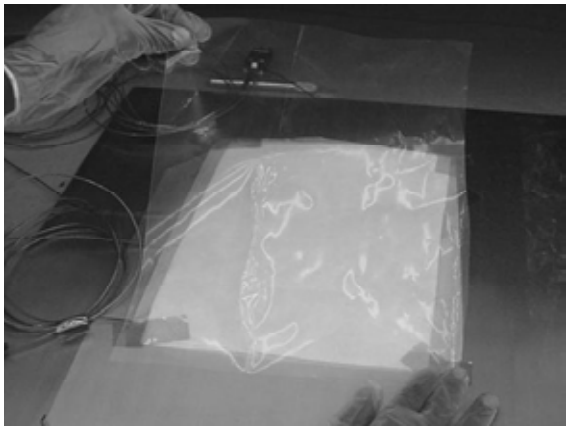

Figure A-25: Place Non-Perforated Release Film

Figure A-26: Place Breather Mat

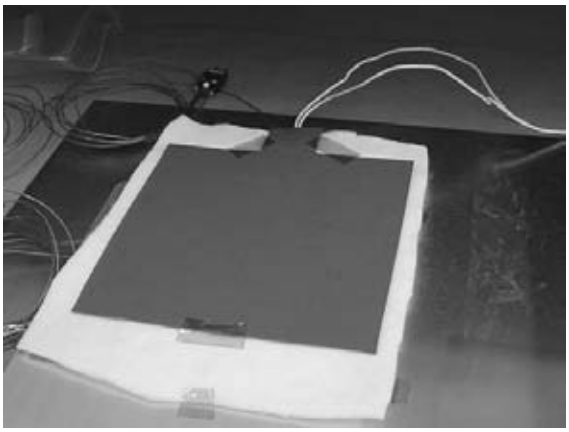

Figure A-27: Place Heat Blanket

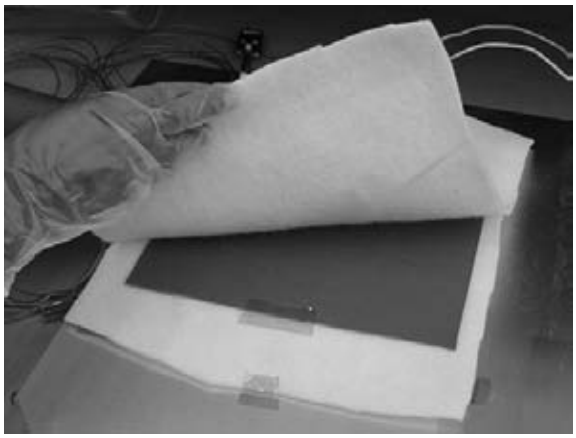

Figure A-28: Place Breather Mat

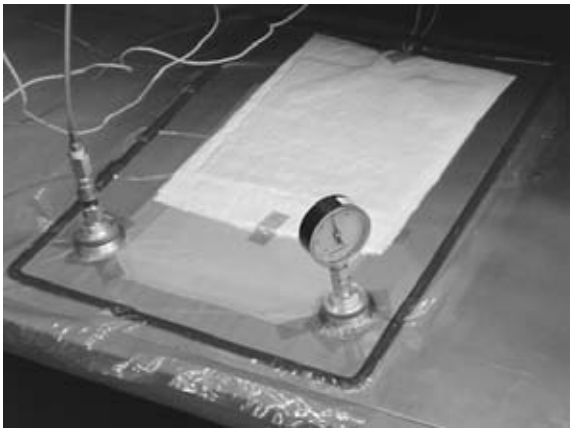

Figure A-29: Install Vacuum Bag

Figure A-30: Program the Heat Control System for Cure Cycle

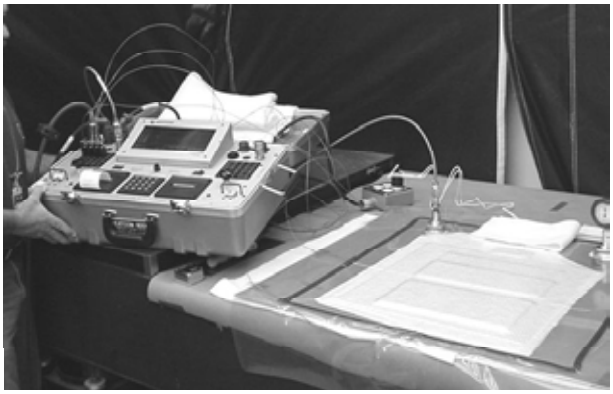

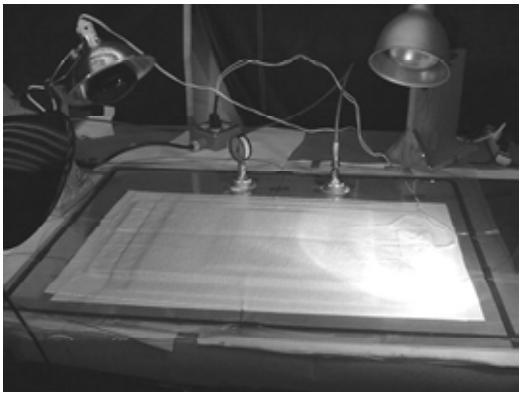

Figure A-31: Hot Bonding Process - Vacuum Bag Pressure with Heat Blanket; Bleeder Cloths for Controlled Resin Bleed; Co-Cure of Primer, Boron-Epoxy Doubler, and Adhesive; Heat Lamps Used to Adjust Local Temperatures

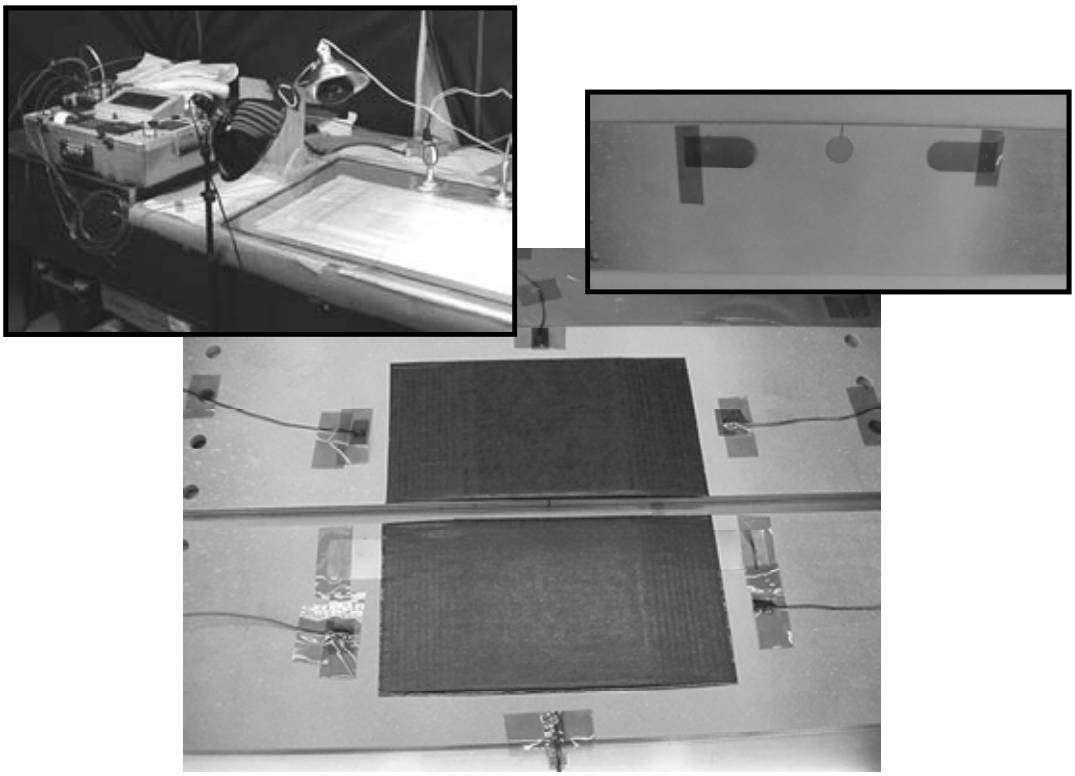

Figure A-32: Completed Specimens with Composite Doublers Installed; Heat Application (left inset), Flaw Inserts Placed Under Doublers (right inset)

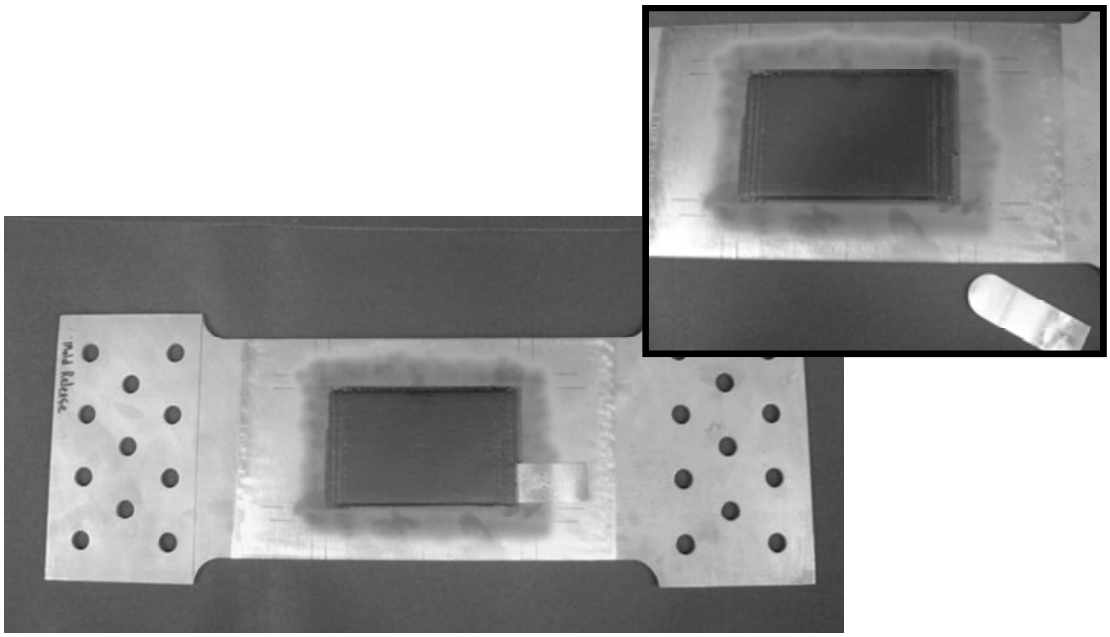

Figure A-33: Composite Doubler Fatigue Specimens After Installation and with Pull Tab Removed to Create Engineered Disbond Flaw (inset)

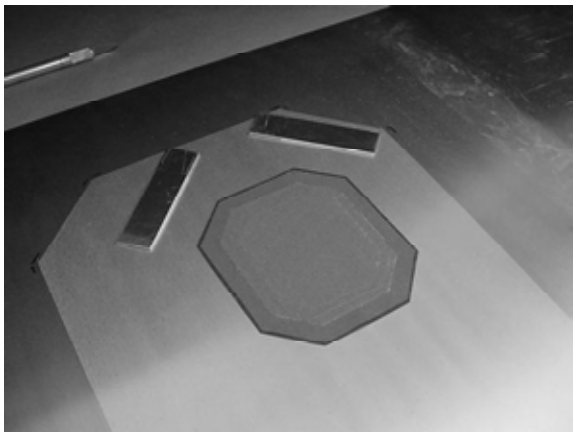

Figure A-34: Finished Product - Red Color is from Adhesive Layer

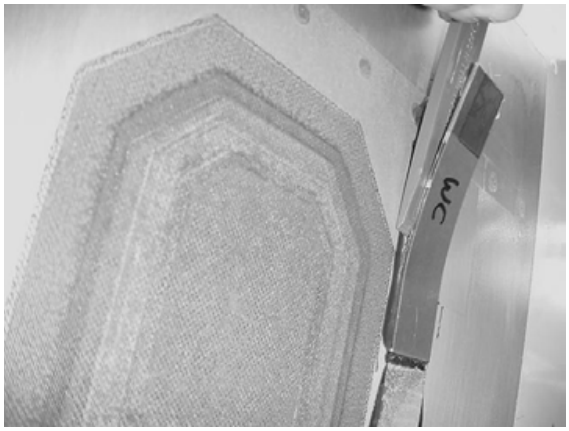

Figure A-35: Remove Witness Coupon Using a Plastic Wedge; Beige Color is From Fiberglass Cover Ply

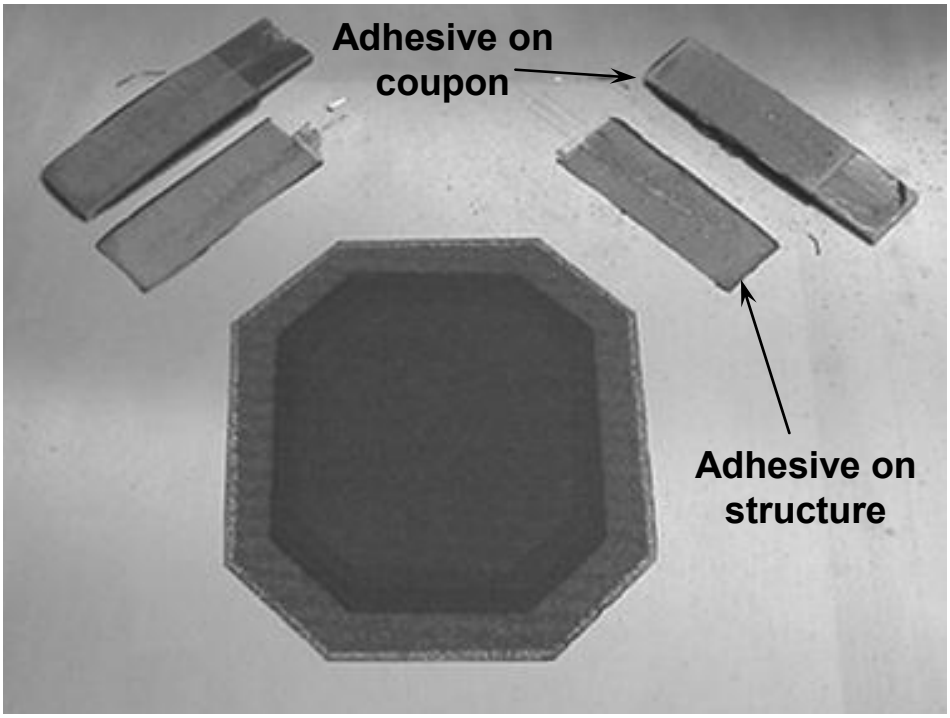

Figure A-36: Witness Coupons Removed - Note Adhesive on Both Coupon and Parent Skin Indicating That Full Strength of Adhesive Has Been Achieved

APPENDIX B

Installation Process for Repairing Carbon Steel Structures Using Bonded Composite Doublers

Installation Process for Repairing Carbon Steel Structures Using Bonded Composite Doublers

Table of Contents

Installation Process for Repairing Carbon Steel Structures Using Bonded Composite Doublers

1.0 GENERAL

This section establishes the procedures for the repair of steel structures using adhesively bonded Boron/epoxy co-cured doublers. This procedure utilizes a 225°F-cure Boron/epoxy structural material. The surface preparation is critical for metal bond repairs. The procedure involves a grit blast surface roughening to enhance mechanical adhesion, followed by the application of Silane & primers to chemically enhance the bonding process.

Typical Composite Doubler Installation - Figure B-1 shows a typical bonded composite doubler repair over a cracked parent steel structure. The doubler consists of a series of Boron/epoxy composite plies that are stacked and debulked to produce a cohesive laminate repair patch. The number of plies and fiber orientation are determined by the nature of the reinforcement required (i.e. stress field and configuration of original structure). The taper at the edge of the doubler is used to produce a gradually increasing stress gradient in the area of primary load transfer. A top ply of fiberglass is installed to supply mechanical and environmental protection for the installation. Surface preparation is the most critical aspect of the doubler installation. This consists of paint removal, solvent clean, light abrasion, grit blasting and chemical treatment (Silane/primer) to ensure proper adhesion. Since the doubler must be installed in the field, vacuum bag pressure and in-situ heat sources (e.g., heat blankets, ceramic heaters) are used to simultaneously cure the composite laminate and adhesive layer.

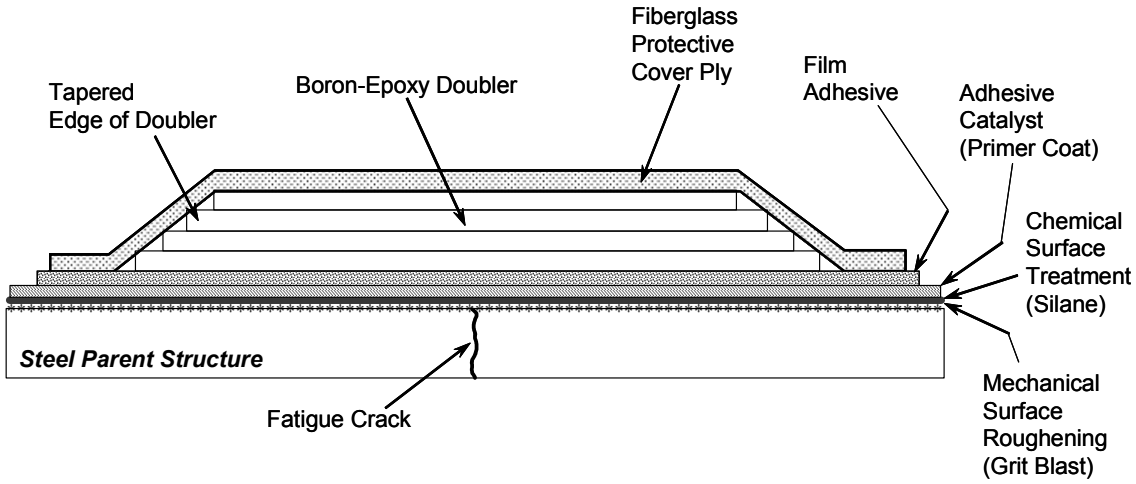

Single heat cycle: co-cure of Silane, primer, adhesive, composite doubler and fiberglass cover ply

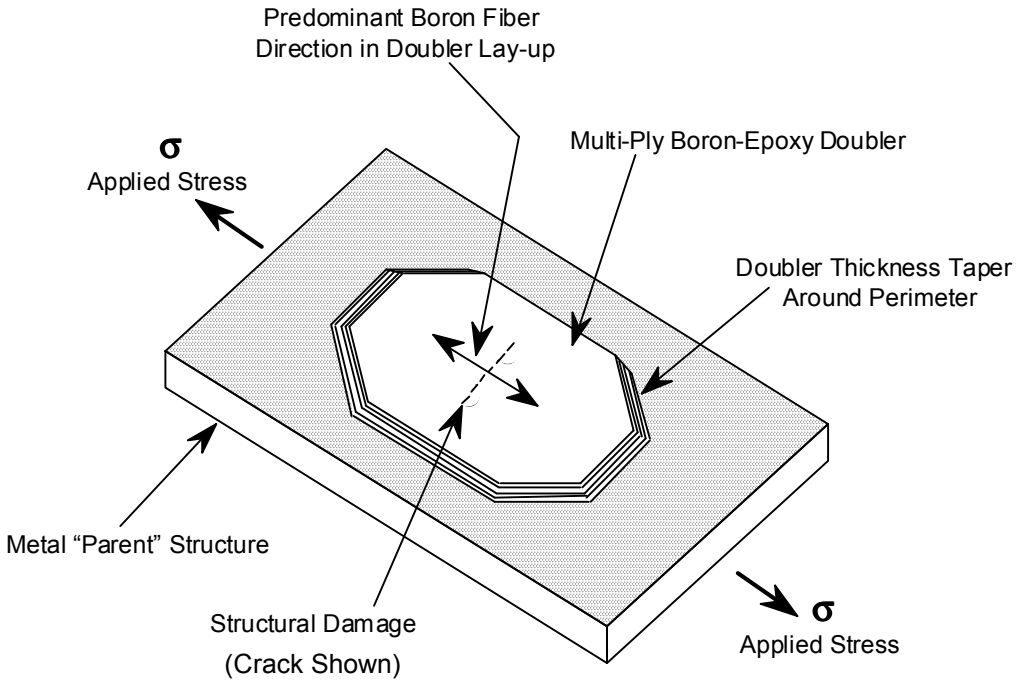

Figure B-1: Schematic and Isometric Views of a Bonded Composite Doubler Repair

2.0 REPAIR CONSIDERATIONS AND PROCESS FLOWCHART

1. Contour of repair shall not be excessive for the thickness of the repair doubler chosen. The application may require a caul plate or special tooling.

2. Repair area surface should have a relatively even surface with local surface anomalies not to exceed .010 inches deep for abrupt thickness changes & 0.25" deep for gradual undulations of the surface.

3. Radius of curvature should not be less 0.5 inches.

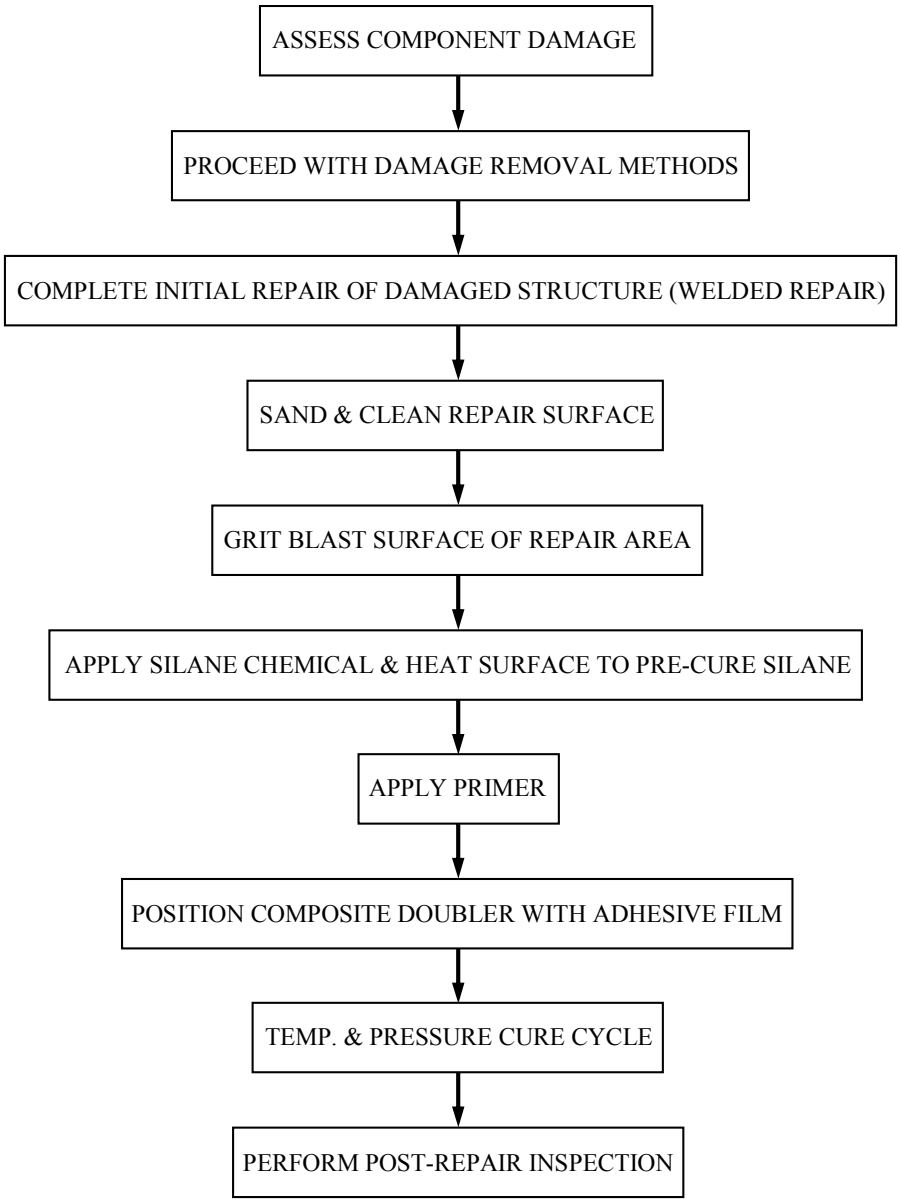

Figure B-2. Repair Flowchart for Installing Composite Laminate on Steel Structure

3.0 TOOLING, EQUIPMENT, AND FACILITY REQUIREMENTS

Processing procedures outlined herein are for preparation, lay-up, and cure of Boron/epoxy repairs. They are to be used only in areas of reasonable cleanliness when temperatures at the repair surface are between 32°-85°F. Protect all bond surfaces from oil mist, exhaust fumes, and gases, soot, rain, dust, and other particulate matter. All equipment requiring calibration shall only be used if it is still within its calibration date.

3.1 Equipment

3.1.1 Pressurizing Devices

A vacuum bag is used to maintain the 17 in.Hg. pressure required to debulk and bleed out excess resin in the Boron/epoxy repair. It is also used to assist in holding repair items, such as heat blankets, insulation layers, and thermocouples in contact with the repair area.

3.1.2 Heating Equipment

Required power and type of heating equipment will be determined by the thickness of the parent structure along with other geometry features of the repair area. Heating equipment shall be compatible with the pressurizing devices. Heating equipment to cure the primer, adhesive and doubler includes:

A. Heat Lamps – Either tungsten filament or quartz tube.

B. Electric Heating Blankets – Electric heating blankets (shown in Figure B-3) are an efficient means of heating the bondline. The direct heating approach achieved with the heat blanket is shown in Figure B-4. The blanket should have 5 Watts/square inch minimum capability and provide continuous heating across the cure area.

C. Hot Bonder – Used for the control of the cure cycle during the bonding of the doubler. It controls the vacuum pressure and the temperatures of the heat blanket and monitors the corresponding thermocouples during the cure cycle. This item must be kept within calibration in order to use for the bonding application.

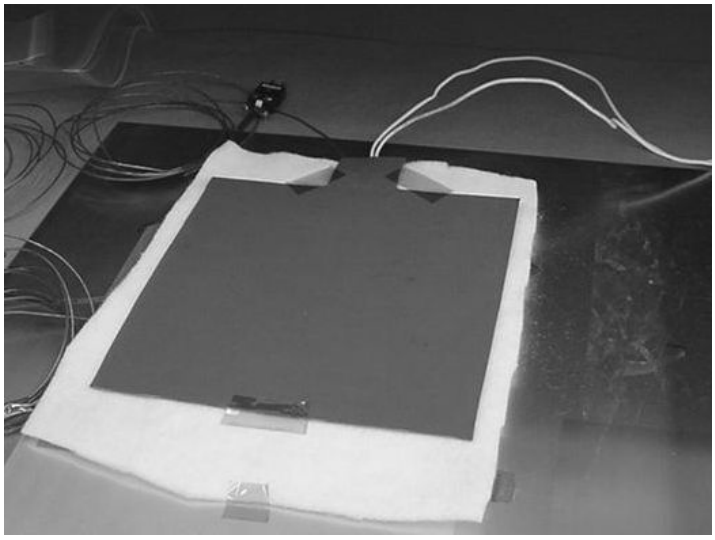

Figure B-3 Heating Blanket with Insulation on Underside

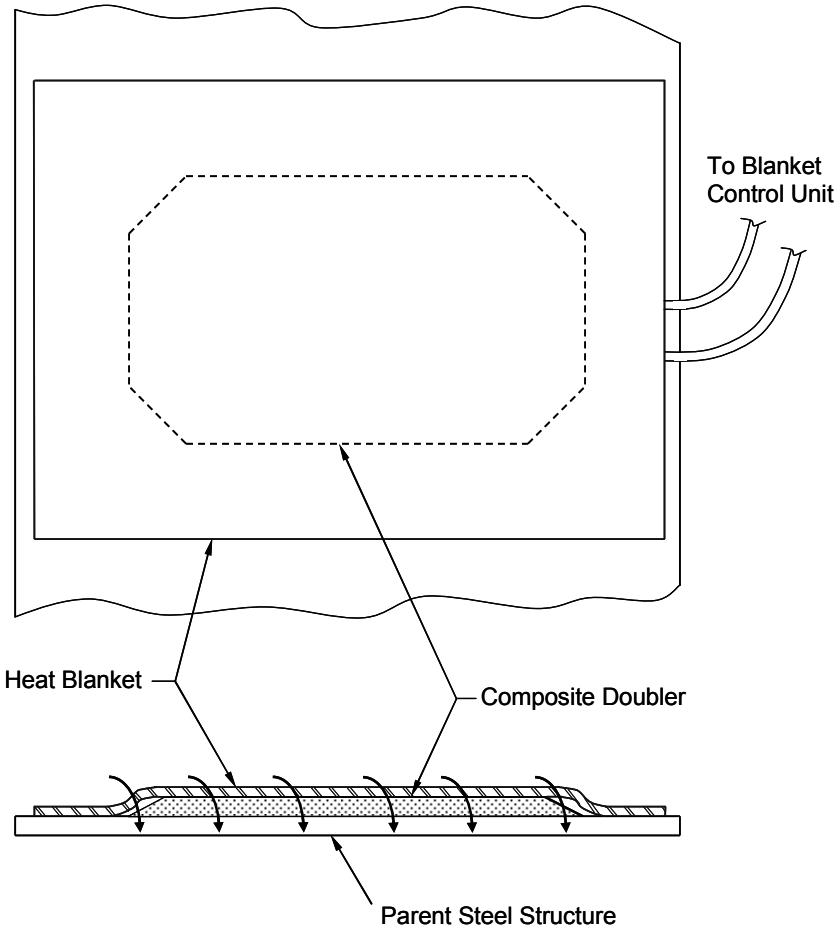

Figure B-4 Basic Concept of Direct Heating Using Heat Blankets

D. Ceramic Heating Elements – Flexible Ceramic Pad Heaters provide an effective way to heat thick structures for doubler repair. The ceramic heaters provide 28 Watts/square inch of heating surface and can provide the projection heating approach shown in Figure B-5. It is crucial to properly locate the heaters such that the target temperatures for the doubler cure cycle can be achieved.

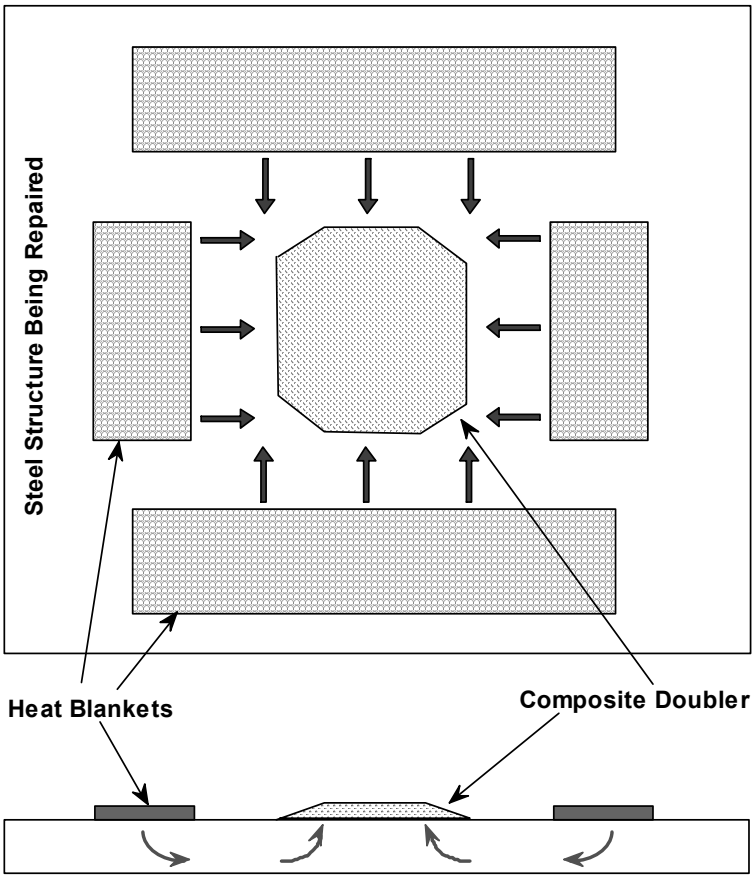

Figure B-5 Basic Concept of Projection Heating

3.1.3 Temperature Control

The temperature in and around the bond area shall be controlled in accordance with the appropriate cure cycle for bonded composite doubler repairs (see section. 10.0). During the heating process, the thermocouples should be monitored at least once per minute for the first 10 minutes, once every 5 minutes until the temperature has stabilized in the cure range, and once every 15 minutes thereafter until cure is complete.

The maximum temperature deviation between any two thermocouples in the curing area shall not exceed 40°F during the ramp-up phase and 25°F during the constant temperature cure phase. Record all readings or, alternately, monitor all readings at the stated intervals until the temperature is stabilized in the cure range. The temperature measuring system shall be capable of measuring temperatures up to 300°F with ±5 °F accuracy. Use 20-gage or finer thermocouple wire. Insulating materials and/or heat lamps may be used as required to improve temperature control or protect selected areas from heat.

3.2 Prohibited Materials

All oils, greases, and silicone compounds shall be prohibited from the immediate repair area during all bonding operations. Do not attempt to perform a bonded repair on any surface that is suspected of being contaminated by silicone compounds or other bond-inhibiting chemicals.

4.0 REPAIR MATERIALS AND SUPPLIES

See Table B-1 (Sheets 1 through 2) for repair materials and supplies needed for doubler repair.

MATERIAL	SUPPLIER
Abrasive cloth (alum. oxide paper, 150 & 220-grit or finer)	Commercially available
Acetone	Fisher Scientific
Adhesive, Film (AF-163)	3M Company Springfield, MO
Adhesive, Film (FM73)	Heatcon Composite Systems Seattle, WA
Air Filters, In-line, Balston models 2104N-1B1-BX and 2104N-1B1-DX	Parker Hannifin Corp, Filtration and Separation Div., Tewksbury, MA
Air Grinder, High Speed (rear exhaust)	Commercially Available
Auto Mixer w/magnetic stirrer (150-250rpm)	Fisher Scientific
Bleeder cloth (10 mil, 2.5 oz., bleeder fabric, 350°F use)	Airtech International Inc. Huntington Beach, CA
Boron/epoxy Prepreg Tape, 5521F/4	Specialty Materials Inc. Lowell, MA
Breather cloth, 10 oz., 400°F cure	Airtech International Inc. Huntington Beach, CA
Breather Cloth, 4 oz., 350°F cure	Airtech International Inc. Huntington Beach, CA
Ceramic Heat Blankets	Cooperheat MQS Inc. Houston, TX
Crown Spra - Tool Jar (#8212)	Fisher Scientific
Crown Spra - Tool Power Pac (#8211)	Fisher Scientific
Crown Spra - Tool spray head (#8213))	Fisher Scientific
Distilled Water	Commercially Available
Fiberglass Cover Ply Material (style 120 glass pre-preg fabric)	Heatcon Composite Systems Seattle, WA
Gloves, latex	Commercially available
Grit Blast System	Clemco Industries Corp. Washington, MO

Table B-1: Composite Doubler Repair Materials and Supplies (sheet 1)

MATERIAL	SUPPLIER
Grit, Aluminum Oxide, 50 Micron	S.S. White Technologies
HeatCon HCS9200 Hot Bonder system (w/thermocouples and heat blankets)	Heatcon Composite Systems Seattle, WA
Methyl Alcohol 99+%	Fisher Scientific
Paper Cutter	Commercially Available
Primer, BR6747-1; Type IA	Cytec Industries West Paterson, NJ
Propanol	Commercially available
Release Fabric, Armalon (peel ply)	National Aerospace Supply San Juan Capistrano, CA
Release Film, Non-perforated	Heatcon Composite Systems Seattle, WA
Respirator with organic cartridge	Commercially available
Sanding Disks Grit (180-grit)	Abrasive Sales Las Vegas, NV
Silane (3-Glycidoxypropyltrimethoxysilane, 98%)	Fischer Scientific (Aldrich Chemical Co. Inc)
Tape, Flash Breaker, 1-inch and 2-inch	Airtech International Inc. Huntington Beach, CA
Vacuum Bag Film (Nylon, Vac-Pac #8171)	Airtech International Inc. Huntington Beach, CA
Vacuum device (Venturi positive air-to vacuum converter or equivalent)	Commercially available
Vacuum Sealant Tape	Heatcon Composite Systems Seattle, WA
Wipes, lint-free (technicloth, cleanroom)	Fisher Scientific

Table B-1: Composite Doubler Repair Materials and Supplies (sheet 2)

5.0 DAMAGE ASSESSMENT

A. This paragraph covers damage assessment methods.

B. Steps in assessing damage are as follows:

(1) Locate damage.

(2) Evaluate damaged area to determine type, depth, and size (see Table B-2).

(3) Re-assess after damage removal. If necessary, complete an Eddy Current Inspection at the end of any welding process to confirm that there is no cracking in or beyond the repaired area.

(4) Record size of repair for doubler sizing and future reference.

Type of Defect	Inspection Method			
	Visual	Eddy Current	Ultrasonic	X-ray
External Damage	X			
Structural Cracks		X	X	X

Table B-2. Typical Methods for Non-Destructive Inspection of Damage

6.0 INITIAL SURFACE PREPARATION-REMOVAL OF ORGANIC SURFACE FINISH

6.1 Paint Removal

A. The following procedures are for removing paint and other finishes in the area of the repair.

B. Procedure for Removal of Organic Surface Finish

(1) Apply aluminum foil or polyester masking tape around repair area approximately 3 inches beyond the doubler footprint on all sides.

(2) Remove paint and primer:

(a) Use approved paint stripper and rinse with tap water.

(b) Use a plastic scraper or lightly apply fine grit sandpaper to complete removal of paint following the application of paint stripper.

WARNING: PAINT STRIPPER IS AN AGENT THAT IS AN IRRITANT. MAKE SURE ALL PERSONS OBEY ALL OF THE PRECAUTIONS WHEN PAINT STRIPPER IS USED.

- DO NOT USE IN AREAS WHERE THERE IS HIGH HEAT, SPARKS, OR FLAMES.
- USE IN AN AREA OPEN TO THE AIR.
- CLOSE THE CONTAINER WHEN NOT USED.

- DO NOT GET PAINT STRIPPER IN THE EYES, ON THE SKIN, OR ON YOUR CLOTHES.
- DO NOT BREATHE THE GAS.

WARNING: REFER TO THE APPLICABLE MANUFACTURER'S OR SUPPLIER'S MSDS FOR:

- MORE PRECAUTIONARY DATA
- APPROVED SAFETY EQUIPMENT
- EMERGENCY MEDICAL AID

TALK WITH THE LOCAL SAFETY DEPARTMENT OR AUTHORITIES FOR THE PROCEDURES TO DISCARD THIS HAZARDOUS AGENT.

6.2 Basic Surface Cleaning and Preparation

- **Note: Safety goggles, latex/rubber gloves, and proper ventilation (exhaust) system must be used when completing initial solvent wipe and degrease steps in this process. Safety goggles and leather gloves should be used when performing the abrade step. In most cases the volume, quantity, and duration of chemical use are low. Exposures are also intermittent because a given operation is seldom carried out continuously for more than 15-30 minutes at a time. See the appropriate MSDS for hazard information and any safety concerns for specific chemicals in use. Note: If an MSDS for a specific chemical is not available, that chemical should not be used.**

- Before starting degrease process ensure that the proper Personnel Protection Equipment (PPE) including latex/rubber gloves, goggles/safety glasses, and proper ventilation is available.

- Wipe off the masked area of the specimen with one of the following solvents: acetone, or isopropyl alcohol. With a lint-free cloth, wipe in one direction, frequently turning the cloth to a clean surface.

- Abrade the repair area using a 180-grit sanding disk with the air grinder set to the proper pressure (80-90 psi). Note: Depending on the hardness of the surface scale, it may be necessary to use a coarser sanding disk to start the paint/scale removal process. However, always finish with a 180-grit sanding disk. Visually check for any signs of corrosion, nicks, or scratches and carefully blend them out, removing the minimum metal possible.

Degrease using the following: methyl alcohol spray down (rinse) followed by acetone spray down (rinse) and wipe. **Note: Ensure proper PPE is being used for degrease and abrade processes. All excess rinse from this step must be captured and disposed of properly per all the applicable requirements.**

7.0 MECHANICAL SURFACE PREPARATION BY GRIT BLASTING

NOTE: This operation has a 2-person requirement to set-up and perform grit blasting. The person doing the grit blasting may need to complete the appropriate (Respiratory Protection) training. The person doing the grit blasting will be required to wear a respirator helmet during blasting. Personnel participating in this task should have completed all the appropriate training required by company guidelines.

- Review Safety and Health Hazards associated with Abrasive Blast Systems for safety issues and operating requirements. Inquire if personnel performing the operation have current training.

- Ensure all required PPE (steel-toe boots, blast suit, leather gloves, ear plugs, respirator helmet, face shields, dust mask, oxygen monitor, and goggles) is on-site. Inspect each item to make sure it is in good working condition (i.e., no tears or holes in blast suit) for each person participating in the operation.

- Set-up area where actual blasting will take place with proper containment for grit media (tarps, or other barriers). Establish barrier and appropriate signage such that no one enters area of grit blasting unless wearing proper protective gear.

- Set-up equipment for each specific operation by determining the placement of each structure to be repaired relative to the grit blast equipment. Special care should be given to the location of the air pump (away from any possible hazardous fumes and dust from blast area). Also, if using a compressor for the pressurized air source ensure its placement is downwind and to the side of the blast area.

- Test the operation of the air pump with respirator connected for proper air pressure (8-10psi) and flow followed by fit adjustments of respirator for user. To prevent excessive heat build-up in the respirator hose, stretch-out the hose and keep it in shaded areas when possible. **(Shut-off respirator air supply pump when not in use.)** The air pump inlet filter should be checked every 100hrs. of operation (per mfr. suggestion). Replace the outlet filter cartridge at least every 200hrs. of operation. Start and stop times of the air pump should be logged on a data card attached to the air pump.

- Oxygen Monitor Set-up - activate the monitor and let it warm-up and stabilize for 3-5 minutes in a known region of acceptable breathing air. Check the readout. It should be at 20.9%-21%. If in 2-3 minutes the monitor is not at the expected level, then adjust the monitor until it does register the appropriate reading.

- Place the oxygen monitor next to the respirator air pump and check at regular intervals (1-5 mins.) during the use of the respirator to insure an acceptable oxygen level. If the oxygen monitor is below the acceptable limit of 19.5%, alert the person using the respirator immediately and halt the blasting operation.

- Ground the grit blast machine to eliminate the possibility of generating static shocks. This can be done using a standard grounding strap.

- Insert appropriate blast nozzle into blast hose and check for any unusual wear.

- Load abrasive into blast machine by pouring it into the concave head through the screen attachment. **The appropriate PPE for this step include latex gloves, goggles, and dust mask.**

- Direct air at ≤ 30psi from compressed air source through air hose to remove any existing moisture. Connect appropriate air filters (Balston BX & DX) in-line with the air source (to remove water and oil from the air supply). Connect a regulator downstream to insure proper air pressure control.

- See Figure B-6 for location of specific valves on grit blast system.

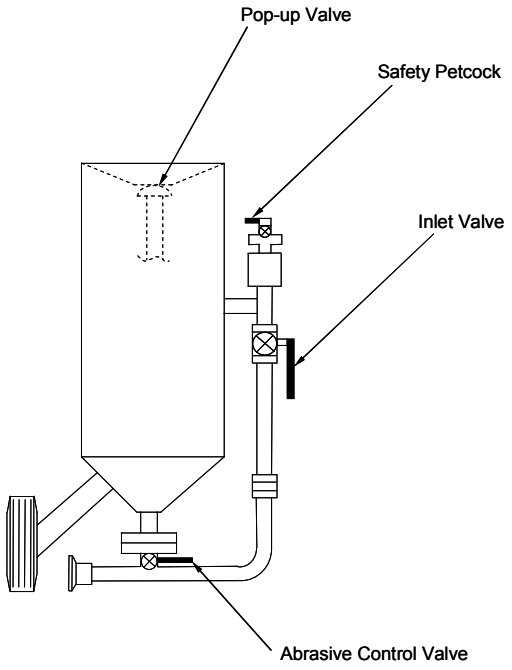

Figure B-6 Grit Blast System with Basic Valve Controls

- Before attaching air hose to blast machine open the safety petcock on the remote control valves, open the inlet valve (handle parallel with pipe) and ensure air pressure from compressor or house air is set to the proper setting and does not exceed the requirements of the blast system (125psi).

- **Always open safety petcock during work breaks and before filling the blast machine with blast media, to prevent unintentional blasting.**

- Ensure that all hoses are properly connected with no air leaks and that all safety cables are connected. (Recommendation: use safety cable when connecting air line to blast machine).

- Adjust air pressure (60-80 psi) at the regulator near the grit blast machine to the appropriate pressure for desired blast results.

- Before starting to blast, establish communication and stop signals between the safety observer and the blaster wearing the respirator helmet. Put on the appropriate protective gear (PPE). The blast operator must wear a blast suit, leather gloves, steel-toed shoes and respirator helmet. Make sure the air pump is on before putting on the respirator helmet. The observer (non-blast operator) also must have on a dust mask, goggles, and latex gloves.

- The start times of the air pump and blast machine should be recorded by the observer.

- Close the inlet valve, to allow the pop-up valve to seal off the filling port. If the pop-up valve does not seal on first attempt try re-opening and closing the inlet valve several times and raising the pressure (≤ 100 psi) if necessary.

- When the pop-up valve seats properly, adjust the abrasive control valve for the proper air/abrasive blend. As a general rule, use as little abrasive as possible. The stream of abrasive coming out of the nozzle should barely discolor the air when seen against a light colored background.

- After the abrasive control valve is properly adjusted and the pressure regulator is set to the proper pressure (60-80 psi), the grit blast process is ready to begin. Note, blasting parameters should be explained to user for consistent surface results. This will include the proper operating pressure, distance nozzle should be from blasting surface (1.50-2.00 inches), setting of abrasive control valve, and proper speed in which to move the nozzle over the surface. The entire surface to be bonded should be scanned at least twice in two perpendicular directions. Once while moving back & forth in the horizontal rows and scan again while moving up & down in vertical rows. Select areas may need to be re-blasted if a visual inspection reveals that the surface finish does not look uniform.

- Note: A certain amount of abrasive surge is normal at start-up. Should the flow of abrasive continue to surge, quickly close and open the inlet valve to stabilize the flow.

- Once blasting is completed open the petcock to reduce the pressure in the system prior to disconnecting the air line. Disconnect the air line from the blast system. Record the stop time on the equipment usage log card attached to the blast machine.

- Collect the spent blast media. All equipment should be cleaned by wiping the excess media from its surfaces. This includes removal of media from any tarps or barriers used to contain the drift of blast media.

Clean-up involves: 1) wiping down adjacent areas covered with the spent blast media, 2) recovering all the spent media by sweeping, and 3) putting spent media into appropriate containers for disposal. Personnel participating in media clean-up must put on appropriate PPE (goggles, latex gloves, and dust mask). If winds cause the spent media to become air borne during cleanup, this work should be completed by personnel wearing the respirator helmet.

- When finished with the respirator system, the safety observer should shut Oxygen Monitor unit off and record the time at the end of the monitoring session.

- Attach the oil and water filters to a compressed air line and use a dusting nozzle to blow any media remaining on the area to be bonded.

8.0 CHEMICAL SURFACE PREPARATION: SILANE TREATMENT METHOD FOR ADHESIVE BONDING

The final surface preparation method is a Silane treatment followed by the primer application.

8.1 Silane Preparation Process

8.1.1 Silane Mixing

- **Note: Safety goggles, latex/rubber gloves, and ventilation (exhaust) system must be used when completing Silane mixing. In most cases the amount of Silane used and the duration of use are low. Exposure times last on average from 1-2 hours during the mixing/application process. See the appropriate MSDS for hazard information and any safety concerns when using Silane. Note: If the current MSDS is not available, then the Silane process should not be started.**

- Mix Silane in a clean glass or polyethylene beaker using a solution of 99 parts (weight or volume) of distilled water and 1 part (+1/-0) of Dow Corning Z6040 Silane (Glycidoxypropyltrimethoxysilane). A 100ml (3.4 oz.) of solution is sufficient to treat a 60 square inch (0.42sq. ft.) area. Approximately 31oz. of Silane mix would be needed to cover a 4 sq. ft. area.

- Place a clean mixing magnet in the beaker. Cover the beaker to avoid contamination and agitate on a magnetic mixer for a minimum of 1-hour prior to use. Continue agitating until the solution is used. Max. solution life is 4 hours after the 1 hour mix.

8.1.2 Silane Application

- When the application area is prepped for Silane treatment, clean a bristle brush with acetone and rinse with distilled water. Use the brush to apply the Silane solution to the repair area for a minimum of 10 minutes after the entire area is wet. **(Note: All excess Silane solution must be captured for proper disposal per all applicable requirements.)**

- While applying the liquid solution, inspect the treated area for water breaks. If a water-break-free surface is not achieved, the process must be restarted at the mechanical surface prep step (grit blast).

- Apply Silane solution to the repair area continuously to maintain a film of solution on the surface throughout the 10-minute time period. Do not allow the surface to dry. **Ensure that the brush does not touch the surrounding uncleaned structure.**

  Note: Complete the following step only if the repair surface does not drain sufficiently on its on accord.

- Connect an air nozzle to approved highly filtered air, and remove the Silane solution from the repair area by starting at the center of the repair area and working outward in all directions. **Do not allow anything to be blown onto the treated area from the surrounding areas and make sure the air pressure is set at ≤ 20 psi before starting.**

8.1.3 Silane Pre-Cure Process

- Place 1-4 thermocouples around the perimeter of the treated area without touching the area to be repaired. The thermocouple ends must be in contact with the surface and taped with high temperature tape. Plug the thermocouples into either a hot bonder or thermocouple reading device.

- Insulate around the repair area (if necessary) to achieve good thermal distribution. Insulation materials must be temperature resistant to at least one and a half times the curing temperature.

- Center infrared lamp(s) or other heating device over the repair area without allowing anything to touch the repair surface. Apply heat to the repair area until all thermocouples are in a range of 120° F to 160° F. Maintain heat for 60 minutes plus 5 minutes, minus 0 minutes, monitoring the thermocouples and adjusting the heat source as necessary. Record temperatures throughout the cure cycle. Prevent cross ventilation to the repair area as much as possible.

It may be necessary to build a temporary screen or curtain from bagging material to prevent wind from crossing the repair site and causing contamination or thermal cooling problems. **If Silane cure temperature exceeds 215°F, the Silane cure process must be started over.**

- The recommended time allowed between Silane drying and application of heat is 30 minutes. This time must not exceed 60 minutes.

- After the 1-hour Silane cure, remove the infrared lamp(s) or other heating devices. Allow the repair area to cool to 100°F or ambient whichever is higher.

- The surface is now ready for primer application.

8.2 Application of Bond Primer (Post Silane)

The application of the primer requires the following safety precautions. The proper PPE must be used when spraying the primer. This includes; latex/rubber gloves, lab coat, a full-face air-purifying respirator (combo cartridge for both vapors & particulate) and, if operating indoors, local exhaust ventilation (e.g., laboratory hood, canopy hood) must be located in the area of the application and operated when applying this primer (Cytec-Fiberite BR6747-1). The user of the respirator must complete the proper training prior to this operation and be approved to use the respirator. The lab room or spray area (20 ft. radius) must be vacated with the exception of the personnel wearing the respirators. See the appropriate MSDS for additional hazard information and any safety concerns when using this primer.
Note: If MSDS is not available, then the primer process should not be started.

Apply Cytec-Fiberite BR 6747-1 adhesive primer onto the bond surface to obtain a cured film thickness of 0.0001 to 0.0004 inch (0.1 to 0.4 mil). Method of application should be with an atomizing sprayer.

8.2.1 Removal of Moisture from Primer

A. Use infrared lamps to drive off water. Apply heat @ 120° - 150° F for 15-20 minutes. Allow structure to cool to less than 100° F.

9.0 FABRICATE WITNESS COUPONS (Peel-Proof Strips)

Witness Coupons for Wedge Tests –For this quality assurance test, two steel strips are bonded to the parent structure immediately adjacent to the doubler. Preparation of the steel strips takes several hours and must be completed before the installation of the doubler is to take place.

As part of the preparation for this process, remove the appropriate primer (BR6747-1) from the refrigerator a half hour prior to the application and mix it well ensuring there is no sediment left in bottom of container. After installation, a plastic or phenolic wedge is used to pry the strips off the structure as shown in Figure B-7. If adhesive is found on both the steel strip and the steel structure, this indicates that the adhesive fractured (cohesive failure) rather than disbonded (adhesive failure). Thus, the surface preparation is good and the full adhesive strength has been achieved. Figure B-8 depicts this surface preparation QA test and the two potential failure modes.

A. Prepare the surface of a 0.060" to 0.070" thick steel sheet with the same surface prep being used on the steel structure. Starting by making a water-break-free surface on the sheet. Next, complete the Silane surface preparation per section 8.0. This includes the application of the appropriate primer.

B. Once completed with surface prep and treatment (Silane), the sheet is ready to be primed using the appropriate primer.

C. Cut the steel sheet into 1" x 4" strips taking precautions to not contaminate the prepped surface. A minimum of two witness coupons are needed for each repair area.

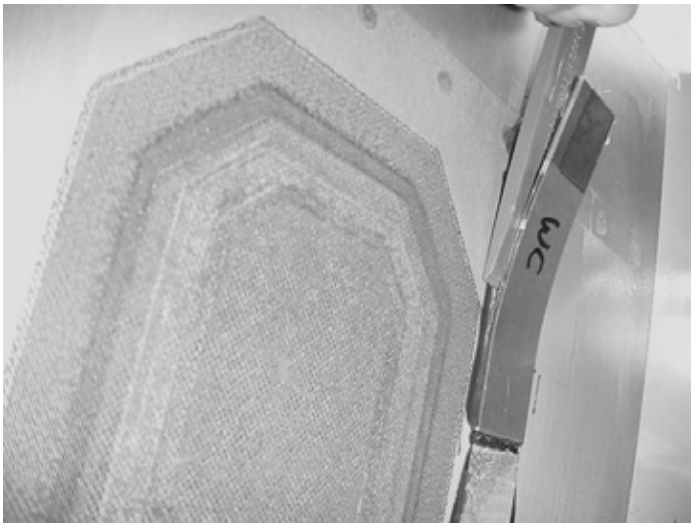

Figure B-7. Plastic Wedge being used to Pry Off Witness Coupon

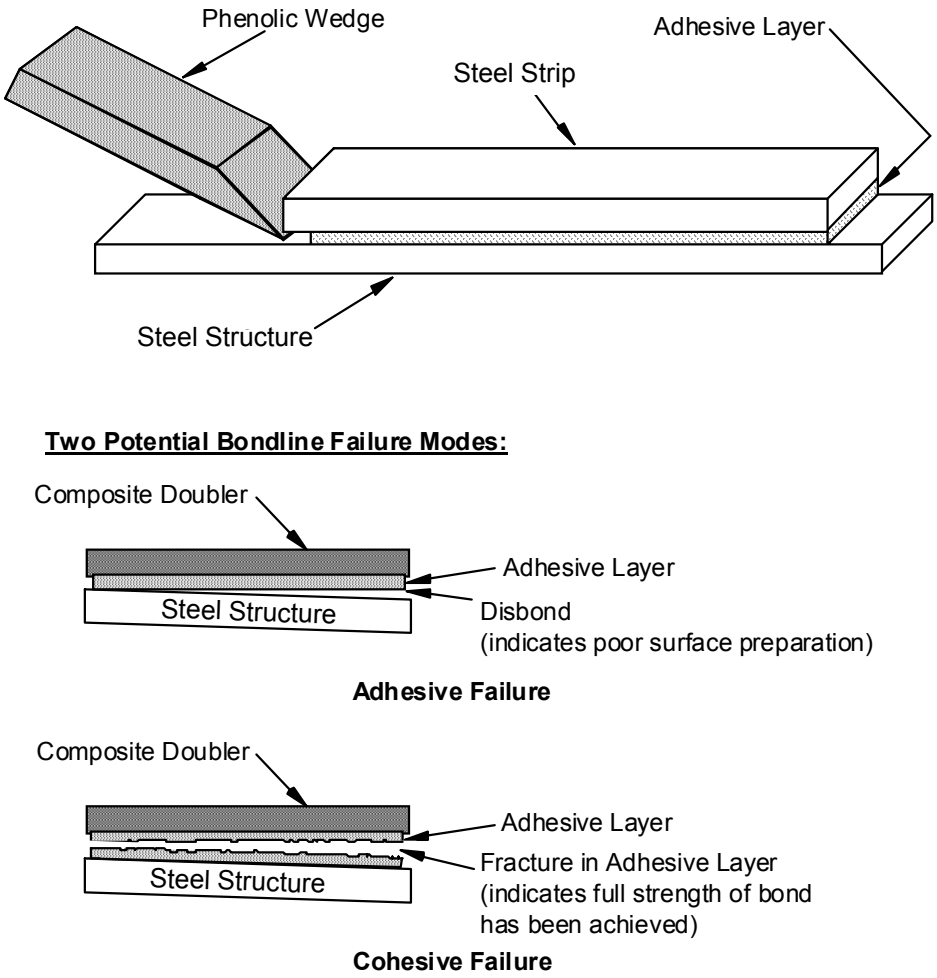

Figure B-8 Use of Witness Coupons in Quality Assurance Wedge Test for Surface Preparation

D. Take witness coupons and wrap a 1" wide piece of flash breaker tape around one end of the coupon ensuring that tape is flush with the end. A 1" x 1" area is now covered with tape as shown in Figure B-9.

E. With the adhesive removed from the freezer cut 1" x 3" strips of the adhesive and apply them to the end of the coupons without the tape as shown in Figure B-9. Once this step is completed and adhesive is stuck to each witness coupon, place them into a clean protective bag and put into the freezer until needed during doubler application.

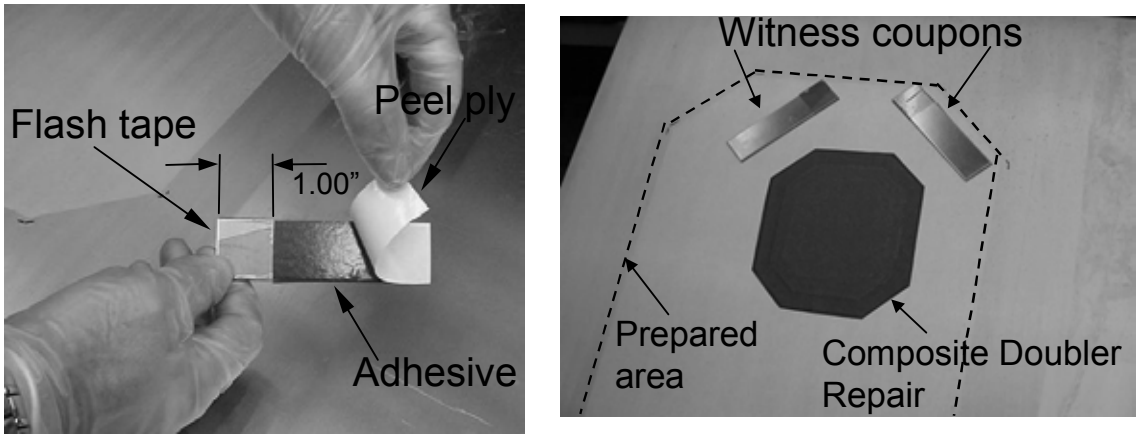

Figure B-9 Application of Adhesive Strips to Witness Coupons and Placement of Coupons Next to Doubler During Cure Process

10.0 BORON/EPOXY DOUBLER REPAIR

10.1 Preparation of Boron/epoxy Doublers

To make optimum use of time, doublers may be assembled prior to or in parallel with the surface preparation operations.

A. Remove the pre-impregnated Boron/epoxy tape from the freezer. Allow the prepreg to thaw at room temperature, not to exceed 100°F, until all condensation has evaporated from the exterior of the bag.

CAUTION: Do not unseal the bag until condensation has completely evaporated.

B. Freezer out-times shall be recorded for all time-and-temperature sensitive material and noted on the roll condition log.

Note: Boron/epoxy manufacturer guarantees 10.5 days out-time at 70°F. Material out time is reduced above 80°F.

C. Boron/epoxy tape shall be cut in an area free from contaminates. Clean, non-contaminating gloves shall be worn during all cutting and handling operations. Uncured tape shall be protected from contamination prior to cure.

D. Boron fibers will dull cutting blades quickly. Ensure that fresh sharp blades are used for all cuts on Boron/epoxy tape. A shearing (paper) cutter, rolling knife blade, or scissors will provide longer cutter life.

E. Boron/epoxy plies shall be cut to the dimensions and fiber orientations of the applicable doubler drawing. Mylar templates can be used to aid the cutting & fiber orientation process.

F. Cut plies shall be layed-up in the drawing stacking order. When possible, layup the doubler in a controlled contamination area then transport the doubler to the repair area.

G. Manually sweep each ply down using a non-contaminating polyethylene sweep or hand roller (see Fig. B-10). Vacuum debulk the layup every 4-6 plies at a minimum (see Figure B-10).

H. Tape material that has gaps between tows greater than 0.03" shall not be used in the fabrication of doublers.

I. Plies shall be applied with the backing paper side facing up. The backing paper shall be carefully removed after the ply has been pressed in place. Note: the first ply is the only ply to be placed with the backing paper down. This backing paper should be left in place for the duration of the doubler lay-up process. Continue until all boron epoxy plies & the fiberglass cover ply have been placed and debulked. The fiberglass cover ply should be larger than the Boron/epoxy doubler footprint by 0.5 inches in all directions.

J. Place assembled doublers into clean protective sealed bags. Place sealed doublers in refrigerated storage unless they will be cured in the next 24 hours.

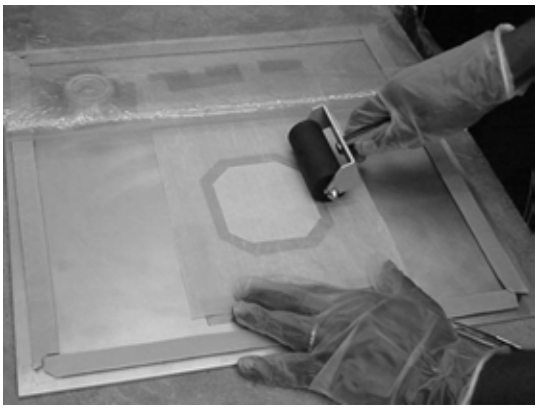

Sweeping down each ply of doubler during lay-up

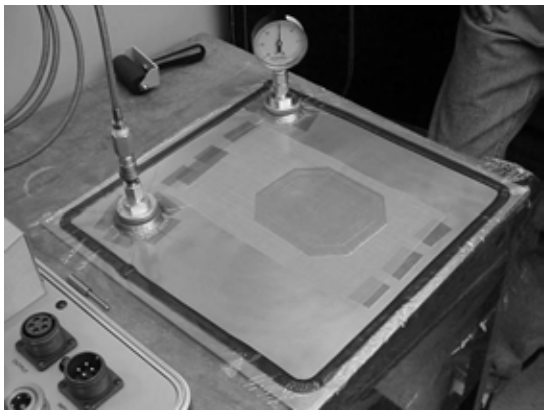

Vaccum debulk of doubler every 4 plies minimum

Figure B-10. Manual Sweep of Each Ply and Vacuum Debulk of Doubler Lay-Up

10.2 Preparation of Film Adhesive

A. Remove film adhesive from the freezer. Allow the adhesive to thaw at room temperature, not to exceed 100°F, until all condensation has evaporated from the exterior of the sealed bag.

Note: Do not unseal the bag until condensation has completely evaporated.

B. Freezer out-times shall be recorded for all time-and-temperature sensitive material and noted on the roll condition log.

Note: Film adhesives have 10 days out-time at 70°F. Material out-time is reduced above 90°F.

C. Film adhesive shall be cut in an area free from contaminates. Clean, non-contaminating gloves shall be worn during all cutting and handling operations. The film adhesive may be pre-kitted in sealed bags alone or with Boron/epoxy material. Return kits to cold storage prior to use and draw as necessary.

D. Cut film adhesive for each bond faying surface. The film adhesive should be placed on the bottom of the doubler and trimmed such that it is larger than the fiberglass cover ply by at least 0.125 inches in all directions. Do not fold or stretch the adhesive film. One or more additional plies of adhesive may be needed in areas with surface irregularities. Small sections of added adhesive should be used to fill local voids and undulations in the surface to provide an even surface for uniform doubler contact/bonding.

10.3 Doubler Installation

The operations of this section apply to the installation of patches to the repair area and the subsequent cure operations. Apply the adhesive and composite doubler to the Silane treated and primed surface using the process described below. Avoid relative movement of the parts being bonded during assembly. Co-cure the adhesive, composite doubler, according to the temperature profiles described below.

10.3.1 Co-Cured Doublers

A. If not already available, remove the film adhesive and doublers from the freezer. Allow the adhesive and doublers to thaw at room temperature, not to exceed 100°F, until all condensation has evaporated from the exterior of the sealed bag.

B. Lightly mark the outline of the repair surface with a non-contaminating marker. Place doubler centerline indicators outside the perimeter of the surface prepped area.

These centerline marks, in both x and y directions, will be used to properly locate the doubler, heat blankets, and insulation materials.

C. Apply film adhesive to the bottom bond surface of the Boron/epoxy doubler. Remove any backing paper from the bottom of the doubler before applying adhesive.

D. Apply the Boron/epoxy doubler & adhesive film to the repair surface in the stack-up and orientation indicated on the engineering drawing. Assure that the film adhesive extends beyond the edge of the cover ply by .125 inches all-around.

10.3.2 Preparation for Cure

A. Apply flash breaker tape around the edge of external details to allow adhesive squeeze-out (flash) to run out onto the tape and aid in post-cure cleanup.

B. When specified by the responsible engineer, a witness coupon shall be fabricated and cured concurrent to the repair doubler as shown in Figure B-9. The witness coupon shall be an adhesive bonded steel lap shear panel per Figure B-9. The lap shear blank surfaces shall be prepared for bonding concurrently with the Silane treatment and priming operations.

C. Bag the doubler laminate in accordance with Figure B-11. Note that one ply of bleeder cloth should be used for each 3-4 plies of Boron/epoxy material in the doubler.

D. Apply vacuum pressure of 17" ± 2"Hg to the bag. Remove the vacuum source and verify that the bag vacuum pressure loss is less than 1"Hg over a 1 minute period. If the leak rate is greater than this find the vacuum leak and repeat this step. If it can be identified that the leak is outside the patch area and the leak path will not be across the patch then the leak is acceptable as long as the proper pressure can be maintained.

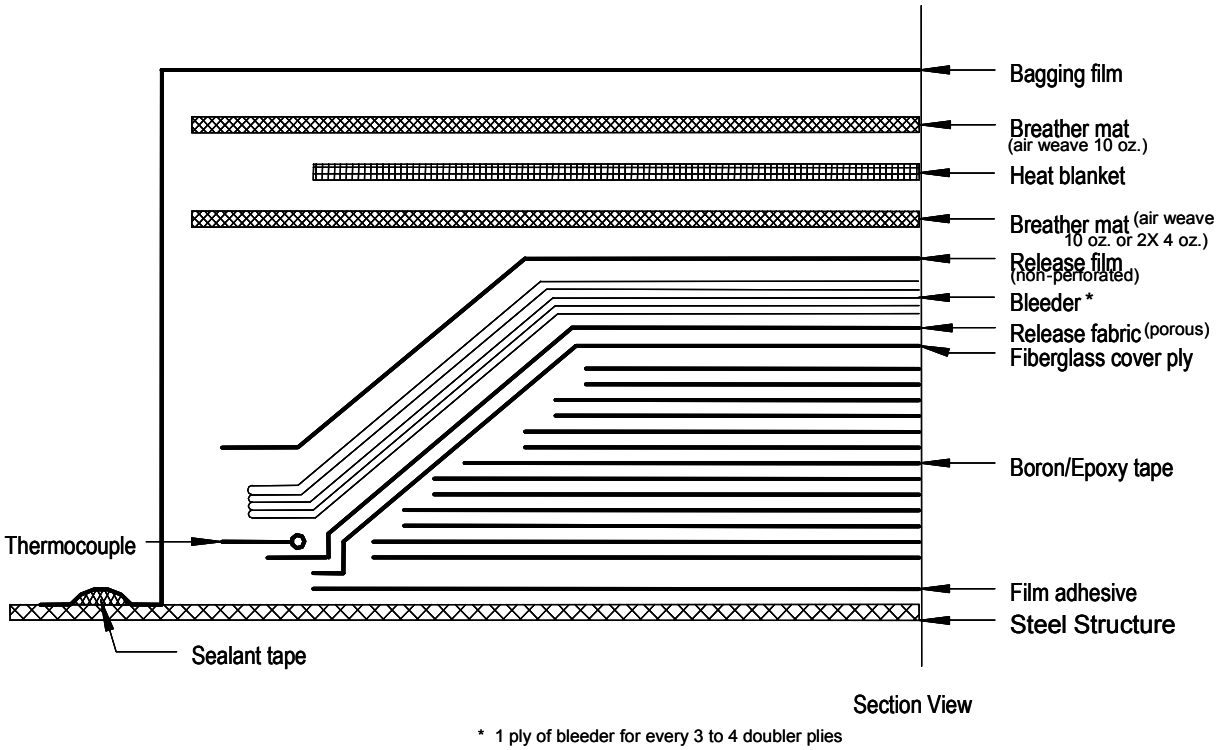

Figure B-11. Vacuum Bagging for Cure of Doubler on Steel Structure

10.3.3 Process for Doubler Cure to Steel Structure

A. Autoclave cure cycles shall be performed in accordance with Figure B-12.

B. When using portable heating equipment for cures, a temperature survey on the repair surface may be desirable. Additional insulation, controller programming changes, additional heaters, and/or other measures may be required to maintain adequate temperature control on some surfaces. At least four thermocouples should be used to monitor and control the temperature in the repair region.

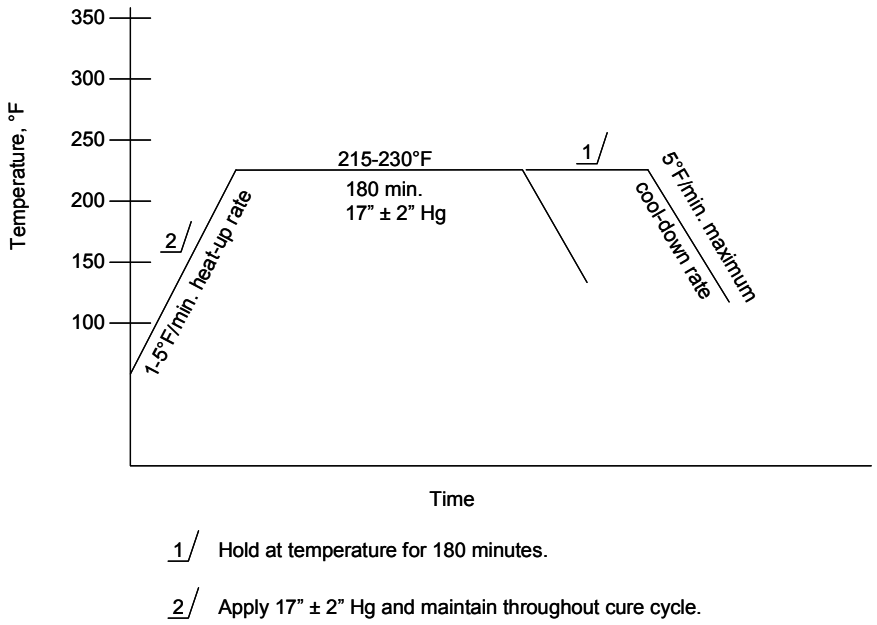

Figure B-12. Cure Cycle for Doubler Installation on Steel Structure

C. Cure cycles achieved with portable heating equipment shall use the following parameters:

(1) Apply 17" ±2"Hg vacuum pressure to the bag.

(2) Ramp from ambient to cure temperature at 1-5°F/minute heat-up rate.

(3) Hold at cure temperature per Table B-3.

CURE TEMPERATURE (°F)	CURE TIME (Min.)
240-255	90+30/-0
215-230	180+30/-0
190-205	360+30/-0

Table B-3. Times at Cure Temperature for Doubler Installation on Steel Structure

(4) Ramp down at 5°F/minute maximum from cure temperature to less than 140°F under full pressure.

D. Remove bagging material from doublers (see finished product shown in Figures B-13 & B-14).

E. Fillet seal periphery of doubler using MIL-S-81733 or equivalent sealant for environmental protection.

F. Prime the steel repair surface, then paint the repair area and the Boron/epoxy doubler using approved paint material.

G. Stencil the following note, in a contrasting color, and locate the note on the Boron/epoxy doubler: "Bonded Repair, Do Not Apply Paint Strippers in This Area".

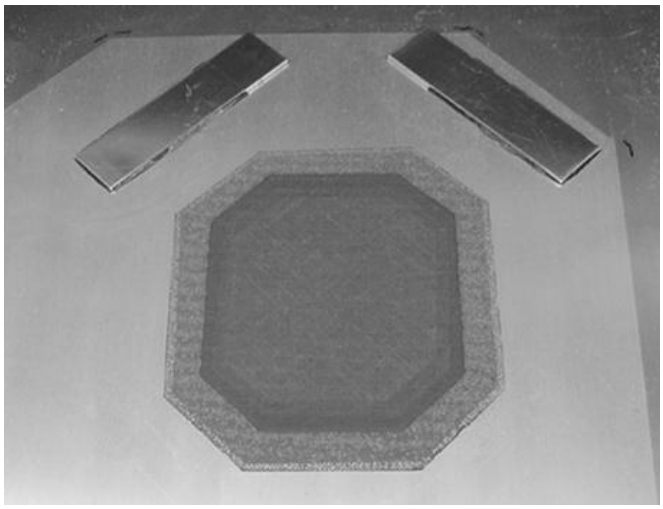

Figure B-13 Sample Composite Doubler Repair with Witness Coupons

Figure B-14 Finished Product – Composite Doubler Repair Installed on Metal Aircraft Structure

11.0 POST-REPAIR INSPECTION

A. Remove witness coupons using a wedge as shown in Figure B-6. If adhesive can be seen on the steel structure and the coupon surface then a cohesive fracture has occurred. This indicates a good surface preparation where the full strength of the adhesive can be achieved.

B. Visually inspect periphery of doubler to ensure that a bead of cured adhesive is evident. An area lacking the bead may indicate a void area. Conduct this inspection before item E in section 10.3.3.

C. Inspect installation using the ultrasonic inspection technique for composite doublers.

D. Disbonds and delaminations in the taper region shall not exceed 0.5 inches in diameter. A maximum of 5% of the central area of the doubler may have delaminations or voids. The central area is defined as the region of the Boron/epoxy doubler that is full thickness. The total number of disbonds and delaminations shall not exceed 2 in any doubler and shall be separated by 3 inches minimum.

E. Flaws found should be reported to engineering for disposition. If repair is defective, remove and repeat repair process.

F. Inspect Boron/epoxy doubler repair at the 6-month and 1-year intervals and thereafter during routine maintenance/inspections of the structure being repaired.

APPENDIX C

Design and Analysis Guidelines for Composite Doubler Repairs

Design and Analysis Guidelines for Composite Doubler Repairs

The guidelines contained in Appendix C are applicable to repairs applied to one side of a defective structural member. The guidelines apply to repair of: 1) cracks in metallic structure, and 2) metallic structure in which damage has been removed. The nomenclature used here is defined at the end of the Appendix.

The steps required for repair design are:

- Calculate the required patch thickness.
- Assess the component criticality and significance of the repair.
- Determine the structural loads appropriate for the design.
- Evaluate the design condition of the repair on the basis of the load capacity of the bond.
- Check the structural integrity of the repaired structure.
- Check the repair and structure for fatigue susceptibility.
- Calculate the required patch dimensions.
- Determine inspection requirements.

CALCULATE THE REQUIRED PATCH THICKNESS

Patch thickness shall restore the original stiffness over the defect. Although a thickness is preferred which provided a stiffness match with the parent structure, a higher stiffness up to 20% above the parent structure stiffness is acceptable. The patch thickness required for a repair is therefore determined from:

$$\frac{E_i t_i}{E_o} \le t_o \le \frac{1.2 E_i t_i}{E_o} \qquad \text{(C-1)}$$

The variables are as shown in Fig. C-1.

DETERMINE THE STRUCTURAL LOADS

The applied load is used to determine the Design Condition for the repair and to verify structural integrity and fatigue resistance. The remote load away from the defect is taken as DUL as determined from:

a. If Design Ultimate Load (DUL) is known, that load shall be used.
b. If Design Limit Load (DLL) is known, the load is taken as 1.5 times the load associated with DLL.
c. Where DUL and/or DLL are not known, design shall be based on the lower value of the load based on a reasoned engineering assessment taking into account issues such as

changes in section in the load path, stress concentrations, net section stresses, fastener bearing strength or buckling load limitations.

EVALUATE THE DESIGN CONDITION OF THE BOND

The level of rigor required to develop repair designs is based on a comparison of the load capacity of the repair adhesive with the design loads, and the significance of the structure being repaired.

Calculate the Potential Load Capacity of a Single Overlap Joint Allowing for Thermal Stresses

The load capacity is given by the lesser value of:

$$P = E_i t_i \left[\left(\alpha_o - \alpha_{i_{eff}} \right) \left(RT - T_{cure} \right) + \left(\alpha_o - \alpha_i \right) \left(T_{oper} - RT \right) \right] + \sqrt{2\eta\tau_p \left(\frac{1}{2}\gamma_e + \gamma_p \right) E_i t_i \left(1 + \frac{E_i t_i}{E_o t_o} \right)} \tag{C-2}$$

and,

$$P = 2E_o t_o \left[\left(\alpha_{i\,eff} - \alpha_o \right) \left(RT - T_{cure} \right) + \left(\alpha_i - \alpha_o \right) \left(T_{oper} - RT \right) \right] + \sqrt{2\eta\tau_p \left(\frac{1}{2}\gamma_e + \gamma_p \right) E_o t_o \left(1 + \frac{E_o t_o}{E_i t_i} \right)} \tag{C-3}$$

where

$$\alpha_{i_{eff}} = \frac{\alpha_i \left(1 + \nu_i \right)}{2} \tag{C-4}$$

Note: adhesive data may be interpolated between known data points.

EVALUATE STRUCTURAL INTEGRITY OF REPAIRED STRUCTURE

A. Determine the Far-Field Stress Associated with DUL

The far-field stress for analysis of the repair is determined from DUL and the thickness of the structure at the defect:

$$\sigma^* = \frac{DUL}{t_i} \tag{C-5}$$

B. Check the Structural Integrity of the Structure at the End of the Patch

The maximum stress in the structure at the end of the patch is estimated from:

$$\sigma^{**} = \Omega_L \sigma^* + \left[E_i \left(\left(\alpha_o - \alpha_{i_{eff}} \right) \left(RT - T_{cure} \right) + \left(\alpha_o - \alpha_i \right) \left(T_{oper} - RT \right) \right) \right] \qquad \text{(C-6)}$$

where Ω_L is the load inclusion factor (see Table C-1) to allow for load attraction into the repair area due to the stiffness added by the patch. A Margin of Safety of 0.2 is recommended where:

$$MOS = \frac{\sigma_{ULT_i}}{\sigma^{**}} - 1 \qquad \text{(C-7)}$$

C. Calculate the Stress Under the Repair

Calculate the localized stress under the repair away from the defect:

$$\sigma_o = \frac{E_i t_i}{\left(E_o t_o + E_i t_i \right)} \sigma^{**} \qquad \text{(C-8)}$$

D. Check the Adhesive Shear Strain

The maximum shear strain in the adhesive (adjacent to the defect) is given by:

$$\gamma_o = \frac{\sigma_o t_i \lambda}{G} \qquad \text{(C-9)}$$

where

$$\lambda^2 = \frac{G}{\eta} \left(\frac{1}{E_i t_i} + \frac{1}{E_o t_o} \right) \qquad \text{(C-10)}$$

If the maximum strain value exceeds the elastic strain limit for the adhesive, the adhesive will be plastic near the defect, and the shear strain is given by:

$$\gamma_o = \frac{\tau_p}{2G} \left(1 + \left(\frac{\sigma_o t_i \lambda}{\tau_p} \right)^2 \right) \qquad \text{(C-11)}$$

E. Calculate the Stress Intensity in a Repaired Metallic Structure

The following step is applicable to repair of cracks in metallic structures using single overlap repairs. The stress intensity for a repaired crack shall be calculated and compared with the fracture toughness of the material. The stress intensity of repaired cracks approaches an

asymptote, a value of stress intensity which the repaired crack never exceeds. The asymptotic stress intensity after repair is given by:

$$K_\infty = \sigma_o \sqrt{\frac{E_i t_i \lambda \eta}{G}} \tag{C-12}$$

for elastic behavior in the adhesive, or

$$K_\infty = \sqrt{\frac{E_i \eta}{G}\left[\sigma_o \tau_p \left(1 + \left(\frac{\sigma_o \lambda t_i}{\tau_p}\right)^2\right) - \frac{\tau_p^2}{3\lambda t_i}\left(1 + 2\left(\frac{\sigma_o \lambda t_i}{\tau_p}\right)^3\right)\right]} \tag{C-13}$$

for plastic behavior in the adhesive.

F. Calculate the Peel Stresses

Peel stresses in adhesive bonds are induced by load path eccentricity. Analytically, peel stresses are determined from vertical equilibrium of shear forces and moments due to load path eccentricity. The maximum peel stress in the adhesive (and the adherend) is given by:

$$\sigma_{c_{\max}} = \tau_p \left(\frac{3E_c' t_o \left(1-\nu^2\right)}{E_o \eta}\right)^{\frac{1}{4}} \tag{C-14}$$

where $\boldsymbol{\tau_p}$ is the shear stress at the end of the adhesive. $\mathbf{E_c'}$ is the effective transverse tensile modulus of the adhesive system. For adherends with the same interlaminar stiffness, the effective transverse stiffness shall be approximated by:

$$\frac{1}{E_c'} = \frac{1}{E_c} + \frac{6}{E_N} \tag{C-15}$$

where $\mathbf{E_N}$ is the tensile elastic modulus of the adherend in the Normal direction and $\mathbf{E_c}$ is the tensile elastic modulus of the adhesive. (The adhesive behavior is influenced by the tensile behavior of the adherends perpendicular to the joint, and in-plane restraint of Poisson's contractions.)

Tapering of patch ends reduces the outer adherend thickness thereby reducing peel stresses. The reduction in peel stresses can be estimated from:

$$\frac{\left(\sigma_{c\max}\right)_{tapered}}{\left(\sigma_{c\max}\right)_{uniform}} = \sqrt{\frac{2}{1+\left(\frac{t_o}{t_e}\right)^3}} \tag{C-16}$$

where $\mathbf{t_e}$ is the thickness at the end of the taper.

To verify the peel resistance of a repair:

1. Compare the peel stresses with the tensile strength of the adhesive, and the through-thickness strength of the adherends. Currently, insufficient reliable data is available for peel strengths for most adhesives. Therefore, the following guidelines are to be applied:
    - For ductile adhesive systems (FM 73, AF 163, FM 300, and FM 300-2): Maximum allowable peel stress is 10,000 psi.

    - For brittle adhesive systems (AF130-1, AF 131): Maximum allowable peel stress is 6,000 psi.

2. In composite materials, peel stresses may result in delamination of the material. Currently, insufficient reliable data is available for through-thickness tensile strengths for most composite resin systems. Therefore, the following guidelines are to be applied:
    - If the **through-thickness tensile strength** is known, the recommended Margin of Safety is 0.2 above the known value.

    - If the **transverse tensile strength** is known, the recommended Margin of Safety is 0.2 above the known value. For all other repairs to composite materials, or for composite patches, the maximum allowable peel stress is 6,000 psi

G. Check the Structural Integrity of the Patch

The maximum stress in the patch is estimated from:

$$\sigma_p = \frac{t_i}{t_o}\sigma^{**} \qquad \text{(C-17)}$$

A Margin of Safety of 0.2 is recommended where:

$$MOS = \frac{\sigma_{ULT_o}}{\sigma_p} - 1 \qquad \text{(C-18)}$$

CHECK THE REPAIR AND STRUCTURE FOR FATIGUE SUSCEPTIBILITY

This method does provide a simple method for elimination of fatigue critical repairs.

A. Calculate the Fatigue Stress

For metallic structures, all repairs are to be designed such that the repair is fatigue resistant if subjected to a constant amplitude fatigue loading (with an assumed fatigue ratio $\mathbf{R} = 0$) with a maximum cyclic load equivalent to the lower value of 40% of $\boldsymbol{\sigma}^*$ used in the assessment of structural integrity.

$$\boldsymbol{\sigma}_\mathbf{f} = 0.4\boldsymbol{\sigma}^* \tag{C-19}$$

B. Check the Fatigue Susceptibility of the Structure at the End of the Patch

The maximum stress in the structure at the end of the patch is estimated from:

$$\sigma^{\#\#} = \Omega_L \sigma_f + \left[\mathrm{E}_i \left(\left(\alpha_o - \alpha_{i_{eff}}\right)\left(RT - T_{cure}\right) + \left(\alpha_o - \alpha_i\right)\left(T_{oper} - RT\right)\right)\right] \tag{C-20}$$

From reference data for the structural material, determine if fatigue damage is anticipated at that stress level.

C. Calculate the Fatigue Stress Under the Patch

Calculate the localized stress under the repair away from the defect:

$$\sigma^{\#} = \frac{E_i t_i}{\left(E_o t_o + E_i t_i\right)} \sigma^{\#\#} \tag{C-21}$$

D. Calculate the Fatigue Shear Strain in the Adhesive at the Defect

Adhesives are fatigue resistant, and when properly designed and implemented, bonded repairs are not susceptible to fatigue. The maximum shear strain in the adhesive (adjacent to the defect) is given by:

$$\gamma_f = \frac{\sigma^{\#} t_i \lambda}{G} \tag{C-22}$$

where $\boldsymbol{\lambda}^2 = \dfrac{\mathbf{G}}{\boldsymbol{\eta}}\left(\dfrac{1}{\mathbf{E_i t_i}} + \dfrac{1}{\mathbf{E_o t_o}}\right)$

If the maximum strain value exceeds the elastic strain limit for the adhesive, the adhesive will be plastic near the defect, and the shear strain is given by:

$$\gamma_f = \frac{\tau_p}{2G}\left(1+\left(\frac{\sigma^{\#} t_i \lambda}{\tau_p}\right)^2\right) \tag{C-23}$$

The adhesive in the repair is considered fatigue resistant if the maximum shear strain is below twice the elastic shear strain limit.

$$\gamma_f < 2 \times \gamma_e \tag{C-24}$$

E. Calculate the Fatigue Stress Intensity in a Repaired Metallic Structure

The stress intensity of repaired cracks approaches an asymptote, a value of stress intensity which the repaired crack never exceeds. The asymptotic stress intensity after repair is given by:

$$K_{\infty f} = \sigma^{\#}\sqrt{\frac{E_i t_i \lambda \eta}{G}} \tag{C-25}$$

for elastic behavior in the adhesive, or

$$K_{\infty f} = \sqrt{\frac{E_i \eta}{G}\left[\sigma^{\#}\tau_p\left(1+\left(\frac{\sigma^{\#}\lambda t_i}{\tau_p}\right)^2\right) - \frac{\tau_p^2}{3\lambda t_i}\left(1+2\left(\frac{\sigma^{\#}\lambda t_i}{\tau_p}\right)^3\right)\right]} \tag{C-26}$$

for plastic behavior in the adhesive.

From reference data for da/dN variation with stress intensity range, the crack growth rate shall be predicted, from which the repair effectiveness may be determined. Alternatively, if fractographic analysis or recorded NDI result has determined growth rates with structure usage hours, an estimate of the stress intensity range reduction shall enable an estimate of inspection intervals from the past crack growth history.

CALCULATE THE REQUIRED PATCH DIMENSIONS

A. Determine the Required Overlap Length

The ***overlap*** length, ***L*** is the minimum distance from the edge of the repair patch to the crack or cut-out. The minimum overlap length is to be sufficient to ensure that the adhesive is never the critical element. To achieve this, the minimum overlap **L** is to be 1.5 times the plastic transfer length necessary to carry the stress:

$$L = \frac{1.5\sigma^* t_i}{\tau_p} \qquad \text{(C-27)}$$

for a single overlap repair.

B. Determine the Overall Patch Length

The minimum overall patch length is twice the overlap length plus the size of the defect. The patch may be longer than this, but in all cases the overlap distance *L* from the edge of the patch to the defect should be observed.

C. Determine the Patch Width

The patch width is usually determined by consideration of patch shape requirements and the required patch overlap length. For repairs to cracked metallic structure, the minimum patch width is such that the patch covers as much of the crack as possible and the patch shall extend at least 1.0 in. ahead of the crack tip at both ends. The sides of the patch shall be aligned with the major load direction.

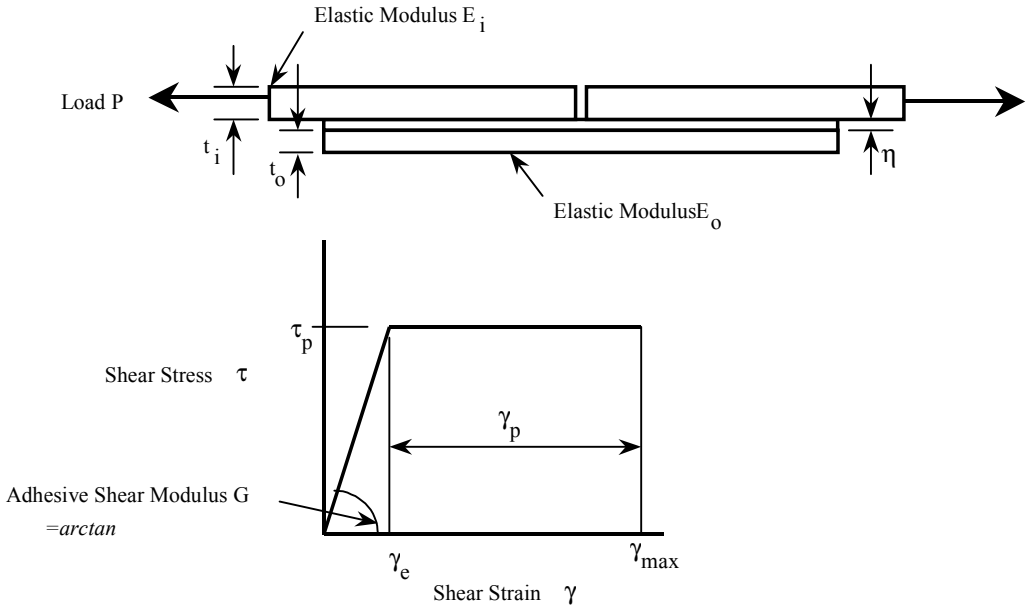

Figure C-1: Single Supported Overlap Joint Geometric and Material Parameters

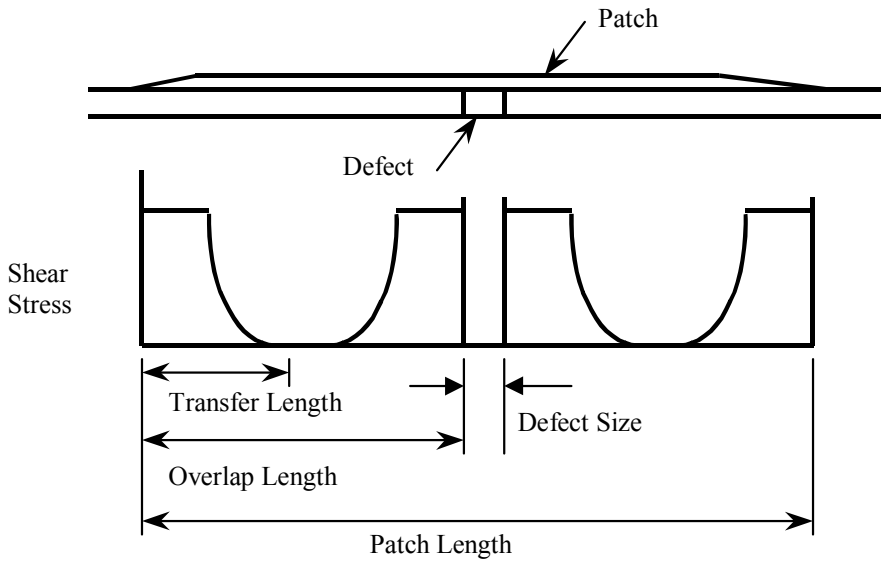

Figure C-2: Relationship Between Transfer Length, Overlap Length and Patch Length

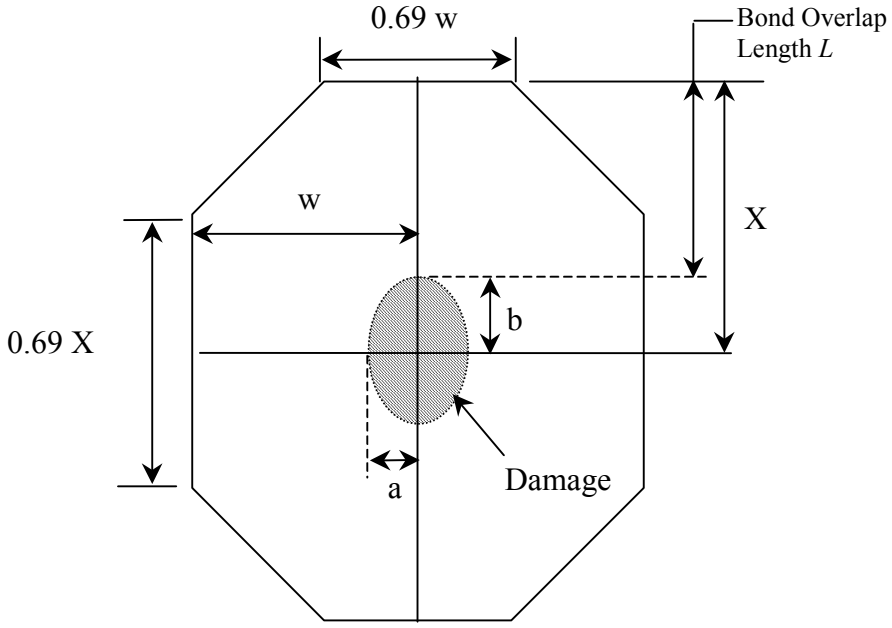

$w \geq a + 25mm$ for cracks OR

$w \geq L + a$ for other damage

$X = L + b$

$X/w \leq 1.0$

Figure C-3: Dimensions of Patches for Optimal Reduction in Load Attraction

$L/w \rightarrow$ $\frac{E_o t_o}{E_i t_i} \downarrow$	1	1.5	3	4
1	**1.18**	**1.20**	**1.22**	**1.23**
1.2	**1.20**	**1.22**	**1.25**	**1.26**
1.4	**1.22**	**1.24**	**1.27**	**1.28**
1.6	**1.24**	**1.27**	**1.29**	**1.30**

Table C-1: Load Inclusion Factor Ω_L for Various Patch Aspect Ratios and Relative Stiffnesses

Material Property	Boron/Epoxy 5521/4
Longitudinal Tension Strength $\mathbf{F_{1T}}$ MPa (ksi)	1520 (220)
Longitudinal Modulus $\mathbf{E_1}$ GPa (Msi)	210 (30)
Ultimate Longitudinal Strain[1] $\boldsymbol{\varepsilon_{1T}}$	0.00733
Longitudinal Compression Strength $\mathbf{F_{1C}}$ MPa (ksi)	2930 (425)
Transverse Tensile Strength F_{2C} Mpa - see Note 1 (ksi)	48.3 (7)
Transverse Modulus[1] $\mathbf{E_2}$ GPa (Msi)	19 (2.7)
In-Plane Shear Strength $\mathbf{F_{12}}$ MPa (ksi)	103 (15)
In-Plane Shear Modulus[1] **G** GPa (Msi)	6.89 (1.0)
Major Poisson's Ratio[1] $\boldsymbol{\nu_{LT}}$	0.21
Minor Poisson's Ratio[1] $\boldsymbol{\nu_{TL}}$	0.04
Thickness per ply $\mathbf{t_{ply}}$, mm. (in.)	0.13 (0.0052)
Longitudinal Thermal Expansion Coefficient $\boldsymbol{\alpha_1}$ x $10^{-6}°C^{-1}$ (x $10^{-6}°F^{-1}$)	4.5 (2.5)
Transverse Thermal Expansion Coefficient[1] $\boldsymbol{\alpha_2}$ x $10^{-6}°C^{-1}$ (x $10^{-6}°F^{-1}$)	29.5 (16.38)

Table C-2: Design Data for Boron/Epoxy 5521/4 Pre-Preg Tape

APPENDIX C NOMENCLATURE

SYMBOL	DESCRIPTION
E_c	Elastic Modulus of Adhesive for the Purposes of Peel Stress Calculation
E_c'	Effective Elastic Modulus of Adhesive for Peel Stress Calculation
E_i	Elastic Modulus Inner Adherend (Structure)
E_o	Elastic Modulus Outer Adherend (Patch)
E_1	Longitudinal Modulus of a Composite Lamina
E_2	Transverse Modulus of a Composite Lamina
F_{1T}	Longitudinal Tensile Strength of a Composite Lamina
F_{1C}	Longitudinal Compression Strength of a Composite Lamina
F_{12}	In-Plane Shear Strength of a Composite Lamina
F_{2T}	Transverse Tensile Strength of a Composite lamina
G	Shear Modulus
$\mathbf{K}_{\infty}$	Stress Intensity Under a Repair for a Repaired Crack at Design Load Case
$\mathbf{K}_{\infty \mathbf{f}}$	Stress Intensity Under a Repair for a Repaired Crack at Fatigue Load Case
DUL	Design Ultimate Load
DLL	Design Limit Load
ULT	Ultimate Strength of Inner Adherend (Structure)
t_i	Thickness Inner Adherend (Structure)
t_o	Thickness Outer Adherend (Patch)
t_{ply}	Thickness of a Composite Lamina
α_i	Thermal expansion coefficient inner adherend (Structure)
α_o	Thermal expansion coefficient outer adherend (Patch)

SYMBOL	DESCRIPTION (continued)
$\alpha_{i_{eff}}$	Effective Thermal expansion coefficient inner adherend (Structure)
ε_{1T}	Ultimate Longitudinal Strain for a Composite Lamina
τ_p	Adhesive plastic shear stress
G	Adhesive shear modulus
η	Adhesive thickness
$\boldsymbol{\nu}_{\mathbf{LT}}$	Major Poisson's Ratio for a Composite Lamina
$\boldsymbol{\nu}_{\mathbf{TL}}$	Minor Poisson's Ratio for a Composite Lamina
$\boldsymbol{\nu}$	Poisson's Ratio
γ_e	Adhesive elastic shear strain limit
γ_p	Adhesive plastic shear strain limit
$\gamma_{\max}$	Maximum shear strain in the adhesive at failure
γ_f	Adhesive Shear Strain at Fatigue Load Case
$\boldsymbol{\sigma}_0$	Stress in Structure Under Patch Away from Defect at Design Load Case
$\boldsymbol{\sigma}^*$	Remote Stress at Design Load Case
$\boldsymbol{\sigma}^{**}$	Stress at the End of the Repair at Design Load Case
$\boldsymbol{\sigma}_{\mathbf{f}}$	Remote Stress at Fatigue Load Case
$\boldsymbol{\sigma}^{\#}$	Stress in Structure Under Patch Away from Defect at Fatigue Load Case
$\boldsymbol{\sigma}^{\#\#}$	Stress at the End of the Repair at Fatigue Load Case
$\boldsymbol{\sigma}_{\mathbf{c}\max}$	Peel Stress in the Adhesive at Design Load Case
$\boldsymbol{\sigma}_{\mathbf{p}}$	Stress in the Patch at Design Load Case
$\boldsymbol{\sigma}_{\mathbf{p}}^{\#}$	Stress in the Patch at Fatigue Load Case

SYMBOL	DESCRIPTION (continued)
Ω_L	Load Attraction Factor
P	Load capacity of the adhesive in the joint
P'	Load capacity of the adhesive in the joint after application of the Adhesive Variation Factor
R	Load ratio for fatigue assessment, as determined by the ratio of minimum cycle load to the maximum cycle load
ΔT	Temperature range from cure temperature to design case temperature
RT	Room Temperature
λ	Elastic exponent
l_e	Elastic load transfer length for the bond
l_p	Plastic load transfer length for the bond
L	Bond overlap length
$\phi_{\max}$	Maximum tolerable defect size for adhesive

DISTRIBUTION

Frances Abrams
Air Force Research Labs/MLMP
2977 Hobson Way
Bldg 653, Rm 215
Wright-Patterson AFB OH 45433-7739

Paulo Anchieta da Silva
Embraer
Av. Brigadeiro Faria Lima 2.170
12227-901 São José dos Campos, São Paulo
BRAZIL

Ted Barber
New Mexico Dept. of Transportation
Bridge Design Section
1120 Cerrillos Road
P.O. Box 1149
Santa Fe, NM 87504

Harold Brashears
Northrop Grumman Ship Systems
PO Box 149 M/S 7000-02
Pascagoula, MS 39568

DOT/RSPA Volpe National Transportation
Systems Center
Environment, Safety and Health
Attn: Aviva Brecher
55 Broadway, DTS-30
Cambridge, MA 02142-1093

Byron Burns
Director Bridge Engineering
Burlington Northern Santa Fe Railway Co.
4515 Kansas Ave
Kansas City, KS 66106-1199

Sandy Butterfield
National Renewable Energy Labs
1617 Cole Blvd. MS 3811
Golden, CO 80401

Joy Cadnar
Pipeline & Hazardous Mat'ls Safety Admin.
1200 New Jersey Avenue SE
Rm E22-334
Washington, DC 20590

David Carroll
University of Illinois
306 Talbot Lab MC-236
104 S. Wright
Urbana, IL 61801

Fu-Kuo Chang
Stanford University
Dept. of Aeronautics and Astronautics
Durand Building Room 250
Stanford, CA 94305

Federal Highway Administration
Attn:Chien-Tan Chang
MS HRDI-01
6300 Georgetown Pike
McLean, VA 22101

Roger Cheng
Dept. of Civil & Environmental Engineering
220 Civil/Electrical Building
University of Alberta
Edmonton, Alberta, Canada, T6G 2G7

Stefano Chiovelli
Syncrude Canada Ltd.,
9421 - 17th Ave.
Edmonton, Alberta, Canada, T6N 1H4

Mark Cookson
Vestas
1881 SW Naito Parkway Suite 100
Portland, OR 97201

William Cox,
Texas Department of Transportation
Director of Bridge Division
125 E. 11th Street
Austin, TX 78701-2483

Sharon Donohoe
Clipper Windpower, Inc.
6305 Carpinteria Ave., Suite 300
Carpinteria, CA 93013

Ken Erdmann
Matrix Service Co.
1105 West Main Parkway
Catoosa, OK 74015

Victor del Valle
Syncrude Canada Ltd.
P.O. bag 4009, MD 0049
Fort McMurray, Alberta, Canada, T9H 3L1

University of California, Irvine
Henry Samueli School of Engineering
Attn: Maria Feng
Irvine, California 92697-2175

Robert Florom
Transportation Technology Center Inc.
55500 DOT Road
PO Box 11130
Pueblo, CO 81001

Earl Franks
New Mexico Dept. of Transportation
2912 E. Pine Street
Deming, NM 88030

Ian Friedlander
Federal Highway Administration
6300 Georgetown Pike
MS - HRDI-03 Rm F211
McLean, VA 22101

Dave Galella
FAA WJ Hughes Technical Center
AJP-6360
Atlantic City Int'l Airport, NJ 08405

Sara Giunta
Research Associate
UTEK Corporation
2109 Palm Avenue
Tampa, FL 33605

Anindya Ghoshal
R & D Applied Mechanics Group
United Technologies Research Center
411 Silver Lane, MS 129-73
East Hartford, CT 06108

Eric Gleason
Director of Public Transportation Division
Texas Department of Transportation
Director of Bridge Division
125 E. 11th Street
Austin, TX 78701-2483

Robert Hawley
BP Exploration Alaska
Alaska Gas Team
900 E. Benson Blvd
Anchorage, AK 99508

Richard Hill
Universal Technology Corporation
1270 North Fairfield Road
Dayton, OH 45432-2600

Russell Hoffman
Director of Engineering
Bath Iron Works
700 Washington Street
Bath, ME 04530

Michael Hoke
President, Abaris Training Resources Inc.
5401 Longley Lane, Suite 49
Reno, NV 89511

Bill Holley
GE Wind Energy Systems
GTTC, MS 100D
300 Garlington Road, P.O. Box 648
Greenville, SC 29602-0648

Larry Ilcewicz
Chief Scientist and Advisor
FAA NRS Composites
1601 Lund Ave. SW
ANM-115N
Renton, WA 98055

Dan Inman
Virginia Tech
Center for Intel. Material Sys. & Structures
Department of Mechanical Engineering
310 Durham Hall, Mail Code 026
Blacksburg, VA 24061

Firdausi Irani
Transportation Technology Center Inc.
55500 DOT Road
PO Box 11130
Pueblo, CO 81001

Semih Kalay
Transportation Technology Center Inc.
55500 DOT Road
PO Box 11130
Pueblo, CO 81001

Gary Kanaby
Knight & Carver Yacht Center
Wind Blade Division Manager
1313 Bay Marina Drive
National City, CA 91950

David Kelsey
Heatcon
7413 Stuart Circle
Warrenton, VA 20187

Jake Kononov
Colorado Department of Transportation
DTD Applied Research and Innovation Branch
Shumate Bldg, 4201 E Arkansas Ave
Denver, CO 80222

Mark Leonard
Colorado Department of Transportation
4201 E. Arkansas Avenue
Staff Bridge Rm 107
Denver, CO 80222

Lane Miller
Pipeline & Hazardous Mat'ls Safety Admin.
PO Box 25082
Oklahoma City, OK 73125

Richard Miller
Utah DOT
4501 South 2700 West
PO Box 148470
Salt Lake City, UT 84114-8470

Steve Millsap
AVP Structures
Burlington Northern Santa Fe Railway Co.
2600 Lou Menk Dr - NOC 3
Fort Worth, TX 76131-2830

Eric Munley
Federal Highway Administration
6300 Georgetown Pike
MS - HRDI-07
McLean, VA 22101

Gerry Nadler
MachineTalker
230 High Street
Acton, MA 01720

Arizona DOT
Attn: Jean Nehme, P.E.
205 S 17th Ave
MD 269E
Phoenix, AZ 85007

Khaled Obaia
Syncrude Canada Ltd.,
9421 - 17th Ave.
Edmonton, Alberta, Canada, T6N 1H4

Kevin O'Brien
U.S. Army Research Laboratory
Vehicle Technology Directorate
NASA Langley Research Center
Hampton, VA 23681

Ruben Pena
Transportation Technology Center Inc
55500 DOT Road
PO Box 11130
Pueblo, CO 81001

James Pitarresi
Binghamton University
Mechanical Engineering
EB S10
PO Box 6000
Binghamton, NY 13902-6000

Damien Reid
Syncrude Canada Ltd.
P.O. bag 4009, MD 0039
Fort McMurray, Alberta, Canada, T9H 3L1

Jeff Register
Aerotechnics
1475 Skyline Rd.
Eagan, MN 55121

Sheila Rimal Duwadi
Federal Highway Administration
6300 Georgetown Pike
McLean, VA 22101

BAE Systems Norfolk Ship Repair
Attn: Larry Rummell
750 West Berkley Avenue
Norfolk, VA 23523

Radovan Sarunac
Booz-Allen-Hamilton
Columbia Square, Suite 480 East
555 Thirteenth Street, N.W.
Washington, DC 20004

Shell Research Center
Westhollow Technology Center
3333 Highway 6 South
Houston, TX 77082-3101

Department of Civil Engineering
The Catholic University of America
Atttn: Edgar Small
620 Michigan Avenue
Washington, DC 20064

Holger Speckmann
AIRBUS Deutschland GmbH
Dept.: ESWNG / Testing Technology
Germany
Huenefeldstr. 1-5
28199 Bremen, GERMANY

Tom Styrbicki
Minnesota Department of Transportation
Bridge Office
3482 Hadley Avenue North
Oakdale, MN 55128

Research and Innovative Technology
Administration (RITA)
Attn: K. Thirumalai
Nassif Building, Room 7110
400 7th St., SW
Washington, DC 20590

Chris Volle
Caterpillar Inc.
27th and Pershing Road
Bldg. W
Decatur, IL 62526

Eric Wetzel
Army Research Laboratory
AMSRD-ARL-WM-MA, Bldg. 4600
Aberdeen Proving Ground, MD 21005

Scott White
University of Illinois
306 Talbot Laboratory, MC-236
104 South Wright Street
Urbana, Illinois 61801-2935

Matt Witte
Transportation Technology Center Inc.
55500 DOT Road
PO Box 11130
Pueblo, CO 81001

Dingyi Yang
Texas DOT Bridge Division
Construction & Maintenance Branch
125 E. 11th Street
Austin, TX 78701

Sandia National Labs:
MS-0116 Alton Romig, 0004
MS-0724 Les Shephard, 6000
MS-1104 Margie Tatro, 6200
MS-1104 Rush Robinett, 6330
MS-1108 Juan Torres, 6332
MS-1108 Annie McIntyre, 6332
MS-1124 Jose Zayas, 6333
MS-1124 Mark Rumsey, 6333
MS-1124 Paul Veers, 6333
MS-0734 Bernard Zak, 6338 (5)
MS-0769 Dennis Miyoshi, 6400
MS-0762 Brad Parks, 6410
MS-0615 Roger Hartman, 6416
MS-0615 Mike Bode, 6416
MS-0615 Waylon Delong, 6416
MS-0615 Tonimarie Dudley, 6038
MS-0615 Gerry Langwell, 6416
MS-0615 Ciji Nelson, 6416
MS-0615 Kirk Rackow, 6416
MS-0615 Dennis Roach, 6416 (30)
MS-0791 Art Shanks, 6417
MS-0782 William Rhodes, 6418
MS-0762 Rebecca Horton, 6420
MS-0757 John Russell, 6423
MS-0768 Basil Steele, 6430
MS-0762 Joe Roesch, 6450
MS-0768 Tommy Woodall, 6460
MS-1003 Phil Heermann, 6470
MS-0768 Billy Marshall, 6480
MS-0123 Donna Chavez, 1011
MS-0123 Henry Westrich, 1011
MS-0847 Peter Wilson, 1520
MS-0557 Randy Mayes, 1521
MS-0847 Tom Baca 1523
MS-0372 Dan Hammerand 1524
MS-0372 John Pott 1524
MS-0372 Jim Redmond 1525
MS-0557 Tom Carne, 1525
MS-1070 Chungnin Wong 1526
MS-0888 Dave Reedy, 1526
MS-0824 G. Sorensen, 1526 department file
MS-1073 Jon Bryan, 1712
MS-1073 Clint Furrer, 1712
MS-1081 Nate Lowrie, 1726
MS-1082 Kent Schubert, 1723
MS-0887 Duane Dimos, 1800
MS-0889 Mike Hosking, 1813
MS-1411 Erik Spoerke, 1816
MS-0885 Jeff Braithwaite, 1826
MS-0885 Justine Johanes, 1810
MS-1245 John Emerson, 2453
MS-1245 David Zamora, 2453
MS-0507 Jim Woodard, 2600
MS-0968 Dan Schmitt, 2611
MS-1064 Stephen Lott, 2614
MS-1219 Walt Caldwell, 5923
MS-1218 Joe Sanders, 5924
MS-1206 Debra Spencer, 5932
MS-1235 Esteban Yepez, 5932
MS-9409 Chris Moen, 8757
MS-9042 James Foulk 8776
MS-0131 Dick Perry, 12130
MS-0899 Technical Library, 9536
MS-9018 Central Technical Files, 8944